ASME
SETTING THE STANDARD
1880 — 2005

# Journal of Engineering for Gas Turbines and Power

Published Quarterly by ASME

VOLUME 127 • NUMBER 2 • APRIL 2005





(**Contents continued on inside back cover**)

**Transactions of the ASME, Journal of Engineering for Gas Turbines and Power** (ISSN 0742-4795) is published quarterly (Jan., April, July, Oct.) by The American Society of Mechanical Engineers, Three Park Avenue, New York, NY 10016. Periodicals postage paid at New York, NY and additional mailing offices. POSTMASTER: Send address changes to Transactions of the ASME, Journal of Engineering for Gas Turbines and Power, c/o THE AMERICAN SOCIETY OF MECHANICAL ENGINEERS, 22 Law Drive, Box 2300, Fairfield, NJ 07007-2300.
**CHANGES OF ADDRESS** must be received at Society headquarters seven weeks before they are to be effective. Please send old label and new address.
**STATEMENT from By-Laws.** The Society shall not be responsible for statements or opinions advanced in papers or ... printed in its publications (B7.1, par. 3).


This journal is printed on acid-free paper, which exceeds the ANSI Z39.48-1992 specification for permanence of paper and library materials. ♾™
♻ 85% recycled content, including 10% post-consumer fibers.

(**Contents continued**)

**Journal of Engineering for Gas Turbines and Power** **APRIL 2005**

**Volume 127, Number 2**



(**Contents continued on facing page**)

(**Contents continued**)

**Journal of Engineering for Gas Turbines and Power** **APRIL 2005**

**Volume 127, Number 2**

## ANNOUNCEMENTS AND SPECIAL NOTES



The ASME Journal of Engineering for Gas Turbines and Power is abstracted and indexed in the following:

*AESIS (Australia's Geoscience, Minerals, & Petroleum Database), Applied Science & Technology Index, Aquatic Sciences and Fisheries Abstracts, Civil Engineering Abstracts, Compendex (The electronic equivalent of Engineering Index), Computer & Information Systems Abstracts, Corrosion Abstracts, Current Contents, Engineered Materials Abstracts, Engineering Index, Enviroline (The electronic equivalent of Environment Abstracts), Environment Abstracts, Environmental Science and Pollution Management, Fluidex, INSPEC, Mechanical & Transportation Engineering Abstracts, Mechanical Engineering Abstracts, METADEX (The electronic equivalent of Metals Abstracts and Alloys Index), Pollution Abstracts, Referativnyi Zhurnal, Science Citation Index, SciSearch (The electronic equivalent of Science Citation Index), Shock and Vibration Digest*

Journal of Engineering for Gas Turbines and Power

# Editorial

In recognition of the 50th anniversary of the ASME International Gas Turbine Institute's annual gas turbine conference, TURBO EXPO '05, this April 2005 issue of the Journal is devoted to papers from the conference's most recent meetings.

About 65–75 percent of Journal papers come from TURBO EXPO. Since the first IGTI gas turbine conference in 1956, a remarkable total of 12,453 refereed papers have been published in conference proceedings and presented at this one annual meeting. Usually, between 25 and 35 percent of conference papers are judged by reviewers to be archival. Thus, for the last half century, I estimate that about 4000 or so have been published in the Journal, in our companion publication *Journal of Turbomachinery*, or in the predecessor of both, the *Journal of Engineering for Power*.

The IGTI First Annual Gas Turbine Conference and Exhibit was held April 16–18, 1956 at the Hotel Statler in Washington, DC. This very first ASME all-gas turbine meeting had 25 exhibitors, six technical sessions, a total of 17 papers and an attendance of about 750. The conference fee was $5 (with papers) and $2 (without papers). By way of contrast, IGTI's 49th gas turbine conference, TURBO EXPO '04 in Vienna, June 14–17, 2004 had 155 exhibitors, 187 technical paper sessions, a total of 732 papers and an attendance of 2443. (It goes without saying that the Vienna conference fees were substantially higher than those of 1956.)

The IGTI gas turbine conference has been ASME's leading international technical meeting from its very beginning. The annual meeting is held in North America and in Europe on alternate years. Currently, more that half of the papers presented are from non-North American parts of the gas turbine community, most coming from Europe and Asia.

The gas turbine is the ''youngest'' of energy converters. The first jet engine-powered flight took place in Germany and the first operation of a gas turbine to generate electrical power occurred in Switzerland, both in 1939. Within five years of this ''birth,'' the organization of IGTI—and of the gas turbine conference—commenced. Here are a few milestones, facts and dates that led to TURBO EXPO:

- On May 8–10, 1944, ASME's 17th National Oil and Gas Power Conference was held mid-continent (wartime) at the Mayo Hotel in Tulsa, OK. The technical program consisted of four sessions (a total of ten technical papers); three on diesel engine technology and one (two papers) on the newly emerging gas turbine. As *Mechanical Engineering* magazine reported: ''Demonstrating the technical interest aroused by the gas turbine, first new prime mover in 50 years, a capacity crowd of approximately 250 attended the first technical session which was devoted to that subject.'' In anticipation of this intense interest in new gas turbine technology, on May 7, 1944, the Executive Committee of the Oil and Gas Power Division voted to form a ten member Gas Turbine Coordinating Committee (GTCC) to provide '' . . . coordination and dissemination of new technical information on the gas turbine through periodic meetings and the presentation of technical papers.'' This newly formed GTCC, with R. Tom Sawyer of the American Locomotive Company as its chairman, was the start of IGTI.
- By March 1947, GTCC had grown to 31 members and had sponsored an increasing number of gas turbine papers at ASME conferences. With its growing membership, the GTCC petitioned ASME for division status, and this was granted on August 14, 1947. Thus the Gas Turbine Power Division was formed, later to be called simply, the Gas Turbine Division (GTD). As the prime organizer (and by then author of the text, *The Modern Gas Turbine*), R. Tom Sawyer was the first chairman, serving for the remainder of 1947.
- The new GTD started in 1948 with three technical committees: Committee on Theory, Committee on Design, and Committee on Application. Over the last 57 years, these three grew into the 17 technical committees which form the backbone of IGTI today.
- As the international gas turbine community grew, the number of papers sponsored by the GTD increased to the point that it was obvious a separate meeting was needed. The first one was held in Washington, DC, in 1956 as mentioned above, with succeeding annual meetings taking place in other US cities. In 1966 Zurich was chosen as the first European site for the gas turbine conference. Not long after, the annual meeting developed into its present schedule of locating in North America and Europe in alternate years.
- As the GTD conferences increased in size in the years after 1956, it became more and more apparent that a separate ASME staff was needed to take over the administration and operation of the Division. In 1978, Donald D. Hill became Director of Operations for the GTD and set up his office in Atlanta, with Sue Collins as his assistant. In 1982, additional staff was hired to take over direct management of the exposition.
- By 1986, the Gas Turbine Division outgrew its divisional status and was made an institute of ASME—the International Gas Turbine Institute—as we know it today. In 1988 the annual gas turbine conference was

renamed TURBO EXPO. Projects and services developed, produced and financed by IGTI have increased, and the professional staff now numbers eight. The Atlanta office is IGTI's headquarters and the hub of its international activity.

This Journal started 125 years ago as a collection of papers on energy conversion technology in the 1880 first volume of the Transactions of the ASME. For the last 50 years, IGTI's annual gas turbine conference has been a major contributor to the Journal. We salute the authors, reviewers, and organizers of TURBO EXPO, as they prepare to present papers and celebrate the 50th gas turbine conference in Reno, Nevada on June 6–9, 2005.

**Lee S. Langston**
**Editor**

# Dr. Max Bentele—Pioneer of the Jet Age

**Cyrus B. Meher-Homji**
Principal Engineer,
Turbomachinery Group,
Bechtel Corporation,
3000 Post Oak Boulevard,
Houston, TX 77056-6503
Fellow ASME

**Erik Prisell**
Chief Engineer,
Defense Materiel Administration (FMV),
Sweden

*This paper documents the pioneering work of Dr. Max Bentele during his long and distinguished career in Germany, the UK, and the United States. His early work on turbojets at the Heinkel-Hirth Corporation in conjunction with his life-long friend, Dr. Hans von Ohain, culminated in the development of the advanced HeS 011 turbojet. Dr. Bentele's pioneering work in the area of blade vibration is documented along with details of his spectacular solution of the turbine blade vibration problem of the Junkers 004B engine which propelled the world's first operational jet fighter—the Me-262. Also covered are his pioneering contributions to turbine blade cooling and blade manufacturing and his important work at Curtiss—Wright and Avco Lycoming prior to his retirement.*
[DOI: 10.1115/1.1807412]

## 1 Introduction

Max Bentele was born on January 15, 1909 in Ulm Germany, graduating from high school in 1927. A visit to the Deutsches Museum in Munich influenced him to study engineering. After his graduation from school, he worked as an apprentice at a ball bearing manufacturer. He enrolled at the Technical University of Stuttgart in the Fall of 1928, to work toward a degree in mechanical and electrical engineering. He obtained his undergraduate degree in 1932 and having completed a thesis on ''Sound dampers for pipelines,'' was awarded a Doctorate in Engineering in 1937. This thesis[1] laid the foundation for his future work in vibrations and dynamics, an area in which he would gain an international reputation. In May 1938 he joined Brandenburgische Motorenwerke (Bramo) in Berlin Spandau, and in late 1938, he joined Hirth-Motoren located in Stuttgart-Zuffenhausen.

## 2 Early Work on Turbosuperchargers at Hirth

Upon joining the applied research department at Hirth Motoren, Dr. Bentele was tasked with the improvement of the specific power, frontal area, and weight of existing Hirth engines. He was appointed Director of the Applied Research Department and worked on the advancement of aeroengine turbocharger design, to facilitate mass production. At that time, Hirth-Motoren was investigating turbocharger technology and had obtained a manufacturing license from DVL (Deutsche Versuchsanstalt für Luftfahrt[2]).

The turbocharger featured a two-stage centrifugal compressor and a single-stage axial flow turbine connected to the compressor by a quill shaft. As the turbine section blading had to withstand temperatures of 1000°C (1832°F) and as no alloys were available to withstand this temperature, air-cooling had to be utilized. The DVL designs featured a solid blade axial turbine with partial admission utilizing one sector for the hot exhaust and one sector for cooling air.

In the summer of 1942, a twin-engine Heinkel He 111, equipped with Junkers V12 Jumo 211 engines utilizing DVL/Hirth turbochargers experienced a turbocharger blade fracture in two turbine blades. A rash of similar failures resulted in a major investigation. DVL, which was the licensor of the turbocharger, stated that they had never experienced any test failures during their test and development programs and felt that the failures were due to problems with the manufacturing processes, material grain size, surface finish, and general machining tolerances. The management at Hirth desperately searched for a way out of this dilemma, even offering a financial award to anyone who could resolve this problem. Dr. Bentele immersed himself in the resolution of this problem.

The DVL/Hirth turbochargers were built in two models with different gas-to-air partial admission ratios of 50/50 and 60/40. The pressure of the exhaust gas before the turbine was much higher than the cooling air. Dr. Bentele intuitively felt that the sudden and alternating changes would induce periodic blade excitation, which under resonance conditions would lead to high vibratory stresses. He hypothesized that these, in combination with the gas and centrifugal stresses, would lead to fatigue cracks. Dr. Bentele embarked on an experimental/analytical program to confirm his hypothesis.

The turbine rotor blade attachment was a fairly rigid fir tree. By striking the blade airfoil, a distinct sound could be obtained. As no frequency analyzer was available, musicians in Dr. Bentele's group were enlisted to help. By stroking the airfoil tip and trailing edge with a violin bow,[3] the bending and tortional mode natural frequencies tones were generated. A piano was then used to match the frequencies. The fundamental bending frequencies of the turbocharger blades were approximately 2000 Hz. Dr. Bentele approximated the frequency changes under operating conditions due to centrifugal stiffening, tightening of the root attachment, and the high operating temperature. He conducted a Fourier analysis to determine the individual harmonics, their orders and their amplitudes. He found that for the 50/50 admission ratio, only odd numbered harmonics occurred, their amplitudes diminishing with their order number. Similar overall declines existed with the 60/40 admission. To determine resonance conditions, Dr. Bentele constructed a frequency-speed diagram, as shown in Fig. 1 (Bentele [1]). It showed that for turbochargers operating with 60/40 admission, the sixth and higher orders were in the operating speed range. For the 50/50 turbocharger design, the fifth order was above the maximum operating speed of 20,000 rpm, and the seventh and higher orders were within. To further corroborate this theory, Dr. Bentele calculated the approximate danger levels of the critical frequencies from the turbine power, gas, and centrifugal force on the blade and the exciting forces based on the Fourier analysis results.

The conditions for the 60/40 turbocharger design is shown in Fig. 2. As can be seen in this figure, the sixth harmonic is more

[1]His thesis was published by VDI as a book.

[2]This was a governmental body similar to NACA in the USA or the RAE in the UK.

Contributed by the International Gas Turbine Institute (IGTI) of THE AMERICAN SOCIETY OF MECHANICAL ENGINEERS for publication in the ASME JOURNAL OF ENGINEERING FOR GAS TURBINES AND POWER. Paper presented at the International Gas Turbine and Aeroengine Congress and Exhibition, Atlanta, GA, June 16–19, 2003, Paper No. 2003-GT-38760. Manuscript received by IGTI, October 2002, final revision, March 2003. Associate Editor: H. R. Simmons.

[3]Stroking the blade tip gave the bending natural frequency. The torsional natural frequency was obtained by stroking the blade tip. This was the first time this technique was employed.

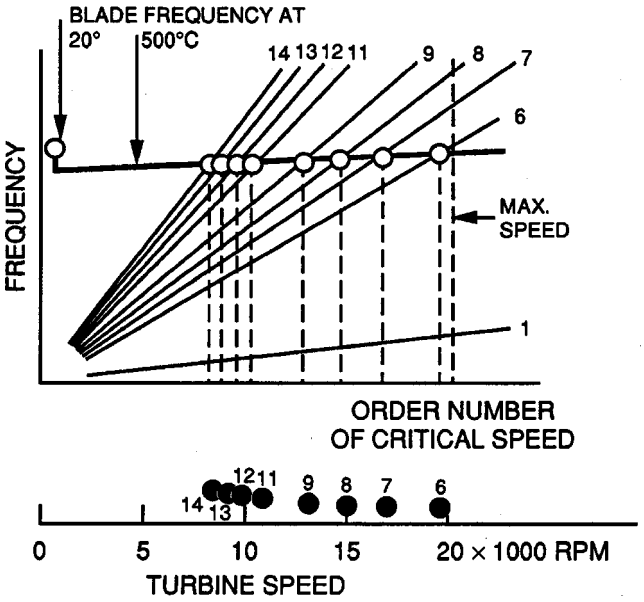


**Fig. 1 Frequency-speed diagram developed by Dr. Bentele for 60/40 admission turbocharger (1942)**

than twice as dangerous as the higher ones due to the higher gas, centrifugal and exciting forces. As the sixth harmonic was near the maximum speed, it could easily be increased by raising the blade natural frequency by shortening the airfoil and increasing its taper. For the 50/50 turbocharger, the seventh harmonic was the most dangerous and occurred for an extended duration during the aircraft climb. As the turbocharger speed could not be avoided, this model was discontinued on Dr. Bentele's recommendation. Dr. Bentele was now able to explain the observed blade losses from the flight times spent in climb and cruise. The results of this elegant analysis established Dr. Bentele as an expert in blade vibrations at Hirth Moteren. DVL, however, still felt that the underlying cause for the failures was manufacturing differences at Hirth, as compared to the turbochargers built at DVL. Dr. Bentele, therefore, requested DVL to provide him with one of their manufactured turbines. Upon receipt of the turbine, the natural blade frequencies were determined and it was recognized that a dangerous seventh-order excitation would occur between 17,500 and 18,400 rpm. The DVL-manufactured turbocharger was installed on a test stand and was vigorously tested resulting in a blade failure, as predicted by Dr. Bentele's theory. The turbine wheel

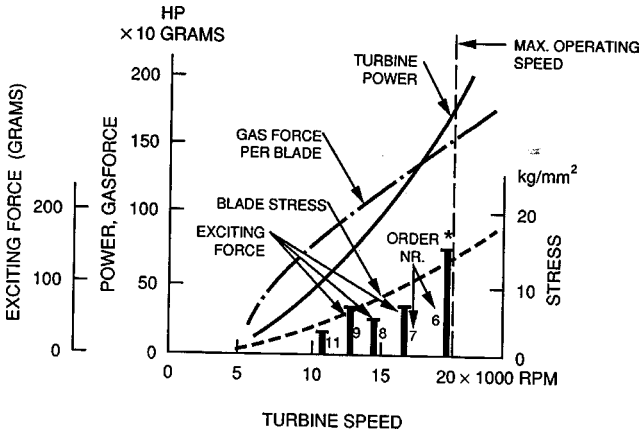


**Fig. 2 Danger level of excitation for different orders (60/40 admission turbine)**

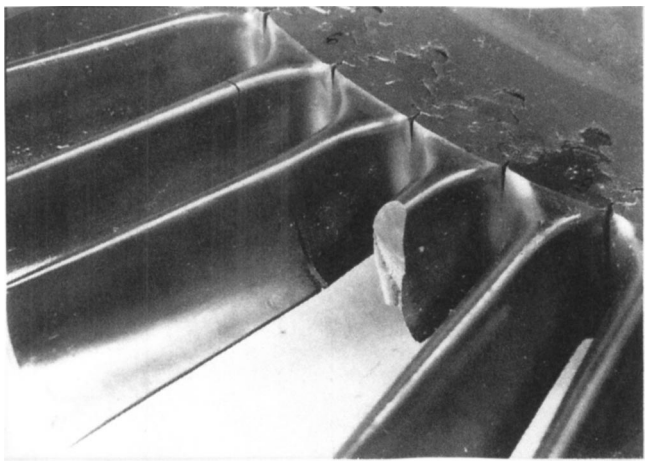

**Fig. 3 Cracked turbocharger blade**

and broken blade is shown in Fig. 3. Vibrations had caused a fatigue crack halfway across the airfoil. The fatigued blade showed classic crack growth, followed by an overload failure. Based on this dramatic demonstration, Dr. Bentele's theory was fully accepted and his recommendations put into effect. This work resulted in Dr. Bentele being established as one of the leading experts in the area of blade vibrations, which would later be confirmed when he resolved blade vibration problems with the Junker Jumo 004 engine. It is also worthwhile noting that his development of a Bentele diagram was made without his knowledge of Campbell's classic work done in 1924 investigating steam turbine disk vibration.[4] Bentele's approach as shown in Fig. 2, however, was unique in that it presented a visualization of the blade vibration danger levels.

## 3 Work Related to Turbine Cooling

Recognizing the inherent problems with partial admission as a means for blade cooling, Dr. Bentele's team investigated several forms of internal blade cooling of the blade and root, studying heat transfer, mechanical design, and manufacturing aspects. Initial efforts were concentrated on hollow convectively cooled turbine blades. While others (mainly the DVL) had experimented with air-cooled blades, Dr. Bentele was able to blend theory and practice and incorporate practical lessons learned to develop workable blading. One of his inventions was the Faltschaufel[5] (folded blade) shown in Fig. 4 that could be mass-produced at an exceedingly low cost.[6]

## 4 German Jet Engine Developments

Turbojet development in Germany initially included two independent programs that were not, at least initially, under the auspices of the German Air Ministry known as the Riechluftfahrtministerium (RLM). As is typical of revolutionary technological changes, these two programs did not initiate at the traditional aeroengine companies but started at Heinkel Airframe and at Junkers Airframe Company. Ultimately, both these programs ended up under Heinkel, however, Heinkel could not capitalize on his position as a jet age pioneer. So great was his disappointment that in his autobiography entitled ''Stormy Life- Memoirs of a Pioneer of the Air Age'' published in 1956, no mention is made of

[4]Wilfred Campbell of the General Electric Company had presented a detailed ASME paper in 1924 entitled ''The Protection of Steam-Turbine Disk Wheels from Axial Vibration.''

[5]A modification of this concept was finally used successfully in turbochargers and finally in the Heinkel-Hirth HeS011 turbojet, and was known as the Topfschaufel (tubular or bootstrap blade). Dr. Bentele is named as a coinventer on the patent.

[6]One manufacturer claimed to manufacture a blade at a rate of 1 Mark and still make a profit.

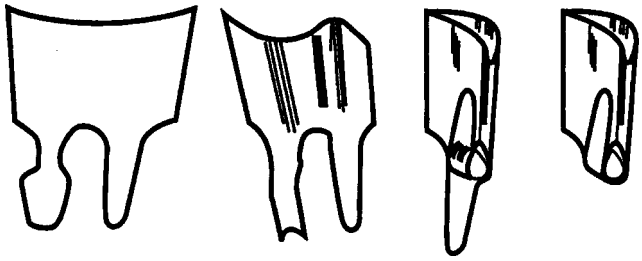

**Fig. 4 Folded turbine blade developed by Dr. Bentele. (Bentele, [1]). The folding process is shown here. Two reinforcement strips increased the blade strength. The inside strip also provided proper distribution of cooling air. Blades would be pinned to the disk with an axial pin.**

any Heinkel-Hirth turbojet development team member's names. Details regarding the overall development of the German jet program and in particular the pioneering work of Dr. Hans von Ohain may be found in Meher-Homji and Prisell [2]. Further details on the history of turbojet development may be found in Constant [3] and Meher-Homji [4,5].

**4.1 Turbojet Engine Development Work at Heinkel.** von Ohain developed the idea of his jet engine while he was a doctoral student at the University of Göttingen. The 24 year old von Ohain was hired by Heinkel and soon headed Heinkel's jet engine development work. Dr. Hans von Ohain received a permanent contract and was named head of Heinkel jet propulsion development after the successful run of his hydrogen demonstrator engine (the HeS 1). After this successful engine run, Heinkel pushed hard for a flight engine and this resulted in the HeS 3B designed by von Ohain. On August 27, 1939, a He 178 piloted by Erich Warsitz made a historic 6 min flight from the Heinkel airfield in Marienehe. This was the first aircraft in the world to fly utilizing a turbojet. Heinkel rushed to inform the RLM of this achievement, but met with indifference as the RLM had more immediate problems of gearing up for the war that was to start within a few days. Later, Heinkel arranged for a demonstration of the He 178 that was observed by the German Air Ministry, but there was little enthusiasm displayed by the Air Ministry representatives.

**4.2 HeS 8A Engine Development for the He 280 Jet Fighter and the Purchase of Hirth Corporation by Heinkel.** Shortly after the demonstration of the He 178 to the RLM, Heinkel started development of a twin engine fighter that was designated the He 280. The aircraft could not use engines of the HeS 3B type because of the large engine diameter and low performance. At this time, however, an axial flow engine (designated the HeS 30) that was being developed by Mueller, who had arrived at the Heinkel Rostock plant, experienced serious development problems. Recognizing that this engine would not be ready in time, von Ohain designed a back-up solution designated the HeS 8 which would employ a radial rotor similar to the HeS 3B combined with an axial vane diffuser and a straight through flow combustor. Only 14 months were available for this development, as the He 280 airframe was developed much faster than its engines. The engine program was done under a RLM contract with the engine getting the first RLM turbojet designation (109-001). Development was not without risks because the specification of the aircraft limited the engine diameter making the axial diffuser function and efficiency together with the straight through combustor very critical. Luckily for Heinkel, von Ohain's HeS 8 engine managed to meet the minimum requirements and was ready in time for the first flight of the He 280 which took place in late March 1941. After the demonstration flight of the He 280, Heinkel finally received permission to purchase Hirth Motoren located at Zuffenhausen near Stuttgart.[7] With the acquisition of Hirth, Heinkel had access to the engineering capabilities and manufacturing know-how of this well-known engine company. The formal name of the company created when Heinkel took over Hirth Motoren was Ernst Heinkel AG-Werk Hirth Motoren (known as Heinkel-Hirth for short). It is interesting to note that when asked during a conference in 1978 [6] what single item von Ohain needed the most during his early development days, he stated that the greatest need was for expertise in the area of blade vibration which, he said, he got from the Hirth Company in the form of Dr. Bentele who was, by then, recognized as the leading expert in Germany specializing in aeromechanics and blade vibration. The close friendship between Dr. von Ohain and Dr. Bentele endured for 57 years right through the passing away of Dr. von Ohain in 1998.

**Table 1 Comparison between the Junkers Jumo 004B and the Heinkel Hirth HeS 011 engines**

| Parameter | Jumo 004 B | HeS-011A |
|---|---|---|
| Manufacturer | Junkers Engine | Heinkel-Hirth |
| Thrust (lbs) | 2000 (8.927 kN) | 2863 (12.75 kN) |
| Weight (lbs) | 1650 (750 kg) | 1950 (885 kg) |
| T/W ratio | 1.21 | 1.44 |
| Length | 152-in. (3860 mm) | 131.6-in. (3343 mm) |
| Frontal diam | 30 in. (760 mm) | 32 in. (805 mm) |
| Air mass flow rate (lb/s) | 46.7 (21.2 kg/s) | 64 (29 kg/s) |
| Pressure ratio | 3.1:1 | 4.2:1 |
| rpm | 8700 | 10,205 |
| Compressor configuration | Eight-stage axial flow | Diagonal stage+three axial stages |
| Turbine configuration | One-stage turbine | Two-stage air cooled |
| Fuel consumption (lb/lb thrust) | 1.4–1.48 | 1.35 |
| Turbine inlet temperature(F) | 1427°F (775°C) | 1427°F (775°C) |

## 5 Design and Development of the Advanced Heinkel-Hirth HeS 011 Turbojet

In 1942 the RLM granted Heinkel-Hirth the contract for a second-generation engine known as the HeS 011 (RLM designation 109-011), which provided a quantum step in specific power and performance. The specifications of this engine were a maximum thrust of 2863 lbs (12.75 kN) with a growth to 3307 lbs (14.7 kN), a weight under 1985 lbs (900 kg), a pressure ratio of 4.2:1, an altitude capability 50,000 ft (15 km), and a specific fuel consumption of less than 1.4 lb/lb-h.

Dr. von Ohain was in charge of the development and Dr. Max Bentele was responsible for component development and managed the development on the compressor and turbine sections of the engine. The best performance parameters attained by the engine in December 1944 were a thrust of 2940 lb (13 kN) at a rotor speed of 10,205 rpm. The leading particulars of the first generation Jumo 004B engine which was in production and the advanced HeS 011 are compared in Table 1. The engine layout is depicted in Fig. 5 (Neville and Silsbee, [7]). Additional details on the engine may be found in Bentele [8], Hirth-Moteren reports [9,10], Aviation Magazine [11], US Navy report [12], Bamford and Robinson [13], and Carter [14].

**5.1 Compressor Section.** The compressor had a single stage inducer row followed by a diagonal compressor[8] (mixed flow) stage and then three symmetric (50% reaction) axial flow compressor stages. As the air exited the first axial inducer stage,

[7]This acquisition was fraught with politics, with Heinkel's rival Messerschmitt reportedly delaying the acquisition for several months.

[8]This was called "Kombinationsverdichter," a layout conceived by Dr. von Ohain.

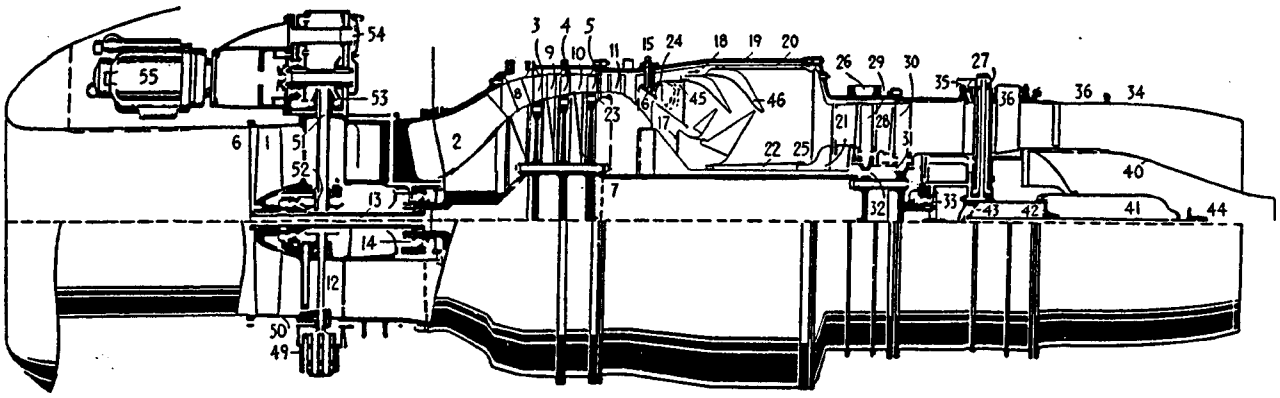


**Fig. 5 Layout of the HeS 011 engine**

the annular passage was reduced by a shaft fairing to the diagonal compressor. The combination of a diagonal stage with axial flow stages was ingenious as it made the operating line very flat and imparted growth potential without incorporating variable geometry that would be required for higher pressure ratios. The double-skinned intake hoods served the dual function of straightening the airflow and housing the accessories, oil tank, and lube oil pump. Both warm air and electric heating were available for anti-icing. A photograph of the compressor section showing the mixed flow stage is shown in Fig. 6.

To develop this compressor, a 1600 kW electric test stand in Zuffenhausen and a steam turbine driven 15,000 hp stand in Dresden were utilized. The rigs allowed the measurement of flow, pressure, and temperature distributions in the flow path and considerable challenges had to be met in designing the mixed flow compressor section. Rather than arriving at an optimal configuration for the axial stages analytically, this was done experimentally using adjustable stators. A variety of settings were tested on the stand and finally this led to satisfactory performance as shown in the compressor map of Fig. 7 (Bentele, [1]). About half of the total pressure ratio of 4.2 was derived by the mixed-flow section (but with moderate efficiency). The axial stages raised the efficiency of the full compressor to 82%. Bentele recounts that during one test, in spite of smooth running of the engine, the occurrence of discrepancies in pressure and temperature readings puzzled the test team. The issue was resolved when a technician appeared holding some broken aluminum blades which he had found at the compressor air exit and inquired if this might be the problem! Evidently, the uniform breakage of the blades did not result in significant unbalance.

**5.2 Combustor.** The combustor was an annular design with airflow being divided into two flow streams by an annular headpiece with a small airflow being routed into the headpiece for mixture preparation and combustion. Most of the air was routed through two of the outer and inner rows of vanes at the end of the combustion chamber and into the mixing chamber to attain the required temperature. The housing wall located around the combustor was protected against radiant heat transfer by an annular insulator around which fresh air from the chamber was circulated. Sixteen equispaced fuel nozzles were utilized with four igniter plugs, two on the lateral axis and two 45° upwards. Bentele indicated that the combustor was a great design challenge and obtaining a satisfactory radial and circumferential temperature profile was not easy given the flow profile emanating from the mixed flow compressor wheel. The combustor was, therefore, a workable design compromise. Dr. Bentele indicated that the combustor was one of his most frustrating assignments—he had reservations

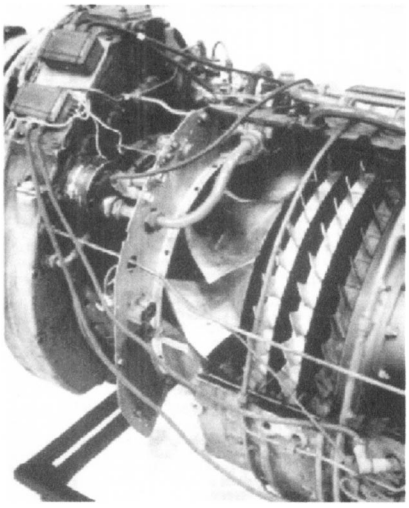

**Fig. 6 Compressor section of the HeS 011**

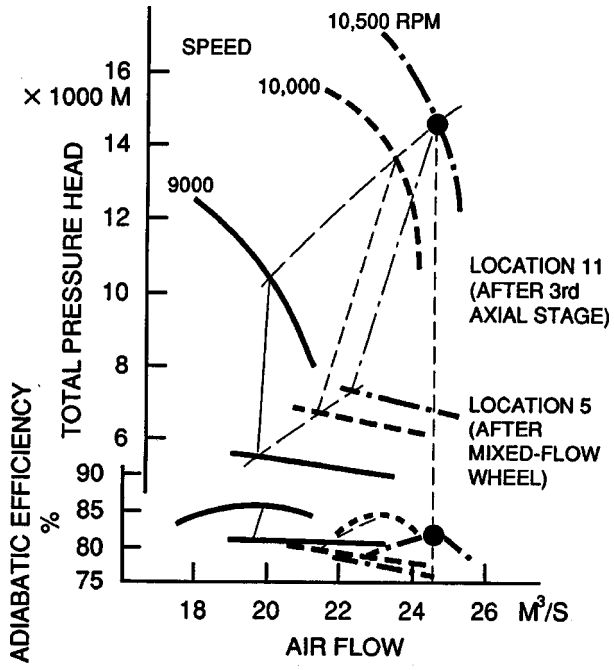


**Fig. 7 HeS 011 compressor map (Bentele, [1])**

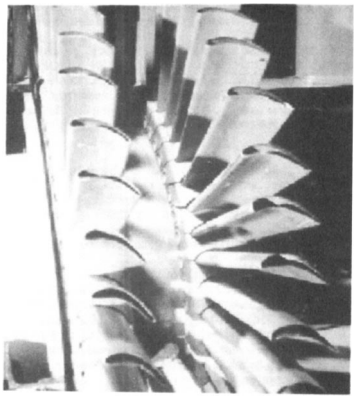

**Fig. 8 Photo of the HeS 011 two-stage air-cooled turbine section**

about too much sheet metal being present in the primary and mixing zones and concerns that small sector testing of an annular combustor would induce false results.[9]

**5.3 Turbine Section.** The HeS 011 had a remarkable two-stage air-cooled turbine section (Fig. 8) designed by Dr. Max Bentele. Two rows of hollow turbine nozzle blades were cooled by air bled off through the annulus after the final compressor stage. This nozzle cooling air was ducted between the combustion chamber and the rotor shaft, which was shielded by an annular insert. Both of the discs had hollow vanes with air being routed to the second stage through holes bored in the first stage. The airflow exited the blades at the tip. The development of the turbine section was most challenging. Initially solid blades were employed and stress rupture occurred at the first stage and fatigue failures at the second stage. The resonance failure was traced to the location of four struts of the rear bearing support and these were eliminated by spacing the struts at unequal angles, thus minimizing the forced excitations that were in resonance with the second-stage rotor blades. A Bentele Diagram of the blading is depicted in Fig. 9. (Hirth-Motoren report, January 1944 [9]).

The final air-cooled blade designed by Dr. Bentele was called ''topfschaufel''[10] and did not utilize any strategic materials. These blades were manufactured starting with a circular plate of austenetic chrome-moly sheet steel from which a closed end tube was drawn in several stages with intermediate heat treatments. As seen in Fig. 10 (Hirth-Motoren Report, April 1944 [10]), wall thickness diminished from 0.079 in. (2 mm) at the root to 0.017 in. (0.45 mm) at the blade tip, so as to match the stresses with the prevailing radial temperature profile. The airfoil shape was then induced and finish machining done. Both the first and second turbine stages utilized this construction and contained an insert for the proper distribution of the cooling air and for damping blade vibration. Further details of the HeS 011's construction, accessories, fuels systems, and controls may be found in Meher-Homji and Prisell [2].

## 6 Planned Variants and Potential Applications of the HeS 011 Engine

On July 15, 1944, the RLM submitted request for proposal number 226/II (known as the ''Emergency Fighter Competition'') to Germany's aircraft manufacturers for the second-generation of jet-powered fighters. The requirements included that this aircraft be powered by a single Heinkel-Hirth HeS 011 turbojet, operate at a level speed of 1000 km/h (621 mph) at 7000 m (22,966 ft) and be armed by four MK 108, 30 mm cannon. The fighter had to have an operating altitude of 14,000 m (45,931 ft), and have a pressurized cockpit. There were several proposals submitted by Focke Wulf, Messerschnmitt, Heinkel and Blohm and Voss, with the Focke Wulf Ta-183 being finally selected. The Ta-183 design concept is shown in Fig. 11. This design was never built in Germany as the war ended prior to its development.

## 7 Resolution of Vibratory Blade Failures on the Junker Jumo 004 B Turbojet

The world's first production turbojet was the Junkers Jumo 004, which was the powerplant for the Messerschmitt Me-262 fighter (Fig. 12). The engine was developed by Dr. Anselm Franz and his design team at Junkers. The Jumo was brought from conceptual design to production in a span of four years. Details of this engine may be found in Meher-Homji [5] and Franz [15]. As Franz had no opportunity to design individual engine components a decision was made to design an experimental engine, the 004A, which would be thermodynamically and aerodynamically similar to the final production engine. The goal in developing the 004A was to have an operating engine in the shortest time frame without consideration for engine weight, manufacturing considerations, or minimizing the use of strategic materials. Based on the results of the 004A engine, the production 004B engine was to be built. On July 18, 1942 the first flight of the Me-262 powered by two Jumo 004A jets took place and lasted for 12 min.

The Jumo 004B engine was available in June 1943 and during the summer, several catastrophic turbine blade failures that resulted in aircraft crashes were experienced when operating at full speed. The Junkers team worked diligently to resolve the problem. The Air Ministry, getting increasingly concerned with the problem, scheduled a conference at the Junkers Dessau plant in December 1943, to be attended by turbine experts from government, industry, and academia. Max Bentele was asked by the ministry to attend this conference.[11] Dr. Bentele listened to the numerous arguments pertaining to material defects, grain size, and manufacturing tolerances. When his turn came, he stated that the underlying cause of the problem was excitation induced by the six combustor cans and the three struts of the jet nozzle housing after the turbine. The combustor and struts excited a sixth-order resonance with the blade bending frequency in the upper speed range. The predominance of the sixth-order excitation was due to the six combustor cans (undisturbed by the 36 nozzles) and the second harmonic of the three struts downstream of the rotor. In the 004A engine, this resonance was above the operating speed range but in the 004B it had slipped because of the slightly higher turbine speed and due to the higher turbine temperatures. Dr. Bentele's elegant analysis allowed the problem to be solved by increasing the blade natural frequency by increasing blade taper, shortening blades by 1 mm, and reducing the operating speed of the engine from 9000 to 8700 rpm. Dr. Bentele's resolution of this problem had a major impact on the operational availability of the Me-262.

## 8 Blade Design Recommendations on the BMW 003 Turbojet

BMW also produced an axial flow turbojet engine (BMW 003) with a thrust of 2,000 lbs (907 kg). The engine had a seven-stage axial compressor with a pressure ratio of 3:1, an annular combustor, and an air cooled turbine that had a very unusual disk attachment as shown in Fig. 13. This attachment was plagued by failures and Dr. Bentele was consulted to resolve the problem. Dr. Bentele found the design overly complex, with the wedge and pin being unnecessary because the centrifugal forces would have held the blade in place. He made several suggestions that allowed trouble-free operation.

[9]When engine runs confirmed this opinion, the combustor was given several nicknames—''Guinea pig,'' ''rat's tail'' and worse! The time was not ripe for an annular combustor of short length, low pressure drop, and high efficiency.

[10]This was a scaled derivitave of the ''topfschaufel'' invented by Dr. Bentele for turbocharger turbines.

[11]At 34 years of age, Dr. Bentele was the youngest person to speak up.

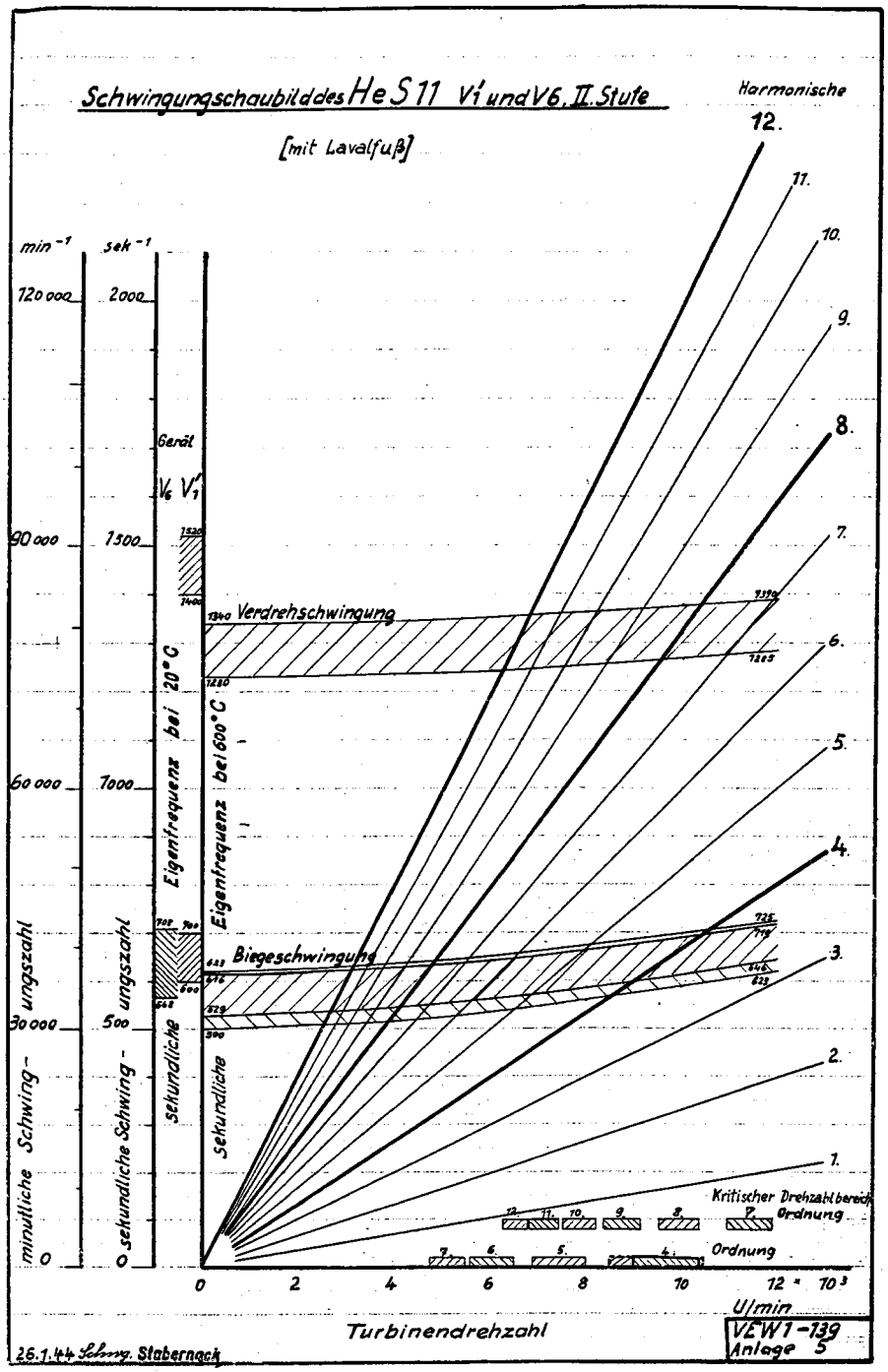


**Fig. 9 "Bentele diagram" showing excitation and natural frequencies (Hirth-Motoren Report, January 1944 [9])**

## 9 Post-War Contributions in Germany and the UK

After the termination of hostilities in Europe, Dr. Bentele met with technical teams put together by the allies who were impressed by the advanced HeS 011 engine. The US Navy decided to build and test these engines. Dr. Bentele interacted with engineers from the Whittle team including R. G. Voysey, and his pioneering work on blading vibration was reviewed with great interest. He also promoted the concept of turbine blade air-cooling but this was not followed up by the allies,[12] who believed that cooling was not needed due to the superior high temperature alloys that they had available.

Dr. Bentele then met Dr. A. T. Bowden of C. A. Parsons of the UK who was interested in automotive applications of the gas turbine. Dr. Bentele was invited to present a monograph to the AVA

[12]It took approximately 10 years before air-cooling was considered in the US and the UK.

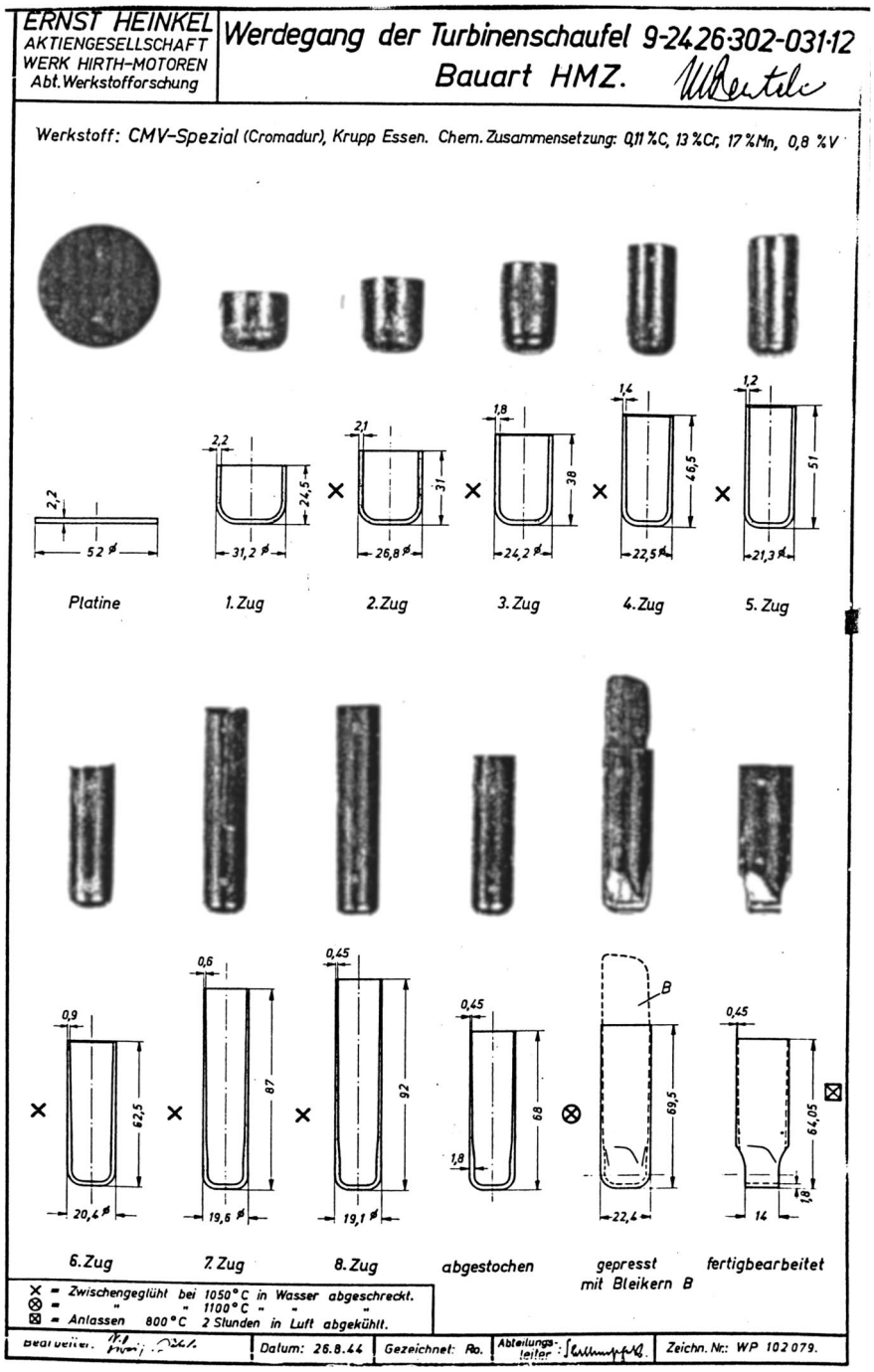


**Fig. 10 Ingenious method of developing air-cooled turbine blade starting with a circular plate 25 mm diameter (Hirth Motoren GmbH report, April 1944 [10])**

on the feasibility of the gas turbine as a vehicle power plant. This monograph covered several investigations of compressor configurations, regenerators, and other practical aspects and included a treatment of regeneration, water injection, ceramic materials, and the concept of a vehicular gas turbine. Because of his contributions to this and other studies, Dr. Bentele was offered a contract from the British Ministry of Supply (MoS) to work on a gas turbine tank engine project that was being developed at Parsons. He contributed significantly to the mechanical design of the engine and in resolving several problems. Dr. Bentele's contributions included the design of a mechanical control system and thermal shock investigations. Because of the special transient operating regime of a tank engine, Dr. Bentele started a systematic

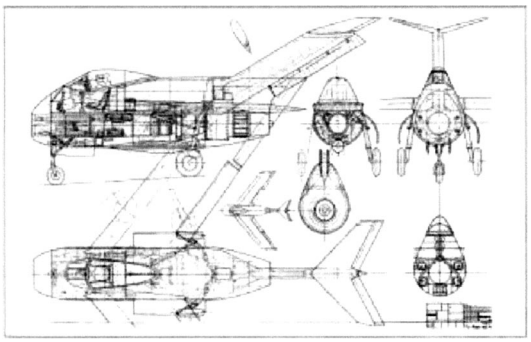

**Fig. 11 Focke Wulf TA-183 with HeS 011 engine**

**Fig. 12 The Me-262 powered by two Junker Jumo 004B turbojets. Dr. Bentele was instrumental in resolving a major operational blade vibration problem with this engine.**

investigation into the thermal shock aspects of turbine blading. The study included an analysis of thermal stresses in a slab for static conditions of constant heat flow and constant temperature difference. Four different materials were considered. Thereafter, transient conditions were modeled where the surface temperatures were suddenly changed. The resulting calculations and models were then extended to shapes approaching those of turbine blades to arrive at a qualitative relationship for the number of thermal cycles to failure. Dr. Bentele and his group verified his thermal shock investigations in test rigs with actual turbine nozzles of their tank engine. The test rigs developed allowed testing to examine the cyclic thermal behavior of blading and combustor walls. A detailed paper was published by Dr. Bentle and Mr. Lowthian [16] which appeared in the February 1952 issue of ''Aircraft Engineer.'' This paper drew an important analogy between thermal shock and vibration phenomena in showing that surface condition, heat treatment, ageing, and varying the amplitude of the applied load had similar effects.

## 10 Work at Heinkel-Hirth (1952–1956)

After his stay in the UK, Max Bentele was persuaded by Ernest Heinkel to rejoin Heinkel at the Stuttgart plant, as Chief of Development. He joined Heinkel in 1952 and Ernst Heinkel relied on his expertise in managing a variety of technical and business issues. Dr. Bentele worked on a range of development initiatives on reciprocating engines and motor scooters that Heinkel was making. Heinkel's heart was, however, set on aviation and he tried to build a team to work on engines. On Heinkel's request, Dr. Bentele served as a consultant to a project involving a gas turbine utilizing thermal compression.[13] Heinkel's most ambitious project was the design of a jet fighter and its engine. The engine was designated as the HeS 053 and borrowed features from the HeS011, and SNECMA's Atar engines. Ultimately the engine and fighter projects were cancelled. In 1955 Curtiss Wright offered Dr. Bentele a job and Dr Bentele emigrated to the USA in 1956 where he joined the Wright Aeronautical Division (WAD) of Curtiss-Wright.

[13]This concept was originally conceived by Dr. Hans von Ohain and had been investigated theoretically and experimentally at Heinkel. The post-war project was run by Max Adolf Müller.

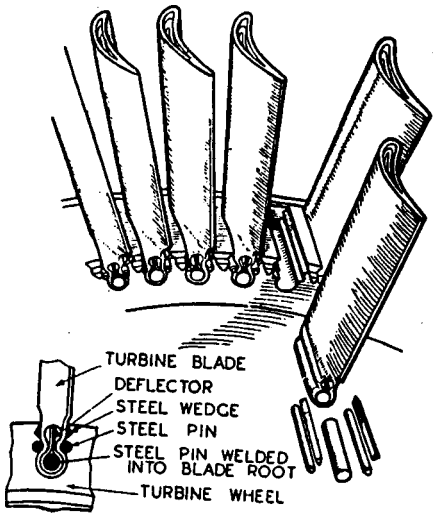


**Fig. 13 Complex blade root design for the BMW 003 engine that resulted in fatigue cracks and failures**

## 11 Contributions at Curtiss-Wright

At Curtiss-Wright Dr. Bentele worked on several projects including detailed studies on turbine blade cooling and transpiration cooling. Several experimental results were developed on a test rig enabling Curtiss-Wright to replace the two-stage turbine design for the J65 engine with a single stage air-cooled design. This development was, however, too late to be put into production. Dr. Bentele was appointed Manager of Mechanical Components for advanced gas turbines and made contributions to blade vibrations caused by forced excitation, rotating stall, and aeroelastic flutter.

In May of 1958, on a Friday afternoon, Dr. Bentele was called into the office of Roy T. Hurley (the President and Chairman of Curtiss-Wright). Hurley handed him a crude plastic 5×6.5 in. model of an engine and said ''That's supposed to be an engine. Find out over the weekend whether it is, and its pros and cons. Report to me on Monday and don't talk to anybody about it!'' On Monday, Dr. Bentele reported his findings in detail to Hurley and then learned that its inventor was Felix Wankel. This was the start of Dr. Bentele's important involvement with this rotary engine and Curtiss-Wright's position as it exclusive licensor of North America. Max Bentele is recognized as an important figure in the development of the Wankel engine and made major contributions to its design. In 1966 he was granted a patent on this engine for burning of a wide range of fuels. By 1966, Curtiss-Wright stopped engine manufacture and restructured itself to be to a major supplier of components to the aerospace and other industries.

## 12 Contributions at Avco Lycoming

In May of 1967, Dr. Bentele joined Avco Lycoming as Consulting Engineer to the Vice President of Engineering. During his career and prior to his retirement in 1974 he made several important contributions including the following.

1. *Solutions to major service problems with the T53 and T55 engines*.[14] Dr. Bentele spearheaded investigation of a rash of disk failures where tennons of aluminum disks holding blade dovetail roots were breaking causing engine failure. In recognition of his worldwide reputation and integrity, Dr. Bentele was selected by the Army Aviation Systems Command (AVSCOM) to chair a blue ribbon panel to find a solution to the problem. It was determined that a failure mode included stress-rupture, high cycle fatigue caused by blade vibrations, and low cycle fatigue due to frequent takeoffs and landing of the helicopter. The solution was a replacement of the disks with a one-piece welded rotor made of titanium.
2. *Development studies of low-power gas turbine engines*. Dr. Bentele worked on a 5 lbs/s flow class gas turbine configuration with a single spool compressor consisting of one axial and one centrifugal stage driven by a single stage axial turbine, a reverse-flow annular combustor, and a power turbine. Details of Dr. Bentele's investigations may be found in Bentele and Laborde [17].
3. *Testing of turbine containment failures*. In the fall of 1970 a containment failure occurred on a T55 engine where power turbine blades had broken off and the bearing support failed under the massive unbalance situation, resulting in control system damage. Dr. Bentele devised an iterative testing

[14]These helicopter engines were the branchildren of Dr. Anselm Franz, designer of the Junker Jumo 004 turbojet that powered the world's first production fighter, the Me-262.

**Fig. 14 Photograph of three jet engine pioneers taken in 1987. Left to right Sir Frank Whittle, Dr. Hans von Ohain, and Dr. Max Bentele.**

method by which stress-rupture failures could be induced at an exact speed thus reducing the number of very expensive tests to a minimum.

## 13 Closure

The long and distinguished career of Dr. Max Bentele has been covered, with an emphasis on his pioneering work on turbojet engines. During WW II he worked on the development of the advanced HeS 011 engine. He made seminal contributions in the area of blade vibration, blade fabrication, air cooling, and turbojet design. While not focused on in this paper, his significant contributions to the development of the Wankel engine earned him the title of the father of the Wankel engine in the USA. A photograph of Dr. von Ohain, Sir Frank Whittle, and Dr. Max Bentele is shown in Fig. 14. This photograph taken in 1987, is the last known photograph of these jet pioneers together. Dr. Bentele is Fellow of the SAE, Associate Fellow of AIAA and member of the VDI. He holds 12 patents. In 1971 The University of Wyoming invited Dr. Bentele to place his technical material in their American Heritage Center. This was done in 1972, thus preserving valuable documents and reports of his contributions to gas turbine and aviation engine technology. Dr. Bentele has been awarded many honors over the years culminating in 2001, with the prestigious ASME R. Tom Sawyer Award, the citation of which reads: ''*For pioneering work in the development of aeroengines and technical contributions in the areas of turbine blade fatigue analysis, blade cooling, and control systems for gas turbine rotary regenerators*.''

For his seminal work on jet engines that started at the dawn of the turbojet revolution, Dr. Bentele will always be remembered as a pioneer of the jet age.


## Acknowledgments

We wish to thank Dr. Max Bentele, for his communications and his correspondence over the years in which he answered several questions and queries about his early work on turbojets. His excellent autobiography ''Engine Revolutions'' has been a valuable reference and covers several fascinating details of the dawn of the jet age in which he played a pivotal role.


## References


[1] Bentele, M., 1991, *Engine Revolutions: The Autobiography of Max Bentele*, SAE, Warrendale, PA.

[2] Meher-Homji, C. B., and Prisell, E., 1999, ''Pioneering Turbojet Developments of Dr. Hans von Ohain—From the HeS1 to the HeS 011,'' ASME Gas Turbine and Aeroengine Conference, Indianapolis, ASME Paper No: 99-GT-228; also in J. Eng. Gas Turbines and Power **122**(2), p. 191 April 2000.

[3] Constant, E. W. II, 1980, *The Origins of the Turbojet Revolution*, John Hopkins University Press, Baltimore, MD, 1980.

[4] Meher-Homji, C. B., 2000, ''The Historical Evolution of Turbomachinery,'' Proceedings of the 29th Turbomachinery Symposium, Texas A&M University, Houston, TX, September 2000.

[5] Meher-Homji, C. B., 1996, ''The Development of the Junkers Jumo 004B—the World's First Production Turbojet,'' 1996 ASME Gas Turbine and Aeroengine Conference, Birmingham, UK, June 10–13, 1996. ASME Paper No. 96-GT-457. Also in ASME Transactions of Gas Turbines and Power **119**4, October 1997.

[6] ''An Encounter Between the Jet Engine Inventors Sir Frank Whittle and Dr. Hans von Ohain,'' 1978, Wright-Patterson Air Force Base, OH, History Office, Aeronautical Systems Division, US Air Force Systems Command.

[7] Neville, L. E., and Silsbee, N. F., 1948, *Jet Propulsion Progress*, McGraw-Hill, New York, 1948.

[8] Bentele, M., 1989, ''Das Heinkel-Hirth Turbostrahltriebwerk HeS011—Vorganger, Characteristiche Merkmale Erkenntnisse,'' Proceedings of Conference on 50 Years of Jet-Powered Flight, Sponsored by the DGLR (German Society for Aeronautics and Astronautics), DGLR Publ. No. 89-05, October 26–27, 1989, Deutsches Museum, Munich, Germany.

[9] Hirth-Motoren GmbH Report, April 1944, VEW 1-139, ''Schwingungsuntersuchungen an der HeS 11—Turbine V1 aund V6 mit Vollschaufeln,'' dated Jan 31, 1944; Max Bentele Papers, American Heritage Center, University of Wyoming.

[10] Hirth-Motoren GmbH Report, April 1944B, VEW 1-140, ''Untersuchung der Fussbefestigung von Topf und Falt-Schaufeln durch Kaltschleuderprufung,'' dated April 16, 1944; Max Bentele Papers, American Heritage Center, University of Wyoming.

[11] ''Design of the German 109-011 A-O Turbojet,'' Aviation, September, 1946.

[12] ''Basic Technical Data on the 109-011 Jet Engine A-O Development Series,'' U.S. Navy Department Bureau of Aeronautics, Third Edition, December 1944.

[13] Bamford, L. P., and Robinson, S. T., 1945, ''Turbine Engine Activity at Ernst Heinkel Atiengesellschaft Werk Hirth-Motoren, Stuttgart/Zuffenhausen,'' Report by the Combined Intelligence Objectives Sub-committee dated May 1945.

[14] Carter, J. L., 1945, *Ernst Heinkel Jet Engines*, Aeronautical Engine Laboratory [AEL], Naval Air Experimental Station, Bureau of Aeronautics, US Navy, June 1945.

[15] Franz, A., 1979, *The Development of the Jumo 004 Turbojet Engine*, 40 Years of Jet Engine Progress, edited by Boyne, W. J. and Lopez, D. S., National Air and Space Museum, Smithsonian, Washington, 1979.

[16] Bentele, M., and Lowthian, C. S., 1952, ''Thermal Shock Tests on Gas Turbine Materials,'' Aircraft Engineering, February, 1952, pp. 32–38.

[17] Bentele, M., and Laborde, J., 1972, *Evolution of Small Turboshaft Engines*, National SAE Aerospace Engineering and Manufacturing Conference, San Diego, CA, October 2–5, 1972, SAE Paper No. 720830.

# Unique Challenges for Bolted Joint Design in High-Bypass Turbofan Engines

**Robert P. Czachor**
Chief Consulting Engineer, Structures,
GE Aircraft Engines,
One Neumann Way,
Cincinnati, Ohio 45215
e-mail: robert.czachor@ae.ge.com

*Bolted joints are used at numerous locations in the rotors and carcass structure of modern aircraft turbine engines. This application makes the design criteria and process substantially different from that used for other types of machinery. Specifically, in addition to providing engine alignment and high-pressure gas sealing, aircraft engine structural joints can operate at high temperatures and may be required to survive very large applied loads which can result from structural failures within the engine, such as the loss of a fan blade. As engine bypass ratios have increased in order to improve specific fuel consumption, these so-called "Ultimate" loads increasingly dominate the design of bolted joints in aircraft engines. This paper deals with the sizing and design of both bolts and lever flanges to meet these demanding requirements. Novel empirical methods, derived from both component test results and correlated analysis have been developed to perform strength evaluation of both flanges and bolts. Discussion of analytical techniques in use includes application of the LS-DYNA™ code for modeling of high-speed blade impact events as related to bolted joint behavior.* [DOI: 10.1115/1.1806453]

## Introduction

This paper deals with a number of unique challenges that large commercial turbofan engines present for the design of bolted joints which secure the engine carcass and rotor components. These circumferential casing/rotor joints typically utilize flat-faced lever-type flanges. Figure 1 illustrates the locations of bolted joints in a typical turbofan engine.

The basic behavior of bolted joints [1] in turbofan engines under normal operation are common to other applications and will not be discussed here. Unique to the turbofan engine, however, are constraints on diameter due to weight and packaging concerns, along with challenging internal pressures, rotational speeds and temperature levels. Transient operation during engine starts, acceleration or deceleration, along with aircraft maneuvers subject these joints to numerous combinations of loads in the course of normal engine operation. In addition, the designs must accommodate so-called "ultimate" loading conditions, such as the large imbalance forces generated by abusive rotor imbalance. Such imbalance can result from loss of a fan blade due to bird strike or other cause. In that event, damage to the joints is acceptable but carcass integrity of the engine generally must be maintained to satisfy FAA requirements. With the latest generation engine fan diameters growing as large as 129 in. (328 cm), these ultimate loads have increased to a point where bolted joints in commercial turbofan engines must push the state of the art to a much more significant extent than in common industrial applications.

Industrial practice [2] provides a basis for sizing bolted joints based primarily on providing adequate sealing against internal liquid or gas pressure. These methods are conservative enough that, in many cases, externally applied loads may safely be ignored. In contrast, the design of aircraft engine bolted joints is dominated by the external loads the joint must support. While leakage control is still a requirement, adequate sealing usually results as the joint is designed to meet other requirements—rarely is it a governing factor in the sizing of the joint. Experience has shown that a variety of design requirements must be satisfied by the aircraft engine joint, including:

1. Prevent joint separation under applied loads during normal operation;
2. Provide transverse-load capability to prevent slippage by means of sufficient joint clamp and flange friction;
3. Prevent air/fluid leakage;
4. Provide strength sufficient to support limit/ultimate dynamic loads due to abusive rotor unbalance;
5. Low cycle fatigue (LCF) life in excess of expected engine lifetime;
6. High-cycle fatigue (HCF) life sufficient to preclude failure with expected levels of normal engine vibration;
7. Provide strength sufficient to support loads due to limit/ultimate aircraft maneuvers.

## Preload and Residual Preload

Assembly of joints for turbofan engines is usually performed with the common torque wrench. Variables such as friction coefficients, assembler technique and torque wrench calibration permits control of clamp only within ±30%. When more accuracy is necessary, torque-angle techniques have been used to reduce this variation to ±20%, but this requires specialized tooling for fastener assembly. Assembly lubricants, such as synthetic engine oil or graphite grease, have been shown to be effective in minimizing clamp variation.

The available clamp is determined through component testing in order to determine the torque-tension or angle-tension relationship. These tests are performed either with force washers or with ultrasonic measurements of bolt elongation. The latter technique requires tensile calibration of the ultrasonic extensometers for each particular type of fastener. Ultrasonic measurement has the advantage of permitting the determination of fastener clamp on production engine assemblies, rather than in the laboratory, which then includes the variables of technician lubrication and assembly technique. (In rare cases, ultrasonic measurement of bolt extension during production assembly has been used to insure clamp variation of less than ±5%.)

During engine operation, three effects serve to reduce this initial assembly clamp. The first is simply thermal expansion, since

Contributed by the International Gas Turbine Institute (IGTI) of THE AMERICAN SOCIETY OF MECHANICAL ENGINEERS for publication in the ASME JOURNAL OF ENGINEERING FOR GAS TURBINES AND POWER. Paper presented at the International Gas Turbine and Aeroengine Congress and Exhibition, Atlanta, GA, June 16–19, 2003, Paper No. 2003-GT-38042. Manuscript received by IGTI, October 2002, final revision, March 2003. Associate Editor: H. R. Simmons.

  

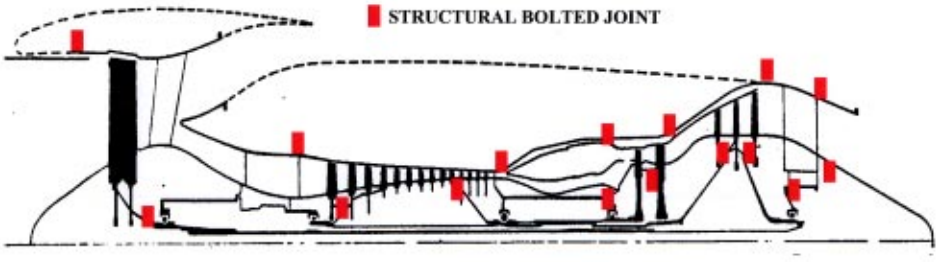


**Fig. 1 Structural bolted joints in a typical turbofan engine**

the fasteners, flanges and any attached bracketry will generally not be made from the same material or operate at the same temperature for engine steady-state or transient conditions. This clamp loss can be simply expressed as:

$$\Delta B = -K_{ET}\left\{ \alpha_B \Delta T_B l_b - \alpha_N \Delta T_N h_n - \sum_1^{NF} (\alpha_F \Delta T_F t_f)_i \right\} \quad (1)$$

Note that the joint combined stiffness term, $K_{ET}$ has been used to account for the load division between bolt load and joint clamp. A less accurate expression, often found in the literature, simply uses the bolt stiffness, $K_{ET}^B$.

A second issue leading to preload loss in turbomachinery is the contraction of the flange thickness due to transverse normal stresses. Tensile hoop stress will exist in a circumferential casing flange due to internal pressure or in a rotating flange due to speed. Flange radial stress levels can also be significant due to thermal gradients. Both will cause Poisson's contraction of the flange thickness and create a further loss in clamp, which can be expressed as:

$$\Delta B = -K_{ET} \sum_1^{NF} \{\mu(\sigma_R + \sigma_H)(t_f^n / E_{ET}^{F,n})\}_n \quad (2)$$

Equations (1) and (2) are derived in Appendix A.

A less obvious effect comes about from the change in the elastic modulus of the joint materials with temperature. A bolted joint is simply a mechanical arrangement of springs and when the joint materials are brought to elevated temperature levels, the change in spring constants due to the reduction in material modulus will create a further loss in preload. This change in bolt load can be expressed as:

$$\Delta B = B_{RT}\{K_{ET}/K_{RT} - 1\} \quad (3)$$

Interestingly, while this effect does reduce the clamp at operating conditions, it alone may not result in a change in bolt strain. Because of this, the cyclic content of bolt stress which is due to the modulus change at temperature in many cases can be safely ignored in the calculation of fastener low-cycle fatigue capability. A derivation of Eq. (3) and an explanation of the effect on bolt strain is provided in Appendix B.

Many characteristics of turbomachinery bolted joint behavior, at least for normal operation, are dependent on the available clamp at operating conditions. Given the variation in assembly clamp and the factors operating to reduce it, providing adequate clamp during engine operation is often a challenge.

## Applied Loads in Operation

Bolted joints in turbomachinery are subjected to a variety of loads in operation that can be broadly categorized as:

1. Axisymmetric loads due to internal pressure, thermal gradients, torque and rotational speed. These loads can act both normal and transverse to the bolt axis.
2. Asymmetric loads or beam-bending loads on the engine, which can be created by rotating imbalance forces, aircraft maneuvers (Including gyroscopic effects from the rotating turbomachinery), aerodynamic forces acting on the engine inlet and nacelle, and the engine thrust. (Since the engine thrust is produced at the engine centerline and reacted at the engine mounts which are offset from the centerline, engine carcass bending results.)
3. Impact loads resulting from failure events where blade fragments may impact the casings in the vicinity of flanges.

Loading conditions are further categorized according to the likelihood of the event and different design criteria applied accordingly. For example, we might require that the joint not separate (lose clamp at the bolt centerline) for normal engine transient and steady state operation combined with normal aircraft maneuvers whereas for a major failure event the criteria would be simply that the flanges and fasteners not fracture.

It can be seen then, that the designer will be faced with the construction of a number of combined load cases for a given joint that must be evaluated against the appropriate design criteria for that condition. These load cases will involve the combination of axisymmetric loads with beam moments and shears due to both maneuvers and imbalance, which will often act in different planes. This often precludes determination of the most limiting bolt location in a joint by simple inspection. It is then necessary to calculate the load on each individual fastener in the joint in order to identify the most highly-loaded fastener.

Furthermore, the load combination/condition and relevant design criteria that will in the end size a given joint will not be known at the point the design is initiated. All possible loadings must be evaluated against the appropriate design criteria before it is established whether a design is satisfactory or otherwise.

## Design Criteria for Normal Operation

Experience has shown that the following criteria must be satisfied for a durable bolted joint when normal operation of the engine and aircraft are considered:

1. Maintain an axial flexibility ratio ($R_a^{ET}$) of less than 0.5, i.e., maintain the clamping member stiffness at no more than 50% of the clamped members. This minimizes cyclic loads on the bolt and improves fatigue life.
2. Provide sufficient bolt length, even where thin flanges are joined, by use of a spacer (thick washer) in the joint. This both improves the joint axial flexibility ratio and ensures sufficient stretch of the bolt at assembly to desensitize the joint from small embedment losses. Longer bolts, having a greater total strain to failure than short bolts, also afford the joint greater ultimate load capability, as will be discussed later in this paper.
3. Provide sufficient clamp to prevent separation of the joint at operating conditions. This criterion ensures adequate sealing, predictable structural stiffness, and satisfactory bolt low-cycle fatigue life.

4. Provide sufficient clamp/flange face friction coefficients to preclude transverse movement of the flanges. Even very small amounts of transverse displacement of the flanges in the clamped condition will produce very high bolt bending stresses and inevitable failure.
5. Related to these criteria is the philosophy that observation of any evidence of movement, such as wear or entrapped debris, at a joint following engine cyclic endurance testing is a clear indication of an unsatisfactory joint design. It has been found that, due to the cyclic nature of aircraft engine operation, even small amounts of movement at a joint will inevitably produce wear, which leads to loss of clamp, increased movement and additional wear until failure results.

## Ultimate Load Capability: Empirical Methods

Having satisfactorily sized a joint to meet the requirements of normal operation, the designer must then examine the ultimate load capability of the joint. Little conservatism is possible consistent with engine weight and space constraints. The design criterion is quite simple: The loadpath must remain intact. First, we can examine the problem of a bolt under ultimate loading conditions which usually results from a large overturning moment (OTM) engine beam-bending load. Such loads can result from an extreme aircraft maneuver or rotor imbalance condition.

A conventional, elastic calculation would simply determine the maximum local shell load associated with the most highly-loaded bolt due to the applied bending load using the formula:

$$P_{\mathrm{SHELL}}=\frac{2M}{NR_S} \tag{4}$$

The derivation of Eq. (4) is provided in Appendix C.

Accounting for the lever action created by the fact that the bolt is offset from the line of action of the shell [3]

$$B_{\mathrm{APPLIED}}=P_{\mathrm{SHELL}}\left[1+\frac{l}{b}\right] \tag{5}$$

Typically, the joint would be past the point of separation on the joint diagram (Fig. 3) for this ultimate condition so preload is not considered in the calculation. The formulation assumes two-dimensional behavior of the circumferential flange and has been found to be reasonably accurate for flanges 20 in. (51 cm) in diameter or larger. The toe reaction at the outer edge of the flange is then simply:

$$R=B_{\mathrm{APPLIED}}-P_{\mathrm{SHELL}} \tag{6}$$

A conservative calculation would then simply compare the resulting bolt stress to the bolt material ultimate strength. Note these simple calculations ignore bolt bending, since, by definition, the bolt is strained near its elongation limit in tension so that little bending capability remains.

Component testing has shown that such elastic calculations are quite conservative. The initial explanation was that a shift in the neutral axis of bending would bring more bolts to their ultimate capability, thus increasing the overall strength of the joint. As illustrated in Fig. 2, this neutral axis shift results since the joint compression load path, which is simply through the heel of the flange where the shells abut, is considerably stiffer than the tensile load path through the bolt, where flange lever action and bolt elongation contribute to substantially more flexibility. Since the joint stiffness in the compressive direction is greater than that in tension, a shift in the neutral axis of bending results in loading additional bolts in tension as shown. An additional contributor is bolt plasticity, since the most highly loaded bolt will not fail when loaded to its ultimate capability, but must also undergo a strain equal to its tensile elongation capability prior to fracture. These effects are illustrated in Fig. 2, where elastic/perfectly plastic behavior has been assumed for the bolts.

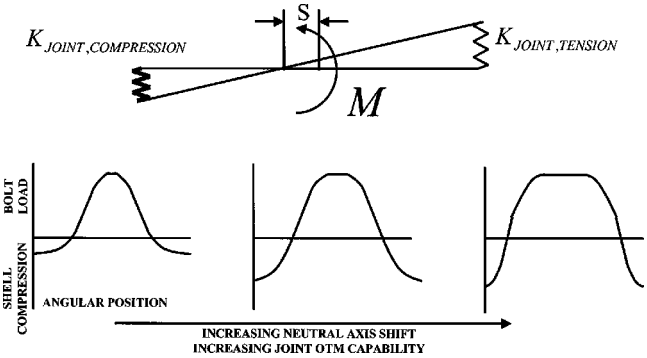


**Fig. 2 Neutral axis shift mechanism for overturning moment loading**

However, experimental measurements of neutral axis shift during component tests failed to reveal the magnitude of shift necessary to account for the observed joint capability. An additional effect, observed from elastic-plastic joint analysis, was that the flange lever action, as described by Eq. (5), decreased when significant bolt plastic strain occurred. The joint diagram for the most highly loaded bolt was found to be described by Fig. 3, which is extended significantly beyond that loading considered in conventional calculations.

Figure 3 describes the load history of the most highly loaded bolt in a joint as the OTM load is applied. Initially, the assembly clamp is reduced as the thermal effects discussed in the previous section occur (point A). As engine normal operating load is applied, the load is absorbed primarily by joint compression relief and some additional bolt load in conventional fashion as described in Ref. [1] (point B). Note that the bolt load in normal operation is actually less than at cold assembly since the thermal effects discussed earlier dominate, rather than the applied load. For normal operation of the turbomachinery, this behavior is typical for high temperature joints. However, what interests us more is the behavior beyond this point.

As the load is further increased, the slope of the bolt load versus applied load changes at the point of separation (point C) where all clamp at the bolt centerline is relieved. However, the flange toe is still in contact due to the flange lever action and the toe reaction is present. As load is increased further and the bolt plastically deforms, the compressive force at the flange toe is relieved, in much the same way as the clamp at the bolt centerline is relieved during the early stages of loading, reducing the slope of the loading curve (point D). In this fashion, flange lever action is decreased. By reducing the rate of bolt load increase with applied load at the most highly loaded bolt, the strength of the joint is enhanced as the load is redistributed to the adjacent, less highly-loaded bolts in much the same manner as occurs due to the neutral axis shift. Both these effects thus combine to afford a much higher joint ultimate load capability than the simple elastic calculation would suggest.

The point of bolt failure (point E) is determined by the total amount of plastic strain that the most highly loaded bolt can sustain. Thus, an explanation for the increased strength of joints with longer bolts is provided. The larger the bolt total elongation capability, the more redistribution of load that will occur and the greater the ultimate strength of the joint.

Data from a number of component tests and correlated elastic-plastic analysis was interrogated, with the aim of providing a simple means for bolt sizing for ultimate load conditions. It was assumed that the basic behavior would be governed by the ratio of the joint tensile stiffness to the compression stiffness. The test data was examined and it was found that a quadratic fit using the flange parameter:

$$K_{\mathrm{FLANGE}}/K_{\mathrm{SHELL}} \tag{7}$$

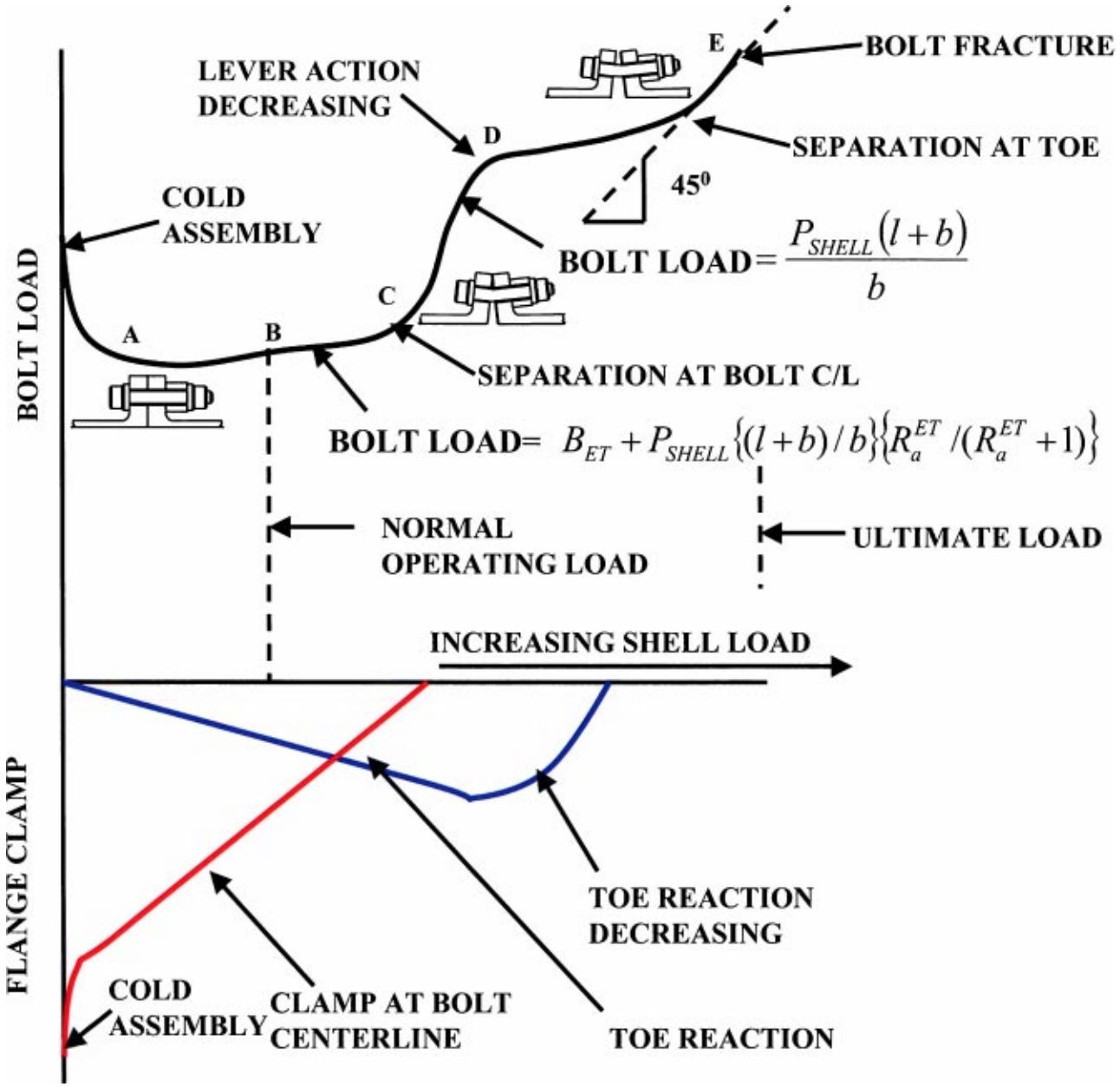


**Fig. 3 The joint diagram for a lever flange at high load levels**

where

$$K_{\text{FLANGE}} = \frac{K_1 K_2 K_3}{K_1 K_2 + K_2 K_3 + K_1 K_3} \quad \text{and} \quad K_{\text{SHELL}} = \frac{K_4 K_5}{K_4 + K_5} \tag{8}$$

and,

$$K_1 = \frac{2E_{ET}^{F,1} R_B \pi (t_f^1/l_1)^3}{N}, \quad K_2 = \frac{2E_{ET}^{F,2} R_B \pi (t_f^2/l_2)^3}{N},$$
$$K_3 = \frac{E_{ET}^B A_{TH} b}{l_B (l+b)} \quad K_4 = \frac{2\pi R_s^1 t_s^1 E_{ET}^{F,1}}{N} \quad K_5 = \frac{2\pi R_s^2 t_s^2 E_{ET}^{F,2}}{N} \tag{9}$$

would provide a simple multiplier for the elastically calculated bolt capability. Correlation results using this parameter are shown in Fig. 4.

Similar component tests were carried out to investigate flange ultimate strength. Calculation methods used in the past, such as the simple calculation of the peak shell load necessary to stress

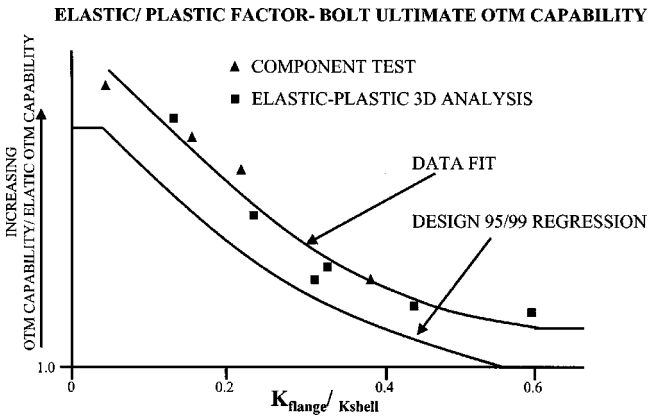


**Fig. 4 Empirical multiplier for bolt capability under OTM load**

**Fig. 5 Typical component test set-up**

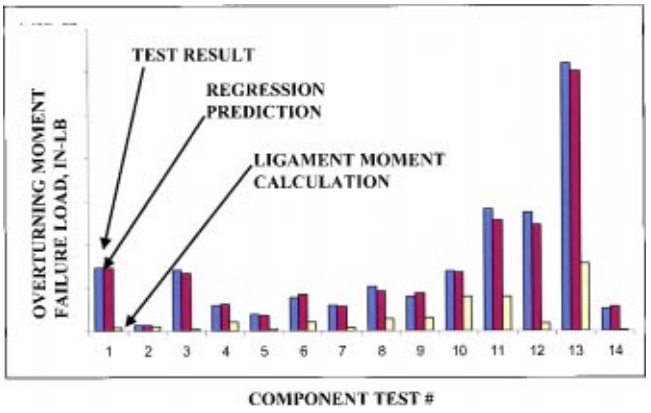


**Fig. 7 Comparison of empirical predictions for flange failure with component test results**

the ligament between boltholes to its full plastic moment capability, were also shown by test to be quite conservative. Since the required flange thicknesses are a major driver for engine weight, a less conservative approach was sought.

An empirical correlation was obtained using the results from a series of 14 component tests. Specimens were prepared from a number of typical engine materials, including INCO 718, M152 steel, aluminum 6061, and titanium alloys. Test flange diameters ranged between 6.6 in. (16.8 cm) to 45 in. (114.3 cm) and flange thickness from 0.055 in. (0.14 cm) to 0.267 in. (0.678 cm), typical of the values in use in aircraft turbomachinery. Tests included both symmetrical (Identical flanges) and nonsymmetrical joints. Figure 5 illustrates a typical component test set-up.

The overturning moment load capability of the flange was found to be described by the relation:

$$\mathrm{OTM}_{\mathrm{ULT}} = \frac{k_1 t^{k_2} UTS^{k_3} (1 + l/b)^{k_4} \left( \frac{K_{\mathrm{FLANGE}}}{K_{\mathrm{SHELL}}} \right)^{k_5}}{(0.2\%YS)^{k_6} (l - D_H/2)^{k_8} R_f^{k_9} t_S^{k_{10}}} NR_S \quad (10)$$

All flange failures initiated near the edge of the fastener head nearest to the shell and progressed from that point in various fashions, primarily dependent on bolt spacing. The tests included cracks that propagated through the shell at the bend tangent of the fillet radius, through the flange thickness at the opposite bend tangent, and pure shear tear-outs. Some typical failures are shown in Fig. 6. Ultimate capability was not affected by the presence of flange scallops between boltholes, which are often used for flange weight reduction in aircraft engine applications.

Figure 7 shows how the empirical correlation compares with

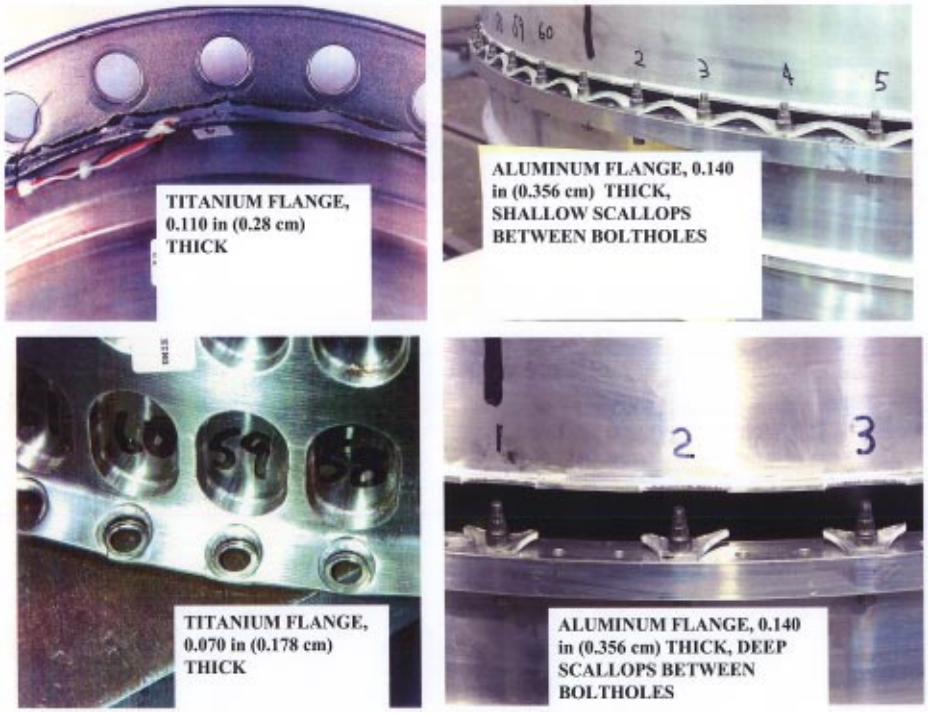


**Fig. 6 Component test flange failures**

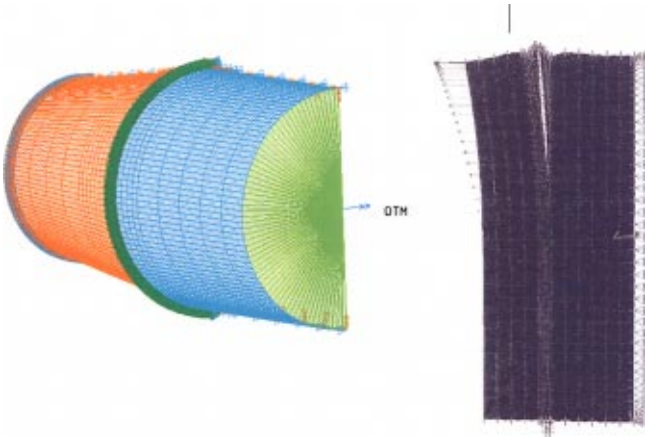


**Fig. 8 Simple plate-beam model used for prediction of bolt OTM capability**

the actual component test results. Also shown for comparison is a conventional handbook fully-plastic moment capability calculation.

## Analytical Methods for Ultimate Capability

As it may be imagined, a degree of conservatism must be included in any empirical component-test based approach to joint design, which is undesirable from a weight standpoint and will necessarily underpredict actual joint capability. Component tests such as described in this paper are both expensive and time-consuming and therefore are not a desirable option as a design tool, particularly in light of efforts to shorten time-to-market of turbomachinery products. Therefore, an effort was undertaken to develop Finite-Element analysis techniques to predict flange and bolt ultimate load capability. An important part of this effort was to show correlation between the analysis and component test results.

The ANSYS® program was used. The general features of the finite element model shown to correlate well for purposes of bolt capability calculation are illustrated in Fig. 8. This is a relatively simple 3D plate model of a 180° sector of the flanged connection. Gap elements are used at the flange faces and elastic-plastic link elements represent the bolts. The bolt is modeled including an additional length to represent the bolt head and nut flexibility. Otherwise, the model is linear. Details such as bolt holes and flange fillet radii are not modeled. Sufficient shell length is included to attenuate the effect of boundary conditions.

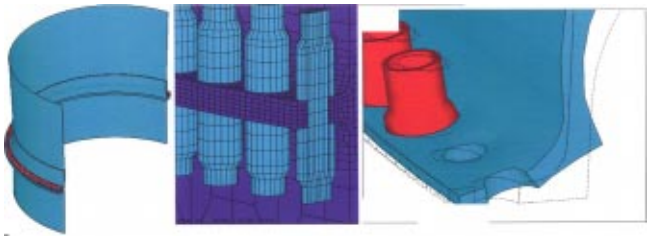

**Fig. 9 Complex model required for accurate prediction of flange capability**

The model is loaded incrementally and failure is predicted when the bolt link elements reach the plastic failure strain level as established by fastener component tests. This strain value is computed from a standard tensile strength test based on the assumption that the measured bolt strain is uniform over the clamped length of the fastener including the dummy length included to account for the head and nut flexibility effects. In reality, the plastic strain in a fastener is concentrated in the first few threads past the nut washer face, but, since the fastener is not modeled in detail, the use of the average plastic extension over this complete length has been used. While a seemingly crude representation of the problem, such models have shown excellent correlation to test results for bolt failure prediction.

Analytical prediction of flange ultimate capability has proven much more difficult. Simple models such as shown in Fig. 8, when used to predict flange failure, were found to deviate from component test results by as much as a factor of 2. It was established that very detailed models were required to simulate the complex interaction between the flanges and the fastener. Detail modeling of the bolt head or nut in contact with the flanges was required along with the inclusion of friction in the solution such that relative movement of the joint elements could occur. An example of the type of model necessary to accurately predict flange ultimate failure is shown in Fig. 9. All elements of this model have plastic properties. Such analysis starts to challenge even current computational capability. Models constructed to this level of

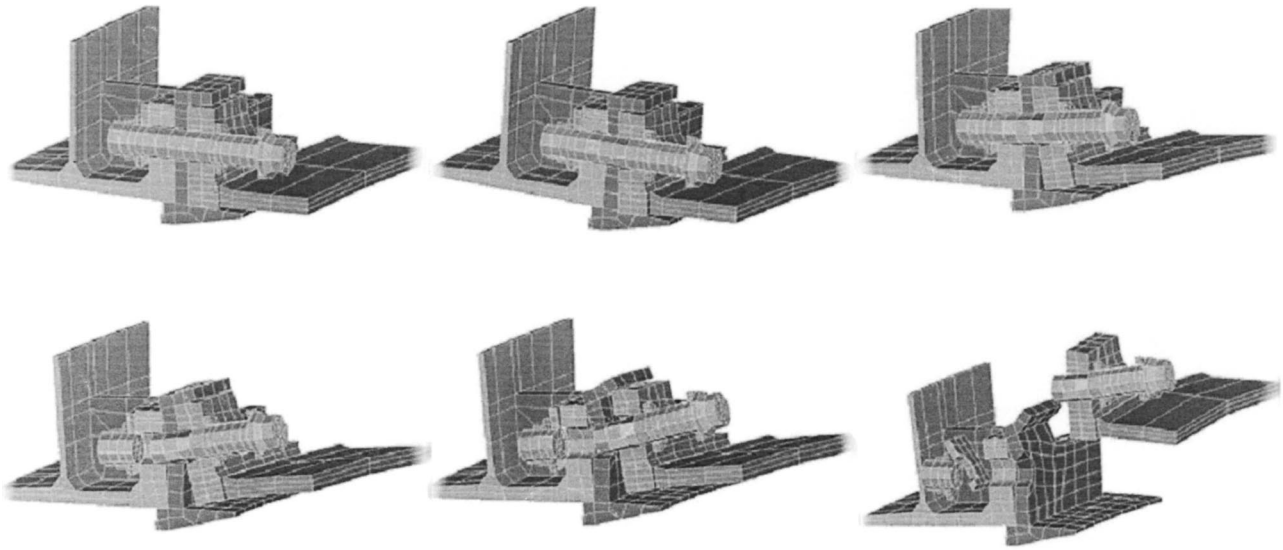

**Fig. 10 LS-DYNA® analysis of a bolted joint in the vicinity of a blade impact on the adjacent casing**

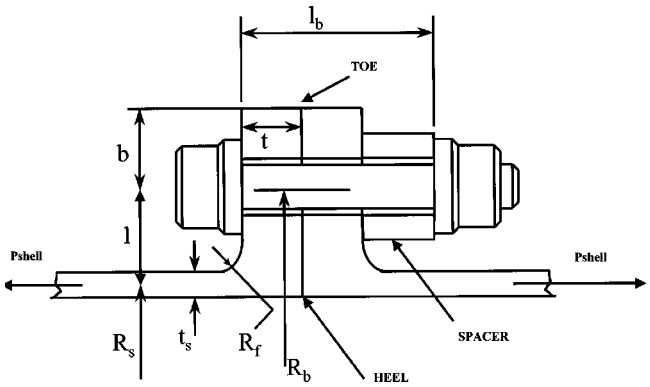


**Fig. 11 Lever flange joint geometry**

detail have achieved correlation with component test results within 15% of the actual failure load. In some cases, correlation within less than 2% has been achieved.

This same, more complex model can, of course, also be used to calculate the ultimate capability of the bolts, although simpler models per Fig. 8 suffice for that purpose.

## The Impact Problem for Blade Containment

A final unique category of bolted joint loads in turbomachinery is that which occurs following a blade failure when the released blade strikes the engine casing with great force. While the casings are designed to prevent blade penetration, bolted joints in the vicinity of the impact will see high loads due to casing deformation during the initial portion of the event, followed by the imbalance-induced cyclic bending loads discussed earlier in this paper. Plastic, radial deflection of the fan casing of over 2 in. (5 cm) will occur in the case of metallic fan casings used on large commercial engines. In order to ensure that the blade or blade fragments are contained and engine carcass integrity is maintained, gross failure of the joints must be prevented during the blade impact although some loss of individual fasteners is acceptable.

The LS-DYNA™ code has been used successfully to predict joint capability under these impact conditions. A model of the engine casing and rotor is run to simulate the blade release, followed by a submodel analysis of a local group of the most highly-loaded fasteners. Shown in Fig. 10 is the sequence of events predicted for an engine/inlet joint for a large fan engine following the release of a fan airfoil and its containment by the casing immediately adjacent to the flange.

The entire sequence of events shown in Fig. 10 occurs in less than 8 ms. Since all elements in the model behave in an elastic-plastic fashion with known failure elongation, failure of any joint element can be directly predicted. Use of high strain-rate material data is necessary for an accurate analysis due to the short duration of the event.

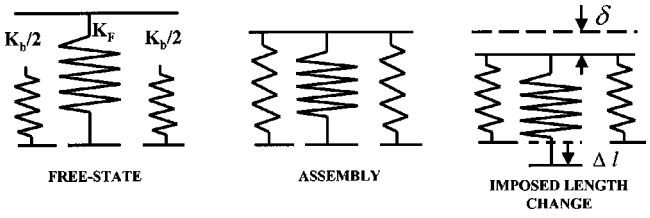


**Fig. 12 Representation of thermal and Poissions mechanism for a bolted joint**

## Conclusions

Bolted joints in turbomachinery are designed to maintain clamp and sealing capacity under normal engine operating conditions, much like other industrial applications. They also must remain intact under extremely high loads associated with engine failure events. Significant insight has been gathered regarding the behavior of lever-flange bolted joints for these severe loading conditions that aid the designer in achieving the necessary capability within the space and weight constraints of the aircraft engine application. (See Fig. 11.)


## Acknowledgments

The author would like to gratefully acknowledge the efforts of E. Baehre, S. Bhattacharjee, A. Mishra, J. Renners, S. Ross, and F. Worthoff as well as the earlier work of C. K. Coombs, all of whom made significant contributions to the work described herein.


## Nomenclature

$\alpha_N$ = nut thermal coefficient of expansion
$\alpha_B$ = bolt thermal coefficient of expansion
$\alpha_F$ = flange thermal coefficient of expansion
$\Delta B$ = change in bolt load from assembly condition
$\Delta l^B_{RT\text{-}ET}$ = change in bolt length from assembly condition to elevated temperature condition
$\Delta T_B$ = delta bolt temperature from assembly condition
$\Delta T_f$ = delta flange temperature from assembly condition
$\Delta T_N$ = delta nut temperature from assembly condition
$\sigma_H$ = hoop, or circumferential flange stress
$\sigma_R$ = Radial flange stress
$\mu$ = Flange Poisson's ratio
$0.2\%YS$ = 0.2% yield strength
$A_{TH}$ = thread equivalent area
$b$ = distance from bolt centerline to flange free edge, also known as toe distance
$B_{\text{APPLIED}}$ = bolt load due to applied external loads in the separated condition, i.e., without preload
$B_{ET}$ = residual preload at operating conditions considering temperature effects
$B_{RT}$ = assembly bolt load
$E^B_{ET}$ = Young's modulus of bolt at elevated temperature
$E^{F,n}_{ET}$ = Young's modulus of flange n at elevated temperature
$D_M$ = thread minor diameter
$h_n$ = nut height
$k_n$ = empirical constant
$K_{RT}$ = joint combined spring constant at elevated temperature $K_{RT}=K^{RT}_B/(1+R^{RT}_a)$
$K_{ET}$ = joint combined spring constant at room temperature $K_{ET}=K^{ET}_B/(1+R^{ET}_a)$
$K_{\text{FLANGE}}$ = spring value representing flange flexibility in the flange parameter used for bolt OTM capability
$K_{\text{SHELL}}$ = spring value representing shell flexibility in the flange parameter used for bolt OTM capability
$K^{SP}_{ET}$ = stiffness of a spacer or washer
$K^B_{RT}$ = series spring combination of the bolt, nut, and spacer stiffness at room temperature
$K^B_{ET}$ = series spring combination of the bolt, nut, and spacer stiffness at elevated temperature
$K^F_{ET}$ = series spring combination of the flange stiffness at elevated temperature
$K^F_{RT}$ = series spring combination of the flange stiffness at room temperature
$K_n$ = spring parameter in the flange parameter used for bolt OTM capability

$K_{ET}^{S}$ = stiffness of the shell portion of the flange at elevated temperature
$l_b$ = bolt effective length; This usually the clamped (grip) length increased by a distance $0.8D_M$ to account for the flexibility of the bolt head and the threads extending into the nut
$l$ = lever distance from casing shell centerline to bolt centerline
$R_a^{ET}$ = the axial flexibility ratio for the joint at elevated temperature, $K_{ET}^{B}/K_{ET}^{F}$
$R_a^{RT}$ = the axial flexibility ratio for the joint at room temperature, $K_{RT}^{B}/K_{RT}^{F}$
$M$ = applied overturning moment load or engine beam-bending moment
$N$ = number of fasteners in the joint
NF = number of flanges in the joint
$\mathrm{OTM_{ULT}}$ = the overturning moment at the point of flange or bolt failure
$P_{\mathrm{SHELL}}$ = maximum shell load at a single bolt due to an applied over-turning moment
$R$ = toe reaction force
$R_B$ = radius to bolt circle
$R_f$ = fillet radius size between the shell and flange face
$R_S^n$ = radius to shell centerline associated with flange $n$
$S$ = distance of neutral axis shift
$t_f^n$ = flange thickness of flange $n$
$t_S^n$ = shell thickness associated with flange $n$

## Appendix A: the Effect of Thermal Expansion and Flange Poisson's Contraction on Bolt Load at Temperature

Both these phenomena, as described by Eqs. (1) and (2), can be represented schematically by considering the bolt deflection ($\delta$) resulting from a change in flange thickness ($\Delta l$) as shown in Fig. 12.

For the bolt, it can be seen that:

$$B_{ET}=B_{RT}-\delta K_{ET}^{B} \tag{11}$$

$$\Delta B=-\delta K_{ET}^{B} \tag{12}$$

For the flange,

$$\Delta B=\{\Delta l-\delta\}K_{ET}^{F} \tag{13}$$

Therefore,

$$\delta=\frac{K_{ET}^{F}\Delta l}{K_{ET}^{B}+K_{ET}} \tag{14}$$

Substituting into (12)

$$\Delta B=-\frac{K_{ET}^{F}K_{ET}^{B}}{K_{ET}^{B}+K_{ET}}\Delta l \tag{15}$$

Using the definition of the joint combined spring constant,

$$K_{ET}=\frac{K_B^{ET}}{(1+R_a^{ET})} \tag{16}$$

We obtain:

$$\Delta B=-K_{ET}\Delta l \tag{17}$$

For thermal expansion, we can consider the change in flange thickness relative to the bolt,

$$\Delta l=\left\{\alpha_B\Delta T_B l_b-\sum_{1}^{NF}(\alpha_F\Delta T_F t_f)_i-\alpha_N\Delta T_N h_n\right\} \tag{18}$$

Substitution of Eq. (18) into Eq. (17) yields Eq. (1).

Considering the effects of Poisson's contraction of the flanges, we obtain the change in flange thickness as:

$$\Delta l=\sum_{1}^{NF}\{\mu(\sigma_R+\sigma_H)(t_f^n/E_{ET}^{F,n})\}_{\mathrm{n}} \tag{19}$$

Substitution of Eq. (19) into Eq. (17) yields Eq. (2).

## Appendix B: the Effect of Elevated Temperature Modulus on Bolt Load and Strain

To determine the impact of the change in modulus on a bolted joint as it is brought to an elevated temperature, we can consider bolt and flange materials with either an identical, or zero, coefficient of expansion but with temperature-dependent moduli. If we consider the fact that any change in bolt length from the assembled condition to the elevated temperature condition must have an equal change in the clamped length of the flange we can write the equation:

$$\frac{B_{RT}}{K_{RT}^{B}}-\frac{B_{ET}}{K_{ET}^{B}}=\frac{B_{ET}}{K_{ET}^{F}}-\frac{B_{RT}}{K_{RT}^{F}} \tag{20}$$

Rearranging this equation yields an expression for the bolt load at temperature:

$$B_{ET}=\frac{B_{RT}K_{ET}^{F}K_{ET}^{B}(K_{RT}^{F}+K_{RT}^{B})}{K_{RT}^{F}K_{RT}^{B}(K_{ET}^{F}+K_{ET}^{B})} \tag{21}$$

The left-hand side of Eq. (20) represents the change in bolt length at temperature due solely to the change in modulus. If we substitute Eq. (21) into (20), we obtain:

$$\Delta l_{RT-ET}^{B}=\frac{B_{RT}}{K_{RT}^{F}}-\frac{B_{RT}K_{ET}^{F}(K_{RT}^{F}+K_{RT}^{B})}{K_{RT}^{F}K_{RT}^{B}(K_{ET}^{F}+K_{ET}^{B})} \tag{22}$$

Reducing further,

$$\Delta l_{RT-ET}^{B}=\frac{B_{RT}}{K_{RT}^{F}}\left\{1-\frac{K_{ET}^{F}(K_{RT}^{F}+K_{RT}^{B})}{K_{RT}^{F}(K_{ET}^{F}+K_{ET}^{B})}\right\} \tag{23}$$

This quantity becomes zero if:

$$\left\{\frac{K_{ET}^{F}}{K_{RT}^{F}}\right\}\left\{\frac{K_{RT}^{B}}{K_{ET}^{B}}\right\}=1 \tag{24}$$

For a given geometry, the stiffness terms in Eq. (24) are only dependent on the modulus. Therefore, if the bolt and flange are constructed of the same materials, or from materials with similar modulus response to temperature, little or no change in bolt strain results from the change in modulus of the joint materials.

Returning to Eq. (21), we can write:

$$B_{ET}=B_{RT}\frac{K_{ET}^{B}\{1+K_{RT}^{B}/K_{RT}^{F}\}}{K_{RT}^{B}\{1+K_{ET}^{B}/K_{ET}^{F}\}} \tag{25}$$

Rearranging further, we obtain

$$B_{ET}=B_{RT}\frac{[K_{ET}^{B}/\{1+K_{ET}^{B}/K_{ET}^{F}\}]}{[K_{RT}^{B}/\{1+K_{RT}^{B}/K_{RT}^{F}\}]} \tag{26}$$

Using the definition of the axial flexibility ratio,

$$R_a=K_{RT}^{B}/K_{RT}^{F} \tag{27}$$

we obtain

$$B_{ET}=B_{RT}\frac{\{K_{ET}^{B}/1+R_a^{ET}\}}{\{K_{RT}^{B}/1+R_a^{RT}\}} \tag{28}$$

Using the definition of the combined joint spring constant,

$$K_{RT}=\frac{K_B^{RT}}{(1+R_a^{RT})} \text{ or } K_{ET}=\frac{K_B^{ET}}{(1+R_a^{ET})} \tag{29}$$

Substituting Eqs. (29) into (28) yields Eq. (3).

## Appendix C: Determination of Maximum Shell Load for an Applied OTM Load

Assuming a sinusoidal distribution of bolt loads, first we must determine the function for the shell load that satisfies the relation:

$$M=\int_0^{2\pi} F(\theta)R_S(\sin\theta)d\theta \tag{30}$$

where

$$F(\theta)=X(\sin\theta) \tag{31}$$

Substituting Eq. (31) into Eq. (30):

$$M=\int_0^{2\pi} X(\sin^2\theta)R_S d\theta = XR_S\left\{\pi-\frac{\sin(4\pi)}{4}\right\}=\pi XR_S \tag{32}$$

Therefore,

$$X=\frac{M}{\pi R_S} \tag{33}$$

Substituting Eq. (33) into Eq. (31) and the result into Eq. (30), then and integrating over a single bolt spacing we have, for a bolt at an arbitrary position $\theta$,

$$\begin{aligned} P_{\text{SHELL}}(\theta)&=\int_{(\theta-\pi/N)}^{(\theta+\pi/N)}\frac{M}{\pi R_S}(\sin\theta)d\theta \\ &=\frac{M}{\pi R_S}\left\{\cos\left(\theta-\frac{\pi}{N}\right)-\cos\left(\theta+\frac{\pi}{N}\right)\right\} \\ &=\frac{2M}{\pi R_S}(\sin\theta)\left(\sin\frac{\pi}{N}\right) \end{aligned} \tag{34}$$

Assuming that, for a large number of bolts,

$$\sin\frac{\pi}{N}=\frac{\pi}{N} \tag{35}$$

we obtain:

$$P_{\text{SHELL}}(\theta)=\frac{2M}{NR}\sin\theta \tag{36}$$

The maximum bolt load is thus given by Eq. (4).

## References


[1] Brickford, J. H., 1995, *An Introduction to the Design and Behavior of Bolted Joints*, 3rd ed., Marcel Decker, Inc., pp. 422–457.
[2] ASME Boiler and Pressure Vessel Code, Section VIII, Division 1, Appendix 2.
[3] Schneider, R. W., 1968, "Flat Face Flanges With Contact Beyond the Bolt Circle," ASME J. Eng. Power, **90**(1), pp. 82–88.

# Detailed Investigation of Heat Flux Measurements Made in a Standard Propane-Air Fire-Certification Burner Compared to Levels Derived From a Low-Temperature Analog Burner

**Abd. Rahim Abu Talib**[1]
e-mail: abrahim@eng.upm.edu.my
Universiti Putra Malaysia,
Department of Aerospace Engineering,
Faculty of Engineering,
43400 Selangor, Malaysia

**Andrew J. Neely**[1]
University of New South Wales,
School of Aerospace and Mechanical Engineering,
Australian Defense Force Academy,
Northcott Drive,
Canberra ACT 2600, Australia
e-mail: a.neely@adfa.edu.au

**Peter T. Ireland**
University of Oxford,
Department of Engineering Science,
Parks Road,
Oxford OX1 3PJ, UK
e-mail: peter.Ireland@eng.ox.ac.uk

**Andrew J. Mullender**
Rolls-Royce plc.,
Fire Precautions Group,
P.O. Box 31,
Derby, DE24 8Bj, UK
e-mail: andy.mullender@rolls-royce.com

*This paper presents detailed heat flux measurements on a flat plate subjected to the ISO2685 [The International Organization for Standardization (ISO), 1992, "Aircraft—Environmental Conditions and Test Procedures for Airborne Equipment—Resistance to Fire in Designated Fire Zones," ISO2685:1992(E)] standard, propane fueled burner used throughout the industry in aero-engine fire-certification. The authors have developed a custom-built heat transfer gauge to measure the heat flux from the burner under isothermal wall conditions. The heat flux from the standard burner is normally calibrated using either a water-cooled copper tube or a Gardon gauge, each sited at a single position in the flame. There are no reports in the literature of a detailed survey of heat flux distribution for the burner and the results are of considerable interest to engineers involved in fire-certification. The reported measurements constitute the first, detailed distribution of heat flux from the actual burner flame during a fire test. These measurements provided benchmark data which allowed the heat flux distribution from the ISO burner to be compared to levels derived from the low-temperature analog burner developed by the authors. The analog burner uses liquid crystals to measure heat transfer coefficient and adiabatic wall temperature on scale models of engine components and provides key data to facilitate the successful design of components used in fire zones. The objective of this paper is to further validate the low-temperature analog burner technique developed by the authors which simulates the standard large propane-air burner for fire-certification in aero engine.* [DOI: 10.1115/1.1806454]

## 1 Introduction

**1.1 ISO2685 Propane-Air Burner.** The ISO propane-air burner is widely used in the UK to certify critical engine components exposed to the danger of fire in aircraft engines. The alternative, Kerosene burner, which is frequently used in the US, is also specified in ISO2685 [1] and in FAA report [2]. In the standard structural fire-test, engine components are immersed in the flame from the ISO burner for a period of 15 min to establish if they are fireproof. This is to verify the structural integrity of the components under flame attack. Therefore it is essential to study the detailed distribution of heat flux within the burner flame. While a full three-dimensional survey would provide the most detail, as the standard specifies a test plane for the location of component surfaces 75 mm downstream from the burner face, the two-dimensional distribution of heat flux at this location is of primary interest.

The large propane-air burner consists of a plenum chamber, burner head and burner face. Mixed propane-air is supplied by 373 copper tubes to the burner head and cooling air is discharged via 332 smaller holes interspersed with the copper tubes in the burner face (Fig. 1). The faceplate acts as a flame stabilizer to prevent back flow into the burner head. The flow rate of the gas and air are adjusted to produce the standard flame characteristic. The ISO standard requires the flame to have the following characteristics: temperature: 1100°C±80°C; heat flux density: 116 $kW\,m^{-2}\pm10\ kW\,m^{-2}$.

ISO2685 [1] requires that the burner flame temperature must be within the required tolerance over at least 25% of the burner area. To this end a rake of thermocouples of specified type and size is recommended. This rake measurement is normally only performed at the single horizontal line specified. During such a calibration, it can be observed that the thermocouples radiate significantly (Fig. 2). Neely et al. [3] reports that due to the large diameter of the thermocouple recommended for the calibration, the effect of radiation from the thermocouple tip significantly reduces the temperature measured in the flame. Once the measured temperature readings (~1100°C) have been corrected for the radiation losses, the actual peak flame temperature is found to be approximately 1900°C, as would be expected from an equilibrium flame calculation. It is noted by the authors that this significant difference between the actual flame temperature and that specified in the standard is not widely understood within the industry.

ISO2685 [1] also requires that the heat flux in the standard

[1]Formerly at the Department of Engineering Science, University of Oxford, Parks Road, Oxford OX1 3PJ, UK.

Contributed by the International Gas Turbine Institute (IGTI) of THE AMERICAN SOCIETY OF MECHANICAL ENGINEERS for publication in the ASME JOURNAL OF ENGINEERING FOR GAS TURBINES AND POWER. Paper presented at the International Gas Turbine and Aeroengine Congress and Exhibition, Atlanta, GA, June 16–19, 2003, Paper No. 2003-GT-38196. Manuscript received by IGTI, October 2002, final revision, March 2003. Associate Editor: H. R. Simmons.

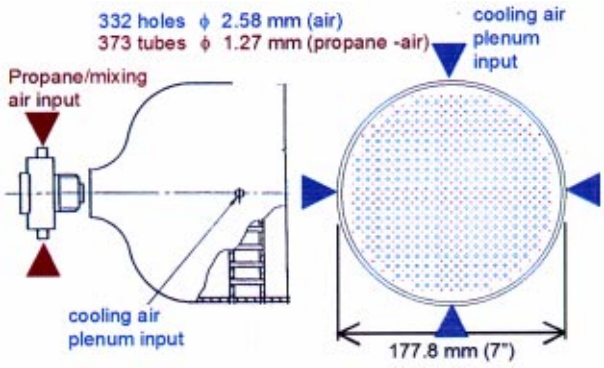


**Fig. 1 ISO2685 standard large (propane-air) fire-test burner [1]**

burner must be calibrated using either a water-cooled copper tube calorimeter or an alternative approved calorimeter. The specified calibration method can only measure a steady heat flux and also has a very slow response. It requires a 3 min warm-up time before the temperature measurements taken. The temperature history of the constant flow of water is monitored for a period of 3 min and used to calculate the average heat flux using the following equation:

$$Q = \frac{\dot{u}\rho c_p \Delta T}{A} \tag{1}$$

where $Q$ is the amount of heat supplied from the flame, $\dot{u}$ is the volume flow rate of the water, $\rho$ is the water density, $c_p$ is the specific heat of water, $\Delta T$ is the temperature difference, and $A$ is the area of the cylinder. This calibration method only provides a single measurement of heat flux integrated over the length of the impingement of the flame onto the copper tube.

**1.2 Heat Flux Measurement.** There are many methods of measuring heat flux such as those reported in Schultz and Jones [4], Jones [5], and Ainsworth et al. [6]. However these methods are unsuitable for surveying the ISO2685 [1] standard flame. A gauge for this purpose must be able to accurately measure the heat flux up to approximately 200 $\mathrm{kW\,m^{-2}}$ and be able to withstand prolonged immersion in a 1900°C flame. For this reason, thin film gauges (TFGs) were chosen to measure the surface temperature of an enamelled-insulating layer attached to a water-cooled metallic plate. As well as maintaining the gauges at a manageable surface temperature, the cooled enclosure accurately prescribes the thermal boundary condition by removing the large step in surface temperature between the gauge and its surroundings seen for uncooled surrounds such as ceramic sheeting.

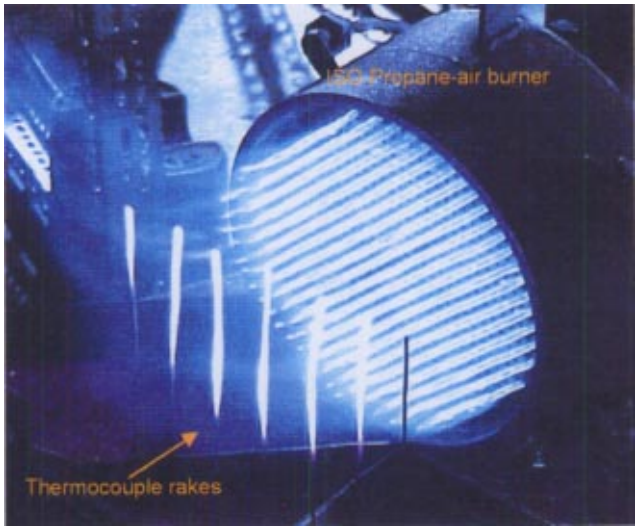


**Fig. 2 ISO burner temperature calibrations**

Thin film gauges were selected to measure the surface temperature due to their fast response and negligible influence on the surface flow field. Additionally they are able to endure elevated surface temperatures.

**1.3 Low-Temperature Analog Technique.** In order to reduce the reliance on conventional fire testing, a new technique has been developed at the University of Oxford, which is faster, cheaper, and provides test data at higher resolution than the standard fire test (Mullender et al. [7]). Initial testing of engine component models using the low temperature technique demonstrated good agreement with metal temperatures from actual ISO burner tests. The validation and development of the low-temperature analogue burner technique is discussed in details by Neely et al. [3,8,9] and Abu Talib et al. [10].

In this approach the high temperature standard fire test (nominally 1900°C) is replaced by tests at close to ambient temperature (approximately 80°C) in which accurate plastic models, surface coated with thermochromic liquid crystal, are immersed in the flow from the low-temperature analog burner to enable the mapping of heat transfer coefficient, $h$, and adiabatic wall temperature, $T_{aw}$, across the surface of the model. The heat transfer coefficient distributions are then input as boundary conditions into a finite-element thermal analysis code, together with knowledge of the component heat-loss due to radiation and where applicable cooling from the by-pass flow, to permit full thermal modeling of the behavior of the component during fire attack.

## 2 Test Facilities and Instrumentation

This section provides detailed descriptions of the instrumentation used in the heat flux measurements and the experimental configuration.

**2.1 Thin Film Gauge.** Thin film gauges are widely used to measure transient and steady state heat transfer. Since the 1970s the technique has been developed and used in a variety of gas turbine applications such as those described in Jones [11,12]. Further application and development of the traditional TFG are described by Epstein [13], Doorly and Oldfield [14,15], and Dunn [16].

A TFG can be used to measure surface temperature and local heat flux when it is used in conjunction with an insulating substrate. The heat transfer rate can be obtained from the steady state one-dimensional conduction equation as follows:

$$q = \Delta T\left(\frac{k}{\Delta x}\right) \tag{2}$$

where $k$ is the substrate thermal conductivity, $\Delta x$ is the thickness of the substrate and $\Delta T$ is the temperature difference across the substrate. The temperature $\Delta T$ across a sheet of known thermal properties and dimensions is measured with the traditional sputtered gauge sensor and a thermocouple is located on the bottom side of this insulating layer in a metal test model. The thermocouple is placed as close as possible to the metal surface. The development of the direct heat transfer gauge is fully explained by Piccini et al. [17].

The TFGs used in the current work consisted of platinum films (approximately 0.04 $\mu$m thick) painted onto the surface of an enamelled Inconel disc (50 mm diameter and 2 mm thick) (Fig. 3). Each platinum TFG is approximately 5 mm long and 1 mm wide. The enamel is assumed to have properties similar to fused quartz with thermal conductivity of approximately 1.36 $\mathrm{W\,m^{-1}\,K^{-1}}$ (Doorly [18]). Inconel-600 (nickel/chromium alloy), which has a good oxidation resistance at high temperature and has a thermal conductivity of 14.8 $\mathrm{W\,m^{-1}\,K^{-1}}$ at room temperature,

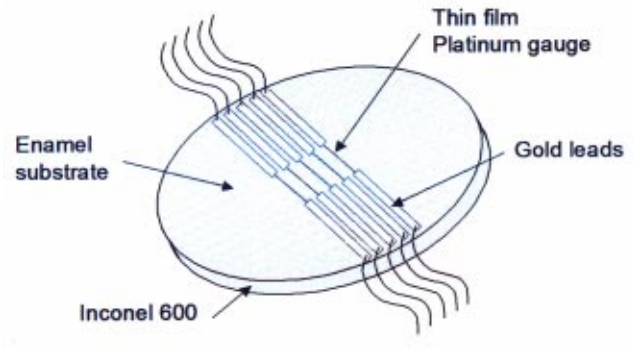


**Fig. 3 Enameled Inconel disk painted with 4 platinum TFGs**

was used as the base of the enamel. The gauges were connected using painted gold leads connected to heavier wire connectors.

*2.1.1 Principle of the TFG.* Resistance of the thin film gauge varies with temperature as shown in the following equation;

$$R = R_o(1 + \alpha_{\text{wb}}\Delta T) \tag{3}$$

where $R_o$ is the resistance of the TFG at room temperature, $\alpha_{\text{wb}}$ is the temperature coefficient of resistance, and $\Delta T$ is the surface temperature rise, $(\Delta T = T_s - T_o)$.

During the test, each TFG is supplied with a small constant current, $I_o$ (approximately 10 A) producing negligible Ohmic heating. The constant current source circuit design was adapted from Anthony et al. [19] (Fig. 4). Four separate constant current sources in parallel were built to supply the current to the circuit. This is to prevent any discontinuity in the current source if one of the thin film gauges is broken. Thus,

$$\Delta T = \frac{R - R_o}{\alpha_{\text{wb}} R_o} = \frac{\Delta R}{\alpha_{\text{wb}} R_o} \tag{4}$$

and,

$$\frac{I_o \Delta R}{I_o R_o \alpha_{\text{wb}}} = \frac{\Delta V}{V_o \alpha_{\text{wb}}} = \Delta T \tag{5}$$

Therefore, the TFG will have a change in electrical resistance $\Delta R$ when it is subjected to a heat load and thus a change in temperature, which results in change in voltage. The surface temperatures measured by the TFGs are combined with the backside temperatures measured by the thermocouples to determine the temperature

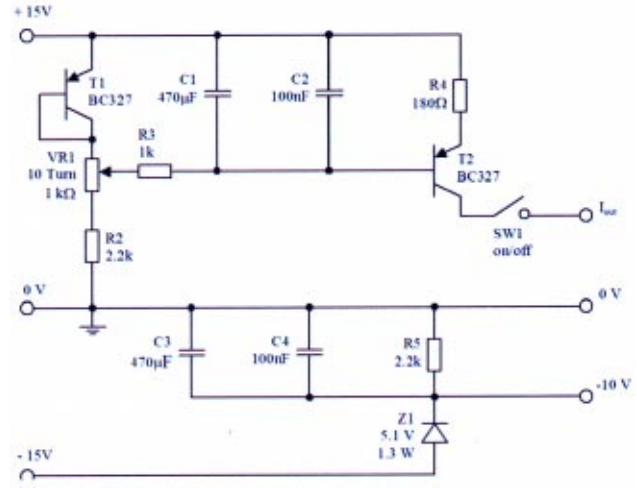


**Fig. 4 TFG Constant current source circuit diagram [20]**

**Table 1 Water bath calibration of the TFG**

| Gauge | $R_o$ | $\alpha_{wb}$ |
|---|---|---|
| 1 | 12.9979 | 0.0026200 |
| 2 | 17.3843 | 0.0026524 |
| 3 | 14.6141 | 0.0025530 |
| 4 | 24.1534 | 0.0026468 |

difference across the Inconel disk. As we have seen from Eq. (2), this temperature difference is proportional to the surface heat flux.

*2.1.2 TFG Water Bath Calibration.* The temperature coefficient of resistance, $\alpha_{\text{wb}}$ of the TFG can be deduced using a thermostatically controlled water bath calibration. From Eq. (3), the resistance of the TFG is directly proportional to the change in surface temperature. Therefore to obtain the $\alpha_{\text{wb}}$ of the TFG, the model with TFGs installed was enclosed in a waterproof plastic bag, to prevent electrical shorting and corrosion, and immersed into a deionized water bath. The water was gradually heated, typically in up to 12 temperature steps using a temperature regulator. Each temperature step was maintained for 180 s to ensure an equilibrium temperature was reached. The temperature was increased from room temperature to 55°C and brought back down to room temperature. The resistance of the TFG was recorded at each time step. A circulator was used to ensure a uniform water temperature in the water bath. $\alpha_{\text{wb}}$ was determined from the slope of the curve representing the resistance, $R$ against $\Delta T$ surface temperature. The calibration was conducted over the range of surface temperatures expected for the real fire test. The $R_o$ and $\alpha_{\text{wb}}$ of each TFG on the enamelled disk are shown in Table 1.

### 2.2 Fire Test Equipments

*2.2.1 Cooling Mechanism.* As stated, a cooling mechanism was required to ensure that the thin film gauges and the insulating substrate were held at a suitable operating temperature in the high temperature flame. A flat copper plate 300 mm×180 mm and 6.2 mm thick was machined with a recess, within which the enamel and instrumented disk was fitted. Three cooling channels, 40 mm wide×1.5 mm deep were machined into the back of the copper plate. Another copper plate, 190 mm×310 mm and 3 mm thick was used as a back plate to seal the cooling channels. The two copper plates were glued and clamped together using gasket sealant and 42 countersunk screws. Water was supplied to and from the channels through the copper backing plate via two copper manifolds 15 mm diameter. The manifolds were soldered to the back of the copper plate to prevent any water leakage.

Wright [20] reported that under a heat flux of 200 kW m$^{-2}$, the enameled Inconel disk was expected to have a temperature difference of about 35°C across it. It was assumed that under equilibrium conditions, the heat flux, from the flame is removed from the gauge by the cooling water inside the channels between the two copper plates. A temperature increase of less than 3°C would require a minimum water flow rate of 287 g s$^{-1}$ as predicted by the following equation:

$$q = \dot{m} c_p \Delta T \tag{6}$$

where $\dot{m}$ is the mass flow rate of water, $c_p$ is the specific heat of water at 20°C, and $\Delta T$ is the temperature difference between the back of the gauge and the water. Wright [20] also showed via calculation that the heat transfer coefficient, $h$, between the enamel surface and the flame was expected to be a factor of 100 times lower than the $h$ between the copper and the cooling water which is 9.2 kW m$^{-2}$ K$^{-1}$. The cooling system described above is sufficient to maintain the rear surface of the copper plate roughly 3°C above the temperature of the water in the channels.

In the heat flux measurements, the flow of water will not maintain a uniform temperature across the plate, as the region beneath the plume will be hotter. However it does help to maintain a

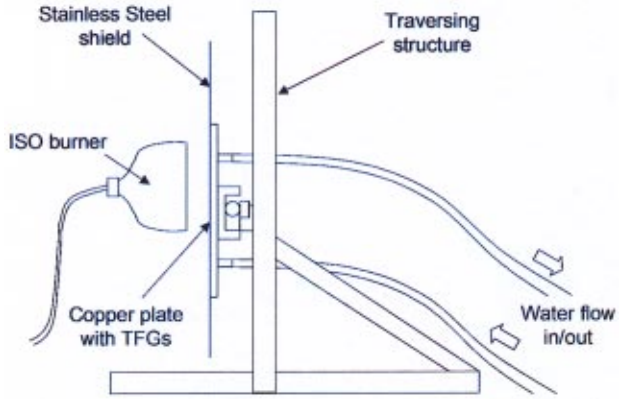


**Fig. 5 Side view schematic of fire test set up**

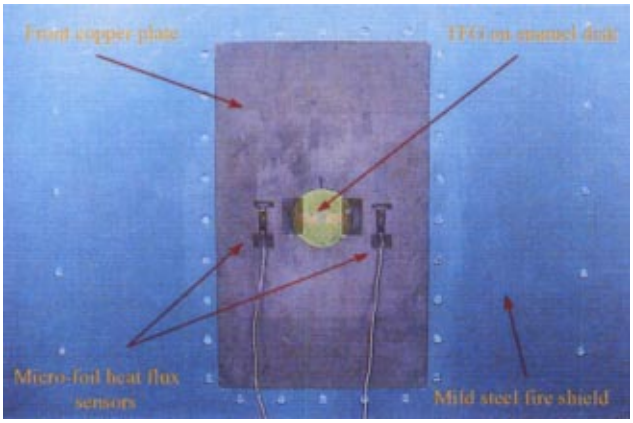


**Fig. 6 TFG water-cooled heat flux gauge system**

steady temperature for the duration of the measurements, as the equilibrium temperature will be reached more quickly. Furthermore it also allows high representative heat fluxes to be measured at low manageable surface temperatures as in the actual tests.

*2.2.2 Traversing Mechanism.* The hollow water-cooled copper plate was flush mounted within a 600 mm×600 mm×3 mm thick steel fire shield. This was done to both protect the vulnerable piping, instrumentation wiring and traversing mechanism from flame impingement and to provide a uniform flat-plate boundary condition across the full extent of the survey. The thin steel fire shield was strengthened by vertical and horizontal ribs to prevent it from buckling. The copper plate was mounted onto a translating frame, which allowed vertical and horizontal traverses. The frame was built in such way to provide a smooth movement for the heat flux measurements to be taken across the flame (Fig. 5).

## 3 Heat Flux Measurements Procedure

This section provides detailed descriptions of the heat flux calibration and the fire test measurements procedure.

**3.1 Heat Flux Calibration.** The term $k/\Delta x$ from Eq. (2) must be experimentally calibrated due to the uncertainty in the enamel thickness, thermal properties and the unknown heat transfer properties of the interface between the Inconel and the buried thermocouples. The TFG heat flux gauge was calibrated at low temperature against two calibrated micro-foil heat flux (Micro-foil heat flux sensor—RdF Corporation, 23 Elm Ave, P.O Box 490, Hudson, NH 03051-0490) sensors as shown in Fig. 6.

The sensors were flush mounted on the enamel surface adjacent to the TFG. A low level of heat flux was applied by a hot air gun and assumed to penetrate the micro-foil heat flux gauge and platinum film equally. Traversing the gauges through the plume core and using only the observed peak values compensated for nonuniformities in the heat flux distribution from the hot air plume. It is noted that micro-foil heat flux sensors were prone to damage at the higher surface temperatures and were therefore not suitable for use in the actual flame experiments. During the calibration, a constant flow of water was supplied into the copper plate to maintain a steady manageable surface temperature at the TFGs for the high levels of heat flux representative of the ISO burner flame. The voltage signals from the TFGs were amplified to enable a better accuracy of the calibration since the voltage changes were very small (approximately 0.5 $\mu$V).

The surface temperature of the enamel was calculated using the knowledge of $R_o$ and $\alpha_{\mathrm{wb}}$. The temperature difference between the surface temperature and the temperature measured by the thermocouple underneath the enamel were used in conjunction with the heat flux measured from the thermopile sensors to determine an equivalent thermal conductivity to thickness ratio $k/\Delta x$ of the substrate.

**3.2 Fire Test Procedure.** The experimental measurements were conducted at a private commercial fire testing cell in the UK. The ISO propane-air burner was set up so as not to impinge on the test plate and ignited. The burner setting was adjusted to get the correct fuel and air mass flow rates and flame temperatures specified by the standard. At the same time, the water to the copper test plate was turned on and was left for approximately 5 min to allow the plate to reach an equilibrium temperature. The data logger was set to continuously record the voltage signals from the TFGs and also the temperature signals from the thermocouples underneath the enameled disk.

To begin the test, the ISO burner was rotated so that the flame impinged directly onto the TFGs on the test plate as shown in Fig. 5. The distance between the burner face and the surface of the TFG was set at 75 mm to conform with ISO2685 [1]. The instrumented plate was moved horizontally and vertically to 29 locations across one half of the test plane, which covered an area of approximately 0.036 $m^2$. It was assumed that the burner flame was nominally symmetrical about a vertical axis. Each location was held for 60 s while the TFG voltage level was recorded. An initial transient voltage was observed as the cooled gauges reached a new equilibrium temperature. The voltage signals were later averaged over the observed equilibrium period for each 60 s step. During the experiment, condensation occurred in front of the cooled copper plate generating a thin film of water dripping to the floor. It is noted that this exothermic condensation process would be expected to have artificially increased the surface temperature readings. It is also noted that this condensation process would also initially occur on any component being heated from ambient temperature in a standard fire test.

## 4 Heat Flux Distribution

The heat flux from the ISO burner can now calculated using information obtained from the heat flux calibration, $k/\Delta x$ and the history of the change in temperature, $\Delta T$ during the fire test. The combination of the value of $k/\Delta x$, obtained from the heat flux calibration, with the distribution of temperature differences across the heat flux sensor, measured in the flame, enables the calculation of the distribution of heat flux to an ambient surface in the ISO burner flame. Figure 7 shows the distribution of heat flux at the test plane across one half of the ISO burner plume. It can be seen that the heat flux distribution from the ISO burner was found to be lower than the specified values required by the standard and the most likely reason for this is given later. Knowledge of distribution of heat flux in the burner plume can be used to benchmark the measurements of local convective heat transfer coefficient made in the test plane of the low-temperature analog burner.

In order to compare the heat flux levels derived from both the low-temperature test and the actual fire-test, the surface tempera-

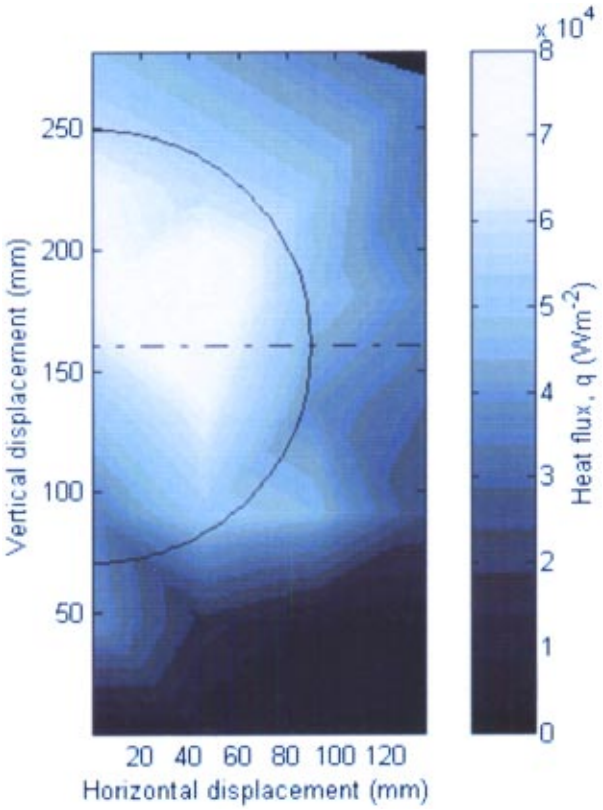


**Fig. 7 Heat flux distribution across half of the test plane of the ISO burner plume (circle and dotted lines indicates the position of burner head)**

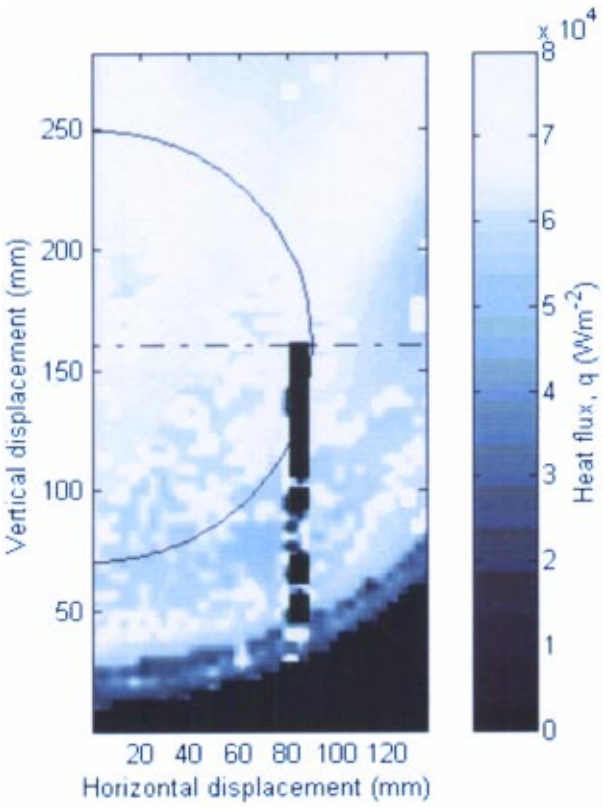


**Fig. 8 Heat flux distribution on half of the test-plane from low-temperature analog burner scaled to flame conditions**

ture distribution from the fire-test is used to calculate the expected heat flux for the low-temperature test. A similar flat plate impingement test has been conducted at low temperature using the low-temperature analog burner, as described in Abu Talib [21]. From the low-temperature test, the distribution of heat transfer coefficient, $h_{LT}$ and adiabatic wall temperature, $T_{awLT}$ is used in conjunction with the surface temperature, $T_{sFT}$ from the fire test to obtain the equivalent heat flux, $q_{LT}$ for the low-temperature test using the following equation.

$$q_{LT} = h_{LT}(T_{awLT} - T_{sFT}) \tag{7}$$

For the low-temperature analog burner tests, the heat transfer coefficient, $h_{LT}$ and adiabatic wall temperature, $T_{awLT}$ must be scaled to the flame temperature conditions (Neely et al. [3]). In the actual ISO burner flame there is a large variation of gas properties through the boundary layer between the gas and wall due to the large temperature gradient. The Nusselt number, Nu is affected by the change in physical properties of the gas ($\rho$, $c_p$, $k$, and $\mu$), which influence the convection of heat across the boundary layer. The gradient of physical properties is not simulated in the low-temperature analog burner case. Therefore a correction procedure is adopted to account for the property variation. The $h$ distribution obtained from the low-temperature test was scaled to ISO burner temperature conditions using a power law applied to the ratio of the gas conductivity, ratio of the Nusselt numbers, and the inverse ratio of the sizes. The ratios of Nusselt number can be first written as:

$$\left(\frac{\mathrm{Nu_{FT}}}{\mathrm{Nu_{LT}}}\right) = \left(\frac{h_{FT}}{h_{LT}}\right)\left(\frac{d_{FT}}{d_{LT}}\right)\left(\frac{k_{LT}}{k_{FT}}\right) \tag{8}$$

The literature for high temperature ratio experiment is very limited (Eckert [22], Kays and Crawford [23], Loftus and Jones [24], Forth [25], and Fitt et al. [26]). However, the approach by Petukov [27] is being employed in this case. Petukov reported limited experimental measurements showing the dependence of Nusselt number ratio on gas to wall temperature ratio for pipe flow. The ratio of the Nusselt number can be expressed as:

$$\left(\frac{\mathrm{Nu_{FT}}}{\mathrm{Nu_{LT}}}\right) = \theta^n \tag{9}$$

where $\theta = (T_s/T_{aw})$ and $n = -0.36$. The distribution of Nusselt number deduced in this manner is then used in conjunction with knowledge of the surface temperature distribution in the flame, as described above, to obtain the expected distribution of heat flux in the flame as displayed in Fig. 8.

The heat flux distribution from the low-temperature test is found to be more uniform compared with the distribution of heat flux from the standard fire-test. This may be due to condensation and evaporation processes occurred during the fire-test. During the heat flux measurements on ISO burner using the TFG, condensation was observed in front of the water-cooled copper plate. The condensation occurred since the surface temperature of the copper (5°C) is lower than the dew point of water (54°C) in the combustion products. The development of water droplets from condensation on the copper plate forms a thin layer of water and flows downwards due to gravitational force. However the water film evaporated along the enameled disk since it has a higher surface temperature. The surface temperature of the enamel disk was 115.74°C when the enamel disk was located at 45 mm above the burner centreline. This indicates that the heat flux distributions obtained from the ISO burner using the TFG system is altered by the heat required for evaporation. The effect of evaporative heat transfer for natural and force convection on vertical plates and horizontal tubes has been investigated by Rose [28]. A simple analysis based on mass transfer analogy has been conducted to estimate the effect of evaporation on the front surface of the TFG

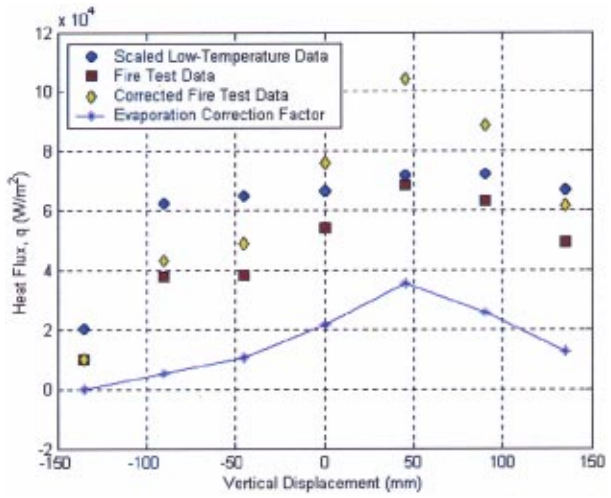


**Fig. 9 Comparison of heat flux data at vertical central displacement of the burner**

enamelled disk. In this analysis the combustion products from the plume were assumed at stoichiometric condition and treated as ideal gas

$$\overline{\mathrm{Nu}}_x = 0.664\,\mathrm{Re}_x^{0.5}\,\mathrm{Pr}^{0.33} \tag{10}$$

A standard Nusselt number correlation [Eq. (10)] for a forced convection on a flat plate is applied to the system at the location of heat flux measurement along the central vertical axis. Equation (10) can then be written as an average Sherwood number, $\overline{\mathrm{Sh}}_x$

$$\overline{\mathrm{Sh}}_x = \frac{\overline{k}_D X}{D} = 0.664\,\mathrm{Re}_x^{0.5}\,Sc^{0.33} \tag{11}$$

$$S_c = \frac{\mu}{\rho D} \tag{12}$$

where $\overline{k}_D$ is the mass transfer coefficient, $D$ is the diffusion coefficient of water, $X$ is the displacement, $S_c$ is the Schmidt number, $\rho$ is the density, and $\mu$ is the viscosity. Using the surface temperature reading from the TFG at the central vertical location in the plume, we can obtain the corresponding value of concentration of water vapor. Therefore the mass flow of water evaporation can be found using the following equation:

$$\dot{m} = \overline{k}_D(c_g - c_\infty) \tag{13}$$

where $\dot{m}$ is the mass flow rate, $c_g$ is the concentration of water vapor, and $c_\infty$ is the concentration of water in the plume. Hence the amount of heat flux due to the evaporation can be estimated. Figure 9 shows a comparison of the corrected heat flux values from fire-test data with the scaled low-temperature analog burner data. It is found that the heat flux distributions along the vertical centerline from the fire-test burner are still less than the levels required by the ISO standard (116 kW $\mathrm{m}^{-2}$) even with the added evaporation correction.

## 5 Wall Temperature Discontinuity Effect

ISO2685 states in Sec. B4.3, "An alternative calorimeter may be used, providing the approving authority agrees to that method of measuring the heat flux density." Therefore apart from the standard water-cooled copper tube calorimeter, the heat flux can be measure using other types of heat flux gauge. The most commonly used heat flux gauge used in the industry with the ISO propane-air burner is the water-cooled Gardon gauge, which is a water-cooled circular disc radiometer. At the private commercial fire testing cell, which the authors conducted these experiments, heat flux

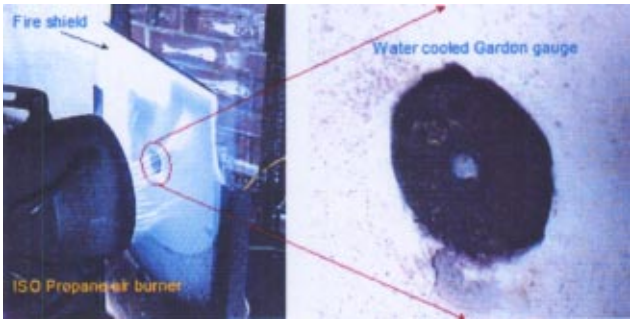


**Fig. 10 Use of a Gardon gauge to measure central heat flux in the ISO burner flame**

from the burner is calibrated using such a Gardon gauge. The gauge consists of a constantan circular foil disk attached to a copper heat sink with a thermocouple connected to the center of the disk. The output of the Gardon gauge indicates the heat flux by measuring the temperature difference between the center and the circumference of the thin foil disk. During the calibration, the Gardon gauge is flush mounted within a sheet of ceramic fire shield as shown in Fig. 10. The gauge is placed 1 in. (25 mm) above the burner centerline.

The Gardon gauge was constructed in such way that it has a nonuniform wall temperature across the measuring plane since only the gauge itself is water-cooled and not the surrounding fire-shield. The buoyant plume from the ISO burner will immediately deflect upwards when it impinges onto the surface surrounding the gauge. Figure 11 clearly shows the development of the thermal boundary layer and hydrodynamic boundary layer on a flat plate. It is assumed that the thermal boundary layer $\Delta$ is always thinner than the hydrodynamic boundary layer $\delta$ for a partially heated surface. $\xi$ represents the separation between the start of the impinging flow and the beginning of the temperature discontinuity between the heated surroundings and the cooled gauge.

The effects of a nonuniform wall temperature distribution have been investigated by Schultz and Jones [4] and Ainsworth [29]. Kays and Crawford [23] give a correlation for Nu to account for nonuniform wall temperature distribution. The local Nusselt number can be written as:

$$\mathrm{Nu}_x = 0.332\,\mathrm{Pr}^{1/3}\,\mathrm{Re}_x^{1/2}\left[1 - \left(\frac{\xi}{x}\right)^{3/4}\right]^{-1/3} \tag{14}$$

where Pr is the Prandtl number, $\mathrm{Re}_x$ is the local Reynolds number, $\xi$ is the unheated starting length, and $x$ is the distance from the

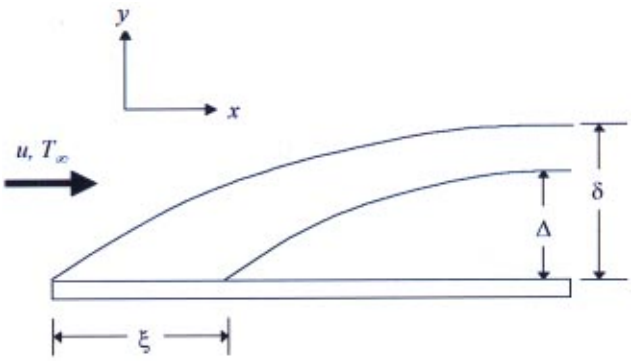


**Fig. 11 Boundary layer development on a plate with an unheated starting length, $\xi$**

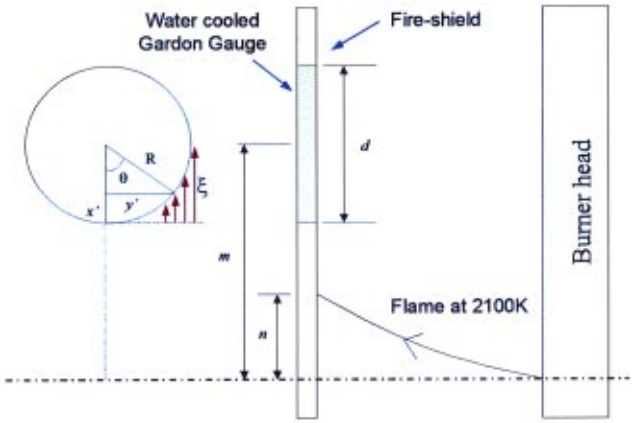


**Fig. 12 Schematic representation of the impingement plume**

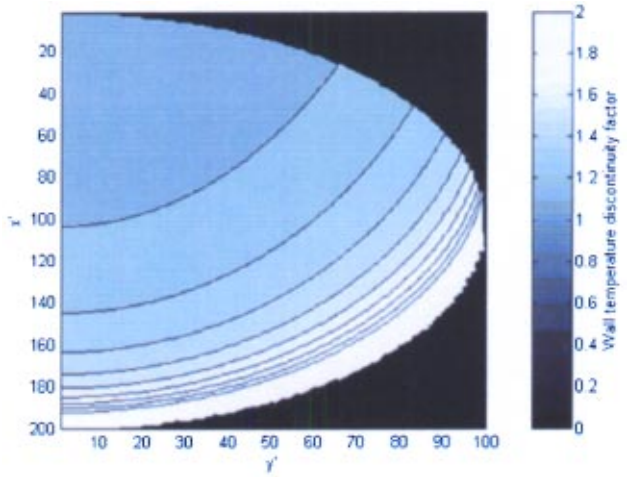


**Fig. 13 Wall temperature discontinuity factor distributions. Average factor=1.467.**

stagnation point. Note that this equation is for a laminar boundary layer but similar equation can be used from a turbulent boundary layer with an uncooled upstream zone.

The above equation is applied to half of the diameter of the Gardon gauge. In this case, the starting section is approximately adiabatic. The discontinuity corresponds to the change from hot wall to cold wall as opposed to the more familiar cold wall to hot wall. The effect of the wall temperature discontinuity and the mathematical solution are independent of the sense of wall temperature change. The gauge is divided into several equally spaced strips. Using MATLAB (The MathWorks Inc, 2001, ''MATLAB—The Language of Technical Computing,'' Ver. 6.1 Release 12.1) software a numerical analysis has been conducted to calculate the unheated starting length factor;

$$\left[1-\left(\frac{\xi}{x}\right)^{3/4}\right]^{-1/3} \tag{15}$$

Figure 12 shows the schematic diagram of the numerical analysis system. The hot plume from the ISO burner will bend upwards towards the plate. *n* represent the distance of the plume rise from the centerline of the burner and *m* is the distance of the Gardon gauge centerline from the burner centerline. The unheated starting length is represented by;

$$\xi=\xi_0+x' \tag{16}$$

where,

$$\xi_0=m-n-(d/2) \tag{17}$$

$$x'=(1-\cos\theta)(d/2) \tag{18}$$

Hence, the distribution of wall temperature discontinuity factor can be evaluated and shown in Fig. 13.

The plume rise is not measured directly and so the effect of the change in the plume rise on the wall temperature discontinuity factor was quantified and is shown in Fig. 14. Inspection of the still photographs from the fire test lead to an estimate of the plume rise as approximately 7 mm. When the discontinuity factor is averaged over the face of the Gardon gauge, it is found that the wall uniformity factor can be approximated by 1.467, assuming a plume rise of 7 mm. This means that the actual heat flux measured using a Gardon gauge mounted in an uncooled fire shield can be overestimated by approximately 46%. In order to obtain an average heat flux signal across the Gardon gauge of about 116 $kW\,m^{-2}$, the technicians at the test cell have to reduce the mass flow rate of the gas supplied to the ISO burner compared to the mass flow from a burner set up with a perfect gauge. For this reason, it is thought not to be surprising that the heat flux measured using the TFG system is lower than the ISO standard requirements.

## 6 Conclusion

A custom built thin film platinum gauge (TFG) calorimeter has been shown to be able to withstand the heat load from the standard ISO2685 propane-air fire-certification burner and used to accurately measure the heat flux distributions across the test plane of the plume. The use of a cooled enclosure around the TFG calorimeter heat flux gauge prescribed the correct form of the thermal boundary layer expected for component testing. The heat flux measured from the ISO burner using a water-cooled circular disk radiometer (Gardon gauge) embedded within an uncooled fire-shield during the burner calibration was significantly lower than the prescribed heat values required by the standard. It is thought that the burner has been adjusted to match the measured heat flux to the level set by the standard. It is thought the heat flux on the ISO burner measured using the Gardon Gauge overestimate the amount of heat load from the burner. The actual heat flux is less than 116 $kW\,m^{-2}$ specified in ISO2685. The levels derived from low-temperature analog burner test scaled to the fire test condition were found to be equivalent to the heat flux measured from the

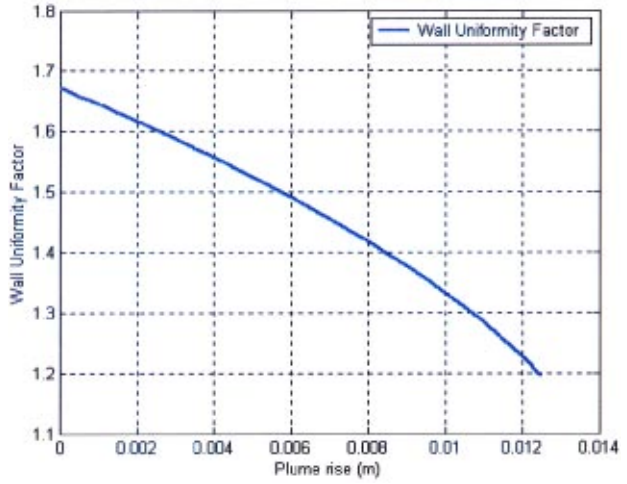


**Fig. 14 Plume rise effects on the wall temperature discontinuity factor**

ISO burner using the water-cooled TFG plate after applying the evaporation correction factor. These low-temperature heat flux measurements provide useful benchmark data and significantly improve the understanding of the nature of the standard flame, helping to facilitate the successful design of components used in fire zones.

## Acknowledgments

The authors wish to thank Rolls-Royce plc for permission to publish this paper. Thanks are also due to the UK Ministry of Defense (MoD) and the UK Department of Trade and Industry (DTI) for their financial support for this work through the Defense Evaluation and Research Agency (DERA), Pyestock. The first author thanks the Malaysian Government and the University Putra Malaysia for their financial support.

## Nomenclature

$\dot{m}$ = mass flow rate ($\mathrm{kg\,s^{-1}}$)
$\dot{u}$ = volume flow rate ($\mathrm{m^3\,s^{-1}}$)
$A$ = area ($\mathrm{m^2}$)
$c$ = concentration ($\mathrm{kg\,m^{-3}}$)
$c_p$ = specific heat capacity ($\mathrm{J\,kg^{-1}\,K^{-1}}$)
$d$ = diameter of the burner (m)
$D$ = diffusion coefficient ($\mathrm{m^2\,s^{-1}}$)
$h$ = heat transfer coefficient ($\mathrm{W\,m^{-2}\,K^{-1}}$)
$I$ = current (A)
$\underline{k}$ = thermal conductivity ($\mathrm{W\,m^{-1}\,K^{-1}}$)
$\overline{k}$ = mass transfer coefficient ($\mathrm{m\,s^{-1}}$)
$m$ = height from burner centerline (m)
$n$ = plume rise (m)
Nu = Nusselt number
Pr = Prandtl number
$Q$, $q$ = total heat load or heat flux ($\mathrm{W\,m^{-2}}$)
R = radius (m)
Re = Reynolds number
Sc = Schmidt number
Sh = Sherwood number
$T$ = temperature (°C)
$u$ = velocity ($\mathrm{m\,s^{-1}}$)
$x$ = substrate thickness, (m)
$X$ = displacement (mm)

### Greek

$\Delta$ = thermal boundary layer (m)
$\delta$ = hydrodynamic boundary layer (m)
$\rho$ = density ($\mathrm{kg\,m^{-3}}$)
$\alpha$ = temperature coefficient of resistance ($\mathrm{K^{-1}}$)
$\xi$ = unheated starting length (m)
$\mu$ = dynamic viscosity ($\mathrm{kg\,m^{-2}\,s^{-1}}$)

### Subscripts

$\infty$ = free stream
$x$ = local
aw = adiabatic wall
FT = fire test
$g$ = gas
LT = low-temperature test
$o$ = ambient surroundings, starting condition
$s$ = surface
wb = water bath

## References

[1] The International Organization for Standardization (ISO), 1992, ''Aircraft—Environmental Conditions and Test Procedures for Airborne Equipment— Resistance to Fire in Designated Fire Zones,'' ISO2685:1992(E).
[2] Federal Aviation Administration (FAA), 1990, ''Draft Advisory Circular, Powerplant Installation and Propulsion System Component Fire Protection Test Methods, Standards and Criteria,'' U.S. Department of Transportation, Advisory Circular No: 20-135.
[3] Neely, A. J., Ireland, P. T., and Mullender, A. J., 1999, ''Pilot Study to Investigate Novel Experimental and Theoretical Fire-Event Modelling Techniques,'' Proceedings, 37th Aerospace Science Meeting, Reno, Nevada, USA. (AIAA-99-09-0326).
[4] Schultz, D. L., and Jones, T. V., 1973, ''Heat Transfer Measurements in Short Duration Hypersonic Facilities,'' AGARD-AG-165, Advisory Group for Aerospace Research and Development (AGARD).
[5] Jones, T. V., 1977, ''Heat Transfer, Skin Friction, Total Temperature and Concentration Measurements,'' Measurement of Unsteady Fluid Dynamic Phenomena, von Karman Institute for Fluid Dynamics.
[6] Ainsworth, R. W., Allen, J. L., Davies, M. R., Forth, C. J. P., Hilditch, M. A., Oldfield, M. L. G., and Sheard, A. G., 1989, ''Developments in Instrumentation and Processing for Transient Heat Transfer Measurements in a Full-Stage Model Turbine,'' ASME J. Turbomach., **111**, pp. 20–27.
[7] Mullender, A. J., Handley, B., Coney, M. H., Ireland, P. T., and Neely, A. J., 2002, ''Model Test Apparatus and Method,'' 6,418,806, USA.
[8] Neely, A. J., Ireland, P. T., and Mullender, A. J., 1998, ''Validation of Novel Low-Temperature Fire Event Modelling Technique,'' Proceedings, Royal Aeronautical Society Conference—Verification of Design Methods by Test and Analysis, London, UK.
[9] Neely, A. J., Abu Talib, A. R., Ireland, P. T., and Mullender, A. J., 2000, ''Development of Low-Temperature Fire-Event Modelling Technique,'' Proceedings, 22nd International Congress of Aeronautical Science (ICAS) Conference, Harrogate, UK.
[10] Abu Talib, A. R., Neely, A. J., Ireland, P. T., and Mullender, A. J., 2001, ''Compact Low-Temperature Analogue of Aero Engine Fire-Certification Burner,'' Proceedings, ASME/IGTi Turbo Expo, New Orleans, Louisiana, USA. (2001-GT-0364).
[11] Jones, T. V., 1988, ''Gas Turbine Studies at Oxford 1969–1987,'' Proceedings, ASME/IGTi Turbo Expo, Amsterdam, The Netherlands. (8-GT-112).
[12] Jones, T. V., 1995, ''The Thin Film Heat Transfer Gauges—A History and New Developments,'' Proceedings, 4th National UK Heat Transfer Conference—IMechE, Manchester, UK.
[13] Epstein, A. H., Guenette, G. R., Norton, R. J. G., and Yuzhan, G., 1986, ''High Frequency Response Heat Flux Gauges,'' Rev. Sci. Instrum., **57**, pp. 639–649.
[14] Doorly, J. E., and Oldfield, M. L. G., 1986, ''New Heat Transfer Gauges for Use on Multilayered Substrates,'' ASME J. Turbomach., **108**, pp. 153–160.
[15] Doorly, J. E., and Oldfield, M. L. G., 1987, ''The Theory of Advanced Heat Transfer Gauges,'' Int. J. Heat Mass Transfer, **30**, pp. 1159–1168.
[16] Dunn, M. G., 1989, ''Phase and Time Resolved Measurements of Heat Transfer and Pressure in a Full Stage Rotating Turbine,'' Proceedings, ASME/IGTi Turbo Expo. (89-GT-135).
[17] Piccini, E., Guo, S. M., and Jones, T. V., 2000, ''The Development of a New Direct-Heat-Flux Gauge for Heat-Transfer Facilities,'' Meas. Sci. Technol., **11**, pp. 342–349.
[18] Doorly, J. E., 1985, ''The Development of Heat Transfer Measurement Technique for Application to Rotating Turbine Blades,'' Ph.D. thesis, Department of Engineering Science University of Oxford, Oxford, UK.
[19] Anthony, R. J., Oldfield, M. L. G., Jones, T. V., and LaGraff, J. E., 1999, ''Development of High-Density Arrays of Thin Film Heat Transfer Gauges,'' Proceedings, 5th ASME/JSME Thermal Engineering Joint Conference, San Diego, USA (AJTE99-6159).
[20] Wright, G., 2000, ''Fire Certification in Aero Engines,'' 4th Year Project Report, Department of Engineering Science, University of Oxford, Oxford, UK.
[21] Abu Talib, A. R., 2003, ''Detail Investigation of the Low-Temperature Analogy of an Aircraft Engine Standard Fire-Test,'' Ph.D. thesis, Department of Engineering Science, University of Oxford, Oxford, UK.
[22] Eckert, E. R. G., 1955, ''Engineering Relations for Friction and Heat Transfer to Surfaces in High Velocity Flows,'' J. Aeronaut. Sci., **22**, pp. 585–587.
[23] Kays, W. M., and Crawford, M. E., 1993, *Convective Heat and Mass Transfer*, 3rd ed., McGraw–Hill.
[24] Loftus, P. J., and Jones, T. V., 1983, ''The Effect of Temperature Ratios on the Film Cooling Process,'' J. Eng. Power, **105**, pp. 615–620.
[25] Forth, C. J. P., 1985, ''An Investigation of Scaling Parameters Governing Film-Cooling,'' Ph.D. thesis, Department of Engineering Science University of Oxford, Oxford, UK.
[26] Fitt, A. D., Forth, C. J. P., Robertson, B. A., and Jones, T. V., 1986, ''Temperature Ratio Effects in Compressible Turbulent Boundary Layers,'' Int. J. Heat Mass Transfer, **29**, pp. 159–164.
[27] Petukhov, B. S., 1970, *Heat Transfer and Friction in Turbulent Pipe Flow With Variable Physical Properties, Advances in Heat Transfer*, **6**, pp. 503–564, Academic Press.
[28] Rose, J. W., 1988, ''Fundamentals of Condensation Heat Transfer: Laminar Film Condensation,'' JSME Int. J., **31**, pp. 357–375.
[29] Ainsworth, R. W., 1976, ''Flow and Heat Transfer Research Related to Turbine Blading, Using Transient Techniques,'' Ph.D. thesis, Department of Engineering Science University of Oxford, Oxford, UK.

# Flow and Thermal Field Measurements in a Combustor Simulator Relevant to a Gas Turbine Aeroengine

**S. S. Vakil**

**K. A. Thole**

Mechanical Engineering Department,
Virginia Polytechnic Institute and State University,
Blacksburg, VA 24061

*The current demands for high performance gas turbine engines can be reached by raising combustion temperatures to increase power output. Predicting the performance of a combustor is quite challenging, particularly the turbulence levels that are generated as a result of injection from high momentum dilution jets. Prior to predicting reactions in a combustor, it is imperative that these turbulence levels can be accurately predicted. The measurements presented in this paper are of flow and thermal fields produced in a large-scale combustor simulator, which is representative of an aeroengine. Three-component laser Doppler velocimeter measurements were made to quantify the velocity field while a rake of thermocouples was used to quantify the thermal field. The results indicate large penetration depths for the high momentum dilution jets, which result in a highly turbulent flow field. As these dilution jets interact with the mainstream flow, kidney-shaped thermal fields result due to counter-rotating vortices that develop.* [DOI: 10.1115/1.1806455]

## Introduction

The flow and thermal fields in a combustor are one of the most complex occurrences in a gas turbine engine and subsequently the most difficult to predict. Typical gas turbine engine combustors for aeroengines have a chamber with a flow area defined by an annulus containing evenly spaced fuel-injection nozzles. Annular combustion chambers have the advantage of requiring less space and weight than cannular chambers, for example, but have the disadvantage of being difficult to obtain both a uniform air-fuel distribution and exit condition.

To evaluate the flow and thermal fields that occur in a typical combustor of an aeroengine and to further our computational predictive methods, a large-scale facility was developed to simulate prototypical combustor flows. Although the simulation presented in this paper has not included the reacting flow thereby not including such effects as the heat release due to combustion, it is important to recognize that we should begin by determining whether we can experimentally and computationally simulate the nonreacting flow field. The heat release, for example, will depend upon the mixing characteristics of the dilution jets. If the dilution jets cannot be accurately simulated under the nonreacting conditions, it would be difficult to simulate the reacting flow field. In particular, predicting the turbulent flow fields for high momentum, normal jets (dilution jets) in crossflow is very difficult. For the design of the facility reported in this paper, nonuniformities in both the span (radial) and pitch (circumferential) directions exiting the combustor have been simulated through the use of cooled combustor walls, ensuring representative near-wall flows, and dilution jets, ensuring representative mainstream flows with high levels of turbulence.

The objective for the work reported in this paper was to quantify the flow and thermal field conditions for a prototypical combustor design that is nonreacting. Predictions of highly separated jets are relevant to that occurring in most aeroengine combustor designs. The dataset reported in this paper can be used for direct comparisons to computational fluid dynamics simulations for the geometry provided. Most often the turbulence produced is underpredicted with standard two-equation turbulence models (typically used in industry). This underprediction results in two concerns. First, the mean flow field will be predicted to have much stronger secondary flows (counter-rotating vortices from the dilution jets) than are actually present. Also, the trajectory of the dilution jets will not be accurately predicted, which make it impossible to track the mixing zones. Second, the mixing characteristics will be underpredicted resulting in a misprediction of the temperature profile entering the turbine. The data provided in this paper gives the community an opportunity to compare their predictions of the flow and thermal field in a scaled-up combustor prior to predicting the more complicated case with reacting flow. After describing the development of the combustor simulator facility, this paper describes the experimentally measured flow and thermal fields.

## Relevant Past Studies

Many experimental studies have been reported in the open literature documenting both experimental and computational data for model combustor flows. The large number prevents a full discussion of all of the results in our paper. None of these studies, however, have provided spatially resolved mean and turbulent flow fields as well as thermal fields for a combustor simulator that includes two rows of staggered dilution jets, and a film-cooled liner wall, which are all upstream of a stator vane sector. The combustor geometry reported in our paper is modeled after a modern aeroengine design in which both liner-cooling and dilution jets are simulated. While a complete summary of the literature documenting combustor-type measurements can be found in Barringer [1], only a few relevant studies will be discussed in our paper.

Since the work presented in our paper is for a nonreacting combustor, it is necessary to address any differences that may occur between the measurements we are reporting and those for a reacting combustor. Zimmerman [2] conducted one of the first investigations that measured combustor-generated turbulence at the exit of a can-type combustor. Turbulence levels, based on local velocities, ranged between 7% (at idle conditions) and 10% (at takeoff

Contributed by the International Gas Turbine Institute (IGTI) of THE AMERICAN SOCIETY OF MECHANICAL ENGINEERS for publication in the ASME JOURNAL OF ENGINEERING FOR GAS TURBINES AND POWER. Paper presented at the International Gas Turbine and Aeroengine Congress and Exhibition, Atlanta, GA, June 16–19, 2003, Paper No. 2003-GT-38254. Manuscript received by IGTI, October 2002, final revision, March 2003. Associate Editor: H. R. Simmons.

conditions). The measurements indicated the same turbulence levels independent of whether combustion took place. Goldstein et al. [3] performed LDV measurements at the exit of two can-type combustors with and without combustion to determine its effect on the velocity and turbulence profiles at the combustor exit. They reported turbulence levels, based upon local velocities, ranging between $25\% < Tu < 35\%$ without reactions and $15\% < Tu < 25\%$ with reactions. The dependence of the turbulence levels upon reactions contradicts the measurements performed by Zimmerman [2] and Moss [4], who showed no dependence.

Cameron et al. [5] conducted detailed spatial mappings of velocity and temperature in the nonreacting and reacting environment of a model gas turbine combustor with a dilution jet, similar to that of our configuration. They concluded that a strong on-axis recirculation zone located upstream of the dilution jets was present in the nonreacting case, but was dissipated in the reacting case. The combustor exit turbulence levels were 25% for the reaction case, but no data was available for the nonreacting case.

While some differences may occur, it is important to recognize data is needed to allow for computational benchmarking. A number of studies have demonstrated the shortfalls of computational predictions for combustor-type flows in that there is an underprediction of the turbulence levels. Predicting the turbulence levels is relatively important if accurate mixing predictions are desired. Gulati et al. [6] measured the mean and rms temperatures at the exit plane of a full-scale, ten-cup, double annular research combustor. Their results indicated that the dilution air had a significant affect on the mean and rms temperature profiles. As the outer row of dilution air was increased, the jets pushed the combustion zone toward the inner liner and increased the peak temperature. While these trends were predicted well by computational models using the standard $k$-$\epsilon$ turbulence model, the model consistently underpredicted the fluctuations at the exit. This trend of underpredicting the turbulence levels is in agreement with the findings of Holdeman [7] and Stitzel [8].

Malecki et al. [9] reported results using the standard $k$-$\epsilon$ turbulence model with wall function near-wall modeling. To overcome the low turbulence level predictions, reduced Schmidt numbers (Sc) were used to compensate for the low turbulence levels in the mixing of the product species. Using this scheme, good agreement was achieved between circumferentially averaged exit temperature profiles from the test rig data and the computational predictions.

Several studies have been reported that discuss the various effects of different combustor features. In the majority of these studies, the dictating features of a combustor flow field are governed by the presence of high momentum dilution jets. Goebel et al. [10], for example, measured velocity, turbulence, and temperature profiles downstream of a reacting small-scale combustor. They found that with an appreciable swirl velocity, the dilution jets acted to disrupt the swirl and actually reduce the turbulence levels. Without swirl and at low swirl velocities, the transverse dilution jets increased the turbulence levels. Stevens and Carotte [11] also experimentally investigated the combustor dilution zone and jet development by focusing on the downstream thermal field in a nonreacting, annular combustor simulator. Their measurements revealed each jet exhibited a kidney-shaped contour, which is a characteristic of jets-in-cross-flow. Liou and Wu [12] made measurements for a nonreacting combustor that consisted of a rectangular duct with two opposing side jets. One finding from the study was that the turbulence was inhomogeneous and anisotropic throughout most regions of the combustor simulator.

Holdeman [7] simulated a nonreacting gas turbine combustion chamber by conducting computations and experiments on the mixing of single, double, and opposed rows of dilution jets with an isothermal or variable temperature mainstream in a confined subsonic cross flow. The principle finding from the investigation was that the momentum flux ratio of the jets dictated the exit velocity and temperature profiles. The results from the cases involving opposed rows of jets revealed that for in-line jets the two streams mixed very rapidly and that the effective mixing height was half the duct height for equal momentum flux ratios on both sides.

In summary, comparing the results from the studies presented in the literature indicate that there are some differences for a reacting and nonreacting flow near the primary zone. Most studies have indicated the importance of simulating the dilution jets. The turbulence levels at the combustor exit that were reported for the studies with reaction, were very similar to those found in the studies without reaction. There was good agreement between computations, which used some form of a two-equation turbulence model, and experiments in predicting dilution jet penetration and combustor exit temperature profiles. The computational models, however, do not have the ability to accurately predict the turbulent mixing that occurs in the dilution zone. As a result of this inability, we believe that it is important to provide data documenting the flow in a combustor environment that is nonreacting. This data provides the first test for computational predictions.

## Experimental Facilities

The development of the combustor simulator used in our study was previously described by Barringer et al. [13]. The geometric scaling factor for the combustor was $9\times$, which allows for good measurement resolution in the experiments. This scaling factor was matched to that of a linear turbine vane cascade that was pre-existing. Note that the turbine vane is not the focus of this paper. Measurements that are presented in this paper include mean and turbulent velocities as well as mean temperatures.

**Experimental Facilities.** Other than performing the measurements in an actual operating engine, it is not feasible to provide a measurement environment with representative turbine engine conditions. In designing this combustor simulator, the parameters that were chosen for a prototypical combustor for aircraft applications included the following: (i) a nondimensional acceleration parameter through the combustor; (ii) a combustor exit velocity that ensured the needed inlet Reynolds number for the downstream turbine section; (iii) coolant-to-mainstream momentum flux ratios of the liner cooling holes and the dilution holes; and (iv) scaled geometric features of a combustor including the film-cooling staggered hole pattern and dilution hole size and placement. Note that the parameters for the prototypical engine combustor are for actual running (hot) operating conditions. The air loading parameter (ALP defined in the nomenclature) for the wind tunnel design was $0.40\times10^{-4}$.

Figure 1 illustrates the wind tunnel containing the combustor simulator and turbine vane test sections. Downstream of a primary heat exchanger is a transition section that divides the flow into three channels that include a heated primary channel, representing the main gas path (center arrows), and two symmetric secondary channels (outer arrows), representing the coolant flow path. Within the transition section of the primary channel, the flow immediately passes through a perforated plate that provides the necessary pressure drop to control the flow splits between the primary and secondary passages. At a distance 2 m downstream of the perforated plate, the flow passes through a bank of heaters followed by a series of screens and flow straighteners. The heater section comprises three individually controlled banks of electrically powered, finned bars supplying a maximum total heat addition of 55 kW. Downstream of the flow straighteners, the heated primary flow enters the combustor simulator. In the combustor simulator, secondary coolant flow is injected into the primary flow passage through cooling panels for the combustor liner and through dilution holes. In addition, the flow is accelerated prior to entering the turbine section. In addition to heat being rejected from the primary heat exchanger, the flow in the secondary passages must pass through a second heat exchanger to further reduce

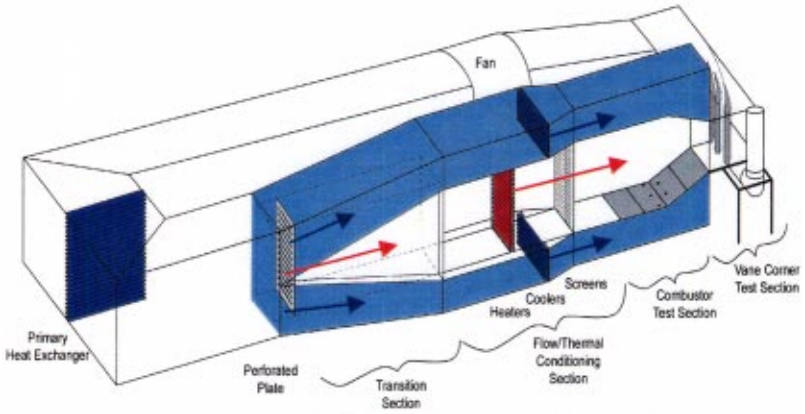


**Fig. 1 Illustration of the wind tunnel facility used for the combustor simulator experiments**

the coolant flow temperature. The flow in the secondary passages is then directed into a large plenum that supplies combustor liner coolant and dilution flow.

The cooling hole pattern in the panels is illustrated in Figs. 2(*a*)–2(*b*). To ensure representative coolant flow splits among the four liner panels and dilution rows, separate supply chambers with adjustable shutters were used. The mass flow exiting the film-cooling holes was set by applying the appropriate pressure ratio between the supply plenum and the exit static pressure. Using previously documented discharge coefficients (Barringer et al. [13]) the mass flows through the panels were determined. The mass flows exiting the dilution holes were set by directly measuring the velocity through the use of a pitot probe installed at the exit of the dilution hole.

The combustor simulator begins at the start of the first panel, as illustrated in Fig. 2(*a*). The cross-sectional area of the simulator at this location is 1 m in height ($H_{in}$) and 1.1 m in width ($W$). At the exit of the simulator, the cross-sectional area is 0.55 m in height and remained 1.1 m in width, giving an area ratio of 1.8. The width was to allow for a span that was slightly greater than a turbine sector while the height was matched to that of the radial extent of a first vane.

The liners for the combustor simulator were a streamwise series of four film-cooled panels that started 2.7 vane chords (1.6 m) upstream of the turbine test section. The first two panel lengths were 39 and 41 cm while the third and fourth panels were 37 and 43 cm. The panels extended across the full width of the test section, which was slightly greater than a scaled turbine sector. The

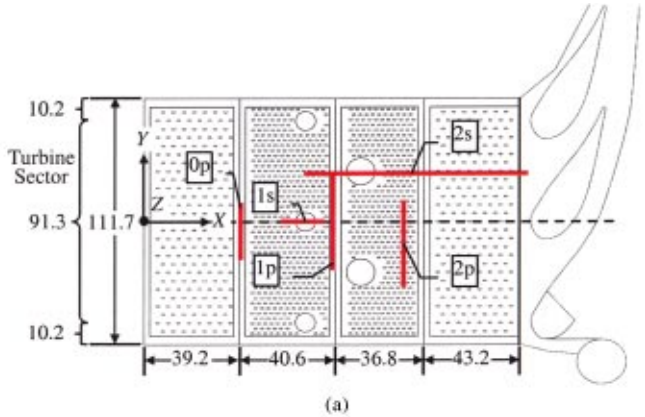


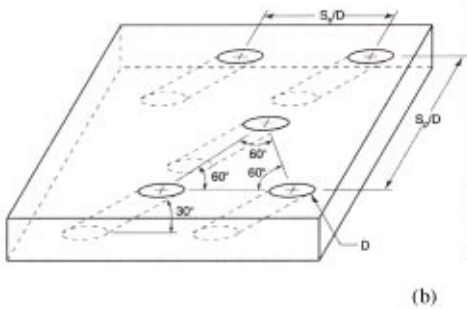


| | $S_y/D$ | $S_x/D$ |
|---|---|---|
| **Panel 1** | 10.1 | 5.8 |
| **Panel 2** | 6.1 | 3.5 |
| **Panel 3** | 6.1 | 3.5 |
| **Panel 4** | 10.1 | 5.8 |
| **Dilution 1** | 60 (5.4 $D_1$) | 90 (8.1 $D_1$) |
| **Dilution 2** | 60 (3.8 $D_2$) | 121 (7.6 $D_2$) |

**Fig. 2 (*a*) Layout and measurements planes for the combustor simulator (dimensions in cm). (*b*) Illustration and description of cooling hole arrangement for liners.**

**Table 1 Summary of Coolant Flow Conditions**

| | % Mass Flow Addition Based on Local Flow Rate | Momentum Flux Ratio Based on Local Mass-Averaged Velocity | Mass Flux Ratio Based on Local Mass-Averaged Velocity | Density Ratio Based on Ups tream Flow Conditions | Ratio of Mass-Averaged Velocity to Inlet Velocity |
|---|---|---|---|---|---|
| Panel 1 | 2.6 | 9 | 3.2 | 1.12 | 1 |
| Panel 2 | 6.3 | 9 | 3.2 | 1.12 | 1 |
| Panel 3 | 5.4 | 9 | 3.2 | 1.12 | 1.6 |
| Panel 4 | 2.2 | 9 | 3.2 | 1.12 | 2.7 |
| Dilution 1 | 18.5 | 128 | 12 | 1.12 | 1 |
| Dilution 2 | 12.5 | 32 | 6 | 1.12 | 1.6 |

first two panels were flat to maintain a constant cross-sectional area while the following two panels were inclined at 15.7 deg to give the required area contraction. The panels were constructed of 1.27 cm thick urethane foam with a low thermal conductivity ($k = 0.037$ W/mK) to allow for adiabatic surface temperature measurements. The dense matrices of film-cooling and dilution holes were cut into the urethane foam using a water jet.

One parameter that is not representative is the coolant-to-mainstream density ratios, which are typically quite high. Typical operating conditions consisted of a flow temperature just downstream of the heater of nominally 50°C and a coolant flow temperature of 20°C. As the coolant flow progressed downstream through the secondary flow channel, there was a small increase in the fluid temperature of nominally 1°C. Although the density ratios were not matched, the jet-to-mainstream momentum flux ratios and percentage of mass flow addition by both the film-cooling and dilution holes were representative. The momentum flux ratio is the parameter that most affects mixing characteristics of jets in cross-flow at high momentum flux ratios. The cooling hole patterns, shown in Fig. 2(*b*), were configured in equilateral triangles and spaced evenly across the panel surface. The diameter of the cooling holes was 0.76 cm, giving an $L/D = 3.3$.

The dilution hole diameters were designed to insure the percent mass addition of the dilution fluid and coolant-to-mainstream momentum flux ratios were representative of that in an engine. This first row of dilution holes has three holes evenly spaced with the center hole being aligned with the center of the simulator (and also the vane stagnation). This first row is located at 43% of the combustor length (0.67 m) downstream of the start of the panels. The dilution holes in the first row have a diameter that is 8.5 cm. The second row of dilution holes was located on the third panel at 57% of combustor length (0.90 m) downstream of the start of the panels. The second row of dilution holes contained two holes having a diameter of 12.1 cm. The two dilution holes were staggered with respect to the first row of holes. The supply chamber for the dilution flow was required to be some distance from the hole exits giving an $L/D$ ratio of 1.5 for both rows. The combustor simulator is symmetric about the vertical mid-span meaning that for each row the dilution holes were aligned with one another in the pitchwise and streamwise directions.

As indicated for the operating conditions of the results reported in this paper in Table 1, 45% of the flow is directed through the primary passage of the combustor simulator while 55% of the flow is directed through the secondary coolant passages for the liner coolant and dilution holes. Of the total cooling flow 36% is injected through the film-cooling holes and 64% is injected through the dilution holes.

**Instrumentation and Measurement Uncertainty.** Thermocouples were used in monitoring inlet and coolant temperatures as well as taking the thermal fields within the combustor. All of the temperature measurements were made using 30-gauge, type E thermocouples that were connected to a data acquisition system through 20-gauge thermocouple extension wire. All of the thermocouples used in this study were made using an argon-gas thermocouple welder that resulted in spherical beads ranging in diameter from a minimum of approximately 0.8 mm to a maximum of ~1 mm. The thermal fields were taken using a 21 probe thermocouple rake. The rake spanned a total distance of 10.2 cm with thermocouples evenly spaced every 5.1 mm. Each thermocouple probe on the rake consisted of a 5.1 cm long, 2.5 mm outer diameter aluminum casing that encapsulated the thermocouple wire. The approximate flow blockage was shown to have no effect on the measured thermal field. Each thermocouple bead is fixed approximately 6.4 mm from the end aluminum shaft in order to minimize heat conduction effects from the aluminum rod to the thermocouple.

Velocities were measured using a two- and three-component laser Doppler velocimeter (LDV). The flow was seeded with olive oil particles that were nominally 1 $\mu$m in diameter. The probability of obtaining a sample was proportional to the speed of the flow; therefore, statistical particle bias corrections were applied to the data by weighting each individual sample based on the residence time of a particle in the probe volume.

In taking flow plane measurements that were aligned with the flow direction, a single fiber-optic LDV probe capable of measuring two components was used. This setup used a 350 mm focusing lens without a beam expander and had a measurement volume of 90 $\mu$m in diameter and 1.3 mm in length. The plane was acquired with the probe perpendicular to the outer wall surface. This allowed for the direct measurement of the local streamwise velocity component, $u$. However, in order to take measurements near the surface of the liner panel, the probe was slightly tilted at 7 deg, whereby there was little effect on the true vertical component measurements.

For the measurements taken in the cross-stream direction where three-component velocity measurements were made, two separate fiber optic probes were used. To allow the measurement volume of the probes to reach the mid-pitch of the combustor simulator, a 2.6 magnification beam expander along with a 750 mm focusing lens were used. With the use of the beam expander, the measurement volume was 73 $\mu$m in diameter and 1.3 mm in length. Using these two probes, the measurements were conducted through a nonorthogonal setup requiring the velocity components to be transformed into the true components. Furthermore, as with the single LDV probe measurements, a tilt was applied to both probes to allow for near-wall measurements. To ensure a single beam crossing, both probes were turned 13 deg toward each other off the cross-stream direction while the vertical tilt angle was set to 7 deg.

In order to compare the day to day repeatability of the test conditions and ensure that the correct velocity transformations were made, the two- and three-component LDV data were compared where streamwise and spanwise measurement planes overlapped. This data is shown in Fig. 3 whereby the measurement times spanned several weeks. The location of this data was just downstream of the first dilution row and in the spanwise middle of

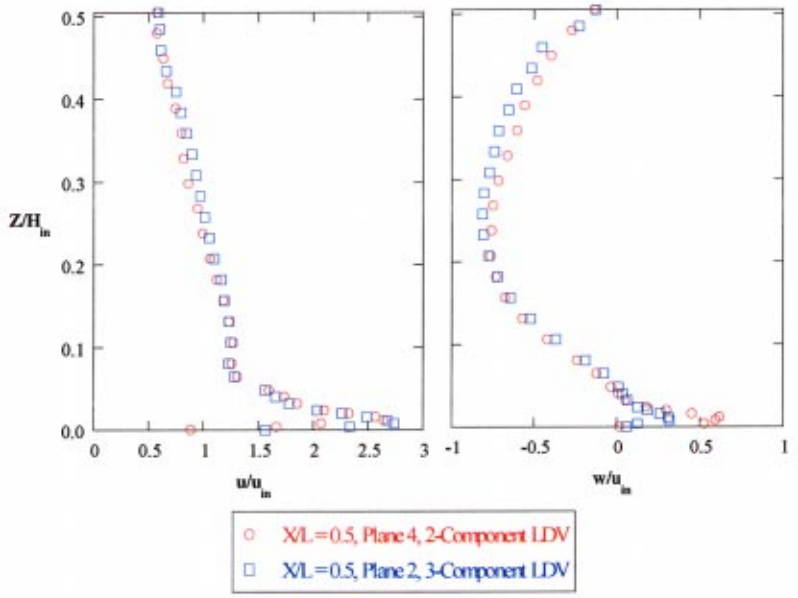


**Fig. 3 Comparisons of two and three-component LDV profiles measured independently in an overlap location just downstream of the first row of dilution**

the outer second row dilution hole. This data indicates consistency of the velocity transformations that were applied to the data as well as the repeatability of the test conditions.

The nominal sampling time for each measurement location was 40 s whereby 15,000 data points were acquired for each component. For the longer 750 mm focusing lens most measurement locations had an average sampling time of approximately 100 s for the same sample size.

The partial derivative and sequential perturbation methods, described by Moffat [14], were used to estimate the uncertainties of the measured values. Precision uncertainties were calculated based on a 95% confidence interval. The precision uncertainty for the streamwise rms velocities was 2.6% while the bias uncertainty for the mean velocity measurements was 1%. The bias and precision uncertainties on the thermal field values, was $\pm 0.04$, giving an uncertainty of 4.5% at $\theta=0.9$ and 12.6% at $\theta=0.3$.

## Measured Flow and Thermal Field Results

The measurements made in this study were taken at a number of different locations within the combustor simulator, as shown in Fig. 2(*a*). These locations were chosen to illustrate the different flow conditions that can occur throughout the combustor and include the following: (i) downstream of the first liner whereby film-cooling holes are present (plane $0p$); (ii) downstream of the first row of dilution holes whereby the jets are being injected at a high momentum flux ratio (planes $1p$ and $1s$); and (iii) downstream of the second row of dilution holes whereby the jets are being injected from a liner wall that is contracting (planes $2p$ and $2s$). The flow conditions that were set are summarized in Table 1 for each of the panel and dilution flows. Note that two different film-cooling flows were studied for the first panel ($I=3$ and 9), but for the remainder of the measurements an $I=9$ condition was set for this panel.

**Liner With Multiple Rows of Film-Cooling Holes.** Thermal field measurements were performed just downstream of the first cooling panel in plane $0p$ for two different flow conditions. The measurement location was at $X/L=0.24$, which is two film-cooling hole diameters downstream of the last row of cooling holes ($X/d=2$) in panel one. The average momentum flux ratios for this panel were set to either $I=3$ or 9, giving an average mass flux ratio for the panels of $M=1.8$ and 3.2, respectively. Fifteen rows of staggered film-cooling holes were present in this panel

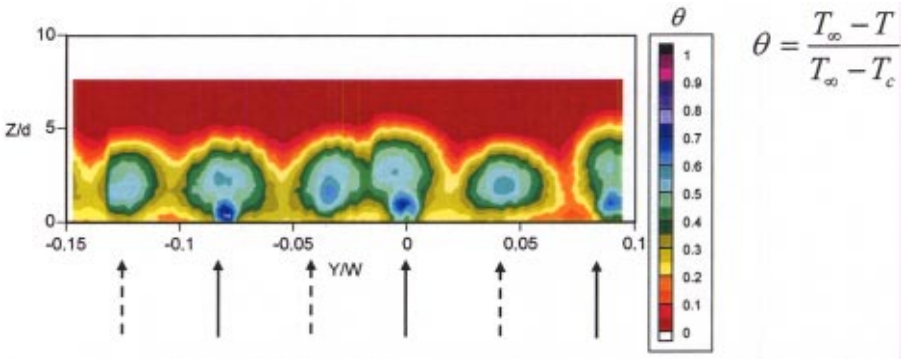


**Fig. 4 Film-cooling thermal field measurements in plane $0p$ with an average liner flow of $I=3$, $DR=1.1$**

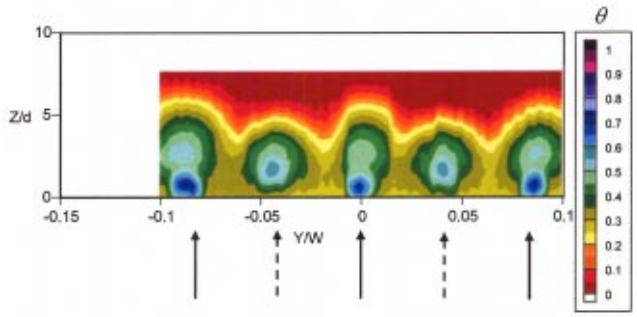


**Fig. 5 Film-cooling thermal field measurements in plane 0*p* with an average liner flow of *I*=9, *DR*=1.1**

with the hole spacing as that indicated in Fig. 2(*b*). While these measurements were conducted, the flow condition for the remaining liner panels was set at the same condition as the first panel ($I=3$ or 9). Figures 4 and 5 show the measured thermal fields for the two blowing conditions. The solid arrows represent the location of the last row of film-cooling holes while the dashed arrows represent the pitch location of the previous row of film-cooling holes. As can be seen by the thermal field measurements, the jets are periodic in the pitch direction across the panel.

Figures 4 and 5 indicate a cooler jet for the row of jets closest to the measurement plane (solid arrows) as compared with the jets of the previous row (dashed arrows). For both flow conditions, the peak temperature contour representing the coolest fluid is located away from the wall. A separated jet condition is expected given the high momentum flux ratio conditions for both cases. The thermal field contours for the row of cooling holes closest to the measurement plane indicate a double-peak with the second peak being at a slightly warmer temperature ($\theta=0.5$) than the primary peak ($\theta=0.7$). The second peak is located just above the coldest peak and is a remnant of the upstream cooling jet at the same pitchwise alignment. Interestingly, the contour levels for the dashed arrows (upstream row) do not have this double peak, which indicates that given enough streamwise distance the streamwise jets merge into one cooler core.

Although the conditions through the holes differ by a large amount of cooling flow, the core of the jets closest to the measurement plane (coldest contour) is nominally at the same temperature level at this location ($\theta=0.7$) for both blowing ratios. There are two real differences between these two cases. First, the penetration depth for the $I=9$ case appears to be greater than the $I=3$ case. Second, and more importantly, the fluid temperature between the jets near the wall appears to be cooler for the $I=9$ case ($0.25<\theta<0.35$) as compared with the $I=3$ case ($0.15<\theta<0.2$).

**Downstream of the First Row of Dilution Holes.** The thermal field measured in the streamwise direction through the first row of dilution jets is shown in Fig. 6. Recall at this location in the combustor simulator, the cross-sectional area of the simulator is the same as that of the entrance. The spanwise distance ($Z$) is normalized by this height ($H_{in}$). The momentum flux ratio for this large dilution jet is $I=128$ while the mass flux ratio is $M=12$.

The contours in Fig. 6 indicate a penetration distance that is approximately 18% of the height before the jet trajectory is bent over by the mainstream flow. Upstream of the jet injection, there is a relatively thick film-cooling layer that is being transported into the free stream by the dilution jet. It is also clear that the temperature gradients are quite high at the jet-mainstream interface near the jet injection, while farther away from the wall the temperature contours are spreading due to the turbulent mixing. The penetration depth of these dilution jets does not extend to the centerline, which is quite probably a result of the opposing jets that are aligned in the pitchwise and streamwise locations.

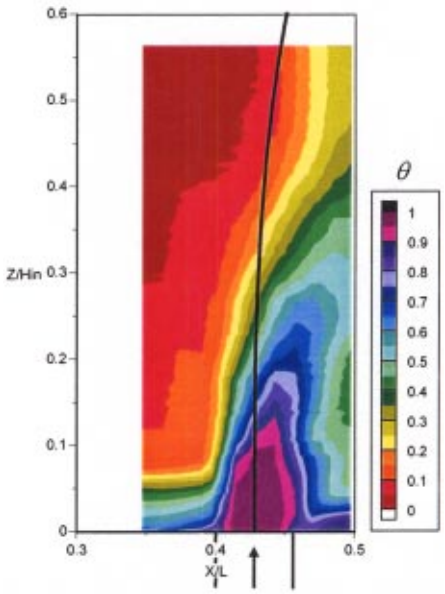


**Fig. 6 Thermal field contours in a streamwise plane through a first row dilution hole (plane 1*s*) with Lefebvre's [15] jet penetration correlation**

The solid line shown in Fig. 6 indicates the penetration distance predicted by the correlation given by Lefebvre [15]. The correlation overpredicts the trajectory of the jet and underpredicts the bending of the jet. One plausible reason for the misprediction may be due to the fact that there is an opposing jet and that these dilution jets are at very high momentum ratios ($I=128$).

Figure 7 shows the measured thermal field for a plane that extends in the pitchwise direction downstream of the first row of dilution jets at a location that is two film-cooling hole diameters downstream of the last row of cooling holes in the second liner. This location is 1.3 hole diameters ($X=1.3D_1$) downstream of the dilution hole whereby this distance is measured from the hole centerline. This larger plane was taken to illustrate the pitchwise symmetry of the dilution flow. These thermal fields indicate that the coolant from the dilution jets has been transported to a region slightly offset from the center of the two lobes of the kidney-shaped vortex. It is important to recognize that the distance be-

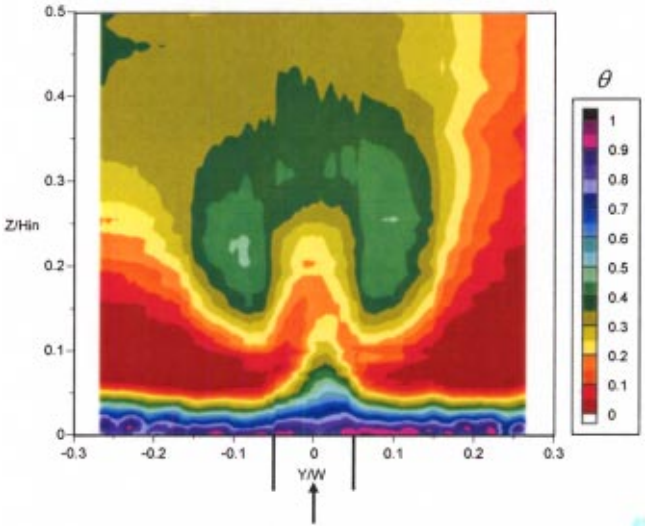


**Fig. 7 Thermal field contours in plane 1*p***

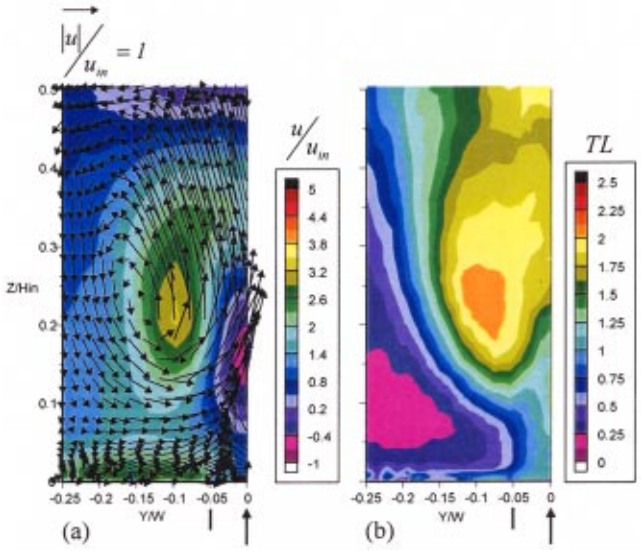


**Fig. 8 Measured (*a*) secondary velocity vectors with contours of $u/u_{in}$ and (*b*) turbulence levels for plane 1*p***

tween the two lobes as illustrated in Fig. 7 is quite large relative to that which would occur for a jet-in-cross-flow without an opposing jet.

At the dilution jet centerline, Fig. 7 illustrates the presence of film cooling near the wall even though there is only one row of cooling holes downstream of the dilution jets and upstream of this measurement plane. It is quite plausible that some of the upstream film-cooling flow has been wrapped around the dilution jet and is present at this location. It is also interesting to note the warmer temperatures that occur as one progresses up from the film-cooling layer to the dilution jet core at $Y/W=0$. The warmest fluid occurs at the same location as the highest negative streamwise velocity contour indicating a strong vortex motion, as will be discussed for Fig. 8.

Figure 8(*a*) shows the secondary velocity vectors ($v$ and $w$) superimposed on the normalized streamwise velocity ($u/u_{in}$) contours in plane 1*p*. The measurement plane was taken across a symmetric section of the combustor simulator. There is a clear kidney-shaped vortex exhibited by the secondary velocity vectors as a result of the shear produced from the jet-mainstream interaction. The velocity contours indicate a strong backward streamwise velocity located at $Z/H_{in}=0.15$ at the hole centerline ($Y/W=0$). The contours indicate velocities as high as three times the inlet velocity near $Y/W=-0.075$ and $Z/H_{in}=0.2$. These high velocities do not coincide with the center of the vortex core. Near the spanwise center of the plane ($Z/H_{in}=0.5$), the streamwise velocity contours indicate a nearly stagnant region as a result of the interaction between the top and bottom dilution jets.

The turbulent flow field was also quantified for the cross-stream plane 1*p*, as shown in Fig. 8(*b*). The turbulence levels were calculated using all three velocity fluctuations and then normalized using the inlet velocity ($u_{in}$). The turbulence levels produced by the jet-mainstream interaction are incredibly high, particularly in the high-velocity region and at the mid-span region where the jets are impacting one another.

**Downstream of the Second Row of Dilution Jets.** The thermal field through the center of the second row of dilution jets is shown in Fig. 9 for plane 2*s*. The second row of dilution jets are injecting near the start of the contraction section of the combustor simulator. The momentum flux and mass flux ratios for these jets are somewhat lower than the first row at $I=32$ and $M=6$.

While the momentum flux ratio is much lower for the second row of dilution jets as compared to the first row, the physical penetration distance is not that different. In comparing the physical penetration distances of the $\theta=0.95$ contour in Figs. 6 and 9

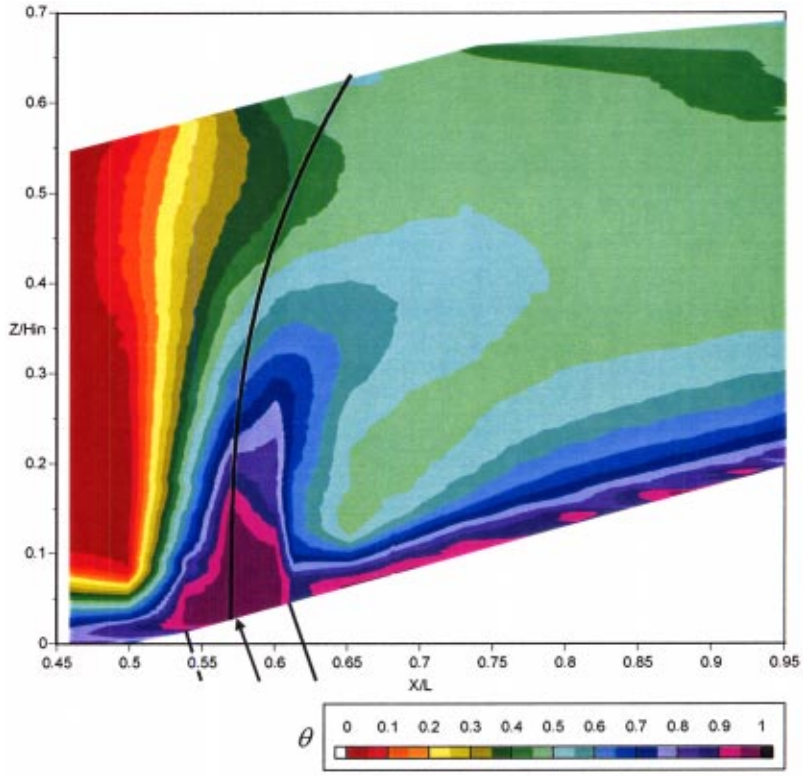


**Fig. 9 Thermal field contours for plane 2*s* showing Lefebvre's [15] jet penetration correlation**

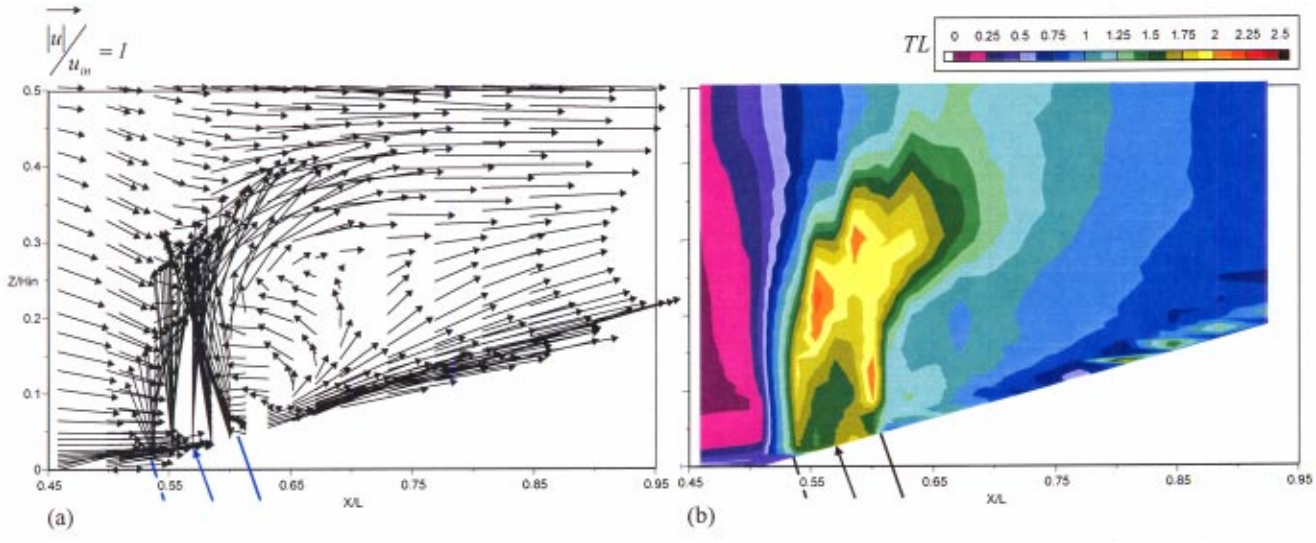


**Fig. 10 (*a*), (*b*) Flow field vectors (left) and contours of turbulence levels (right) for plane 2*s*, downstream of the second row of dilution jets**

for the two rows of dilution holes, the $Z/H_{in}$ penetration depth for each is 0.1 and 0.12, respectively. In relating this distance to the respective hole diameters, however, there is a different answer. The first row of jets penetrated to a $Z/D_1=1.2$ while the second row of jets only penetrated only to $Z/D_2=0.95$. The solid line in Fig. 9 indicates the dilution jet trajectory predicted by Lefebvre's correlation [15]. As with the higher momentum dilution jets, the correlation predicts the trajectory of the dilution flow fairly accurately near the liner panels; however, the bending of the dilution flow is underpredicted as the jet penetration continues into the mainstream. It is worth mentioning that Lefebvre's correlation for this lower momentum dilution jet seems to fit better than it did for the higher momentum first row dilution jets.

Similar to that of the first row of holes, the thermal gradients reduce in magnitude at the jet-mainstream interface as one progresses farther from the wall. Figure 9 also indicates the presence of a cooler bulge near $X/L=0.65$ with a thermal contour level of $\theta=0.45$. This cooler region is a result of the lateral spreading of the cooler fluid from the first dilution row.

The thermal field contours for the near-wall fluid indicate a relatively thick layer upstream of the dilution jet. Just downstream of the dilution jets, however, the layer is much thinner but there is still coolant present. The coolant that is present near the wall downstream of the injection is there, despite the fact that there is some streamwise distance (one dilution hole diameter) between the dilution location and the film-cooling injection location. While the film-cooling layer near the wall is relatively thin just downstream of the dilution injection, this layer becomes relatively thick caused by the increased turbulence levels generated from the dilution jet-mainstream interaction.

Two-component LDV measurements were made for the streamwise plane 2*s* given the symmetric nature of this location (the $v$-component was nominally zero). The streamwise velocity vectors in Fig. 10(*a*) indicate a downward velocity as the flow approaches the dilution injection location. This downward velocity is thought to be the result of the mainstream flow being deflected away from the jet-to-jet impingement of the first row of dilution at the mid-span center. The velocity vectors indicate that most of the jet is exiting from the downstream portion of the dilution hole, but are pointed toward the upstream direction. This is consistent with the thermal field contours presented in Fig. 9. These high velocities have enough momentum to have a jet trajectory that is directed upstream.

Downstream of the jets, the velocity vectors indicate a very large recirculation region, which is characterized by warmer fluid behind the dilution jet. Near the wall, it is clear that there is also reversed flow just downstream of the jet. The coolant present near the wall may be in fact transported to this region from the downstream film-cooling holes, which is consistent with the thinner coolant layer. The closest film-cooling injection is located at $X=1D_2$ downstream on the dilution injection. Near $X/L=0.75$, which is slightly greater than two dilution hole diameters ($X=2D_2$) downstream of the jet injection, is the end of the recirculating region.

The vectors also indicate that the flow has been accelerated both in the near wall region, due to the film-cooling jets, and above the jet injection near the mid-span, due to the dilution jet blockage. As the flow exits the combustor, the streamwise profiles still have remnants of these faster regions.

Figure 10(*b*) shows the turbulent flow field measurements for

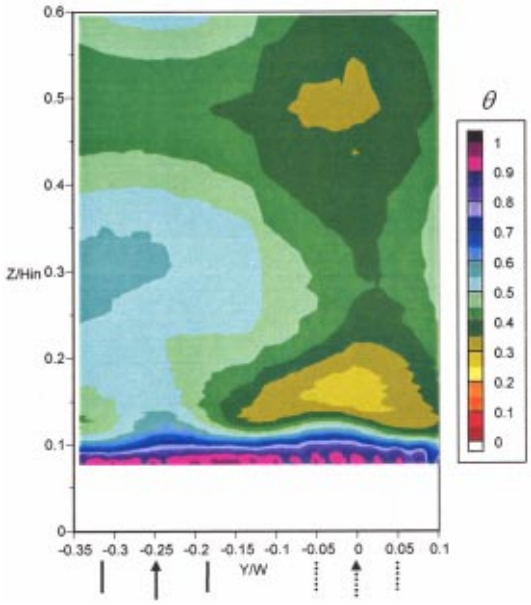


**Fig. 11 Thermal field contours in plane 2*p* downstream of the second row of dilution**

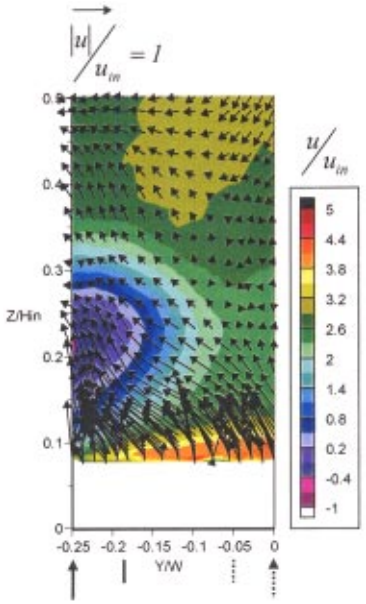


**Fig. 12 Secondary velocity vectors with contours of the streamwise velocities in plane 2*p***

plane 2*s*. The peak turbulence levels, which occur at the jet-mainstream interface, are 2.2 times greater than the inlet velocity. It is important to recognize that at the dilution jet injection location, the mass-averaged velocity is 2.7 times that of the inlet velocity (indicated in Table 1) as a result of the mass flow injection from the first row of dilution jets and the film-cooling addition. The jet turbulence itself is relatively lower than that occurring as the jet interacts with the mainstream flow. In the jet recirculating region, the turbulence levels are very high, considering the fact that the local flow velocities in this region are relatively low. The near-wall turbulence that is generated is also relatively high due to the film-cooling injection. As the flow exits the combustor, the levels relative to the local exit velocity are on the order of 20%.

Figure 11 shows the thermal field contours downstream of the second row of dilution jets (plane 2*p*) for a region larger than the symmetric locations to illustrate the thermal field symmetry. Note that both jets inject to approximately the same spanwise location relative to the mid-span. The dashed lines represent the spanwise injection location of the first row of dilution holes while the solid lines represent the second row of dilution holes. At this streamwise location, which is one dilution hole diameter downstream of the second row of dilution holes ($X=1D_2$), the coldest temperature contour for the dilution flow is $\theta=0.55$ located at $Y/W=-0.25$ at about $Z/H_{in}=0.3$. The warmer fluid shown near $Y/W=0$ at $Z/H_{in}=0.15$ is a remnant of the warm fluid that is trapped in the recirculating region downstream of the first row of dilution jets. A similarly warm region is located just above that region near the mid-span, which is a result of warmer fluid penetrating between the opposing first row of dilution jets.

Figure 12 shows the secondary velocity vectors superimposed on the streamwise velocity contours at the same plane 2*p* only with a smaller measurement region as compared with Fig. 10. At this location, it is clear that there is no evidence from the vectors as to a strong kidney vortex as there was in the case of the first row of dilution holes. The high turbulence levels, as will be illustrated in the upcoming figures, have caused a reduction in the swirl velocities. There is a strong upward flow that is a result of the contraction section of the combustor. The streamwise velocities indicate that the flow has accelerated to about three times the inlet velocity near the mid-span. At a span of approximately 25% of the inlet height, there is a near zero velocity just downstream of the dilution holes, similar to that of the first row of dilution jets, which is caused by the jet blockage. To illustrate the anisotropic behavior of the turbulence of the dilution jets, Figs. 13(*a*)–13(*c*) show the measured fluctuations for all three velocity components. As can be seen, all three contour plots illustrate a very different behavior. The highest fluctuation levels in this plane are 1.75 times that of the inlet velocity. It is important to remember that at this location the mass-averaged velocity is 2.7 times faster than the inlet velocity, which still translates to average rms levels that

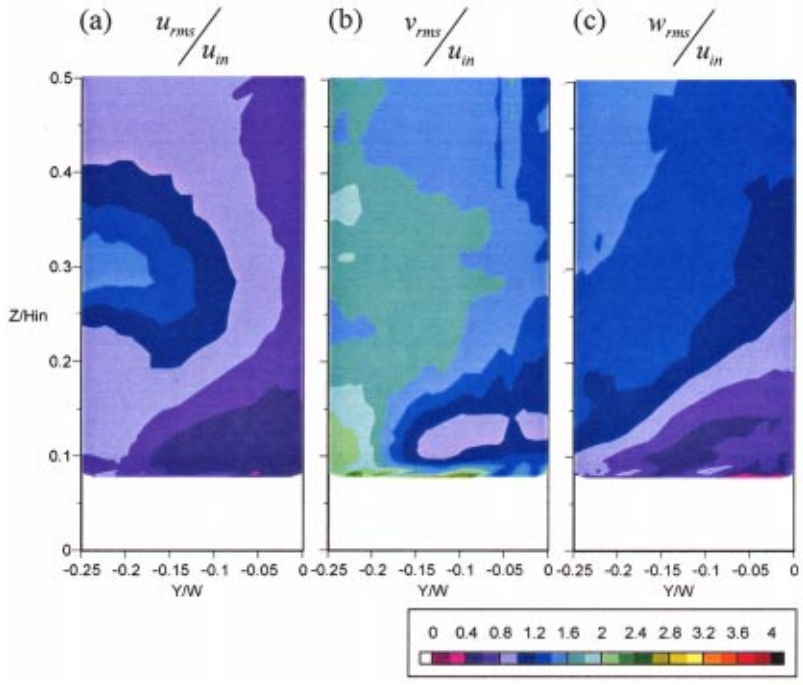


**Fig. 13 (*a*)–(*c*) Contours of the rms fluctuations for the flow in plane 2*p***

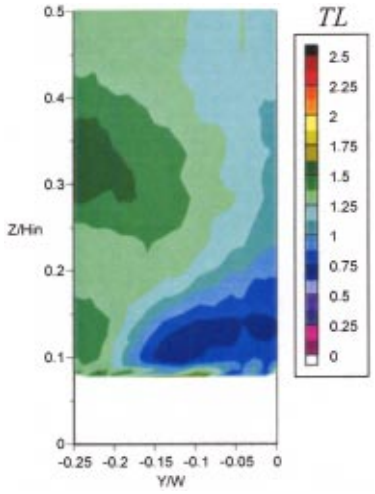


**Fig. 14 Contours of turbulence levels in plane 2*p***

are 0.65 times the local mass averaged velocity. The peak streamwise velocity fluctuations occurs at $Z/H_{in}=0.3$ and $Y/W=-0.25$, which coincides with the core of the jet (as indicated by the thermal field contours in Fig. 11). The peak spanwise velocity fluctuations ($v_{rms}$), which are slightly higher at 2.1 times the inlet velocity, occur near the liner wall just below the core of the jet. Similar to the streamwise fluctuations, the peak spanwise fluctuations occur at the core of the jet and above.

The turbulence levels for the pitchwise plane, which is a combination of the fluctuations for all three velocity components, is shown in Fig. 14 for plane $2p$. For the second row of injection ($Y/W=-0.25$), the peak level coincides with a region slightly higher than the core of the jet. While the levels are much lower, the peak region for the first row of dilution jets coincides more closely with the mid-span.

## Conclusions and Recommendations

The results of this study indicate the complexity of the flow that occurs in a typical aeroengine combustor. While these results were acquired with a nonreacting flow, it is important to have a place to begin when it comes to making comparisons with computational predictions. In particular, it is important that we are able to understand how the interactions take place between rows of dilution jets and liner film-cooling. The resolution of the measured data presented in this paper was only made possible through scaling up of a combustor.

The measurements indicate the dominance of the dilution jets on the flow and thermal fields. Kidney-shaped thermal fields were present as the result of the dilution jet-mainstream interaction. One notable feature was the spreading of the two kidney lobes that resulted from the impacting of the jets. Downstream of the dilution jet injection, there was a large recirculating region that transported warm fluid into the region just downstream of the injection. While the near-wall film of coolant is much thinner just downstream of the dilution holes, there is still coolant present. To determine whether the coolant was transported by vortices wrapping around the dilution jet or transported by the reverse flow downstream of the dilution jet is not known at this time. Further work needs to be conducted to determine the true mechanism that is important for combustor cooling strategies.

The turbulence levels were measured to be extremely high throughout the combustor as well as highly anisotropic. It is clear as to why current two-equation turbulence models underpredict these turbulence levels given the model assumptions of isotropic turbulence. The exit turbulence levels, based on the local average exit velocity were 20%.

Further studies need to be done to evaluate cooling schemes along the liner wall and ensure good coverage near the dilution holes. More detailed measurements are needed near the dilution holes to evaluate these cooling schemes. Given the results presented in this paper, it is possible to compare computational predictions with measured flow and thermal fields.

## Acknowledgments

The authors gratefully acknowledge United Technologies—Pratt and Whitney for their support of this work.

## Nomenclature

ALP = air loading parameter, $ALP=P_0^{1.75}A_{ref}D_{ref}^{0.75}e^{T/300}/\dot{m}$, Lefebvre [15]
$d$ = film cooling hole diameter
$D_1$, $D_2$ = dilution hole diameters for first and second rows
$H_{in}$ = combustor inlet height
$I$ = momentum flux ratio, $I=\rho_c U_c^2/\rho_\infty U_\infty^2$
$L$ = film cooling hole length, combustor simulator length
$\dot{m}$ = mass flow rate
$M$ = mass flux ratio, $M=\rho_c U_c/\rho_\infty U_\infty$
$P$ = vane pitch
$S_s$, $S_p$ = streamwise, pitchwise film cooling hole spacing
$T$ = temperature
TL = turbulence level, $TL=0.33(u_{rms}^2+v_{rms}^2+w_{rms}^2)^{0.5}/u_{in}$ (3-comp.) and $TL=0.5(u_{rms}^2+w_{rms}^2)^{0.5}/u_{in}$ (2-comp.)
$u$, $v$, $w$ = local, mean velocity components
$X$, $Y$, $Z$ = coordinate system shown in Fig. 2(a)
$W$ = combustor inlet width

### Greek

$\rho$ = density
$\nu$ = kinematic viscosity
$\theta$ = nondimensional temperature, $\theta=(T_\infty-T)/(T_\infty-T_c)$

### Subscripts

ave = spatial average
rms = root mean square
$\infty$ = free-stream conditions (primary flow)
$c$ = coolant conditions (secondary flow)

## References

[1] Barringer, M. D., 2001, "Design and Benchmarking of a Combustor Simulator Relevant to Gas Turbine Engines," Master's thesis, Virginia Polytechnic Institute and State University.
[2] Zimmerman, D. R., 1979, "Laser Anemometer Measurements at the Exit of a T63-C20 Combustor," National Aeronautics and Space Administration, NASA Lewis Research Center, Contract No. NAS 3-21267.
[3] Goldstein, R. J., 1983, "Velocity and Turbulence Measurements in Combustion Systems," Exp. Fluids, **1**, pp. 93–99.
[4] Moss, R. W., 1992, "The Effects of Turbulence Length Scale on Heat Transfer," Ph.D. dissertation, Department of Engineering Science, University of Oxford, Report No. OUEL 1924/92.
[5] Cameron, C., Brouwer, J., Wood, C., and Samuelson, G., 1989, "A Detailed Characterization of the Velocity and Thermal Fields in a Model Can Combustor With Wall Jet Injection," ASME J. Eng. Gas Turbines Power, **111**, pp. 31–35.
[6] Gulati, A., Tolpadi, A., VanDuesen, G., and Burrus, D., 1995, "Effect of Dilution Air on the Scalar Flowfield at Combustor Sector Exit," J. Propul. Power, **11**, pp. 1162–1169.
[7] Holdeman, J. D., 1993, "Mixing of Multiple Jets With a Confined Subsonic Crossflow," Prog. Energy Combust. Sci., **19**, pp. 31–70.
[8] Stitzel, S. M., 2001, "Flow Field Computations of Combustor-Turbine Interaction in a Gas Turbine Engine," Master's thesis, Virginia Polytechnic Institute and State University.
[9] Malecki, R., Rhie, C., McKinney, R., Ouyang, H., Syed, S., Colket, M., and Madhabushi, R., 2001, "Application of an Advanced CFD-Based Analysis

System to the PW6000 Combustor to Optimize Exit Temperature Distribution—Part I: Description and Validation of the Analysis Tool,'' ASME Paper No. 2001-GT-0062.
[10] Goebel, S., Abauf, N., Lovett, J., and Lee, C., 1993, ''Measurements of Combustor Velocity and Turbulence Profiles,'' ASME Paper No. 93-GT-228.
[11] Stevens, S. J., and Carotte, J. F., 1990, ''Experimental Studies of Combustor Dilution Zone Aerodynamics, Part I: Mean Flowfields,'' J. Propul. Power, **6**, pp. 297–304.
[12] Liou, T. M., and Wu, Y. Y., 1992, ''LDV Measurements of the Flowfield in a Simulated Combustor With Axial and Side Inlets,'' Exp. Therm. Fluid Sci., **5**, pp. 401–409.
[13] Barringer, M. D., Richard, O. T., Walter, J. P., Stitzel, S. M., and Thole, K. A., 2001, ''Flow Field Simulations of a Gas Turbine Combustor,'' ASME J. Turbomach., **124**, pp. 508–516.
[14] Moffat, J. R., 1988, ''Describing the Uncertainties in Experimental Results,'' Exp. Therm. Fluid Sci., **1**, pp. 3–17.
[15] Lefebvre, A. H., 1999, *Gas Turbine Combustion*, Taylor & Francis, Philadelphia, PA.

# The Use of Helmholtz Resonators in a Practical Combustor

**Iain D. J. Dupère**

**Ann P. Dowling**

Department of Engineering,
University of Cambridge,
Cambridge CB2 1PZ, United Kingdom

*The drive to reduce emissions has led to the development of lean premixed combustors. However, lean premixed combustion is often associated with combustion oscillations which can be so severe that they can cause structural damage to the engine. Since the associated frequencies are typically of the order of hundreds of Hertz, there is a need for a compact device to absorb the noise which drives the oscillation. Helmholtz resonators are commonly used as absorbers of incident acoustic power. In addition they are relatively compact. However, their use in combustors creates practical issues, such as placement within the chamber, neck length, and cooling, which need to be addressed. In this paper we consider these practical problems and describe how to overcome them in a real combustor.* [DOI: 10.1115/1.1806838]

## 1 Introduction

Low $NO_x$ combustion can be achieved using lean premixed systems. Here the temperature is more evenly distributed and the peak temperature lower, leading to low $NO_x$ production. Unfortunately, low $NO_x$ combustors are often associated with combustion instabilities which can be so severe that structural damage to the engine occurs. Helmholtz resonators are commonly used to damp incident acoustic waves in a number of applications (see, for example [1–6]). Helmholtz resonators have the advantage that they require a relatively small volume to damp oscillations at the relatively low frequencies found in combustion systems and thus provide a useful damping mechanism for combustion oscillation [1,3]. In order to control oscillations, they must communicate with the combustor itself. This places practical constraints upon their design, limiting their performance.

The need to incorporate the Helmholtz resonator so that it can communicate with the combustion chamber places strong constraints upon the aperture size, neck length, and volume of the Helmholtz resonator. In particular, the neck length needs to be relatively long and this results in a compromise between the absorption obtained at the peak and the frequency range over which significant absorption is obtained. A systematic approach for choosing the parameters is developed and described in this paper. We also consider the case of a neck which is long in comparison with the wavelength and its practical use in an engine.

We consider two types of configuration: no mean flow and with a mean flow. The mean flow may be either tangential across the face of the aperture or be like a cooling flow through the aperture. A combination of a cooling flow with a tangential flow is also possible. The no flow case is associated with nonlinear absorption of sound which depends upon the amplitude of the neck pressure, which in turn depends upon the incident acoustic energy, the combustor geometry, and the location of the neck. We describe this regime by using a model developed by Cummings [7] for the nonlinear behavior of an aperture and compare our results with an experiment, obtaining good agreement.

In the presence of a mean flow the absorption coefficient is linear (i.e., independent of neck pressure) and associated with the convection of unsteadily shed vorticity from the neck of the resonator. However, it still depends upon the combustor geometry and the location of the neck. Both tangential and cooling flows are modeled by using a Rayleigh conductivity first derived by Howe and his co-workers for each flow regime separately. In the presence of a tangential mean flow the convecting vorticity can also interact with the downstream edge of the aperture and generate sound. This can be overcome by rounding the downstream edge or by combining the tangential flow with cooling through the neck. Finally we draw some conclusions.

Contributed by the International Gas Turbine Institute (IGTI) of THE AMERICAN SOCIETY OF MECHANICAL ENGINEERS for publication in the ASME JOURNAL OF ENGINEERING FOR GAS TURBINES AND POWER. Paper presented at the International Gas Turbine and Aeroengine Congress and Exhibition, Atlanta, GA, June 16–19, 2003, Paper No. 2003-GT-38429. Manuscript received by IGTI, October 2002, final revision, March 2003. Associate Editor: H. R. Simmons.

## 2 Practical Helmholtz Resonators

**2.1 Introduction.** Helmholtz resonators consist of a chamber and a neck as illustrated in Fig. 1. Oscillation occurs when the mass of gas in the neck vibrates against the gas in the chamber. They can simply consist of a perforation in a plate above the chamber [8], the end correction acting as the neck. In the absence of a mean flow, absorption of incident sound is related to the nonlinear viscous damping of the flow in the neck region, and the absorption is only significant near resonance. This mechanism ultimately ensures that the neck velocity remains finite. Furthermore, a significant proportion of the incident sound energy will only be absorbed at high acoustic amplitudes. This phenomenon can be modeled by an appropriate nonlinear model such as proposed by Cummings [7]. A similar model applied to Helmholtz resonators was successfully used by Bellucci et al. [1].

In the presence of a mean flow incident acoustic waves cause unsteady vortex waves to be shed at the edges of the aperture which is swept away by the mean flow. This convecting vorticity acts as a sink to the incident sound near the upstream edge.

In this paper, we consider the acoustic response of an idealized system consisting of a resonator chamber connected to a pipe containing incident sound energy via an aperture. The problem can be separated into three features: the acoustic properties of the combustion chamber, the local absorption due to a finite pressure difference between the pipe and the Helmholtz resonator chamber, and the enhancement of the absorption due to resonance. When the neck of the Helmholtz resonator consists of an aperture in a pipe wall connecting it to the resonator chamber, the local absorption is characterized by the Rayleigh conductivity. This was derived by Howe and his co-workers for mean flow both through the aperture [9] and for tangential flow across it [10]. A correction is required for the finite wall thickness. Howe's model has been used extensively in the literature to model the interaction between sound and mean flow in a wide variety of applications, including Helmholtz resonators [2,4–6,11–17].

In a practical system, space will often prevent Helmholtz resonators from being attached to the region of interest via a short neck. We consider, therefore, practical resonators with notable physical lengths. Initially the Rayleigh conductivity for the neck is assumed to be a known complex quantity $\kappa = \gamma - i\delta$.

  

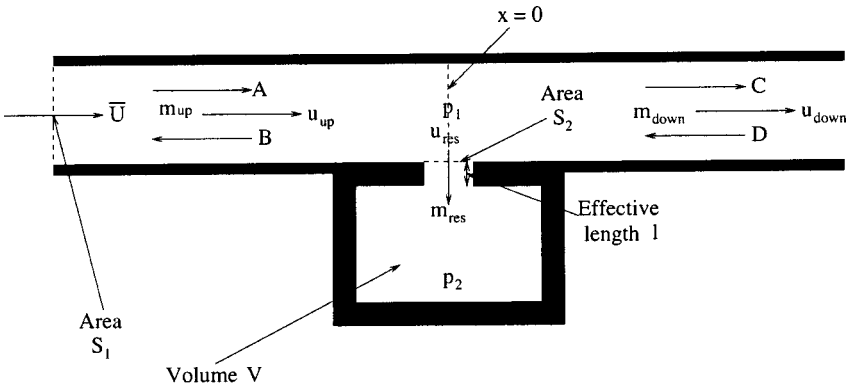


**Fig. 1 An illustration of a real Helmholtz resonator attached to a pipe**

Consider the system illustrated in Fig. 1. This consists of an infinitely long pipe of cross-sectional area $S_1$, to which a Helmholtz resonator chamber is attached at $x=0$ via a neck of effective length $l$ and area $S_2$. An incident sound wave, whose complex amplitude is $A$ at $x=0$, propagates along the pipe from left to right from $x=-\infty$ to $x=0$. A second incident acoustic wave, with complex amplitude $D$, propagates from right to left from $x=+\infty$ to $x=0$. At $x=0$, a right propagating wave, of complex amplitude $C$, is generated by the combination of transmission of wave $A$ and reflection of wave $D$. Similarly a left propagating wave, of complex amplitude $B$, is generated in the left-hand part of the pipe. In addition unsteady flow of speed $u_{HR}$ and mass flow $m'_{HR}$ enters the Helmholtz resonator through the neck and a low Mach number (which may be zero) mean flow flows along the pipe from left to right. We neglect viscous effects, except at the opening.

We begin by equating the change of mass inside the chamber to the unsteady neck flow:

$$V\frac{\partial \rho'_2}{\partial t}=\overline{\rho}S_2u'_{HR},\Rightarrow i\omega V\rho'_2=\overline{\rho}S_2u'_{HR} \tag{1}$$

for harmonic excitation of angular frequency $\omega$. If we further assume that the unsteady flow inside the resonator chamber is isentropic, then we can relate the fluctuating resonator chamber pressure, $p'_2$, to the fluctuating density, $\rho'_2$, and hence to the neck velocity via Eq. (1) to give

$$p'_2=\overline{c}_2^2\frac{\overline{\rho}u'_{HR}S_2}{i\omega V} \tag{2}$$

The acoustic pressure waves on either side of the resonator are related (from energy or momentum considerations) by

$$A(1+M)+B(1-M)=C(1+M)-D(1-M) \tag{3}$$

The behavior of the neck is linear in the presence of a mean flow, but nonlinear with no mean flow. We consider the nonlinear behavior first.

*2.1.1 Non-Linear Theory.* Following Cummings [7] the acoustic velocity, $u'_1$ is given by

$$p'_1-p'_2=l\frac{\partial u'_1}{\partial t}+\frac{c}{2}u'_1|u'_1| \tag{4}$$

$$=i\omega lu'_1+\frac{c}{2}u'_1|u'_1| \tag{5}$$

where $l$ is the effective length of the Helmholtz resonator neck and $c$ is the discharge coefficient describing the nonlinear behavior of the neck. Both the effective neck length, $l$, and the discharge coefficient, $c$, are determined experimentally. Substituting for $p'_2$ into equation (5),

$$p'_1=u'_1i\left(\omega l-\frac{\overline{c}^2\overline{\rho}\overline{S}}{\omega V}\right)+\frac{c}{2}u'_1|u'_1| \tag{6}$$

For low amplitudes, the nonlinear real part of the right-hand side of Eq. (6) is small and so little absorption of sound energy occurs. The imaginary part then gives resonance at the frequency given by classical theory.

Nonlinear equation (6) is solved numerically for the acoustic velocity, $u'_1$, for a given neck pressure amplitude, $p'_1$, which can also be related to the downstream waves $C$ and $D$ using Eq. (3). $u'_1$ can be related to the incident acoustic velocities by considering the conservation of acoustic mass flow, i.e.,

$$\overline{\rho}A_1\left(\frac{A-B}{\overline{\rho c}}\right)=\overline{\rho}\overline{S}u'_1+\overline{\rho}A_1\left(\frac{C-D}{\overline{\rho c}}\right) \tag{7}$$

Equation (7) together with Eq. (3) can be solved to give the incident and reflected waves $A$ and $B$.

Equations (3) and (7) together with equation (6) are used to predict the four acoustic waves, $A$, $B$, $C$ and $D$, for a range of sound pressure levels. We present our results in terms of the absorption coefficient, defined as the fraction of incident energy which is absorbed, since we are interested in absorption,

$$\text{i.e.,}\quad \Delta=1-\left(\frac{|B|^2+|C|^2}{|A|^2+|D|^2}\right) \tag{8}$$

Sample results are shown in Fig. 2 which is for a neck pressure of 165 dB which also shows comparison with experimental measurements. The experimental arrangement is described in the Appendix. The agreement between the theory and the experiment is good. Although much of the literature on Helmholtz resonators is concerned with predicting the resonant frequency (see, for example, Chanaud [11,12]), a number of other studies have also found good agreement with experiment for the amplitude response [1,4–6,13–17]. At the peak 65% of the incident sound is absorbed. Even at 135 dB the peak absorption is between 50% and 60% depending upon the configuration. However, the absorption characteristics include a distinct minimum. This results from a pressure node at the neck of the Helmholtz resonator. This has two effects. The first, and most obvious, is that the sound pressure levels found in practice will be low near this frequency. Second, when the unsteady pressures nearly cancel at the neck of the resonator, specific neck pressure levels can only be achieved with large incident sound waves. The unsteady velocity into the resonator, $u'_1$, however, is solely a function of this neck pressure amplitude [see Eq. (6)] and so will not be affected by the presence of the node. Thus the actual amount of energy absorbed is purely a function of the neck pressure and the behavior of the resonator. The incident acoustic energy, and thus the fraction of energy which is absorbed, however, also depend upon the amplitude of

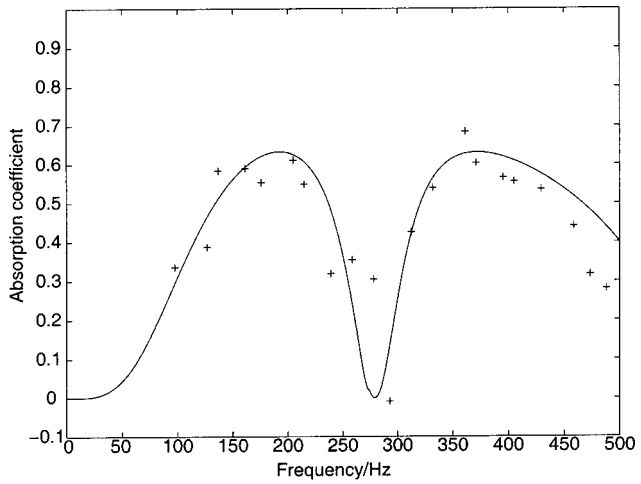


**Fig. 2 Comparison between the measured and predicted absorption coefficient as a function of frequency for an incident sound pressure amplitude of 165 dB with a closed end. + experimental measurement, ——— theory.**

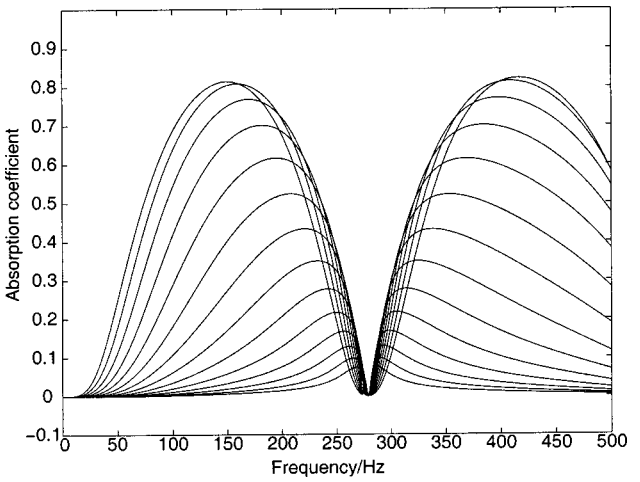


**Fig. 4 The predicted absorption coefficient as a function of frequency for a range of incident sound pressure amplitudes from 120 to 185 dB with increments of 5 dB. The lowest graph is for 120 dB.**

the incident waves required to generate the neck pressure. Thus when the neck is situated near to a pressure null, the fraction of acoustic energy which is absorbed will always be small.

To confirm the effect of the node, comparison is made in Fig. 3 between the predicted and measured absorption for a different configuration with an open end. The symbols represent the measured values and the solid line represents the predicted behavior. Here the minimum shifts to a frequency of 350 Hz.

Figure 4 summarizes the effect of amplitude, showing the predicted absorption coefficients as a function of frequency for sound pressure levels of between 120 and 185 dB, in steps of 5 dB. With a sound pressure level at the neck of 120 dB, absorption occurs only over a very narrow frequency range and the maximum absorption coefficient is less than 10%. There is a minimum in absorption at a frequency of about 275 Hz, corresponding to the frequency at which there is a pressure node at the opening, at all amplitudes, as discussed above. As a result there are two maxima in absorption either side of the node.

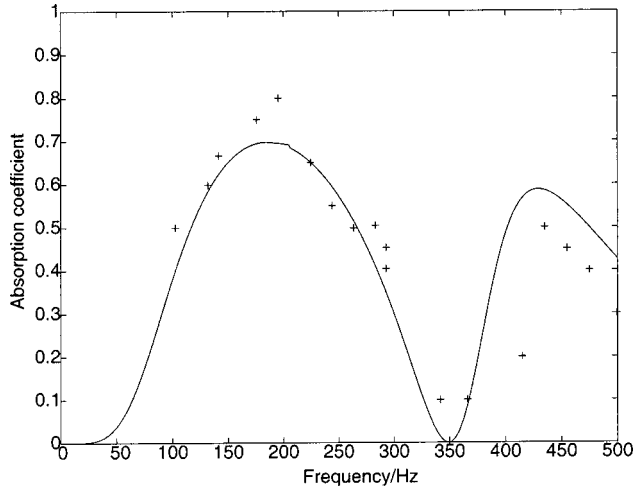


**Fig. 3 Comparison between the measured and predicted absorption coefficient as a function of frequency for an incident sound pressure amplitude of 170 dB with an open end. + experimental measurements, ——— theory.**

*2.1.2 Linear Theory.* To quantify the unsteady mass flow rate into the Helmholtz resonator we relate it to the fluctuating pressure difference across the neck via the Rayleigh conductivity defined as

$$(p_1' - p_2')\kappa = \overline{\rho} i \omega S_2 u_{HR}' \tag{9}$$

where $\kappa$ is a complex quantity which we choose to write as $\kappa = \gamma - i\delta$, following Howe [9,10]. $\gamma$ represents the inertance of the neck and is related to the effective length of the neck. $\delta$ relates to the reactance of the neck or opening and thus to any generation (or absorption) of acoustical energy (e.g., by vortex shedding) associated with the neck. The negative sign is used so that positive $\delta$ relates to absorption of sound.

Since the resonator chamber pressure is related to this acoustic velocity via Eq. (2) we can rewrite Eq. (9) as an equation for $u_{HR}'$ in terms of the acoustic pressure above the neck, $p_1'$, as follows:

$$\rho u_{HR}' = \left( \frac{p_1'(\gamma - i\delta)}{i\omega S_2 - i(\gamma - i\delta)\overline{c_2}^2 S_2 / \omega V} \right) \tag{10}$$

All acoustic energy absorbed or generated is associated with the mean acoustical energy flux into the resonator via the neck.

$$\text{i.e., absorption } \propto -\overline{p_1' \overline{\rho} u_{HR}' S_2}$$

The acoustical pressure $p_1'$ describes the amplitude of the incident acoustic waves and the mode shape of the pipe (or combustion chamber) to which the resonator is attached. We take this as our reference and therefore suppose its phase to be zero. Thus only the real part of $u_{HR}'$ contributes to the generation or absorption of acoustical energy.

Evaluating the real part of Eq. (10) we have

$$\Re(\overline{\rho} u_{HR}') = -p_1' \delta \left( \frac{\omega S_2}{\alpha^2 \delta^2 + (\omega S_2 - \alpha\gamma)^2} \right) \tag{11}$$

where

$$\alpha = \frac{\overline{c_2}^2 S_2}{\omega V} \tag{12}$$

giving an absorption

$$\frac{p_1'^2}{\overline{\rho}} \delta \left( \frac{\omega S_2^2}{\alpha^2 \delta^2 + (\omega S_2 - \alpha\gamma)^2} \right) \tag{13}$$

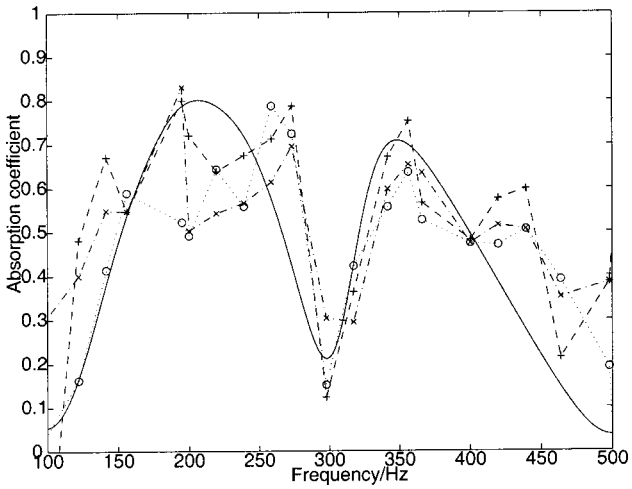


**Fig. 5 The variation of acoustic absorption coefficient with frequency for a Helmholtz resonator with a sound pressure level at the neck opening of 155 dB and in the presence of a mean pipe flow Mach number of 0.04. ——— theory, ∘ ··· 145 dB, × –·– 150 dB, + ——— – 155 dB.**

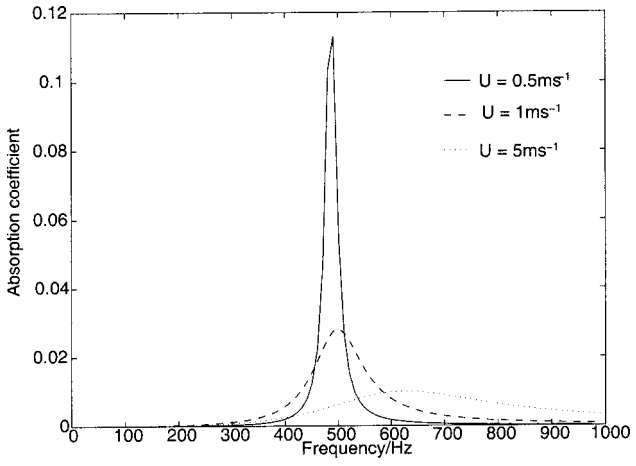


**Fig. 6 A graph showing the variation of absorption coefficient with frequency for three different mean aperture velocities, for a practical Helmholtz resonator with a finite neck length**

Comparison between theory and experimental measurements of the absorption obtained by this mechanism is shown in Fig. 5 for a sample cross flow Mach number of 0.04. Here the Rayleigh conductivity used for the predictions is taken from Howe's model [10]. Similar results have also been obtained for a cooling flow and a combination of a cooling flow and a cross flow (also from Howe's model) and were presented in a previous paper [18]. The absorption is shown for a variety of amplitudes of unsteady pressure at the neck and shown to have little effect on the overall absorption, which is reasonably high here. As before the minimum absorption occurs when the resonator neck is near a pipe node. Notice that at this temperature and with a relatively short neck the absorption is high and occurs over a broad range of frequencies. This ceases to be the case at higher temperatures and with long necks as would be required if it were to be implemented in a real combustion chamber. The practical implications of this are discussed below.

**2.2 Discussion.** For low amplitude sound waves in the absence of a mean flow, the Rayleigh conductivity of the neck is purely imaginary (i.e., $\delta=0$), leading to the denominator of Eq. (13) being purely imaginary and becomes zero when

$$\omega S_2=\alpha\gamma, \text{ i.e., when } \omega=\overline{c_2}\sqrt{\frac{\gamma}{V}} \tag{14}$$

Since $\gamma=S_2/l_{effective}$, the familiar formula for the resonant frequency of a Helmholtz resonator is recovered. Here the unsteady flow velocity into the Helmholtz resonator is large, and nonlinear effects become important. This limits the velocity and leads to some sound absorption, as described above. In the presence of a mean flow, however, $\delta$ has a nonzero value, leading to absorption away from resonance. Since the imaginary part of the denominator in Eq. (13) can still be set to zero at the frequency defined by Eq. (14), this might be supposed to enhance the absorption for modest $\delta$. When this occurs Eq. (13) becomes

$$\text{absorption}=\frac{p_1'^2}{\overline{\rho}}\left(\frac{\gamma^{3/2}V^{1/2}}{\delta\overline{c_2}}\right) \tag{15}$$

since $\omega S_2=\alpha\gamma$. It is clear from Eq. (15) that the absorption at the conventional resonance frequency is inversely proportional to $\delta$. This occurs because $\delta$ describes the local absorption of the neck irrespective of its acoustics environment. For very small but finite $\delta$, there is a little absorption at most frequencies. Near resonance, however, the large neck velocities enhance the absorption. As $\delta$ increases, noticeable absorption occurs over a broader range of frequencies. However, at resonance the effect of the increased ''local'' absorption is to suppress resonance, reducing the peak absorption. This is illustrated in Fig. 6, which shows the variation in absorption coefficient of one Helmholtz resonator at three different flow conditions. All configurations are for mean flow through the aperture. The volume of the resonator chamber is chosen to give peak absorption at 500 Hz for the lowest neck velocity, which has the greatest peak absorption. The Rayleigh conductivity used in the calculations to produce Fig. 6 is from Howe et al.'s solution for an aperture in an infinitely thin plate [10], as before, with a correction applied to account for the physical length of the neck. Since the Rayleigh conductivity, and $\gamma$ in particular, is a function of Strouhal number and hence frequency, the frequency at which peak absorption occurs varies slightly between the three configurations. This has not been compensated for here since the magnitude of the absorption depends upon $\alpha'$, which is itself a function of the volume. Nevertheless, it is clear from Fig. 6 that increasing $\delta$ gives absorption over a broader range of frequencies, but at the expense of peak absorption. This has strong consequences for the use of Helmholtz resonators in combustion systems. If the resonators are to have a significant effect in damping the oscillations, then it is essential that they are attached to the combustion chamber itself. However, the high temperatures in the combustion chamber result in complicated liners and a cooling system. As a result the neck of the Helmholtz resonator will often have to be several centimeters long. The damping described by Fig. 6 suggests that this limits the overall performance of the resonator, leaving the designer to choose the balance between the maximum absorption achieved and the frequency range over which this absorption occurs. Unfortunately, the current understanding of the instability does not presently give an *a priori* estimate of the amount of absorption required.

The other factors which appear in Eq. (15) are $\gamma$; the sound speed in the Helmholtz resonator chamber, $\overline{c_2}$; the volume of the Helmholtz resonator chamber, $V$; the mean density, $\overline{\rho}$; and the acoustic pressure above the aperture, $p_1'$. $\gamma$ describes the inertance of the aperture per unit area and is large for large radius and short neck length. In common with $\delta$, $\gamma$ is proportional to the aperture diameter. Since $\gamma$ has a higher power in Eq. (15) than $\delta$, the absorption increases with aperture size. The absorption is inversely proportional to the sound speed and so we require a small sound speed, and thus a low temperature in the Helmholtz resonator chamber for high absorption. The volume of the resonator chamber, $V$, is constrained to give resonance at the desired fre-

quency by Eq. (14). However, since the resonant frequency is related to $\gamma/V$, the volume must also increase as $\gamma$ increases to keep the resonant frequency constant. The increased volume also increases the absorption. The mean density, $\overline{\rho}$, affects both the incident sound and the absorption equally and so has no effect upon the proportion of incident sound which is absorbed. The acoustic pressure above the aperture, $p_1'$, is determined by the incident sound energy and the mode shape in the pipe or combustion chamber containing the incident sound waves.

The requirements for good acoustic performance, defined as high absorption over as wide a frequency range as possible, are therefore summarized as large aperture, large volume, short neck and low temperature. One might also be interested, however, in the total amount of absorption over the entire frequency range of interest. This is considered next.

**2.3 The Total Energy Absorbed.** The total amount of acoustic energy absorbed over a range of frequencies $\omega_1$ to $\omega_2$ can be determined by multiplying Eq. (13) by $S_2$ and integrating with respect to $\omega$:

$$\text{Total absorption} = \int_{\omega_1}^{\omega_2} p_1' \Re(u) S_2 \, d\omega = I$$

$$= \int_{\omega_1}^{\omega_2} \left( \frac{p_1'^2 \delta \omega S_2^2}{\overline{\rho}(\alpha^2 \delta^2 + (\omega S_2 - \alpha\gamma)^2)} \right) d\omega \quad (16)$$

If $\gamma$ and $\delta$ are assumed to have constant values over this frequency range, Eq. (16) can be solved directly to give

$$I = \frac{p_1'^2}{\overline{\rho}} \left( \frac{\delta}{4} \right) \ln[\alpha'^2 \delta^2 + (\omega^2 S_2 - \alpha'\gamma)^2]_{\omega_1}^{\omega_2} + \frac{p_1'^2}{\overline{\rho}} \left( \frac{\gamma}{2} \right) \times \left[ \tan^{-1} \left( \frac{\omega^2 S_2 - \alpha'\gamma}{\alpha' \delta} \right) \right]_{\omega_1}^{\omega_2} \quad (17)$$

where

$$\alpha' = \omega\alpha = \frac{\overline{c_2}^2 S_2}{V} \quad (18)$$

Over the full frequency range, $\omega=0$ to $\omega=\infty$, $\delta$ and $\gamma$ will vary, and so Eq. (17) cannot be used to evaluate the overall acoustic energy absorption directly. However, since it is valid for all frequency ranges for which $\delta$ and $\gamma$ can be considered constant, it can be used to give a piecewise estimate of the overall absorption. We consider three cases: maximum $\delta$ for $\omega^2 S_2 \gg \alpha'\gamma$ (case 1), maximum $\delta$ for $\omega^2 S_2 \approx \alpha'\gamma$ (case 2) and maximum $\delta$ for $\omega^2 S_2 \ll \alpha'\gamma$ (case 3). Since $\omega^2 S_2 = \alpha'\gamma$ at the resonant frequency of the Helmholtz resonator in the absence of a mean flow, and maximum $\delta$ occurs when the local absorption is maximum; these conditions correspond to the three possibilities for the relative positions of maximum local absorption and the no flow resonant frequency of the Helmholtz resonator.

*2.3.1 Case 1.* This occurs when the mean flow speed associated with the aperture is large and the aperture diameter is small. The first term in Eq. (17) is only significant when the $\omega^2 S_2 \gg \alpha'\gamma$ and is proportional to $\delta$. Since $\delta$ is maximum in this range for case 1, the first term is maximum for case 1. In practice, $\delta \propto r$ (for fixed mean flow speed and frequency), where $r$ is the radius of the aperture. Hence greatest absorption is achieved if the limit is achieved with a large aperture mean velocity rather than with a small aperture diameter. The second term in Eq. (17) is also only significant when $\omega^2 S_2 \gg \alpha'\gamma$. Since $\delta$ is significant in this range, the second term evaluates to $(p_1'^2/\overline{\rho})\gamma\pi/4$. $\gamma$ describes the aperture inertance, and is greatest for a small neck length. Like $\delta$, $\gamma$ is proportional to $r$ and so large diameter apertures are beneficial.

*2.3.2 Case 2.* This occurs for modest mean flow velocities and aperture diameters. The first term in Eq. (17) is not significant for case 2, since $\delta$ is small when $\omega^2 S_2 \gg \alpha'\gamma$. The second term in Eq. (17) depends upon the range of frequencies for which $\delta$ is close to its maximum. When this range is small, then the only significant contributor to this term is when $\omega^2 S_2 \gg \alpha'\gamma$ and $\delta$ is small. Then the term evaluates to $\approx (p_1'^2/\overline{\rho})\gamma\pi/4$ as for case 1. When this range is large, however, $(\omega^2 S_2 - \alpha'\gamma)/\delta$ can be large and negative and so this term can be as large as $(p_1'^2/\overline{\rho})\gamma\pi/2$ for large $\alpha'\gamma$. As for case 1 this term is greatest for a short neck length and a large aperture diameter. It is also worth noting that the total acoustic energy absorption over a range of frequencies is less dependent upon a frequency range than is the case for case 1. This implies that if the overall absorption over a range of frequencies is the same for two arrangements, one for case 1 and one for case 2, the acoustic absorption at any given frequency will be greatest for case 2.

*2.3.3 Case 3.* This occurs for small mean aperture velocities and large aperture diameters. As for case 2, the first term in Eq. (17) will not be significant since $\delta$ is small when $\omega^2 S_2 \gg \alpha'\gamma$. The second term in Eq. (17) has small $\delta$ for most of the frequency range and so will be $\approx (p_1'^2/\overline{\rho})\gamma\pi/2$. Once again, overall absorption is improved with a short neck length and a large aperture diameter. Unlike cases 1 and 2, however, increasing the aperture diameter brings the conditions nearer to the limit described by case 3. Indeed the diameter is only restricted by the condition that the aperture diameter be small in comparison with the wavelength.

It is notable that the most significant factors in determining the total amount of energy absorbed over a range of frequencies are the relative positions of the frequency for peak $\delta$ and the resonant frequency of the Helmholtz resonator, and the range of frequencies chosen. The absolute magnitude of $\delta$ is only important in determining the overall absorption for the first term in Eq. (17) which is only significant when the frequency at which $\delta$ is maximum occurs for $\omega^2 S_2 \gg \alpha'\gamma$, i.e., for case 1. The second term in Eq. (17) is nearly independent of $\delta$ and depends nearly exclusively on the range of frequencies and the relative positions of the two optimum frequencies.

**2.4 The Resonant Frequency for Large Local Damping.** In the discussion, so far, the local absorption by the aperture, for a given fluctuating pressure difference across it, has been assumed to have been small (i.e., $\delta$ has been assumed small). However, for sufficiently large aperture diameters near the optimum Strouhal number, $\delta$ can become significant. This is particularly true in practical systems where the physical length of the neck can be nonnegligible and so $\gamma$ is small. It is worth noting, therefore, the effect this has on the frequency at which maximum absorption is achieved. Since absorption is proportional to the real part of the unsteady velocity, this frequency can be obtained by differentiating Eq. (13) with respect to $\omega$ (for constant $\gamma$ and $\delta$) and equating to zero. This gives

$$\frac{p_1'^2}{\overline{\rho}} \delta S_2 \left( \frac{-S_2^2\omega^4 - 2S_2\alpha'\gamma\omega^2 + 3\alpha'^2(\gamma^2 + \delta^2)}{(\alpha'^2\delta^2 + (\omega^2 S_2 - \alpha'\gamma)^2)^2} \right) \quad (19)$$

Equating to zero and solving the quadratic equation we have

$$\omega_{res} = \overline{c_2} \left( \sqrt{\frac{\sqrt{4\gamma^2 + 3\delta^2} - \gamma}{V}} \right) \quad (20)$$

Note that this reduces to the no flow result in the limit $\delta \to 0$. Equation (20) can be substituted into Eq. (11) to give the peak absorption:

$$\frac{p_1'^2}{\overline{\rho}} V^{1/2} \delta \left( \frac{(\sqrt{4\gamma^2 + 3\delta^2} - \gamma)^{3/2}}{4\overline{c_2}(\delta^2 + 2\gamma^2 - \gamma\sqrt{4\gamma^2 + 3\delta^2})} \right) \quad (21)$$

This reduces to

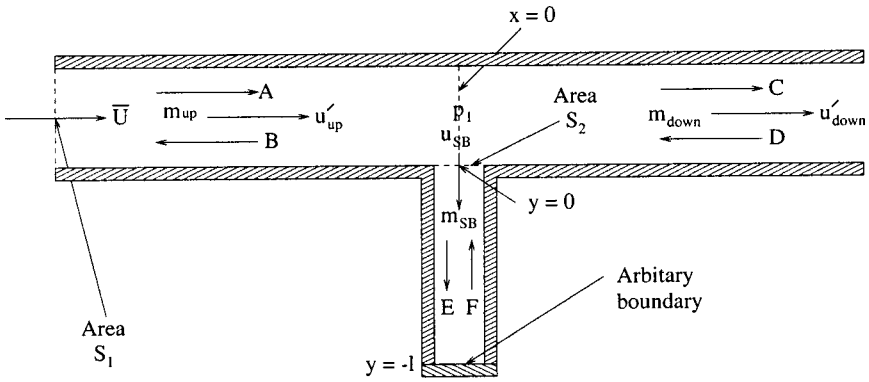


**Fig. 7 An illustration of a side-branch resonator with an arbitrary base attached to a pipe**

$$\text{absorption} = \frac{p_1'^2}{\overline{\rho}} \frac{V^{1/2}\gamma^{3/2}}{4\overline{c}_2 S_2 \delta} \tag{22}$$

when $\gamma \gg \delta$. This differs by a factor of 4 from the peak absorption given by Eq. (15). This occurs because in the limit $\delta \to 0$, the greatest absorption becomes infinite and is not a formal maximum. The formal maximum occurs at a slightly higher frequency where the absorption is lower. It has already been noted, however, that absorption occurs over a narrow band of frequencies in this limit. Broadband absorption occurs in the limit $\delta/\gamma \to \infty$. In this limit the frequency from Eq. (20) becomes

$$\omega_{res} = \overline{c}_2 \left( 3^{1/4} \left( \frac{\delta}{V} \right)^{1/2} \right) \tag{23}$$

and the absorption becomes

$$\text{absorption} = p_1' V^{1/2} \frac{\delta^{1/2}}{4\overline{c}_2} \tag{24}$$

Thus for large damping the amplitude of the peak absorption increases with $\delta$. In practice, however, the absorption predicted by Eq. (24) is small except for very large volumes and such large aperture diameters that the assumption that the aperture is compact becomes invalid.

**2.5 Conclusions.** In practical systems, physical constraints imposed by the system to be damped can have a strong effect upon the performance of Helmholtz resonators. A reliable damper would be one which provides high absorption over a large range of frequencies, with high absorption at the peak frequency. This requires a short neck, a large aperture diameter, a large resonator chamber volume, and a low temperature within the resonator. In addition the resonator should be positioned as near to an acoustic anti-node as possible. In practice all these factors are constrained. As a result designers have a trade off between high absorption at the peak and broadband absorption. This trade off can be controlled via the mean flow speed through the aperture. In designing Helmholtz resonators, designers should first choose as large an aperture diameter, as short a neck length, and as low a resonator chamber temperature as physical constraints permit. Second, they should choose the volume of the Helmholtz resonator to give resonance at the required frequency. Third, the mean velocity through the aperture is chosen to set the Strouhal number of the aperture. The absorption should be calculated at this stage to check that the absorption is both broadband and significant. If space will allow, multiple Helmholtz resonators positioned around the circumference can be used to extend the bandwidth for absorption. Where circumferential modes are important, as is often the case in combustors, circular symmetry means that with only one Helmholtz resonator, it is always possible to have a pressure node at the neck of the Helmholtz resonator and when this is the case the resonator will have no effect. Since their presence changes the boundary conditions this can be the case even if a node does not exist at that position when there are no resonators in place and is in fact always the case. More than one Helmholtz resonator can be used to avoid this and then the circumferential spacing required would depend upon the order of the circumferential mode.

## 3 Side Branch Resonators

Although Helmholtz resonators are a compact way to absorb at a particular frequency, it was shown above that a compromise is set up between obtaining high absorption at the peak and obtaining absorption over a range of frequencies. This problem can be overcome by using a side branch resonator where space permits.

Consider the geometry illustrated in Fig. 7. Two incident sound waves, one with complex amplitude $A$ propagating from left to right in the left-hand portion of the pipe, and one propagating from right to left with complex amplitude $D$ in the right-hand portion of the pipe, propagate along an infinite pipe of cross-sectional area $S_1$ towards $x=0$. At $x=0$, $y=0$; both pipes are attached to a side branch of length $l$ and area $S_3$ via an aperture of area $S_2$ and Rayleigh conductivity $\kappa$. Through a combination of reflection and transmission of incident waves $A$ and $D$, two outgoing waves ($B$, propagating from right to left in the left-hand part of the pipe, and $C$, propagating from left to right in the right-hand portion of the pipe) are generated. As before a mean flow of low Mach number (which may be zero) flows from left to right along the pipe. An acoustic wave of complex amplitude $E$ propagates in the negative $y$-direction towards $y=-l$ where it is reflected to give a second acoustic wave of complex amplitude $F$ towards $y=0$. The complex amplitudes $A$, $B$, $C$, $D$, $E$ and $F$ are all referenced to $x=0$, $y=0$. The factor $e^{-i\omega t}$ is suppressed throughout. At the end of the side branch (i.e., at $y=-1$) an arbitrary boundary exists which could be a solid wall, an open end, a chamber, or some other boundary. The viscous effects are ignored everywhere except in determining the Rayleigh conductivity of the aperture. In a practical system, the infinite pipe could be replaced with a finite length pipe by relating waves $C$ and $D$ via a reflection coefficient at the end of the pipe.

The acoustic velocity entering the side-branch, $u'_{SB}$, is related to the pressure difference across the aperture via the Rayleigh conductivity:

$$(p_1' - (E+F))\kappa = \overline{\rho} i \omega S_3 u'_{SB} \tag{25}$$

For an arbitrary reflection at $y=-l$ we define the reflection coefficient $R$ as $F=RE$. Hence

$$E = \frac{\kappa p_1'}{(1+R)\kappa + i\alpha(1-R)} \tag{26}$$

and

$$u'_{SB}=\left(\frac{E-F}{\overline{\rho c_1}}\right)=\frac{\kappa p'_1(1-R)}{(1+R)\kappa+i\alpha(1-R)} \tag{27}$$

where

$$p'_1=\frac{p'_1}{\overline{\rho c_1}}, \quad \alpha=\frac{\omega S_3}{\overline{\rho c_2}}$$

Equation (27) relates the unsteady velocity into the side branch, $u'_{SB}$, to the local acoustic pressure, $p'_1$, and the acoustic properties of the aperture (characterized by the Rayleigh conductivity, $\kappa$) and the reflection coefficient, $R$. Absorption or generation of acoustic energy is related to that part of the acoustic velocity, $u'_{SB}$, 180 deg out of phase (or in phase for generation) with the local acoustic pressure, $p'_1$. As for the conventional Helmholtz resonators, we assume that $p'_1$ is entirely real and take the real part of the velocity. Taking $R=R_0(\cos(\phi)+i\sin(\phi))$ and $\kappa=\gamma-i\delta$,

$$|\Delta|^2\Re\left(\frac{u'_{SB}}{p'_1}\right)=(\gamma^2+\delta^2)(1-R_0^2)+\alpha\delta(2R_0\cos(\phi)-(1+R_0^2)) \tag{28}$$

where

$$|\Delta|^2=(\gamma^2+\delta^2)(1+R_0^2+2R_0\cos(\phi))+\alpha^2(1+R_0^2-2R_0\cos(\phi)) +4\gamma\alpha R_0\sin(\phi)+2\alpha\delta(R_0^2-1) \tag{29}$$

This simplifies when $R_0=1$:

$$\Re\left(\frac{u'_{SB}}{p'_1}\right)=\left(\frac{\alpha\delta(\cos(\phi)-1)}{\text{denominator}}\right) \tag{30}$$

$$\text{where denominator}=(\gamma^2+\delta^2)(1+\cos(\phi))+\alpha^2(1-\cos(\phi))+2\gamma\alpha\sin(\phi))$$

Notice that since $\cos(\phi)\leqslant 1$, and $\alpha(=\omega S_2/\overline{\rho c_2})$ and the denominator $(=|\Delta|^2)$ are always positive, Eq. (30) is always negative for a positive $\delta$, i.e., the side-branch resonator with simple reflection at $y=l$ always absorbs when there is absorption at $y=0$. In contrast with the Helmholtz resonators, however, the denominator of Eq. (30) can become zero even in the presence of absorption at the neck because of the phase difference between the acoustic waves $E$ and $F$ resulting from the length of the side branch. As the denominator tends to zero the real part of acoustic velocity into the side branch rises. This gives rise to increased absorption. The absorption cannot be greater than the incident sound energy, however, and, so, as the acoustic velocity rises, the resonator responds by enforcing a node near the aperture. In practice, however, the numerator also becomes zero when

$$\cos(\phi)=1 \tag{31}$$

and so overall best absorption is achieved for small $\alpha$ so that the denominator vanishes near $\cos(\phi)=-1$. Small $\alpha$ requires a large sound speed (and thus a large temperature) and a low side tube area, which has an adverse affect on the area over which sound is absorbed. As a result, side tube resonators are likely to be restricted in their range of absorption as the absorption will drop to zero near $\cos(\phi)=1$ and it is difficult to arrange for the denominator to become zero (and thus obtain the maximum absorption) at frequencies greatly removed from this minimum. Side branch resonators also have the disadvantage that they require a much greater volume to absorb at the required frequency than is the case for Helmholtz resonators.

## 4 Conclusions

In this paper, we have discussed the effects of practical constraints on the acoustic performance of absorbers. It has been shown that the need for high temperatures and long necks for Helmholtz resonators leads to a compromise between broadband absorption and high peak absorption. In designing an absorber, therefore, designers should first try to arrange for the neck length to be as short as possible and for the aperture size to be as large as possible. The volume is then chosen to give maximum absorption at the required frequency. The Strouhal number of the neck flow is chosen to give the desired balance between broadband absorption and high peak absorption. Where space allows, multiple resonators should be used and spaced around the combustor in order to increase the bandwidth. This is also beneficial since with only one Helmholtz resonator the change in the mode shape will result in a pressure node at the resonator neck resulting in no damping.

Side branch resonators provide an alternative absorber, but these take up a great deal of space and have a number of frequencies in which the absorption drops to zero.


## Acknowledgments

The work contained in this paper was sponsored by Rolls Royce plc. as part of the ESPR project under the guidance of Bryn Jones. We are also grateful to Dr. Ivor Day for his help in the design of the experiment.


## Nomenclature

- $A, B, C$ = complex amplitude of acoustic waves
- $D, E, F$ = complex amplitude of acoustic waves
- $M$ = Mach number$=\overline{U}/\overline{c_1}$ in the pipe
- $R$ = reflection coefficient
- $S$ = cross-sectional area
- $U$ = velocity
- $V$ = volume of resonator chamber
- $c$ = speed of sound, discharge coefficient
- $p$ = pressure
- $\alpha$ = positive real function
- $\gamma$ = real part of Rayleigh conductivity
- $\delta$ = negative imaginary part of Rayleigh conductivity
- $\kappa$ = Rayleigh conductivity
- $\rho$ = fluid density
- $\omega$ = angular frequency

### Subscripts

- 1 = pipe
- 2 = aperture
- 3 = side branch

### Superscripts

- $\overline{\ }$ = mean value
- $'$ = perturbation

## Appendix: Experimental Arrangement

Figure 8 shows an illustration of the experimental set up used. The pressure oscillation between 50 and 500 Hz is provided by pumping air through a rotary valve. The flow rate of air through the main pipe is measured with a flow meter. The Helmholtz resonator consists of a nylon cylinder of radius 62 mm bounded by a nylon cylinder at one end and a metal plate at the other. The metal plate has a 12.5 mm diameter circular aperture at the center which separates it from the test pipe. The plate is flat on the side of the nylon cylinder, but curved on the other side so that it smoothly meets the test pipe. The volume of the resonator chamber is varied by adjusting the position of the piston between 5 and 20 cm from the metal plate. The aperture has sharp edges.

The acoustic waves upstream and downstream of the resonator are measured using three kulites in each section of the pipe and applying the two microphone technique of Seybert and Ross [19]. The kulites are also calibrated in the way suggested by Seybert and Ross [19]. Two additional kulites, one below the resonator neck and one in the resonator chamber, are also used to measure $p'_1$ and $p'_2$, respectively.

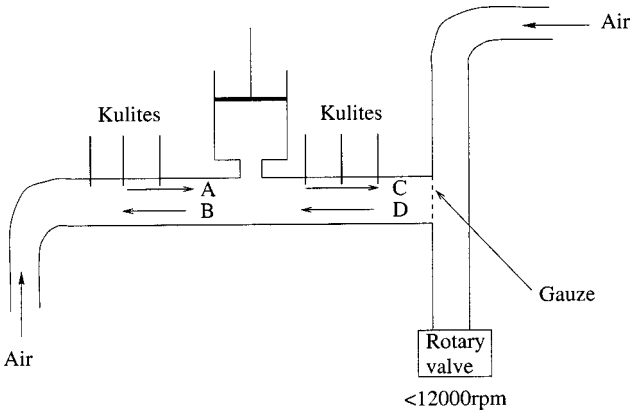


**Fig. 8 Experimental rig used for high amplitude incident waves, with and without mean flow**

## References


[1] Bellucci, V., Flohr, P., Paschereit, C. O., and Magni, F., 2001, ''On the use of Helmholtz Resonators fo Damping Acoustic Pulsations in Industrial Gas Turbines,'' Technical Report 2001-GT-0039, ASME TURBO EXPO 2001, June 4–7, 2001, New Orleans, LA.

[2] Doria, A., 2000, ''A Simple Method for the Analysis of Deep Cavity and Long Neck Acoustic Resonators,'' J. Sound Vib., **232**(4), pp. 823–833.

[3] Gysling, D. L., Copeland, G. S., McCormick, D. C., and Prosnia, W. M., 2000, ''Combustion System Damping Augmentation With Helmholtz Resonators,'' ASME J. Eng. Gas Turbines Power, **122**, pp. 269–274.

[4] Selamet, A., Dickey, N. S., and Novak, J. M., 1995, ''Theoretical, Computational and Experimental Investigation of Helmholtz Resonators With Fixed Volume: Lumped Versus Distributed Analysis,'' J. Sound Vib., **187**(2), pp. 358–367.

[5] Selamet, A., Radavich, P. M., Dickey, N. S., and Novak, J. M., 1997, ''Circular Concentric Helmholtz Resonators,'' J. Acoust. Soc. Am., **101**(1), pp. 41–51.

[6] Walker, B. E., and Charwat, A. F., 1982, ''Correlation of the Effects of Grazing Flow on the Impedance of Helmholtz Resonators,'' J. Acoust. Soc. Am., **72**(2), pp. 550–555.

[7] Cummings, A., 1984, ''Acoustic Nonlinearities and Power Losses at Orifices,'' AIAA J., **22**, pp. 786–792.

[8] Dowling, A. P., and Ffowcs Williams, J. E., 1983, *Sound and Sources of Sound*, Ellis Horwood, Chichester, UK.

[9] Howe, M. S., 1979, ''On the Theory of Unsteady High Reynolds Number Flow Through a Circular Aperture,'' Proc. R. Soc. London, Ser. A, **366**, pp. 205–223.

[10] Howe, M. S., 1996, ''The Influence of Tangential Mean Flow on the Rayleigh Conductivity of an Aperture,'' Proc. R. Soc. London, Ser. A, **452**, pp. 2303–2317.

[11] Chanaud, R. C., 1994, ''Effects of Geometry on the Resonance Frequency of Helmholtz Resonators,'' J. Sound Vib., **178**(3), pp. 337–348.

[12] Chanaud, R. C., 1997, ''Effects of Geometry on the Resonance Frequency of Helmholtz Resonators. Part ii,'' J. Sound Vib., **204**(5), pp. 829–834.

[13] Jungowski, W. M., and Grabitz, G., 1987, ''Self-Sustained Oscillation of a Jet Impinging Upon a Helmholtz Resonator,'' J. Fluid Mech., **179**, pp. 77–103.

[14] Khosropour, R., and Millet, P., 1990, ''Excitation of a Helmholtz Resonator by an Air Jet,'' J. Acoust. Soc. Am., **88**(3), pp. 1211–1221.

[15] Meissner, M., 1987, ''Self-Sustained Deep Cavity Oscillations Induced by Grazing Flow,'' Acustica, **62**, pp. 220–228.

[16] Nelson, P. A., Halliwell, N. A., and Doak, P. E., 1981, ''Fluid Dynamics of a Flow Excited Resonance. Part I: Experiment,'' J. Sound Vib., **78**(1), pp. 15–38.

[17] Nelson, P. A., Halliwell, N. A., and Doak, P. E., 1983, ''Fluid Dynamics of a Flow Excited Resonance. Part II: Flow Acoustic Interaction,'' J. Sound Vib., **91**(3), pp. 375–402.

[18] Dupère, I. D. J., and Dowling, A. P., 2002, ''The Absorption of Sound by Helmholtz Resonators With and Without Flow,'' Technical Report 2002–2590, 8th AIAA/CEAS Aeroacoustics Conference, June 17–19, 2002, Breckenridge, CO.

[19] Seybert, A. F., and Ross, D. F., 1977, ''Experimental Determination of Acoustic Properties Using a Two Microphone Random Excitation Technique,'' J. Acoust. Soc. Am., **61**, pp. 1362–1370.

# Surface-Stabilized Fuel Injectors With Sub-Three PPM $NO_x$ Emissions for a 5.5 MW Gas Turbine Engine

**Steven J. Greenberg**

**Neil K. McDougald**
e-mail: nmcdougald@alzeta.com

**Christopher K. Weakley**

**Robert M. Kendall**

ALZETA Corporation,
2343 Calle del Mundo,
Santa Clara, CA 95054

**Leonel O. Arellano**
Solar Turbines,
2200 Pacific Highway,
San Diego, CA 92186

*ALZETA Corporation has developed surface-stabilized fuel injectors for use with lean premixed combustors which provide extended turndown and ultralow* $NO_x$ *emission performance. These injectors use a patented technique to form interacting radiant and blue-flame zones immediately above a selectively perforated porous metal surface. This allows stable operation at low reaction temperatures. A previous ASME paper (IJPGC2002-26088) described the development of this technology from the proof-of-concept stage to prototype testing. In 2002 development of these fuel injectors for the 5.5 MW turbine accelerated. Additional single-injector rig tests were performed which also demonstrated ultralow emissions of* $NO_x$ *and CO at pressures up to 1.68 MPa (16.6 atm) and inlet temperatures up to 670°K (750°F). A pressurized multi-injector "sector rig" test was conducted in which two injectors were operated simultaneously in the same geometric configuration as that expected in the engine combustor liner. The multi-injector package was operated with various combinations of fired and unfired injectors, which resulted in low emissions performance and no adverse affects due to injector proximity. To date sub-3 ppm* $NO_x$ *emissions with sub-10 ppm CO emissions have been obtained over an operating range of 0.18–1.68 MPa (1.8–16.6 atm), inlet temperatures from 340 to 670K (186–750°F), and adiabatic flame temperatures from 1740 to 1840K (2670–2850°F). A full scale multi-injector engine simulation is scheduled for the beginning of 2003, with engine tests beginning later that year.* [DOI: 10.1115/1.1839920]

## Introduction

ALZETA Corporation is developing a surface-stabilized combustion system for industrial turbine applications capable of sub-3 ppm emissions of oxides of nitrogen ($NO_x$) with simultaneous low emissions of carbon monoxide (CO) and unburned hydrocarbons. Surface-stabilized combustion is a simple approach which can maximize the emissions benefit of lean fuel/air premixing by increasing flame stability, and doing so in a compact and flexible manner. This paper will discuss progress towards deploying this technology, already commercially successful in atmospheric boilers and process heaters, in gas turbine engines. The application of surface-stabilized combustion to gas turbines is being developed under the name nanoSTAR™.

Low emissions of oxides of nitrogen ($NO_x$), as well as carbon monoxide and unburned hydrocarbons can be achieved with thorough fuel/air mixing and control of the adiabatic flame temperature of that mixture below about 1920 K (3000°F). One of the great difficulties with such lean premixed systems has been maintaining flame stability in the narrow flame temperature range between high $NO_x$ production and lean flame extinction. Aerodynamically stabilized injectors have very narrow ranges of operation, necessitating multiple injector staging (up to four stages in some systems) or piloting [1]. Such dry low $NO_x$, or DLN systems, have been successfully deployed to achieve sub-25 ppm $NO_x$ emissions in several gas turbine applications, and in some cases much lower. To date, however, such systems have not been refined to reliably achieve sub-3 ppm $NO_x$ emission levels.

A more recent development has been the demonstration of catalytic combustors in gas turbine engines which can achieve sub-3 ppm $NO_x$ emissions [2]. These combustors use a catalyst to stabilize gas phase combustion at temperatures less than 1645 K (2500°F). However, precious metal catalyst life is greatly limited at temperatures above 1310 K (1900°F), and temperatures considerably higher than 1365 K (2000°F) are required to realize acceptable CO and HC emissions. Methods have been developed to circumvent these problems, but they introduce additional complexities and limitations that result in incompatibility with a number of existing gas turbine configurations unless extensive engine modifications are performed.

Surface-stabilized combustion is a simple approach that extends the operating range of lean premixed systems to achieve sub-3 ppm $NO_x$ emissions. The technology has advanced through proof-of-concept testing in pressurized rigs and demonstration in a 1 MW test engine. Prototype injectors for the 5.5 MW Taurus 60 have been designed, built, and rig tested. The present work is focused on addressing operational and design issues relevant to an annular combustion liner configuration. Specifically, the ability to ignite at pressure, operate with adjacent fired and unfired injectors, and determine the optimal distance between injectors. Additional single injector tests were performed at higher inlet temperature and pressure to establish the feasibility of applying nanoSTAR to higher pressure ratio engines. The successful results from these tests support continued development of nanoSTAR with full combustor testing and engine testing planned for the coming year.

## Technology

The particular style of surface-stabilized combustion inherent in NanoSTAR injectors is best described as laminar blue-flame combustion stabilized by significant velocity gradients above a porous metal-fiber mat. The operation of this type of surface-stabilized

Contributed by the International Gas Turbine Institute (IGTI) of THE AMERICAN SOCIETY OF MECHANICAL ENGINEERS for publication in the ASME JOURNAL OF ENGINEERING FOR GAS TURBINES AND POWER. Paper presented at the International Gas Turbine and Aeroengine Congress and Exhibition, Atlanta, GA, June 16–19, 2003, Paper No. 2003-GT-38489. Manuscript received by IGTI, October 2002, final revision, March 2003. Associate Editor: H. R. Simmons.

  

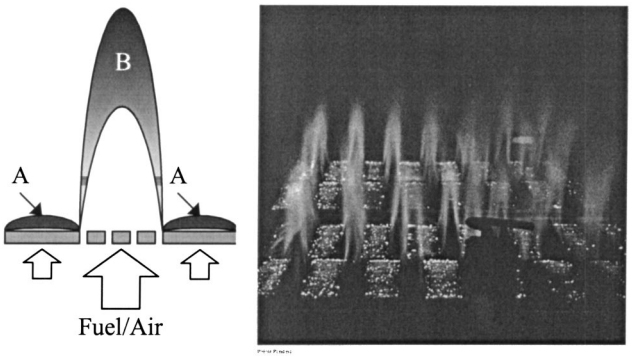


**Fig. 1 Surface-stabilized combustion**

combustion is characterized by the schematic to the left of Fig. 1, which shows premixed fuel and air passing through the metal fiber mat in two distinct zones.

In the porous-only zone true surface combustion (A) is realized. Under lean conditions this will manifest as very short laminar flamelets, but under rich conditions the surface combustion will become a diffusion-dominated reaction stabilized just over a millimeter above the metal matrix, which proceeds without visible flame and heats the outer surface of the mat to incandescence. This type of radiant surface combustion can be seen between the laminar flamelets to the right of Fig. 1.

Portions of the metal fiber mat are perforated to allow higher mass flux (B). In these zones stretched laminar flames are established that are anchored by the adjacent surface combustion. This produces the distinctive flame pattern seen in the right-hand picture of Fig. 1. The specific perforation arrangement and pattern control the size and shape of the laminar flamelets. The perforated zones operate at flow velocities of up to ten times the laminar flame speed producing a factor of 10 stretch of the flame surface and resulting in large laminar flamelets. The alternating arrangement of laminar blue flames and surface combustion allows high firing rates to be achieved before flame lift-off occurs, with the surface combustion stabilizing the long laminar flames by providing a pool of hot combustion radicals at the flame edges.

At atmospheric operation, nominal injector output would be 3.15 MW/m$^2$ (1.0 million Btu/h/ft$^2$), so an injector with a fired area of 0.047 m$^2$ (0.5 ft$^2$) would have a capacity of 146.5 kW (500,000 Btu/h). Assuming the firing rate of the injector increases linearly with pressure, the surface firing rate (SFR) remains constant as pressure increases. This results in a compact injector size for a given capacity in high pressure systems. Therefore the 146.5 kW (500,000 Btu/h) injector at 0.1 MPa (1 atm) becomes nominally a 1465 kW (5 million Btu/h) injector at 1 MPa (10 atm). Put another way, based on a gas turbine with a heat rate of 10,000 Btu/kW/h and a combustion pressure of 10 atm, only about one square foot of injector surface area would be required for every megawatt of gas turbine output.

NanoSTAR injectors are constructed of small metal fibers which are compressed and sintered, resulting in an all-metal structure. This porous pad is perforated to produce a proprietary arrangement of perforation zones. The perforated metal fiber pads have a very low pressure drop but excellent flow uniformity. They also display excellent durability in fired service. In an atmospheric cycling test, a nanoSTAR metal fiber pad withstood over 15,000 ignition/cooling cycles over a 30 day period without a significant loss in operability. Further material and oxidation studies are to be conducted to estimate injector life which is expected to exceed 8000 h. Figure 2 depicts an injector in a gas turbine combustor liner.

The laminar blue flame combustion zones created by the surface stabilization contribute to lower $NO_x$ emissions in three ways. The dominant mechanism is the expected benefit from using fully premixed fuel and oxidizer, resulting in a uniform temperature across the reaction zone, and lean burning, resulting in reaction temperatures below the 1920 K (3000°F) limit for thermal $NO_x$ formation. The second is the much lower residence time in the hot combustion zone. The peak temperatures are realized in the combustion front formed by each laminar flamelet which, like that of a Bunsen injector flame, is very thin. So the residence time in the peak flame temperature zone for a nanoSTAR injector is a fraction of that of a typical aerodynamically stabilized injector. The third mechanism is a more rapid postflame cooling of each blue-flame zone via the gas phase radiation mechanism. By spreading the flame over a larger surface, the gas layer thickness at any specific location on the injector is thin (relative to that of a conventional injector) and can more rapidly transfer energy as a result.

These mechanisms combine in a nanoSTAR injector to produce lower $NO_x$ emissions than a typical lean premixed aerodynamically stabilized injector. Figure 3 shows a comparison between nanoSTAR injector emission results from a high-pressure rig test and perfectly premixed aerodynamically stabilized emission re-

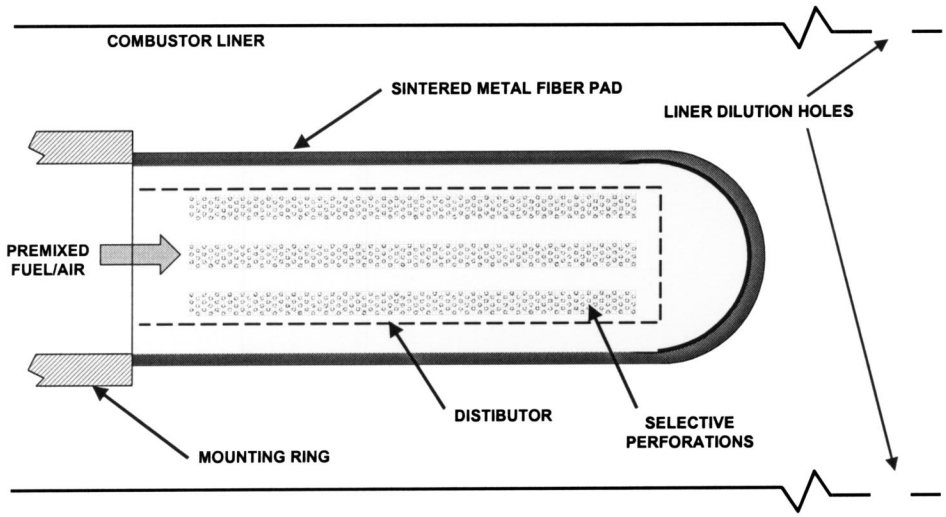


**Fig. 2 Surface-stabilized nanoSTAR injector**

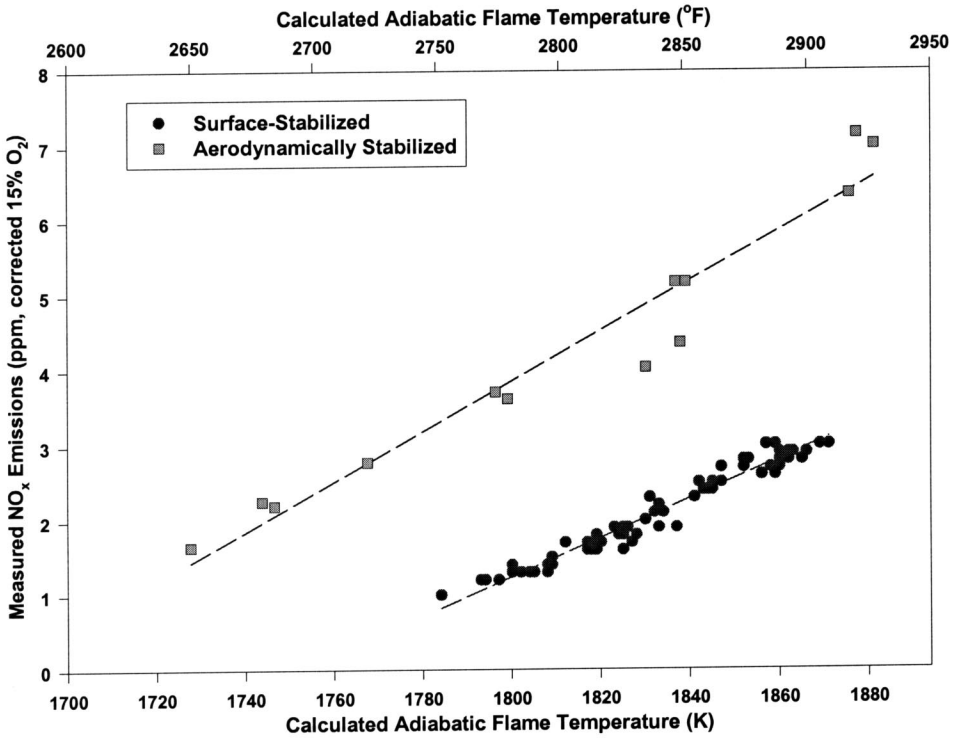


**Fig. 3 Surface-stabilized compared to aerodynamically stabilized emission results; both tests conducted at 1.01 MPa (10 atm) pressure and 535–590 K (500–600°F) inlet temperatures**

sults from a 1990 paper by Leonard and Correa [3]. In both cases the tests were conducted at 1.01 MPa (10 atm) and 535–590 K (500–600°F) inlet temperatures.

In addition to lower emissions with a wide turndown window, nanoSTAR injectors can be designed to fit within existing combustor liners and fitted to existing fuel/air premixers without extensive modification to the combustion equipment or pressure case. Furthermore, they require no extraordinary control schemes or equipment beyond that which would be required for an aerodynamically stabilized lean-premixed injector.

## Past Work

A previous ASME paper (IJPGC2002-26088) described the development of nanoSTAR from the proof-of-concept stage to prototype testing [4]. These tests were part of a development program pursued after a relationship was established between ALZETA and Solar Turbines. The initial target applications were Solar gas turbines in the 5–7 MW range.

Initial proof-of-concept tests occurred at the National Energy Technology Laboratory's (NETL) Low Emission Combustion Test and Research facility in Morgantown, West Virginia. These high-pressure rig tests demonstrated operability and low emissions in a simulated gas turbine environment. The surface-stabilized injector was shown to operate stably over a pressure range of 0.18–1.24 MPa (1.8–12.2 atm) at the nominal values of flame temperature and mass flow, so the operating envelope of the injector was shown to be large. $NO_x$ emissions, at the lowest flame temperatures, were generally below 2 parts per million (corrected to 15% $O_2$) and at times below 1 ppm. The highest value recorded was less than 3.5 ppm.

After the success of the testing at NETL, additional proof-of-concept tests were conducted at Solar Turbines' San Diego facilities. The most significant of these was a demonstration on an operating gas turbine engine, which demonstrated the ability of a nanoSTAR injector to provide stable operation through the start ramp and across the engine load range. An existing modified 1 MW Solar Saturn engine was used. The engine is outfitted with an external side-mounted combustor that allowed for easy hardware modification and instrumentation. The side-mounted design also provides variable geometry in the form of butterfly valves to control the air flow split between the primary and dilution zones.

On the first day of testing, the surface-stabilized injector took the engine through the start ramp to the point of starter drop-out, the idle point where combustion provides enough energy to maintain air flow through the engine. By the second day of testing stable operation up to 92% engine speed was achieved. Figure 4 shows the gas producer speed and $NO_x$ emissions from this test run. No effort was made to optimize emissions performance as operational characteristics of the technology were the focus of the demonstration. However, $NO_x$ emissions were well below the typical dry low $NO_x$ value of 25 ppm (15% $O_2$). On the third and final day of testing the start ramp was completely automated. The engine was brought to idle speed entirely by the control system except for manual adjustment of the air flow split. As control algorithms were developed, several system shutdowns occurred, and the nanoSTAR injector responded with reliable ignition and performance through several start ramps. The engine was operated to 95% speed before a high temperature limit upstream of the turbine section (unrelated to the surface-stabilized injector) prevented further increase.

The proof-of-concept tests confirmed that nanoSTAR technology can operate under the conditions of pressure and temperature found in a gas turbine engine, and can in fact provide the motive power for an actual engine. The next phase was to design, test, and demonstrate a prototype injector for Solar's Taurus 60 engine.

First, the technology itself was refined based on the results of the previous tests. A new generation of monolithic nanoSTAR injectors were produced. This produced a simplified combustion surface free of welds or other joints, and allowed the injectors to

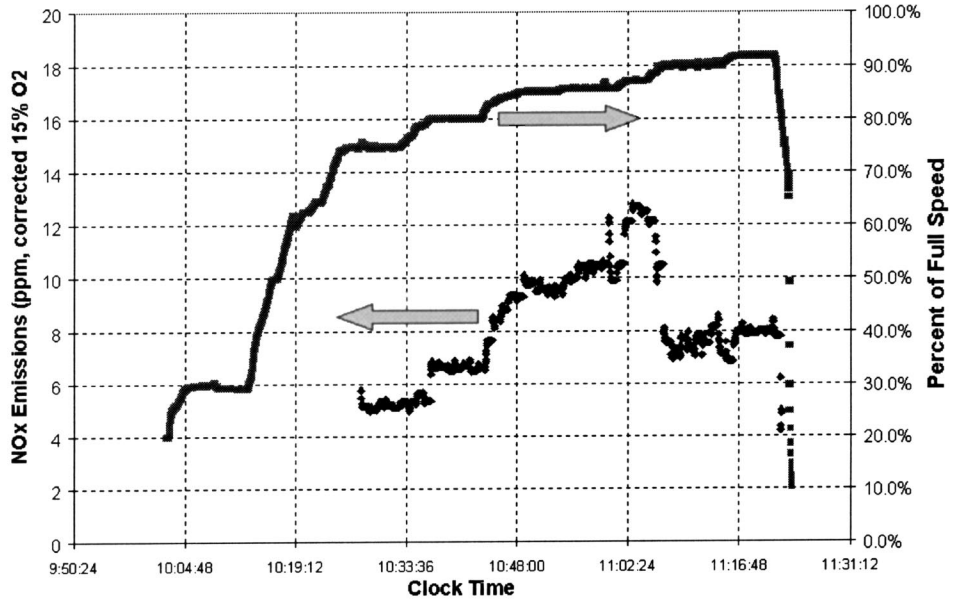


**Fig. 4 Gas producer speed and $NO_x$ emissions from Saturn test run**

be produced in a variety of shapes to interface with any particular combustor liner. An example of the resulting injector head is shown in Fig. 5 during an atmospheric test.

An extensive program of single-injector rig tests was conducted at Solar's high-pressure test rig facility. The prototypes were tested under a variety of conditions, ranging from near atmospheric all the way up to simulated full-load conditions. The injector demonstrated stable operation at each of ten pressure, temperature, and fuel flow combinations targeted. At a pressure and air preheat designed to simulate a full-load operating condition (1.24 MPa (12.2 atm), 640 K (690°F) inlet temperature), the fuel flow was reduced to near lean blowout in an effort to identify a point of optimal emissions. In this range, several data points were collected with $NO_x$ emissions less than 3 ppm and CO emissions less than 25 ppm. A final data point was collected with $NO_x$ emissions less than 2 ppm, but CO emissions had jumped to about 80 ppm. Figure 6 shows a plot of $NO_x$ and CO emissions versus AFT.

## Present Work: Multiple Injector Tests

All previous testing of nanoSTAR injectors at Solar Turbines had involved a single injector firing in conjunction with a cooled liner wall. However, nearly all proposed engine configurations would require numerous individual injectors to be placed inside an annular combustor liner. This creates a situation where the fired surface of one injector will be exposed to the fired surfaces of other injectors just inches away. At this stage in the development program, it was necessary to determine an optimal separation distance for two neighboring injectors in a Solar engine. Interactions between a fired injector and a neighboring unfired injector would also be investigated.

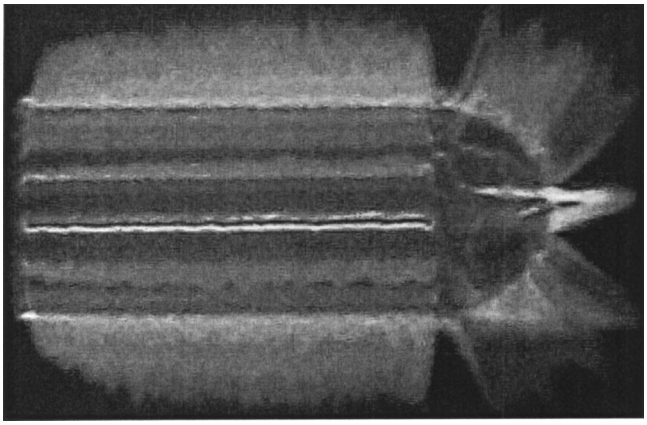

**Fig. 5 NanoSTAR injector during atmospheric testing**

Testing was conducted with a set of identical and replicable injectors. The tests involved a set of two injectors placed side by side in a rectangular liner approximating a sector of the combustor annulus of a Solar Taurus 60 engine (hence the term ''sector rig'' tests). This two-injector configuration allowed investigation of all relevant operating modes. One side of each injector was exposed to the adjacent injector, while the other side faced a hot, insulated wall.

The proximity testing made use of an existing sector rig at Solar Turbines. This rig was initially designed and used to simultaneously test up to three DLN injectors inside a simulated sector of a Taurus 60 combustor liner. The pressure vessel of the rig underwent minor repairs and was pressure tested. The combustor liner, Fig. 7, was completely rebuilt for the test. The top and bottom of the liner were backside cooled while the ends were lined with ceramic insulation board. This configuration creates a thermal environment similar to that found in an engine. The liner has a rectangular cross section, which adequately simulates the large radius of curvature in the Taurus 60 engine. The rig and the liner both feature accommodations for a direct-spark igniter.

The inlet ''dome'' of the liner was redesigned in order to minimize air leakage into the primary zone at the injector/liner interface. Injectors are flange mounted and can easily be replaced if necessary. The dome also features a sliding mechanism that allows for continuous variation of the injector separation distance. This distance can be adjusted from 5 in. down to 3 in., with approximately 3 in. being the target for most engine designs. The interior of the dome is lined with ceramic insulation board.

Instrumentation and data collection in the sector rig were similar to that of previous single-injector rigs. Two quartz sight glasses were installed to allow optical access to each injector via video cameras connected to monitors in the control room. Emission

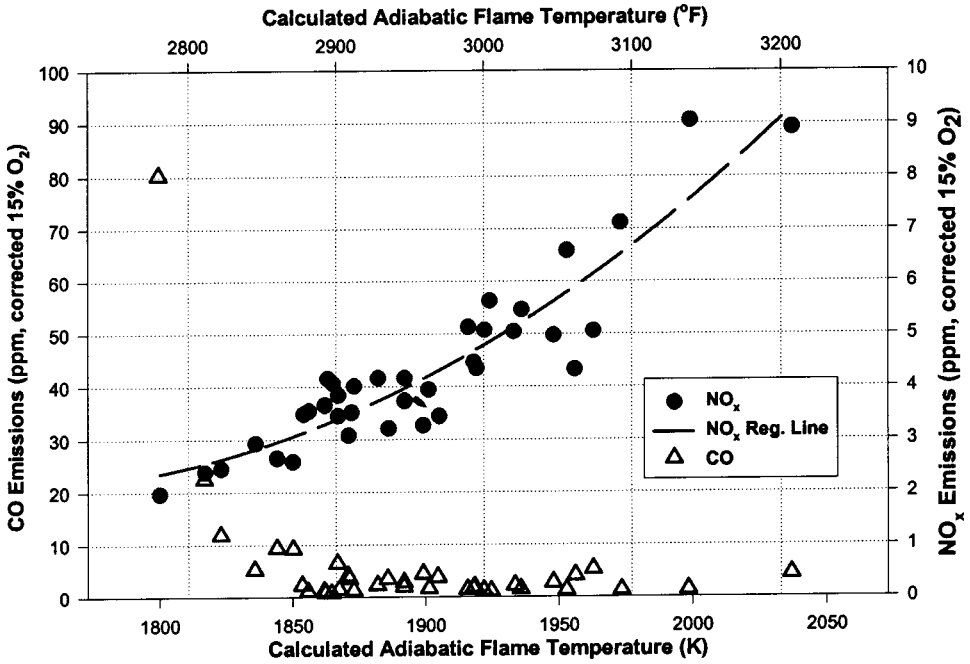


**Fig. 6 Emissions versus calculated adiabatic flame temperature**

probes drew samples from a number of discrete tubes arrayed across the exit plane of the combustor liner. These samples were combined and sent to the emissions train for continuous sampling of $NO_x$, CO, HC, $O_2$, and $CO_2$ concentrations. Thermocouples and hydrocarbon sample tubes installed on each injector allowed accurate online calculation of the AFT for each injector. Pressure losses for the combustor as a whole and for each injector individually were read with pressure transducers. Combustor inlet and exit temperatures and liner temperatures were measured. All data were continuously sampled and electronically recorded throughout the test.

The first issue to be addressed during sector rig testing was that of pressurized ignition. Many of the potential schemes for achieving engine turndown involve turning certain injectors, or zones of those injectors, on and off at different points in the engine loading cycle. A characterization of ignition of one unfired injector by an adjacent fired injector is critical to the development of these control schemes. Ignition tests were conducted at a variety of inlet pressures, inlet temperatures, and airflow rates that simulate full and part load turbine speed conditions. In each case, one injector was fired at a steady-state condition while the other injector remained unlit with only air flowing through the surface. An appropriate amount of fuel was then supplied to the second injector, and the resulting ignition event studied.

The second focus of the sector rig tests was steady-state testing with two injectors firing simultaneously. Beginning at 5 in. separation distance, the two injectors were tested through a range of simulated engine operating conditions, including a Taurus 60 full-load condition. Visual observations of both injectors were made during testing in order to identify any potential surface nonuniformities. Emissions data were gathered in an attempt to determine if emissions are impacted by injector-to-injector interactions. Lean blowout testing was also conducted to identify any effect on stability from the multi-injector configuration. As testing progressed the injectors were moved closer together and portions of the tests were duplicated. At a separation distance commensurate with the Taurus 60 engine (approximately 3 in.), a longer steady-state test was conducted.

The final focus of investigation was steady-state tests with one fired injector and one unfired injector. Single-injector testing has indicated that the presence of cold airflow directed at or across the injector surface can potentially lead to combustion instabilities and poor emissions. In this configuration, which is integral to many of the engine turndown schemes, the cold air flowing through the surface of the unfired injector will likely have some interaction with the combustion on the surface of the fired injector. This interaction was studied at each separation distance by testing one injector through a matrix of simulated engine operating conditions while the other injector admitted airflow but remained unfired.

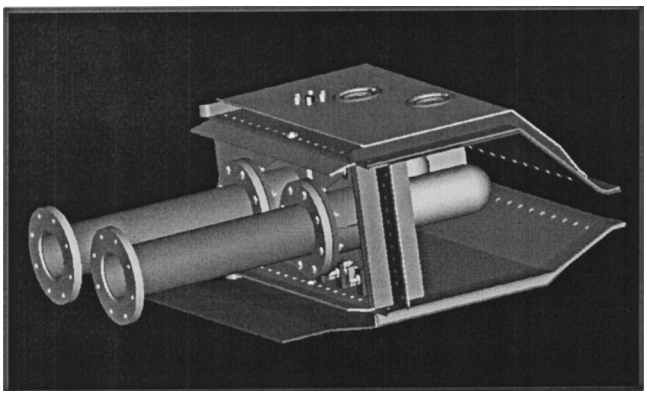

**Fig. 7 Solid model of sector rig liner with two nanoSTAR injectors installed**

## Multiple Injector Results

Testing proceeded initially over six days, with the injectors being moved closer together on succeeding days (Fig. 8). Day one was a shakedown test with only one injector installed, while day 6 was a durability test performed at the last separation distance. At each injector separation distance a full day of testing was conducted during which firing with only one and with both injectors

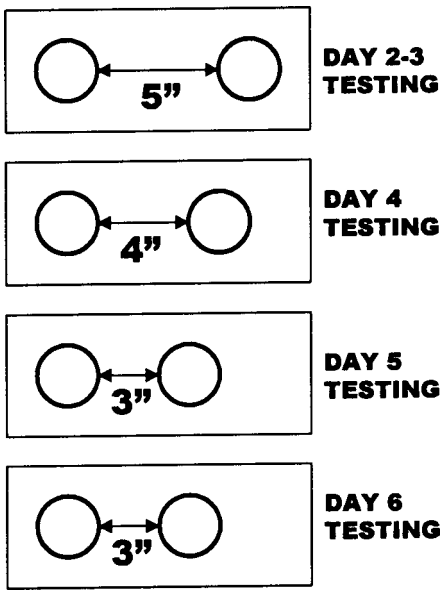


**Fig. 8 Injector separations on successive days of testing**

was attempted, pressurized ignition behavior was evaluated, and emissions data were collected. After each day of testing the injectors were visually inspected.

Table 1 summarizes the pressures at which ignition of the second injector was conducted while the first injector was fired. As can be seen from the chart, most tests were conducted at low to intermediate pressures. This is because pre-test cycle analyses indicated that these pressures corresponded to engine operating conditions where pressurized ignition would be necessary for successful low emissions performance.

**Table 1 Pressurized ignition summary**

| Testing | No. of ignitions | Pressures (atm) |
|---|---|---|
| Day 3 | 5 | 1.3, 2.1, 3.6, 4.8, 6.5 |
| Day 4 | 8 | 2.2, 3.1, 4.2, 5.9, 6.8, 7.9, 8.9, 10.0 |
| Day 5 | 7 | 1.7, 2.2, 3.3, 3.4, 4.5, 6.9, 7.7 |
| Day 6 | 2 | 7.4, 9.6 |

On days 3 and 4 the ignitions were smooth and repeatable. At no point were there significant combustion dynamics or pressure oscillations during these ignitions. On day 5, some of the pressurized ignitions took place at high injector SFR (near 1.4), resulting in unusually high velocities through the surface. Under these conditions there were some small measured pressure oscillations during ignition, which disappeared once the second injector was fully burning. At nominal to low SFRs there were no observable dynamics or oscillations, just as in the previous tests. Injector separation distance did not appear to affect pressurized ignition behavior.

On Day 2 extensive testing was performed with one injector fired and one not. The presence of the unfired injector did not appear to influence the stability of the fired injector. Turndown and $NO_x$ emissions were similar to those observed in previous single-injector tests. However, the presence of the second injector did affect CO emissions. Figure 9 shows CO emissions from four days of testing whenever the one-injector-fired configuration was run. Emission levels were mostly in the 50–100 ppm range (corrected to 15% $O_2$) even at higher AFTs. Relatively cool air from adjacent unfired injectors quenches CO oxidation that normally occurs in the liner volume. Within the range tested, the injector separation distance did not affect this tendency.

The final series of tests were with both injectors firing at all simulated operating conditions and the three separation distances. When fired in this configuration the observed steady-state interaction between the two injectors was minimal. There was no interaction between the laminar flamelets established on the surface of each injector, and the sections of the injectors facing each other did not glow excessively from radiant heating. No excessive combustion dynamics or pressure oscillations were observed.

Figures 10 and 11 show the $NO_x$ and CO emissions when both injectors were fired at the three separation distances tested. $NO_x$ emissions less than 3 ppm and CO emissions less than 25 ppm were achievable. The CO emissions were higher than those observed during single-injector testing. One potential explanation is

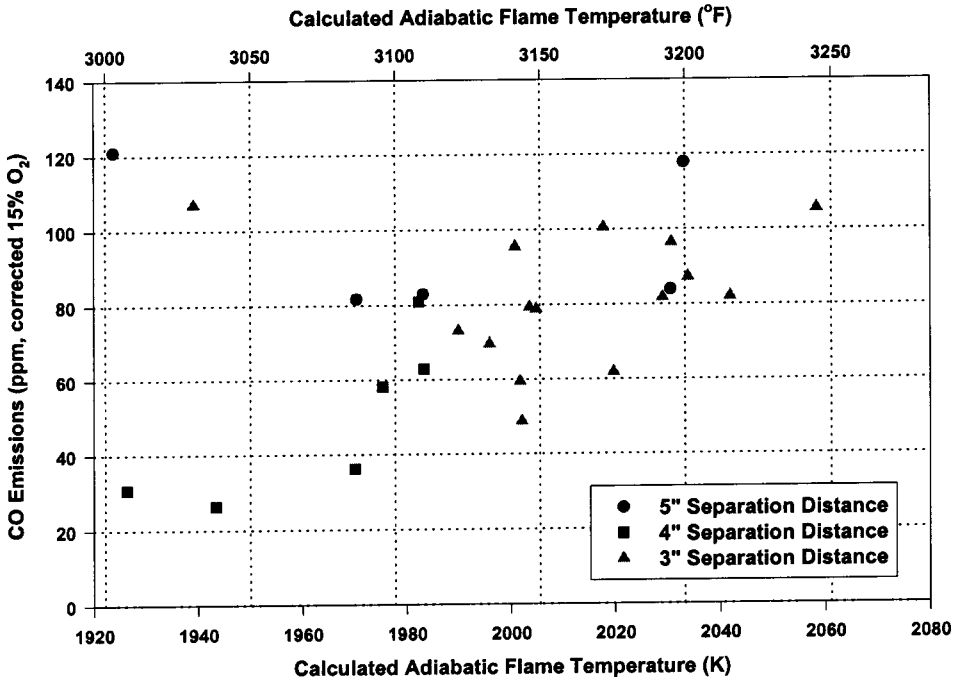


**Fig. 9 CO emissions during one fired/one unfired tests**

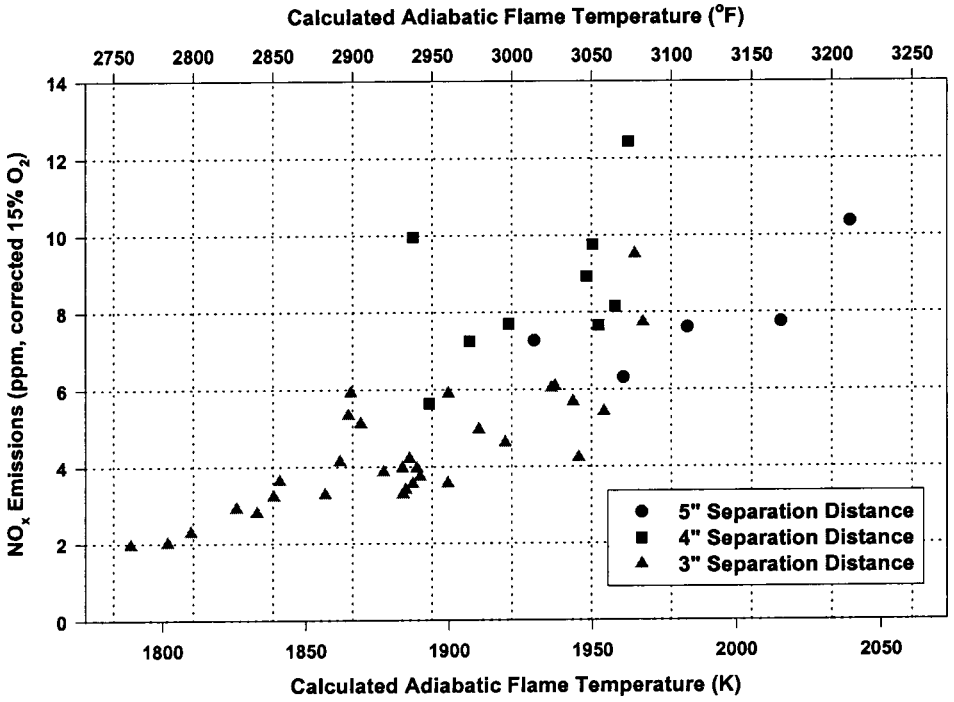


**Fig. 10 $NO_x$ emissions for both injectors fired**

that purge/cooling air from the two quartz viewports was observed impinging on the surface of both injectors, to such an extent that flames in those areas were deflected by the flow. This could have driven higher CO emissions than those observed during single-injector testing. Also note that the emissions performance is independent of the injector separation distance.

The firing of two injectors in close proximity to each other appears to have no adverse effect on the $NO_x$ emissions when compared with single-injector tests. Figure 12 shows the measured $NO_x$ emissions from the 3 in. separation tests plotted with the $NO_x$ emissions from a previous single-injector test with another nanoSTAR injector.

Day 6 included an "endurance test" in which both injectors were run for a full day. In total, over all days of testing, the total fired run time on the first injector exceeded 40 h, while the total run time on the second injector exceeded 20 h, including 22 pressurized starts. After the entire program of testing the two injectors

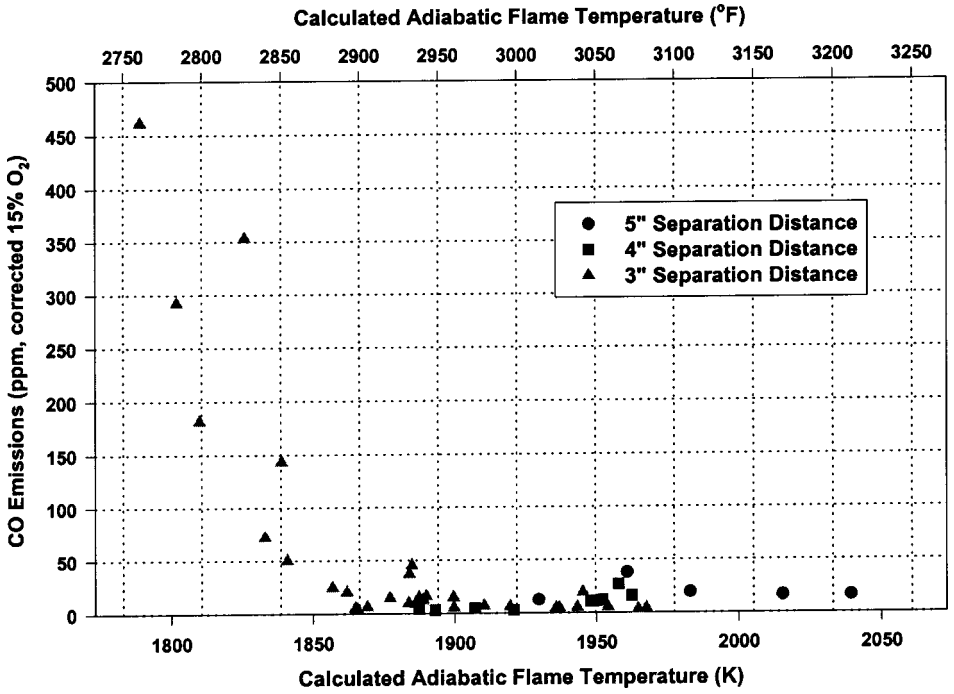


**Fig. 11 CO emissions for both injectors fired**

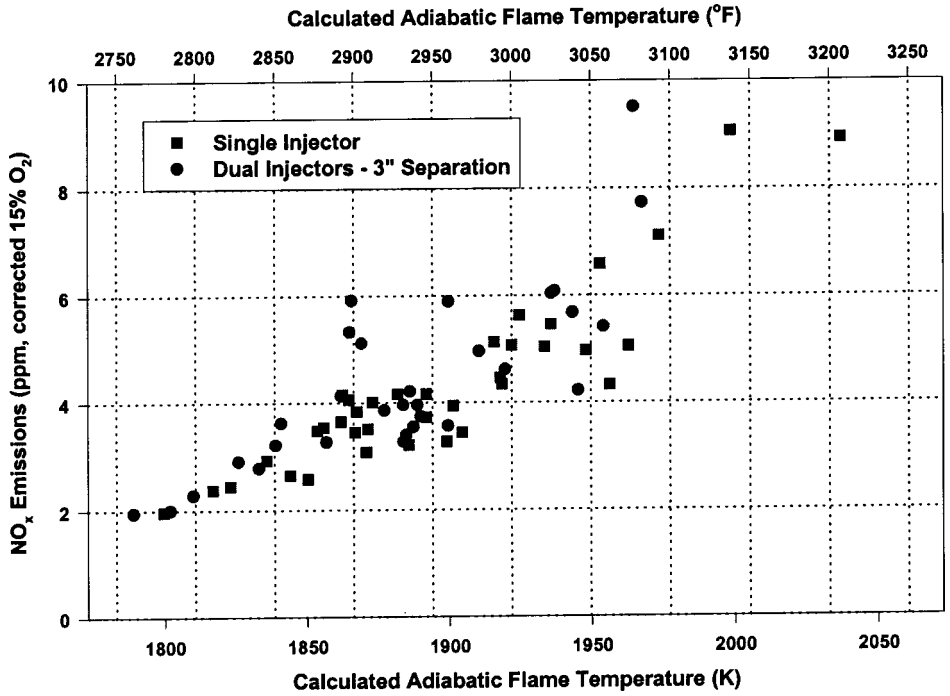


**Fig. 12 Comparison of day 6 $NO_x$ data with data from a single injector test on Dec. 7, 2001**

were examined and neither showed any signs of excessive aging due to the proximity testing. Figure 13 shows before and after pictures of the first injector.

## Higher Pressure Operation

Previous tests at multiple facilities clearly established the viability of nanoSTAR surface-stabilized combustion technology at pressures and volumetric heat release rates consistent with industrial gas turbines with pressure ratios up to 12. Higher inlet temperatures and pressure ratios are required to increase engine efficiency and are encountered in higher output engines such as Solar Turbines' 13.5 MW Titan 130. This engine operates at a pressure ratio of 16 as opposed to 12 for the Taurus 60. To assess the feasibility of applying the technology to higher pressure ratio engines, a prototype Taurus 60 nanoSTAR injector was rig tested under simulated Titan 130 pressure and temperature conditions.

As in previous tests the injector was ignited at near-atmospheric conditions and ramped through a series of pressure/temperature combinations, however, this time the ramp was continued beyond Taurus 60 full load conditions, ultimately reaching 1.68 MPa (16.6 atm) and 670 K (750°F). At these elevated pressure and inlet temperature conditions, the injector displayed greatly enhanced

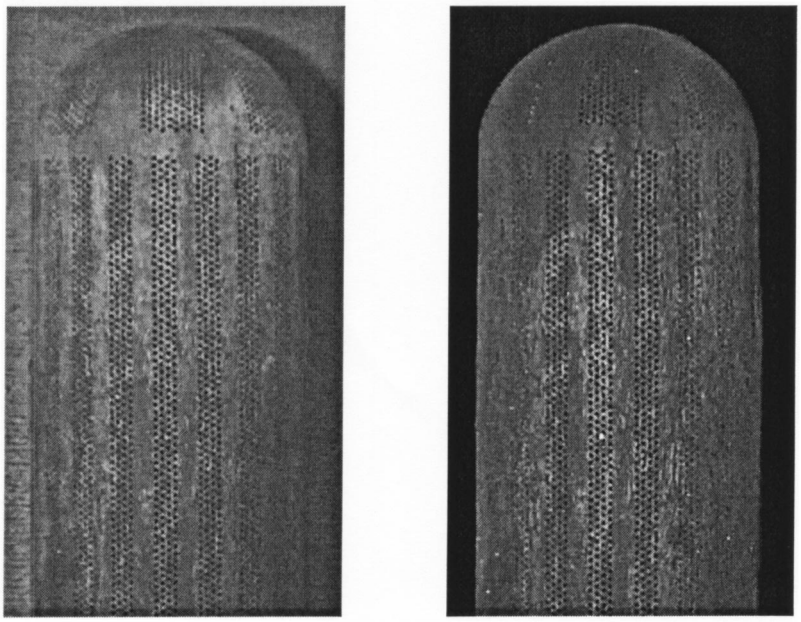

**Fig. 13 Pictures of the first sector rig injector before testing (left) and after testing**

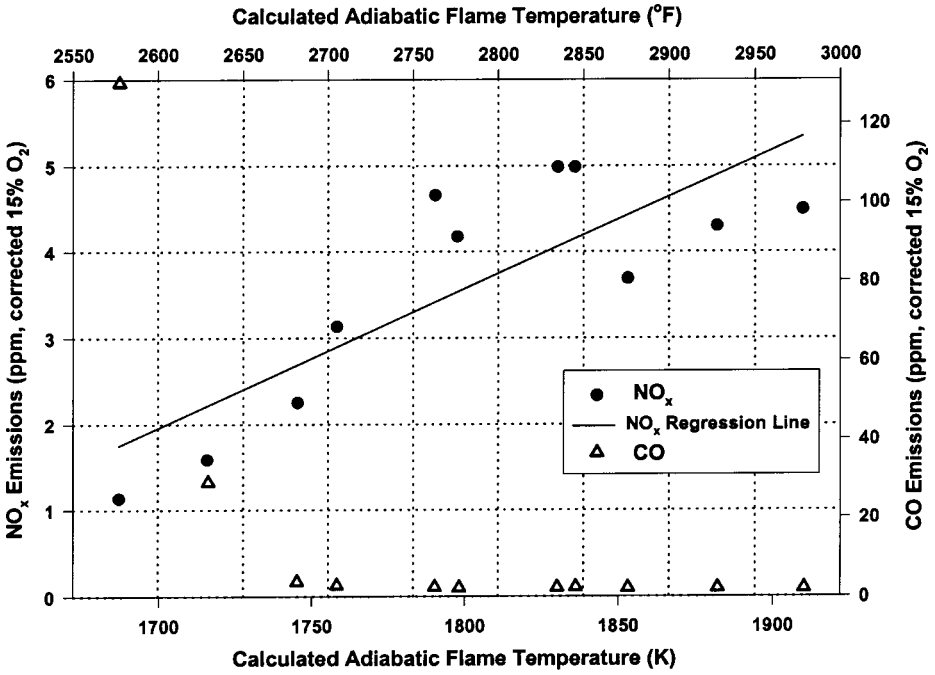


**Fig. 14 $NO_x$ and CO emissions at 116 MPa (16 atm) versus AFT**

stability over previous tests at 12 atm and below. A lean blowout ramp was conducted and the injector was able to reach an AFT below 1685 K (2575°F) prior to flameout. $NO_x$ emissions as low as 1.1 ppm were recorded, though CO had climbed above 100 ppm at that point. More reasonable CO emissions of 29 ppm were displayed at a flame temperature of 1710 K (2618°F) and corresponding $NO_x$ emissions of 1.6 ppm. The crossover point where $NO_x$ and CO emissions were equal was around 3 ppm and a flame temperature around 1755°K (2700°F). Figure 14 shows measured emissions of CO and $NO_x$ at the nominal 1.6 MPa (16 atm) pressure condition.

During these tests the nanoSTAR injector displayed stable, low-emissions operation in the 1.20–1.68 MPa (12–16 atm) range and throughout a broad range of surface firing rates and adiabatic flame temperatures. After testing, the injector was inspected and displayed no physical change, and indeed after 10 h of intensive testing and multiple ignition starts the injector appeared virtually the same as it did prior to testing. In addition, the lower emissions and increased lean stability at the higher operating pressure indicate that the nanoSTAR injector benefited in terms of stability from the higher inlet temperature without paying the expected emissions penalty. Although $NO_x$ emissions are higher with increased preheat at any given flame temperature, this effect is more than counteracted by the increase in lean stability. The net effect is that lower overall $NO_x$ emissions are attainable at the increased temperature and pressure conditions encountered in the Titan 130 engine.

## Conclusion

The extensive tests conducted with two injectors in close proximity demonstrated sustainable operation down to 3 in. of separation as required for application in the Taurus 60 without modification of the combustion liner. $NO_x$ emissions when both injectors are fired were unchanged from previous single-injector tests. Detrimental interaction between the two injectors when fired together was not observed, and neither injector was damaged in any way by proximity firing. Pressurized ignition was successful and was repeated at several pressures with no observable combustion dynamics and little pressure fluctuations.

The one issue identified during the proximity testing was that CO emissions appeared higher when one injector was fired while the other was not. Two facts might mitigate this effect operationally, however. One is that for the majority of the test points the CO emissions in this configuration were between 50 and 100 ppm (corrected 15% $O_2$). Thus, a small increase in the combustor volume may reduce CO to the targeted level. The second is that all cycle analyses conducted on both the Taurus 60 and Titan 130 cycle data indicate that situations involving unfired injectors only arise below about 60% load. Therefore higher CO emissions due to nonfiring some injectors would only be a part-load effect. CO emissions lower than 25 ppm could be expected at higher engine loads. This issue still requires further investigation.

Recent rig tests by ALZETA and Solar Turbines have clearly demonstrated the viability of nanoSTAR surface-stabilized fuel injectors under operating conditions of 1.68 MPa (16.6 atm) and 670 K (750°F) inlet temperatures. Ultralow emissions of $NO_x$ ($<3$ ppm) and CO ($<10$ ppm) were demonstrated at these higher pressure and temperature conditions.

ALZETA and Solar Turbines are continuing with the next phase of deploying nanoSTAR technology, which will be a multi-injector full scale rig test in the first quarter of 2003. Engine testing is scheduled to begin later that same year.

## Acknowledgments

This work was funded in part by the California Energy Commission and the U.S. Department of Energy.

## Nomenclature

AFT = Adiabatic Flame Temperature; a value calculated from the inlet temperature, pressure, fuel/air ratio, and fuel composition.

SFR = Surface Firing Rate; injector firing rate per square foot of injector fired surface area per atmosphere of pressure. Closely tied to injector pressure drop and firing rate.

## References


[1] Vandervort, C. L., 2001, "9 ppm $NO_x$/CO Combustion System for "F" Class Industrial Gas Turbines," ASME J. Eng. Gas Turbines Power, **123**, pp. 317–321.

[2] Yee, D. K., Lundberg, K., and Weakley, C. K., 2001, "Field Demonstration of a 1.5 MW Industrial Gas Turbine With a Low Emissions Catalytica Combustion System," ASME J. Eng. Gas Turbines Power, **123**, pp. 550–556.

[3] Leonard, G. L., and Correa, S. M., 1990, "$NO_x$ Formation in Premixed High-Pressure Lean Methane Flames," Fossil Fuel Combustion Symposium 1990, S. N. Singh, ed., American Society of Mechanical Engineers, New York, pp. 69–74.

[4] Weakley, C. K., Greenberg, S. J., Kendall, R. M., McDougald, N. K., and Arellano, L. O., 2002, "Development of Surface-Stabilized Fuel Injectors With Sub-Three ppm $NO_x$ Emissions," ASME Paper No. IJPGC2002-26088, presented at the 2002 International Joint Power Generation Conference, Phoenix, AZ, 24–26 June, 2002.

# Measurement of Smoke Particle Size and Distribution Within a Gas Turbine Combustor

**K. D. Brundish**

**M. N. Miller**[1]
e-mail: mnmiller@qinetiq.com

**C. W. Wilson**

QintiQ,
Farnborough,
Hants GU14 OLX, United Kingdom

**M. Jefferies**
Rolls-Royce Plc,
Derby, United Kingdom
e-mail: mark.j.Jefferies@rolls-royce.com

**M. Hilton**

**M. P. Johnson**
e-mail: m.p.Johnson@reading.ac.uk

J. J. Thompson Physics Laboratory,
University of Reading,
Whiteknights,
Reading, United Kingdom

*The objective of the work described in this paper was to identify a method of making measurements of the smoke particle size distribution within the sector of a gas turbine combustor, using a scanning mobility particle sizing (SMPS) analyzer. As well as gaining a better understanding of the combustion process, the principal reasons for gathering these data was so that they could be used as validation for computational fluid dynamic and chemical kinetic models. Smoke mass and gaseous emission measurements were also made simultaneously. A "water cooled," gas sampling probe was utilized to perform the measurements at realistic operating conditions within a generic gas turbine combustor sector. Such measurements had not been previously performed and consequently initial work was undertaken to gain confidence in the experimental configuration. During this investigation, a limited amount of data were acquired from three axial planes within the combustor. The total number of test points measured were 45. Plots of the data are presented in two-dimensional contour format at specific axial locations in addition to axial plots to show trends from the primary zone to the exit of the combustor. Contour plots of smoke particle size show that regions of high smoke number concentration once formed in zones close to the fuel injector persist in a similar spatial location further downstream. Axial trends indicate that the average smoke particle size and number concentration diminishes as a function of distance from the fuel injector. From a technical perspective, the analytical techniques used proved to be robust. As expected, making measurements close to the fuel injector proved to be difficult. This was because the quantity of smoke in the region was greater than 1000 mg/m$^3$. It was found necessary to dilute the sample prior to the determination of the particle number concentration using SMPS. The issues associated with SMPS dilution are discussed.*
[DOI: 10.1115/1.1839921]

## Introduction

With respect to gas turbine engines, the radiation emitted by smoke particles is detrimental to combustor and turbine blade life. Smoke emissions also pose a threat to health and the environment. Although some legislation currently exists for smoke emissions, it is likely that more stringent pollution control will be forthcoming.

Currently the only reliable way of determining the smoke concentration is by using experimental test rigs. If, however, a reliable smoke model were to be evolved, then considerable cost savings could be the net result as expensive rig testing could be reduced or eliminated.

## Experimental Configuration

Within this section the hardware configuration will be examined. In order to provide sufficient data for computational fluid dynamic (CFD) model validation full gas analysis measurements were made in addition to the smoke measurements presented.

**High Pressure Test Rig Configuration.** A section from a fully annular aero, gas turbine combustor was used in this work. The sector combustor encompassed an arc of approximately 70 deg and comprised four air-spray fuel injectors. Since the combustor was not fully annular, water-cooled sidewalls were placed at either side. The area within the combustor which encompassed the two central fuel injectors has been shown to be representative of a fully annular combustor [1,2]. The segments next to the wall of the combustor are not representative because of wall quenching, and recirculation effects. Measurements were therefore restricted to the two central segments.

A test rig has been in use for some years at QinetiQ, Pyestock in Hampshire U.K, which has the unique ability of being able to extract gaseous samples from within the volume of a gas turbine combustor. The test rig has the capability of supplying inlet air temperatures up to 900 K, air mass flow rates up to 5 Kg/s and pressures up to 10 bar. The arrangement of the facility is illustrated in Fig. 1. The main components of the rig are compressor, heater, fuel system, exhaust system, sample probe with traversing gear, and combustion chamber.

Combustion products were extracted from different axial planes in the combustor using an intrusive gas sample probe as identified in Fig. 2. Data presented within this paper were measured at planes B, D, and F. Plane B is located at the exit of the primary zone, with plane D downstream of the dilution ports and plane F at the combustor exit. The total number of test points measured in planes B, D, and F were 11, 19 and 17, respectively.

The gas sample was designed so that the gaseous sample is conditioned to a temperature (423 K$\pm$15) where no further chemical reactions are likely to occur and no condensation takes place. A heated stainless steel sample line connected to the sample probe was used to convey the sample from the combustor to the gas analysis system. This sample acquisition system incorporates high pressure back purge air, which could be maintained at a pressure of about 1500 Pa, and was used to stop fuel flowing down the sample line at light-up. The backpurge system was actuated by a valve that allowed almost instantaneous changes between the sample or backpurge air and was also used to maintain a clear passage in the sample probe.

[1]To whom correspondence should be addressed.

Contributed by the International Gas Turbine Institute (IGTI) of THE AMERICAN SOCIETY OF MECHANICAL ENGINEERS for publication in the ASME JOURNAL OF ENGINEERING FOR GAS TURBINES AND POWER. Paper presented at the International Gas Turbine and Aeroengine Congress and Exhibition, Atlanta, GA, June 16–19, 2003, Paper No. 2003-GT-38627. Manuscript received by IGTI, October 2002, final revision, March 2003. Associate Editor: H. R. Simmons.

  

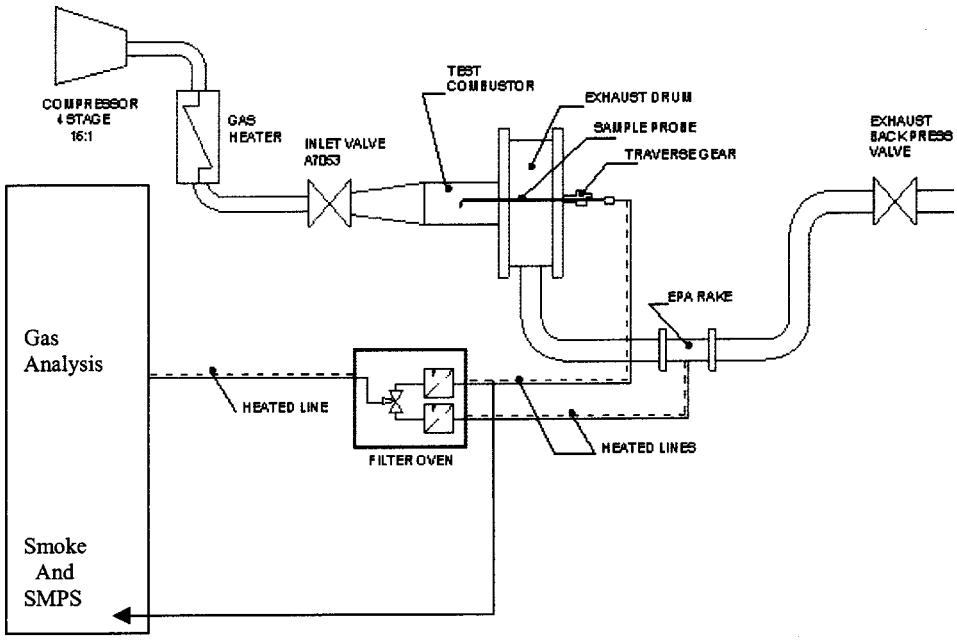


**Fig. 1 Schematic representation of test rig**

The probe was intrusive, however it was designed to minimize the interference with the local environment. The inlet orifice diameter was 1.5 mm and the outside diameter of the sample probe was 10 mm. Smaller diameters could not be used because the physical strength of the sample probe would be insufficient and distortion would result. The traverse mechanism used to drive the probe had 4 deg of movement which were pitch, yaw, translation and rotation. Each of the 4 deg of movement were measured using individual potentiometers. Before rig testing, the position of the sample probe was determined through calibration. The gaseous samples entered the sample probe under rig pressure; excessive sample was spilled close to the sample probe. Although the sample flow was not perfectly isokinetic, perturbations in the sample train were not significant.

**Smoke Mass Instrumentation.** The mass of smoke from the primary to the exit zone of a gas turbine combustor has been shown to vary by three orders of magnitude [3]. Due to this large variation in smoke concentration, it was necessary that two different analytical techniques were used. In the first, a standard filter stain technique was employed, whereby a filter paper was used to trap a quantity of smoke from a fixed volume of sample gas. A reflectometer was then used to determine the concentration of smoke present, the result of which was expressed as the SAE smoke number [4]. This technique was generally used at the exit of a gas turbine where the smoke concentrations were likely to be low. The instrument used to make the measurements was a Richard Oliver smoke meter (Part number MK1 1023).

When making measurements inside the combustor an optical technique was used. A visible light SIGRIST nephalometer, which works on the principle of deflecting the optical beam at an angle of 15 deg was used [5]. It should be noted that although the instrument is an optical device, the smoke sample is extracted from within the combustor and fed to the analyzer. The calibrated range of the SIGRIST was from 10 to 1000 mg/m$^3$, although the

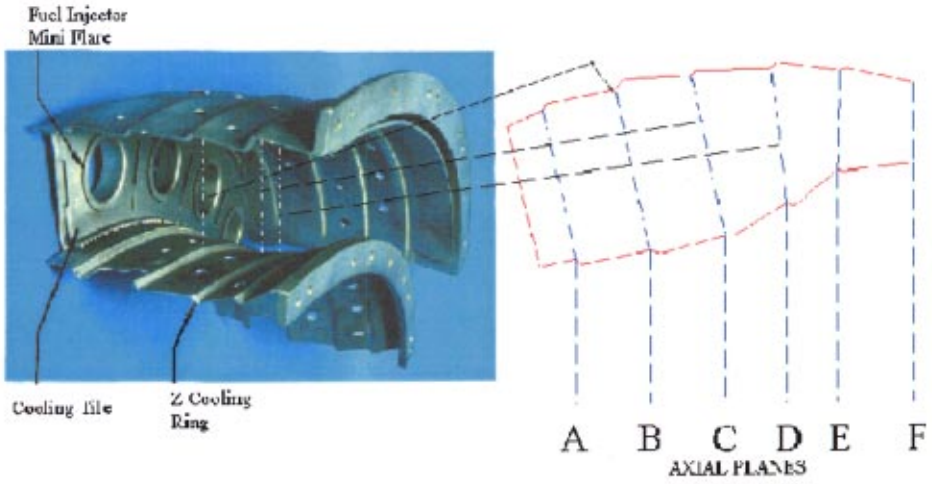


**Fig. 2 Generic sector of combustor**

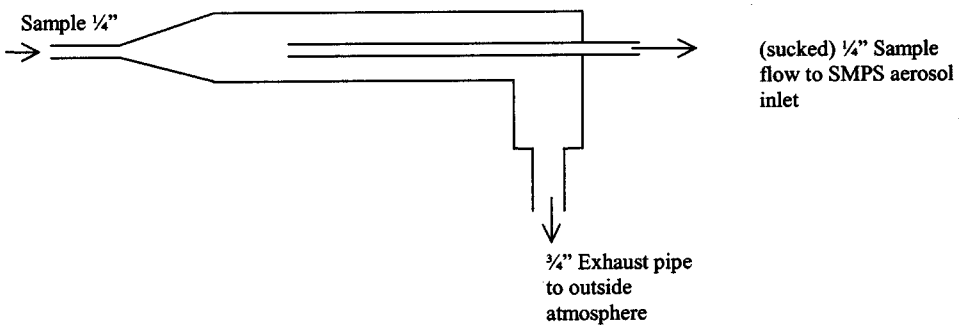


**Fig. 3 Pressure regulation system**

analyzer read up to 2000 mg/m$^3$. The SIGRIST was initially calibrated against a known mass of smoke generated by a combustor [6]. Subsequent checks on the optics were undertaken using reflective rods. Maximum errors associated with the optical technique have been found to be ±25%.

**SMPS Instrumentation.** In order to determine the number concentration and size distribution of the smoke particulates, a TSI, scanning mobility particle sizing (SMPS) analyzer was used. The SMPS system measures the size distribution of aerosols in the size range from 14 to about 800 nm using an electrical mobility detection technique. The SMPS analyzer was connected to the same dedicated smoke sample line which also incorporated the SIGRIST and the SAE measuring instruments. A direct comparison between the different analytical techniques could then be made. It was important when using the SMPS analyzer that the sample was fed at a constant pressure. This was achieved by reducing the sample pressure to near atmospheric. This reduction in pressure must be achieved with minimal disruption to the flow in order to reduce effects on smoke measurements and was achieved using the configuration identified in Fig. 3.

The sample is expanded slowly into a large volume that is vented to atmosphere downstream. A small percentage of the sample flows into the SMPS instrument through a secondary sample tube located in the center of the large volume. This ensures that the pressure is reduced while maintaining sample fidelity.

The SMPS system measures the size distribution of particulates using an electrical mobility technique. A radioactive Kr-85 source is used to neutralize and charge incoming particulates. The charged particles then enter a classifier where they are sequentially separated by electrostatic repulsion.

After the sample has been ''classified'' by the SMPS, the sample was drawn, by a pump, through a condensation particle counter (CPC) to determine number concentration.

**Sample Dilution.** In order to make SMPS measurements within the combustor; it was necessary to dilute the gaseous sample before determination of the particle size and distribution. There are several reasons why the sample must be diluted prior to measurement. The main ones are related to water of combustion concentration, particulate number concentration, and coagulation of smoke particulates in the sample line.

Particulate number concentration is a concern when values exceed 1E7 particles/cm$^3$ for any given size range. This instrument is not able to measure such high values and defaults to a statistical approach (photometric effect). Dilution reduces the likelihood of this occurring as the particle number counts are reduced.

Water of combustion only becomes a problem if the dewpoint of the gaseous water is exceeded and particulates are lost in the condensate. Heating the sample lines to 423 K ensures no condensation takes place in the sample line. It was not, however, possible to heat the lines within the SMPS analyzer, therefore the dew point has to be adjusted by dilution so that none of the particulates are lost due to condensation.

Coagulation of smoke particulates occurs when the individual particles collide and stick to each other [7]. Upon initial coagulation, more and more of the particulates collide, thus forming ever-larger particulates. When initially formed, smoke particulates are very small, these particulates upon coagulating diminish in number but increase in size. The effect of coagulation is shown in Fig. 4 which shows smoke particulates magnified 310,000 times. It can be seen that when they coagulate they become larger and lose their spherical shape. This image, although collected from an aero engine, was not acquired from the combustor used in this work. Diluting the sample reduces the proximity of the particulates to each other thus increasing the mean free path before collision and possible coagulation occurs.

The dilution air was generated using a compressor and then filtered by using a two stage BOLSTEN filtering system. This system removes particles down to a size of 0.01 $\mu$m, as well as water and oil. The total particulate number concentration for this filtered air was measured using the SMPS and found to be between 20 and 50 particles/cm$^3$. The need for filtering the dilution air was shown by checking ambient air concentration values in the test control room which were found to be between 3000–8000 particles/cm$^3$. The dilution air line was heated to 423±5 K for a length of about 1 m prior to joining a Y piece. The Y piece allowed the dilution air to merge with the gas sample as depicted in Fig. 5. The reason that the air was heated was to offset any potential effects upon the sample.

The gas analysis system was used to determine the dilution ratio of the sample. The gas analysis facility consisted of a suite of gas analyzers, which were used to determine the concentration of pollutants. The analysers that were available are shown in Table 1.

It can be seen from Table 1 that the CO and $CO_2$ analyzers

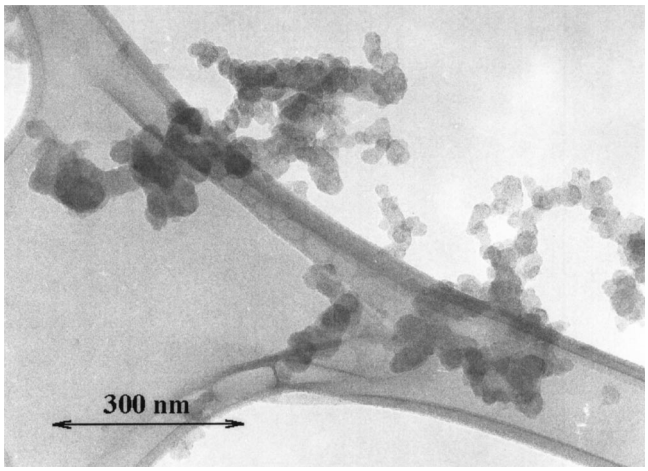


**Fig. 4 Smoke particulates magnified 310,000 times**

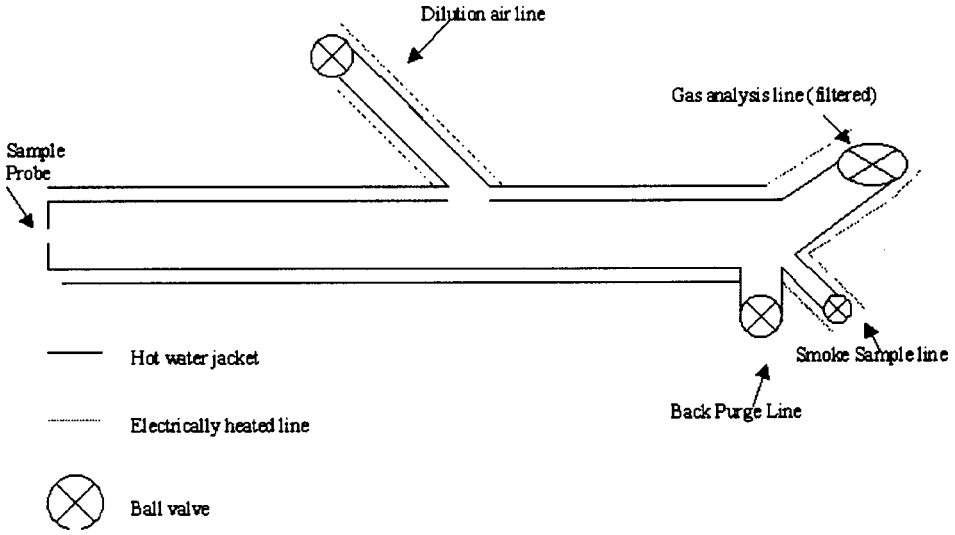


**Fig. 5 Layout of the dilution system**

covered a number of ranges to enhance the accuracy of the measurements. With the cycles considered, the $CO_2$ concentration between the combustor face and the exit of the combustor could vary between 0.5% and 15%, hence the need for two analyzers. The gas analysis system used conforms to the requirements of the International Civil Aviation Organization, July 1993 [8].

Dilution was determined by taking a gas analysis measurement before and after the dilution air was added to the sample. NO, $NO_X$, $O_2$, $CO_2$, total hydrocarbons and CO were measured at each of the test points. The most stable chemical species, however, was $CO_2$, and this was used to determine the dilution ratio. Two individual $CO_2$ analyzers were used to measure the concentration of the specific species, and the ranges of the two analyzers were 0%–2% and 0%–15%.

The dilution ratio as determined by $CO_2$ was checked against values obtained using $NO_X$ ($NO_2+NO$) and the results obtained were in good agreement. Although $NO_X$ could be used to determine the dilution ratio, NO and $NO_2$ measured individually could not. This is because of possible chemical reactions occurring in the sample line prior to the measurement of the species. The maximum uncertainty associated with the dilution ratio was $\pm 11\%$ at dilution ratios up to 35, while at a dilution ratio of 150 the uncertainty was $\pm 23\%$.

**Line Losses.** Work undertaken by Hurley [9] has shown that smoke particulates are lost on the walls of the sample line as they are transported to the smoke measuring equipment. Hurley derived the following line loss equation (*E*1). The equation takes into account factors such as velocity, composition of sample line, line diameter, and length:

$$n/n_0 = \exp(-(1.05E-4V+2.27E-4)L/DV), \qquad (E1)$$

**Table 1 Analysers used**

| Type of analyzer | Technique | Range % |
|---|---|---|
| Carbon dioxide | Infrared | 0–15 |
| Carbon dioxide | Infrared | 0–2 |
| Carbon monoxide | Infrared | 0–0.05 |
| Carbon monoxide | Infrared | 0–1 |
| Carbon monoxide | Infrared | 0–15 |
| Total HC | Flame ionization | 0–10 |
| Hydrogen | Chromatography | 0–10 |
| Oxygen | Paramagnetic | 0–30 |
| Nitrogen oxides | Chemiluminescense | 0–0.1 |

where $n/n_0$=The ratio of smoke particles coming out of the sample line ($n$) to those entering the line.

$V$=velocity (m/s)

$L$=sample line length (m)

$D$=sample line internal diameter (m)

The calculated line loss found for the operating conditions used in this work was found to be between 21% and 24%. All data presented in this paper have been corrected for line loss.

**Summary of Experimental Configuration.** A number of factors affect the accuracy of the SMPS measurements, some of which are reduced through the use of dilution and conditioned sample lines. The experiment has been configured to minimize all of the associated errors, although it is not possible to determine an overall systematic error, the smoke measurements performed will be compared to more traditional techniques to gain confidence in the data. Although it is desirable to maximize the dilution ratio, the sensitivity of the gas analysis measurement system presented a practical limitation. SMPS measurements had not been previously performed within the combustor and as a consequence the minimum required dilution was unknown at the commencement of the testing and had to be derived experimentally.

## Determination of Minimum Dilution Ratio

**Dilution Effects With Respect to Probe Location.** Smoke and gas analysis measurements were made at a number of axial planes within the combustor: B, D, and F as illustrated in Fig. 2. Preliminary tests were undertaken to ascertain the effect of dilution upon the particulate number concentration in each of the axial planes.

Figure 6 shows a plot of normalized particulate number concentration versus particulate size for an individual test point taken within plane F. The diluted data have been multiplied by the dilution factor as determined from the gas analysis measurements. The dilution value as determined from the $CO_2$ measurements was found to be 19. The mean particle size for the diluted sample was found to be 50 nm while for the undiluted test point the value was 52 nm. The fact that the mean particle size does not significantly change suggests that coagulation is not a problem in this axial plane.

Figure 7 shows a diluted test point multiplied by the dilution factor, and also the undiluted test point acquired at the same spatial location in plane D. Gas analysis measurements at this test point suggest that the dilution ratio was 19. The value for the mean particle size of diluted sample was found to be 67 nm while

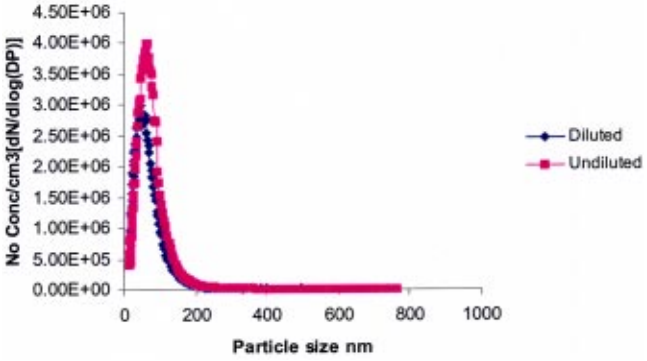


**Fig. 6 Diluted and undiluted Plane F**

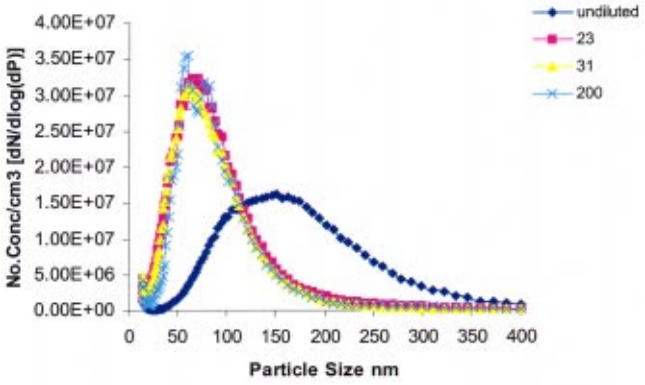


**Fig. 8 Varied dilution and undiluted Plane D**

for the undiluted sample the value was 201 nm. Although it appeared that there was little effect of dilution in plane F, it can be seen that the effect in plane D is pronounced. This shift in particulate size shows that coagulation effects were significant. A similar result, not reported here, was found in plane B although the difference in particle size and dilution factors was more pronounced.

The above plots show that for planes B and D dilution is necessary, although for plane F it is less significant. The combination of change in particle size and number concentration with the addition of dilution air suggests the effect of coagulation is the dominant factor. Unsurprisingly the effects are more pronounced the closer the sample is taken to the fuel injector and thus optimum dilution ratio must be determined for each plane.

**Effect of Increasing Dilution Air.** It was important to establish the effect of varying the amount of dilution air in the sample. This was necessary because it is likely that there is a minimum amount of dilution air required to avoid coagulation of the sample in the sample line. At a discrete sample point in plane D of the combustor, the dilution ratio was varied and the results are shown in Fig. 8.

Again, Fig. 8 shows the diluted data multiplied by the dilution ratio (in this case 23, 31, and 200) calculated from the gas analysis. The mean particle sizes with respect to increasing dilution ratio were 63, 61, and 67 nm respectively, while the undiluted sample had a value of 129 nm. It can be seen that the geometric mean particle size distribution does not change significantly when dilution ratios of between 23 and 200 are used. This result shows that for test running purposes, a dilution ratio of 23 in plane D of the combustor will produce representative results, and this value was used. It is, however, possible that if localized rich spots are encountered then this dilution value may prove inadequate. In plane F the geometric mean particle size does not significantly alter when the sample is diluted, however minimum dilution ratios of 14 were used to ensure that there was no dewing of the water in the sample line.

In plane B a dilution test was undertaken but problems with probe blockage were encountered. This was because it took a minimum of 4 min to acquire the SMPS scan, plus the time required to determine the dilution ratio. It should be noted that smoke concentration levels in this zone were sometimes greater than 1000 mg/m$^3$, hence probe blockages became more common. Prior to installing the SMPS into the system, the time taken to acquire test data was about 2 min and this generally resulted in few problems with probe blockage. At the onset of a test it was not possible to set the dilution air flow to a dilution ratio of, for example, 23 and expect the value to remain constant from one test location to the next. It was found that when moving the probe from one spatial location to the next, the density and pressure of the sample significantly changed and so the dilution ratio had to be adjusted for each test point. This in itself was time consuming and increased the probability of probe blockage.

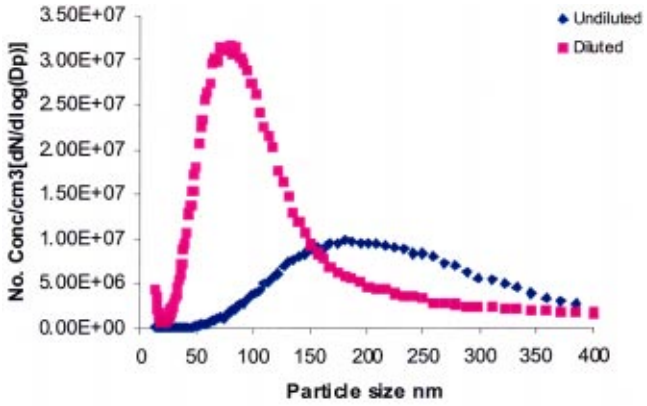


**Fig. 7 Diluted and undiluted Plane D**

## Experimental Results

With confidence in the experimental configuration determined, more detailed measurements were performed in Planes F, D, and B. Both SMPS and smoke mass measurements were performed and are compared. The total number of diluted sample points measured in planes F, D, and B were 17, 19, and 11 respectively. The data presented have been corrected for both line losses and dilution.

**SMPS Measurements.** Figure 9 shows a two-dimensional contour plot of the total smoke number concentration (expressed as particles/cm$^3$) for plane F. The test points were about 10 mm apart and formed a grid over the area shown. It can be seen from this plot that the distribution across the axial plane is not symmetrical but biased towards the right hand side of the combustor. The reason for this is that this location coincides approximately with the position of one of the fuel injectors.

This region of high smoke number concentration can also be seen in axial planes D and B as shown in Figs. 10 and 11, respectively. This pattern shows that should a region of high smoke be formed in the primary zone of the combustor, it generally persists through to the exit plane.

**Smoke Mass Measurements.** The smoke mass as determined by the SIGRIST optical smoke meter has been plotted for planes D and B and are shown in Figs. 12 and 13, respectively. It should be noted that all data points acquired for plane B have been included in the plot. This is despite the fact that some are above the

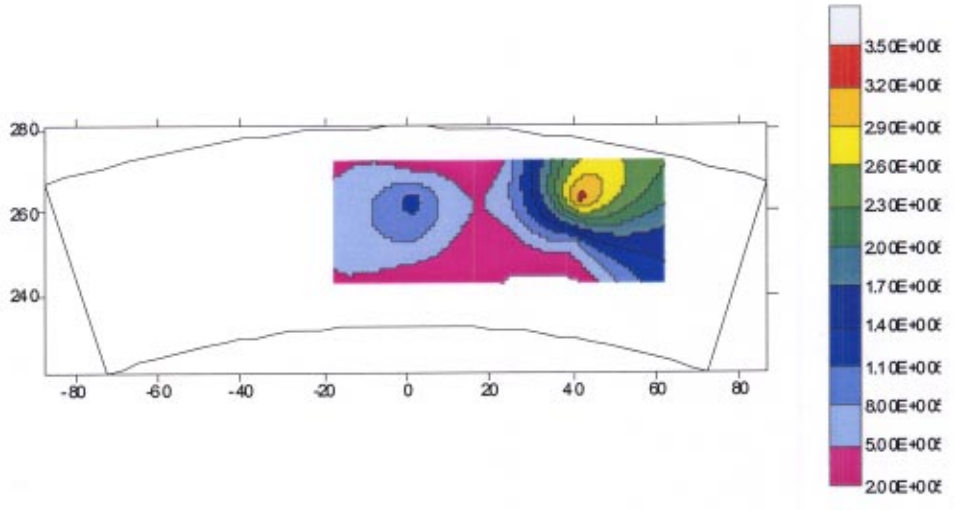


**Fig. 9 Particulate number concentration Plane F**

calibrated range of the SIGRIST and are therefore extrapolated concentration values. They have been included to show the trends and not provide definitive quantitative values.

The trends observed in these two plots show reasonable qualitative agreement between particulate number concentration contours measured using SMPS, Figs. 10 and 11, and mass concentration profiles measured using SIGRIST.

In plane F of the combustor, it was not possible to measure the smoke (mass) concentration using the optical technique (SIGRIST). This was because the observed values were too low to be determined using this analytical method. The values determined from the SAE technique are shown in Fig. 14 and the trends again show a good agreement with particulate number concentration as shown in Fig. 9.

**Comparison Between SMPS and Smoke Mass Measurements.** The SMPS analyzer does not have the capability of measuring the mass of smoke particulates. However, the software accompanying the instrument does calculate the volume of the particulates from their size and number concentration. In order to establish how the two techniques compare, plots of smoke mass as determined by SIGRIST versus volume as determined by SMPS are illustrated. As well as providing a means of comparison between the two techniques, the gradient of the best fit line allows the determination of the density. Figure 15 shows the measurements for plane B while Fig. 16 shows the measurements for plane D. Smoke mass concentration values greater than 1000 $mg/m^3$ have been omitted from the plot (plane B only) as they were outside the calibration range of the instrument. With respect to plane F, the SAE values were converted to a mass concentration by an empirical correlation which was determined at QinetiQ [3]. It was necessary to measure the smoke in this plane using the filter stain technique because the smoke concentration was so low that the SIGRIST could not be used. The problem with this comparison, however, is that the SAE measured values were very low and the error associated with the analytical technique is $\pm 3$ SAE units. With the exception of one test point which was SAE 9 the rest of the values were all less than 4, therefore the errors are large.

It can be seen that the agreement between the two techniques is reasonably good in plane B. The agreement between the data in plane D shows good agreement along part of the data set. It can be seen that there is one point with a mass of 5.6E-8 which shows massive deviation from the rest of the data. Statistically; it would have been justifiable to eliminate this point, however there are reasons to suppose it may be correct. It has therefore been left in

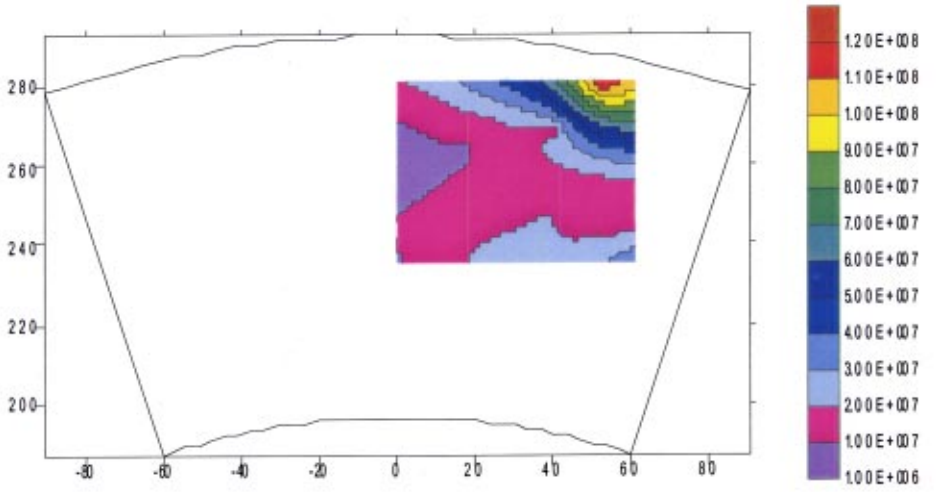


**Fig. 10 Particulate number concentration Plane D**

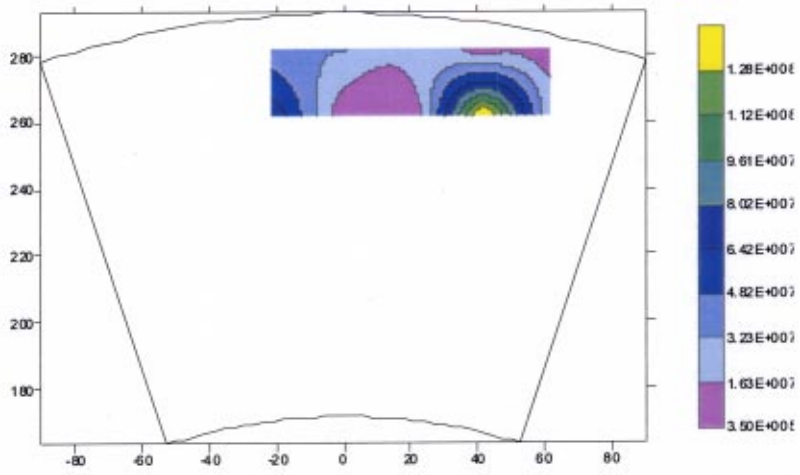


**Fig. 11 Particulate number concentration Plane B**

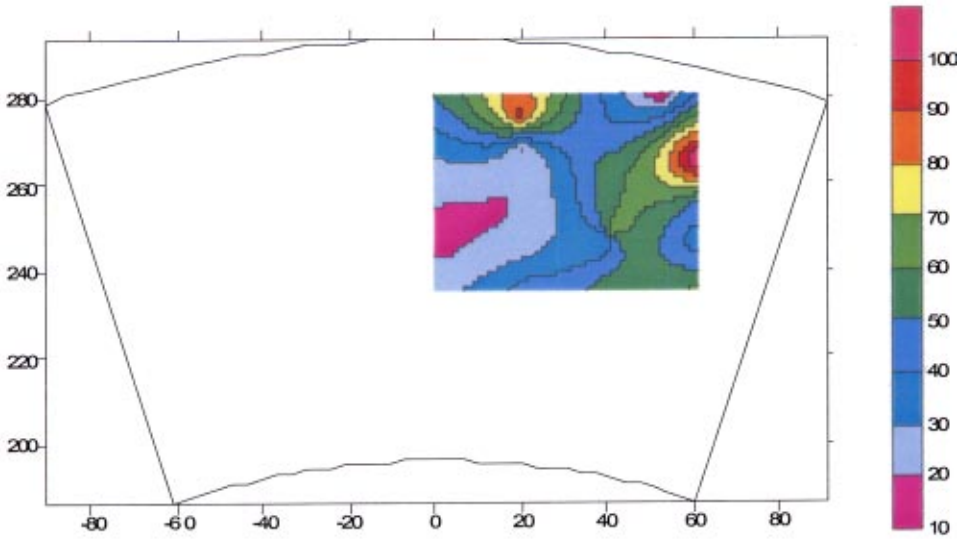


**Fig. 12 Smoke mass mg/m$^3$ Plane D**

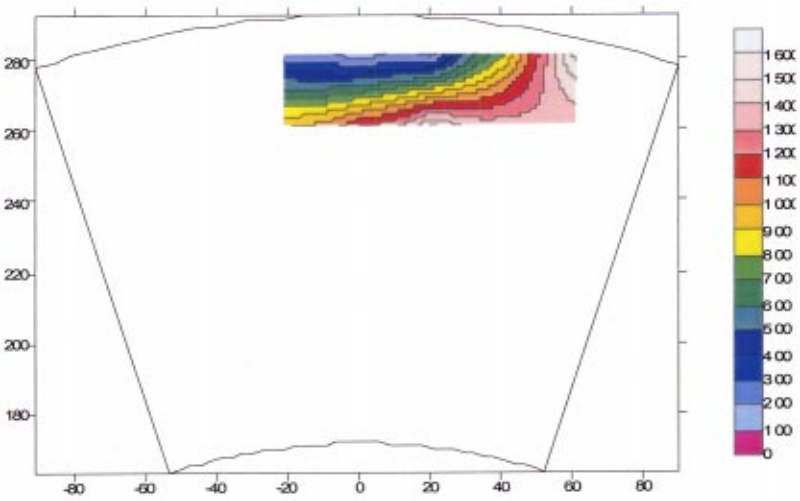


**Fig. 13 Smoke mass mg/m$^3$ Plane B**

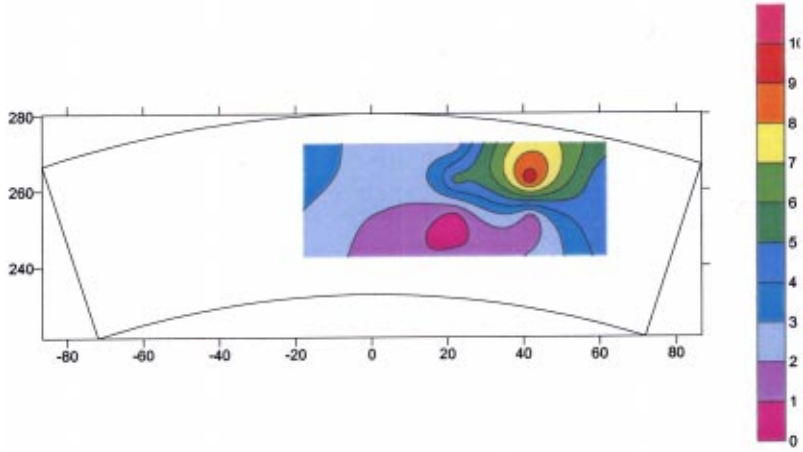


**Fig. 14 SAE Plane F**

the data set. The main justification for leaving it in is related to the nonspherical nature of the particulates (Fig. 4). The volume as calculated from the SMPS software is reliant upon the pareticulates being spherical for accurate determination. It is a possibility that at this particular point a larger particle of carbon was shed from the combustor. It is also a possibility that the residence time through the combustor was also variable, thus producing particulates with varying degrees of roundness.

The gradient of the plot (mass/volume) gives an average value for particulate density. The plots shown in Figs. 15 and 16 have best lines fitted alone with error lines corresponding to $\pm 20\%$ which are the known errors with respect to the SMPS. The average density calculated for plane B was 2520 kg/m$^3$ $\pm 505$ while the value calculated for plane D was 2079 kg/m$^3$ $\pm 405$. It is recognized by the authors that the best-fit line suggested in Fig. 16 is subjective.

In plane F of the combustor two separate best fit lines were used to determine an average value for density, as shown in Fig. 17. The two lines span the data set, which has a wider spread and less agreement than for planes B and D. The reason for the large degree of spread in part can be attributed to the large error associated with the SAE measurements at these low concentrations. Other factors such as the nonspherical nature of the particulates may also contribute. This manifests itself in an incorrect volume measurement as calculated from the number and size of the particulates. The density values calculated from plane F for the two separate lines were 68 and 480 kg/m$^3$; these values are, however, subject to an error of about $+100\%$. The range of the values could therefore be between 132 and 960 kg/m$^3$.

Although errors are high when examining smoke particle density in this way, a trend of changing density is readily apparent (see Fig. 17). The density decreases from Plane B to Plane F (combustor exit) with values ranging from 3025 to 132 kg/m$^3$. Unpublished work undertaken at QinetiQ suggests a mean value of about 1500 kg/m$^3$, while Sunderland and Faeth [10] suggest a value of 1850 kg/m$^3$. The values obtained are therefore seen as reasonable.

**Axial Trends.** Although the number of data points measured is not large enough to obtain definitive mass weighted average values, some conclusions may be drawn from the arithmetic mean values.

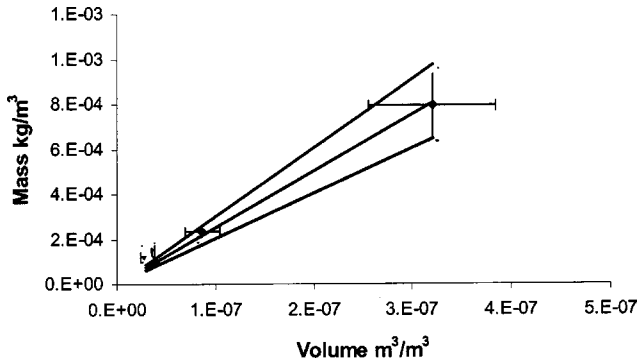


**Fig. 15 Comparison between SMPS and Sigrist Plane V**

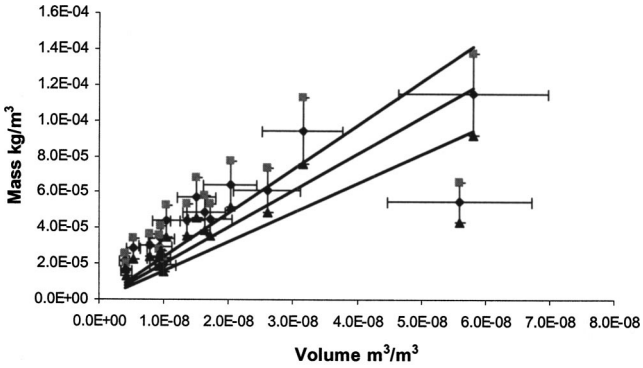


**Fig. 16 Comparison between SMPS and Sigrist Plane D**

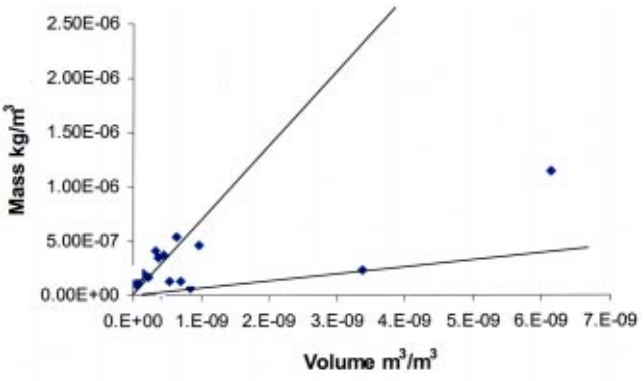


**Fig. 17 Comparison between SMPS and SAE Plane F**

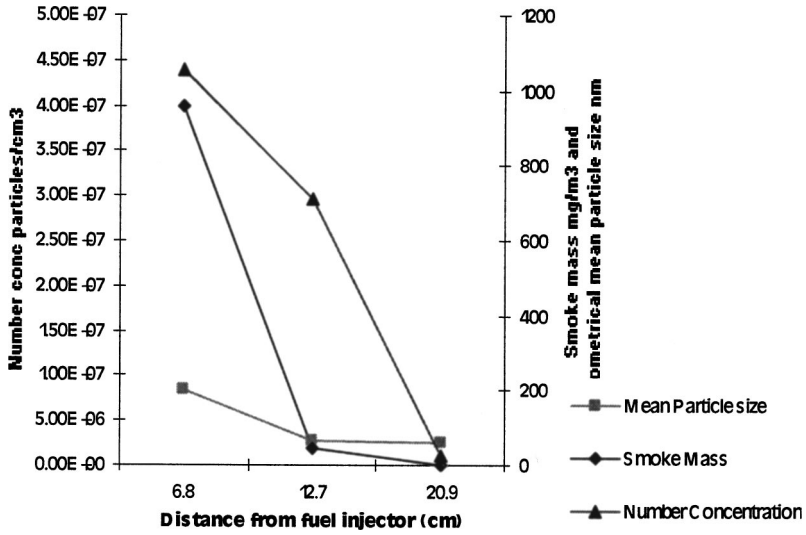


**Fig. 18 Average axial trends**

Figure 18 shows arithmetic averages of mean particle size, smoke mass, and number concentration against axial location. Expressed as mass of smoke in $mg/m^3$, the average values for planes F, D, and B were 0.3, 44, and 958. It can be seen from these values that there are three orders of magnitude change from the primary zone to the exit of the combustor. The corresponding average smoke number concentration for these respective planes is 1.08E6, 3.08E7, and 4.4E7 while the average mean particle size for planes F, D, and B was found to be 60, 68, and 200 nm, respectively.

It can be seen that the smoke number concentration and mass are at a maximum value in plane B and then diminish as a function of distance. It can also be seen that the geometric mean particle size diminishes as a function of distance.

## Conclusions and Recommendations

The SMPS analyzer has been used to determine the smoke number concentration and distribution at discrete test points at three axial planes of a generic annular combustor.

In axial planes F and D the minimum dilution ratio was determined which removed coagulation and water vapor effects and minimized dilution measurement uncertainties. It was not possible to determine a minimum dilution ratio in plane B of the combustor because of probe blockage. The maximum uncertainty in the measurements was associated with measurements in plane F where the smoke mass values were very low.

From SMPS and smoke mass measurements density values were calculated for each of the axial planes. The values found for planes B, D, and F, respectively, were $2520\pm505$, $2079\pm405$ $kg/m^3$, and between $68+68$, and $480+480$ $kg/m^3$. It was shown that the density of the smoke particulate decreases as a function of distance from the fuel injector.

Arithmetic averages for each plane show a three order of magnitude decrease in smoke mass from the primary zone exit to the combustor exit. Smoke number concentrations decrease from 4.4E7 to 1.08E6 with a particle size decrease from 200 to 60 nm. Although the limited data set has highlighted bulk changes in soot parameters, further measurements are required in order to provide a robust data set for soot model development and validation. Further work is necessary in the determination of optimum dilution ratios. In order to determine the optimum value for plane B, modifications will have to be made to the sample probe to allow a greater amount of sample flow.

## Acknowledgments

The authors would like to acknowledge the financial assistance of the Applied Research Program of the UK Ministry of Defense.

## Nomenclature

| | | |
|---|---|---|
| CO | = | carbon monoxide (ppm) |
| $CO_2$ | = | carbon dioxide (%) |
| HC | = | unburnt hydrocarbons (ppm) |
| NO | = | nitrogen monoxide (ppm) |
| $NO_X$ | = | oxides of nitrogen (ppm) |
| $O_2$ | = | oxygen (%) |
| SMPS | = | scanning mobility particle sizer |
| CFD | = | computational fluid dynamics |
| SCR | = | sector combustion rig |
| CPC | = | condensation particle counter |

## References

[1] Mosier, S. A., and Roberts, R., 1973, ''Low-Power Turbopropulsion Combustor Exhaust Emissions, Theoretical Formulation and Design Assessment,'' Pratt and Whitney Aircraft, Technical Report No. AFAPL-TR-73-36, Volume 1.
[2] Mosier, S. A., and Roberts, R., 1974, ''Low-Power Turbopropulsion Combustor Exhaust Emissions, Demonstration and Total Emission Analysis and Prediction,'' Pratt and Whitney Aircraft, Technical Report No. AFAPL-TR-73-36, Volume 2.
[3] Hurley, C. D., 1993, ''Smoke Measurements Inside a Gas Turbine Combustor,'' AIAA/SAE/ASME/ASEE 29th Joint Propulsion Conference and Exhibit June 28–30, Monterey, CA.
[4] Aerospace Recommended Practice, 1997, SAE ARP1179. ''Aircraft Gas Turbine Engine Exhaust Smoke Measurement,'' Rev. C.
[5] SIGRIST photometer AG. CH-6373 Enneburgen.
[6] Girling, S. P., and Hurley, C. D., 1990, ''Development and Characterization of a Smoke Generator for the Calibration of Aerosol Emissions From Gas Turbine Engines,'' Aerosol Sci. Technol., **13**, pp. 8–19.
[7] Green, H. L., and Lane, W. R., 1957, ''Particulate Clouds: Dusts, Smokes and Mists.,'' pp. 126–163, E.&F.N. Spon Ltd., London.
[8] International Standards and Recommended Practices. Environmental Protection, Annex 16, 1993, *Aircraft Engine Emissions*, 2nd ed., International Civil Aviation Organization (ICAO).
[9] Hurley, C. D., 1996, ''AEROTRACE Measurement of Particulates From an Engine Combustor,'' Proc. International Colloquium, Paris, 15–18 October.
[10] Sunderland, P. B., and Faeth, G. M., 1996, ''Soot Formation in Hydrocarbon/Air Laminar Jet Diffusion Flames,'' Combust. Flame, **105**, pp. 132–146.

# Experimental Investigation of the Interaction of Unsteady Flow With Combustion

**K.-U. Schildmacher**

**R. Koch**

Institute of Thermal Turbomachinery,
University of Karlsruhe,
Kaiserstrasse 12,
76128 Karlsruhe, Germany

*In order to reduce the dimensions of the combustor, swirl stabilized flames are used in heavy duty gas turbines. In our recent investigation of the swirling flow at a single heavy duty gas turbine burner under nonreacting conditions typical instabilities like precessing vortex cores and vortex shedding have been found (Schildmacher et al., Proceedings of the 6th European Conference on Industrial Furnaces and Boilers). In the present paper the experimental investigations will be discussed. Combustion instabilities have been analyzed by phase-locked laser doppler anemometer measurements. For the reacting flow, also combustion instabilities could be detected. The amplitude increases strongly with the equivalence ratio. The frequency of the oscillations for reacting conditions has been found to be slightly shifted towards lower frequencies compared to those of the corresponding nonreacting flow. In addition, for the reacting flow a linear and nonlinear range of oscillations could be discriminated.* [DOI: 10.1115/1.1789512]

## Introduction

Strong limitations of $NO_x$ emissions imposed by legislation forced the gas turbine industry in recent years to adopt premixed lean combustors which lead to a significant decrease of emissions [1]. However, premixing burners of present gas turbines exceed the emission level of an ideal premixed flame by a factor of about 2 which is mainly to be attributed to nonperfect air-fuel mixing. As pointed out by Kraemer et al. [2], spatial mixing is quite perfect in most cases, but temporal fluctuations degrade the mixing quality. These temporal fluctuations of the mixing can be caused by vortex shedding or Kelvin-Helmholtz instabilities [3].

Although precessing vortex cores and vortex shedding have been investigated in a lot of publications of nonreacting swirling flows [4] not very much is known about the impact of these flow instabilities on combustion [5]. In order to analyze instability mechanisms of the reacting flow in detail, a spatially and time- and phase-resolved flow field analysis using LDA has been performed. The oscillating reacting flow was analyzed at different sound levels. The LDA investigations were supported by pressure fluctuation measurements which where also used to synchronize the laser doppler anemometer. In the paper, first the transparent test rig will be described and a short outline of the measurement technique will be given. In the main part, the cold flow instabilities will be reviewed briefly and then the instabilities of the reacting flow will be discussed.

## Burner

In this study, a single test burner of industrial size was investigated within an atmospheric test rig (Fig. 1). It is fired by natural gas. The burner (Fig. 2) is operated in a combustor casing which provides excellent optical access for velocity measurements by LDA. The combustion chamber has a square cross section with a truncated pyramid shape at the exit.

The burner air passage consists of two concentric annular swirlers. The inner axial swirler has nozzles for pilot and nonpremixed gas. At the outer diagonal swirler, the gas is injected through holes in the swirler blades in order to enhance premixing with the air.

Contributed by the International Gas Turbine Institute (IGTI) of THE AMERICAN SOCIETY OF MECHANICAL ENGINEERS for publication in the ASME JOURNAL OF ENGINEERING FOR GAS TURBINES AND POWER. Paper presented at the International Gas Turbine and Aeroengine Congress and Exhibition, Atlanta, GA, June 16–19, 2003, Paper No. 2003-GT-38644. Manuscript received by IGTI, Oct. 2002, final revision, Mar. 2003. Associate Editor: H. R. Simmons.

## Burner Operation Conditions

The burner can be operated either in nonpremixed or premixed mode [6]. In case of nonpremixed operation, the natural gas is injected solely through the nonpremixing nozzles. In premixed mode, the premixing gas nozzles and to a minor extent the pilot nozzles are used. In both modes, the air is fed through the axial as well as through the diagonal swirler passages with the same flow split.

In the gas turbine at nominal operation conditions, the burner is operated in premixed mode with pilot gas injection for better flame stabilization. Under test rig conditions, the pilot gas injection is not necessary for stable combustion. In order to prevent any disturbance of the premixed flame by the pilot burner, no pilot gas was used. In this study, the investigations have been performed in premixed mode with a constant air volume flow at atmospheric pressure. The air was pre-heated to 673 K. The Reynolds number at the burner mouth was $10^5$ and the thermal power varied between 420 kW ($\phi$=0.5) and 810 kW ($\phi$=0.83).

## Experimental Techniques

The velocity field was investigated by a two-dimensional (2D) laser doppler anemometer (LDA) (Fig. 3) in back-scattering mode. The axial and tangential velocities have been recorded in the $x$-$r$ plane (Fig. 2). The air stream was seeded by $Al_2O_3$ particles of an average diameter of 1 $\mu$m. The data rate was 4–20 kHz in the main flow and the validation rate was 60–90% for a duration of 20 s per measurement position. Close to the center where the recirculation zone of the flame is located, the data rate dropped sometimes to less than 1 kHz.

In addition, the LDA investigations were accompanied by pressure fluctuation measurements. Due to the high temperatures in the combustion chamber, the quartz pressure sensor was implemented into the air plenum of the burner where the air temperature is 673 K. The pressure signal was conditioned by a bandpass filter of ±2.5 Hz half width around the pronounced peak frequency at 254 Hz. This filter signal was also used to synchronize the burst spectrum analyzers of the LDA (Fig. 3). In contrast to the nonoscillating flow, the LDA-particle distribution over time is not uniform. The instantaneous records exhibit a much higher particle rate at moments of high velocities [7]. Thus velocity biasing had to be taken into account when determining the time-averaged velocities of the oscillating flow [8,9].

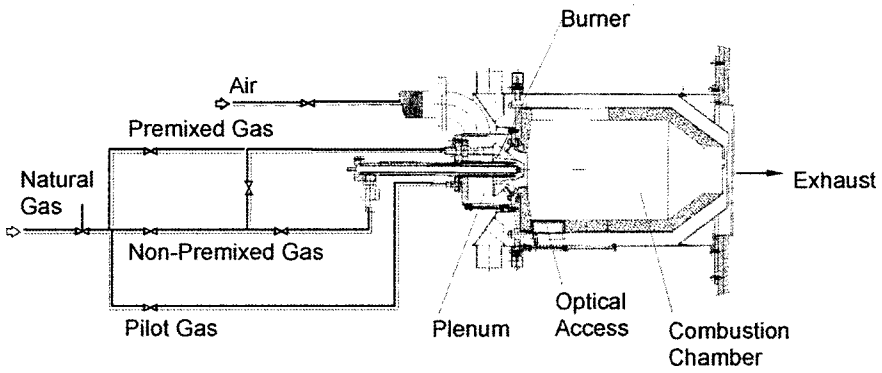


**Fig. 1 Sketch of the test rig**

## Review of Cold Flow Instabilities

Investigations of the nonreacting flow [10] reveal a pronounced frequency of the instabilities which is proportional to the air flow (constant Strouhal number) (Fig. 4). This phenomenon was attributed to vortex shedding at the burner mouth. An accompanying large eddy simulation of the nonreacting flow [11] revealed that there is a precessing vortex core which triggers vortex shedding in the shear flow region at the burner mouth. In addition, investigations of the fuel concentration for nonreacting conditions showed that alternating pattern of rich and lean fuel concentrations is generated by vortex shedding (Fig. 5), through the time-averaged fuel concentration is axis symmetrical and much more homogeneous [10]. For comparison, the corresponding operation point of the reacting flow is indicated in Fig. 4. The reacting flow was investigated at constant air flow.

## Reacting Flow Analysis

**Combustion Stability.** As indicated previously, under reacting flow conditions the air flow was kept constant and the equivalence ratio was varied by modifying the fuel flow.

The pressure fluctuations of the combustion oscillations were found to strongly increase with the equivalence ratio (Fig. 6). At $\phi=0.66$ first oscillations could be detected by the pressure transducer. The pressure amplitude at the peak frequency was just twice as high as the turbulent combustion noise at nominal operating conditions without oscillations ($\phi=0.5$).

Audible oscillations started at an equivalence ratio greater than 0.71 with a pressure amplitude of the pronounced frequency peak that is five times higher than the turbulent combustion noise. In

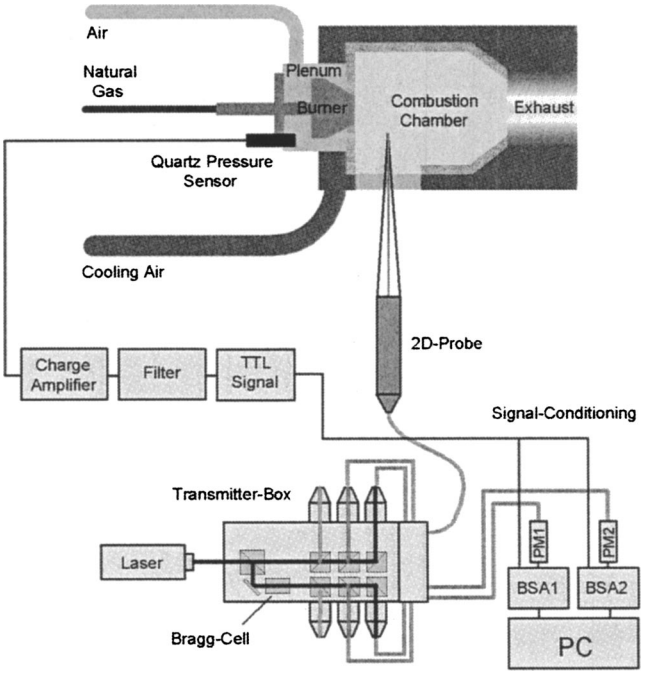


**Fig. 3 Experimental setup for the LDA investigations**

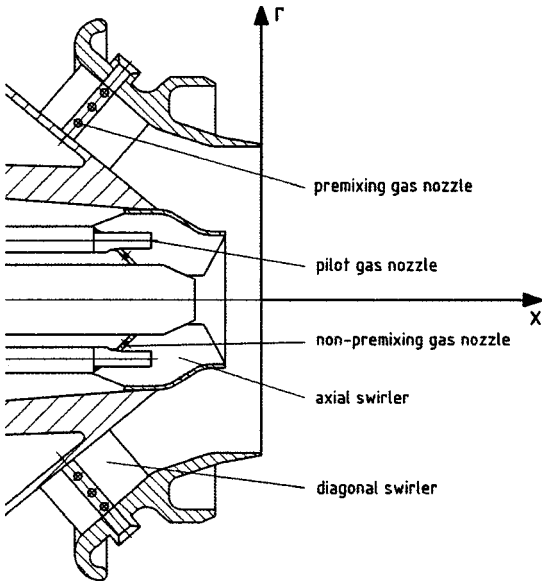


**Fig. 2 Sketch of the burner**

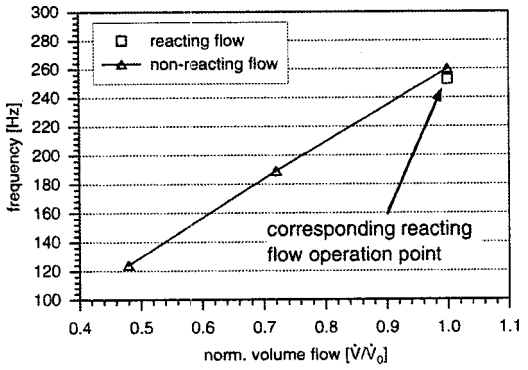


**Fig. 4 Frequency of instability**

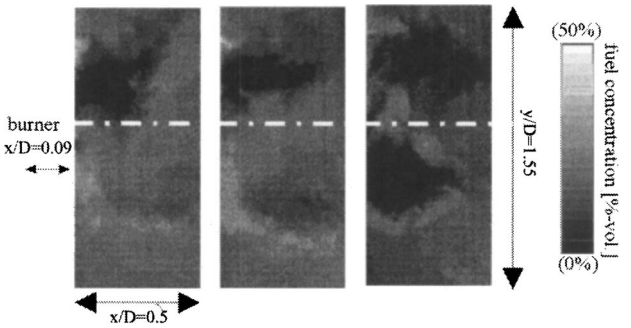


**Fig. 5 Instantaneous fuel concentration for premixed operation (nonreacting flow)**

the transition region at $\phi \approx 0.75$, the sound level was not constant over time but fluctuated between quiet and loud. At $\phi > 0.77$, the oscillations became loud with a pressure amplitude that was more than 50 times higher compared to the turbulent combustion noise at nominal operation. The pressure fluctuation amplitudes of the quiet oscillations are 3.2% of the amplitude of the loud oscillations. This observation indicates that for the present burner the amplitudes steadily grow with increasing equivalence ratio in contrast to a sudden excitation which can observed in other combustion systems.

**Self-Excited Combustion Instabilities at High Oscillation Sound Level.** Subsequently, the flow fields, as recorded by LDA, will be compared. Nonoscillating flow conditions at $\phi = 0.66$ and the oscillating flow condition exhibiting weak ($\phi = 0.71$) and strong pressure fluctuations ($\phi = 0.83$) will be considered.

Figure 7 shows the time-averaged axial velocity field at high oscillation level ($\phi = 0.83$). The flame is stabilized in regions of high velocity gradients and therefore is very sensitive to instabilities like vortex shedding which are possibly triggering combustion oscillations. The signal of the pressure sensor which is located inside the air plenum (Fig. 3), was used as reference signal for phase angle matching. All plots of the velocity measurements are referenced to the phase angle of the pressure fluctuations at the air plenum (Fig. 8). From the phase-locked LDA data records, mean fluctuations have been derived by averaging over 5000 periods. These averaged data revealed different phase shifts and wave forms depending on the location. At the reaction zone ($x/D = 0.63$, $r/D = 0.56$), the highest fluctuations of the axial as well as the tangential component were detected (Fig. 7). The averaged phase-locked RMS values were nearly constant over the phase angle. At a position radially further outward ($x/D = 0.63$, $r/D = 0.75$) the highest mean axial velocities are present. There, the

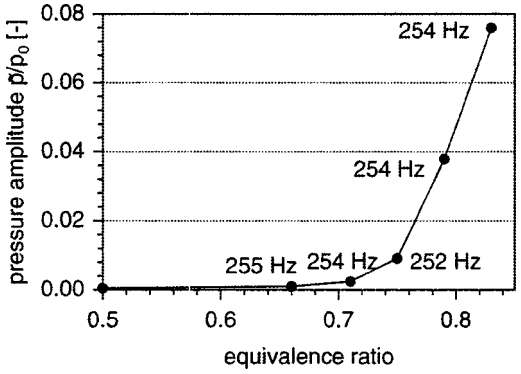


**Fig. 6 Pressure amplitude and oscillation frequency for different equivalence ratios**

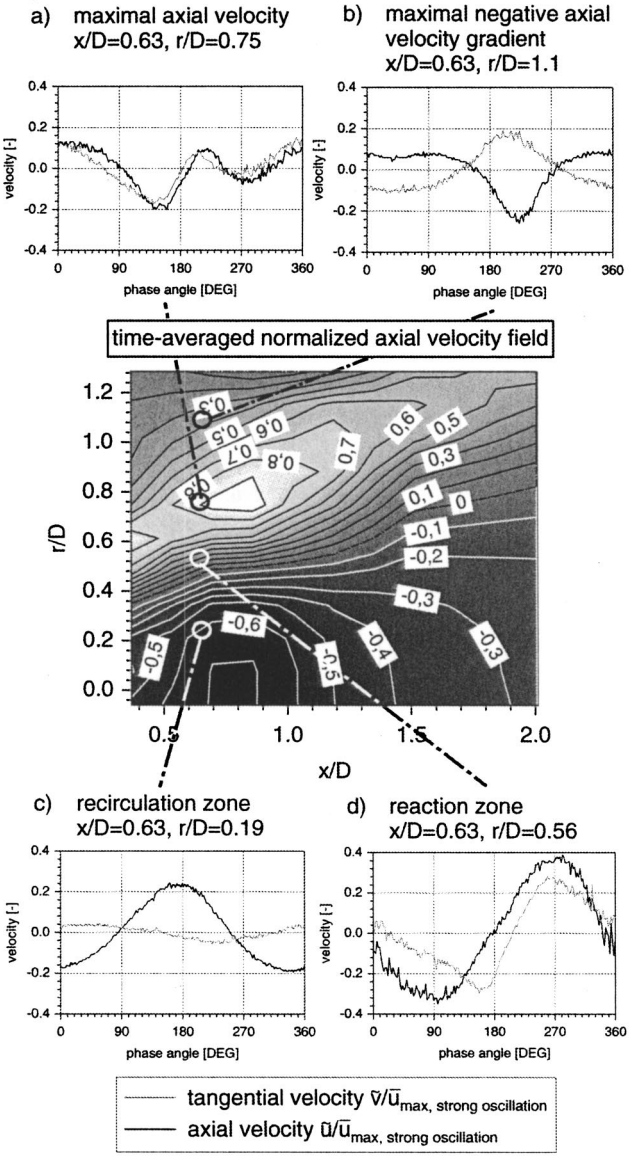


**Fig. 7 Normalized axial velocity field and normalized local phase-locked velocity fluctuations at high oscillation sound level ($\phi = 0.83$)**

axial as well as tangential velocity fluctuations revealed the first harmonic frequency which must be attributed to nonlinear effects. This phenomena was only detected at equivalence ratios greater than 0.75. In the recirculation zone at $x/D = 0.63$, $r/D = 0.19$ strong oscillations of the tangential velocity were detected which may be caused by mushroom shaped ring vortices.

The swirl has a major impact on flame stabilization. In Fig. 9 the local velocity ratio $v/u$ is plotted over the phase angle for different positions and an equivalence ratio of 0.83. Regions which may trigger combustion instability are characterized by strong fluctuations. The fluctuations of the velocity ratio have

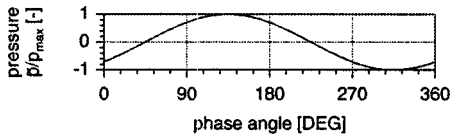


**Fig. 8 Pressure amplitude at the air plenum**

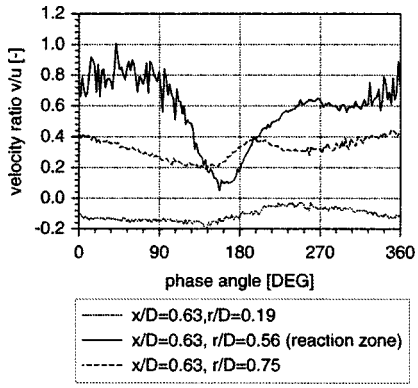


**Fig. 9 Phase-locked velocity ratio $v/u$ at high pressure fluctuations**

been analyzed on basis of the LDA data. The data reveal, the strongest fluctuation of $0.1 \leqslant v/u \leqslant 0.8$ are found in the reaction zone ($x/D=0.63$, $r/D=0.56$). Because of the periodicity of the signal, the fluctuations must be attributed to coherent structures. The plot also indicates that for a short time at around 150 deg phase angle, swirl stabilization of the flame is interrupted which may cause to strong strain rates in the reaction zone and local flame quenching. Outside the recirculation zone only minor fluctuations of the velocity ratio were recorded.

**Self-Excited Combustion Instabilities at Low Oscillation Sound Level.** For an equivalence ratio of $\phi=0.71$ barely audible oscillations have been detected. The amplitude of the pressure oscillations was more than thirty times smaller compared to strong oscillations but five times higher than the turbulent combustion noise (Fig. 6). Figure 10 shows the flow field and the phase-locked velocity fluctuations at different positions. Everywhere inside the combustion chamber the frequency of the velocity fluctuations was identical to that of the pressure oscillations. Higher harmonic frequencies amplitude compared to operation at high oscillation level, the velocity fluctuations were reduced only by a factor of 4.

The velocity ratio $v/u$ only varied between 0.35 and 0.5 (Fig. 11), and due to the reduced strain rate the flame was more stable.

**Fluctuations Close to the Onset of Combustion Oscillation.** As stated previously, the first onset of combustion oscillations was detected at an equivalence ratio of 0.66. The time-averaged velocity field at $\phi=0.66$ was quite similar to that of the weakly oscillating flow at $\phi=0.71$.

Due to the small amplitude of the pressure oscillations that was just twice as high as the turbulent combustion noise, it was not possible to generate a useful trigger signal for synchronization of the burst spectrum analyzers. Therefore subsequently frequency spectra will be used for the analysis. For extracting the spectral data, the resampling method was adopted [12,13].

The frequency spectra of the local axial and tangential velocities are shown in Fig. 12. Generally, a pronounced frequency peak was not found for the stable operating conditions. Very small sinusoidal velocity fluctuations at about 254 Hz could only be detected in the axial component at regions of high velocities ($x/D=0.37$, $r/D=0.56$). Comparing the spectra obtained for the reacting case (Fig. 12) to those of the corresponding nonreacting flow case, the coherent flow structures which are present in the nonreacting flow and which cause the pronounced frequency peak at 263 Hz are not reproduced under reacting flow conditions.

Moreover, even in the flow field upstream of the reaction zone (e.g., $x/D=0.37$, $r/D=0.56$) no fluctuations are present. This emphasizes the strong impact of the heat release on the generation of coherent flow structures. This observation is also confirmed by Fig. 13. The frequency and the corresponding Strouhal number

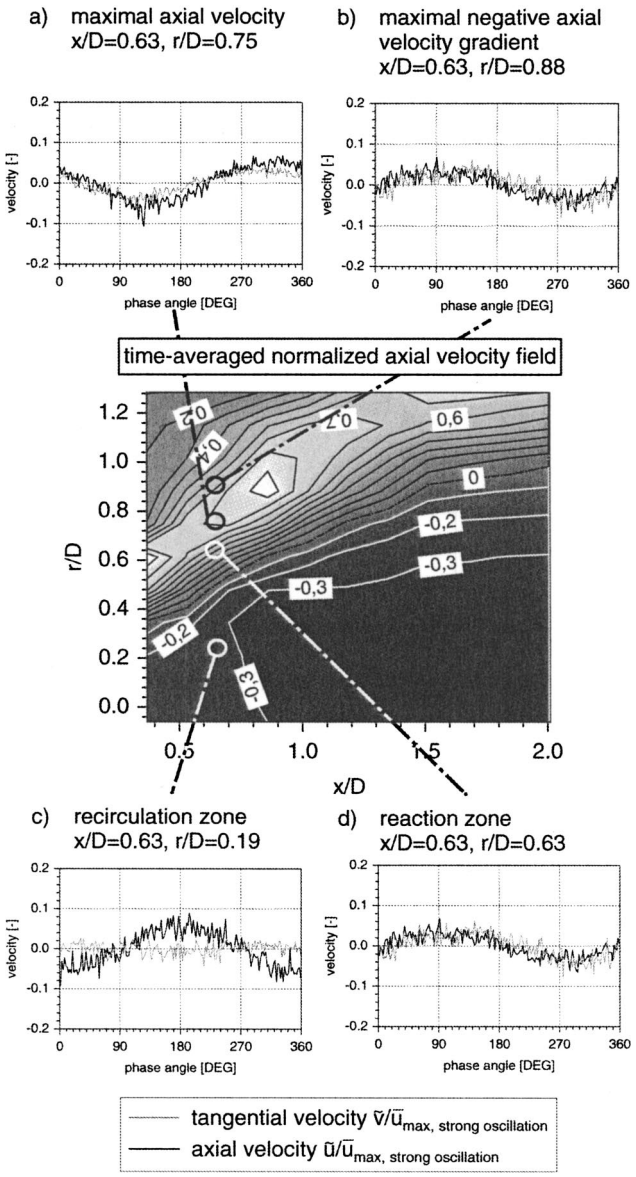


**Fig. 10 Normalized axial velocity field and normalized local phase-locked velocity fluctuations at low oscillation sound level ($\phi=0.71$)**

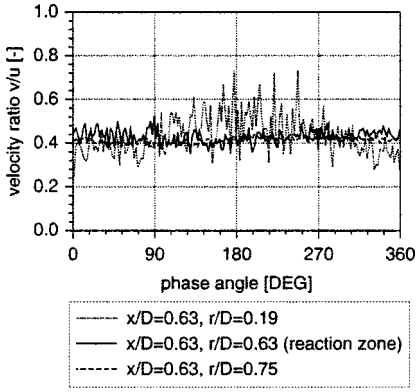


**Fig. 11 Phase-locked velocity ratio $v/u$ at low pressure fluctuations**

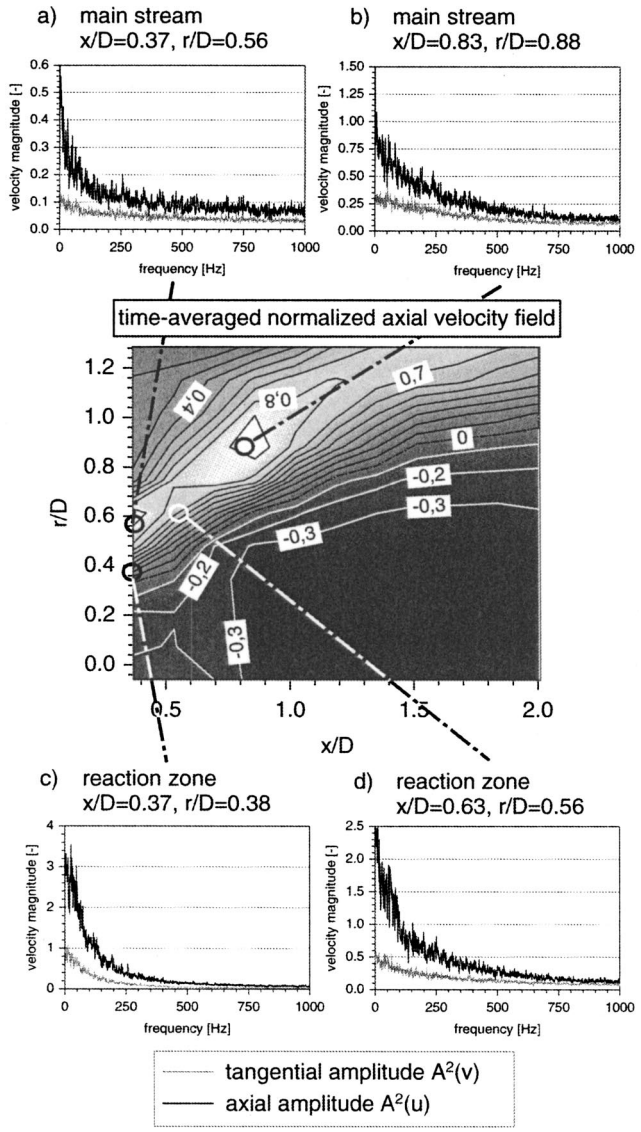


**Fig. 12 Normalized axial velocity field and power spectra without oscillations ($\phi$=0.66)**

St$=f_{St}D/c_{\infty}$ of the oscillations are plotted for nonreacting and reacting conditions over the normalized volume flow. For the nonreacting flow, the frequency increases linearly to volume flow resulting in a constant Strouhal number. Such an observation may be attributed to vortex shedding [3,10]. For reacting flow conditions, however, the frequency only slightly changes with normalized flow and the Strouhal number decreases. This leads to the

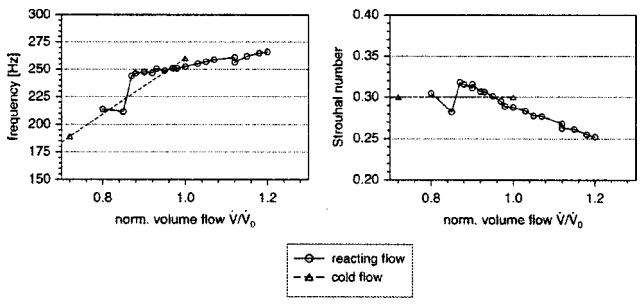


**Fig. 13 Frequency of instability and Strouhal number**

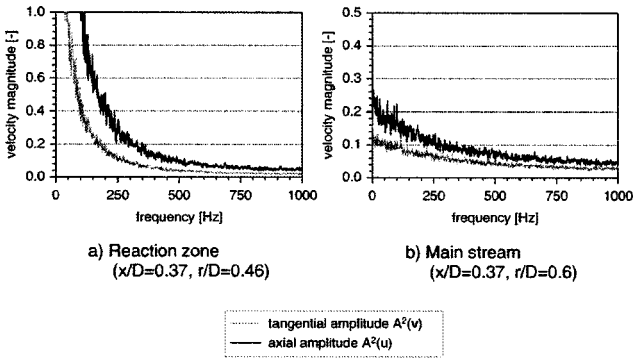


**Fig. 14 Power spectra of velocities without oscillations at $\phi$=0.5**

conclusion that for self-excited reacting conditions, the resonant frequencies are linked to the acoustic eigenfrequencies of the combustion system which do not depend much on the burner air flow.

## Conclusion

In order to study the impact of flow instabilities such as precessing vortex cores and vortex shedding on combustion, the unsteady reacting flow has been investigated by phase-locked LDA measurements. The velocity fluctuations of the reacting flow at different equivalence ratios ($\phi$=0.66; $\phi$=0.71; $\phi$=0.83) have been recorded and compared to those of the nonreacting flow.

At an equivalence ratio of 0.66 no audible pressure fluctuations could be detected and in the spectrum of the velocity fluctuations no pronounced peak was found. For the same flow conditions, but for the nonreacting flow, a predominant frequency peak was found which could be attributed to coherent flow structures. Comparing the spectra of the velocity fluctuations of nonreacting to those of reacting flow, the pronounced frequency peak previously found under nonreacting conditions was not present under reacting conditions. This observation indicates that the heat release has such a strong impact on the onset of coherent structures in flow.

At equivalence ratios lower than 0.66, a pronounced frequency peak could not be detected either by the LDA (Fig. 14) or by the quartz pressure sensor. For nonaudible oscillation at $\phi$=0.66 only axial oscillation modes were identified, indicating that the onset of combustion oscillation is mainly triggered by axial-acting fluctuations. A Strouhal number about 0.25 could be associated with the presence of these vortex rings [14].

Increasing the equivalence ratio to 0.71, weak oscillations were found. The amplitude of the oscillations increased steadily (not suddenly) when increasing the equivalence ratio. The frequencies of these weak oscillations correspond to the acoustic eigenfrequencies of the combustion system and do not change with air flow. The velocity oscillations are of sinusoidal shape and of the same frequency as the pressure oscillation. This indicates that the instability can still be described by linear acoustics. The velocity ratio $v/u$ showed small fluctuations that did not compromise stable combustion.

In the transient region ($\phi$=0.75) the sound level alternated between quiet and loud. A small increase of the equivalence ratio to $\phi$>0.75 led to very strong pressure oscillations but only to a small increase of the velocity fluctuations. The flow began to oscillate strongly and higher harmonic frequencies could be detected in the velocity fluctuations. The velocity oscillations are so strong that additional coherent structures such as ring vortices are generated which may be the reason for the first harmonic frequency found in the main flow region. In this region clearly a nonlinear acoustic mechanism is present. Strong fluctuations of the velocity ratio $v/u$ between 0.1 and 0.8 were detected, and thus the swirled stabiliza-

tion of the flame was disturbed periodically for a short time. This mechanism seems to have a major impact on the combustion stability.


## Acknowledgment

This study was supported by the EC under contract ENK5-CT-2000-00060 (PRECCINSTA) which is gratefully acknowledged.


## Nomenclature

$A$ = amplitude, magnitude
BSA = burst spectrum analyzer
$c$ = velocity
$c_\infty$ = axial velocity at the burner exit
$D$ = burner outlet diameter
$f$ = frequency
$f_{St}$ = Strouhal frequency
$p$ = pressure
PM1,
PM2 = photomultiplier
$r$ = radial direction
RMS = root-mean-square value
St = Strouhal number
$u$ = axial velocity
$\dot{V}$ = volume flow
$v$ = tangential velocity
$x$ = axial direction
$y$ = normal direction
$\phi$ = equivalence ratio

### Subscripts

0 = nominal operation, design point
max = maximum

### Superscripts

$\bar{}$ = time-averaged component
$\tilde{}$ = periodical component
$'$ = turbulent component

## References


[1] Lefebvre, A. H., 1974, ''Pollution Control in Continuous Combustion Engines,'' Fifteenth Symposium on Combustion, Combustion Inst., Pittsburgh, pp. 1169–1180.
[2] Kraemer, H., Dinkelacker, F., Huth, M., Leipertz, A., Poeschl, G., and Lenze, M., 1999, ''Optimization of the Mixing Quality of a Real Size Gas Turbine Burner With Instantaneous Planar Laser-Induced Fluorescence Imaging,'' ASME Paper No. 99-GT-135.
[3] Coats, C. M., 1996, ''Coherent Structures in Combustion,'' Prog. Energy Combust. Sci., **22**, pp. 427–509.
[4] Gupta, A. K., Lilley, D. G., and Syred, N., 1984, ''Swirl Flows,'' ABACUS Press.
[5] Gutmark, E. J., Shadow, K. C., and Yu, K. H., 1994, ''Methods for Enhanced Turbulence Mixing in Supersonic Shear Flows,'' Appl. Mech. Rev., **47**(2), pp. 375–417.
[6] Prade, B., Streb, H., Berenbrink, P., Schetter, B., and Pyka, G., 1996, ''Development of an Improved Hybrid Burner—Initial Operating Experience in a Gas Turbine,'' ASME Paper No. 96-GT-43.
[7] Schildmacher, K.-U., Koch, R., Krebs, W., Hoffmann, S., and Wittig, S., 2002, ''Experimental Investigation of Unsteady Flow Phenomena in High Intense Combustion Systems,'' *Proceedings of the 6th European Conference on Industrial Furnaces and Boilers*.
[8] Loseke, A. H., and Gould, R. D., 1991, ''A Comparison of Velocity Bias Correction Techniques in Laser-Doppler-Velocimetry,'' ASME Fluid Measurement and Instrumentation Forum, **108**, pp. 63–68.
[9] McLaughlin, D. K., and Tiedermann, W. G., 1973, ''Biasing Correction for Individual Realization of Laser-Doppler-Anemometer Measurements in Turbulent Flow,'' The Physics of Flow, **16**, pp. 2082–2088.
[10] Schildmacher, K.-U., Koch, R., Krebs, W., Hoffmann, S., and Wittig, S., 2000, ''Experimental Investigations of the Temporal Air-Fuel Mixing Fluctuations and Cold Flow Instabilities of a Premixing Gas Turbine Burner,'' ASME Paper No. 2000-GT-0084.
[11] Schlueter, J., Schoenfeld, T., Poinsot, T., Krebs, W., and Hoffmann, S., 2001, ''Characterization of Confined Swirl Flows Using Large Eddy Simulations,'' ASME Paper No. 2001-GT-0060.
[12] Host-Madsen, A., 1994, ''A New Method for Estimation of Turbulence Spectra for Laser Doppler Anemometry,'' 7th International Symposium on Applications of Laser Techniques of Fluid Mechanics, Lisbon.
[13] Host-Madsen, A., and Caspersen, C., 1981, ''Spectral Analysis—A Modern Perspective,'' Proc. IEEE, **69**(11), pp. 1380–1419.
[14] Laufer, J., and Monkewitz, P., 1978, ''The Influence of the Dominant Large Scale Structures on the Initial Instability of a Low-Speed Circular Jet,'' Bull. Am. Phys. Soc., **23**, p. 1008.

**J. Eckstein**

**E. Freitag**

**C. Hirsch**

**T. Sattelmayer**

Lehrstuhl fur Thermodynamik,
Technische Universitat Munchen,
85747 Garching,
Germany

**R. von der Bank**

**T. Schilling**

Rolls-Royce Deutschland Ltd. & Co. KG,
Combustor Aerodynamics,
Eschenweg 11,
15827 Dahlewitz, Berlin, Germany

# Forced Low-Frequency Spray Characteristics of a Generic Airblast Swirl Diffusion Burner

*The low-frequency response of the spray from a generic airblast diffusion burner with a design typical of an engine system has been investigated as part of an experimental study to describe the combustion oscillations of aeroengine combustors called rumble. The atomization process was separated from the complex instability mechanism of rumble by using sinusoidal forcing of the air mass flow rate without combustion. Pressure drop across the burner and the velocity on the burner exit were found to follow the steady Bernoulli equation. Phase-locked particle image velocimetry measurements of the forced velocity field of the burner show quasisteady behavior of the air flow field. The phase-locked spray characteristics were measured for different fuel flow rates. Here again quasi-steady behavior of the atomization process was observed. With combustion, the phase-locked Mie-scattering intensity of the spray cone was found to follow the spray behavior measured in the noncombusting tests. These findings lead to the conclusion that the unsteady droplet Sauter mean diameter mean and amplitude of the airblast atomizer can be calculated using the steady-state atomization correlations with the unsteady burner air velocity.* [DOI: 10.1115/1.1789515]

## Introduction

The demand for significant reductions of pollutant emissions like $NO_x$ and smoke from gas turbine aeroengines has motivated continuous improvement of the combustion processes within the constraints of the engine operation. New concepts of fuel atomization, pre-vaporization, and staged injection have been developed or are currently being tested for their operability. However, with the improvements gained, thermoacoustic combustion instabilities known and feared for their destructive potential in stationary gas turbines have also become more prominent in aeroengines. During recent years intense scientific efforts were undertaken to understand and specify the underlying driving mechanisms (e.g., Refs. [1–3]). A particular combustion instability of aeroengine combustors is related to the fuel spray atomizers used. It exhibits a low-frequency oscillation between 50 and 150 Hz at idle and subidle conditions, commonly called ''rumble.'' In engine design practice, certain atomizers or combinations of fuel injector and combustor have become known as being particularly rumble prone, yet a standard procedure to predict and to prevent a given designs susceptibility to this kind of instability has still to be formulated [4]. Work in this area was performed by Zhu et al. who formulated a computational fluid dynamics (CFD) model to numerically simulate the response of a two-dimensional (2D) model combustor to forcing of the fuel and air streams [5] as well as the onset of self-excited oscillation [6]. In this paper we provide the experimental results which clarify one of the key mechanisms of the rumble instability, i.e., the fuel atomization. A generic airblast atomizer with a design typical for current systems has been incorporated into a thermoacoustic combustor test rig simulating rumble conditions. To isolate the effect of acoustic oscillation upon the atomization, the forced response of the atomizer has been investigated under noncombustion conditions. Phase-locked measurements of the pressure velocity coupling at the burner, the combustor velocity field, as well as the associated spray diameter spectra were taken to provide a clear picture of the unsteady atomization process. The conclusions were verified using Mie scattering of the spray cone in the combusting environment. For all measurements, a periodically forced air flow in the frequency range 50–150 Hz was provided at different mean air mass flows (AMFs) and fuel mass flows (FMFs), covering the typical range of rumble.

## Experimental Setup

In this section, the experimental setup, the measurement techniques and the error estimates pertaining to the data presented in the results section are being presented. Also, the operational parameters of the experiments are given.

**Test Facility.** The single sector test rig, in which the measurements were conducted under atmospheric pressure conditions, is sketched in Fig. 1. Harmonic forcing on the electrically pre-heated air flow is created by a siren. The siren works on the principle of a rotating disc in an axial flow. The rotor has rectangular orifices passing double sine shaped apertures on the stator plate. Practice has shown that a sinusoidal excitation is well achieved if the air leakages around the rotor are kept small. The siren is driven by a 1.1-kW induction motor. The rotation speed is controlled by a frequency converter, producing excitation frequencies up to 850 Hz. In order to adjust the excitation amplitudes, the siren unit has a bypass valve, which allows the alteration of the air mass flow ratio between the siren and the bypass passage.

A supply tube connects the siren to the combustion chamber. The supply tube has a circular cross section with 124-mm inner diameter, and its length is adjustable from 850 to 1450 mm. In this way tube resonance effects may be used or avoided to further control the forcing amplitude. For the measurements presented here the maximum supply tube length was used. The acoustics of the supply were shown to be 1D using the ten equally spaced microphone ports in the far field of the siren. The supply tube and the combustion chamber are connected with an adapter piece accommodating the injector/burner investigated. A thermocouple gives the air temperature at the injector inlet. The mean and oscillating pressure drop over the injector are determined by corresponding pairs of pressure taps and microphone ports close to the burner inlet and outlet planes.

Contributed by the International Gas Turbine Institute (IGTI) of THE AMERICAN SOCIETY OF MECHANICAL ENGINEERS for publication in the ASME JOURNAL OF ENGINEERING FOR GAS TURBINES AND POWER. Paper presented at the International Gas Turbine and Aeroengine Congress and Exhibition, Atlanta, GA, June 16–19, 2003, Paper No. 2003-GT-38646. Manuscript received by IGTI, Oct. 2002, final revision, Mar. 2003. Associate Editor: H. R. Simmons.

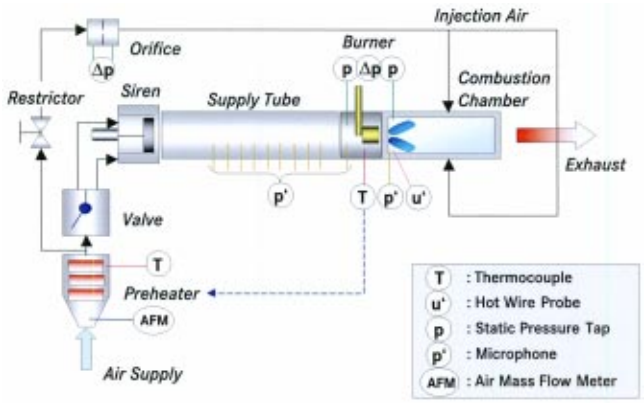


**Fig. 1 (Color online) Schematic representation of the test rig**

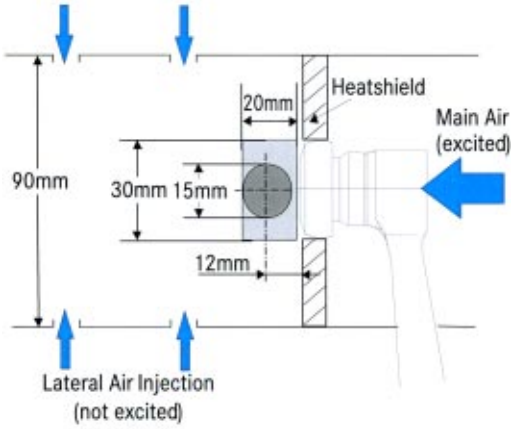


**Fig. 2 (Color online) Schematic representation of the position of the PIV-investigation area (light gray) and the Malvern laser beam (dark gray) in the vertical center plane of the combustion chamber relative to the injector outlet**

The combustion chamber has a square cross section, and measures 90×90×300 mm. Exchangeable side plates allow a flexible adaptation to the requirements of the measurement techniques applied. The primary combustion zone is optically accessible by exchangeable quartz windows. A hot-wire probe can be mounted 3 mm downstream of the burner outlet for the determination of the acoustic velocities. Ignition is achieved using a spark plug. For the combustion chamber, an acoustic open end condition can be assumed, since the exhaust tube measures 500 mm in diameter and does not contain a silencer.

The generic airblast diffusion injector/combustor system investigated is of the rich-quench-lean type, such that holes for secondary air injection were provided in the top and bottom plates of the combustion chamber, meeting the aerodynamic and stoichiometric operating conditions. The hole pattern and location was derived from the real (annular) liner geometry. The hole diameters were determined from the original air distribution on the basis of CFD. The air flow through these holes is diverted from the main flow upstream of the siren valve and is controlled by a flow restrictor valve with a corresponding measurement orifice. Dilution, film and liner cooling in the downstream part of the combustion chamber were omitted since they do not contribute to the formation of the primary zone aimed at in the current investigation.

**Measurement Techniques and Data Analysis.** A major requirement in the current experiments is to capture phase locked data. For this the siren shaft provides a reference signal, such that the exact forcing frequency and the phase angle of all measurements relative to the forcing can be determined. For the time-resolved measurement of the acoustic velocity, a 5-$\mu$m constant temperature anemometer (CTA) hot-wire probe has been used. It was located 3 mm downstream of the injector exit in the horizontal centerplane of the combustion chamber. The position of the probe was chosen such that the maximum velocity and at the same time a low local turbulence level was obtained, to make the measurement representative of the acoustic burner velocity. Additionally, the dynamic pressure drop over the burner has been measured by means of two $\frac{1}{4}$-in. microphones being located directly upstream and downstream of the burner. The acquisition of the acoustic data (pressures and velocities) is controlled by a multichannel-I/O board (300 kHz, 12 bit). The microphone channels and the CTA channel were sampled with 10 kHz each. Time-domain sequences of 10,000 samples each were taken and Fourier transformed. Then the amplitude and phase of each signal at the forcing frequency were stored. Finally, the averages were computed for all measurement sets from a given operating condition. The errors of the CTA velocity measurements are estimated to be below ±3.5% relative error and those of the microphone pressure amplitudes to be below ±5% relative error.

Phase-locked PIV and spray measurements were obtained by means of a hardware trigger. The rectangular reference signal is used to start a programmable counter on a PCI board, which triggers the measurement devices on completion of the preselected countdown.

*Particle Image Velocimetry (PIV).* PIV was employed to determine the flow field in the central longitudinal section of the combustion chamber. For detailed data at the combustor outlet, a region in the vicinity of the injector exit was investigated which measured 20×32 mm starting 1 mm downstream of the combustor front as shown in Fig. 2. 100 vector maps were recorded and averaged to obtain the flow field data at every measured phase angle. The recording of the air velocity field took place without spray and flame. Oil droplets were used as seeding. The PIV light-sheet was also used for spray visualization by Mie scattering. Comparison of the PIV data with CTA data of corresponding cases leads to a relative error estimate of about ±3% of the measured velocity.

*Malvern Particle Sizing.* The Spraytec Particle Sizer was used to characterize the spray at the injector exit under nonignited conditions. The measurement volume made up by the laser beam had a diameter of 15 mm and was located at a distance of 12 mm downstream of the injector exit in the horizontal center plane of the combustor (see Fig. 2). The recordings have been performed phase triggered, taking 1250 samples at a sampling frequency of 2.5 kHz. For the ambient temperature spray measurements, repeatability and consistency checks make the SMD size measurements rather reliable. At elevated temperatures, beam steering caused by density gradients may introduce a considerable source of error. Again repeatability and consistency were checked, e.g., by comparing the measured temperature dependence of the SMD with the temperature scalings known from literature [7]. From the typical data scatter an error bar of ±5% is estimated for the SMD measurements.

**Operating Conditions.** The measurement points were derived from the startup operating conditions of the real combustor. They are characterized by low pressures inside the combustion chamber (1.2–3.6 bars), moderate air temperatures (maximum 430 K) and low AFR's in the combustion zone (18–40, without dilution). Since measurements were to be performed at ambient pressure, the preheating temperatures were maintained and the air and fuel mass flows were adapted such that the AFR of the primary zone and the characteristic pressure losses over the burner were retained. For the spray measurements without combustion, a mixture of 90% ethanol and 10% water was used as fuel which

shows good agreement with the properties of kerosene (maximum 10% deviation on the main physical properties determining spray formation).

The parametric study included steady-state and unsteady measurements. The steady-state measurements were performed to characterize the general atomization behavior of the burner and the corresponding flow field and comprised a variation of:

1. Air temperature: 290 K (ambient) and 430 K
2. Air mass flow: $\dot{m}/\dot{m}_0 = 0.8-2.0$ in 13 different AMF's
3. Fuel mass flow: 1.0, 1.3, and 1.8 g/s, covering the whole range of AFR's occuring in the real engine.

For the unsteady measurements, external forcing has been applied at frequencies between 50 and 150 Hz, corresponding to the usual rumble frequencies. The unsteady measurements were conducted for the same temperature and FMF conditions as for the steady-state case, but only for selected burner AMF of $\dot{m}/\dot{m}_0 = 1.0, 1.6$.

## Theoretical Analysis

For the interpretation of the data shown in the results section a few derivations are needed, which are provided in the following sections. The pressure velocity coupling for a quasi-steady injector, the droplet motion time scale and its evaporation time, and finally a relation between Mie scattering intensity droplet diameter and velocity are being introduced.

**Quasi-Steady Pressure Velocity Coupling.** The measured flow field as well as the pressure and velocity measurements at the burner suggest that the burner response to the forcing is quasi-steady in the low-frequency range. To verify this notion, the quasi-steady relation between the amplitudes of burner velocity and pressure drop is derived from a perturbation expansion using the perturbations of pressure and velocity in the steady Bernoulli equation. Due to the very large area ratio between the supply tube and the burner channels, the supply tube may be treated as a plenum chamber, neglecting the contribution of the air velocity to the total pressure. For a low Mach number flow from a plenum through the burner channels, the total pressure balance from the plenum to the burner exit is given by

$$\Delta p = \frac{\rho}{2} u^2 (1+\zeta_B). \tag{1}$$

Introducing the perturbed values of pressure $p+p'$ and velocity $u+u'$ into Eq. (1) and subtracting from this the equation of the averages, the following perturbation equation is obtained:

$$p' = \rho u u' (1+\zeta_B). \tag{2}$$

Referring the left and right sides to the respective averages, the quasi-steady relation of relative pressure and velocity perturbations results:

$$\frac{1}{2}\frac{p'}{\Delta p} = \frac{u'}{u}. \tag{3}$$

Equation (3) means that for a quasi-steady burner response the relative velocity amplitude will be half the relative pressure drop amplitude.

**Droplet Motion Time Scale.** The dynamical behavior of the spray is characterized by the time scale of droplet motion. An estimate for this time scale can be obtained from the equation of motion of a simple spherical droplet for a constant air velocity. This way the frequency limits of a quasi-steady behavior of the spray in an unsteady air flow can be assessed. This is needed when discussing the forced spray SMD measurement results. Following Hinze [8] the equation of motion of a spherical particle reduces to the balance of inertia and drag force,

$$\rho_f \frac{\pi d^3}{6}\frac{du_f}{dt} = -\frac{\rho_a}{2} c_w \frac{\pi d^2}{4}(u_f-u_a)\|u_f-u_a\|. \tag{4}$$

For a droplet Reynolds number in the range $1<\mathrm{Re}<1000$ the drag coefficient $c_w$ is well approximated by an augmented Stokes-type law [9],

$$c_w = \frac{24}{\mathrm{Re}}(1+0.15\,\mathrm{Re}^{0.68}) \tag{5}$$

with

$$\mathrm{Re} = \frac{d\|u_f-u_a\|}{\nu_a}. \tag{6}$$

With this expression inserted into Eq. (4), the following mildly nonlinear ordinary differential equation for the droplet velocity is obtained:

$$\frac{du_f}{dt} = -18\frac{\nu_a \varepsilon}{d^2}(1+0.15\,\mathrm{Re}^{0.68})(u_f-u_a). \tag{7}$$

Solving this equation for typical droplet diameters, it is found that the deviation from the Stokes drag relation is only relevant in the initial acceleration of the droplet, when the slip velocity is large. It is found that a characteristic time scale $\tau$ can be defined analogously to the linear case by

$$\frac{1}{\tau} = 18\frac{\nu_a \varepsilon}{d^2} \tag{8}$$

which will scale the solutions of Eq. (7) for zero initial droplet velocity. In the linear case, $\tau$ gives the time in which the droplet has accelerated to 63% of the gas velocity, whereas in the nonlinear case 63% of the gas velocity are reached after about $1/3\tau$.

**Time Scales of Evaporation.** For the higher air temperature measurements, droplet evaporation may influence the size measurements. Therefore time scales of droplet heating $t_h$ and droplet evaporation $t_v$ have been estimated for the typical operation conditions using the simple $d^2-t$ law, which has been shown to work reasonably well for volatile liquids like ethanol [10,11]. As suggested there, the property values have been determined at the average temperature between the liquid boiling point $T_s$ and the air temperature $T_a$. Droplet flight was simulated using Eq. (7) between the atomizer lips as the virtual start and the measurement volume. This resulted in an average droplet slip of 50% of the air speed, which was used to determine the droplet Reynolds number Eq. (6).

The total evaporation time used to estimate the importance of the process for the current measurements is the sum of both times $t_h+t_v$. For the low AMFs where the SMD is around 55 $\mu$m the total evaporation time is estimated at around 11 ms, whereas for the high AMF with SMD of around 20 $\mu$m a time of 6.2 ms is obtained. To assess the influence of droplet evaporation on the measured diameter, these time scales are compared with the mean flight time calculated integrating Eq. (7) between the atomizer lip and the measurement volume. For the given setup the ratio of residence to evaporation time scale is 0.06 for the 55-$\mu$m and 0.02 for the 20-$\mu$m droplets, indicating that this effect may be neglected when comparing to the other measurement uncertainties.

**Spray Visualization Analysis.** Apart from extracting the spray geometry from phase-locked average pictures of Mie scattering light sheet tomography, the intensity oscillation of the scattered light was analyzed. In dilute spray the average intensity observed from Mie scattering depends on droplet diameter and number density approximately as

$$\frac{I}{I_0} = \left(\frac{d}{d_0}\right)^2 \frac{N}{N_0} \overset{\dot{m}_f=\text{const!}}{\approx} \left(\frac{d}{d_0}\right)^2 \left(\frac{d}{d_0}\right)^{-3} = \frac{d_0}{d}. \tag{9}$$

For a constant fuel mass flow rate, the particle number ratio in the second term of Eq. (9) can be expressed by droplet diameter. For the current atomizer under steady-state conditions the droplet diameter and air velocity correlate well with

$$\frac{d}{d_0} = \left(\frac{u_{a,0}}{u_a}\right)^{\xi}, \quad \xi > 1. \tag{10}$$

Given Eqs. (10) and (9), the measured intensity amplitude can be transformed into a velocity amplitude,

$$\frac{u_a'}{u_{a,0}} = \frac{1}{\xi}\frac{I'}{I_0}. \tag{11}$$

With this equation and given the steady atomizer characteristics, relative velocity amplitudes may be calculated from relative Mie intensity amplitudes for quasisteady behavior of the atomizer. Thus it provides an easy check for quasi-steady spray behavior.

## Results

**Pressure Velocity Coupling Under Forcing.** In Fig. 3, the comparison of the amplitudes of half the relative pressure drop oscillation measured with microphones and the relative velocity oscillation measured with the hot wire are compared for three mean flowrates: 1, 1.3, and 1.6 times the reference air mass flow rate.

The correlation between the relative velocity amplitude and half the relative pressure amplitude is very good. Therefore Eq. (3) holds, which means that the burner flow responds quasi-steady to the low-frequency forcing. The small differences observed between velocity and pressure amplitudes, seen in particular for the higher frequencies at the lowest flow rate ($p'/2p$ and $u'/u$ for $\dot{m}/\dot{m}_0 = 1$), decrease with increasing flow rate. This is due to the signal-to-noise ratio of the CTA which improves with mean velocity. For increasing flow rate the relative amplitudes achieved at the burner are seen to decrease, because the rising burner back pressure reduces the relative forcing amplitude.

**Velocity Field Under Forcing.** Figure 4 shows the velocity distribution at the burner exit for a forcing at 90 Hz. On the left half of the picture, the contour lines represent two fixed levels of air velocity magnitude at ten different phase angles with a phase separation of $\Delta\varphi = 36$. The spread of the superposed contours gives an impression of the injector's velocity response and shows how the swirling jet velocity grows and diminishes during the forcing period.

On the right half of Fig. 4 the contourlines of equal relative velocity are shown. These are obtained by normalizing the local phase-averaged velocities with the injector exit velocity of the respective phase angle. The contours coincide, meaning that the velocity field is invariant during the forcing cycle. Therefore the aerodynamic behavior of the injector is quasi-steady for the frequency range considered, which is in line with the pressure-velocity coupling discussed above.

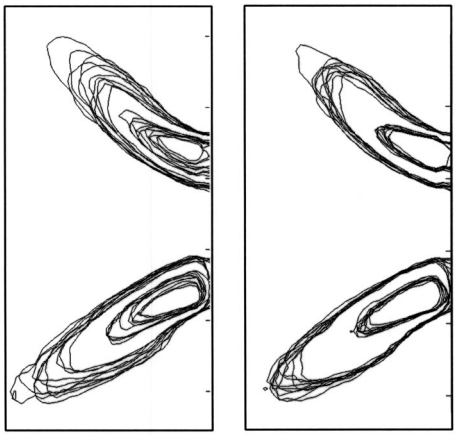

**Fig. 4 Phase-locked velocity field at 90 Hz without combustion: the left half shows two contour levels of velocity magnitude for all ten phase angles, the right half shows the same field scaled with the average velocity at the burner exit**

**Stationary Atomization Measurements.** Figure 5 shows the measured SMD of the burner for different AMF's and two air temperatures. As typical for airblast atomizers, the SMD is dominated by the air mass flow rate and relative atomization velocities at the atomizer lip. For relative AMF>1.5 and low viscosity fuel, the atomization process is solely governed by the Weber number We. Referring to the relation given in Ref. [7]:

$$\frac{\mathrm{SMD}}{L_c} \propto \mathrm{We}^{-x}. \tag{12}$$

For the current data an exponent $x \approx 0.8$ with respect to the AMF variation and $x \approx 0.5$ for the temperature change is obtained. This is in agreement with the typical values for air blast atomizers found in the literature [7,12]. A possible reason for the different values of $x$ may be secondary spray breakup. With decreasing relative AMF<1.5 the disruptive forces decrease strongly, which tends to decrease the slope of the curve in this range. According to the stationary curves in Figs. 6 and 7, the SMD is fairly insensitive to changing FMF, giving only a 10% diameter increase for almost double fuel flow rate.

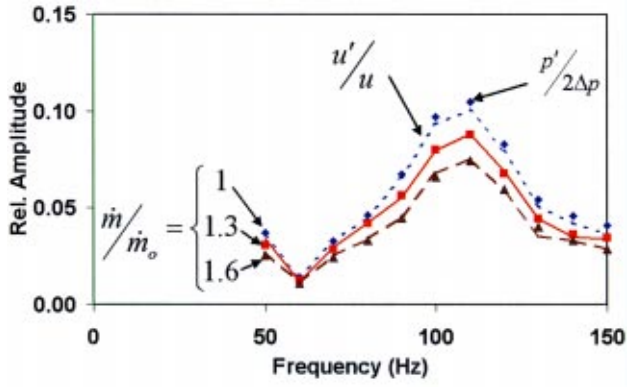


**Fig. 3 (Color online) Comparison of measured pressure amplitudes (symbols) and velocities (lines) over frequency for three mass flow rates in a noncombusting environment**

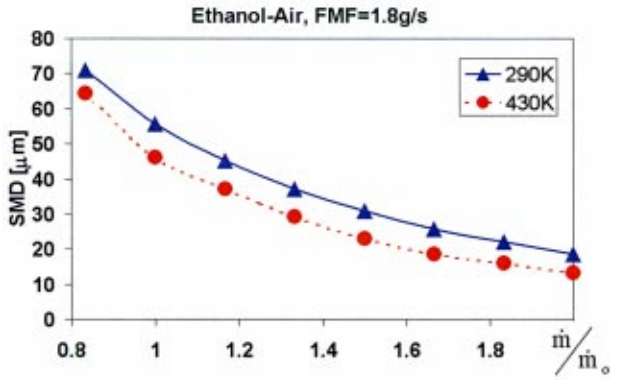


**Fig. 5 (Color online) SMD over relative AMF for different preheating temperatures in the stationary, noncombusting case**

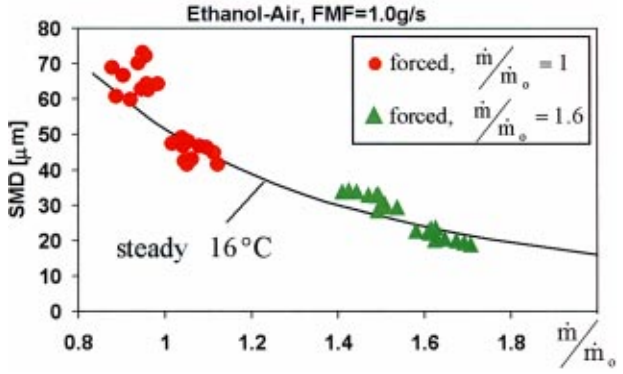


**Fig. 6 (Color online) Comparison of unsteady SMD (symbols) data with the steady atomization curve at 1.0-g/s fuel mass flow rate**

**Atomization Measurements With Forcing.** The atomization of the forced spray was measured using the Malvern particle sizer for a relative AMF of $\dot{m}/\dot{m}_0=1.0$ and 1.6, fuel flow rates of 1 and 1.8 g/s, 290 K air temperature, and frequencies between 50 and 150 Hz. From the time series of SMD, the diameter mean and amplitude were extracted. To compare with the steady data, only the momentary SMD values for the maximum and minimum velocity phase have been plotted in Figs. 6 and 7 together with the SMD curves obtained from the steady-state atomization experiments.

For the higher air mass flow rates at $\dot{m}/\dot{m}_0=1.6$, the comparison is good, showing quasi-steady behavior of the atomizer. For lower air flow rate at $\dot{m}/\dot{m}_0=1.0$, the droplet SMD and thus its motion time scale, Eq. (8) increases to the same magnitude as the forcing period. Now, convection will bias the drop size distribution in the measurement volume towards larger droplets, since larger droplets from the low velocity phase still continue to reach the measurement volume during the high velocity phase. Therefore the time series of drop size becomes assymmetric between the low and high velocity phases, leading to larger SMD amplitudes at the forcing frequencies. For the 1.0-g/s fuel flow rate, Fig. 6, the comparison at the lower AMF is better than in Fig. 7, which is consistent with a 20% lower droplet time scale. Therefore it seems that the deviations seen are mainly an intrinsic measurement problem related to the measurement technique employed [13].

**Spray Cone Angle, Mie Scattering Intensity.** In order to assess the applicability of the forced spray behavior under nonignited conditions to the case with combustion, the spray cone in the

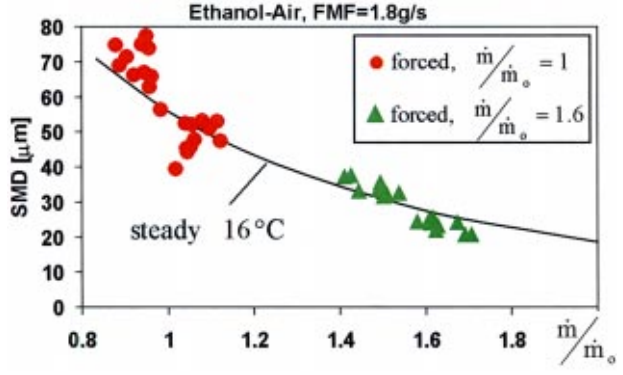


**Fig. 7 (Color online) Comparison of unsteady SMD (symbols) data with the steady atomization curve at 1.8-g/s fuel mass flow rate**

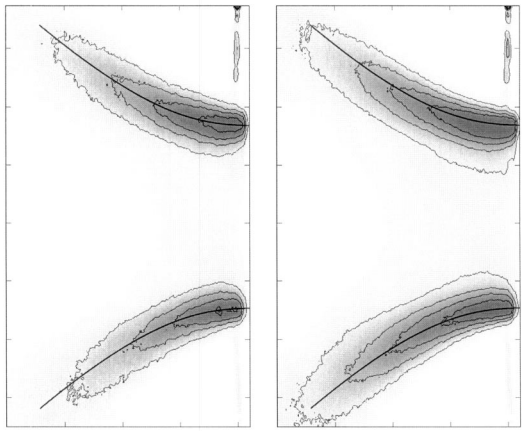

**Fig. 8 Mie scattering images of the spray cone with combustion at $\dot{m}/\dot{m}_0=1.6$, fuel flow rate of 1.3 g/s, $T_{air}=430$ K, and $f=130$ Hz. The contours show constant levels of scattered intensity. Left half: minimum velocity phase; right half: maximum velocity phase. Crown lines show constant spray geometry.**

combusting environment has been analyzed by means of Mie scattering. Figure 8 shows two phase-averaged pictures at minimum and maximum velocity phases with constant levels of Mie scattering intensity, which were averaged over 150 individual recordings. The intensity of the scattered light varies during the period due to the variation of droplet number and size with the air velocity as seen by the fixed contourlines. But the crown lines on the intensity contours of both phase angles coincide, showing that the underlying spray geometry does not vary with the periodic velocity oscillation.

Figure 9 shows the comparison of relative burner air velocity and mean Mie scattering intensity oscillation for the same operation point taken from phase locked PIV measurements. To obtain the intensity amplitude, a sinusoidal fit was used, which is also shown.

Taking into account the average convective time delay of the spray ($\approx$10 deg at 130 Hz), the net phase angle difference between the scattering intensity and velocity trace is negligible, which means that the spray response to velocity forcing is in phase. Using Eq. (11) with a velocity exponent of $\xi=1.6$ (taken from the static atomization behavior shown in the second previous subsection) the quasi-steady velocity amplitude is calculated from the Mie intensity amplitude. A relative velocity amplitude of 5.4% results, which compares well with 5.3% measured velocity amplitude. The validity of Eq. (11) implies that quasi-steady atomiza-

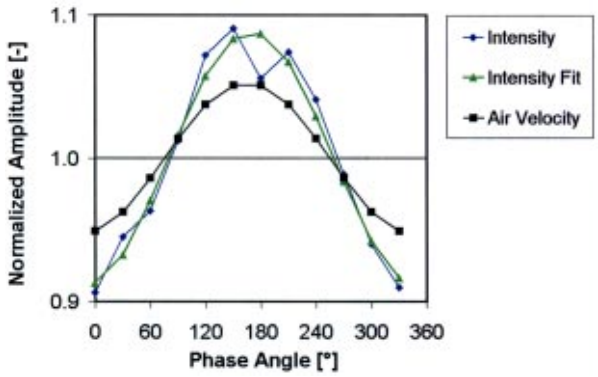


**Fig. 9 (Color online) Air velocity and Mie scattering intensity fluctuation for the spray at 130-Hz excitation**

tion behavior is also found under combustion conditions and that the momentary fuel mass flow rate in the spray is constant.

## Findings and Conclusions

The atomization behavior of a generic airblast atomizer with a design typical for aeroengine systems has been investigated under forced oscillation, which yields the following findings.

- The pressure velocity coupling of the burner air flow obeys the steady Bernoulli equation in the frequency range investigated.
- The phase-averaged velocity field of the cold flow in the combustor has an invariant distribution throughout the oscillation period.
- The phase-locked SMD measurements for oscillating air flow lie on the steady atomization curve. Agreement is good for higher mean air flow rate, but the deviations observed at lower mean air flow rate are most probably measurement bias.
- In the case of combustion, the basic spray geometry is unaffected by the forcing. The measured Mie scattering intensity oscillation obeys a quasi-steady relation derived for a constant fuel mass flow rate.

Our experimental findings lead to the conclusion that a quasi-steady description of an airblast atomizer in the context of low-frequency combustion oscillations like rumble is appropriate. Thus the instantaneous SMD may be calculated using the momentary velocity data and the steady-state correlation between velocity and SMD. The constant fuel mass flow rate will lead to substantial fluctuations of the equivalence ratio which could be the reason for rumble. The design of the generic airblast atomizer used here further suggests that this conclusion should also hold for typical systems used in aeroengines today.

## Acknowledgments

It is gratefully acknowledged that the experimental work presented in this paper has been supported by the European Commission as part of the GROWTH program ''Instability Control of Low Emissions Aero Engine Combustors'' (ICLEAC) under Contract No. G4RD-CT-2000-00215.

## Nomenclature

AFR = air fuel ratio of the primary zone
AMF = air mass flow [g/s]
$c_w$ = drag coefficient
$c$ = heat capacity [J/(kg K)]
$d$ = droplet diameter [m]
FMF = fuel mass flow [g/s]
$h$ = enthalpy [J]
$I$ = light intensity [W/m$^2$]
$L_c$ = characteristic atomizer dimension [m]
$N$ = droplet number
Nu = Nusselt number
$p$ = pressure [Pa]
Pr = Prandtl number
Re = Reynolds number
SMD = Sauter mean diameter [$\mu$m]
$T$ = temperature [K]
$t$ = time [s]
$u$ = velocity [m/s]
We = Weber number
$\varepsilon$ = density ratio; $\varepsilon = \rho_a / \rho_f$
$\lambda$ = thermal conductivity [W/(m K)]
$\nu$ = dynamic viscosity [m/s$^2$]
$\rho$ = density [kg/m$^3$]
$\tau$ = characteristic time scale [s]
$\zeta$ = pressure loss coefficient

### Subscripts

$( )_a$ = air
$( )_B$ = burner
$( )_f$ = fuel
$( )_h$ = heating
$( )_p$ = for constant pressure
$( )_v$ = vaporization
$( )_0$ = reference

### Superscripts

$( )'$ = perturbation, amplitude

## References

[1] Paschereit, C. O., Polifke, W., Schuermanns, B., and Mattson, O., 1998, ''Investigation of the Thermoacoustic Characteristics of a Lean Premixed Gas Turbine Burner,'' ASME Paper 98-GT-582.
[2] Sattelmayer, T., 2000, ''Influence of the Combustor Aerodynamics on Combustion Instabilitites From Equivalence Ratio Fluctuations,'' ASME Paper 2000-GT-0082.
[3] Polifke, W., Paschereit, C. O., and Döbbeling, K., 2001, ''Constructive and Destructive Interference of Acoustic and Entropy Waves in a Premixed Combustor With a Choked Exit,'' Int. J. of Acoustics and Vibration, **6**(3), pp. 135–146.
[4] Cohen, J. M., Hibshman, J. R., Proscia, W., Rosfjord, T. J., Wake, B. E., McVey, J. B., Lovett, J., Ondas, M., DeLaat, J., and Breisacher, K., 2000, ''Experimental Replication of an Aeroengine Combustion Instability,'' ASME Paper 2000-GT-0093.
[5] Zhu, M., Dowling, A. P., and Bray, K. N. C., 1999, ''Combustion Oscillations in Burners With Fuel Spray Atomizers,'' ASME Paper 99-GT-302.
[6] Zhu, M., Dowling, A. P., and Bray, K. N. C., 2000, ''Self-Excited Oscillations in Combustors With Spray Atomizers,'' ASME Paper 2000-GT-0108.
[7] Lefebvre, A. H., 1983, *Gas Turbine Combustion*, First ed., Hemisphere, New York.
[8] Hinze, J. O., 1979, *Turbulence*, Second ed., McGraw-Hill, New York.
[9] Krämer, M., 1988, ''Untersuchungen zum Bewegungsverhalten von Tropfen in turbulenter Strömung im Hinblick auf Verbrennungsvorgänge,'' Ph.D. thesis, TH Karlsruhe.
[10] Turns, S., 2000, *An Introduction to Combustion*, Second ed., McGraw-Hill, New York.
[11] Kneer, R., 1993, ''Grundlegende Untersuchungen zur Sprühstrahlausbreitung in hochbelasteten Brennräumen,'' Ph.D. thesis, TH Karlsruhe.
[12] Sattelmayer, T., 1985, ''Zum Einfluss der ausgebildeten, turbulenten Luft-Flüssigkeitsfilm-Strömung auf den Filmzerfall und die Tropfenbildung am Austritt von Spalten geringer Höhe,'' Ph.D. thesis, TH Karlsruhe.
[13] Wittig, S., Aigner, M., Sakbani, K., and Sattelmayer, T., 1984, ''Optical Measurements of Droplet Size Distributions: Special Considerations in the Parameter Definition for Fuel Atomizers,'' AGARD-CP-353, Paper 13.

# Experimental Study of Surface and Interior Combustion Using Composite Porous Inert Media

**T. L. Marbach**

**A. K. Agrawal**

School of Aerospace and Mechanical Engineering,
University of Oklahoma,
Norman, OK 73019

*Combustion using silicon carbide coated, carbon–carbon composite porous inert media (PIM) was investigated. Two combustion modes, surface and interior, depending upon the location of flame stabilization, were considered. Combustion performance was evaluated by measurements of pressure drop across the PIM, emissions of* $NO_x$ *and CO, and the lean blow-off limit. Data were obtained for the two combustion modes at identical conditions for a range of reactant flowrates, equivalence ratios, and pore sizes of the PIM. Results affirm PIM combustion as an effective method to extend the blow-off limit in lean premixed combustion.* [DOI: 10.1115/1.1789516]

## Introduction

Reduction of pollutant emissions is one of the most important goals of combustion research today. Many new technologies aimed at reducing nitric oxides ($NO_x$), carbon monoxide (CO), and unburned hydrocarbons (UHCs) have arisen to meet increasingly stringent emissions regulations. The most direct method of controlling emissions is to control the flame temperature. Variable geometry combustion and advanced fuel atomization and mixing techniques are being used to reduce emissions from lean premixed (LPM) combustion. Staged combustion, including the rich-burn, quick-quench, lean-burn (RQL) combustor, selective catalytic reduction (SCR) and direct catalytic combustion are other methods of reducing emissions [1]. Direct catalytic combustion offers the potential to greatly reduce $NO_x$ emissions by decreasing the reaction gas temperature of lean premixed fuel and air [2].

Combustion stabilized with the use of porous inert media (PIM) is another technique that is capable of achieving low emissions. A flame can be stabilized on the surface or in the interior of a PIM as illustrated by Fig. 1. For a flame stabilized on the surface, the energy released by the reaction is transferred to the porous surface, which in turn emits it to the surroundings, such as in radiant burners. A portion of the energy is radiated and conducted upstream to preheat the reactants in the preheat zone. A surface burner with high radiant output and low $NO_x$, CO and UHC output is feasible by optimizing the pore size, geometry, and thermophysical properties of the PIM, fuel/air flowrates, and equivalence ratio ($\Phi$). Recently, Alzeta Corporation demonstrated combustion at gas turbine conditions, stabilized above a porous sintered injector surface comprised of high temperature metal fibers [3]. They reported firing rates on the order of 30 $MW/m^2$ at 10-atmospheric pressure. Initial results show that the combustor simultaneously achieved single digit emissions of $NO_x$, UHCs and CO. Ontko et al. [4] used sintered tungsten, formed into a truncated cone, to extend the turndown ratio in porous surface combustion. Low $NO_x$ and CO emissions were simultaneously obtained.

Although heat transfer mechanisms similar to surface combustion serve as the basis of interior combustion, the amount of heat transferred in each mode can be significantly different. During surface combustion, heat is transferred from the reaction zone to the PIM at and slightly below the burner surface. However, interior combustion allows heat transfer to the PIM both at the reaction zone and downstream by interfacial convection between the products and the porous structure. The result of this additional convective heat transfer is the potential for increased preheating of reactants and consequently a greater control of flame stability and temperature, leading to ultra low $NO_x$ combustion.

The concept of recirculating energy from products to reactants or the ''excess enthalpy flame'' was introduced by Hardesty and Weinberg [5]. PIM combustion research has been reviewed by Howell et al. [6], Viskanta [7], and Trimis and Durst [8]. Kotani and Takeno [9] found that a porous burner increased the laminar flame speed by more than an order of magnitude. Subsequently, various aspects of combustion with PIM have been investigated experimentally and numerically. Hsu et al. [10] used two porous ceramic cylinders of different pore sizes stacked together. The flame was stabilized at the interface of two blocks over a range of mixture flow rates for a given equivalence ratio. A similar concept of bilayered reticulated ceramic burner with an upper layer with larger pores and a lower layer with smaller pores to improve the stable operating regime was used by Rumminger et al. [11]. Pickenacker et al. [12] have developed several commercial concepts involving combustion inside the PIM.

A critical component of PIM combustion is the porous material. Important characteristics of the porous structure are the maximum operating temperature and thermophysical properties such as absorptivity, emissivity, and thermal conductivity. Materials used in experimental porous burners are wide ranging, with ceramics being the most common. Although porous ceramics have good thermal resistance, they suffer from structural damage caused by repeated start-up and shutdown and therefore, are not suited for gas turbine applications. In recent years, new materials have become available with advancements in manufacturing techniques. One such example is the carbon–carbon (C–C) composite with carbon fiber reinforcement imbedded in a carbon matrix. Properly fabricated C–C composites have the highest specific strength (strength/weight) of any known material and retain their strength to over 2775 K [13]. The drawback of C–C composites is their inability to resist oxidation at temperatures above 775 K. An oxidation-resistant coating of high temperature materials such as silicon carbide (SiC), rhenium, hafnium, or iridium may be deposited on the composite structure by the chemical vapor deposition technique. These porous materials offer structural rigidity as well as thermal/oxidation resistance required for combustion at gas turbine operation conditions.

The objective of this research is to study combustion performance of a SiC coated, C–C composite foam designed to operate continuously at temperatures above 1675 K without significant thermal or structural degradation. Figure 2 depicts a SiC coated,

Contributed by the International Gas Turbine Institute (IGTI) of THE AMERICAN SOCIETY OF MECHANICAL ENGINEERS for publication in the ASME JOURNAL OF ENGINEERING FOR GAS TURBINES AND POWER. Paper presented at the International Gas Turbine and Aeroengine Congress and Exhibition, Atlanta, GA, June 16–19, 2003, Paper No. 2003-GT-38713. Manuscript received by IGTI, Oct. 2002, final revision, Mar. 2003. Associate Editor: H. R. Simmons.

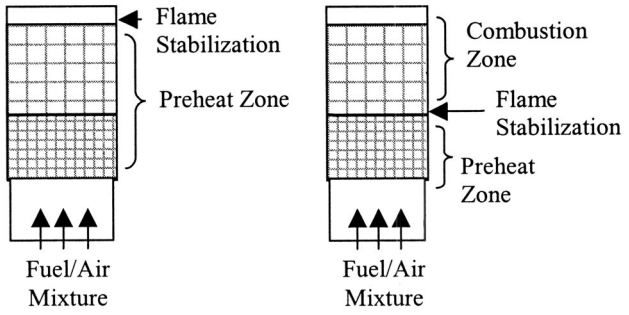


**Fig. 1 Schematic representation of (*a*) surface combustion, (*b*) interior combustion**

C–C composite porous material of 4 pores per cm (ppcm). The overall goal is to gain insight to advance PIM burners for gas turbines and other combustion applications. Past experimental investigations of combustion in PIM have focused on either surface or interior combustion. In the present study, both surface and interior combustion modes were investigated at identical operating conditions to compare the performance. The operating parameters include fuel/air mixture flowrate, equivalence ratio, and the pore sizes of the PIM. The combustion performance was characterized by measurements of pressure loss and emissions of $NO_x$ and CO.

## Experimental Setup

The burner, depicted in Fig. 3, is comprised of four sections: the fuel/air inlet section, the fuel/air mixing section, the PIM section, and the emissions shield. Each section is constructed of stainless steel square tubing of 4.04 cm by 4.04 cm inside cross section and a wall thickness of 0.48 cm. The 15.2 cm long fuel/air mixing section is comprised of a 2.54 cm thick, 32 ppcm porous-piece at the upstream end to assist fuel/air mixing, with free space making up the remaining mixing length. The PIM section is 10.2 cm long, with four 2.54 cm thick porous pieces arranged in various configurations of 4, 8, 12, and 32 ppcm material.

The porous pieces are sanded to fit precisely into the PIM section. A tight fit is critical because space between porous material and combustor wall could cause the flame to propagate around the PIM. A shield is used downstream of the PIM section for emissions measurements without entraining the ambient air. A set of pressure taps is located near the exit of the fuel/air mixing section to monitor the pressure drop across the PIM. The product gases are discharged through the emission shield at atmospheric pressure.

The combustion air is supplied by an air compressor, dried, and measured upstream of the burner by a laminar flow element calibrated for 0–300 standard liters per minute (slpm). The natural gas fuel is supplied from a compressed gas cylinder, controlled by a needle valve, and metered by a mass flow meter calibrated in the 0–60 slpm range. Air and fuel enter the experimental setup at a temperature of about 300 K. A quartz extraction probe with a tapered tip to quench the reactions is used to sample the products. The sample is passed through water traps prior to the measurements of CO, $NO_x$, and $O_2$ concentrations using electrochemical sensors. The uncertainty of emissions measurement is $\pm 2$ ppm. Emissions data are reported on an uncorrected dry basis. The pressure drop across the combustion section was measured with a $\pm 12.5$ cm $H_2O$ pressure transducer.

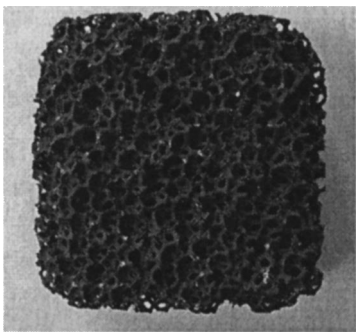

**Fig. 2 SiC coated, C–C composite PIM of 4 ppcm**

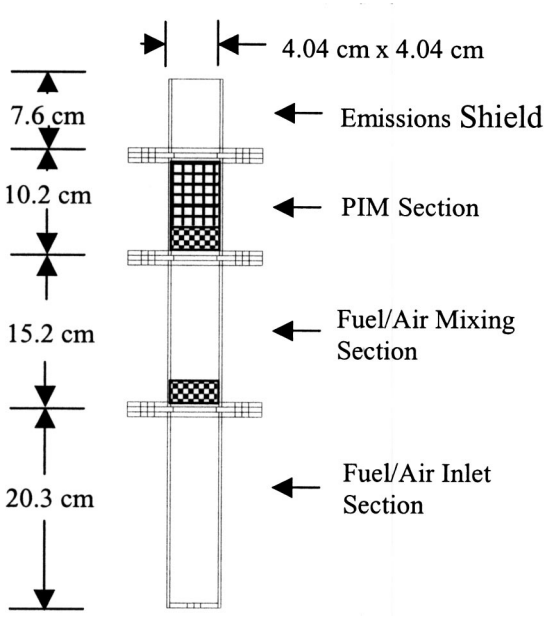


**Fig. 3 Schematic diagram of the experimental setup**

At each set of operating parameters, surface and interior combustion data were obtained. The switch from surface to interior combustion was made by reducing the mean fuel/air mixture inlet velocity ($v$) to about 0.4 m/s and increasing the equivalence ratio to about 0.8, which caused the flame to propagate upstream into the PIM. Once interior combustion was established, the mean inlet velocity was increased and the equivalence ratio was decreased to the desired values.

## Results and Discussion

The baseline configuration for the experiment was defined as 32-8-8-8. This refers to the PIM section filled with one 32 ppcm piece (preheat zone), followed by three 8 ppcm pieces (combustion zone). The baseline conditions were defined as $\Phi = 0.60$ and $v = 1.0$ m/s. Parameters varied during experiments include equivalence ratio, mixture inlet velocity, preheat zone pore size, and combustion zone pore size. Both surface and interior combustion were established at identical conditions, allowing direct comparison of the performance of the two combustion modes.

Several differences between surface and interior combustion are notable. As seen in Fig. 4(*a*) surface combustion results in the characteristic blue flat flame of lean premixed combustion. However, as Fig. 4(*b*) depicts, interior combustion emits an orange glow from the radiating PIM. Audibly, surface combustion produced sound similar to that from a Bunsen burner, while interior combustion was virtually silent. This is a result of the muffling effect of the porous material between the flame front and burner exit. Consequently, the resolution of noise-related instabilities by interior combustion is a significant benefit in LPM gas turbine combustion systems.

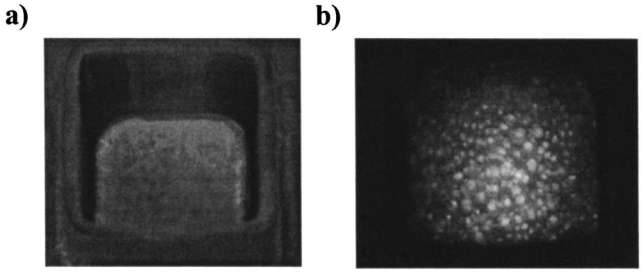


**Fig. 4 Visual images at baseline conditions (*a*) surface combustion, (*b*) interior combustion**

## Pressure Drop

Pressure drop resulting from cold flow through the PIM ranged from 0 to 1% of the operating pressure. Figure 5 presents the percent pressure drop across various individual porous pieces (each 2.54 cm thick) and the baseline configuration (32-8-8-8) at a range of flow rates. As expected, the pressure drop increases with the flowrate. Note that the measured pressure drop across the 32-8-8-8 configuration is within 5% of that calculated by adding the pressure drop across the individual pieces. Figure 6 presents percent pressure drop for surface and interior combustion over a range of flow rates. With surface combustion, the pressure drop in the PIM is virtually the same as that for cold flow. Interior combustion, however, more than doubles the pressure drop in the PIM section, in part, because of the higher velocity of the product gasses moving through the PIM. Results suggest that pore size and thickness of the PIM region are important to minimize the pressure drop for practical applications.

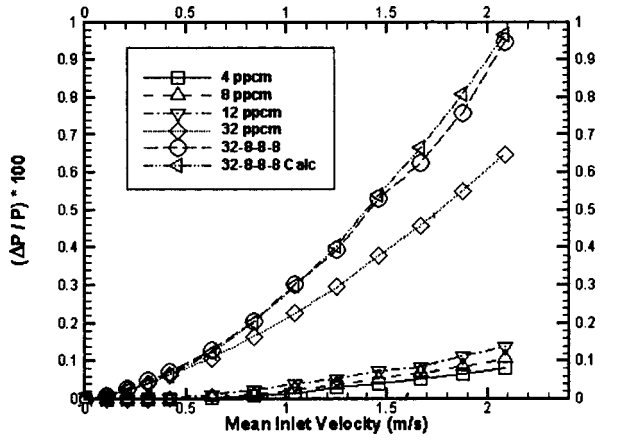


**Fig. 5 Effect of pore size on cold flow pressure drop**

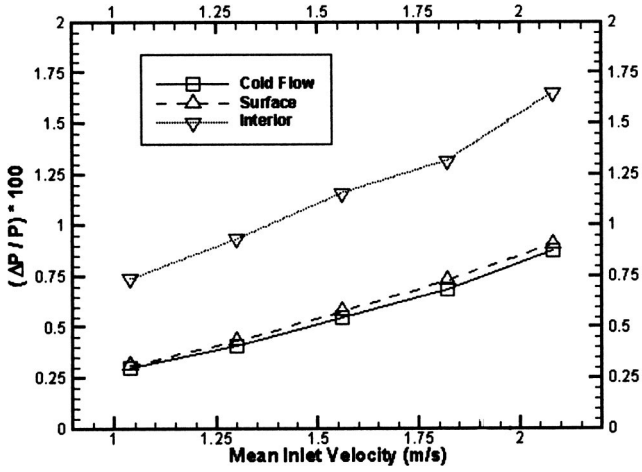


**Fig. 6 Effect of combustion on pressure drop for baseline configuration (32-8-8-8), Φ=0.6**

## CO and $NO_x$ Emissions

First, experiments were conducted to determine the uniformity and length of the reaction zone. To quantify this, emissions profiles at baseline conditions were (a) in the flow direction (vertical) along the combustor midpoint and (b) in the transverse (horizontal) direction at a vertical plane $z=63$ mm above the PIM surface.

Figure 7 presents data for $NO_x$ and CO emissions of surface and interior combustion versus vertical distance ($z$) above the PIM surface. Both $NO_x$ and CO emissions of interior combustion are constant throughout the entire length of the emissions shield. Therefore, all of the $NO_x$ and CO are generated within the PIM. However, surface combustion concentrations change radically near the PIM surface. CO concentration increases sharply as the emissions probe is lowered into the flame front. $NO_x$ concentrations decrease sharply as the probe is moved into the flame. Results show that the $NO_x$ formation was completed within $z=15$ mm from the PIM surface. The CO oxidation however continued downstream until about $z=35$ mm.

Figure 8 presents $NO_x$ and CO concentrations of surface and interior combustion versus horizontal distance ($y$) from the combustor midpoint at $z=63$ mm. Evidently, the CO and $NO_x$ emissions are nearly constant over the entire width for the two combustion modes. Emissions profiles obtained with leaner mixtures showed CO increasing and $NO_x$ decreasing near the combustor wall, which suggests a quenching effect of heat loss through the wall. Based on these results, the combustor midpoint at $z=63$ mm was selected for all subsequent emissions measurements, representing the postreaction zone.

**Effect of Reactant Flow Rate.** Figures 9(*a*) and 10(*a*) present data for $NO_x$ emissions versus equivalence ratio at various mean inlet velocities for surface and interior combustion, respectively. At a given equivalence ratio, the $NO_x$ concentration is weakly dependent on the mean inlet velocity, varying over a factor of 2. Khanna et al. [14] produced similar results, citing constant $NO_x$ emissions over a range of flame speeds or mixture flowrates. $NO_x$ increased exponentially with equivalence ratio, suggesting thermal mechanism as the primary source of $NO_x$ generation. Single digit $NO_x$ concentrations are obtained in both combustion modes for equivalence ratios of up to 0.65. Figures 9(*b*) and 10(*b*) present CO concentrations for surface and interior combustion, respectively. Figure 9(*b*) shows that the CO concentration at a given equivalence ratio is nearly independent of the flowrate for surface combustion. Khanna et al. [14] observed similar results to those depicted in Fig. 9(*b*); little dependence of CO concentration on reactant flow rate. The CO concentration increases with equivalence ratio, similar to the trend observed in nozzle-stabilized LPM flames [15]. Mital et al. [16] also observed increasing CO concentration with increasing equivalence ratio from interior combustion using reticulated ceramics. Data presented at the lowest equivalence ratio in Figs. 9 and 10 correspond to the lean blow-off limit. Results show that the equivalence ratio at the lean blow-off limit increases with increasing mean inlet velocity.

In general, the CO concentration for interior combustion increases with equivalence ratio as shown in Fig. 10(*b*). In this case, a significant flowrate effect is observed, especially at lower flowrates. Note that the combustor was air-cooled by natural convection to prevent overheating and structural damage to the stainless steel enclosure. At low flowrates, a larger fraction of heat released is believed to be lost to the surroundings. The resulting decrease in the flame temperature could affect the oxidation reactions to produce larger CO concentrations. The fractional heat loss is expected to diminish at higher flow rates, which show minor effect on CO emissions.

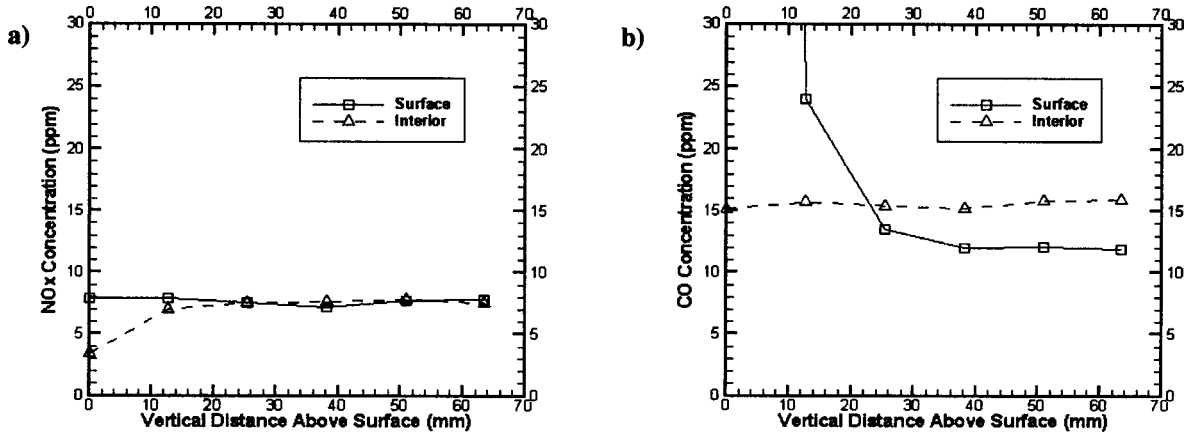


**Fig. 7 Effect of vertical measurement location on emissions (*a*) $NO_x$ and (*b*) CO**

**Surface Versus Interior Combustion.** $NO_x$ and CO concentrations versus equivalence ratio for surface and interior combustion at various flow rates are compared in Fig. 11 for $v = 1.0$ m/s. Results show that the combustion mode has little impact on $NO_x$ concentration at a given equivalence ratio. Interior combustion extends the lean blow-off limit, offering further $NO_x$ reduction. At the baseline conditions, the lean blow-off limit for surface combustion is about 0.58 while that for interior combustion is 0.55. Theoretically, this extension of the lean blow-off limit corresponds to a decrease in flame temperature of about 50 K. CO concentrations of the two combustion modes follow a similar trend with equivalence ratio, although interior combustion results in slightly higher concentrations, attributed to a higher fraction heat loss as explained above.

**Effect of Combustion Zone Pore Size.** Thermal feedback to reactants in both combustion modes depends upon the geometry of the PIM. To examine this issue, surface combustion experiments were conducted with 4, 8, 12, and 32 ppcm PIM and interior combustion experiments were conducted only with 4 and 8 ppcm PIM because smaller pores would quench the flame. Results in Figs. 12(*a*) and 13(*a*) show a relatively weak trend of larger

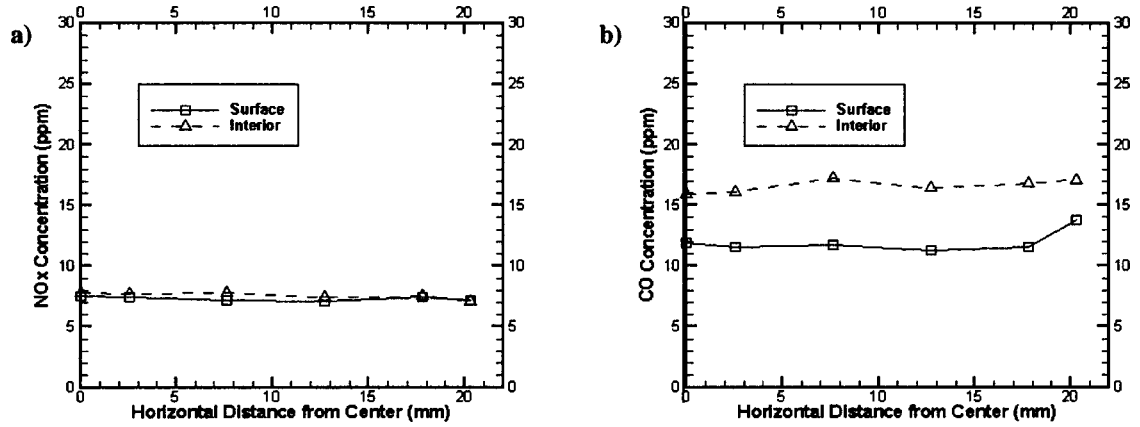


**Fig. 8 Effect of horizontal measurement location on emissions (*a*) $NO_x$ and (*b*) CO**

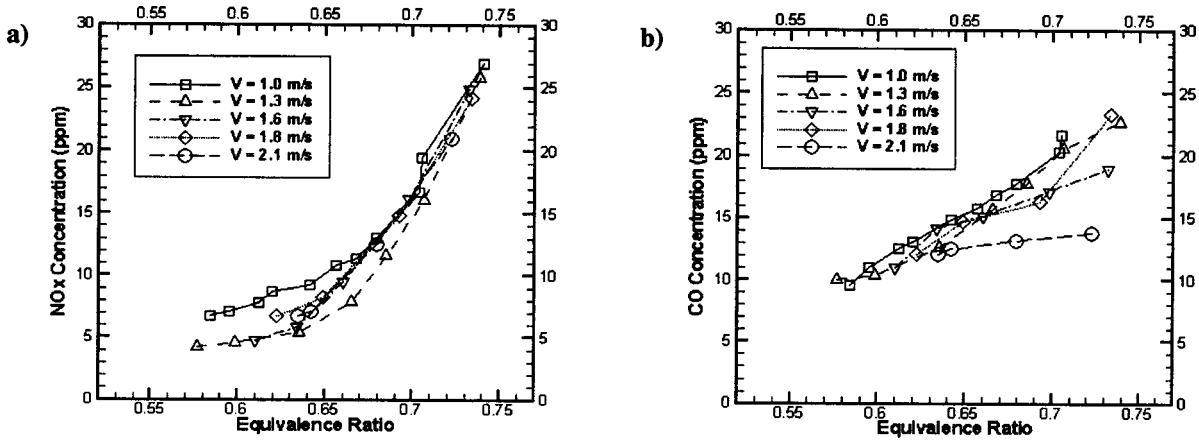


**Fig. 9 Effects of mean inlet velocity on emissions from surface combustion, (*a*) $NO_x$ and (*b*) CO**

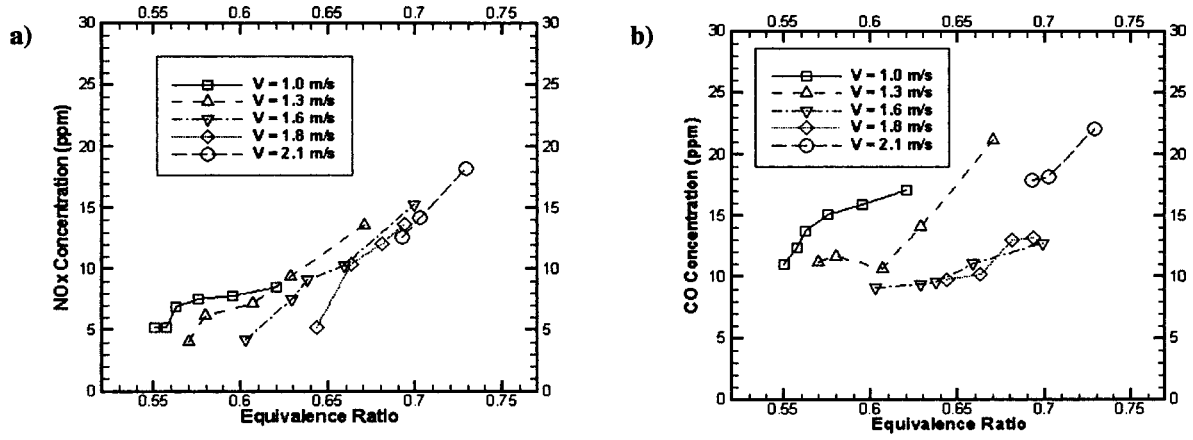


**Fig. 10 Effects of mean inlet velocity on emissions from interior combustion, (*a*) $NO_x$ and (*b*) CO**

pores resulting in higher $NO_x$ emissions at a given equivalence ratio. The PIM with larger pores has smaller optical thickness compared to that of a PIM with smaller pores. Therefore, it is plausible that the higher $NO_x$ generation of the large pore PIM (32-4-4-4) is an effect of the greater preheating of reactants by radiation from the flame zone. Detailed measurements near the flame front are therefore necessary to fully explain these observations.

Figures 12(*b*) and 13(*b*) present CO concentration versus equivalence ratio for various combustion zone pore sizes, respectively, for surface and interior combustion. In both cases, CO concentration increases with decreasing pore size. Several phenomena may be responsible for this trend. In case of surface combustion, increased flame length and residence time with larger pores would assist oxidation reactions to reduce CO emissions. Furthermore, as discussed above, a porous structure with smaller pores has a larger optical thickness than a similar porous structure with larger pores. Therefore, less heat is radiated upstream and less preheating of reactants occurs. The decrease in preheating is akin to the flame

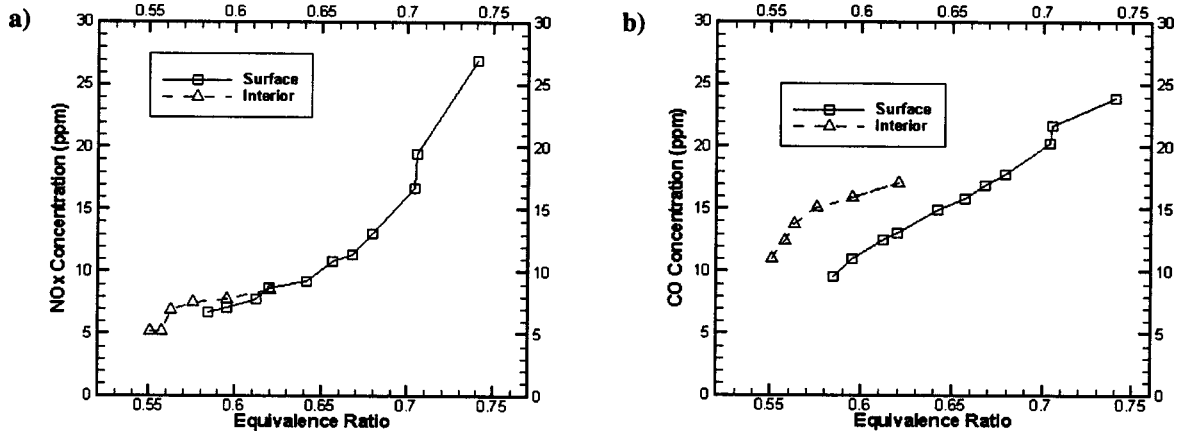


**Fig. 11 Emissions measurements for the two combustion modes, (*a*) $NO_x$ and (*b*) CO**

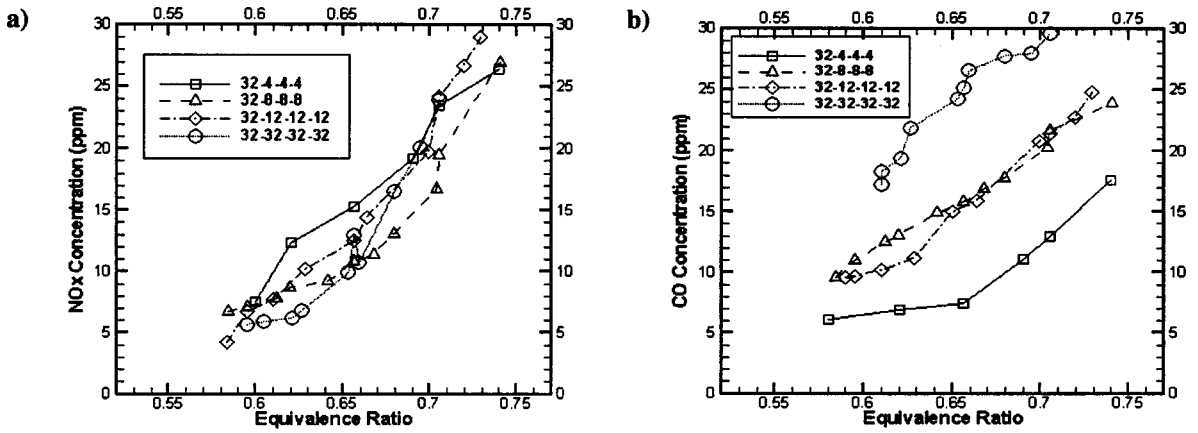


**Fig. 12 Effect of combustion zone pore size on emission from surface combustion at $v = 1.0$ m/s, (*a*) $NO_x$ and (*b*) CO**

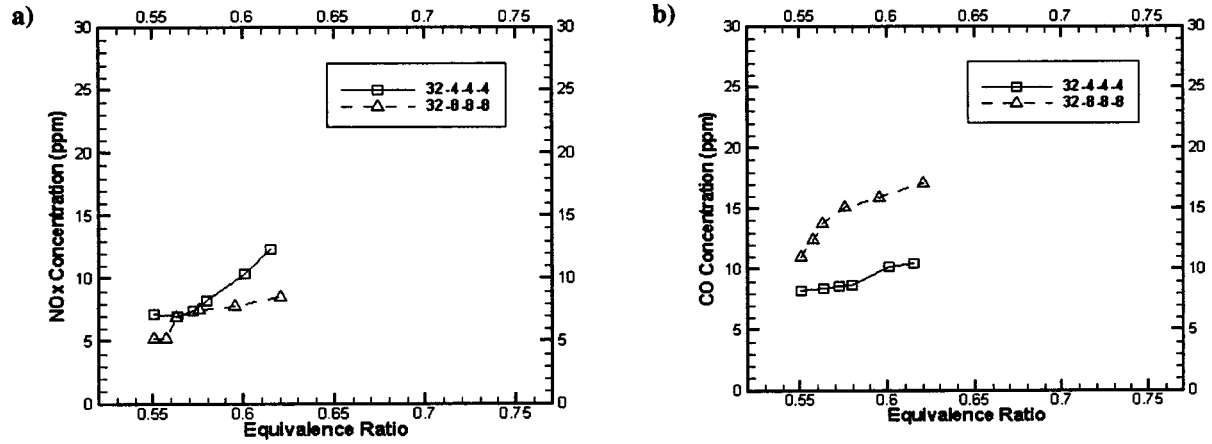


**Fig. 13 Effect of combustion zone pore size on emission from interior combustion at $v=1.0$ m/s, (*a*) $NO_x$ and (*b*) CO**

leading to higher CO emissions. Flow dynamics on the pore size scale level is another factor affecting CO concentration. Small pores cause greater redirection of the gases moving through the structures, resulting in increased local velocities. The increased velocity results in a higher strain rate for small pore size structures, leading to higher CO concentrations at a given equivalence ratio.

**Preheat Zone Pore Size.** The degree of reactant preheating for interior combustion is largely dependent upon pore size of the preheat zone. The size of the pores in this region must be small to enough to quench the flame and eliminate flashback. However, the pores should be large enough to allow significant thermal feedback to the reactants. The effect of upstream pore size on emissions for interior combustion is presented in Fig. 14. At a given equivalence ratio, $NO_x$ concentrations for the two preheat zone pore sizes tested were virtually identical. Figure 14(*b*) shows a noticeable reduction in CO concentration with larger preheat zone pore size, suggesting more effective preheating of reactants. Extension of the lean blow-off limit with large pore size further substantiates this observation. No flashback occurred at any of the conditions with the 32 ppcm preheat region. However, flashback occurred with the 12 ppcm preheat region at equivalence ratios above 0.58 and mean inlet velocity of 1.0 m/s. This result indicates that the preheat region pore size should be optimized to increase the heat transfer upstream and to quench the reaction at the most likely flashback conditions.

## Concluding Remarks

SiC coated, C–C composite foam structures, offering superior structural and thermal integrity at gas turbine operating conditions, were investigated as PIM for combustion. Methane/air flames were stabilized on the surface and interior of the PIM at identical operating conditions, allowing for a direct comparison of the two combustion modes. Simultaneous $NO_x$ and CO emissions of less than 10 ppm were obtained for a range of equivalence ratios and mean inlet flowrates. While surface combustion produced noise typical of a flat flame burner, interior combustion was virtually silent. The main results of this study are summarized in the following:

(1) Surface combustion resulted in only slight increase in pressure drop in the PIM compared to that in cold flow. However, interior combustion increases the pressure drop by more than a factor of 2.
(2) For both combustion modes, the $NO_x$ concentration was weakly dependent upon the flow velocity or PIM pore size. $NO_x$ concentration increased exponentially with equivalence ratio, suggesting thermal mechanism as the primary source of $NO_x$ generation.
(3) For both combustion modes, the CO concentration increased with increasing equivalence ratio. The CO concentration decreased with increasing PIM pore size.

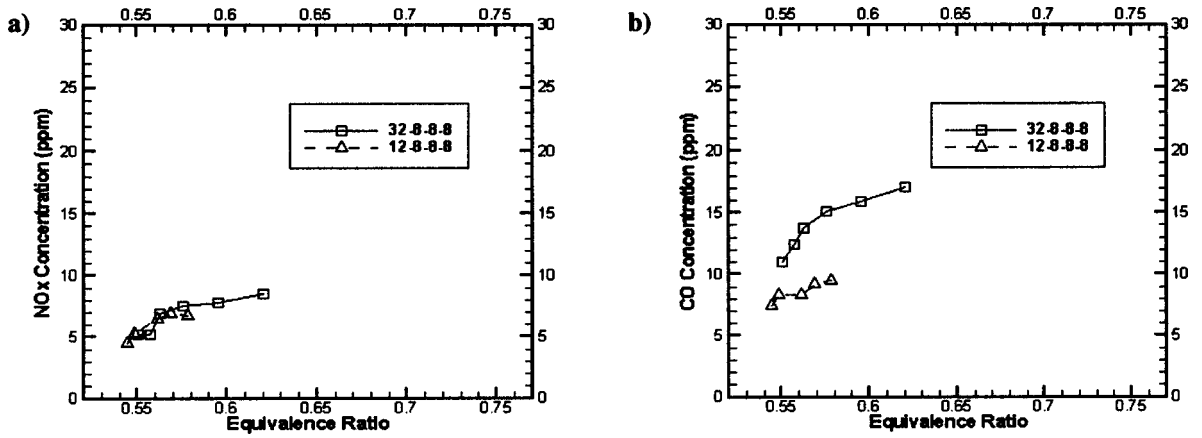


**Fig. 14 Effect of preheat zone pore size on emissions from interior combustion at $v=1.0$ m/s, (*a*) $NO_x$ and (*b*) CO**

(4) Interior combustion extended the lean blow-off limit over surface combustion at all conditions tested.
(5) Increasing pore size extended the lean blow-off limit in both combustion modes. The increase in pore size is however constrained by the increased potential of flashback.

The experimental results of this study affirm PIM combustion as an effective method of extending the blow-off limit in lean premixed combustion. Experimental investigation provides evidence that a PIM combustor producing single-digit $NO_x$ and CO concentrations is feasible. Furthermore, interior combustion in the PIM proved more effective in recovering the flame energy to preheat the reactants. Thermal feedback in the preheat zone of interior combustion could be utilized to prevaporize the fuel in liquid fuel applications. Gas turbine applications would benefit from the extended lean blow-off limit, low $NO_x$ and CO emissions, elimination of noise and noise-related combustion instabilities, flashback prevention, and duel-fuel capability feasible with interior combustion in PIM. Further research is however required to characterize and optimize performance of thermal/oxidation resistant, high-strength materials considered in this study before PIM combustion is implemented in gas turbine applications.

## Acknowledgments

This work was supported by the U.S. Army Research Laboratory and the U.S. Army Research Office under Grant No. DAAD 190210082.

## References

[1] Lefebvre, A. H., 1995, ''The Role of Fuel Preparation in Low-Emissions Combustion,'' ASME J. Eng. Gas Turbines Power, **177**, pp. 617–654.
[2] Dalla Betta, R. A., Schlatter, J. C., Nickolas, S. G., Cutrone, M. B., Beebe, K. W., Furuse, Y., and Tsuchiya, T., 1997, ''Development of a Catalytic Combustor for a Heavy-Duty Utility Gas Turbine,'' ASME J. Eng. Gas Turbines Power, **119**, pp. 844–851.
[3] Sullivan, J. D., Kendall, R. M., and McDougald, N. K., 2000, ''Development of a Low Emission Gas Turbine Combustor,'' AFRC International Symposium, Newport Beach, CA.
[4] Ontko, J. S., 2000, National Energy Technology Laboratory (private communication).
[5] Hardesy, D. R., and Weinberg, F. J., 1976, ''Converter Efficiency in Burner Systems Producing Large Excess Enthalpies,'' Combust. Sci. Technol., **12**, pp. 153–157.
[6] Howell, J. R., Hall, M. J., and Ellzey, J. L., 1996, ''Radiation Enhanced/Controlled Phenomena of Heat and Mass Transfer in Porous Media,'' Prog. Energy Combust. Sci., **22**, pp. 121–145.
[7] Viskanta, R., 1995, ''Interaction of Combustion and Heat Transfer in Porous Inert Media,'' in *Transport Phenomena in Combustion*, edited by S. H. Chan, pp. 64–87, Taylor and Francis.
[8] Trimis, D., and Durst, F., 1996, ''Combustion in a Porous Medium-Advances and Applications,'' Combust. Sci. Technol., **121**, p. 153.
[9] Kotani, Y., and Takeno, T., 1982, ''An Experimental Study on Stability and Combustion Characteristics of an Excess Enthalpy Flame,'' Proc. Combust. Institute, **19**, pp. 1503–1509.
[10] Hsu, P. F., Evans, W. D., and Howell, J. R., 1993, ''Experimental and Numerical Study of Premixed Combustion Within Nonhomogeneous Porous Ceramics,'' Combust. Sci. Technol., **90**, pp. 149–172.
[11] Rumminger, M. D., and Dibble, R. W., 1996, ''Gas Temperature above a Porous Radiant Burner: Comparison of Measurements and Model Predictions,'' Proc. Combustion Institute, **26**, pp. 1755–1762.
[12] Pickenaker, O., Pickenacker, K., Wawrzinek, K., Trimis, D., Pritzkow, W. E. C., Muller, C., Goedtke, P., Papenburg, U., Adler, J., Standke, G., Heymer, H., Tauscher, W., and Jansen, F., 1999, ''Innovative Ceramic Materials for Porous-Medium Burners,'' Interceram, **48**, pp. 1–12.
[13] Sherman, A. J., Tuffias, R. H., and Kaplan, R. B., ''Refractory Ceramic Foams: A Novel New High Temperature Structure,'' http://www.ultramet.com/foamtech.htm.
[14] Khanna, V., Goel, R., and Ellzey, J. L., 1994, ''Measurements of Emissions and Radiation for Methane Combustion Within a Porous Medium Burner,'' Combust. Sci. Technol., **99**, pp. 133–142.
[15] Bhargava, A., Kendrick, D. W., Colket, M. B., and Sowa, W. A., 2000, ''Pressure Effect on NO*x* and CO Emissions in Industrial Gas Turbines,'' ASME 2000-GT-0097.
[16] Mital, R., Gore, J. P., and Viskanta, R., 1997, ''A Study of the Structure of Submerged Reaction Zone in Porous Ceramic Radiant Burners,'' Combust. Flame, **111**, pp. 175–184.

# Diagnosis for Loose Blades in Gas Turbines Using Wavelet Analysis

**Meng Hee Lim**
Research Officer
e-mail: mhlim@citycampus.utm.my

**M. Salman Leong**
Professor
e-mail: salman@citycampus.utm.my

Institute of Noise and Vibration,
University of Technology,
54100 Kuala Lumpur,
Malaysia

*The application of wavelet analysis to diagnose loose blades condition in gas turbines is examined in this paper. Experimental studies were undertaken to simulate loose blades condition occurring in gas turbines in an attempt to understand vibration response associated with loose blades under different operating conditions. Results showed that loose blades were undetectable under steady state operating condition. During turbine coast down, a loose blade could be detected based on the impactic signals induced by the loose blades on the rotor and thus excited the natural frequencies of the rotor assembly. Results from the coast down condition showed that wavelet analysis was more sensitive and effective than Fourier analysis for loose blade diagnosis. The severity, the number, and the configuration of the loose blades could be potentially estimated based on the pattern of the coast down wavelet map.* [DOI: 10.1115/1.1772406]

## 1 Introduction

Blade faults represent a major and common source of problem in power generation gas turbines. Over the years, extensive research had been undertaken on this subject. Previous work reported in the literature included studies on the characteristics of various blade faults and potential diagnostic methods. Reviews on this subject were published by Meher-Homji [1–4] among others. The reviews showed emphasis on blade faults involving blade rubs, blade cracks, foreign object damage (FOD) or loss part, blade deformation (creeping and bending), blade fouling, blade mistuning, and blade fatigue failure. To the author's knowledge, it was Kuo [5] who attempted to address the problem of loose blades in gas turbine. Dynamic response and characteristics of loose blades in gas turbines are therefore less quantified. There appeared to be limited effective diagnostic method in the detection of loose blades in gas turbine. When loose blade is suspected in gas turbines, the methods used usually involved methods more suitable for conventional faults. These include blade passing frequencies (BPF) monitoring (suitable for blade rubbing), performance monitoring method (suitable for blade fouling), and pressure measurement method (suitable for blade deformation). Such methods are often exclusively suitable for a specific blade fault only and are less effective or sensitive in detecting other blade faults. It is therefore very unlikely to find a unifying method which is well suited to diagnose all kinds of blade faults that could possibly occur in gas turbines. Furthermore, these methods are usually based on the measurement (either vibration, pressure, noise, etc.) taken during the steady-state operating conditions. It is also often the case that changes (in vibration, pressure or noise) resulting from a defect or fault may not appear in all operating speeds ranges. It was intention of this work to examine vibration response of loose blade under different operating conditions (steady-state operating condition and coast down condition), and to formulate suitable diagnostic methods from this experimental study. In this paper, the potential of the wavelet analysis method to be used for diagnosis of loose blades was examined and compared against conventional Fourier analysis method.

Contributed by the International Gas Turbine Institute (IGTI) of THE AMERICAN SOCIETY OF MECHANICAL ENGINEERS for publication in the ASME JOURNAL OF ENGINEERING FOR GAS TURBINES AND POWER. Paper presented at the International Gas Turbine and Aeroengine Congress and Exhibition, Atlanta, GA, June 16–19, 2003, Paper No. 2003-GT-38091. Manuscript received by IGTI, October 2002, final revision, March 2003. Associate Editor: H. R. Simmons.

## 2 Experience of a Loose Blade Problem

Loose blades, and more pertinently intermediate packing pieces which are used as spaces in securing individual blades, had been known to occur in some commercial gas turbines (for example, ABB gas turbines, [6]). The experience of the authors related to four-unit commercial open cycle gas turbines used in power generation. The axial flow compressor section of the gas turbine had 21 blading stages. The compressor stator and rotor blades were made of high-tensile ferrite chrome steel, and manufactured partly by precision forging and part milling. The blades were fitted into the radial grooves of the rotor and compressor casing and were separated by the intermediate pieces (Fig. 1). Rotor blades of the first ten stages were fitted directly in the rotor shaft by fir tree roots, while the blades for the remaining stages are rooted in the intermediate pieces. It was at these latter stages that the problem of loose blade problem was more prevalent due to the root or attachment design of the intermediate pieces.

From previous inspections on the turbines, visual observations showed that some intermediate pieces, particularly from stages 11 to 21 protruded out and/or had cracks at the roots (see Fig. 2). This fault could potentially result in further secondary failures, particularly foreign object damage (FOD), if the roots of the intermediate pieces completely failed. In addition to the cracked root(s), blades in the vicinity were also found loose. Copper rings (Fig. 1) used in the assembly beneath the loose blade were found flattened; hence providing the room for the blades to loosen. This suggested that the root cause of the cracks on intermediate pieces could originate from the loose blades at this particular location. It was likely that the space provided by the flattened ring and rotor grooves enabled the loose blade to rattle (vibrate), with similar rattling of the intermediate pieces. Cracks eventually developed at the roots of the intermediate pieces.

Some power plant operators in the Asia Pacific region are increasingly faced with the dilemma to operate their gas turbines beyond recommended running hours (EOH) stipulated by the manufacturers due to continuous electricity load demand and economic pressure for plant availability (Ng and Zahir [6]). The demands in pressing electricity load despatch appeared to be a common occurrence in the power generation industry world wide. Manufacturers (OEM) recommend preventive maintenance, including blades replacement, on the basis that life expectancy of components is reached upon specific running hours. The necessity and experience of the Connaught Bridge Power Station (CBPS) of a public utility company in Malaysia, and the experience of the

  

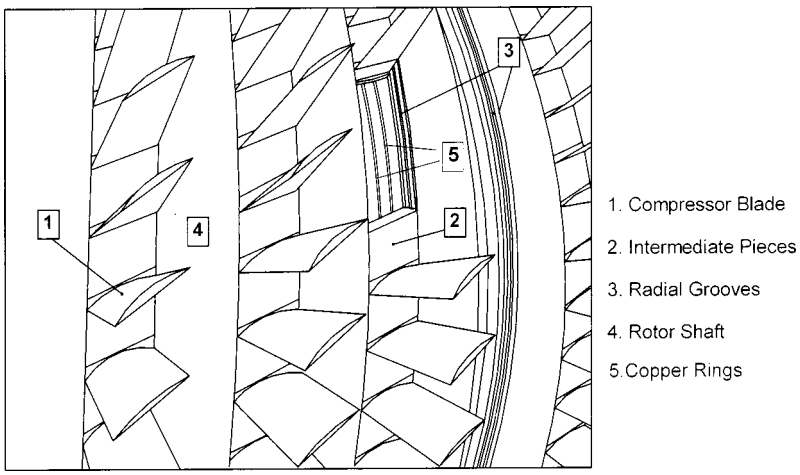


**Fig. 1 Basic configuration of compressor rotor and its pertinent components (Ng and Zahir [6])**

authors in assisting the Station in seeking out feasible vibration monitoring and assessment for blades looseness and cracks on these actual gas turbines, lead to experimental studies to be undertaken in the laboratory.

## 3 Experiment Test Rig

A test rig consisting of sub-assemblies of rotor-shaft, blades and intermediate locking pieces, drive and casing was designed for a laboratory study of typical loose blade dynamic response. A hollow rotor of 300 mm nominal diameter was used on the basis of a practical working dimension (and machining constraints). Blades were located onto radial grooves in similar manner to the above industrial gas turbines, although simplified for the purpose of this experimental study. Flat blades were used to avoid undue complications in attempting to replicate the aerodynamic profile of an actual blade. Other basic features such as blade incidence angle, width, length and thickness were nevertheless maintained. The test rotor had 12 blades. A photograph showing an overall view is given in Fig. 3, and the blade assembly is given in Fig. 4. The test rig incorporated elements which were considered important for understanding the behavior of loose blade. A slackness adjuster and locking mechanism was incorporated into each blade such that controlled looseness could be induced in each blade.

Experiments were undertaken to quantify a tight and induced fault condition. Three different conditions were incorporated in this study. The first condition was such that only a single loose blade (abbreviated as ''S'') was introduced into the test rig. This condition was designed to examine whether if the effect of a loose blade could be differentiated in the vibration spectrum of the rotor bearing measured under rotation. Fourier analysis and wavelet analysis were undertaken to confirm its viability and sensitivity to detect the loose blade. The second loose blade condition was induced such that all implanted loose blades were seated in adjacent

**Fig. 3 View of the experimental test rig**

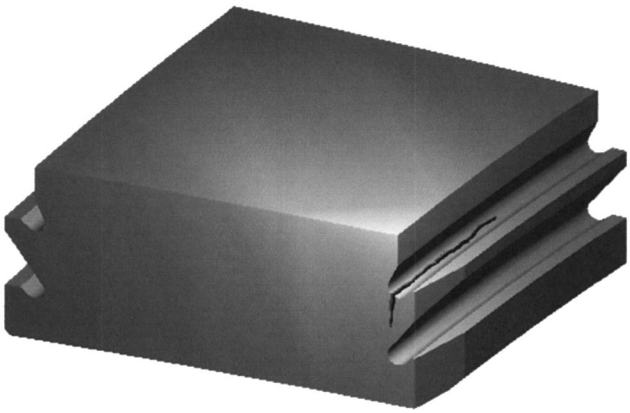

**Fig. 2 Typical crack location on intermediate pieces (Ng and Zahir [6])**


**Fig. 4 Photograph showing blade assembly with intermediate locking pieces**

position (abbreviated as ''A''). This condition was intended to examine the effect of adjacent loose blades on the vibration signal of the rotor bearing. The third case involved loose blades seated randomly, i.e., scattered (abbreviated as ''R'') in the rotor rig. This condition was intended to compare with test condition number two whereby the results of these two conditions would provide an indication as to whether the position of the loose blade would affect the measured vibration signals. All loose blade conditions were investigated with 1 mm and 2 mm looseness severity, respectively, (such quantum of looseness (free play or slackness) are typically found in the above mentioned gas turbines). It was realized that the vibration resulting from a defect or a fault such as the loose blade might not appear at all operating speeds. The characteristics of these loose blade conditions were examined for two different operating conditions—typically the steady-state speed condition, and the coast down condition.

## 4 Signal Processing

The vibration spectrums of steady state operating condition were measured in the span of 0 Hz to 500 Hz with frequency resolution of 0.625 Hz. This setting allowed the blade passing frequency (BPF) (12 blades×20 Hz (operating frequency)=240 Hz) and its second harmonic (480 Hz) to be included in the vibration spectrums. BPF is the frequency inherent in all rotating blades assembly. Literature had reported applications of BPF in blade faults diagnosis since the 1970s. Mitchell (1975), for example, showed that the relational changes in the blade passing frequency (BPF) and its harmonics provide useful information for blade faults diagnosis (cited in Meher-Homji [3]). The use of vibration analysis for blade faults diagnosis was also studied by Simmons [7,8], Parge et al. [9], and Parge [10]. They have confirmed that by observing the relative changes in the BPF and its harmonics amplitude; the blade faults can be possibly detected. The use of BPF in blade faults diagnostic had been documented in various text (Hewlett Packard application note 243 [11], and Mitchell [12], for example). It was documented that the increase of sidebands indicates blade faults has occurred. The blade-passing profile is also used as the fundamental parameter in some novel signal analysis methods for blade faults diagnosis such as the wavelet analysis (refer Aretakis [13]) and artificial intelligent (refer to Kuo [5]).

Synchronous time averaging method is typically used to average-time waveforms measured in moderately steady-state operating condition. The averaged-time waveforms were then analyzed with Fourier analysis method to yield the frequency spectrum. With this operation, interference of the noise signals on the vibration spectrum was minimized to obtain a more accurate spectrum. Synchronous time averaging was used in the data acquisition process.

The resolution and the maximum span of vibration time waveforms are critical in wavelet analysis. In this case, the time waveforms of steady-state operating condition were measured for a total of 1.6 s (1/0.625) with the sampling frequency of 1280 Hz (0.000781 s time resolution). This setting was found to produce fine and clear wavelet map for steady-state operating condition monitoring. The vibration spectrums of the coast down condition were measured from 0 Hz to 1600 Hz. This setting was used to ensure capture of structural natural frequencies excitation of the experimental rig during the coast down. Waterfall measurements of coast down condition were taken for every 0.5 s for a total of 24 s until stand still condition. The time waveforms of coast down condition were recorded for the last 9 s with sampling frequency of 1792 Hz (or 0.000558 s time resolution) only due to memory storage capacity constraint of the vibration analyzer.

## 5 Selection of Wavelet Parameters

Wavelet is a ''small wave,'' which has its energy concentrated in time, fairly similar to an impulse waveform over time. Pure sine wave (which is also the basis of Fourier analysis), in contrast to wavelet, typically do not have its waveform (sinusoid) limited in time (i.e., repeated over time). While a sinusoid is smooth and predictable, wavelet on the other hand tends to be irregular and asymmetric (refer to Sidney [14]). The irregular shape of wavelet renders it suitable for the detection of nonstationary signals with discontinuity or sharp changes. Whereas its nature of compactly supported in time (energy concentrated in time) enables signals to be analyzed in time and frequency domain simultaneously. Therefore, the driving impetus behind wavelet analysis is their property of being localized in time as well as in frequency (scale). This provides the time-frequency representative of the signal. Continuous wavelet transform (CWT) is defined as the sum over all time of the signal, $f(t)$ multiplied by scaled, shift versions of the wavelet function, as represented in Eq. (1).

$$C(\text{scale},\text{position}) = \int_{-\infty}^{\infty} f(t)\,\psi(\text{scale},\text{position},t)\,dt \qquad (1)$$

where $f(t)$ is the signal, $\psi$ is the wavelet function, and $C$ is the resulted wavelet coefficient.

The results of CWT are many wavelet coefficients, $C$ in function of scale and position. Multiplying each coefficient by the appropriately scaled and shifted wavelet yields the constituent wavelets of the original signal.

Two different wavelet analysis settings were performed on the vibration signal obtained from the steady-state operating condition. These results were then displayed on different graphs known as the global wavelet map and local wavelet map. Global wavelet map (with lower scale resolution and larger span) was obtained from the wavelet analysis to provide an overall view of the dynamics of the entire time waveform. Local wavelet map (with higher scale resolution and shorter span) is simply a zoomed version of the global wavelet map particularly around the BPF (240 Hz) level. This display allowed a close monitoring of the BPF for loose blade diagnosis. To perform the wavelet analysis on the entire measured length of coast down time waveform is indeed a laborious task, which required relatively long computation time in a standard desktop PC. Therefore, only a portion of the coast down signal (last 2 seconds) was extracted to perform the wavelet analysis in the computer. There are two different transformation methods that could be used for wavelet analysis. There are the continuous wavelet transform (CWT) and the discrete wavelet transform (DWT). DWT is implemented to reduce the computation time required in wavelet analysis by calculating the wavelet coefficients at the scale and position based on the powers of two. On the other hand, CWT operates at every scale from the minimum scale (highest frequency) of the original signal up to the maximum scale (lowest frequency) that determined. CWT is also continuous in its shifting: during computation, the analyzing wavelet is shifted smoothly over the full domain of the analyzed signal. The wavelet map produced by CWT is therefore smoother and provide better visualisation for feature recognition purpose. On this basis, then CWT method was chosen in this experimental work.

There are numerous wavelet families available for wavelet analysis of a signal. The selection of the wavelet families for signal analysis depends on its characteristics of that family such as the shape of the wavelet: symmetry, the number of vanishing moments, and the regularity. The wavelet family is important to the pattern of the wavelet map representing the signal in hand. Coiflet (level 5) wavelet was chosen for wavelet analysis of the experimental signal based on the fact that Coiflet (level 5) wavelet is fairly symmetrical and regular in shape (see Fig. 5).

Wavelet map plotted with this wavelet was found to be fairly symmetrical and smooth for the display of the vibration signals measured from the experiment. Wavelet analysis in this work was performed using the Wavelet Toolbox embedded in Matlab (an integrated technical computing software).

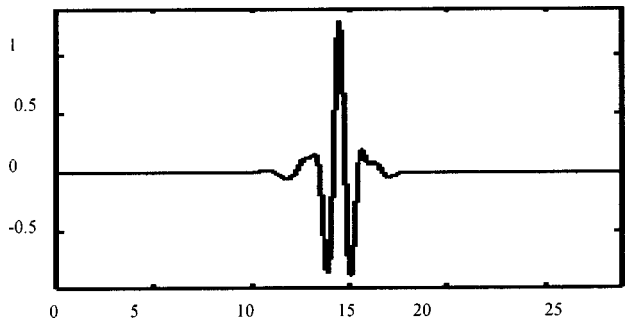


**Fig. 5 Coiflet (level 5) wavelet**

## 6 Experimental Results and Discussions

**6.1 Steady-State Operating Condition.** Comparing the baseline (good) condition and loose blade condition number one (single loose blade with 1 mm and 2 mm looseness severity), it could be seen that there was no noticeable changes on the steady state vibration spectrums; (Fig. 6). With loose blade condition number two (adjacent effect with three and six loose blades), vibration spectrums (Fig. 7) were almost identical to the baseline condition (Fig. 6). Even with increased looseness severity and increased number of loose blade (e.g., Case 4 in Fig. 7), the BPF and sidebands (220 Hz or 260 Hz) amplitudes remained almost unchanged or unaffected. It could be inferred that under steady state operating condition (1200 rpm), the loose blades did not result in any appreciable change to the vibration signals and loose blades could not be detected in the vibration spectrums. Under the steady-state operating condition, the centrifugal force would keep the loose blade at the most extended outer position in the rotor groove hence rendering the loose blade condition similar to the baseline condition with all blades firmly seated in a tight position. It could be concluded that the loose blade condition in the test rig could not be readily detected under the steady-state operating condition. It was however reported by Kuo [5] that loose blade could be diagnosed under the normal operating condition by using multi-vibration sensor system with FFT analysis combined together with neural network and fuzzy logic for pattern recognition based on an experimental model. Differences in findings between this work and Kuo, however, could be explained by the physical differences in the test rig. Kuo's work was based on an angular displaced (loose) blade from its regular position, which free play is not necessarily in the radial direction only. The loose blade examined the study in this work involved a vertical displaced looseness solely in the radial direction.

From the global wavelet maps shown in Fig. 8, it could be seen that the vibration signals of steady state operating condition were dominated by the periodical components. The first-order running speed (20 Hz) was clearly seen from the extracted wavelet coefficients at scale 44 (20 Hz) from the wavelet map. It was also seen that the dominating frequencies of the vibration signals were at the scale of 1 to 10 or corresponding to 800 Hz to 100 Hz in frequency spectrum. This suggested that the BPF (240 Hz) was also included in the region. Figure 9 shows the zoomed wavelet map (termed as local wavelet map) particularly at the scales 1 to 6 to capture changes in BPF when loose blade conditions were induced in the experiment. By inducing one and three loose blades on the blade assembly, there was no appreciable change found in the local wavelet maps, which distinguished the loose blade condition from the baseline condition (Compare Figs. 9(*a*), 9(*b*), and 9(*c*)). These findings were in good agreement with the findings found above that suggested that during the steady-state operating condition, the centrifugal force will displace the blade in an extended position, which therefore would be similar to baseline condition.

**6.2 Coast Down Condition.** As typical in any machinery coast down, resonant frequencies would be excited as the rota-

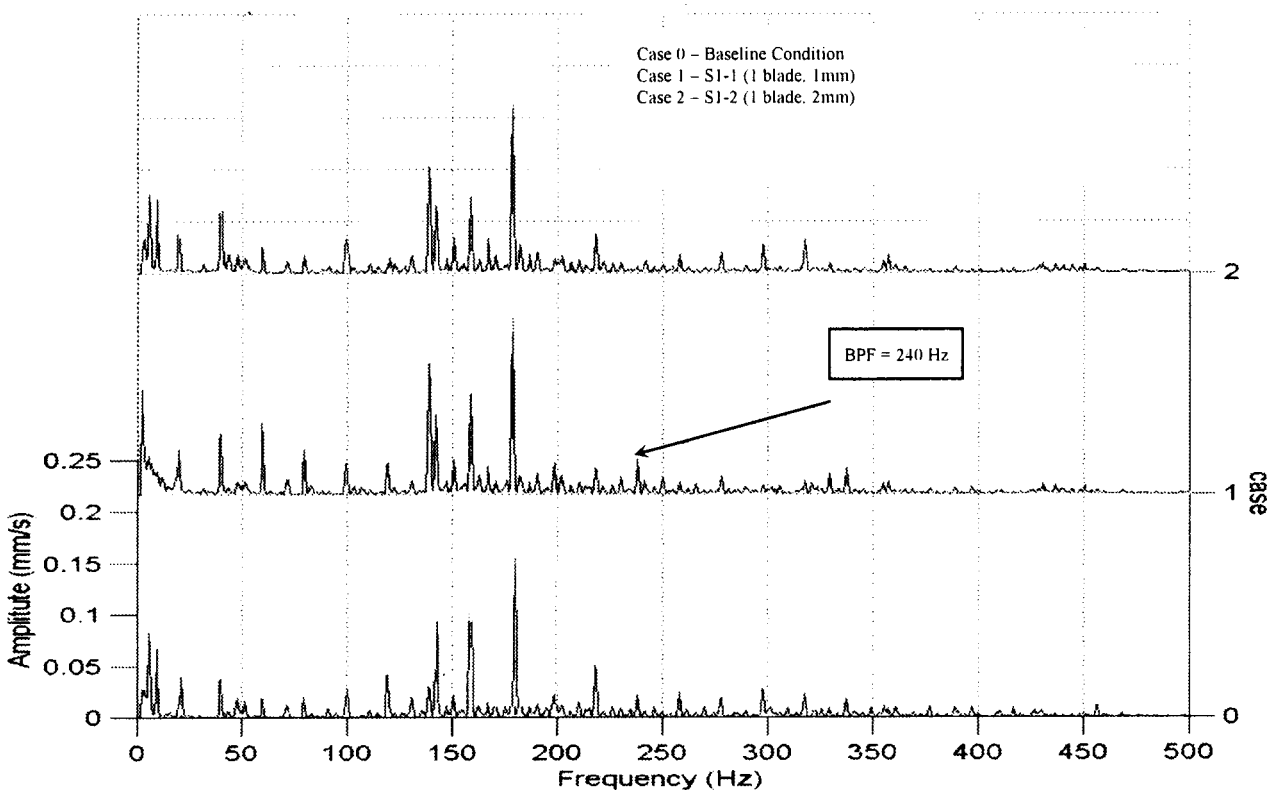


**Fig. 6 Comparison of baseline and faulty condition 1**

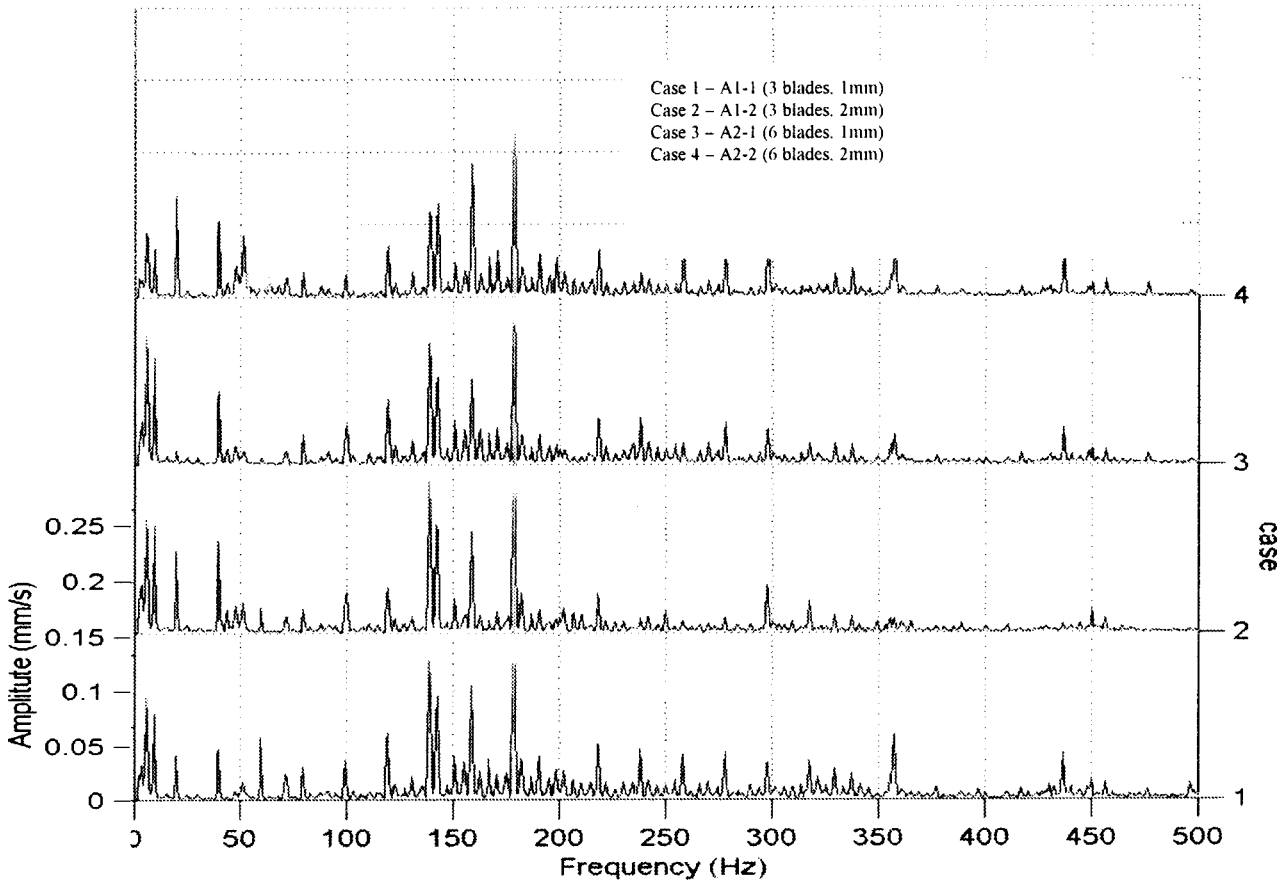


**Fig. 7 Comparison of faulty condition 2**

tional speed coincides with the natural frequency of the rotor and structure. Waterfall plots of FFT vibration spectrum were examined for all test conditions. For the baseline, and a single loose blade conditions, the waterfall plots were found to be normal (i.e., with resonant peaks at critical speeds), and thereafter at low speeds clean (i.e., no additional peaks) (Fig. 10(*a*) and Fig. 10(*b*)).

However, by increasing the looseness severity of that single loose blade to 2 mm, some minor ripples were noted in the region of 400 Hz to 800 Hz (see Fig. 10(*c*)). By increasing the number of loose blades from one to three blades, it could be seen that the ripples increase accordingly (refer to Fig. 10(*d*)). This finding suggested that the loose blade may have triggered a series of impact

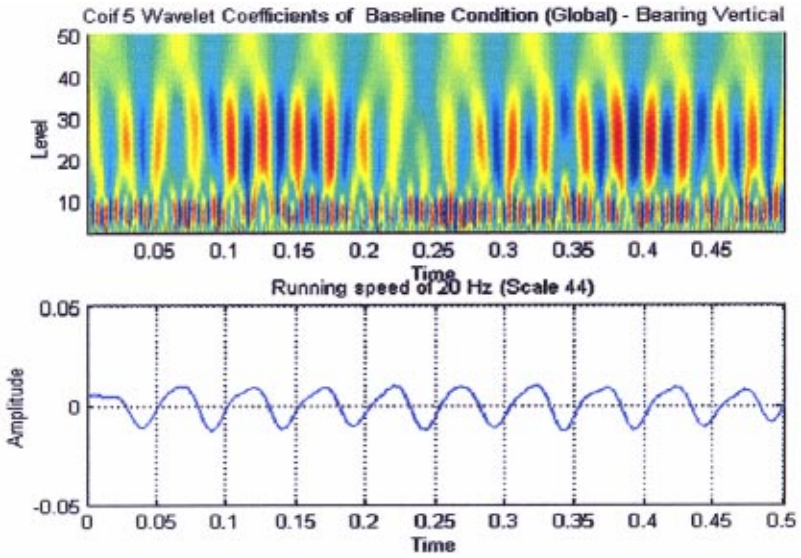


**Fig. 8 Typical global wavelet map**

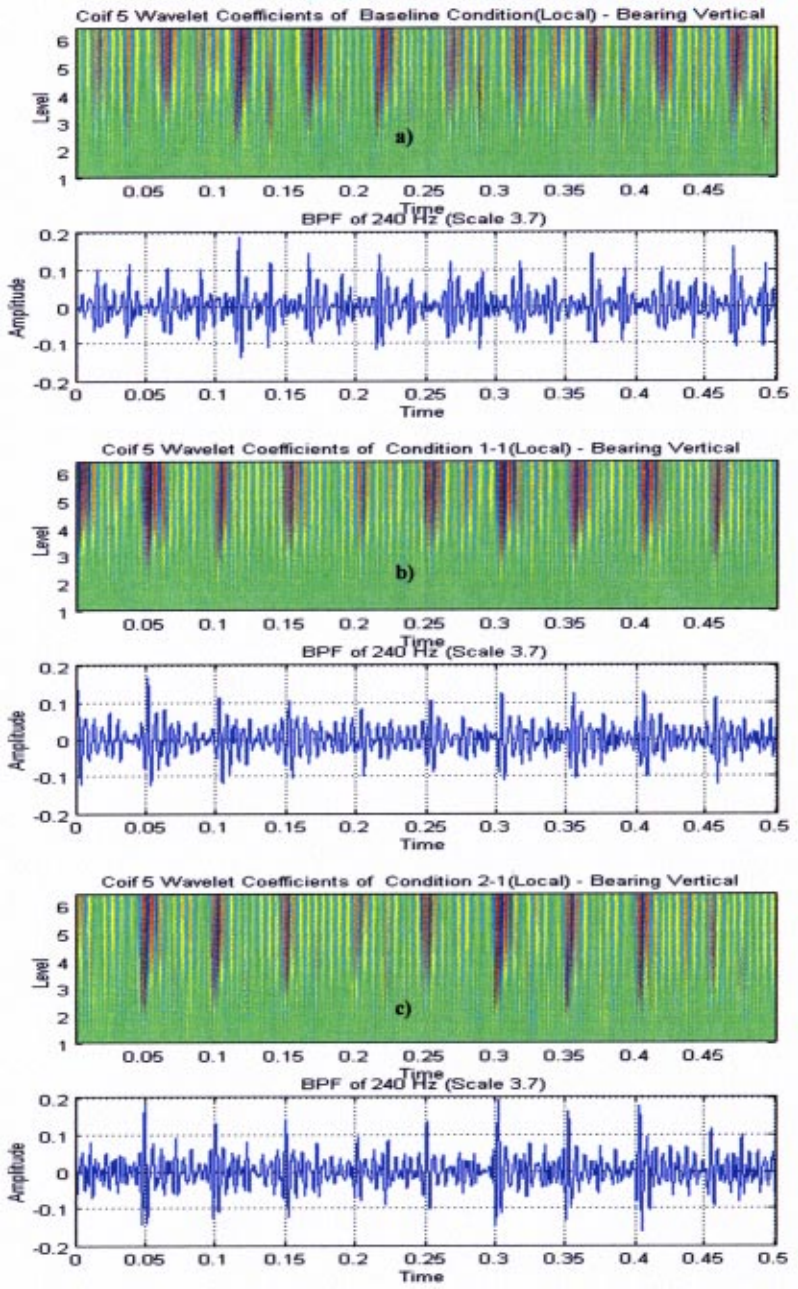


**Fig. 9 Local wavelet maps: (*a*) baseline, (*b*) condition no. 1 (one blade, 1 mm), (*c*) condition no. 2 (three blades, 1 mm)**

on the rotor, which excited its natural frequency of the experimental rig. These impacts could only happen during the last 10 s of coast down when the weight of the loose blade was greater than the centrifugal force. It was seen that there was no significant difference between three loose blades and six loose blades conditions even though it was thought reasonably that the total energy of impact was proportional to the number of loose blades (comparing Figs. 10(*d*) and 10(*e*)). In addition, the different in loose blades configuration (adjacent and random loose blades positions) could not be differentiated in waterfall profiles (comparing Figs. 10(*d*) and 10(*e*)). Notwithstanding the above, it is acknowledged that the differences in the waterfall plots with fault condition were not readily apparent. This makes it even more less applicable in real machines.

In the baseline (good) condition, the coast down wavelet map was clean (see Fig. 11(*a*)). With a nominal loose blade condition of a single loose blade and minimum looseness severity of 1 mm, significant changes were noted in the wavelet maps. Relatively high amplitude components in the region of 1–10 scale or corresponding to 1000 Hz to 150 Hz along the time scale was observed (Fig. 11(*b*)). This suggested that light impacts had occurred thereby exciting natural frequencies which was evident in the wavelet map. It was seen that increasing the looseness severity from 1 mm to 2 mm, resulted in greater change consistent with increase in impact (compare the gray color tone of impacts in Figs. 11(*b*) and 11(*c*)). The increase in the number of loose blades from one blade to three and six blades resulted in longer impact duration as seen in wavelet maps, Figs. 10(*d*) and 10(*e*). Examining the total impact time seen in wavelet maps provided a basis of estimate in the number of loose blade. It was found that the greater the looseness severity the higher the impact energy would be seen in the wavelet maps. Changes in intensity as represented

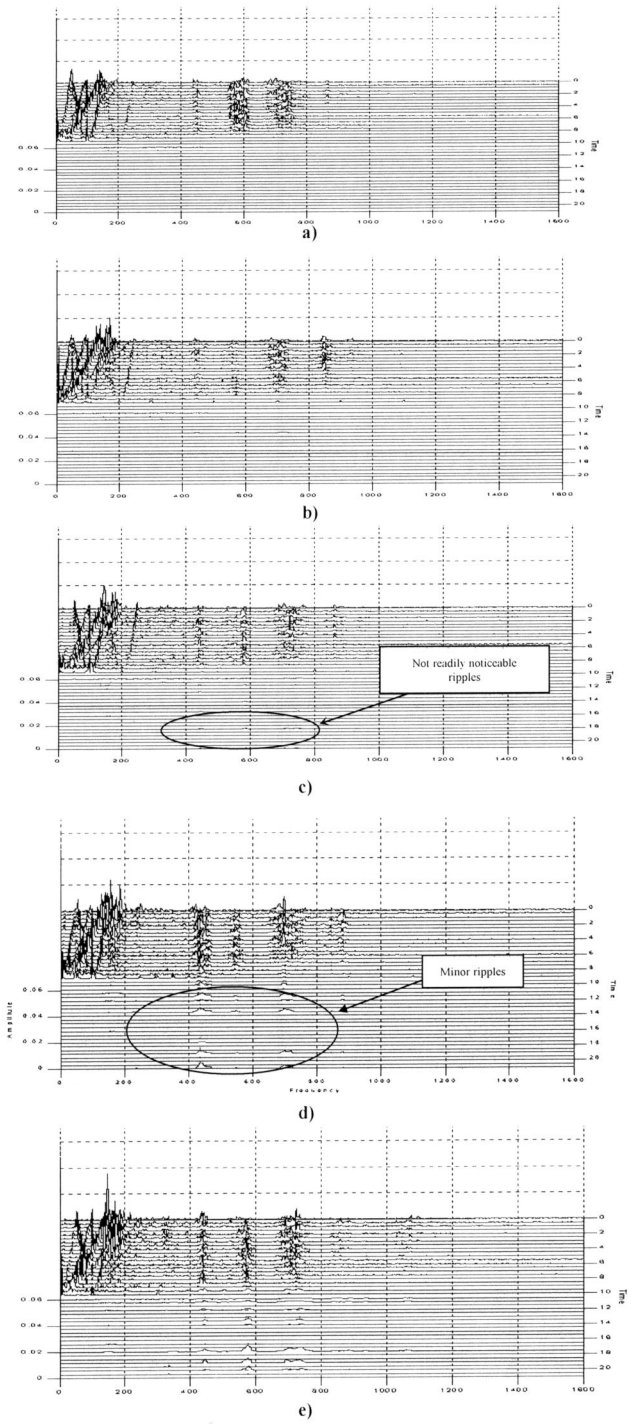


**Fig. 10 Waterfall plots: (*a*) baseline, (*b*) condition no. 1 (1 mm), (*c*) condition no. 1 (2 mm), (*d*) condition no. 2 (three blades, 2 mm), (*e*) condition no. 3 (six blades, 2 mm)**

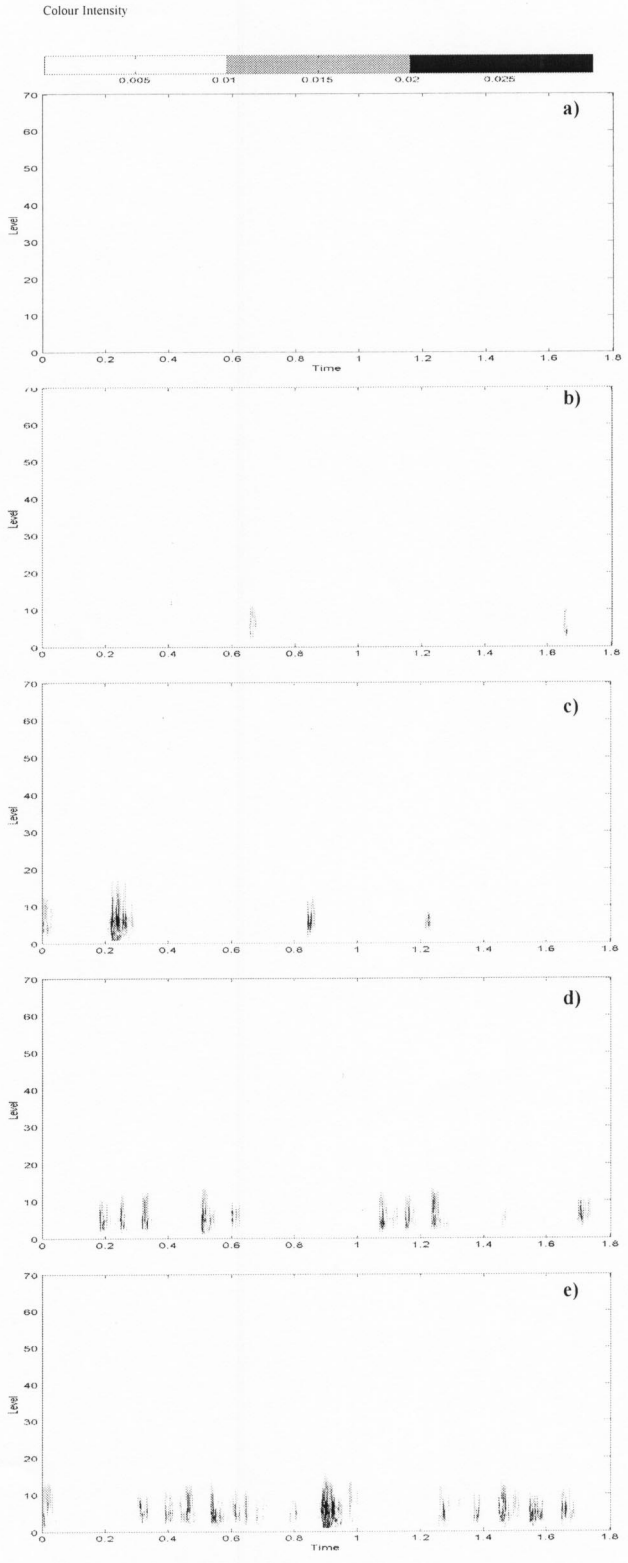


**Fig. 11 Coast down wavelet maps: (*a*) baseline, (*b*) condition no. 1 (1 mm), (*c*) condition no. 1 (2 mm), (*d*) condition no. 2 (three blades, 2 mm), (*e*) condition no. 3 (six blades, 2 mm)**

at the color in the wavelet map, indicated severity of looseness. Differences in loose blades configuration (adjacent and random loose blades position) could be fairly estimated based on the time duration taken for the two consecutive impacts as seen on the wavelet maps (compare Figs. 11(*d*) and 11(*e*)). In conclusion, loose blade was detectable in the wavelet map during the coast down condition. The looseness severity, the number of loose blades, as well as the configuration of the loose blades could be differentiated based on the pattern of the wavelet maps.

**6.3 Discussion.** Some important and significant findings of this experiment are summarized as follows:

1. It was shown that the loose blade conditions were undetectable under steady-state operating condition, either by using the

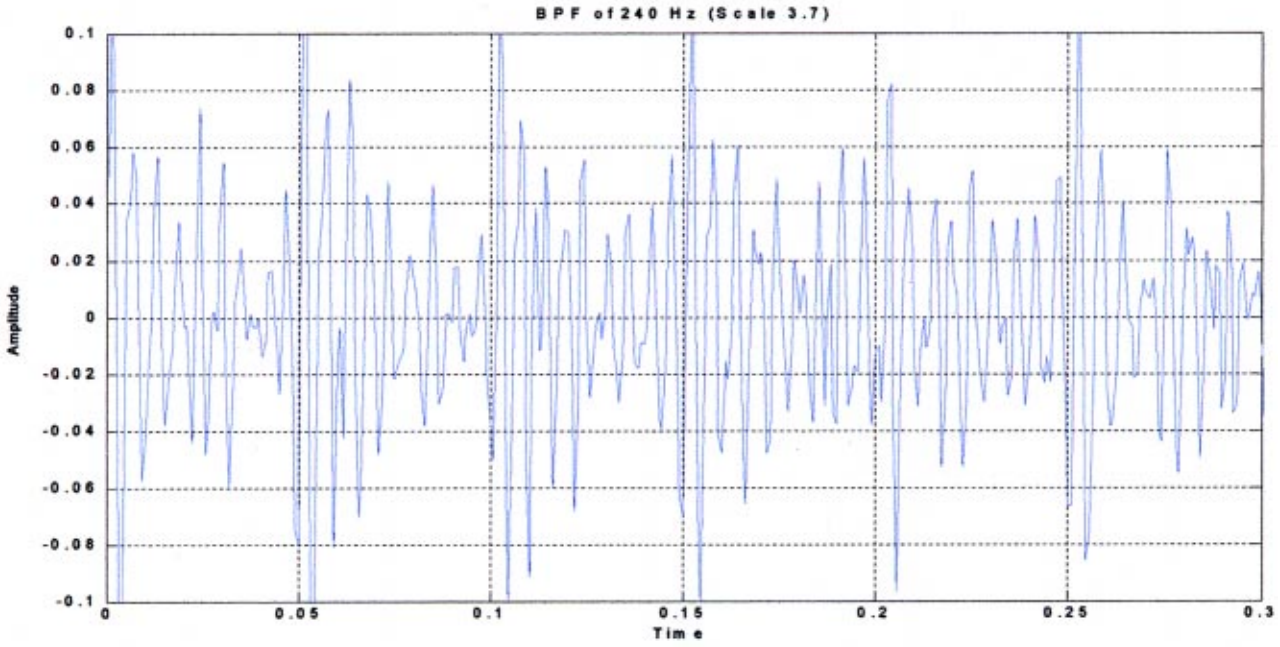


**Fig. 12 Zoomed BPF time waveform**

Fourier analysis method or wavelet analysis method. It was only during the coast down condition, that a loose blade could be detected based on the impacts imposed by the loose blade, which excited the natural frequency of the rotor system. This suggests that not all kinds of blade faults could be readily detected during normal or steady-state operating condition.

2. Wavelet analysis was shown to be more sensitive than the conventional FFT waterfall in detecting loose blade. This was evident from changes in the wavelet map with a single loose blade with nominal (1 mm) looseness, which was not obvious in FFT waterfall plots. This was due to the fact that the impacts signals are nonstationary signals, which would be better analyzed by time-frequency analysis method such as wavelet analysis. Conventional Fourier analysis was more suitable for deterministic and stationary signal. When Fourier analysis method is used to analyze these nonstationary impactive signals such as those generated by loose blade, these signals would be normalized over the entire time series. These impactive signals would therefore be masked by noise or more prominent frequency components present in the frequency spectrums. This observation was in agreement with findings of Aretakis and Mathioudakis [13] that the wavelet analysis allows local features and hidden details of a signal to be identified that makes it useful for condition monitoring in turbomachiney components, where the detection of small changes in dynamic quantities is important.

3. Over the years, frequency spectrum (BPF) of Fourier analysis has been used as the primary tool to diagnose blade faults in gas turbines. It was however noted from this work that wavelet analysis is superior over Fourier analysis for loose blade detection. Wavelet map provides a good illustration to visualize the dynamics response of a mechanical system. It could show simultaneously the periodicity and the transient components of vibration signal. This offers an advantage over the Fourier analysis where the transient signals would be normalized, and only the averaged energy of particular frequencies band is shown in the frequency spectrum. Aretakis and Mathioudakis [13] had showed that the extracted wavelet amplitude differences near BPF was viable in diagnosing twisted blade and fouled blade.

4. In addition, the extracted BPF time waveform provides better visualization on the pressure profile trailing each blade. There were ten peaks found in the local wavelet map plotted for the duration of ten cycles (see Figs. 9(*a*) to 9(*c*)). These peaks were better seen in the BPF time waveforms extracted from the local wavelet map (the lower diagram of every local wavelet maps in Fig. 9). For clearer view, the enlarged BPF time waveform is shown in Fig. 12.

It was found that in one rotational (0.05 s), there were approximately 12 pressure gradients, which represented 12 pressure profiles imposed by each blade on the experimental rig. This method is potentially suitable for diagnosis of blade deformation faults (such as crack, FOD, loss part, and erosion and corrosion) that introduce changes to the blade surface or geometry. This in turn would potentially alter the BPF time waveform profiles. Wavelet analysis has the capability to extract BPF time waveform from the raw vibration signal. The extracted BPF time waveform could then be used as the raw signal inputted into the wavelet analysis for the second time for feature recognition (fault recognition) purposes. This method (referred as ''dwi-wavelet analysis'') in some ways are similar in intent of Cepstrum analysis used in vibration analysis. This method seems promising for blade faults diagnosis particularly for blade deformations faults. Figure 13 showed the simulated blade passing time waveform for good and faulty blade. Minor distortion of BPF time waveform (due to blade deformation) would not be obvious in Fourier analysis spectrum. This minor alteration on the blade passing time waveform could, however, be clearly detected with wavelet analysis (compare Figs. 13(*a*) and 13(*b*)). This illustrates the feasibility that BPF should be treated as nonstationary signal and blade fault could therefore be potentially detected with ''dwi-wavelet'' analysis. This could introduce a new paradigm for blade faults diagnosis whereby BPF is no longer treated as stationary signal (as the case with frequency spectrum) but would be recognized as a nonstationary signal. This is then well suited for time-frequency analysis method such as wavelet analysis.

This method, if combined with the phase information could be able to detect the number and the position of the faulty blades which is never possible using the Fourier analysis (since the time

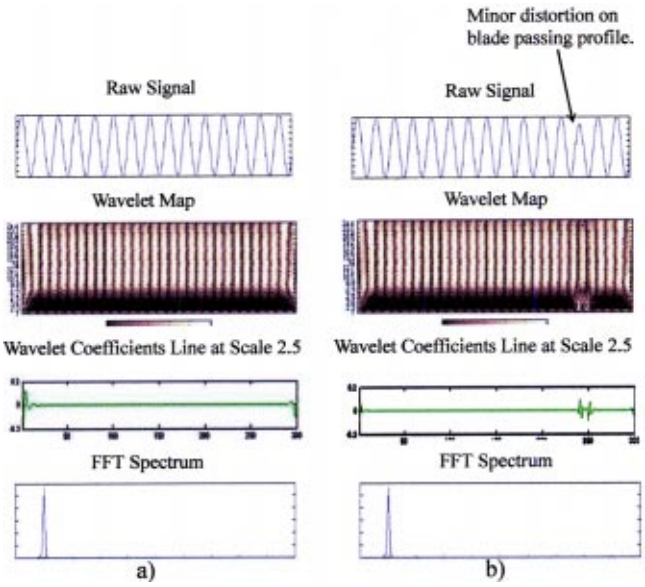


**Fig. 13 Wavelet analysis (*a*) good condition (*b*) with fault**

information is lost). On-going work is still in progress to confirm the feasibility of this proposition in the diagnosis of blade faults in gas turbines.

## 7 Conclusion

Some level of understanding on the characteristics of the loose blades under different operating conditions (steady state operating condition and coast down condition) was achieved in this experimental study. It could be observed that during the steady-state operating condition, loose blade conditions resembled the baseline condition (all blades in tight condition) due to the centrifugal force. It was towards the very end of the coast down process that loose blade could result in a series of impacts on the rotor that excited the natural frequencies of the test rig. This finding when extrapolated to a real world application in the detection of loose blades condition in commercial gas turbine, confirmed that coast down signals should be measured and analyzed. In the experimental study, it was shown that wavelet analysis was more sensitive to detect the loose blade condition and could reasonably estimate the severity, the number of the loose blades and the loose blade configurations implanted in the test rig. The question that remained to be answered was how the impacts signals could be captured by an accelerometer if the rotor to blade weight's ratio was large? Would the impact signal be overwhelmed by the more prominent signal or noise? How well this method will perform in a more complex environment of an actual gas turbine shall require a pilot study on actual gas turbines correlated with observation of physical faults and maintenance post-mortem.

## Acknowledgments

The authors acknowledged the cooperation and kind assistance in the form of site experience, access and field information of the Connaught Bridge Power Station (CBPS) of the Malaysian National Utility Company (Tenaga Nasional Berhad) in this work.

## References

[1] Meher-Homji, C. B., 1995, ''Blading Vibration and Failures in Gas Turbines: Part A—Blading Dynamics and the Operating Environment,'' ASME Paper No. 95-GT-418.
[2] Meher-Homji, C. B., 1995, ''Blading Vibration and Failures in Gas Turbines: Part B—Compressor and Turbine Airfoil Distress,'' ASME Paper No. 95-GT-419.
[3] Meher-Homji, C. B., 1995, ''Blading Vibration and Failures in Gas Turbines: Part C—Detection and Troubleshooting,'' ASME Paper No. 95-GT-420.
[4] Meher-Homji, C. B., 1995, ''Blading Vibration and Failures in Gas Turbines: Part D—Case Studies,'' ASME Paper No. 95-GT-421.
[5] Kuo, R. J., 1995, ''Intelligent Diagnosis for Turbine Blade Faults Using Artificial Neural Network and Fuzzy Logic,'' Eng. Applic. Artif. Intell., **8**, pp. 25–34.
[6] Ng, B. H., and Zahir, I., 2000, ''Managing the Risk of Extended EOH of ABB Gas Turbines at Connaught Bridge Power Station,'' Report of Connaught Bridge Power Station, Klang, paper also available at website URL: http://www.egat.or.th/asean_cc/news/paper06.doc
[7] Simmons, H., 1986, ''A Non-Intrusive Method for Detecting HP Blade Resonance,'' ASME Paper No. 86-JPGC-Pwr-36.
[8] Simmons, H., 1987, ''Non-Intrusive Detection of Turbine Blade Resonance,'' Third EPRI Conference on Incipient Failure Detection in Power Plants,'' Philadelphia, PA.
[9] Parge, P., Trevillion, B., and Carle, P., 1989, ''Machinery Interactive Display and Analysis System Description and Applications,'' *Proceedings of the First International Machinery Monitoring and Diagnostic Conference*, Sept. 11–14, Las Vegas, NV, pp. 176–182.
[10] Parge, P., 1990, ''Non-Intrusive Vibration Monitoring for Turbine Blade Reliability,'' *Proceedings of Second International Machinery Monitoring and Diagnostic Conference*, Oct. 22–25, pp. 435–446.
[11] Hewlett Packard, ''The Fundamental of Signal Analysis,'' Application Note 243.
[12] Mitchell, John S., 1981, *An Introduction to Machinery Analysis and Monitoring*, PennWell Publishing Company, Tulsa, OK.
[13] Aretakis, N., and Mathioudakis, K., 1997, ''Wavelet Analysis for Gas Turbine Fault Diagnostics,'' ASME J. Eng. Gas Turbines Power, **119**, pp. 870–876.
[14] Sidney Burrus, C., Ramesh, A. G., and Guo, H. T., 1998, *Introduction to Wavelets and Wavelet Transforms*, Prentice-Hall Englewood Cliffs, NJ.

# Aircraft Turbofan Engine Health Estimation Using Constrained Kalman Filtering

**Dan Simon**
Electrical Engineering Department,
Cleveland State University,
1960 East 24th Street,
Cleveland, OH 44115
e-mail: d.j.simon@csuohio.edu

**Donald L. Simon**
U.S. Army Research Laboratory,
NASA Glenn Research Center,
21000 Brookpark Road,
Cleveland, OH 44138
e-mail: donald.l.simon@grc.nasa.gov

*Kalman filters are often used to estimate the state variables of a dynamic system. However, in the application of Kalman filters some known signal information is often either ignored or dealt with heuristically. For instance, state-variable constraints (which may be based on physical considerations) are often neglected because they do not fit easily into the structure of the Kalman filter. This paper develops an analytic method of incorporating state-variable inequality constraints in the Kalman filter. The resultant filter is a combination of a standard Kalman filter and a quadratic programming problem. The incorporation of state-variable constraints increases the computational effort of the filter but significantly improves its estimation accuracy. The improvement is proven theoretically and shown via simulation results obtained from application to a turbofan engine model. This model contains 16 state variables, 12 measurements, and 8 component health parameters. It is shown that the new algorithms provide improved performance in this example over unconstrained Kalman filtering.* [DOI: 10.1115/1.1789153]

## Introduction

For linear dynamic systems with white process and measurement noise, the Kalman filter is known to be an optimal estimator. However, in the application of Kalman filters there is often known model or signal information that is either ignored or dealt with heuristically [1]. This paper presents a way to generalize the Kalman filter in such a way that known inequality constraints among the state variables are satisfied by the state-variable estimates.

The method presented here for enforcing inequality constraints on the state-variable estimates uses hard constraints. It is based on a generalization of the approach presented in Ref. [2], which dealt with the incorporation of state-variable equality constraints in the Kalman filter. Inequality constraints are inherently more complicated than equality constraints, but standard quadratic programming results can be used to solve the Kalman-filter problem with inequality constraints. At each time step of the constrained Kalman filter, we solve a quadratic programming problem to obtain the constrained state estimate. A family of constrained state estimates is obtained, where the weighting matrix of the quadratic programming problem determines which family member forms the desired solution. It is stated in this paper, on the basis of Ref. [2], that the constrained estimate has several important properties. The constrained state estimate is unbiased (Theorem 1 below) and has a smaller error covariance than the unconstrained estimate (Theorem 2 below). We show which member of all possible constrained solutions has the smallest error covariance (Theorem 3 below). We also show the one particular member that is always (i.e., at each time step) closer to the true state than the unconstrained estimate (Theorem 4 below). Finally, we show that the variation of the constrained estimate is smaller than the variation of the unconstrained estimate (Theorem 5 below).

The application considered in this paper is turbofan engine health-parameter estimation [3]. The performance of gas turbine engines deteriorates over time. This deterioration can affect the fuel economy and impact emissions, component life consumption, and thrust response of the engine. Airlines periodically collect engine data in order to evaluate the health of the engine and its components. The health evaluation is then used to determine maintenance schedules. Reliable health evaluations are used to anticipate future maintenance needs. This offers the benefits of improved safety and reduced operating costs. The money-saving potential of such health evaluations is substantial, but only if the evaluations are reliable. The data used to perform health evaluations are typically collected during flight and later transferred to ground-based computers for post-flight analysis. Data are collected each flight at approximately the same engine operating conditions and corrected to account for variability in ambient conditions and power-setting levels. Typically, data are collected for a period of about 3 s at a rate of about 10 or 20 Hz. Various algorithms have been proposed to estimate engine health parameters, such as weighted least squares [4], expert systems [5], Kalman filters [6], neural networks [6], and genetic algorithms [7].

This paper applies constrained Kalman filtering to estimate engine component efficiencies and flow capacities, which are referred to as health parameters. We can use our knowledge of the physics of the turbofan engine in order to obtain a dynamic model [8,9]. The health parameters that we try to estimate can be modeled as slowly varying biases. The state vector of the dynamic model is augmented to include the health parameters, which are then estimated with a Kalman filter [10]. The model formulation in this paper is similar to previous NASA work [11]. However, Ref. [11] was limited to a 3-state dynamic model and 2 health parameters, whereas this present work includes a more complete 16-state model and 8 health parameters. In addition, we have some a priori knowledge of the engine's health parameters: we know that they never improve. Engine health always degrades over time, and we can incorporate this information into state constraints to improve our health-parameter estimation. (This is assuming that no maintenance or engine overhaul is performed.) This is similar to the probabilistic approach to turbofan prognostics proposed in Ref. [12]. The simulation results that we present here show that the Kalman filter can estimate health-parameter deviations with an average error of less than 5%, and the constrained Kalman filter performs even better than the unconstrained filter.

It should be emphasized that in this paper we are confining the problem to the estimation of engine health parameters in the presence of degradation only. There are specific engine fault scenarios that can result in abrupt shifts in filter estimates, possibly even

Contributed by the International Gas Turbine Institute (IGTI) of THE AMERICAN SOCIETY OF MECHANICAL ENGINEERS for publication in the ASME JOURNAL OF ENGINEERING FOR GAS TURBINES AND POWER. Paper presented at the International Gas Turbine and Aeroengine Congress and Exhibition, Atlanta, GA, June 16–19, 2003, Paper No. 2003-GT-38584. Manuscript received by IGTI, October 2002, final revision, March 2003. Associate Editor: H. R. Simmons.

indicating an apparent improvement in some engine components. An actual engine-performance monitoring system would need to include additional logic to detect and isolate such faults.

## Kalman Filtering

Consider the discrete linear time-invariant system given by

$$x_{k+1}=Ax_k+Bu_k+w_k,$$
$$y_k=Cx_k+e_k, \tag{1}$$

where $k$ is the time index, $x$ is the state vector, $u$ is the known control input, $y$ is the measurement, and $\{w_k\}$ and $\{e_k\}$ are uncorrelated zero-mean white-noise input sequences. We use $Q$ to denote the covariance of $\{w_k\}$ and $R$ to denote the covariance of $\{e_k\}$, and $\bar{x}$ to denote the expected value of $x$. The problem is to find an estimate $\hat{x}_{k+1}$ of $x_{k+1}$ given the measurements $\{y_0,y_1,\ldots,y_k\}$. We will use the symbol $Y_k$ to denote the column vector that contains the measurements $\{y_0,y_1,\ldots,y_k\}$. The Kalman filter can be used to solve this problem as follows:

$$K_k=A\Sigma_k C^T(C\Sigma_k C^T+R)^{-1}, \tag{2}$$

$$\hat{x}_{k+1}=A\hat{x}_k+Bu_k+K_k(y_k-C\hat{x}_k), \tag{3}$$

$$\Sigma_{k+1}=(A\Sigma_k-K_kC\Sigma_k)A^T+Q, \tag{4}$$

where the filter is initialized with $\hat{x}_0=\bar{x}_0$, and $\Sigma_0=E[(x_0-\bar{x}_0)\times(x_0-\bar{x}_0)^T]$. It can be shown [13] that the Kalman-filter estimate has several attractive properties. It is unbiased, and of all affine estimators, it is the one that minimizes the variance of the estimation error. In addition, if $x_0$, $\{w_k\}$, and $\{e_k\}$ are jointly Gaussian, then the Kalman-filter estimate is the one that maximizes the conditional probability density function of the state given the measurement history.

## Kalman Filtering With Inequality Constraints

This section extends the well-known results of the preceding section to cases where there are known linear inequality constraints among the state components. Also, several important properties of the constrained filter are discussed. Consider the dynamic system of Eq. (1) where we are given the additional constraint

$$Dx_k\leq d_k, \tag{5}$$

where $D$ is a known $s\times n$ constant matrix, $s$ is the number of constraints, $n$ is the number of state variables, and $s\leq n$. It is assumed in this paper that $D$ is full rank, i.e., that $D$ has rank $s$. This is an easily satisfied assumption. If $D$ is not full rank that means we have redundant state constraints. In that case we can simply remove linearly dependent rows from $D$ (i.e., remove redundant state constraints) until $D$ is full rank. Three different approaches to the constrained state estimation problem are given in this section. The time index $k$ is omitted in the remainder of this section for ease of notation.

**The Maximum Probability Method.** In this section we derive the constrained Kalman-filtering problem by using a maximum probability method. From Ref. [[13], p. 93ff.] we know that the Kalman-filter estimate is that value of $x$ that maximizes the conditional probability density function $P(x|Y)$. The constrained Kalman filter can be derived by finding an estimate $\tilde{x}$ such that the conditional probability $P(\tilde{x}|Y)$ is maximized and $\tilde{x}$ satisfies the constraint of Eq. (5). Maximizing $P(\tilde{x}|Y)$ is the same as maximizing its natural logarithm. So the problem we want to solve can be given by

$$\max \ln P(\tilde{x}|Y)\Rightarrow\min_{\tilde{x}}(\tilde{x}-\bar{\tilde{x}})^T\Sigma^{-1}(\tilde{x}-\bar{\tilde{x}}),$$
$$\text{such that } D\tilde{x}\leq d. \tag{6}$$

Using the fact that the unconstrained state estimate $\hat{x}=\bar{\tilde{x}}$ (the conditional mean of $x$), we rewrite the above equation as

$$\min_{\tilde{x}}(\tilde{x}^T\Sigma^{-1}\tilde{x}-2\hat{x}^T\Sigma^{-1}\tilde{x})\text{such that } D\tilde{x}\leq d. \tag{7}$$

Note that this problem statement depends on the conditional Gaussian nature of $\hat{x}$, which in turn depends on the Gaussian nature of $x_0$, $\{w_k\}$, and $\{e_k\}$ in Eq. (1).

**The Mean-Square Method.** In this section we derive the constrained Kalman-filtering problem by using a mean-square minimization method. We seek to minimize the conditional mean-square error subject to the state constraints.

$$\min_{\tilde{x}} E(\|x-\tilde{x}\|^2|Y)\text{such that } D\tilde{x}\leq d, \tag{8}$$

where $\|\cdot\|$ denotes the vector two-norm. If we assume that $x$ and $Y$ are jointly Gaussian, the mean-square error can be written as

$$E(\|x-\tilde{x}\|^2|Y)=\int (x-\tilde{x})^T(x-\tilde{x})P(x|Y)dx \tag{9}$$

$$=\int x^Txp(x|Y)dx-2\tilde{x}^T\int xP(x|Y)dx+\tilde{x}^T\tilde{x}. \tag{10}$$

Noting that the Kalman-filter estimate is the conditional mean of $x$, i.e.,

$$\hat{x}=\int xP(x|Y)dx, \tag{11}$$

we formulate the first-order conditions necessary for a minimum as

$$\min_{\tilde{x}}(\tilde{x}^T\tilde{x}-2\hat{x}^T\tilde{x})\text{such that } D\tilde{x}\leq d. \tag{12}$$

Again, this problem statement depends on the conditional Gaussian nature of $\hat{x}$, which in turn depends on the Gaussian nature of $x_0$, $\{w_k\}$, and $\{e_k\}$ in Eq. (1).

**The Projection Method.** In this section we derive the constrained Kalman-filtering problem by directly projecting the unconstrained state estimate $\hat{x}$ onto the constraint surface. That is, we solve the problem

$$\min_{\tilde{x}}(\tilde{x}-\hat{x})^TW(\tilde{x}-\hat{x})\text{such that } D\tilde{x}\leq d, \tag{13}$$

where $W$ is any symmetric positive-definite weighting matrix. This problem can be rewritten as

$$\min_{\tilde{x}}(\tilde{x}^TW\tilde{x}-2\hat{x}^TW\tilde{x})\text{such that } D\tilde{x}\leq d. \tag{14}$$

The constrained estimation problems derived by the maximum probability method of Eq. (7) and the mean-square method of Eq. (12) can be obtained from this equation by setting $W=\Sigma^{-1}$ and $W=I$, respectively. Note that this derivation of the constrained estimation problem does not depend on the conditional Gaussian nature of $\hat{x}$; i.e., $x_0$, $\{w_k\}$, and $\{e_k\}$ in Eq. (1) are not assumed to be Gaussian.

**The Solution of the Constrained-State Estimation Problem.** The problem defined by Eq. (14) is known as a quadratic programming problem [14,15]. There are many algorithms for solving quadratic programming problems, almost all of which fall in the category known as active set methods. An active set method uses the fact that it is only those constraints that are active at the solution of the problem that are significant in the optimality conditions. Assume that $t$ of the $s$ inequality constraints are active at the solution of Eq. (14), and denote by $\hat{D}$ and $\hat{d}$ the $t$ rows of $D$ and $t$ elements of $d$ corresponding to the active constraints. If the

correct set of active constraints was known a priori then the solution of Eq. (14) would also be a solution of the equality-constrained problem

$$\min_{\tilde{x}}(\tilde{x}^T W\tilde{x} - 2\hat{x}^T W\tilde{x}) \text{such that } \hat{D}\tilde{x} = \hat{d}. \tag{15}$$

This shows that the inequality-constrained problem defined by Eq. (14) is equivalent to the equality-constrained problem defined by Eq. (15). Note that $\tilde{x}$ depends entirely on $\hat{x}$ at each time step. Although the equation for $\hat{x}$ is recursive as seen in Eq. (3), the equation for $\tilde{x}$ is not recursive. Therefore, an inequality-constrained Kalman filter that uses active set methods to enforce the constraints completely reduces to an equality-constrained Kalman filter, even though the active set may change at each time step. The equality-constrained problem was discussed in Ref. [2], in which there is no assumption that the constraints remain constant from one time step to the next. Therefore, those results can be used to investigate the properties of the inequality-constrained filter.

**Properties of the Constrained State Estimate.** In this section we examine some of the statistical properties of the constrained Kalman filter. We use $\hat{x}$ to denote the state estimate of the unconstrained Kalman filter, and $\tilde{x}$ to denote the state estimate of the constrained Kalman filter as given by Eq. (14), recalling that Eqs. (7) and (12) are special cases of Eq. (14).

*Theorem 1.* The solution $\tilde{x}$ of the constrained state estimation problem given by Eq. (14) is an unbiased state estimator for the system given by Eq. (1) for any symmetric positive definite weighting matrix W. That is,

$$E(\tilde{x}) = E(x). \tag{16}$$

*Theorem 2.* The solution $\tilde{x}$ of the constrained state estimation problem given by Eq. (14) with $W = \Sigma^{-1}$, where $\Sigma$ is the error covariance of the unconstrained estimate given in Eq. (4), has an error covariance that is less than or equal to that of the unconstrained state estimate. That is,

$$\text{Cov}(x - \tilde{x}) \leq \text{Cov}(x - \hat{x}). \tag{17}$$

At first this seems counterintuitive, since the standard Kalman filter is by definition the minimum variance filter. However, we have changed the problem by introducing state-variable constraints. Therefore, the standard Kalman filter is no longer the minimum variance filter, and we can do better with the constrained Kalman filter.

*Theorem 3.* Among all the constrained Kalman filters resulting from the solution of Eq. (14), the filter that uses $W = \Sigma^{-1}$ has the smallest estimation error covariance. That is,

$$\text{Cov}(x - \tilde{x}_{\Sigma^{-1}}) \leq \text{Cov}(x - \tilde{x}_W) \quad \text{for all } W. \tag{18}$$

*Theorem 4.* The solution $\tilde{x}$ of the constrained state estimation problem given by Eq. (14) with $W = I$ satisfies the inequality

$$\|x_k - \tilde{x}_k\| \leq \|x_k - \hat{x}_k\| \quad \text{for all } k, \tag{19}$$

where $\|\cdot\|$ is the vector two-norm and $\hat{x}$ is the unconstrained Kalman-filter estimate.

*Theorem 5.* The error of the solution $\tilde{x}$ of the constrained state estimation problem given by Eq. (14) with $W = I$ is smaller than the unconstrained estimation error in the sense that

$$\text{Tr}[\text{Cov}(\tilde{x})] \leq Tr[\text{Cov}(\hat{x})], \tag{20}$$

where $\text{Tr}[\cdot]$ indicates the trace of a matrix, and $\text{Cov}(\cdot)$ indicates the covariance matrix of a random vector.

The above theorems all follow from the equivalence of Eqs. (14) and (15), and the proofs presented in Ref. [2]. We note that if any of the *s* constraints are active at the solution of Eq. (14), then strict inequalities hold in the statements of Theorems 2–5. The only time that equalities hold in the theorems is if there are no active constraints at the solution of Eq. (14); that is, if the unconstrained Kalman filter satisfies the inequality constraints.

## Turbofan Engine Health Monitoring

The high-performance turbofan engine model used in this research is based on a gas turbine engine simulation software package called DIGTEM (digital turbofan engine model) [8,16]. DIGTEM is written in Fortran and includes 16 state variables. It uses a backward difference integration scheme because the turbofan model contains time constants that differ by up to four orders of magnitude.

The nonlinear equations used in DIGTEM can be found in Refs. [8,9]. The time-invariant equations can be summarized as follows:

$$\begin{aligned} \dot{x} &= f(x,u,p) + w_1(t), \\ y &= g(x,u,p) + e(t). \end{aligned} \tag{21}$$

$x$ is the 16-element state vector, $u$ is the 6-element control vector, $p$ is the 8-element vector of health parameters, and $y$ is the 12-element vector of measurements. The noise term $w_1(t)$ represents inaccuracies in the model, and $e(t)$ represents measurement noise. The state variables and their nominal values at the selected operating point are as follows:

- Low-pressure turbine (LPT) rotor speed (9200 rpm)
- High-pressure turbine (HPT) rotor speed (11900 rpm)
- Compressor volume stored mass (0.91294 lbm)
- Combustor inlet temperature (1325 R)
- Combustor volume stored mass (0.460 lbm)
- HPT inlet temperature (2520 R)
- HPT volume stored mass (2.4575 lbm)
- LPT inlet temperature (1780 R)
- LPT volume stored mass (2.227 lbm)
- Augmentor inlet temperature (1160 R)
- Augmentor volume stored mass (1.7721 lbm)
- Nozzle inlet temperature (1160 R)
- Duct airflow (86.501 lbm/s)
- Augmentor airflow (194.94 lbm/s)
- Duct volume stored mass (6.7372 lbm)
- Duct temperature (696 R)

The turbofan controls and their nominal values are as follows:

- Combustor fuel flow (1.70 lbm/s)
- Augmentor fuel flow (0 lbm/s)
- Nozzle throat area (430 $\text{in.}^2$)
- Nozzle exit area (492 $\text{in.}^2$)
- Fan vane angle ($-1.7°$)
- Compressor vane angle (4.0°)

The health parameters and their nominal values are as follows:

- Fan airflow (193.5 lbm/s)
- Fan efficiency (0.8269)
- Compressor airflow (107.0 lbm/s)
- Compressor efficiency (0.8298)
- HPT airflow (89.8 lbm/s)
- HPT enthalpy change (167.0 Btu/lbm)
- LPT airflow (107.0 lbm/s)
- LPT enthalpy change (75.5 Btu/lbm)

The turbofan measurements and their nominal values and signal-to-noise ratios (SNRs) are as follows:

- LPT rotor speed (9200 rpm, SNR=150)
- HPT rotor speed (11900 rpm, SNR=150)
- Duct pressure (34.5 psia, SNR=200)
- Duct temperature (696 R, SNR=100)
- Compressor inlet pressure (36.0 psia, SNR=200)
- Compressor inlet temperature (698 R, SNR=100)
- Combustor pressure (267 psia, SNR=200)

- Combustor inlet temperature (1325 R, SNR=100)
- LPT inlet pressure (70.0 psia, SNR=100)
- LPT inlet temperature (1780 R, SNR=70)
- Augmentor inlet pressure (31.8 psia, SNR=100)
- Augmentor inlet temperature (1160 R, SNR=70)

The SNR values above are based on NASA experience and previously published data [17]. Sensor dynamics are assumed to be high enough bandwidth that they can be ignored in the dynamic equations [17]. Equation (21) can be linearized about the nominal operating point by using the first-order approximation of the Taylor-series expansion. This gives a linear small-signal system model defined for small excursions from the nominal operating point:

$$\delta\dot{x} = A_1\delta x + B\delta u + A_2\delta p + w_1(t),$$
$$\delta y = C_1\delta x + D\delta u + C_2\delta p + e(t). \tag{22}$$

We note that

$$A_1 = \frac{\partial f}{\partial x},$$
$$A_1(i,j) \approx \frac{\Delta\dot{x}(i)}{\Delta x(j)}. \tag{23}$$

Similar equations hold for the $A_2$, $C_1$, and $C_2$ matrices. We obtained numerical approximations to the $A_1$, $A_2$, $C_1$, and $C_2$ matrices by varying $x$ and $p$ from their nominal values (one element at a time) and recording the new $\dot{x}$ and $y$ vectors in DIGTEM.

The goal of our turbofan engine health monitoring problem is to obtain an accurate estimate of $\delta p$, which varies slowly with time. We therefore assume that $\delta p$ remains essentially constant during a single flight. We also assume that the control input is constant, so $\delta u = 0$. (In reality, $\delta u \neq 0$, which complicates the problem and will give different results than we present in this paper. This will be explored in further work.) This gives us the following equivalent discrete time system [[18], p. 90ff.]:

$$\delta x_{k+1} = A_{1d}\delta x_k + A_{2d}\delta p_k + w_{1k},$$
$$\delta y_k = C_1\delta x_k + C_2\delta p_k + e_k, \tag{24}$$

where $A_{1d} = \exp(A_1 T)$ and $A_{2d} = A_1^{-1}(A_{1d} - I)A_2$ (assuming that $A_1$ is invertible, which it is in our problem). We next augment the state vector with the health-parameter vector [11] to obtain the system equation

$$\begin{bmatrix} \delta x_{k+1} \\ \delta p_{k+1} \end{bmatrix} = \begin{bmatrix} A_{1d} & A_{2d} \\ 0 & I \end{bmatrix} \begin{bmatrix} \delta x_k \\ \delta p_k \end{bmatrix} + \begin{bmatrix} w_{1k} \\ w_{2k} \end{bmatrix},$$
$$\delta y_k = \begin{bmatrix} C_1 & C_2 \end{bmatrix} \begin{bmatrix} \delta x_k \\ \delta p_k \end{bmatrix} + e_k, \tag{25}$$

where $w_{2k}$ is a small noise term (uncorrelated with $w_{1k}$) that represents model uncertainty and allows the Kalman filter to estimate time-varying health-parameter variations. The discrete time small signal model can be written as

$$\begin{bmatrix} \delta x_{k+1} \\ \delta p_{k+1} \end{bmatrix} = A \begin{bmatrix} \delta x_k \\ \delta p_k \end{bmatrix} + w_k,$$
$$\delta y_k = C \begin{bmatrix} \delta x_k \\ \delta p_k \end{bmatrix} + e_k, \tag{26}$$

where the definitions of $A$ and $C$ are apparent from a comparison of the two preceding equations. Now we can use a Kalman filter to estimate $\delta x_k$ and $\delta p_k$. Actually, we are only interested in estimating $\delta p_k$ (the health-parameter deviations), but the Kalman filter gives us the bonus of also estimating $\delta x_k$ (the excursions of the original turbofan state variables). Note that four of the state variables are directly measured with good SNRs. The Kalman-filter equations automatically use this information to improve its estimate of all of the state variables and generate the optimal state estimate.

It is known that health parameters do not improve over time. That is, $\delta p(1)$, $\delta p(2)$, $\delta p(3)$, $\delta p(4)$, $\delta p(6)$, and $\delta p(8)$ are always less than or equal to zero and always decrease with time. Similarly, $\delta p(5)$ and $\delta p(7)$ (the two turbine airflow parameters) are always greater than or equal to zero and always increase with time. In addition, it is known that the health parameters vary slowly with time. As an example, since $\widetilde{\delta p}(1)$ is the constrained estimate of $\delta p(1)$, we can enforce the following constraints on $\widetilde{\delta p}(1)$:

$$\widetilde{\delta p}(1) \leq 0,$$
$$\widetilde{\delta p}_{k+1}(1) \leq \widetilde{\delta p}_k(1) + \gamma_1^+,$$
$$\widetilde{\delta p}_{k+1}(1) \geq \widetilde{\delta p}_k(1) - \gamma_1^-, \tag{27}$$

where $\gamma_1^+$ and $\gamma_1^-$ are nonnegative factors chosen by the user that allows the state estimate to vary only within prescribed limits. Typically we choose $\gamma_1^- > \gamma_1^+$ so that the state estimate can change more in the negative direction than in the positive direction. This is in keeping with our a priori knowledge that this particular state variable never increases with time. Ideally we would have $\gamma_1^+ = 0$ since $\delta p(1)$ never increases. However, since the state-variable estimate varies around the true value of the state variable, we choose $\gamma_1^+ > 0$. This allows some time-varying increase in the state-variable estimate to compensate for a state-variable estimate that is smaller than the true state-variable value.

These constraints are linear and can therefore easily be incorporated into the form required in the constrained filtering problem statement of Eq. (5). If the state constraints are nonlinear they can be linearized as discussed in Ref. [2]. Note that this does not take into account the possibility of abrupt changes in health parameters due to discrete damage events. That possibility must be addressed by some other means (e.g., residual checking [3]) in conjuction with the methods presented in this paper.

## Simulation Results

We simulated the methods discussed in this paper using MATLAB. We simulated a steady-state 3 s burst of engine data measured at 10 Hz during each flight. The nonlinear DIGTEM software described in the preceding section was used to generated the measurement data. Each data collection was performed at the single operating point shown earlier in this paper. The signal-to-noise ratios were determined on the basis of NASA experience and previously published data [17] and are shown earlier in this paper. The Kalman filter was relinearized around the state estimates every 50 flights. We used a $1\sigma$ process noise in the Kalman filter equal to approximately 1% of the nominal state values to allow the filter to be responsive to changes in the state variables. We set the $1\sigma$ process noise for each component of the health-parameter portion of the state derivative equation to 0.01% of the nominal parameter value. This was obtained by tuning. It was small enough to give reasonably smooth estimates, and large enough to allow the filter to track slowly time-varying parameters. For the constrained filter, we chose the $\gamma$ variables in Eq. (27) such that the maximum allowable rate of change in $\widetilde{\delta p}$ was the sum of a linear and exponential function that reached 9% after 500 flights in the direction of expected change, and 3% after 500 flights in the opposite direction. The true health-parameter values never change in a direction opposite to the expected change. However, we allow the state estimate to change in the opposite direction to allow the Kalman filter to compensate for the fact that the state estimate might be either too large or too small. We set the weighting matrix $W$ in Eq. (14) equal to $\Sigma^{-1}$ in accordance with Theorem 3.

We simulated an exponential degradation of the eight health parameters over 500 flights. The initial health-parameter estima-

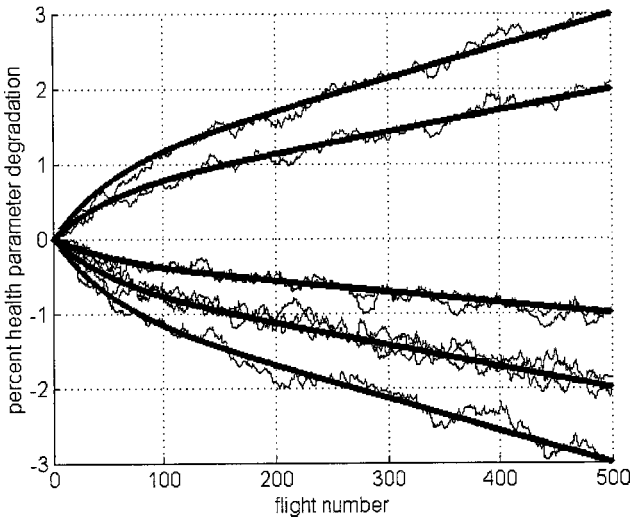


**Fig. 1 Unconstrained Kalman-filter estimates of health parameters. True health-parameter changes are shown as heavy lines. Filter estimates are shown as lighter lines.**

tion errors were taken from one-sided normal distributions with standard deviations of 0.5% of their nominal values. The simulated health-parameter degradations were representative of turbofan performance data reported in the literature [19]. We ran 30 Monte Carlo simulations like this, each with a different noise history and different initial estimation errors. Figures 1 and 2 show the Kalman filter's performance in a typical case when the initial estimation errors are zero. Both simulations represented in the figures have the same "random" measurement noise. Table 1 shows the performance of the filters averaged over all 30 simulations. The standard Kalman filter estimates the health parameters to within 4.66% of their final degradations. The constrained filter estimates the health parameters to within 3.90% of their final degradations. These numbers show the improvement that is possible with the constrained Kalman filter.

The improved performance of the constrained filter comes with a price, and that price is computational effort. The constrained filter requires about four times the computational effort of the unconstrained filter. This is because of the additional quadratic programming problem that is required. However, computational effort is not a critical issue for turbofan health estimation since the filtering is performed on ground-based computers after each flight.

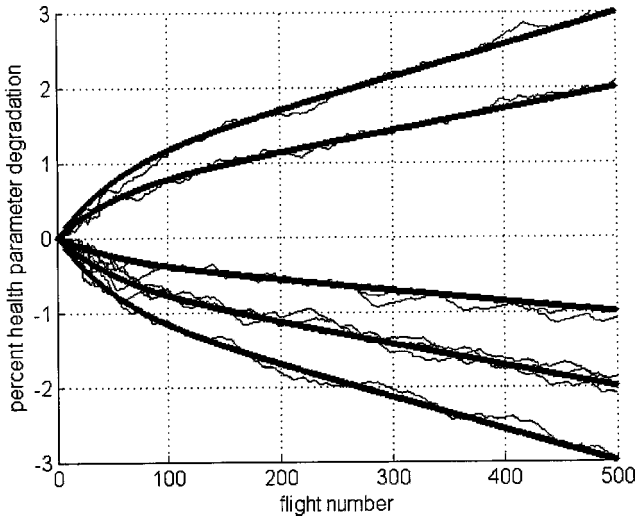


**Fig. 2 Constrained Kalman-filter estimates of health parameters. True health-parameter changes are shown as heavy lines. Filter estimates are shown as lighter lines.**

**Table 1 Kalman-filter estimation errors. The numbers shown are rms estimation errors averaged over 30 simulations where each simulation had a linear-plus-exponential degradation of all eight health parameters. The numbers show the error between the estimated and actual degradation as percentages of the degradation at the final time.**

| | Estimation error (%) | |
|---|---|---|
| Health parameter | Unconstrained | Constrained |
| Fan airflow | 4.81 | 4.41 |
| Fan efficiency | 5.85 | 4.60 |
| Compressor airflow | 3.43 | 2.73 |
| Compressor efficiency | 4.82 | 3.80 |
| HPT airflow | 3.09 | 2.39 |
| HPT enthalpy change | 4.48 | 3.76 |
| LPT airflow | 4.54 | 4.26 |
| LPT enthalpy change | 6.28 | 5.22 |
| Average | 4.66 | 3.90 |

Note that the Kalman filter works well only if the assumed system model matches reality fairly closely. The method presented in this paper, by itself, will not work well if there are large sensor biases or hard faults due to severe component failures. A mission-critical implementation of a Kalman filter should always include some sort of residual check to verify the validity of the Kalman-filter results [20], particularly for the application of turbofan engine health estimation considered in this paper [3].

It can be seen from the figures that although the constrained filter improves the estimation accuracy, the general trend of the state-variable estimates does not change with the introduction of state constraints. This is because the constrained filter is based on the unconstrained Kalman filter. The constrained filter estimates therefore have the same shape as the unconstrained estimates *until* the constraints are violated, at which point the state-variable estimates are projected onto the edge of the constraint boundary. The constrained filter presented in this paper is not qualitatively different than the standard Kalman filter; it is rather a quantitative improvement in the standard Kalman filter.

## Conclusion

We have presented an analytic method for incorporating linear state inequality constraints in a Kalman filter. This maintains the state-variable estimates within a user-defined envelope. The simulation results demonstrate the effectiveness of this method, particularly for turbofan engine health estimation.

If the system whose state variables are being estimated has known state-variable constraints, then those constraints can be incorporated into the Kalman filter as shown in this paper. However, in implementation, the constraints enforced in the filter might be more relaxed than the true constraints. This allows the filter to correct state-variable estimates in a direction that the true state variables might never change. This is a departure from strict adherence to theory, but in practice this improves the performance of the filter. This is an implementation issue that is conceptually similar to tuning a standard Kalman filter.

We saw that the constrained filter requires a much larger computational effort than the standard Kalman filter. This is due to the addition of the quadratic programming problem that must be solved in the constrained Kalman filter. The engineer must therefore perform a tradeoff between computational effort and estimation accuracy.

## Acknowledgments

This work was funded by the NASA Aviation Safety Program, NASA Glenn Research Center, Cleveland, Ohio.

## References


[1] Massicotte, D., Morawski, R., and Barwicz, A., 1995, ''Incorporation of a Positivity Constraint Into a Kalman-Filter-Based Algorithm for Correction of Spectrometric Data,'' IEEE Trans. Instrum. Meas., **44**, pp. 2–7.

[2] Simon, D., and Chia, T., 2002, ''Kalman Filtering With State Equality Constraints,'' IEEE Trans. Aerosp. Electron. Syst., **39**, pp. 128–136.

[3] Doel, D., 1994, ''TEMPER—A Gas-Path Analysis Tool for Commercial Jet Engines,'' ASME J. Eng. Gas Turbines Power, **116**, pp. 82–89.

[4] Doel, D., 1994, ''An Assessment of Weighted-Least-Squares-Based Gas Path Analysis,'' ASME J. Eng. Gas Turbines Power, **116**, pp. 366–373.

[5] DePold, H., and Gass, F., 1999, ''The Application of Expert Systems and Neural Networks to Gas Turbine Prognostics and Diagnostics,'' ASME J. Eng. Gas Turbines Power, **121**, pp. 607–612.

[6] Volponi, A., DePold, H., Ganguli, R., and Chen, D., 2000, ''The Use of Kalman Filter and Neural Network Methodologies in Gas Turbine Performance Diagnostics: a Comparative Study,'' ASME J. Eng. Gas Turbines Power, **125**, pp. 917–924.

[7] Kobayashi, T., and Simon, D. L., 2001, ''A Hybrid Neural Network-Genetic Algorithm Technique for Aircraft Engine Performance Diagnostics,'' 37th AIAA/ASME/SAE/ASEE Joint Propulsion Conference, Salt Lake City, UT.

[8] Daniele, C., Krosel, S., Szuch, J., and Westerkamp, E., 1983, ''Digital Computer Program for Generating Dynamic Turbofan Engine Models (DIGTEM),'' NASA Technical Memorandum 83446.

[9] Szuch, J., Krosel, S., and Bruton, W., 1982, ''Automated Procedure for Developing Hybrid Computer Simulations of Turbofan Engines,'' NASA Technical Paper 1851.

[10] Friedland, B., 1969, ''Treatment of Bias in Recursive Filtering,'' IEEE Trans. Autom. Control, **AC14**, pp. 359–367.

[11] Lambert, H., 1991, ''A Simulation Study of Tubofan Engine Deterioration Estimation Using Kalman Filtering Techniques,'' NASA Technical Memorandum 104233.

[12] Roemer, M., and Kacprzynski, G., 2000, ''Advanced Diagnostics and Prognostics for Turbine Engine Risk Assessment,'' IEEE Aerospace Conference, Big Sky, MT., pp. 345–353.

[13] Anderson, B., and Moore, J., 1979, *Optimal Filtering*, Prentice-Hall, Englewood Cliffs, NJ.

[14] Fletcher, R., 1981, *Practical Methods of Optimization*, Vol. 2: *Constrained Optimization*, Wiley, New York.

[15] Gill, P., Murray, W., and Wright, M., 1981, *Practical Optimization*, Academic, New York.

[16] Daniele, C., and McLaughlin, P., 1984, ''The Real-Time Performance of a Parallel, Nonlinear Simulation Technique Applied to a Turbofan Engine,'' *Modeling and Simulation on Microcomputers*, R. Swartz, ed., Society for Computer Simulation, San Diego, CA, pp. 167–171.

[17] Merrill, W., 1984, ''Identification of Multivariable High-Performance Turbofan Engine Dynamics From Closed-Loop Data,'' J. Guid. Control Dyn., **7**, pp. 677–683.

[18] Chen, C., 1999, *Linear System Theory and Design*, Oxford University Press, New York.

[19] Sasahara, O., 1985, ''JT9D Engine/Module Performance Deterioration Results From Back to Back Testing,'' International Symposium on Air Breathing Engines, Beijing, pp. 528–535.

[20] Gelb, A., 1974, *Applied Optimal Estimation*, MIT Press, Cambridge, MA.

# Adaptive Myriad Filter for Improved Gas Turbine Condition Monitoring Using Transient Data

**Vellore P. Surender**

**Ranjan Ganguli**
Mem. ASME

Department of Aerospace Engineering,
Indian Institute of Science,
Bangalore 650012, India

*The removal of noise and outliers from measurement signals is a major problem in jet engine health monitoring. In this study, we look at the myriad filter as a substitute for the moving average filter that is widely used in the gas turbine industry. The three ideal test signals used in this study are the step signal that simulates a single fault in the gas turbine, while ramp and quadratic signals simulate long term deterioration. Results show that the myriad filter performs better in noise reduction and outlier removal when compared to the moving average filter. Further, an adaptive weighted myriad filter algorithm that adapts to the quality of incoming data is studied. The filters are demonstrated on simulated clean and deteriorated engine data obtained from an acceleration process from idle to maximum thrust condition. This data was obtained from published literature and was simulated using a transient performance prediction code. The deteriorated engine had single component faults in the low pressure turbine and intermediate pressure compressor. The signals are obtained from T2 (IPC total outlet temperature) and T6 (LPT total outlet temperature) engine sensors with their nonrepeatability values that were used as noise levels. The weighted myriad filter shows even greater noise reduction and outlier removal when compared to the sample myriad and a FIR filter in the gas turbine diagnosis. Adaptive filters such as those considered in this study are also useful for online health monitoring, as they can adapt to changes in quality of incoming data.*
[DOI: 10.1115/1.1850491]

## Introduction

Gas turbines are important and expensive mechanical systems that are used for power generation and aircraft propulsion. Monitoring the health of such systems is an important engineering problem. Aircraft jet engines are fitted with four basic measurements: low rotor speed, high rotor speed, exhaust gas temperature, and fuel flow rate. These measurements lead to four measurement deviations or deltas that are the difference from the measurements of the damaged engine and the undamaged or baseline engine. These measurement deltas are the health signals which are very important for health monitoring since they contain information about the condition of the gas turbine engine [1,2]. A key problem in condition monitoring is the presence of high levels of noise and outliers in the data. Another problem is the presence of sudden trend shifts in gas path measurements that can occur due to so-called ''single faults'' or repair events. It has been found from an analysis of engine data that most faults in gas turbine engines are preceded by a sudden increase in one or more measurements [3]. These ''single faults'' result in a step change in the gas path measurements. Besides ''single faults,'' gas turbines undergo deterioration over time, which shows up as a gradual increase in the gas path measurement deltas. It has been found from a study of revenue service data that these measurements follow a low-order polynomial variation with respect to time and a linear approximation is quite accurate [4–6]. Some studies have looked at deriving algorithms for removing noise from gas turbine measurement deltas. In [3], the exponential average filter was suggested as an alternative to the FIR moving average filter. The authors also suggest rules of thumb for removing outliers based on the logic that it is not physically possible for any one measurement to change and for the other measurements to not change. Such points were classified as outliers. Some studies have looked at median-type filters for denoising gas path health signals. However, these algorithms are based on median-type filters and have a time delay [7,8]. Since data on aircraft power plants are obtained only once or twice per flight, the time delay is a handicap. Other researchers have looked at neural network based approaches for denoising gas path health signals [9].

The test signals used in this paper are for transient data. It is possible to use both steady-state and transient data for diagnostics. However, good steady-state data may not be available under all operating conditions. For example, military engines can operate up to 70% of the time in unsteady conditions [10]. In addition, some faults may be amplified under transient conditions. Several authors have looked at engine diagnostics with transient data [10–13]. Some studies address the problem of fault detection and a few have looked at the assessment of the fault magnitude. Neural network and genetic algorithms have been used for the fault isolation problem. While the neural approach is robust to the presence of some level of noise in data, all fault isolation algorithms benefit from prior signal processing. Since transient data is acquired online at a reasonably high rate, we study an online adaptive signal processing method in this paper, which can be useful for data cleaning prior to fault isolation and visual display to human engineers.

Linear filtering algorithms used in practical applications are limited to the cases of Gaussian noise and show performance degradation in the presence of impulsive contamination. The class of myriad filters has been proposed for filtering highly noisy data [14–17]. In this study, we look at the myriad filter as a substitute for the moving average filter that is widely used in the gas turbine industry.

## Myriad Filter

Myriad filters are nonlinear filters whose development was motivated by the properties of $\alpha$-stable distributions, a family of heavy-tailed densities that have been proposed for robust non-

Contributed by the International Gas Turbine Institute (IGTI) of THE AMERICAN SOCIETY OF MECHANICAL ENGINEERS for publication in the ASME JOURNAL OF ENGINEERING FOR GAS TURBINES AND POWER. Paper presented at the International Gas Turbine and Aeroengine Congress and Exhibition, Vienna, Austria, June 13–17, 2004, Paper No. 2004-GT-53080. Manuscript received by IGTI, October 1, 2003; final revision, March 1, 2004. IGTI Review Chair: A. J. Strazisar.

Gaussian signal processing in impulsive noise environments [14]. Using an $\alpha$-stable noise model leads to a noise removal processor that performs nonlinear operations on the data and is good at outlier removal. Myriad filters have a solid theoretical basis, and are inherently more powerful than median filters.

The myriad filter is defined as a running-window filter outputting the sample myriad of the elements in the window. In the case that all the weights are unitary [14], this filter is referred as the ''unweighted myriad filter'' or simply as the myriad filter. The myriad filter is then defined as

$$\hat{\beta}_K = \arg\left( \min_{\beta} \prod_{i=1}^{N} [K^2 + (x_i - \beta)^2] \right). \tag{1}$$

The myriad is the argument $\beta$ that minimizes the product expression in the above equation. The myriad filters can be controlled by adjusting the linearity parameter $K$ [16]. The larger the value of $K$, the closer the behavior of the myriad to a linear estimator. As the myriad moves away from the linear region (large values of $K$) to lower values, the estimator becomes more nonlinear and resistant to the presence of impulsive noise.

We use a five-point myriad filter that represents a small window. Distortion to sharp edges in the signal that can precede ''single faults'' is minimal. This filter can be evaluated by using the following polynomial that is obtained from Eq. (1) by using $N=5$:

$$f(\beta) = (K^2 + (x_1 - \beta)^2) * (K^2 + (x_2 - \beta)^2) * (K^2 + (x_3 - \beta)^2) * (K^2 + (x_4 - \beta)^2) * (K^2 + (x_5 - \beta)^2) \tag{2}$$

The myriad is the value $\beta$ that minimizes $f(\beta)$, where it lies between $[x_1, x_5]$, where $x_1$ and $x_5$ are the minimum and maximum values in the sample. We see from Eq. (2) that $f(\beta)$ for the five-point filter myriad is a polynomial in $\beta$ of order ten. In general, $f(\beta)$ for an $N$-point myriad is a polynomial of order $2N$. To find the value of the myriad, we need to find the roots of $f'(\beta)$ and find the value of $\beta$ among the root values that give the lowest $f(\beta)$. The myriad filters are compared in this study to FIR (Finite Impulse Response) moving average filters of equal length. The FIR filter is defined as

$$\hat{x} = \sum_{i=1}^{N} w_i x_i, \tag{3}$$

where the weights sum to one. When the weights are equal, a moving average filter is obtained. The five-point moving average FIR filter is defined as

$$\hat{x} = \frac{x_1 + x_2 + x_3 + x_4 + x_5}{5}, \tag{4}$$

where each weight is equal to 1/5. Note that the myriad filter becomes the moving average as $K \to \infty$. Defining $f_i(\beta) = (K^2 + (x_i - \beta)^2)$, Eq. (2) can be written as

$$f(\beta) = \prod_{i=1}^{5} f_i(\beta) \tag{5}$$

Then,

$$f'(\beta) = f_1' f_2 f_3 f_4 f_5 + f_1 f_2' f_3 f_4 f_5 + \cdots + f_1 f_2 f_3 f_4 f_5' = 0 \tag{6}$$

Dividing by $f_1 f_2 f_3 f_4 f_5$ gives

$$\frac{f_1'}{f_1} + \frac{f_2'}{f_2} + \cdots + \frac{f_5'}{f_5} = 0 \tag{7}$$

where $f' = -2(x_i - \beta)$. The above equation can be written as

$$\frac{x_1 - \beta}{1 + \frac{(x_1 - \beta)^2}{K^2}} + \frac{x_2 - \beta}{1 + \frac{(x_2 - \beta)^2}{K^2}} + \cdots + \frac{x_5 - \beta}{1 + \frac{(x_5 - \beta)^2}{K^2}} = 0 \tag{8}$$

As $K \to \infty$, $(x_i - \beta)^2 / K^2 \to 0$, which yields

$$\beta = \frac{(x_1 + x_2 + x_3 + x_4 + x_5)}{5} \tag{9}$$

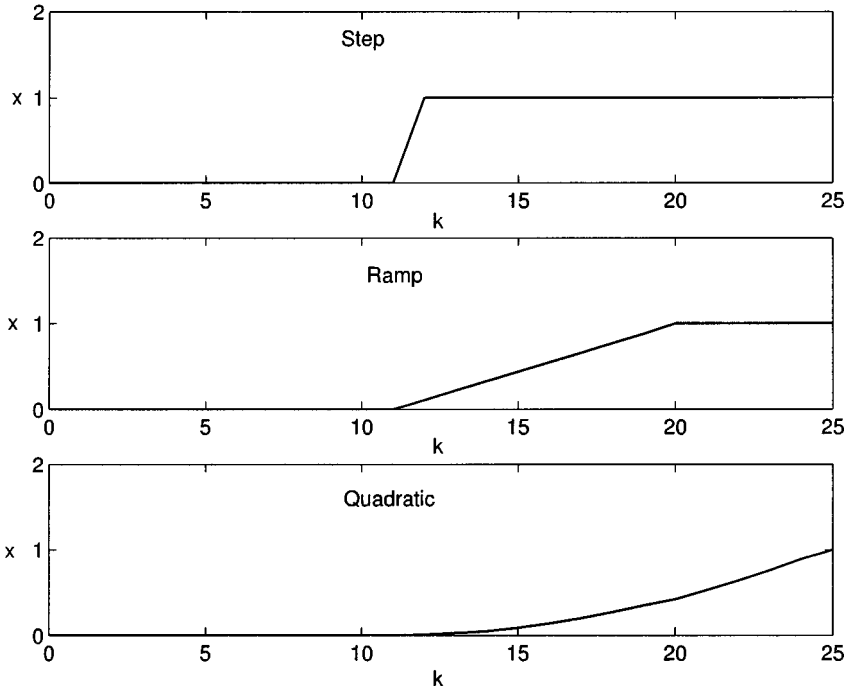


**Fig. 1 Test signals**

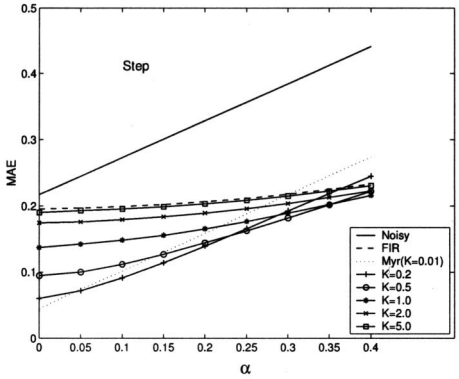


(a) Step Signal.

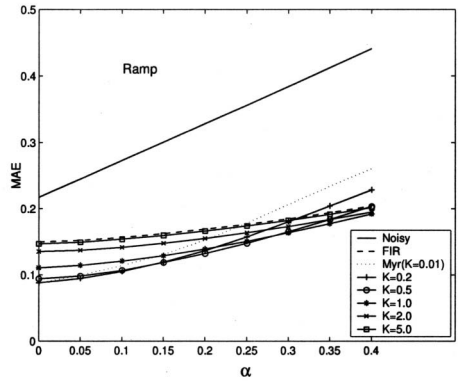


(b) Ramp Signal.

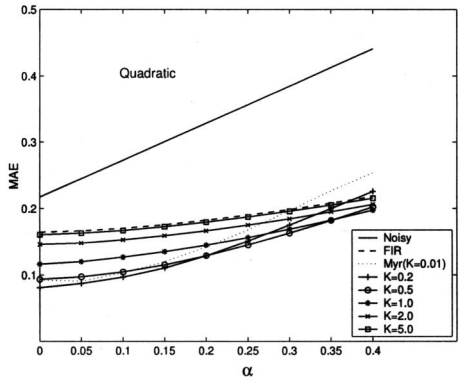


(c) Quadratic Signal.

**Fig. 2 Effect of linearity parameter *K* on five-point myriad filter for MAE**

a moving average FIR filter. Thus we see that this filter is analogous to the FIR filter unlike the median filters and may be used in the same manner as the moving average is used in the gas turbine industry.

## Numerical Experiments

The signals that are considered for preliminary numerical experiments are (1) the Step signal, (2) the Ramp signal and (3) the Quadratic signal and are shown in Fig. 1. Later in this paper, more realistic gas path signals are considered. However, the numerical experiments conducted here allow the selection of the value of the parameter $K$ which is critical to the performance of the myriad filter.

The step signal simulates a single fault event in the gas turbine. The ramp and quadratic signal simulate long term deterioration. The signal is created using

$$x = x^0 + \alpha\varepsilon + \theta \tag{10}$$

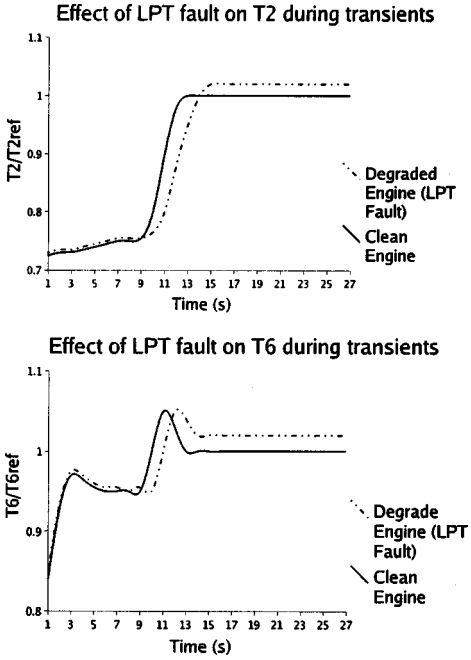


**Fig. 3 Clean and degraded signals during LPT fault on the acceleration process**

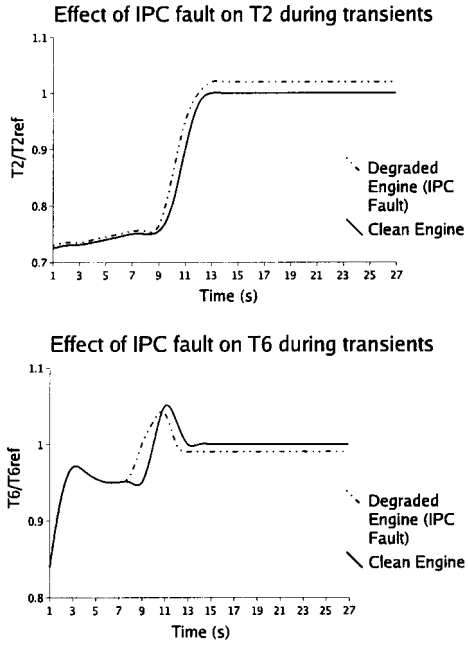


**Fig. 4 Clean and degraded signals during IPC fault on the acceleration process**

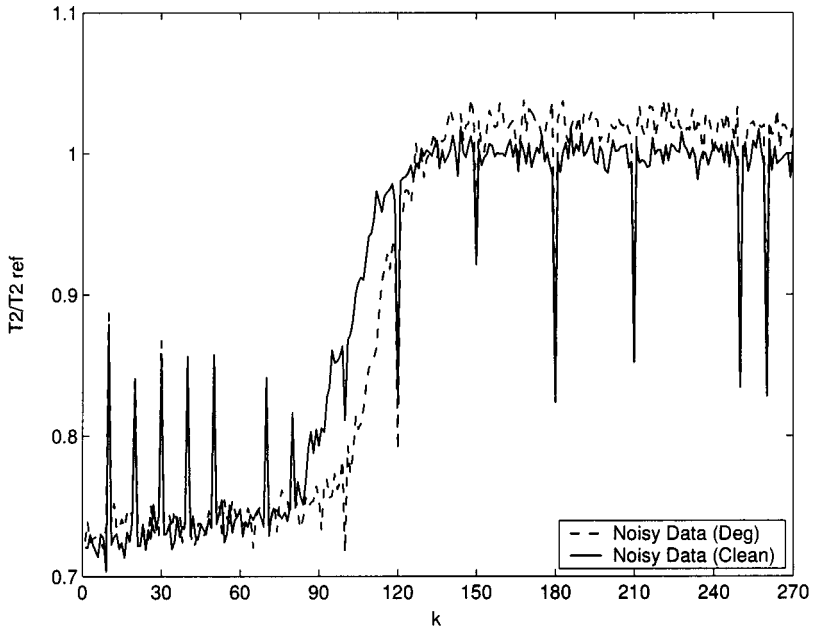


(a) Noisy data on LPT T2 engine for α=0.008.

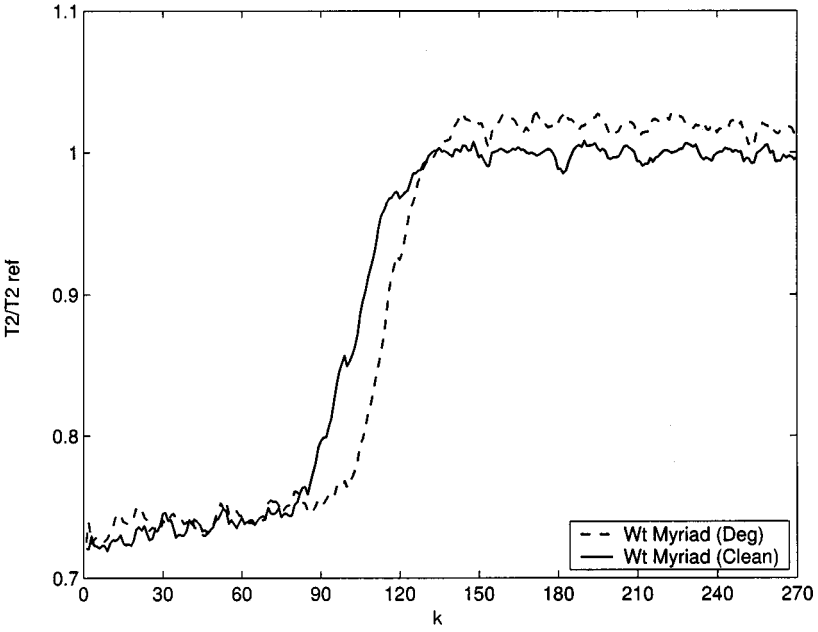


(b) Filtered data on LPT T2 engine for α=0.008.

**Fig. 5 Clean and degraded signals during LPT fault on the acceleration process for T2**

where $x^0$ is the root signal, $\varepsilon$ accounts for Gaussian noise and $\theta$ for non-Gaussian outliers. Here $\alpha$ is a parameter called noise level that allows us to control the level of noise in the data. A $\Psi$ filter performs the following operations that returns the filtered signal from the corrupted signal.

$$y = \Psi(x) = \Psi(x^0 + \alpha\epsilon + \theta) \tag{11}$$

The following error measures will be used to analyze the myriad filter performance over a sample of $N$ points by comparing the filtered signal with the root signal

$$\text{MAE} = \sum_{i=1}^{N} \frac{|(y - x^0)|}{N} \tag{12}$$

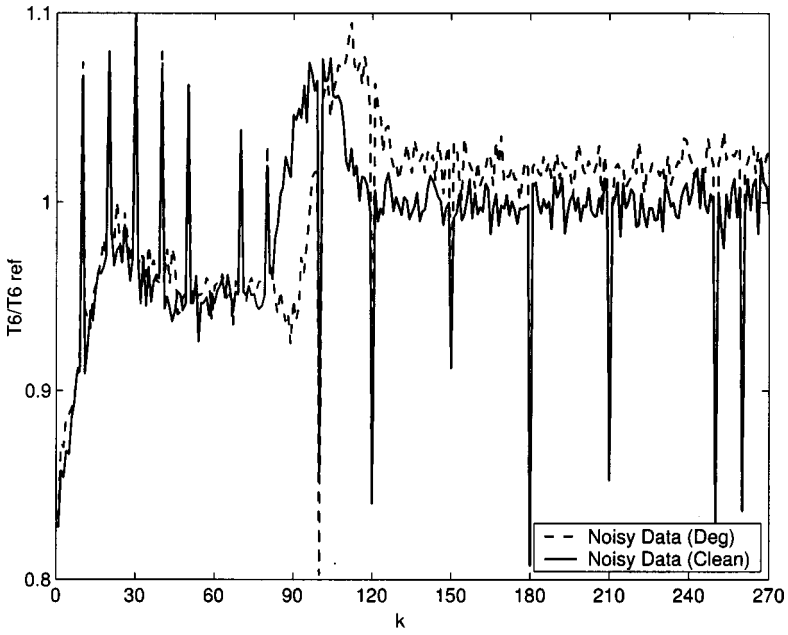


(a) Noisy data on LPT T6 engine for $\alpha$=0.008.

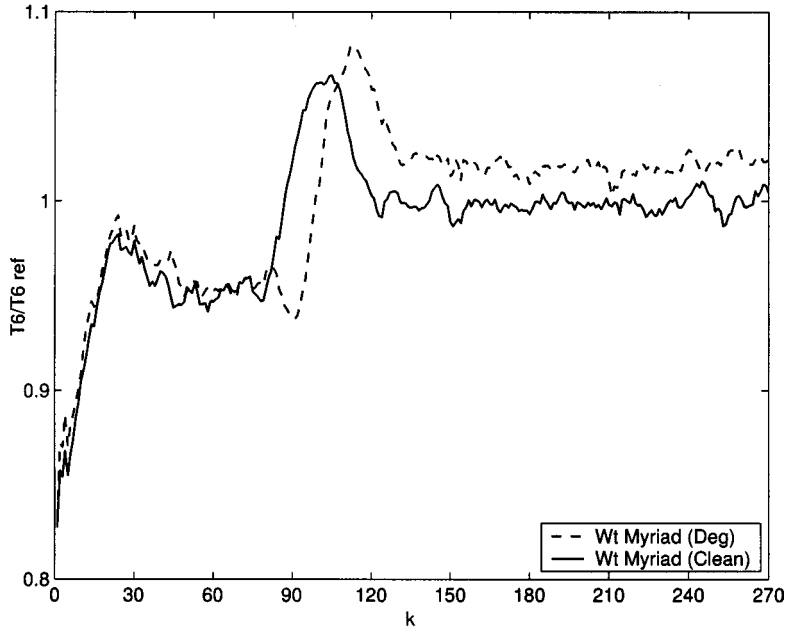


(b) Filtered data on LPT T6 engine for $\alpha$=0.008.

**Fig. 6 Clean and degraded signals during LPT fault on the acceleration process for T6**

The error measures used are the mean absolute error (MAE) that are widely used in signal processing and is particularly sensitive to the presence of outliers and edges in the data. The three ideal test signals are shown in Fig. 1, which show a signal from discrete time $k=1$ until $k=25$. These signals correspond to the step change in the measurements, a linear variation and a quadratic variation. Five outliers are added to test the robustness of the filter to impulses: $\theta(7)=-1.0$; $\theta(18)=1.0$; $\theta(10)=0.75$; $\theta(14)=-0.75$; $\theta(22)=-1.5$. Gaussian noise at various levels is added for the numerical experiments. Since the maximum value of the test signals is one and the minimum value is 0, by varying the noise level $\alpha$ between 0 and 0.4, a wide variety of signal to noise ratios found in typical gas path measurements can be simulated.

The effects of the linearity parameter $K$ on MAE is studied on the step, ramp edge, and quadratic signals for the five-point filter. The simulation results for step, ramp, and quadratic signal for different values of $K$ on MAE are shown in Fig. 2 with various noise levels in the data. For the five-point filter, low values of $K$

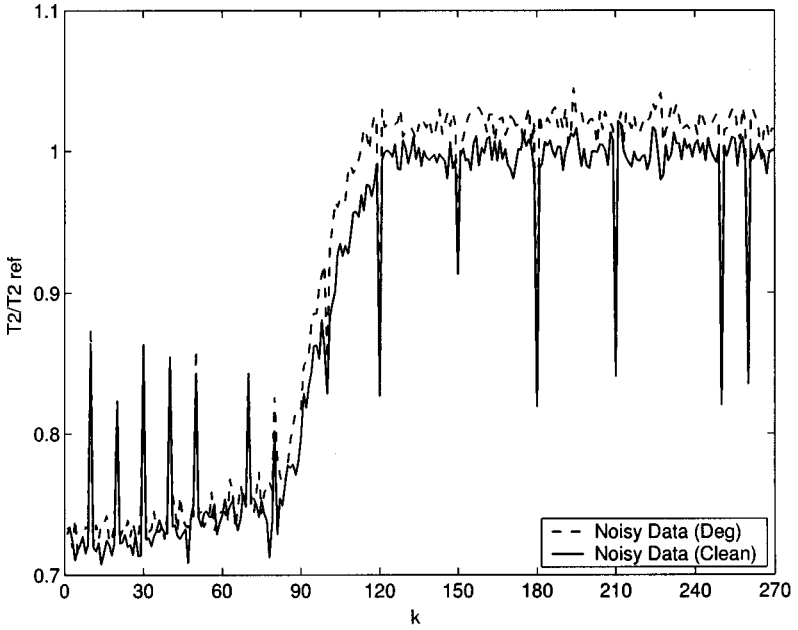


(a) Noisy data on IPC T2 engine for α=0.008.

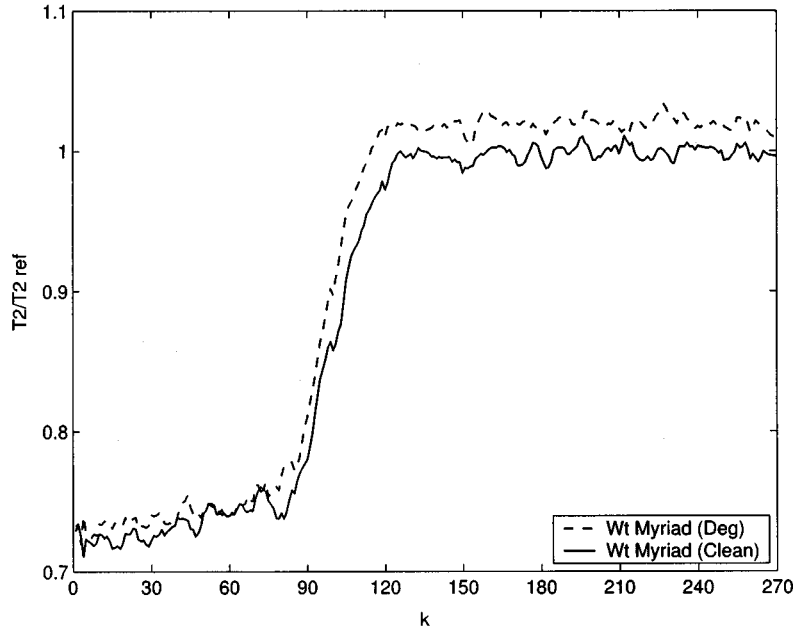


(b) Filtered data on IPC T2 engine for α=0.008.

**Fig. 7 Clean and degraded signals during IPC fault on the acceleration process for T2**

(such as $K=0.01$) cause the myriad performance to become worse than the FIR at higher noise levels. For high values of $K$ such as $K=5$, the myriad filter approaches the FIR filter in performance. Since gas path signals have reasonably low levels of noise and have more possibility for outlier contamination, a value of $K=0.1$ is selected.

## Gas Turbine Transient Signal

The trajectories for a clean and deteriorated engine are presented during an acceleration process. The deteriorated engine had single component faults in LPT (low pressure turbine) and IPC (intermediate pressure compressor) implanted, respectively. The signals of LPT fault and IPC fault on T2 and T6 during transients are obtained from [18]. These ideal signals are shown in Fig. 3 and Fig. 4.

The noise level $\alpha$ of 0.004 is the level of noise used in [18]. We use $\alpha=0.004$ and $\alpha=0.008$ to simulate conditions with normal data and low quality data, respectively. Outliers are also added to the signals. The noisy signals are shown in Figs. 5(*a*), 6(*a*) and 7(*a*). Tables 1–2 show the MAE values on the T2 measurements.

**Table 1 MAE for T2 engine with $\alpha$=0.004**

| | LPT T2 | | IPC T2 | |
|---|---|---|---|---|
| Filter | Degraded | Clean | Degraded | Clean |
| FIR | 0.1149 | 0.1101 | 0.1085 | 0.1090 |
| MYRIAD | 0.0740 | 0.0694 | 0.0666 | 0.0690 |
| WMYRIAD | 0.0549 | 0.0503 | 0.0483 | 0.0503 |

**Table 2 MAE for T2 engine with $\alpha$=0.008**

| | LPT T2 | | IPC T2 | |
|---|---|---|---|---|
| Filter | Degraded | Clean | Degraded | Clean |
| FIR | 0.1237 | 0.1136 | 0.1222 | 0.1277 |
| MYRIAD | 0.0829 | 0.0735 | 0.0817 | 0.0871 |
| WMYRIAD | 0.0669 | 0.0550 | 0.0635 | 0.0722 |

**Table 3 MAE for T6 engine with $\alpha$=0.004**

| | LPT T6 | | IPC T6 | |
|---|---|---|---|---|
| Filter | Degraded | Clean | Degraded | Clean |
| FIR | 0.1162 | 0.1111 | 0.1066 | 0.1148 |
| MYRIAD | 0.0681 | 0.0648 | 0.0588 | 0.0671 |
| WMYRIAD | 0.0521 | 0.0498 | 0.0459 | 0.0519 |

**Table 4 MAE for T6 engine with $\alpha$=0.008**

| | LPT T6 | | IPC T6 | |
|---|---|---|---|---|
| Filter | Degraded | Clean | Degraded | Clean |
| FIR | 0.1260 | 0.1247 | 0.1203 | 0.1254 |
| MYRIAD | 0.0773 | 0.0791 | 0.0729 | 0.0782 |
| WMYRIAD | 0.0634 | 0.0638 | 0.0593 | 0.0645 |

Results for both the clean and degraded engines are shown. Tables 3–4 shows the MAE values for the T6 measurements. There is a considerable reduction in the MAE using the myriad filter with $K=0.1$, compared to the FIR filter. Again, results for both the clean and degraded engine are shown. The results for the weighted myriad filter shown in these tables will be discussed later in this paper.

## Weighted Myriad Algorithm

A problem in the myriad filter discussed above is in the selection of the linearity parameter $K$. Weighted myriad filters provide a way to avoid the selection of the linearity parameter.

Consider a set of observations $\{x_i\}_{i=1}^N$ and a set of filter weights $\{w_i\}_{i=1}^N$. Define the observation vector $\mathbf{x}\triangleq[x_1,x_2,\ldots,x_N]^T$ and the weighted vector $\mathbf{w}\triangleq[w_1,w_2,\ldots,w_N]^T$. For a given $K>0$, the WMyF (weighted myriad filter) output is given by [10]

$$\hat{\beta}_K(\mathbf{w},\mathbf{x})\triangleq \text{myriad}(K;w_1\circ x_1,w_2\circ x_2,\ldots,w_N\circ x_N)$$

$$=\arg\min_\beta G_K(\beta,\mathbf{w},\mathbf{x}) \tag{13}$$

The function

$$G_K(\beta,\mathbf{w},\mathbf{x})\triangleq\prod_{i=1}^{N}[K^2+w_i(x_i-\beta)^2] \tag{14}$$

is called the weighted myriad objective function since it is minimized by the weighted myriad and $w_i\circ x_i$ denotes the weighting operation in Eq. (13). As shown in Appendix A,

$$\hat{\beta}_{K1}(\mathbf{w}_1,\mathbf{x})=\hat{\beta}_{K2}(\mathbf{w}_2,\mathbf{x}),\quad \text{if}\quad \frac{\mathbf{w}_1}{K_1^2}=\frac{\mathbf{w}_2}{K_2^2} \tag{15}$$

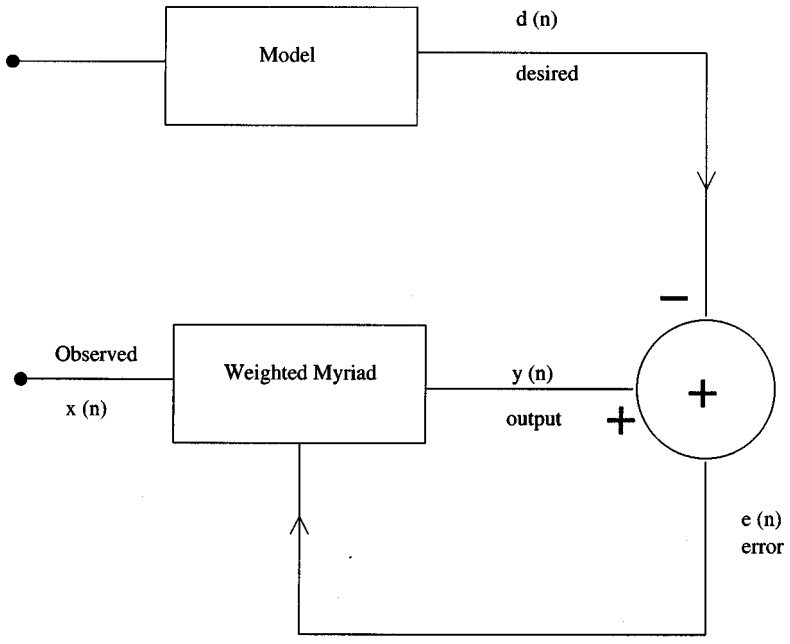


**Fig. 8 Schematic for adaptive filter optimization**

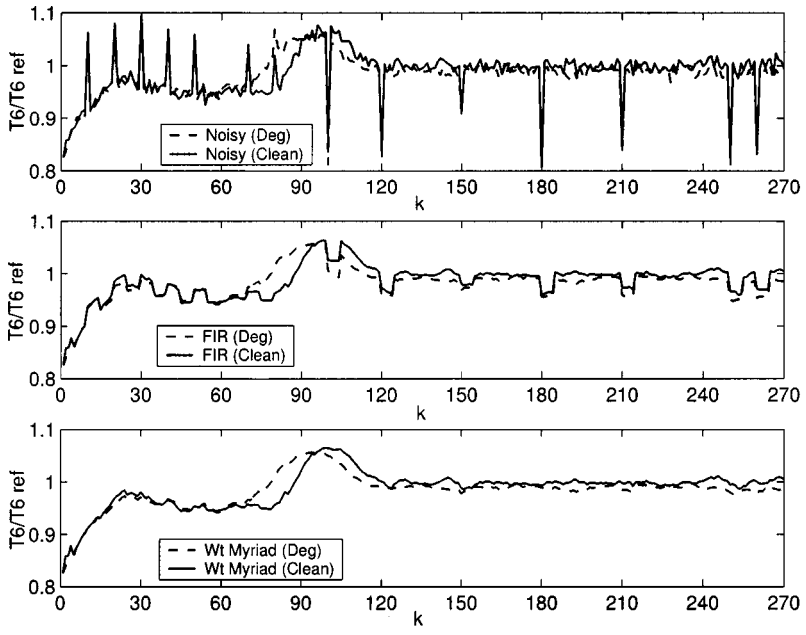


(a) Comparison of filters using outliers on IPC T6 engine for α=0.008.

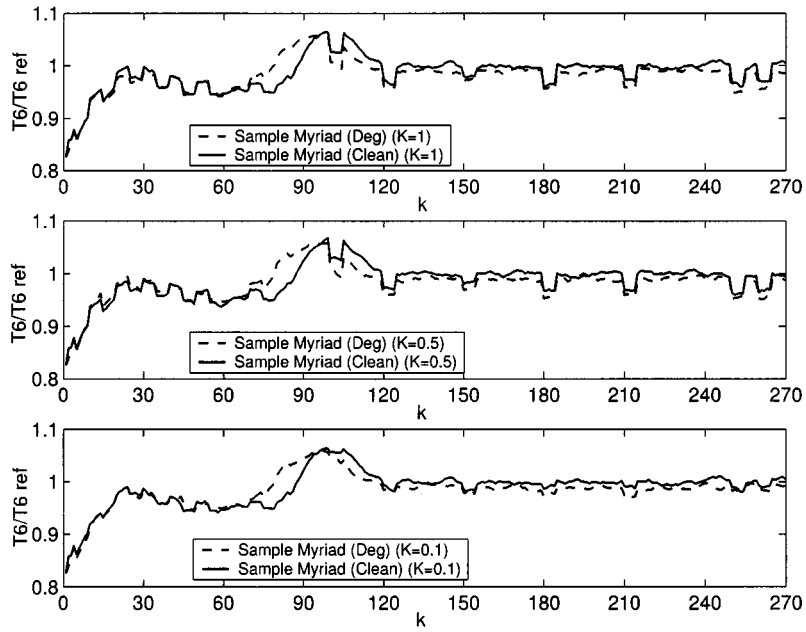


(b) Sample myriad filter using outliers on IPC T6 engine for α=0.008.

**Fig. 9 A comparison of filters**

Thus the filter output depends on $\mathbf{w}/K^2$. Thus the problem of finding the optimal linearity parameter $K$ is avoided by using the weighted myriad filter. However, the problem of finding the appropriate value of $K$ is now replaced by finding the appropriate weight vector. In general, the myriad is the global minima among several local minimum points of $G(\beta)$. To compute the myriad, one needs to find the roots of polynomial $G'(\beta)$, and test all the local minima to find the global minima.

## Adaptive Weighted Myriad Filter Algorithm

For applications where the statistics of the signal are unknown or time varying, the adaptive algorithm is very useful. For gas path measurements, historical data is often used to obtain representative numbers for measurement uncertainty. However, it is likely that the uncertainty changes for different outliers and engines and for different operating conditions. The adaptive algo-

rithm avoids the need for this simplification. An adaptive steepest descent method algorithm is used to optimize the filter weights. The update is computationally comparable to the least mean absolute deviation (LMAD) algorithm. The weight update algorithm is given as

$$w_i(n+1) = P\left( w_i(n) + \mu \,\mathrm{sgn}[e(n)] \left\{ \frac{(y-x_i)}{\left[1+\frac{w_i}{K^2}(y-x_i)^2\right]^2} \right\}(n) \right) \tag{16}$$

where $e(n)=y(n)-d(n)$ is the error at the nth iteration, $d$ is the desired signal, $y(n)$ is the WMyF output at the $n$th iteration, $n$ is the number of iterations, $\mu$ is the step size, $w_i(n)$ denotes the $i$th weight at the $n$th iteration, $P[u]$ is set to a small positive value $\varepsilon$ if $u<0$. The derivation of the algorithm is condensed from [14] and is given in Appendix B. The above algorithm is started with weights equal to 1 at iteration $n=1$, $K=0.1$, and $\mu=5.0\times10^{-3}$. The proposed schematic of the adaptive filter is shown in Fig. 8.

In applications where non-Gaussian processes naturally arise in practice, the myriad-based algorithms lead to significant advantages. In gas turbine applications, the presence of outliers in the data is well known. The weighted myriad filters have the potential to perform significantly better than both linear and median filters in Gaussian and non-Gaussian environments. For applications where the statistical characteristics of the underlying signals may be unknown, varying adaptive algorithms are used. A disadvantage of the myriad filter is its complicated definition and implementation compared to the linear filters. However, once implemented, this is hidden from the user.

## Simulation Results

This adaptive algorithm was evaluated through a computer simulation example involving denoising gas turbine measurements contaminated with Gaussian noise. The trajectories for a clean and deteriorated engine are considered for this problem. In our simulation example, the degraded signal and clean signal were chosen that had single component faults: LPT (low pressure turbine) and IPC (intermediate pressure compressor) faults. The signal is corrupted by adding noise level $\alpha=0.004$ [18] yielding the noisy observed signal. A further noise level of $\alpha=0.008$ is also used.

The objective of this adaptive algorithms is to train the weighted myriad to converge the filter weights that minimize the absolute value of the error signal $e(n)$ between the filter output signal $y(n)$ and desired signal $d(n)$. This adaptive algorithm is a simple, fast, and practical weighted myriad filter algorithm. This achieves a lower MAE than the FIR and sample myriad at comparable convergence speeds as shown in the results in Tables 1–4. The weighted myriad filter has the best outputs and lowest mean errors. The effects of 5-point filter are plotted with $\alpha=0.008$ for the noisy data and weighted myriad in Figs. 5–7.

In this case, we took both a degraded signal and a clean signal for a T2 LPT engine sensor signal. Figure 5(*a*) shows the noisy data, for both a degraded and a clean engine. The weighted myriad filtered data is shown in Fig. 5(*b*) for the degraded and clean engine signal. Similarly, the effects of LPT T6 for both the degraded and clean signal are plotted with noisy data in Fig. 6(*a*) and for the weighted myriad data in Fig. 6(*b*). The results for the IPC engine sensor signal for the T2 engine for the degraded and clean signal are also plotted in Fig. 8. Figure 7(*a*) shows the noisy data, for both degraded and clean engine and Fig. 7(*b*) shows the filtered data. From these figures, and results in Tables 1–4, it is clear that considerable noise reduction is obtained using the weighted myriad filter. The outcome of different filters such as FIR, sample myriad, and weighted myriad are compared and studied. From Fig. 9(*a*) we can see that the weighted myriad filter shows much better performance and outlier removal when compared to the FIR filter, which is not able to remove the outliers. The sample myriad filter results are plotted in Fig. 9(*b*) for different values of $K$. It is clear from the results that the sample myriad can be controlled by adjusting the linear parameter $K$, whereas the adaptive weighted myriad filter provides a way to avoid the selection of the linear parameter $K$. However, a low value of $K=0.1$ appears to work quite well for the signals in this study. Note that the sample myriad used the value $K=0.1$ in this study and the values of $K$ that give good results may change for a different type of signal and noise characteristics.

This paper therefore offers two approaches to denoising gas path signals. The first is based on the simple myriad and uses a suitable value of $K$ based on representative signals and known statistics of the system. Our results show that $K=0.1$ works quite well for signals polluted by outliers. This approach is suitable for ground based diagnostics systems. The sample myriad and filter is implemented as a MATLAB program using built in functions that calculate the roots of polynomials and are simple and fast. The second approach is the powerful weighted myriad approach that adapts to changes in both signals and their statistics and is especially suitable for online applications. The adaptive myriad is implemented using the weight update Eq. (*B*16) in Appendix A using MATLAB. While the adaptive myriad is a useful tool for outlier contaminated gas path measurements, the optimum weightings are not known until all the available data is processed. Thus there is a lag caused by the filter. Engine faults result in a change in the engine state measured over many samples, and should not affect the myriad filter. Abrupt faults will not be impacted by filters with a low window length and gradual faults that develop slowly over time will also not be impacted. However, any intermittent faults may be impacted as they can appear as outliers to the filter. Note that the full power of the adaptive filter can be better demonstrated with real data. That is a subject of future work.

## Conclusions

In this study, we look at the myriad filter as a substitute for the moving average filter that is widely used in the gas turbine industry. Results with transient gas path measurement signals show that the myriad filter has good noise reduction qualities when compared to moving average FIR filters. There is considerably more noise reduction obtained by the myriad filter when compared to the FIR filters. The results show that there is good outlier removal by the weighted myriad filter, which is an important element of a filter. The adaptive weighted myriad filter shows even greater noise reduction when compared to the sample myriad and FIR filter in the gas turbine diagnosis. The use of such a filter prior to performing fault isolation and detection functions is likely to lead to improved performance of the diagnostic system.

## Nomenclature

- arg = argument function
- $d$ = desired signal
- $e$ = filtering error
- $G_k(\beta)$ = weighted myriad function
- IPC = intermediate pressure compressor
- $K$ = linearity parameter
- $k$ = discrete time
- LPT = low pressure turbine
- MAE = mean absolute error
- $n$ = iteration number of weighted myriad
- sgn = signum function
- T2 = IPC total outlet temperature
- T6 = LPT total outlet temperature
- $x$ = noisy input signal
- $x^0$ = ideal input signal
- $y$ = output of myriad filter
- $w$ = weights of myriad filter

$\alpha$ = noise level
$\varepsilon$ = Gaussian noise
$\hat{\beta}_k$ = sample myriad
$\mu$ = step size
$\theta$ = non-Gaussian outliers

## Appendix A: Filter Weights and the Linearity Parameter

Using negative weights results in the potential instability of the filter so it is defined using positive weights: $w_i \geqslant 0$, $i=1,2,\ldots,N$. The WMyf output is the value of $\beta$ at its global minimum of $G_K(\beta)$. For $w_i \geqslant 0$ and $K>0$, $G(\beta)>0$ for all $\beta$. Furthermore, $G_K(\beta)$ is a polynomial in $\beta$ of degree $2N$. The myriad $\hat{\beta}$ is defined as the minimum value of $G_K(\beta)$ and occurs at one of the roots of $G'_K(\beta)$,

$$G'_K(\hat{\beta})=0. \tag{A1}$$

Differentiating (8) gives

$$G'_K(\beta)=\sum_{j=1}^{N} 2w_j(\beta-x_j)\prod_{\substack{l=1\\ l\neq j}}^{N}[K^2+w_l(\beta-x_l)^2] \tag{A2}$$

which is a polynomial of degree $2N-1$ with as many as $2N-1$ real roots. Using (8) and (12), we get

$$G'_K(\beta)=2G'_K(\beta)\sum_{j=1}^{N}\frac{w_j(\beta-x_j)}{K^2+w_j(\beta-x_j)^2} \tag{A3}$$

Since $G'_K(\beta)>0$, the filter output $\hat{\beta}$ must satisfy

$$\sum_{j=1}^{N}\frac{\frac{w_j}{K^2}(\hat{\beta}-x_j)}{1+\frac{w_j}{K^2}(\hat{\beta}-x_j)^2}=0 \tag{A4}$$

The above equation shows that even if the value of $K$ is changed the same filter output is obtained provided the weights are suitably scaled. Therefore,

$$\hat{\beta}_{K1}(\mathbf{w}_1,\mathbf{x})=\hat{\beta}_{K2}(\mathbf{w}_2,\mathbf{x}) \quad \text{if} \quad \frac{\mathbf{w}_1}{K_1^2}=\frac{\mathbf{w}_2}{K_2^2} \tag{A5}$$

## Appendix B: Optimal Filter Weights

In order to find the optimal weights, the steepest descent method can be used to minimize the MAE cost function $J(w)$ [14] where

$$J(\mathbf{w},K)=E\{|y_K(\mathbf{w},\mathbf{x})-d|\} \tag{B1}$$

and $E\{\cdot\}$ is the statistical expectation and $d$ is the desired signal. Here $d$ can be generated by an onboard model of the engine. The following algorithm is used to update the filter weights

$$w_i(n+1)=P\left[w_i(n)-\mu\frac{\partial J}{\partial w_i}(n)\right] \tag{B2}$$

where $w_i(n)$ denotes the $i$th weight at the $n$th iteration, $\mu>0$ is the step size of the update, and $P[\cdot]$ is defined as

$$P[u]\triangleq u, \quad u>0$$
$$0, \quad u\leqslant 0 \tag{B3}$$

In practice $P[u]$ is set to a small positive value $\epsilon$ if $u\leqslant 0$. Differentiating (Eq. (A5)) we obtain;

$$\frac{\partial J}{\partial w_i}(n)=E\left\{\operatorname{sgn}[y(n)-d(n)]\frac{\partial y}{\partial w_i}(n)\right\} \tag{B4}$$

Since a lack of knowledge of signal statistics makes evaluation of statistical expectation $E$ difficult, an instantaneous estimate for the gradient is used. Putting (Eq. (B3)) into (Eq. (B2)) yields,

$$w_i(n+1)=P\left\{w_i(n)-\mu\operatorname{sgn}[e(n)]\frac{\partial y}{\partial w_i}(n)\right\} \tag{B5}$$

where $e(n)=y(n)-d(n)$ is the error at the $n$th iteration. To find $\partial y/\partial w_i$ for a given $K$, we can write Eq. (A1) as

$$G'_K(y)=2G_K(y,w,x)\sum_{j=1}^{N}\frac{w_j(y-x_j)}{K^2+w_j(y-x_j)^2} \tag{B6}$$

Consider $K$; the other weights and input vector $x$ are constant. Then,

$$G'(y)=2G(y,w_i)H(y,w_i) \tag{B7}$$

where

$$H(y,w_i)\triangleq\sum_{j=1}^{N}\frac{w_j(y-x_j)}{K^2+w_j(y-x_j)^2} \tag{B8}$$

Since $G'(y)=0$,

$$G(y,w_i)H(y,w_i)=0 \tag{B9}$$

Since $G(y,w_i)\geqslant 0$,

$$H(y,w_i)=0 \tag{B10}$$

Differentiating the above equation with respect to $w_i$ yields

$$\frac{\partial H}{\partial y}\cdot\frac{\partial y}{\partial w_i}+\frac{\partial H}{\partial w_i}=0 \quad \frac{\partial y}{\partial w_i}=-\frac{\frac{\partial H}{\partial w_i}}{\frac{\partial H}{\partial y}} \tag{B11}$$

$$\frac{\partial H}{\partial w_i}=\frac{\partial}{\partial w_i}\sum_{j=1}^{N}\frac{w_j(y-x_j)}{K^2+w_j(y-x_j)^2}=\frac{1}{K^2}\left\{\frac{(y-x_i)}{\left[1+\frac{w_j}{K^2}(y-x_i)^2\right]^2}\right\} \tag{B12}$$

$$\frac{\partial H}{\partial y}=\frac{\partial}{\partial y}\sum_{j=1}^{N}\frac{w_j(y-x_j)}{K^2+w_j(y-x_j)^2}=\sum_{j=1}^{N}\frac{w_j}{K^2}\cdot\frac{1-\frac{w_j}{K^2}(y-x_j)^2}{\left[1+\frac{w_j}{K^2}(y-x_j)^2\right]^2} \tag{B13}$$

Putting Eq. (B12) and Eq. (B11) in Eq. (B10) we get

$$\frac{\partial y}{\partial w_i}=\frac{\left\{\frac{-(y-x_i)}{\left[1+\frac{w_j}{K^2}(y-x_i)^2\right]^2}\right\}}{K^2\left\{\sum_{j=1}^{N}\frac{w_j}{K^2}\frac{1-\frac{w_j}{K^2}(y-x_j)^2}{\left[1+\frac{w_j}{K^2}(y-x_j)^2\right]^2}\right\}} \tag{B14}$$

Putting Eq. (A5) into Eq. (A4) and adding a stability constant $\alpha$ yields

$$w_i(n+1)=P\left(\begin{array}{l} w_i(n)+\mu\ \mathrm{sgn}[e(n)]\dfrac{\left\{\dfrac{(y-x_i)}{\left[1+\dfrac{w_j}{K^2}(y-x_i)^2\right]^2}\right\}(n)}{K^2\left\{a+\displaystyle\sum_{j=1}^{N}\dfrac{w_j}{K^2}\dfrac{1-\dfrac{w_j}{K^2}(y-x_j)^2}{\left[1+\dfrac{w_j}{K^2}(y-x_j)^2\right]^2}\right\}(n)} \end{array}\right) \tag{B15}$$

We can remove the denominator from the update term in the above equation as it does not effect the direction of the gradient estimate or the values of the final weights. This leads to

$$w_i(n+1)=P\left(\begin{array}{l} w_i(n)+\mu\ \mathrm{sgn}[e(n)]\left\{\dfrac{(y-x_i)}{\left[1+\dfrac{w_j}{K^2}(y-x_i)^2\right]^2}\right\}(n) \end{array}\right) \tag{B16}$$

## References


[1] Volponi, A. J., and Urban, L. A., 1992, ''Mathematical Methods of Relative Engine Performances Diagnostics,'' SAE Trans., Journal of Aerospace Technical Paper 922048, p. 101.

[2] Doel, D. L., 2003, ''Interpretation of Weighted-Least-Squares Gas Path Analysis Results,'' J. Eng. Gas Turbines Power, **125**, pp. 624–633.

[3] DePold, H., and Gass, F. D., 1999, ''The Application of Expert Systems and Neural Network to Gas Turbine Prognostics and Diagnostics,'' J. Eng. Gas Turbines Power, **121**, pp. 607–612.

[4] Fasching, W. A., and Stricklin, R., 1982, CF6 Jet Engine Diagnostics Program, Final Report 1, NASA/CR-165582.

[5] Glenny, D. E., 1988, ''Gas Path Analysis and Engine Performance Monitoring in a Chinook Helicopter,'' Paper 25 AGARD-CP-448 1, Engine Condition Monitoring Technology and Experience.

[6] Mathioudakis, K., Kamboukos, P. H., and Stamatis, A., 2002, ''Turbofan Performance Deterioration Tracking Using Non-Linear Models and Optimization Techniques,'' J. Turbomach., **124**, pp. 580–587.

[7] Ganguli, R., 2002, ''Noise and Outlier Removal From Jet Engine Health Signals Using Weighted FIR Median Hybrid Filters,'' Mech. Syst. Signal Process., **16**, pp. 967–978.

[8] Ganguli, R., 2003, ''Jet Engine Gas Path Measurement Filtering Using Center Weighted Idempotent Median Filters,'' J. Propul. Power, **19**, pp. 930–937.

[9] Lu, P. J., and Hsu, T. C., 2002, ''Application of Autoassociative Neural Network on Gas-Path Sensor Data Validation,'' J. Propul. Power, **18**, pp. 879–888.

[10] Li, Y. G., 2003, ''A Gas Turbine Diagnostic Approach With Transient Measurements,'' Proc. Inst. Mech. Eng., Part A, J. Power Energy, **217**, pp. 169–177.

[11] Eustace, R. W., Woodyatt, B. A., Merrington, G. L., and Runacres, A., 1994, ''Fault Signatures Obtained From Fault Implant Tests on an F404 Engine,'' J. Eng. Gas Turbines Power, **116**, pp. 178–183.

[12] Merrington, G. L., 1988, ''Identification of Dynamic Characteristics for Fault Isolation Purposes in a Gas Turbine Using Closed-Loop Measurements,'' *Engine Condition Monitoring-Technology and Experience*, AGARD-CP-448.

[13] Merrington, G. L., 1994, ''Fault Diagnosis in Gas Turbines Using a Model-Based Technique,'' J. Eng. Gas Turbines Power, **116**, pp. 374–380.

[14] Kalluri, S., and Arce, G. R., 1998, ''Adaptive Weighted Myriad Filter Algorithms for Robust Signal Processing in Alpha-Stable Noise Environments,'' IEEE Trans. Signal Process., **46**, pp. 322–334.

[15] Gonzalez, J. G., and Arce, G. R., 2002, ''Statistically-Efficient Filtering in Impulsive Environments: Weighted Myriad Filters,'' EURASIP J. Appli. Signal Process., **1**, pp. 4–20.

[16] Gonzalez, J. G., and Arce, G. R., 2001, ''Optimality for the Myriad Filter in Practical Impulsive-Noise Environments,'' IEEE Trans. Signal Process., **49**, pp. 438–441.

[17] Kalluri, S., and Arce, G. R., 2000, ''Fast Algorithm for Weighted Myriad Computation by Fixed Point Search,'' IEEE Trans. Signal Process., **48**, pp. 159–171.

[18] Ogaji, S. O. T., Li, Y. G., Sampath, S., and Singh, R., ''Gas Path Fault Diagnosis of a Turbofan Engine From Transient Data Using Artificial Neural Networks,'' ASME Paper GT2003-38423.

# Transient Analysis of and Control System for Advanced Cycles Based on Micro Gas Turbine Technology

**Alberto Traverso**
e-mail: alberto.traverso@unige.it

**Federico Calzolari**

**Aristide Massardo**

TPG-DiMSET,
Università di Genova,
Genova, Italy

*Microturbines have a less complex mechanical design than large-size gas turbines that should make it possible to fit them with a more straightforward control system. However, these systems have very low shaft mechanical inertia and a fast response to external disturbances, such as load trip, that make this very difficult to do. Furthermore, the presence of the recuperator requires smooth variations to the Turbine Outlet Temperature (TOT), when possible, to ensure reduced thermal stresses to the metallic matrix. This paper, after a brief overview of microturbine control systems and typical transients, presents the expected transient behavior of two advanced cycles: the Externally Fired micro Gas Turbine (EFmGT) cycle, where the aim is to develop a proper control system set-up to manage safe part-load operations at constant rotational speed, and a solar Closed Brayton Cycle (CBC), whose control system has to ensure the maximum efficiency at constant rotational speed and constant Turbine Inlet Temperature (TIT).*
[DOI: 10.1115/1.1839918]

## 1 Introduction

Microturbines are now considered ready to conquer energy markets thanks to their flexibility and low maintenance, which should make them extremely cost effective in the near future [1]. Nevertheless, the microturbine control system represents a key problem for stable operation at different working conditions, ensuring a flexible usage of the machine. The experience gained in large-size turbine control systems [2] can also be profitably exploited in the microturbine field, but the time scale of the phenomena are extremely reduced due to the small mechanical inertia of the shafts, which make microturbines difficult systems to control.

This paper focuses, first, on the simulation of the transient behavior in both the simple and the recuperated cycle of the micro Gas Turbine (the calculated data have been checked previously with experimental ones, thanks to collaboration with ENEL [3]), and secondly, on extensions to microturbine-based advanced cycles, such as an Externally Fired micro Gas Turbine cycle (EFmGT) and a Closed Brayton Cycle (CBC) for solar applications, which are presented in detail. The former is actually under construction at ANSALDO Ricerche (ARI) laboratories, where experimental activities will be undertaken in order to assess its off-design performance (off-design calculated performance and transient behavior are presented in [4]). The latter represents a case-study that has been conducted in collaboration with the Italian Space Agency (ASI) to assess the control system to be implemented on this type of cycle, which is attractive because it offers better performance and greater compactness than other static generators [5–7].

When a microturbine cycle is modified into an Externally Fired cycle (EFmGT), the large thermal inertia of the heat exchanger section becomes the most influential parameter acting on the transient behavior of the plant. Moreover, the coupling of the long-term response of the heat exchangers with the short-term response of the turbine rotor requires a suitable control system to protect the machine from unstable behavior and dangerous operating regions, which may affect component life.

On the other hand, as far as a Closed Brayton Cycle (CBC) for space applications is concerned, the relatively smooth transients should be controlled to continually provide maximum efficiency, which leads to a reduction of weight and cost for the whole system in the end.

At present, the transient behavior and control systems, such as Humid Air Cycle (mHAT) [8] and hybrid systems based on Molten Carbonate or Solid Oxide Fuel Cells (MCFC-SOFC), of other advanced cycles are also under investigation at the TPG laboratories [9].

## 2 mGT Transient Analysis: TRANSEO Code

The TRANSEO code, employed for the simulations presented here, is under continuous development at the TPG laboratories. It exploits the MATLAB© and Simulink visual environment for the off-design, transient and dynamic analyses of advanced energy systems based on microturbine technology.

Its modular structure allows any type of system to be built and run: now the general structure of the code has been established, and the on-going work is basically aiming at increasing, improving, and assessing the components of the standard library. TRANSEO has already been used for the off-design calculations in [4].

From the point of view of the transient analysis, it is worthy mentioning the technique used for the data transfer between two adjoining components. TRANSEO applies the interconnecting volume approach, where a volume is interposed between two consequent components. Each component is in charge of calculating its own mass inflow or mass outflow, while each plenum has to define the boundary conditions in terms of pressure and temperature. In the plenum, the total temperature is maintained while the total pressure is assumed to be equal to the static pressure. This means that a plenum carries out an adiabatic transformation where the flow kinetic energy is dissipated: as a consequence, plenums should be inserted where velocity is negligible, while the real kinetic-pressure transfers should be managed within each component. In this way, the connecting standard exposed in [10] can

Contributed by the International Gas Turbine Institute (IGTI) of THE AMERICAN SOCIETY OF MECHANICAL ENGINEERS for publication in the ASME JOURNAL OF ENGINEERING FOR GAS TURBINES AND POWER. Paper presented at the International Gas Turbine and Aeroengine Congress and Exhibition, Atlanta, GA, June 16–19, 2003, Paper No. 2003-GT-38269. Manuscript received by IGTI, Oct. 2002, final revision, Mar. 2003. Associate Editor: H. R. Simmons.

  

easily be handled as a subcase of this protocol. Moreover, there is a basic theoretical difference from other approaches adopted in open literature [11,12]: in those cases the interconnecting plenum volumes are often assumed to be equal to the downstream or upstream component volume, in order to reproduce their fluidodynamic inertia. This type of ''superposition of the effects'' is often used but has still not been verified in detail (in principle it is only applicable to linear systems). For this reason, TRANSEO locates all the fluidodynamic, thermal and mechanical inertia in each component, while plenum volumes are assumed to be equal to the actual interconnecting ducts of the plant or small enough not to affect the results. In the latter case, a time-characterization of the plenum becomes mandatory in order to ensure that it has no influence on the simulation results. To help the user, TRANSEO automatically produces a special time-characterization of all the main components of the plant: in this way the most influential components can be highlighted and the proper sample time and plenum volumes selected [13].

Referring to the plenum, the plenum unsteady governing equations of continuity and energy can be expressed as follows:

$$\frac{\partial(\rho R)}{\partial t} = \frac{R(\dot{m}_{\text{in}} - \dot{m}_{\text{out}})}{V} \tag{1}$$

$$\frac{\partial p}{\partial t} = \frac{kR}{c_p V}((\dot{m}c_p T)_{\text{in}} - (\dot{m}c_p T)_{\text{out}}) \tag{2}$$

The perfect gas state law is used to calculate the updated temperature once pressure $p$ and density $\rho$ are known. The momentum equation is not necessary as the internal transformation inside the plenum is pre-established and the mass inflows and outflows are given as known inputs, as stated above. Starting from (1) and (2), applying a mass flow step or temperature step to the plenum, the following time characteristic constants can be found:

$$\tau = \frac{\rho V}{k\dot{m}} \tag{3}$$

The time value expressed by (3) can be compared to the characteristic time of the real components of the plant, then the volume for the plenum can be properly chosen: from TPG experience, it is sufficient to have a characteristic time for the plenum of two orders of magnitude lower than the lowest characteristic time of the components.

Thanks to its modular organization, TRANSEO is, at the moment, composed of more than 25 modules including rotating components, heat exchangers and fuel cells.

## 3 Microturbine: Control System and Transients

At present it is still quite difficult to collect data on the main parameter settings in the control system of a microturbine engine because they are either quite new products that have not yet become common in the energy market or the manufacturers have tried to keep the data confidential. For these reasons the control system for a sample microturbine was set in order to provide the model with quite stable behavior close to the design point and allow the system a 50% maximum load decrease, which is a reasonable limit, also confirmed by some field data [3,14].

Owing to the fast response of the microturbine shaft to external disturbances, the fuel valve is a key-component of the control system and it needs to be fast enough to allow significant load changes. In this paper, all the results have been produced by implementing a PID (Proportional, Integral, Derivative) controller for the valves. With regard to the rotor revolutions, a threshold of 5% overspeed has been set: if such a limit is passed, fuel is definitively cut and the machine stops (the same if the TOT threshold is overcome).

The fuel valve model is illustrated in Fig. 1: a linear relationship between the valve fractional opening (FO) and the fuel mass flow rate has been considered (the pressure drop is supposed to be

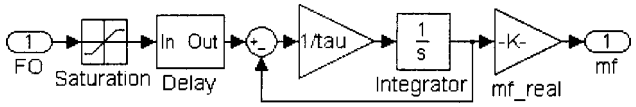


**Fig. 1 Scheme of the fuel valve**

almost fixed). Two sequential delays act on the actual valve opening position: a constant delay (0.01 s) and a first order delay based on a time constant (0.2 s). The former represents the most critical parameter because during such a period the valve doesn't actually regulate and instability may occur.

In the EFmGT and CBC configurations, a general-purpose valve model has also been employed: the model is similar to the fuel valve one, except for the nonlinear relationship between the mass flow rate and fractional opening, which can be chosen from three predefined characteristic curves: gate, disk and globe valves [15]. Also in this case, the two delays have been assumed equal to 0.01 s and 0.2 s, respectively.

Figure 2 reports the transient response of the simple and recuperated cycle microturbine, employed in the advanced cycles described here: the machine used for the analysis was an Elliott Energy Systems TA-80R (80 kWe). The only difference between the two systems is the presence of the recuperator in the recuperated cycle, which introduces a large thermal inertia into the system. The recuperator model is analyzed in [4].

In the case study, the control system reacts against a sudden load decrease of 25%. The recuperated system presents less prompt behavior due to the lower initial value of the fuel valve fractional opening: this is justified by its higher efficiency, which allows the fuel consumption to be almost halved. Furthermore, if the time scale should be extended up to 500–600 s, after the fast transient caused by the load step change, the recuperated cycle would show a relatively ''slow'' transient until the final steady

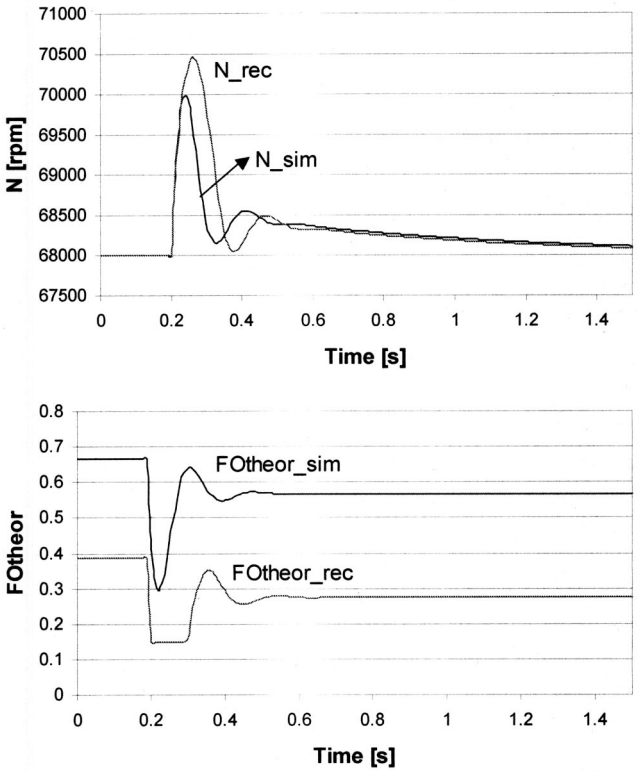


**Fig. 2 Simple and recuperated cycle response to a load step decrease of 25%: rotational speed and fractional opening of fuel valve versus time**

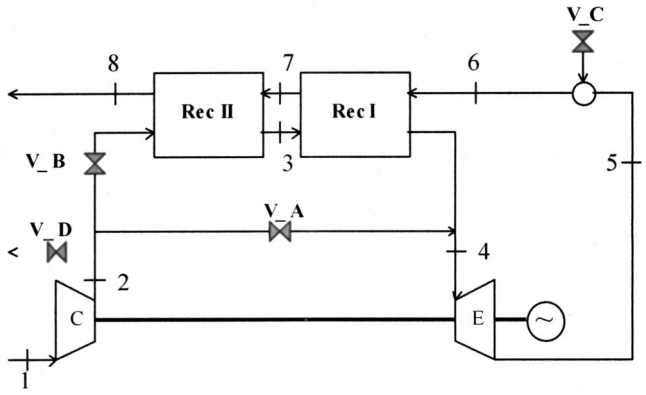


**Fig. 3 EFmGT pilot plant: main regulation valves**

state value, because of the recuperator thermal inertia. The complete transient response of the recuperated cycle is reported in [3], where a preliminary comparison with experimental data is included.

## 4 Advanced Cycles Based on Micro Gas Turbine Technology

The transient behavior analysis of simple and recuperated micro Gas Turbine cycles was the necessary step for proceeding with the study of the two advanced configurations, the EFmGT and the CBC, considered in this paper.

**4.1 Externally Fired Micro Gas Turbine (EFmGT).** The collaboration between the Thermochemical Power Group (TPG) and ANSALDO Ricerche (ARI) has resulted in the design and the installation of an Externally Fired micro Gas Turbine at the ARI Laboratories [14], which represents a possible concept for future commercial applications.

The original configuration of the microturbine recuperated cycle (Elliott TA-80R) has been modified with the introduction of an additional high temperature heat exchanger, which should substitute the combustion chamber. The latter, which will be used only during the system start-up, will normally stand off because the necessary heat will be delivered by an external atmospheric combustion chamber fed with the expander exhausts (Fig. 3). Four valves are employed to control the EFmGT, *V_A* for the air bypass of the recuperators, *V_B* for maintaining a constant pressure drop across *V_A*, *V_C* for the fuel to the external combustor, *V_D* as an emergency valve for the compressor bleed.

Such a control scheme allows the control system to be uncoupled between a fast-response control loop, which is based on *V_A* and has to prevent the microturbine rotor from reaching an excessive speed, and a long-response control loop consisting of *V_C*, which should maintain *V_A* at its nominal position (5% open) and optimize cycle performance. *V_A* must be in accord with the shaft response: this makes it a fairly critical device because of the low shaft mechanical inertia; *V_C* only needs to be tuned to the heat exchanger thermal inertia, which is the main inertia of the whole system. Furthermore, a PID controller has been used for commanding *V_A* while a simpler PI for *V_C*: in fact, the effect of fuel flow variation on the cycle is strongly smoothed by the heat exchanger thermal inertia, which acts as a low-frequency filter.

The expected on-design and off-design performance of such a plant [4] shows that, even if the variable rotational speed should be regarded as the best option for controlling the plant, the constant speed strategy has been chosen in order to allow a simpler control system to be implemented and to avoid the microturbine rotor reaching dangerous resonance speeds. The high temperature heat exchanger is of metallic type (superalloy), because the experimentation is devoted to understanding and measuring the transient behavior of such a configuration rather then its peak performance: this forces the TIT to reach the upper limit of 800°C, which will be decreased to 750°C during the experimental activities to ensure the durability of the system and to prevent it from dangerous faults.

At present an Elliott TA-80R microturbine has been installed and tested successfully in a recuperated cycle. The high temperature heat exchanger will come soon, and then the complete EFmGT, with the new control system, should be available for operating and testing. The field data obtained will provide the necessary basis for the validation of the simulated data and for a final review of the parameter settings of the controllers as the model presented here has been used to design the actual EFmGT control system.

**4.2 Closed Brayton Cycle (CBC).** The second advanced cycle analyzed in the paper is a regenerative CBC for space application. The plant layout is shown in Fig. 4 [16].

The working fluid is a helium–xenon mixture with molecular weight equal to 40 kg/kmol. The main components of the cycle are: the receiver, which has to collect solar energy, to store it in a phase-change eutectic salt ($LiF–CaF_2$) and to transfer it to the working fluid; the cooler, which refrigerates the working fluid and ejects the low temperature heat into space via the radiator device; the radial turbomachinery, consisting of the compressor, expander and electrical generator, all assembled on a single rotating shaft; the recuperator, which recovers the exhaust heat from the expander outlet and transfers it to the compressed air. This cycle has been studied in the past for its excellent qualities in terms of compactness and efficiency when compared to a photovoltaic gen-

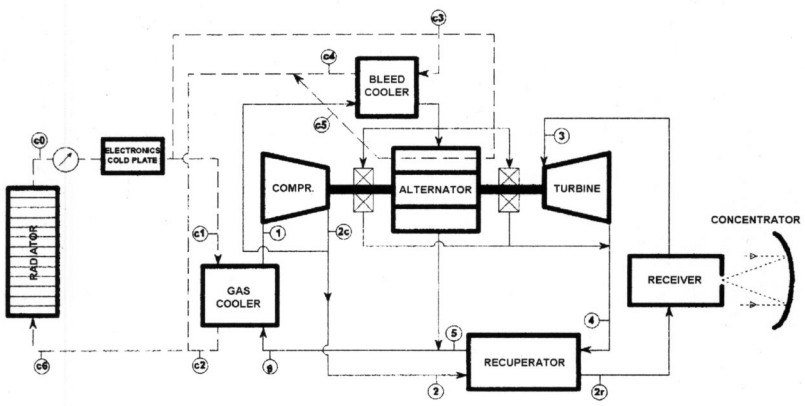


**Fig. 4 CBC plant layout**

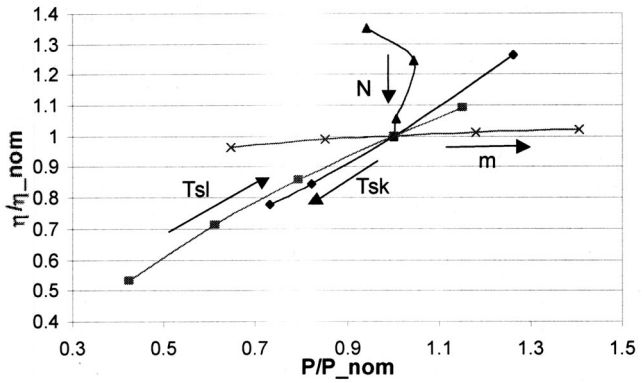


**Fig. 5 CBC: off-design performance with different parameter variations**

erator. A CBC electrical generator is to be installed in the International Space Station, together with an auxiliary photovoltaic plant, in order cover the load demand during the orbit around the Earth.

This work mainly focuses on a possible implementation and validation of the variable-mass control strategy for the plant. In fact, in a closed cycle the total circulating mass content can be varied by introducing or bleeding mass from/to an auxiliary storage tank (accumulator): this regulation has been shown to be extremely effective in reducing the power output while maintaining high conversion efficiency in a very large range of working conditions, as shown in Fig. 5.

The plant seems to benefit from $N$ decrease, thanks to the increased efficiency: this is due to the nonoptimal choice of the nominal working point of the cycle, which takes advantage of the lower pressure ratio.

CBC on-design conditions are reported in Table 1, which also illustrates the basic assumptions for the temperatures of the cycle: the difference between the $T_{sink}$ and the $T_{inc}$ is due to the presence of an intermediate coolant closed loop in between the gas and the radiator. $V\_tot$ is the total volume in the CBC where the working fluid is constrained: this value should be kept as low as possible in order to allow a small accumulator for the working fluid to be considered.

## 5 Transient Behavior of EFmGT

The first part of the results deals with the fast microturbine response (1–2 s) dominated by the shaft mechanical inertia. The second part is concerned with the long-term response of the cycle due to the influence of the heat exchangers, which do not show significant variations before about 50 s. The main load functions that have been considered are reported in Table 2, while Table 3 refers to the main assumptions on plant inertia. The shaft mechanical inertia has been deduced in accordance with the available data [14]; the recuperator Rec II has been designed with an original code for compact heat exchanger sizing developed by the TPG [17]; preliminary information about Rec I has been communicated by the manufacturer [14].

**Table 1 CBC nominal characteristics**

| |
|---|
| $P=24$ kW |
| $\eta=15.8\%$ |
| $\beta=3.8$ |
| $N=68\,000$ rpm |
| $T_{sink}=200$ K |
| $T_{ing}=296$ K |
| TIT$=1008$ K |
| $V\_tot=0.6$ m3 |
| $\dot{m}=0.83$ kg/s |

**Table 2 Load variations and transient period**

| No. | Power step | Short transient period | Long transient period |
|---|---|---|---|
| I | +2% | ~2 s | ··· |
| II | −70% | ~2 s | ~2000 s |

The short-term transients mainly concern the shaft and the bypass valve. In this case, the temperature along the exhaust line is not monitored because it does not change significantly in such a short period of time, differently from $N$ that is, instead, the driving-factor.

With regard to the load function I (Table 2), Fig. 6 illustrates the variation of $N$ over time, at different load increases. A 2% variation has been found to be the maximum allowable step that is sustainable by the machine without a nonrecoverable deceleration of the rotor. This limitation is basically due to the 5% nominal opening of the bypass valve: higher load fluctuations could be controlled for higher values, but the nominal efficiency would be significantly affected [4].

Figure 7 reports the main short transient system parameters during load function II (Table 2). The relevant time gap between the command to the bypass valve fractional opening (FOtheor) and the real fractional opening (FOreal) demonstrates the strong influence of bypass valve delays on system reaction. Due to the very prompt signal from the control system, it appears evident that a faster setting of the PID controller would not lead to significant improvements in cycle response as the bypass valve could hardly regulate in a shorter time: so, in the EFmGT regulation the bypass valve is shown to be as critical an element as the fuel valve in a conventional microturbine cycle.

The by-passed air, not reported, can reach even 60% of total intake air: this requirement is the main design specification for the valve. If the load suddenly dropped more than 70%, the shaft would pass the maximum limit of 5% overspeed and the machine would stop.

The short-term transients are mainly influenced by the bypass valve, whose unsteady behavior strongly drives the rotor dynamics in the first 1–2 s of the cycle simulation. After that, the heat

**Table 3 Main inertia of EFmGT cycle**

| | |
|---|---|
| Shaft mechanical inertia [kg·m$^2$] | $3.8\cdot10^{-3}$ |
| Rec I mass (internal matrix) [kg] | 1600 |
| Rec I mass (vessel) [kg] | 200 |
| Rec II mass (internal matrix) [kg] | 100 |
| Rec II mass (vessel) [kg] | 10 |

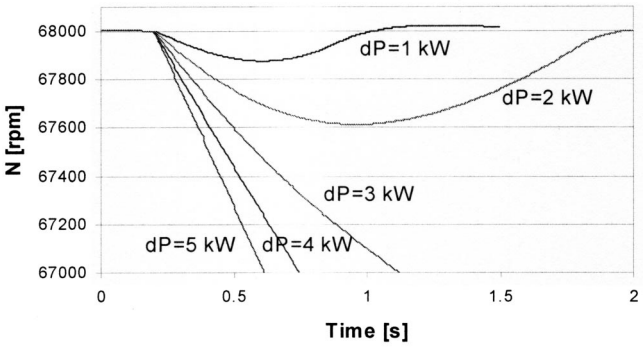


**Fig. 6 EFmGT: shaft response to different load step increases (starting from 50 kW)**

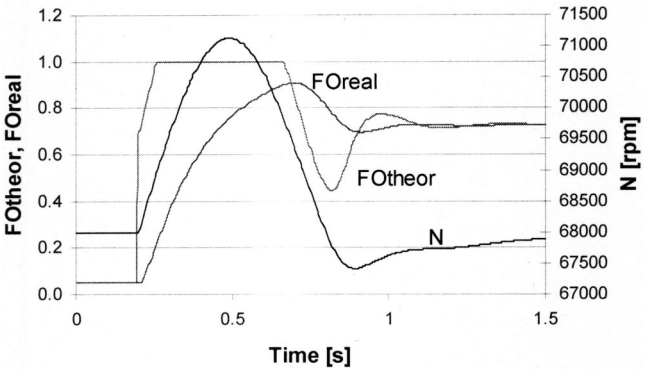


**Fig. 7 EFmGT: response to a load step decrease (Case II, Table 2)**

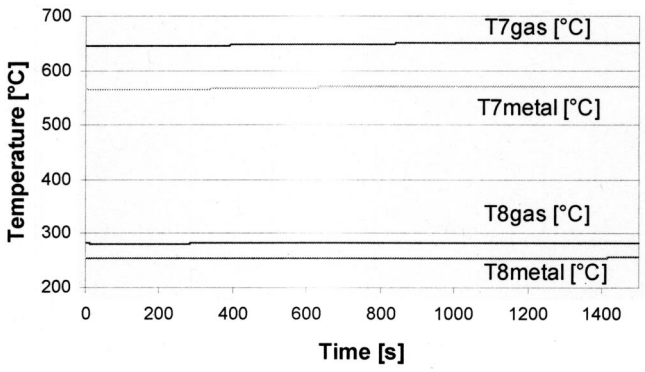


**Fig. 9 EFmGT: Rec II response to a load step increase (Case I, Table 2). Exhaust and recuperator metallic matrix temperatures are recorded against time.**

exchanger thermal inertia slowly leads the plant to the final steady conditions: these long-term transients are driven by the fuel valve of the external combustor, because the rapid response of the bypass valve can always keep the rotor speed almost constant.

Figure 8 reports the fractional opening of the fuel valve during the whole transient, for two different values of the gain in the PI controller for Case I of Table 2. Unlike bypass valve delays, fuel valve delays become almost negligible for the proper regulation of the system, due to the high time constants of the phenomena under control. In this case, the fuel valve controller has been set in order to obtain a stable rather than a quick time response from the system since the latter may cause instability (later shown in Fig. 12): for this reason, the lower value for $K$ (0.00025) has been chosen. The typical duration of an EFmGT transient can be estimated as greater than 1000 s. In this case, the temperature variations at the interconnecting points (gas and metal) of the heat exchangers are almost negligible because of the large heat capacity of these devices as shown in Fig. 9.

The control of the load step decrease (Case II, Table 2) was more critical. In fact, after the short-term transient regulation operated by the bypass valve, this should follow the smooth variations of the TIT (caused by fuel flow changes) by maintaining $N$ almost constant, as illustrated in Fig. 10. Since the fuel valve controller is based on the bypass fractional opening (the set point value is 5%), the fuel valve is pushed to significantly reduce the fuel flow during the first 500 s of the transient until it reaches its minimum value. If this threshold is too low, when the bypass valve returns to the nominal opening, after almost 2000 s, the whole cycle is too cold and the heat exchanger thermal inertia prevents the system from quickly elevating the TIT to the required level, despite the bypass valve being completely closed: so, the rotor velocity drops and the machine stops. To avoid this, a higher inferior limit for the fuel valve fractional opening has been set, taking it closer to EFmGT cycle idle conditions (the fractional opening limit has been assumed to be equal to 50%).

The large amount of bypassed mass flow, especially during the first 500 s of the transient, leads to a significant decrease in the cooling flow on the cold side of the heat exchangers. This situation is potentially dangerous for the recuperator, which could be fed with very high temperature exhausts coming from the Rec I outlet (Point 7 in Fig. 3). The simulation results reveal that such critical operating conditions are very likely to happen in the actual plant: in fact, Fig. 11 shows a quick rise of T7 (both for the gases and for the internal metallic matrix of the recuperator) which, however, terminates after the first 250 s of the transient.

Owing to the low steady state temperature of the matrix (~580°C), it never reaches the safety threshold of 650°C [14], but it clearly shows a significant increase of almost 70°C in the first 250 s. In an actual plant, where high performance is pursued and high steady state temperatures are required, this situation (partial load rejection) is supposed to be an issue and the T7 needs to be carefully monitored.

So, the conclusion of the off-design analysis [4], that no forbidden operating points at steady state conditions limit the EFmGT pilot plant management, must be completed by this relevant limitation to the experimental activities during transient operations.

Finally, a simulation of a likely load ramp has been performed in order to distinguish the best setting for the PI controller of the fuel valve. The ramp starts from 40 kW and reaches the value of 43 kW after 300 s, that is with a constant slope of 0.01 kW/s. Two different values of gain are tested, as shown in Figs. 12 and 13.

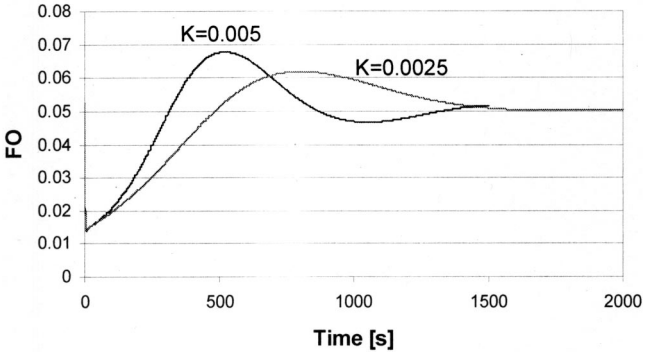


**Fig. 8 EFmGT: bypass valve FO response to a load step increase (Case I, Table 2): two different gains (K) of the fuel valve PI have been considered**

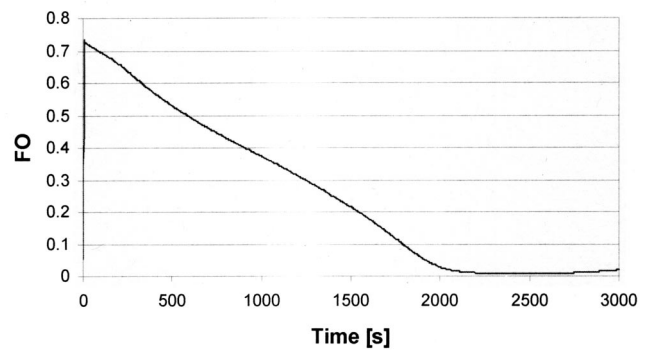


**Fig. 10 EFmGT: bypass valve FO response to a load step decrease (Case II, Table 2)**

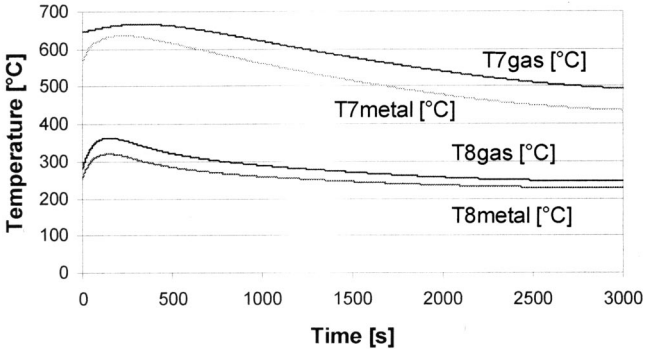


**Fig. 11 EFmGT: Rec II response to a load step decrease (Case II, Table 2). Exhaust and recuperator metallic matrix temperatures are recorded against time.**

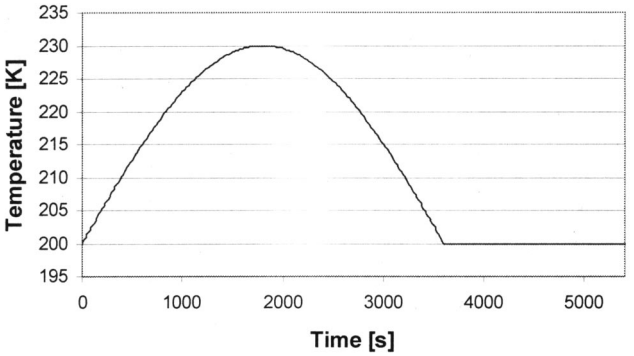


**Fig. 14 CBC: sample variation of sink temperature during the orbit ($T_{sk}$)**

The instability caused by too high a value of the PI gain is evident, and the lower value must be chosen in order to avoid dangerous fluctuations in the system at a frequency close to 0.005 Hz, which could affect the life of the heat exchanger. However, the bypass valve manages to maintain $N$ at its nominal value.

## 6 Transient Behavior of the Closed Brayton Cycle

During an orbit of the Earth, the CBC system will encounter periodic shadow and insulation phases lasting approximately 90 min (5400 s) [18]: this forces the cycle to continuously work in unsteady conditions. While the receiver has to be properly designed to store and supply the necessary heat to the CBC at almost constant temperature, the radiator is affected by the $T_{sk}$ variation, and indirectly transposes such variations on the cycle with a delay, due to its thermal inertia. So, a sample function for $T_{sk}$ has been considered, as shown in Fig. 14 [19,20]: 60 min (sinusoidal variation) for the insulation period and 30 min for the shadow period (constant value).

During the transient, the cycle is supposed to maintain constant rotational speed and the TIT, in order to minimize the thermal stresses to the rotating parts and keep efficiency as high as possible. The resulting power can be used directly by the space station or dissipated into the parasitic-load radiator. The control system acts on the cycle in order to keep the TIT constant by adding or subtracting working fluid in the accumulator. Two valves are employed: a feed valve upstream from the compressor, and a bleed valve downstream. The two PI controllers must also ensure zero fractional opening of the valves at steady state conditions.

Figure 15 shows the percentage change of the main cycle parameters during the whole transient: the TIT is successfully kept almost constant but power and efficiency are greatly affected, since both show a decrease of almost 40% from the on-design conditions. While $T_{sk}$ reaches its peak after 1800 s, the other properties follow with a delay of about 40 s. However, the mass flow delay is up to 200 s, because of the time that is required by the control system to update the current mass content according to the actual operating point.

The mass exchange between the cycle and the accumulator is reported in Fig. 16. During the transient, mass is first added to and then subtracted from the cycle, which, in fact, shows an increase of the impeller delivery pressure ($p_{outc}$) along the entire $T_{sk}$ rise

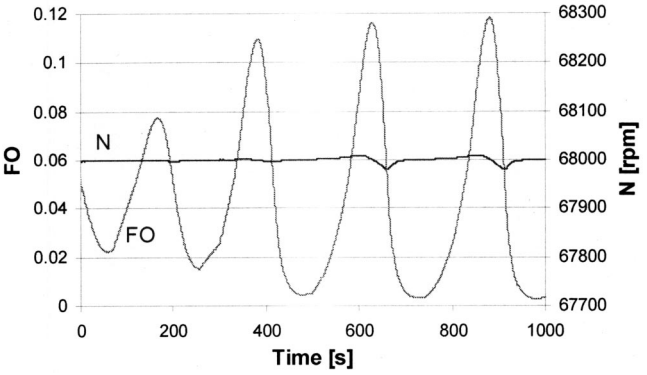


**Fig. 12 EFmGT: bypass valve and shaft response to a load ramp (+0.01 kW/s) from 40 kW to 43 kW (PI gain K=0.005, unstable)**

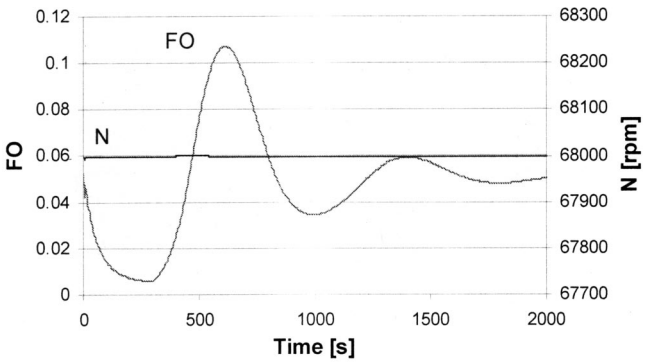


**Fig. 13 EFmGT: bypass valve and shaft response to a load ramp (+0.01 kW/s), from 40 kW (PI gain K=0.005, unstable)**

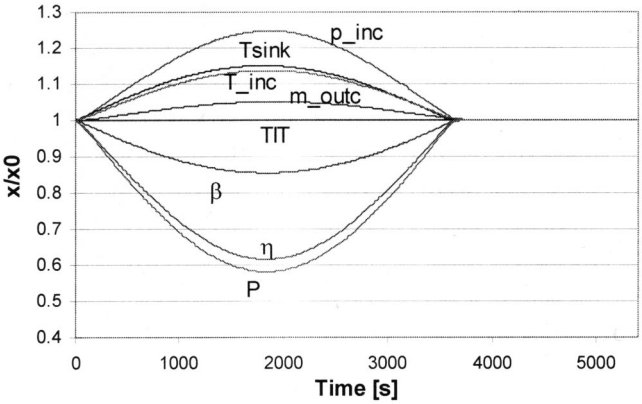


**Fig. 15 CBC: percentage variation of the main parameters during the orbit**

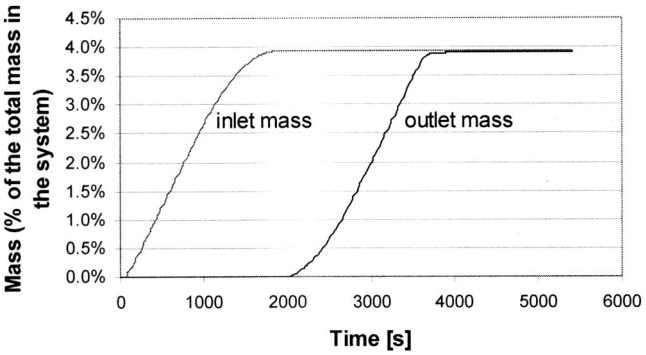


**Fig. 16 CBC: mass exchange between the cycle and the mass accumulator during the orbit**

(Fig. 15). Figure 16 also demonstrates that the accumulator must be able to store at least 4% of the total working fluid in the cycle, this being its major design specification.

The receiver supplies the necessary heat as shown in Fig. 17: the solar energy is stored during the insulation period only, but must be smoothly released during the complete orbit. The simulation estimates a total energy requirement of about 800 MJth and an electricity production of 107 MJel, which leads to an average cycle efficiency of 13.4% for the complete orbit.

Finally, an accidental case has been considered, where the regulation valve response is assumed to be unexpectedly delayed by 30 s (Fig. 18). At the beginning of the transient, the system presents large fluctuations in all the main parameters, caused by the fast reaction of the control system, which is not followed by the regulation valves. The instability is attenuated only after the first

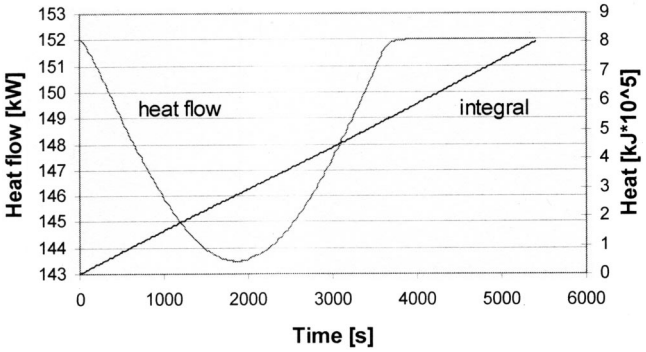


**Fig. 17 CBC: instantaneous heat flow rate (kW) and integral heat (kJ) supplied by the receiver during the orbit**

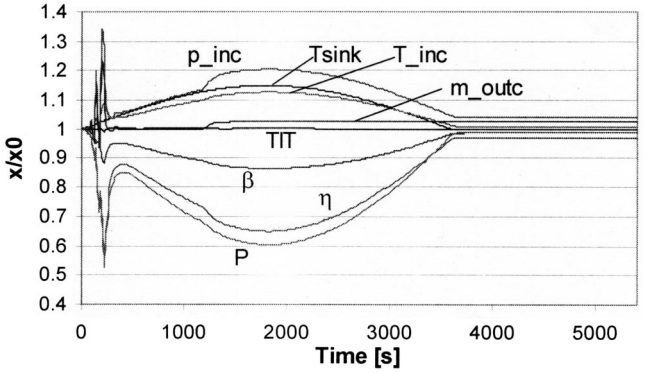


**Fig. 18 CBC: percentage variation of the main parameters during the orbit (accident: delayed motion of the control valves)**

400 s. However, since the TIT succeeds in being almost constant despite the unstable oscillations, the cycle seems to be able to sustain such an accidental situation, showing good features in terms of robustness and reliability.

## 7 Conclusions and Future Work

Microturbines are characterized by nervous dynamic behavior, due to the low mechanical inertia of the shaft, necessitating the use of fast control systems and valves.

The TRANSEO code has been shown to be a flexible and robust code for transient simulations of microturbine-based advanced cycles.

The results obtained for the EFmGT show that, even if the steady-state points during part-load are always feasible, transients may cause the plant to run into forbidden areas, which are especially dangerous for the recuperator, where the exhaust inlet temperature is the main variable to be monitored and to be kept under the safe limit of 650°C.

The CBC, when regulated by varying the total mass in the circuit using a mass accumulator, shows good performance and stability over the entire operating range, even when a fault occurs in the control valves.

Other advanced cycles, such as Humid Air Cycle (mHAT) and hybrid systems based on MCFC of SOFC, are also under investigation at the TPG laboratories using the TRANSEO code.

## Acknowledgments

This work has been partially sponsored by a contract to TPG-DiMSET from the Agenzia Spaziale Italiana (ASI) under Grant No. ASI-I/R/135/00 and by Contract No. 9/2000 from ANSALDO Ricerche (ARI).

## Nomenclature

$C$ = compressor
Cc = combustion chamber
CBC = closed Brayton cycle
$c_p$ = specific heat at constant pressure [kJ/kg K]
$c_v$ = specific heat at constant volume [kJ/kg K]
$E$ = expander
EFmGT = externally fired micro gas turbine
FO = fractional opening
$\dot{m}$ = mass flow rate [kg/s]
$K$ = controller gain
$N$ = rotational speed [rpm]
$p$ = pressure [Pa]
$P$ = power [kW]
$P\_nom$ = nominal power [kW]
$R$ = gas constant [J/kg K]
PI = proportional integral controller
PID = proportional integral derivative controller
Rec = recuperator
$T$ = temperature [K]
TIT = turbine inlet temperature [K]
TOT = turbine outlet temperature [K]
$V$ = volume [$m^3$]
$V\_tot$ = total volume of the CBC [$m^3$]

### Greek letters

$\eta$ = efficiency
$\beta$ = pressure ratio
$\rho$ = density [$kg/m^3$]

### Subscripts

in = inlet
inc = compressor inlet
out = outlet
outc = compressor outlet
sk = space sink

sl = salt
t = total

## References


[1] Rodgers, C., ''Microturbine Cycle Options,'' ASME paper No. 2001-GT-0552.
[2] Rowen, W. I., 1992, ''Simplified Mathematical Representation of Single Shaft Gas Turbines in Mechanical Drive Service,'' Turbomachinery Inter., **33**, pp. 26–32.
[3] Cerelli, E., ''Theoretical Modelling and Experimental Measurements of Microturbine Cycles for Distributed Trigeneration,'' 2002, Master thesis, TPG-DiMSET, Università di Genova, Italy.
[4] Traverso, A., Magistri, L., Scarpellini, R., and Massardo, A. F., ''Demonstration Plant and Expected Performance of An Externally Fired Micro Gas Turbine for Distributed Power Generation,'' ASME Paper No. 2003-GT-38268.
[5] Agazzani, A., and Massardo, A., 1995, ''Advanced Solar Dynamic Space Power Systems, Part I: Efficiency and Surface Optimization,'' ASME Trans. J. Solar Energy Eng., **117**, pp. 265–273.
[6] Agazzani, A., and Massardo, A., 1995, ''Advanced Solar Dynamic Space Power Systems; Part II: Detailed Design and Specific Parameters Optimization,'' ASME Trans. J. Solar Energy Eng., **117**, pp. 273–281.
[7] Massardo, A. F., Tagliafico, L. A., Fossa, M., and Agazzani, A., 1997, ''Solar Space Power System Optimization With Ultralight Radiator,'' J. Propul. Power, **13**, pp. 560–564.
[8] Parente, J., Traverso, A., and Massardo, A. F., ''Micro Humid Air Cycle. Part A: Thermodynamic and Technical Aspects,'' ASME Paper 2003-GT-38326.
[9] Magistri, L., Bozzo, R., Costamagna, P., and Massardo, A. F., ''Simplified Versus Detailed SOFC Reactor Models and Influence on the Simulation of the Design Point Performance of Hybrid Systems,'' ASME Paper 2002-GT-30653.
[10] Schobeiri, M. T., Attia, M., and Lippe, C., 1994, ''GETRAN: A Generic, Modularly Structured Computer Code for Simulation of Dynamic Behavior of Aero- and Power Generation Gas Turbine Engines,'' J. Eng. Gas Turbines Power, **116**, pp. 483–494.
[11] Crosa, G., Fantini, L., Ferrari, G., Pizzimenti, L., and Trucco, A., ''Steady State and Dynamic Behavior of an Indirect Fired Gas Turbine Plant,'' ASME paper 98-GT-167.
[12] Pilidis, P., and Maccallum, N. R. L., ''A General Program for the Prediction of the Transient Performance of Gas Turbines,'' 1985, ASME Paper 85-GT-265.
[13] Calzolari, F., ''Transient Behavior and Control System for Advanced Cycles Based on Micro Gas Turbine Technology,'' 2002, Master thesis, TPG-DiMSET, Università di Genova, Italy.
[14] ''Externally Fired Micro Gas Turbine for Distributed Power Generation,'' 2002, ANSALDO Ricerche, Research Contract No. 9/2000, Final Report.
[15] White, F. M., 1994, *Fluid Mechanics*, 3rd ed., McGraw–Hill, New York, pp. 335–341.
[16] Korakianitis, T., Hochstein, J. I., and Zou, D., ''Prediction of Transient Thermodynamic Response of a Closed-Cycle Regenerative Gas Turbine,'' ASME Paper 93-GT-136.
[17] Rio, R., 2001, ''Regenerated Microturbines for Distribuited Power Generation: Thermoeconomic Assessment,'' Master thesis, TPG-DIMSET, Università di Genova, Genova, Italy.
[18] ''Closed Brayton Cycle for Space Applications: Off-Dedign and Transient Analysis,'' Agenzia Spaziale Italiana (ASI), Grant No. ASI-I/R/135/00, Final Report.
[19] Bons, R., Hanlon, J., and Spencer, S., 1988, ''Predicting the Behavior of Solar Dynamic Closed Brayton Cycle Power Conversion Systems,'' ASME Trans. J. Eng. Gas Turbines and Power, **110**, pp. 636–640.
[20] Harper William, B., Boyle, Jr., Robert V., and Kudija, Charles T., 1990, ''Solar Dynamic CBC Power for Space Station Freedom,'' ASME Paper 90-GT-70.

# Integrated Pyrolysis Regenerated Plant (IPRP): An Efficient and Scalable Concept for Gas Turbine Based Energy Conversion From Biomass and Waste

**Francesco Fantozzi**
Dipartimento di Ingegneria Industriale,
Universitá degli Studi di Perugia,
Via G. Duranti 1A/4,
06125 Perugia, Italy
e-mail: fanto@unipg.it

**Bruno D'Alessandro**
Ingegneria dei Materiali,
Universitá degli Studi di Perugia,
Loc. Pentima Bassa 21,
05100 Terni, Italy
e-mail: dalessandro@mach.ing.unipg.it

**Umberto Desideri**
Dipartimento di Ingegneria Industriale,
Universitá degli Studi di Perugia,
Via G. Duranti 1A/4,
06125 Perugia, Italy
e-mail: umberto.desideri@unipg.it

*A massive effort towards sustainability is necessary to prevent global warming and energy sources impoverishment: both biomass and waste to energy conversion may represent key actions to reach this goal. At the present, state of the art available technologies for biomass and waste to energy conversion are similar and include low to mid efficiency grate incineration or fluidized bed combustion with steam power cycles or mid to high efficiency gas turbine based cycles through integrated gasification technology. Nevertheless, these plants are all available from mid-to-high scale range that can be highly intrusive on protected areas and socially unacceptable. This paper proposes an innovative, low cost, high efficiency plant in which the residue is gasified in the absence of oxygen (pyrolysis), in a rotary kiln, by means of a highly regenerative gas turbine based cycle. Pyrolysis is preferred to gasification, because the syngas obtained has a higher low heating value and produces char or tar as a by-product with an interesting energy content to be re-utilized inside the cycle. Different plant configurations are proposed and discussed through principal thermodynamic variables parametric analysis. Results show that very interesting efficiencies are obtainable in the 30–40% range for every plant scale. This fact shows how IPRP technology can provide an interesting alternative to traditional technologies, especially for the small size (below 5MW). Moreover, the IPRP technology provides a unique solution for microscale (below 500 kW) power plants, opening a new and competitive possibility for distributed biomass or waste to energy conversion systems where low environmental and social impact turns into higher interest and positive dissemination effect.* [DOI: 10.1115/1.1789513]

## 1 Introduction

The energy conversion of biomass and/or waste (B&W) is addressed as one of the key issues to reach sustainability and to meet the goals of the Kyoto Protocol [1]. The best available technology for B&W electric energy conversion is still the grate-based incineration with a net electric efficiency lower than 30% and a minimum plant size for economical feasibility above 2 MWe. Higher efficiencies may be obtained through an intermediate conversion (gasification, anaerobic digestion) that turns B&W into a medium-low calorific fuel gas that can be used in a high efficiency cycle based on internal combustion engine (ICE) or gas turbine (GT) but still at a demonstrative stage. Nevertheless, the higher capital cost and the more complicated arrangement of these plants maintains the minimum size for economical feasibility still on the medium to high scale, as briefly summarized in Table 1. This turns into relative big plants and B&W supply chain that may be considered intrusive for protective areas and socially unacceptable. For small to micro scale conversion, externally fired cycles are promising but still at a demonstration level due to material problems for hot air heat exchangers technology [4,5].

B&W energy conversion is therefore hampered because:

• it is feasible on medium to big scale that is often considered intrusive and socially unacceptable;

• there are no technologies available for the small–micro scale that benefits of the intrinsic distributed nature of B&W.

This paper analyzes the integrated pyrolysis regenerated plant (IPRP), a new concept for B&W energy conversion, that puts together both high performance and plant simplicity and it is also scalable even to the micro scale. The plant is based on an intermediate conversion of B&W to a medium-high LHV gas through pyrolysis (a well-known process [6–13]) in a rotary kiln reactor. The syngas obtained fuels a GT and the exhaust gases from the GT are fed back to the reactor providing the energy required to maintain the pyrolysis process. If necessary it is possible to increase the enthalpy content of the GT exhaust gases through combustion of the residual tar/char produced by pyrolysis. With reference to other pyrolysis based combined cycle [14] the IPRP technology is simpler and more economic because it does not require a bottoming steam cycle.

## 2 Plant Description

Figure 1 shows the plant layout analyzed in the present work. The rotary-kiln pyrolyzer (PYRO) is fed by the generic residual fuel (RF) through a hopper. The rotary-kiln pyrolyzer is built as a tube in tube heat exchanger where the inner cylinder represents the pyrolysis reaction chamber where the RF degrades to syngas, tar and char in absence of oxygen. The hollow space between the two cylinders is the flow path for the hot gases exhausted from the GT, which provide the heat necessary to pyrolyze the RF. Exhaust gases from the pyrolyzer may be used to preheat GT primary air in a recuperator (REC, when present), before being conveyed to the filtering section and to the stack. Syngas obtained from pyrolysis

Contributed by the International Gas Turbine Institute (IGTI) of THE AMERICAN SOCIETY OF MECHANICAL ENGINEERS for publication in the ASME JOURNAL OF ENGINEERING FOR GAS TURBINES AND POWER. Paper presented at the International Gas Turbine and Aeroengine Congress and Exhibition, Atlanta, GA, June 16–19, 2003, Paper No. 2003-GT-38653. Manuscript received by IGTI, October 2002, final revision, March 2003. Associate Editor: H. R. Simmons.

  

**Table 1 Biomass to energy conversion plant efficiencies [2,3]**

| Technology | Building Status | Fuel | Plant Capacity | Efficiency |
|---|---|---|---|---|
| Travelling Grate Average Zurn / NEPCO | Existing | Wood | 25 MW | 29% |
| Travelling Grate McNeil (USA) | Existing | Wood | 50 MW | 30% |
| Circulating Fluidized Bed Händelőverket CHP (S) | Existing | Wood | 46 MW | 32% |
| Bubbling Fluidised Bed Delano I plant (USA) | Existing | Agr. Waste | 27 MW | 29% |
| Vibratine Grate Enkőping (S) | Under construction | Wood | 28 MW | 33% |
| IGCC Värnamo (S) | Existing | Wood chips | 6 MW | 32% |

is cleaned in a cyclone (CYCLO), to remove solid residual particles, and in a wet scrubbing section (SCR), to remove chemical aggressive compounds that may damage the GT. The SCR also cools the syngas to condense water vapor and tars and to lower the work required by following syngas compression (COMP SYN); syngas is eventually injected in the GT combustion chamber (CC). Thermal energy of GT exhaust gases may be recuperated in the regenerator (REG, when present) to provide additional heat to the GT primary air. Depending on the layout considered, and for some values of the operational parameters, the enthalpy content of exhaust gases to the pyrolyzer may not be sufficient to maintain pyrolysis. In this case it is possible to increase the exhaust gases enthalpy through a post combustion in TAR CC of tars and chars produced by pyrolysis.

Four different plant layouts will be considered in the following analysis; they are descriptive of four different heat recovery solutions. Exhaust gases from the GT will be always forwarded to the PYRO but they may previously be used to regenerate the Joule cycle in REG or they can regenerate the Joule cycle after exiting the PYRO in REC or both. Table 2 shows the different plant layouts that will be considered.

**Case A: Simple Cycle.** The Joule cycle in the GT is not regenerated; exhaust gases from the GT are conveyed directly to PYRO and from PYRO to the stack. This case is also the reference case.

**Case B: Cycle With REC.** The Joule cycle in the GT is regenerated by exhaust gases from PYRO; they enter PYRO directly from the GT and eventually they enter REC, where primary air is preheated, and then conveyed to the stack.

**Case C: Cycle With Both REC and REG.** The Joule cycle in the GT is two times regenerated: a first time by the exhaust gases from the turbine and a second time by the exhaust gases from PYRO; at the GT outlet they enter REG and preheat primary air before it enters the CC. Exhaust gases are then conveyed to PYRO and eventually they enter REC, where primary air is heated again. Finally they are conveyed to the stack.

**Case D: Cycle With REG.** The Joule cycle in the GT is regenerated by exhaust gases from GT; they enter REG and preheat primary air from the compressor. Exhaust gases are eventually conveyed to PYRO and from PYRO to the stack.

## 3 Objectives

An efficiency evaluation and optimization of the plant will be carried out, for the four different plant layouts, by varying main thermodynamic parameters in order to identify the best performing arrangement with respect to the possible size of the plant.

Main objectives of the study will be:

1. to determine the efficiency of the IPRP plant as a function of its main design variables (GT Compression Ratio ($\beta$), Turbine Inlet Temperature (TIT), Pyrolysis Temperature ($T_p$) and GT Regeneration Ratio (RR) as defined in Eq. (1));
2. to point out their influence on plant performance and their mutual interference;
3. to determine the values of the above-described variables that yield to best IPRP overall efficiency and to compare it to the SOA.
4. to compare the performance of the four different plants and to determine the working envelope;
5. to evaluate the compatibility of these values with different size commercial GT design values in order to evaluate the feasibility and scalability of the recuperated IPRP.

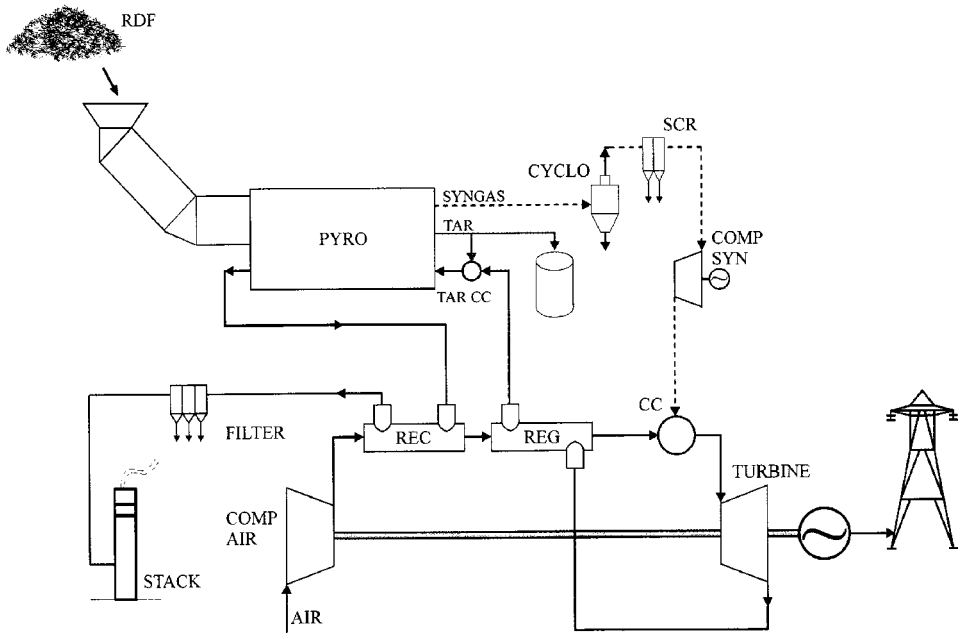


**Fig. 1 Plant layout**

Table 2 Different layouts considered

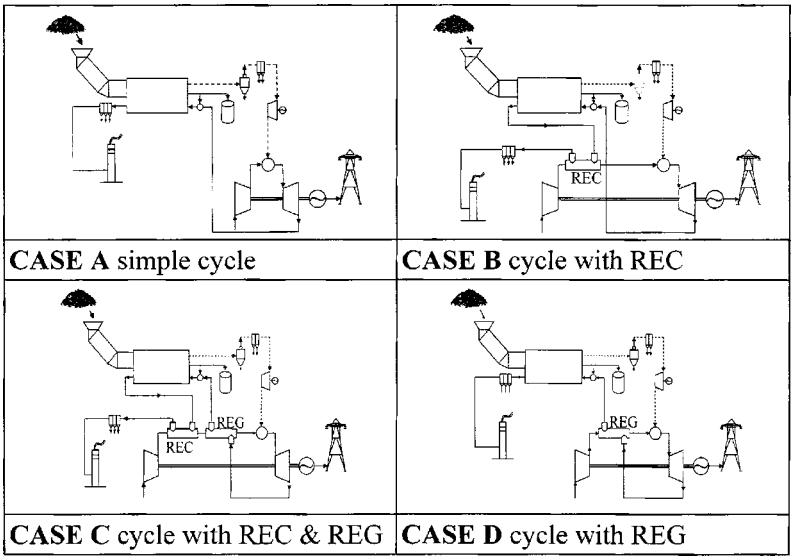


CASE A simple cycle | CASE B cycle with REC

CASE C cycle with REC & REG | CASE D cycle with REG

Some typical results are extendable from the previous analysis carried out in Ref. [15] such as:

- an increase in $\beta$ will increase the GT efficiency but not necessarily the overall plant efficiency, because less energy will be available from GT exhaust gases and also the work required to compress the syngas will increase [16,17];
- a similar conclusion may be obtained when discussing an increase in the TIT or in $T_p$ that yields more syngas from RF pyrolysis but requires as well more heat to be provided by tar or external fuel combustion.
- higher RR yield to higher efficiencies but more tar energy (TE) is requested because GT exhaust gases will have a lower enthalpy content, and if residual tar is not enough an external fuel supply will be required. These preliminary conclusions will be more evident after the following section.

## 4 Methodology

Through software modeling the overall plant performance was determined as a function of four design variables that were varied in an adequate range and with an adequate step as described in Table 3. Specific work, plant efficiency, and residual energy available from tar-char production are the results that will be considered and discussed.

Plant modeling was carried out with homemade software that utilizes thermodynamic relations, energy balances and data available in literature. This approach was preferred to proprietary software because power plant simulation softwares that are commercially available also require a major user effort to define not-off-the-shelf components such as a pyrolysis reactor.

**4.1 Pyrolysis Reactor Modeling.** The reactor was simulated in the steady state and no transient or kinetic behavior is considered both for heat transfer and pyrolysis reaction. The equilibrium temperature, where reactor, pyrolysis products, and exhaust gases to stack are assumed, is the pyrolysis temperature $T_p$.

Pyrolysis products percentages and LHV as a function of pyrolysis temperature were obtained from data available in literature and in particular for plastic waste (composition is shown in Table 4) pyrolyzed in an externally heated laboratory-scale rotary-kiln pyrolyzer [18]. The yield of pyrolysis products is shown in Fig. 2.

As different residues behave in different ways when heat is provided, data utilized may only be representative for a high plastic content residue as RDF can be, with an insignificant char production, when compared to tar production (Fig. 2). However, different residues may yield to different pyrolysis products but the energy balance shall be maintained, therefore lower tar production usually results in higher char production (i.e., biomass) and vice versa.

The assumption that is made is that since in this study we are interested only in char/tar energy content (and not in their composition) every reference to tar energy it is assumed to be extendable to char energy, therefore the results obtained may be generalized to any RF, as far as trends are concerned. This assumption is confirmed when considering biomass in Sec. 7 that pyrolyzes

Table 3 Parametrization of the simulations

| Parameter | Range | Step |
|---|---|---|
| Pyrolysis temperature ($T_p$) | 823K–1123K | 100K |
| Compression ratio ($\beta$) | 2 – 30 | 1 |
| Regeneration Ratio * | 25% – 75% | 25% |
| Turbine Inlet Temperature (TIT) | 1000K – 1500 K | 100K |
| * Defined as in section 4.2 | | |

Table 4 Primary analysis and ultimate analysis of the raw materials (dry air basis) [18]

| Proximate analysis | [wt.%] |
|---|---|
| Moisture | 0.17 |
| Ash | 0.06 |
| Volatile matter | 99.77 |
| Fixed carbon | 0 |
| **Ultimate analysis** | **[wt.%]** |
| Carbon | 89.28 |
| Hydrogen | 13.66 |
| Nitrogen | 0.06 |
| Sulfur | 0.02 |
| Oxygen | 0 |
| | |
| LHV [kJ/Kg] | 34,440 |

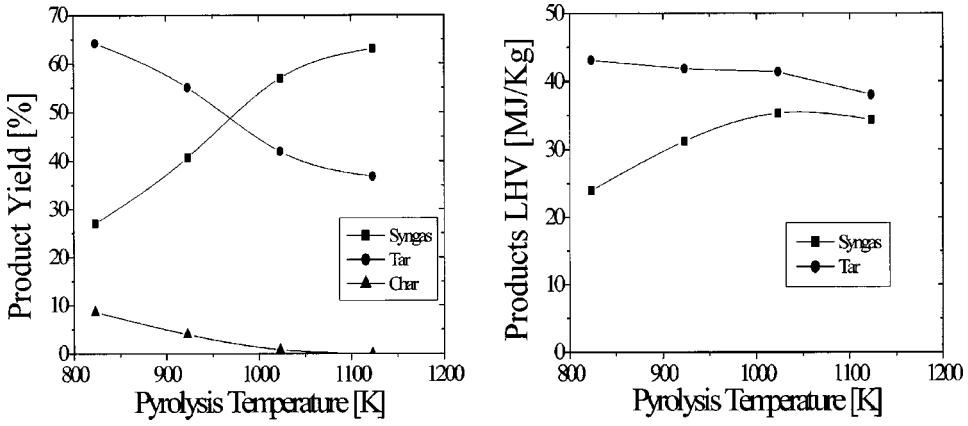


**Fig. 2 Pyrolysis products yield (left) [18] and LHV (right) [18]**

mainly to char. Therefore, from now on, every reference to tar will be extended to char as well if considering a RF that pyrolyzes mainly to char and syngas, i.e., biomass.

The energy required for pyrolysis was assumed as the sum of different contributions obtained in Ref. [19] for rubber whose behavior was considered coherent with the results shown in Ref. [18] for plastic waste as heat capacity and heat of reaction are similar. This methodology yield to results that are coherent and comparable to the results obtained equalling endothermic and esothermic reactions as in Ref. [20] for biomass.

The different energy contributions are listed below:

(a) Heat capacity of the feedstock to the reaction temperature considered in Ref. [19];

(b) Vaporization energy of pyrolysis reactants [19];

(c) Heat of reaction as in Ref. [19];

(d) Heat capacity of products to the $T_p$,

where the only item that is sensibly dependent from $T_p$ is the last one, (d).

**4.2 Other Components Modeling.** An energy balance in the pyrolyzer was used to estimate the additional energy required to increase GT exhaust gases temperature to $T_p$ by tar or external fuel combustion. Char LHV was not considered assuming that the small yield would not be significant for final results.

GT, compressor, and heat exchangers were simulated according to ideal conditions while irreversibilities were introduced through efficiencies as described in Table 5 that also shows other technical assumptions of the simulation.

The GT regenerator (REG), in particular, was modelled considering the RR defined as the ratio between the recovered energy on primary air, and the theoretical recoverable energy from GT exhaust gases assuming that they were cooled to the compressor outlet air temperature as described in Eq. (1),

$$\mathrm{RR} = \frac{\dot{m}_{\mathrm{Air}} Cp_{\mathrm{AV,Air}} (T_{\mathrm{REG,Out}} - T_{\mathrm{REG,In}})}{\dot{m}_{\mathrm{Eg}} Cp_{\mathrm{AV,Eg}} (T_{\mathrm{T,Out}} - T_{\mathrm{REG,In}})}. \quad (1)$$

Coming to the recuperator (REC) it was assumed that it has always priority when a REG is also present because the enthalpy of exhaust gases from PYRO would otherwise be lost. No RR was considered when discussing REC, which will always preheat primary air to a temperature which is 50 K lower than the considered $T_p$.

**4.3 Exclusions.** State of the art for tar combustion and eventual problems will not be discussed in the present paper; also the gas treatment section analysis will be neglected assuming that syngas is cooled to 50°C in the humid filter and that the entire fraction of water vapor is condensed. Also no consideration is made on acid vapors treatment and eventual dioxins production and abatement. These issues represent the technical barriers of the IPRP technology and will be discussed in other works.

Finally the GT combustion chamber, usually designed for conventional fuels, will require some adaptation, especially in the fuel injection nozzles due to low LHV fuel gas [21], but they are not analyzed in the present work.

**4.4 Normalization.** The analysis was carried out referring all mass and energy flows to 1 Kg RF in input to the pyrolyzer that yields to different syngas production rate, depending on $T_p$ (Fig. 2). With this approach the higher the syngas production the higher the GT power output but also the work required for its compression to the GT CC operational pressure, with this latter as a function of $\beta$.

## 5 Results for Specific Work

We will consider in the following the specific GT work as the work produced by the GT when it is fuelled by the quantity of syngas obtained from the pyrolysis of 1 Kg of RF. The specific syngas compression work is the work required to compress the amount of syngas produced by 1 Kg of RF pyrolyzed, from ambient pressure to the GT CC pressure. Therefore the GT specific work is referred to 1 Kg of residue fuelled to the plant and not, as usual, to 1 Kg of working fluid. This means that the air mass flow

**Table 5 Technical assumption used in the simulation**

| | Parameter | Value |
|---|---|---|
| **Air** | $P_{air,in}$ | 101325 Pa |
| | $T_{air,in}$ | 288K |
| **Syngas** | $P_{syn,in}$ | 101325 Pa |
| | $T_{syn,in}$ | 323K |
| **Efficiencies** | Air Compressor | 80% |
| | Syngas Compressor | 80% |
| | Turbine | 90% |
| | Combustion | 98% |
| | Tar combustion | 90% |
| | Pyrolyser heat exchange | 90% |
| | REG & REC heat exchange | 90% |
| **Pressure losses** | Combustion Chamber | 5% |
| | Fuel injection nozzle | 3% |

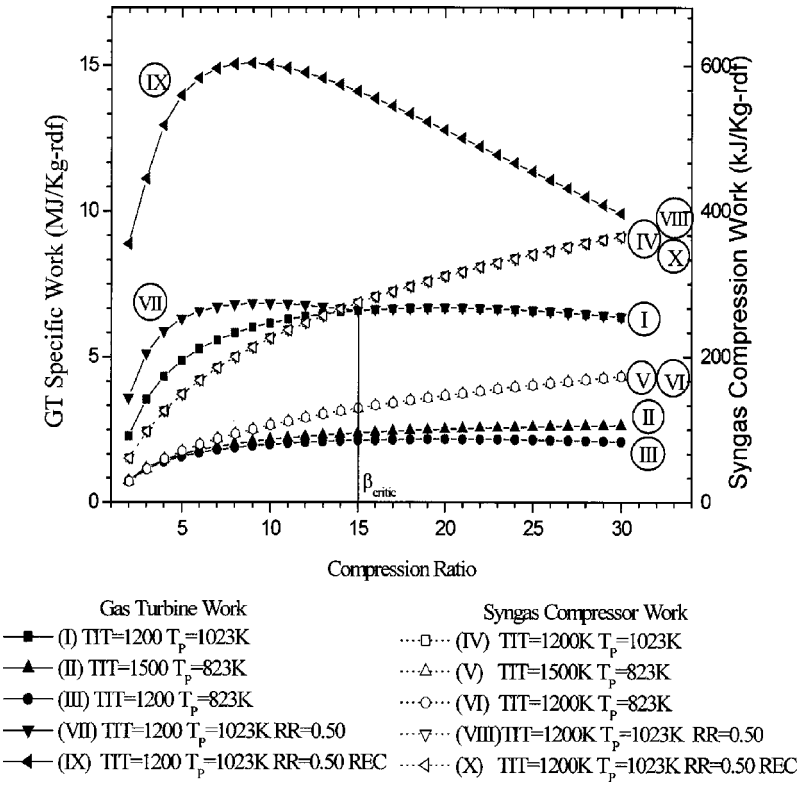


**Fig. 3 Effect of TIT and $T_p$ on specific work**

considered in the GT analysis is the quantity necessary to burn the syngas produced by the pyrolysis of 1 Kg of RF, given a value of air/fuel ratio. For a better understanding of the dependence of the IPRP efficiency from main variables, Fig. 3 shows the specific GT and syngas compression work as a function of $\beta$ considering two different TIT's and $T_p$'s, and the presence of REC and REG. We will now discuss separately the effect of the different variables.

**5.1 Effect of TIT.** Increasing the TIT, while maintaining $T_p$ constant, results in a slight increase of the GT work because the area inside the Joule cycle has increased (curves II and III). No modification in the syngas compression work is experienced (curves V and VI) because syngas production does not vary when keeping $T_p$ constant (Fig. 2).

**5.2 Effect of $\beta$.** An increase in $\beta$ produces, as a well-known effect, an increase in the GT work with a decreasing slope as $\beta$ increases. The slope inverts its sign at low TIT's therefore the GT specific work may decrease for high values of $\beta$ (curves I and III) while the slope maintains a positive sign at high TIT's (curve II). Syngas compression work always increases while increasing $\beta$.

**5.3 Effect of $T_p$.** The effect of a variable $T_p$ is a consequence of the different yield of pyrolysis products. In particular, an increase in $T_p$ results in a higher syngas rate of production (Fig. 2) therefore more fuel available: the GT specific work is increased (curves I and III) as well as the syngas compression work (curves IV and VI).

**5.4 Effect of REG.** Regeneration produces as a well known effect, an increase in GT efficiency. Since we keep syngas production constant for a given $T_p$, the effect of REG turns into an increase flow of working fluid, if we want to consume the whole syngas produced, therefore the final effect is that of an increase of the GT specific work.

The increase is evident at low values of $\beta$ and decreases while increasing $\beta$ until it reaches a critical value ($\beta_{\text{critic}}$) above which the exhaust gases temperature is too low and there is no need for a REG. From this point the regenerated and not regenerated GT specific work curves (I and VII) are coincident. Obviously an increase in the RR increases also GT specific work for $\beta < \beta_{\text{critic}}$. Syngas compression work is not affected by regeneration because the amount of syngas produced is only dependent on $T_p$ therefore the curves are coincident (IV and X).

**5.5 Effect of REC.** The effect of REC is always positive increasing the GT specific work (increasing the GT efficiency as above stated) with respect to the simple cycle and also to the regenerated one (curves IX, I, and VII). As in the previous case the syngas compression specific work is not affected and the curves are coincident (IV, VII, and X).

## 6 Results for Efficiency

Coming to efficiency, the previously described interaction between thermodynamic parameters has also to deal with the heat required to maintain the pyrolysis process. Tar (char) production depends on pyrolysis temperature (Fig. 2) which is slightly lower than the gas temperature at TAR CC outlet. Therefore the higher the pyrolysis temperature the higher the quantity of tar (char) to be burnt to rise GT exhaust gases temperature, therefore TAR residual energy may be sufficient (case b) or not (case a) to meet pyrolysis temperature.

**(a) Additional Energy Input Required.** The higher the pyrolysis temperature the lower the tar production (Fig. 2) therefore there will be cases in which tar combustion is not enough to rise GT exhaust gases temperature to the value required for pyrolysis and this is often the case when REG is present. In this case an external fuel (natural gas) will be considered, sacrificing efficiency, instead of sacrificing the GT specific work. The value of $\beta$ that is indicative of an external fuel requirement will be marked with a vertical line between the plant efficiency point and the TE point, the line is marked with the $\mathbf{Q_{ext}}$ symbol. The eventual inte-

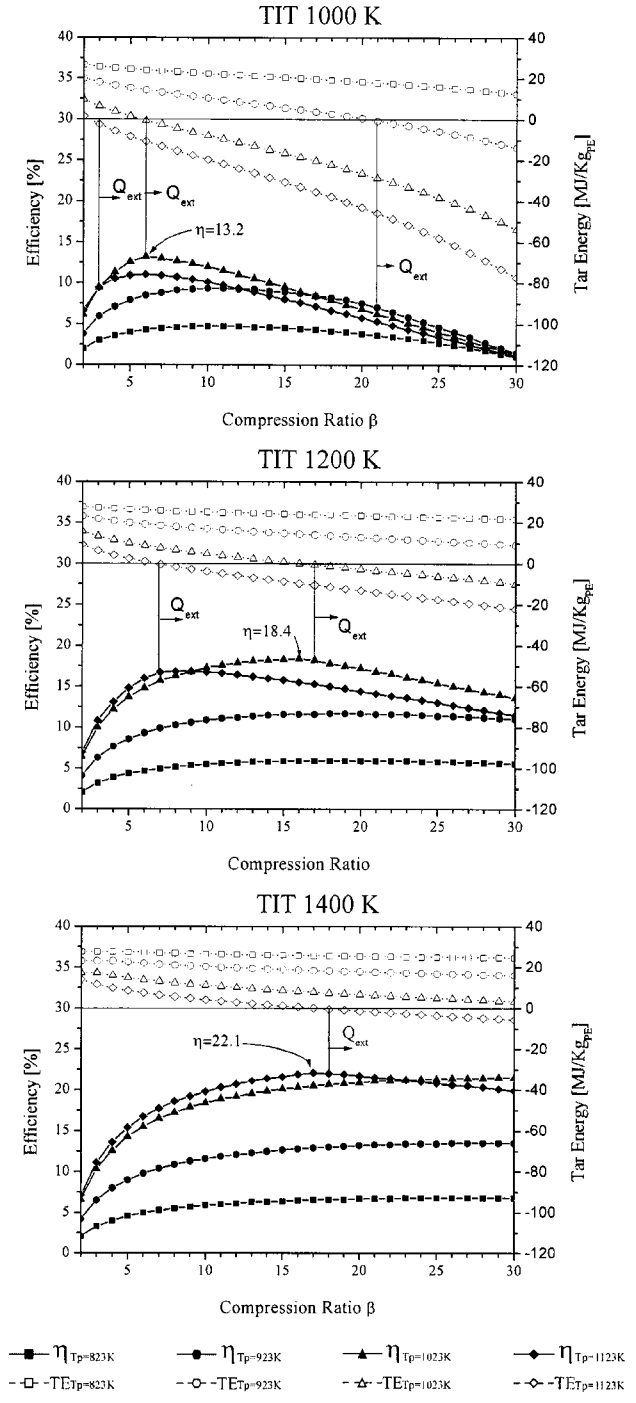


**Fig. 4 Results for the simple cycle (Ref. [15])**

gration of an external fuel will be indicated by a negative value of available energy for tar (char), which also means that the plant is not self-sufficient.

**(b) No Additional Energy Input Required.** On the other hand, some cases will show an excess of tar production with respect to the quantity required for pyrolysis, therefore the residual tar production will be considered as positive value of available energy. In this case the plant is self-sufficient and is also by-producing tar and/or char with interesting energy content. Tar/char residual energy, however, is not considered when calculating efficiency as it is considered to be stocked and utilized for startups.

Plant efficiency is therefore defined as the ratio between the net power output of the plant and the energy provided by 1 Kg of RF and eventually with natural gas,

$$\eta = \frac{\text{specific work (GT} - \text{COMP}_{\text{syn}})}{\text{LHV}_{\text{RF}} + \phi \text{LHV}_{\text{NG}}} \tag{2}$$

**Case A: Simple Cycle.** Results are collected in three charts, shown in Fig. 4, one for each TIT examined. Each graph was obtained plotting overall plant efficiency (continuous lines on lower part of the graph and left side scale) and tar residual energy (dashed lines on the upper part of the graph, right side scale) versus the GT compression ratio. Different lines are representative of different pyrolysis temperature (symbols are described on the attached table).

The lines referred to the pyrolysis temperature of 1023 K are frequently higher than the others. It depends, as shown in Fig. 2, on the better performance of the pyrolyzer for $T_p = 1023$ K. According to pyrolysis data, the difference between the line at $T_p$ of 1123 and 1023 K is very small because the production of syngas at 1123 K is similar to the production at 1023 K.

Referring to graph at TIT=1400 K of Fig. 4 the overall plant efficiency increases with $\beta$ following the usual trend of GT except for $T_p = 1123$ K and high values of $\beta$. In this case the temperature of GT exhaust gases is quite low and tar combustion is not enough to rise it to $T_p$. An external fuel is needed forcing TE to negative values and the overall plant efficiency to diminish with a discontinuity in the trend.

Referring to $T_p$, the plant efficiency increases with $T_p$ as far as TE is positive; when TE becomes negative the gap between the plant efficiency for $T_p = 1123$ K and for $T_p = 1023$ K decreases and, in some cases curve overlapping is experienced.

Decreasing the TIT the plant performance decreases because GT efficiency decreases and also because a higher amount of tar is needed. Let us also notice that decreasing the TIT the value of $\beta$ corresponding to best efficiency points also decreases.

IPRP technology appears therefore to be suitable at every GT scale because decreasing the TIT (it is typical when reducing the GT size) the best plant efficiency point moves to lower $\beta$ (also typical of reduced GT size). Figure 5 shows the best efficiency points obtained at operational parameters typical of three different GT sizes:

- microturbines ($\beta$=4 and low TIT) show very low values for plant efficiency (11.3–13.1%);
- medium size aeroderivative GT ($\beta$=12 and medium high TIT) show low overall plant efficiency (17.9–20.7%);
- big size heavy duty GT ($\beta$=20, high TIT) show acceptable plant efficiency (20–23.3%).

Maximum obtainable efficiencies are usually lower than SOA technologies, however, the results are encouraging for further op-

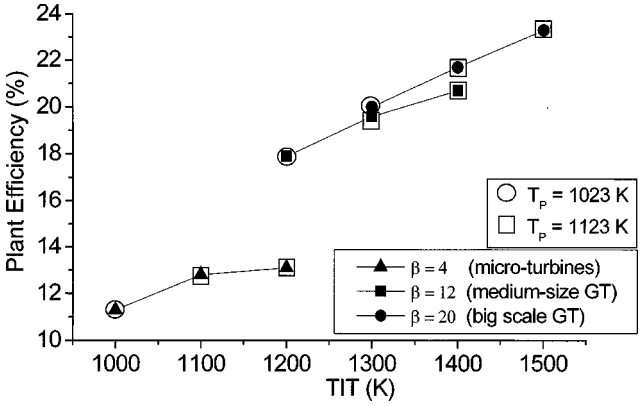


**Fig. 5 Plant efficiency versus TIT for the simple cycle (Ref. [15])**

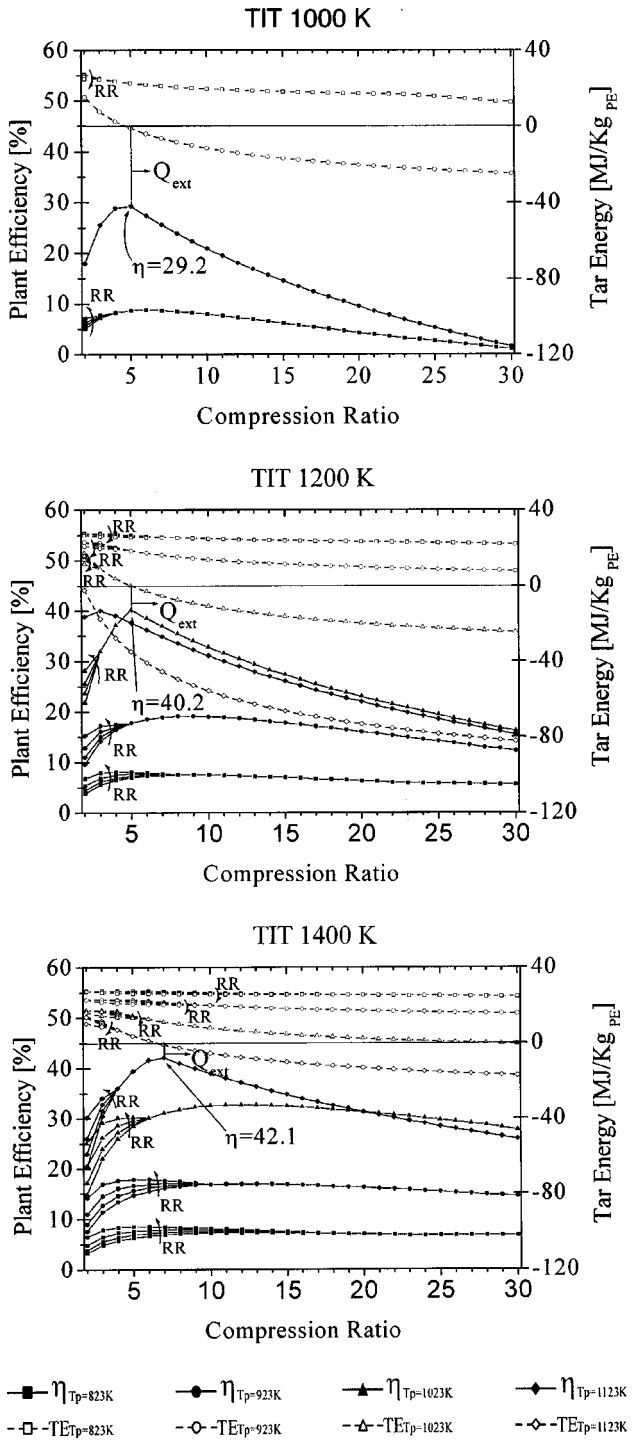


**Fig. 6 Results for case B and case C cycle with REC and REC & REG**

timization of the IPRP technology. This is to be considered particularly for micro-scale plants where no SOA is available (Ref. [15]).

**Cases B and C: Cycle With REC and Both REC & REG.** According to the above-mentioned methodology, REC presence was always privileged, with respect to REG presence, because it is always not convenient to convey to stack high-temperature exhaust gases from PYRO. This fact results in very few occasions in which REG presence is worthy and always for low values of $\beta$, where GT exhaust temperature is still higher than air temperature at REC outlet (assumed 50 K lower than $T_p$).

Moreover, as we have observed in Fig. 3, regeneration is not effective for $\beta > \beta_{critic}$ therefore curves at different RR may be discussed only for values of $\beta$ lower than the critic value. For the above-mentioned reasons Fig. 6 shows together the results of case B and case C by plotting curves at different RR. In those areas where multiple RR are possible, the null value of RR will be descriptive of the plant without REG (case B).

The trends of efficiency curves are similar to the ones obtained for case A but are all shifted to higher values of efficiency due to the positive effect of regeneration.

When TIT is lower than $T_p$ the enthalpy of exhaust gases from PYRO is sufficient to heat up primary air to the TIT at REC outlet and there would be no need for additional syngas firing in the CC. These cases were not included in Fig. 6 because this paper does not deal with externally fired cycles. Therefore for TIT=1000 K we have only two values of $T_p$ that are significant.

The effect of REG is evident at low values of $\beta$ where efficiency increases with increasing RR while TE decreases because more tar is necessary due to the lower temperature of GT exhaust gases.

Increasing the TIT results in higher efficiencies, higher flexibility because more $T_p$ are available and higher TE, therefore more cases in which the plant is self-sufficient.

Decreasing the $T_p$ results also in lower efficiencies but also in lower air temperature at REC outlet making regeneration possible in REG. Therefore the lower the $T_p$ the higher the range of $\beta$ that allow the use of a REG. In any case best efficiency points are always obtained where no regeneration is possible therefore without REG.

Best efficiency points as a function of TIT are shown in Fig. 7 only for case C because no best point was experienced for the B configuration. The overall plant efficiency is always comparable to the SOA of much more complicated IGCC arrangements where there is also a costly bottoming steam cycle that the proposed IPRP technology does not require.

Best efficiency points are always obtainable at low values of $\beta$ making case C arrangement more suitable for small scale plants than big ones. This peculiarity is also evident when considering the scalability of the technology. The graph of Fig. 8 shows the results grouped for GT scale. It is noticeable that efficiency decreases when shifting from microturbines to heavy duty GT.

Nevertheless, efficiency obtainable in compatibility with GT operational parameters are always in the 30–40% range making IPRP technology competitive with the available technologies at every scale.

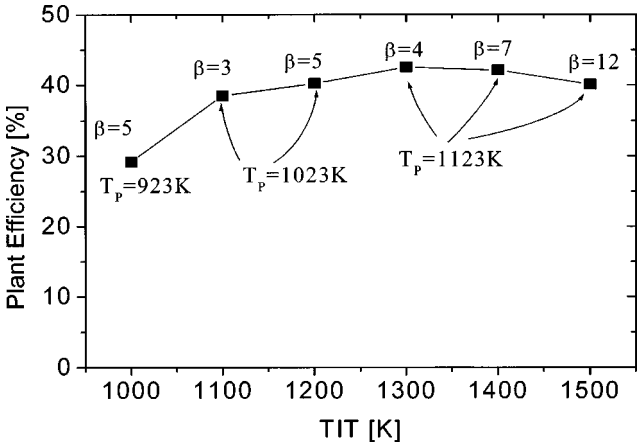


**Fig. 7 Best efficiency points for case C**

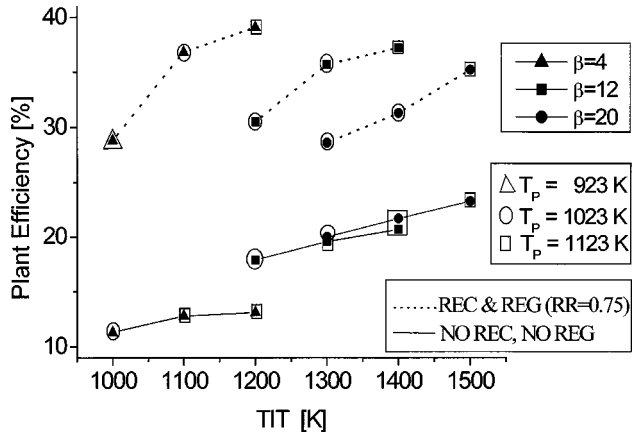


**Fig. 8 Best efficiency points for typical GT size parameters for case C**

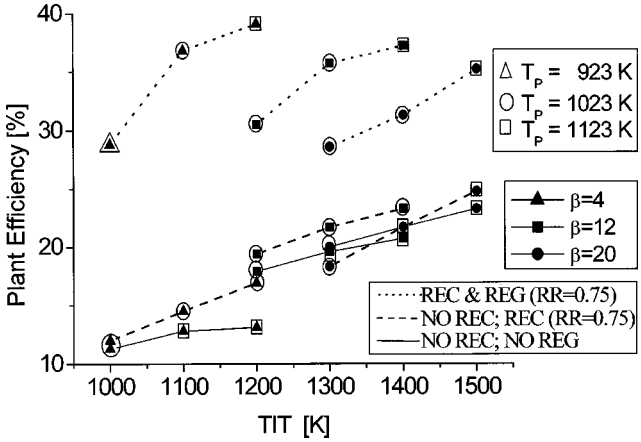


**Fig. 9 Comparison of plant efficiency in case A**

**Case D: Cycle With REG.** As we have seen in the previous section, the case with only REG is not very significant anymore having revealed that REG together with REC is most of the time not necessary. Moreover, being in this case exhaust gases from PYRO directly conveyed to stack, a lot of heat available is not reused inside the cycle therefore lower efficiencies are expected.

In this optic only the final results grouped for GT size will be shown for case D in Fig. 9 together with the previous ones so that a comparison will be possible.

**Table 6 Primary analysis and ultimate analysis of the raw materials [22]**

| Proximate analysis | [wt.%]* |
|---|---|
| Ash | 8.4 |
| Volatile matter | 77.3 |
| Fixed carbon | 14.3 |
| **Ultimate analysis** | **[wt.%]** |
| Carbon | 46.7 |
| Hydrogen | 4.8 |
| Nitrogen | 0.7 |
| Sulfur | 0.1 |
| Oxygen (difference) | 47.7 |
| | |
| LHV [kJ/Kg] | 17,120 |
| * Dry basis | |

Figure 9 shows clearly how the benefits of adding a REG to the simple cycle are less important than the benefits of adding a REC. However, GT may be commercially available with REG while introducing a REC into a commercial package could be economically not convenient especially in the micro scale. The positive effect of REG is evident at low $\beta$ typical of microturbines that are commercially available with REG.

## 7 Extension of the Results to Biomass

The plant behavior in the case C arrangement that gave best results was then reproduced considering biomass as a fuel. Data available in literature [22] were used to simulate biomass pyrolysis, the heat required for pyrolysis was obtained with the previously applied methodology using the heat of reaction found in Ref. [20] (see Table 6).

The pyrolysis behavior of biomass is shown in Fig. 10 where it is evident that the LHV of the syngas obtainable is quite lower than the LHV of the syngas obtainable from the pyrolysis of plastic. Syngas yield is also lower, with respect to data provided in Fig. 2, therefore a lower plant efficiency is expected. Moreover, plastic wastes pyrolysis results in a high production of tar and a very small production of char (and this latter was neglected), biomass pyrolyzes both to tar and char. Only char was considered in the simulation therefore char residual energy is quite low and the plant is often not self-sufficient. Results obtained are shown in Fig. 11.

Results show clearly that biomass halves the efficiencies obtainable with the IPRP technology with respect to the waste fu-

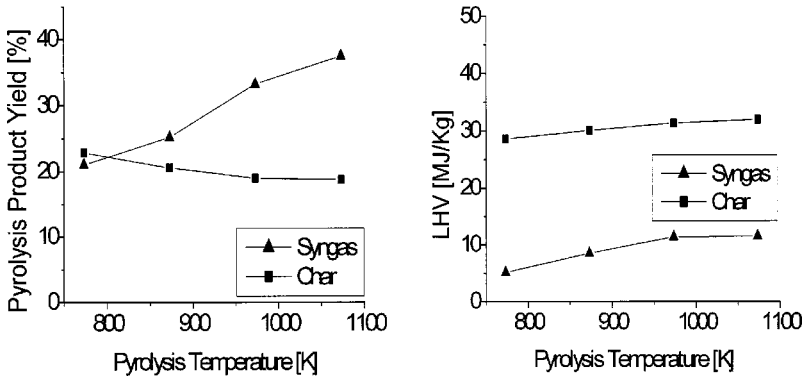


**Fig. 10 Pyrolysis products yield (*a*), LHV (*b*), and heat required for the pyrolysis (*c*) [22]**

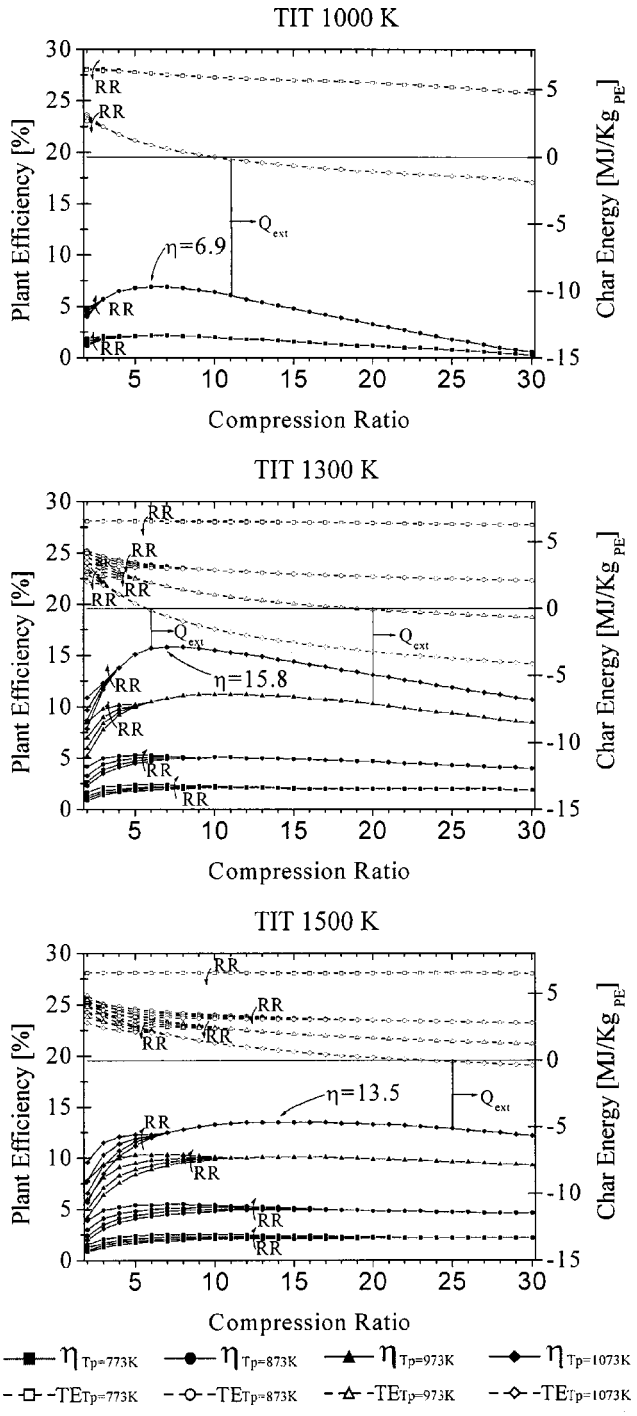


**Fig. 11 Results obtained for case C biomass fueled**

elled scenario. Best efficiency point show poor efficiencies for the microscale (around 7%) and encouraging values for the intermediate scale (around 16%). It has to be noted that this result is also affected by the use of char in post-combustion and not both char and tar therefore reducing prematurely the growing trend of efficiency curves in Fig. 11. This was assumed for technical reasons concerning the difficulty of burning tar in a char burner.

## 8 Conclusions

This paper analyzes an innovative solution for waste and biomass to energy conversion. The plant combines a rotary kiln pyrolyzer and a gas turbine fuelled by the pyrolysis gas produced from the thermal degradation of residual fuels. The exhaust gases from the gas turbine provide the heat required to maintain pyrolysis while additional energy may be supplied by post-combustion of tars and chars produced by pyrolysis. Four plant configuration were analyzed with different heat recovery solutions and for each of them performance was evaluated by varying main thermodynamic parameters.

When fueled with a plastic-behaving residue, results obtained for the simple cycle with no regeneration show best efficiencies that range from 11% for microscale plants to 23% for big scale plants. The possibility of regenerating the Joule cycle with the exhaust gases exiting the pyrolyzer strongly enhances plant performance especially on the medium to small scale with results that range between 30 and 40%. Using a recuperated GT improves efficiency only at low values of pressure ratio therefore it may be utilised only on the microscale.

When fueled with a wood-behaving residue the results obtained show similar trends but the efficiencies are halved due to the lower energetic content of the pyrolysis gas and the use of only char in post-combustion.

IPRP technology is a scalable concept because best efficiency points are obtainable for combinations of operational parameters that are consistent with microturbines, aeroderivative, and heavy duty GT's.

IPRP technology can perform as available technologies but at a lower capital cost because no bottoming steam cycle is required. Moreover, IPRP technology provides a solution for the micro scale where there are no available technologies.

Critical points of the proposed technology may be found in variable yields and energy content of pyrolysis products that may jeopardize performance and produce combustion irregularities in both the GT and TAR CC, and in syngas cleaning, that shall guarantee optimal performance of the syngas compressor and of the GT.

A laboratory scale rotary kiln was built at the University of Perugia [23] providing experimental data on pyrolysis to back up numerical simulation and the design of a microscale (70 kWe) IPRP pilot plant [24] that is being built at the Terni facility of the University of Perugia with regional co-funding.

## Nomenclature

B&W = biomass and waste
$Cp$ = specific heat at constant pressure
CC = combustion chamber
COMP = compressor
CYCLO = cyclone
GT = gas turbine
ICE = internal combustion engine
IGCC = integrated gasification combined cycle
LHV = low heating value
$\dot{m}$ = mass flow
$P$ = pressure (Pa)
PYRO = pyrolyzer
$Q$ = heat ($MJ/Kg_{RF}$)
RDF = refuse derived fuel
REC = recuperator
REG = regenerator
RF = residual fuel
RR = regeneration ratio
SCR = scrubber
SOA = state of the art
SYN = syngas
$T$ = temperature (K)
TE = tar energy (from residual tar (char) combustion)
TIT = turbine inlet temperature
$W$ = specific work ($J/Kg_{RF}$)
$\beta$ = compressor pressure ratio
$\phi$ = specific additional fuel consumption ($kg_{NG}/kg_{RF}$)

### Subscripts

Air = air
av = average
Eg = exhaust gases
Ext = external
In = inlet
NG = natural gas
Out = outlet
*P* = pyrolysis
RDF = refuse derived fuel
REG = regenerator
RF = residual fuel
Syn = syngas
T = turbine

## References


[1] UN Convention on Climate Change, 1997, Report of the conference of the parties on its third session, held at Kyoto from 1 to 11 December, FCCC/CP/1997/7/Add. 1.

[2] van den Broek, R., Faaij, A., and van Wijk, A., 1996, ''Biomass Combustion for Power Generation,'' Biomass Bioenergy, **11**, pp. 271–281.

[3] Stàhl, K., and Neergaard, M., 1998, ''IGCC Power Plant for Biomass Utilisation, Värnamo, Sweden,'' Biomass Bioenergy, **15**, pp. 205–211.

[4] Elmegaard, B., Henriksen, U., and Qvale, B., 2002, ''Thermodynamic Analysis of Supplementary-Fired Gas Turbine Cycles,'' *Proceedings of the Conference "ECOS 2002"*.

[5] Elmegaard, B., Qvale, B., Carapelli, G., and De Faveri, P., 2001, ''Open-Cycle Indirectly Fired Gas Turbine for Wet Biomass Fuels,'' *Proceedings of the Conference "ECOS 2001*,'' July 4–6, Istanbul, Turkey.

[6] Solantausta, Y., Bridgwater, A. V., and Beckman, D., 1995, ''Feasibility of Power Production With Pyrolysis and Gasification Systems,'' Biomass Bioenergy, **9**, pp. 257–269.

[7] Bridgwater, A. V., Elliot, D. C., Fagernas, L., Gifford, J. S., Mackie, K. L., and Toft, A. J., 1995, ''The Nature and Control of Solid, Liquid and Gaseous Emissions From the Thermochemical Processing of Biomass,'' Biomass Bioenergy, **9**, pp. 325–341.

[8] Demirbas, A., 2001, ''Carbonisation Ranking of Selected Biomass for Charcoal, Liquid and Gaseous Products,'' Energy Convers. Manage., **42**, pp. 1229–1238.

[9] Demirbas, A., 1997, ''Calculation of Higher Heating Values of Biomass Fuels,'' Fuel, **76**, pp. 431–434.

[10] Demirbas, A., 2000, ''Mechanism of Liquefaction and Pyrolysis Reactions of Biomass,'' Energy Convers. Manage., **41**, pp. 633–646.

[11] Di Blasi, C., and Branca, C., 2000, ''Evaluation of the Performance of a Novel Straw Pyrolysis Reactor,'' 1st World Conference on Biomass for Energy and Industry, Sevilla, Spain, 5–9 June, pp. 1767–1770.

[12] Di Blasi, C., Signorelli, G., Di Russo, C., and Rea, G., 1999, ''Product Distribution From Pyrolysis of Wood and Agricultural Residues,'' Ind. Eng. Chem. Res., **38**, pp. 2216–2224.

[13] Di Blasi, C., Signorelli, G., and Portoricco, G., 1999, ''Countercurrent Fixed-Bed Gasification of Biomass at Laboratori Scale,'' Ind. Eng. Chem. Res., **38**, pp. 2571–2581.

[14] Roy, C., and Morin, D., 1998, ''Efficient Electricity Production From Biomass Through IPCC Power Plants,'' 4th International Conference on Greenhouse Gas Control Technologies (GHGT4), Interlaken, Switzerland.

[15] Fantozzi, F., D'Alessandro, B., and Bidini, G., 2003, ''IPRP—Integrated Pyrolysis Regenerated Plant—Gas Turbine and Externally Heated Rotary-Kiln Pyrolysis as a Biomass and Waste Energy Conversion System. Influence of Thermodynamic Parameters,'' Proc. Inst. Mech. Eng., Part A: J. Power Energy **217**, pp. 519–527.

[16] Fantozzi, F., Di Maria, F., and Desideri, U., 2001, ''Micro-Turbine Fuelled by Pyrolysis Gas,'' *Thermodynamic Analysis, Proceedings of the POWERGEN Europe Congress and Exhibition*, Helsinki.

[17] Fantozzi, F., Di Maria, F., and Desideri, U., 2002, ''Integrated Micro-Turbine and Rotary Kiln Pyrolysis System as a Waste to Energy Solution for a Small Town in Central Italy—Cost Positioning and Global Warming Assessment,'' ASME Paper GT-2002-30652.

[18] Li, A. M., Li, X. D., Ren, Y., Chi, Y., Yan, J. H., and Cen, K. F., 1999, ''Pyrolysis of Solid Waste in a Rotary Kiln: Influence of Final Pyrolysis Temperature on the Pyrolysis Products,'' J. Anal. Appl. Pyrolysis, **50**, pp. 149–162.

[19] Yang, J., and Roy, C., 1996, ''A New Method for DTA Measurement of Enthalpy Change During the Pyrolysis of Rubbers,'' Thermochim. Acta, **288**, pp. 155–168.

[20] Arcangioli, S., Gamberi, F., Milli, A., and Scapecchi, N., ''Analysis of an Indirectly Biomass-Fired Gasturbine Engine Integrated With Pyrolysis for Supplementary Firing,'' Biomass Gasification Group, Department of Mechanical Engineering, Technical University of Denmark (DTU) Internal Report.

[21] Neilson, C. E., 1998, ''LM2500 Gas Turbine Modifications for Biomass Fuel Operation,'' Biomass Bioenergy, **15**, pp. 269–273.

[22] Encinar, J. M., Gonzalez, J. F., and Gonzalez, J., 2000, ''Fixed-Bed Pyrolysis of Cynara Cardunculus L. Product Yields and Compositions,'' Fuel Process. Technol., **68**, pp. 209–222.

[23] Frantozzi, F., and Desideri, U., 2004, ''Micro Scale Rotary Kiln Slow-Pyrolysis for Syngas and Char Production from Biomass and Waste: Reactor and Test Bench Realization,'' ASME Paper GT-2004-54186.

[24] Bidini, G., Moriconi, A., Rossi, D., and Fantozzi, F., 2004, ''IPRP—Integrated Pyrolysis Regenerated Plant Rotary Kiln Pyrolyzer and Microturbine for Distributed Energy Conversion from Biomass—A 70 Kw Demonstration Unit in Central Italy,'' *Proceedings of the Second World Conference and Technology Exhibition on Biomass for Energy Industry and Clilmate Protection*, May, Rome.

**Shoko Ito**
e-mail: shoko1.ito@toshiba.co.jp

**Hiroshi Saeki**

**Asako Inomata**

**Fumio Ootomo**

**Katsuya Yamashita**

**Yoshitaka Fukuyama**[1]

Toshiba Corporation,
Yokohama, Japan

**Elichi Koda**

**Toru Takehashi**

**Mikio Sato**
e-mail: satomiki@criepi.denken.or.jp

Central Research Institute of Electric Power Industry,
Yokosuka, Japan

**Miki Koyama**

**Toru Ninomiya**
e-mail: ninomiyator@nedo.go.jp

New Energy and Industrial Technology Development Organization,
Tokyo, Japan

# Conceptual Design and Cooling Blade Development of 1700°C Class High-Temperature Gas Turbine

*In this paper we describe the conceptual design and cooling blade development of a 1700°C-class high-temperature gas turbine in the ACRO-GT-2000 (Advanced Carbon Dioxide Recovery System of Closed-Cycle Gas Turbine Aiming 2000 K) project. In the ACRO-GT closed cycle power plant system, the thermal efficiency aimed at is more than 60% of the higher heating value of fuel (HHV). Because of the high thermal efficiency requirement, the 1700°C-class high-temperature gas turbine must be designed with the minimum amount of cooling and seal steam consumption. The hybrid cooling scheme, which is a combination of closed loop internal cooling and film ejection cooling, was chosen from among several cooling schemes. The elemental experiments and numerical studies, such as those on blade surface heat transfer, internal cooling channel heat transfer, and pressure loss and rotor coolant passage distribution flow phenomena, were conducted and the results were applied to the conceptual design advancement. As a result, the cooling steam consumption in the first stage nozzle and blade was reduced by about 40% compared with the previous design that was performed in the WE-NET (World Energy Network) Phase-I.* [DOI: 10.1115/1.1806456]

## Introduction

In regard to the greenhouse effect, there is a global and strong demand to reduce $CO_2$ emissions by the improvement of the thermal efficiency of power plants. The project entitled ACRO-GT-2000 was sponsored by the New Energy and Industrial Technology Development Organization of Japan (NEDO) and conducted from fiscal year 1999 to 2001. The aim of the project, which was the successor project to WE-NET Phase-I, was the development of a 500 MW class thermal power plant with more than 60% HHV efficiency by using methane ($CH_4$) fuel instead of hydrogen ($H_2$) in the WE-NET project and free from $CO_2$ emission due to recovery of the $CO_2$ from exhaust gas. The purpose of the new project is to promote the near-term realization of a highly efficient power plant by utilizing more general and practical fuel, $CH_4$. And a fundamental system study of a high-efficiency closed cycle power generation system has been performed and reported by Koda et al. [1].

Several system studies have been performed for the $CO_2$ recovery power generation systems by other researchers. Jackson et al. [2] studied the closed topping cycle system for a $CO_2$ and $H_2O$ gas mixture with the sequestration of $CO_2$. Jeriche et al. [3] reported the conceptual design of a prototype 100 MW class Graz cycle power plant. In both cases, 1500°C (2370°F)-class gas turbine was assumed.

The present system features the introduction of the $CH_4$-$O_2$ combustion system and the 1700°C (3090°F)-class high-temperature gas turbine. It is well known that the increase in turbine inlet temperature has a strong impact on the thermal efficiency enhancement. However, the gas turbine working temperature rise results in the increase of the coolant flow rate, under the turbine blade, with the same cooling structure, material, and thermal barrier coating (TBC). And the increase of the coolant consumption deteriorates the thermal efficiency of the plant. So, for the realization of high-temperature gas turbine, the development of a more efficient cooling structure, a more durable base-metal and a more effective insulation coating are essential.

The cooling structure selected for the first stage nozzle and blade was a hybrid cooling scheme that was developed and verified by a high-temperature cascade experiment in the former project, WE-NET [4,5] To minimize the coolant flow rates, various elemental experiments and numerical studies have been carried out.

[1]Currently at Japan Aerospace Exploration Agency, Tokyo, Japan. E-mail: fukuyama.yoshitaka@jaxa.jp

Contributed by the International Gas Turbine Institute (IGTI) of THE AMERICAN SOCIETY OF MECHANICAL ENGINEERS for publication in the ASME JOURNAL OF ENGINEERING FOR GAS TURBINES AND POWER. Paper presented at the International Gas Turbine and Aeroengine Congress and Exhibition, Atlanta, GA, June 16–19; 2003, Paper No. 2003-GT-38352. Manuscript received by IGTI, October 2002, final revision, March 2003. Associate Editor: H. R. Simmons.

  

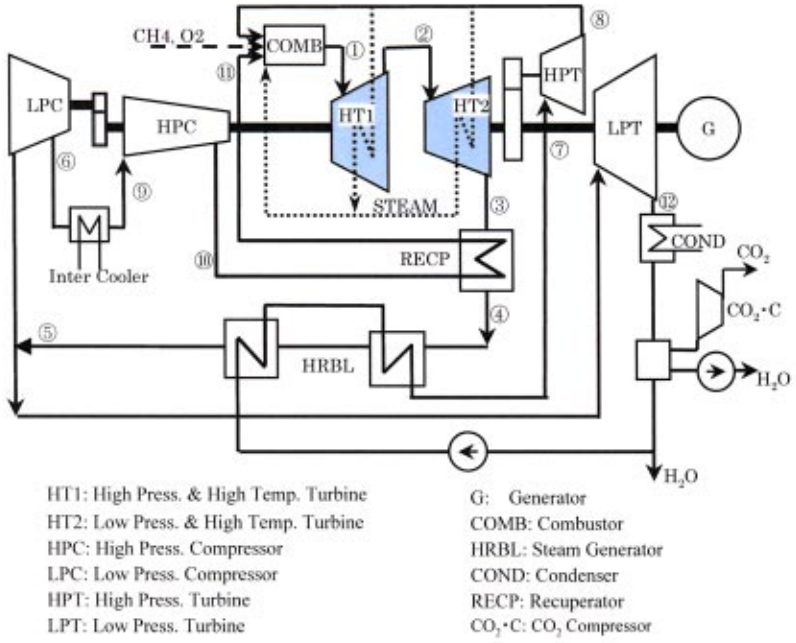


**Fig. 1 Schematic diagram of $CO_2$ recovery power generation system**

A conceptual design and cooling blade development studies of 1700°C-class high-temperature gas turbine are reported in this paper.

## System and Conceptual Design of High-Temperature Turbine

Figure 1 shows the schematic diagram of the ACRO-GT system. And Table 1 summarizes the flow condition at selected node of Fig. 1. The system consists of a closed Brayton cycle part with $CH_4$-$O_2$ combustion and a Rankine cycle part utilizing the waste heat of the Brayton cycle. The Brayton cycle is comprised of a low-pressure compressor (LPC), a high-pressure compressor (HPC), a combustor (COMB), and two high-temperature turbines (HT1, HT2). The inlet temperature and pressure of HT1 selected were 1700°C (3090°F) and 4.51 MPa (0.654 ksi). The Brayton cycle working fluid is a mixture of $H_2O$ and $CO_2$, which was generated by $CH_4$ and $O_2$ combustion. The exhaust gas of HT2 exchanges heat with high-pressure steam from HPC at recuperator (RECP) and then heats the feed water from condenser (CON) in the heat recovery boiler (HRBL). The steam generated by HRBL is rated at 543°C 31 MPa (1010°F/4.50 ksi) and is led to a high-pressure turbine (HPT). The outlet steam of HPT is used as the coolant of HT1 and HT2 and is finally fed into COMB. The HRBL exhaust gas is divided into two and fed into a low-pressure turbine (LPT) and a low-pressure compressor (LPC). Part of the gas that was expanded in LPT is then led to the condenser (CON). Since $CO_2$ is not liquefied there, it is separated from water at CON and exhausted as pure $CO_2$ by the $CO_2$ compressor ($CO_2$-C).

**Table 1 Flow condition at selected nodes**

| Node | Flow rate (kg/s) | Temperature (°C) | Pressure (MPa) |
|---|---|---|---|
| ① | 277.94 | 1700 | 4.513 |
| ② | 309.4 | 1271.4 | 1.47 |
| ③ | 309.4 | 717.6 | 0.112 |
| ④ | 309.4 | 627.4 | 0.1064 |
| ⑤ | 309.4 | 106.5 | 0.1013 |
| ⑥ | 119.22 | 347.9 | 0.7189 |
| ⑦ | 96.9 | 543 | 31.0 |
| ⑧ | 96.9 | 310.9 | 6.579 |
| ⑨ | 134.69 | 170.9 | 0.7045 |
| ⑩ | 134.69 | 454.5 | 5.0 |
| ⑪ | 134.69 | 600 | 4.75 |
| ⑫ | 190.18 | 40.2 | 0.0085 |

Figure 2 shows the cross-sectional view and the shaft arrangements. The high-temperature turbines HT1 and HT2 are driven at different rotational speeds. The HT1 shares the shaft with HPC and the HT2 shares the shaft with LPT and Generator (G). These shaft arrangements and the rotational speeds are decided based on the evaluation of turbine aerodynamic efficiency and structural integrity of the rotating components. Figure 3 shows the relationship between adiabatic efficiency and rotational speed for HT1. Generally, the aerodynamic efficiency of a turbine increases with the increase of rotational speed.

One of the critical points besides the turbine is the productivity of high-temperature and the large size connection duct between HT1 and HT2. The cooling and structural design of this connection duct depends on the load of HT1, namely, the outlet temperature of HT1. The higher the gas temperature becomes, the greater is the need for cooling. And the relatively large surface area of the connection duct necessitates the consumption of a large amount of coolant, which directly results in the decrease of thermal efficiency. Therefore, the stage number of HT1 should be larger to lower the HT1 outlet temperature.

Figure 4 indicates the gas-path configuration of HT1 under the two rotational speeds of 9500 and 6000 rpm. As the figure shows, if the peripheral speed and volume flow rate are kept constant, the increase of the shaft rotational speed results in the decrease of the gas path radius and also the increase of the blade height. From the blade structural design viewpoint, the higher the aspect ratio of the blade (height/chord) is, the higher the centrifugal force acting on the blade becomes. Therefore, the last stage long blade becomes difficult to realize with the increase of the rotational speed. From these design trade-offs, 9500 rpm/3-stage design was selected for HT1. Under this condition, the outlet temperature of HT1 is about 1300°C (2370°F) and the connection duct manufac-

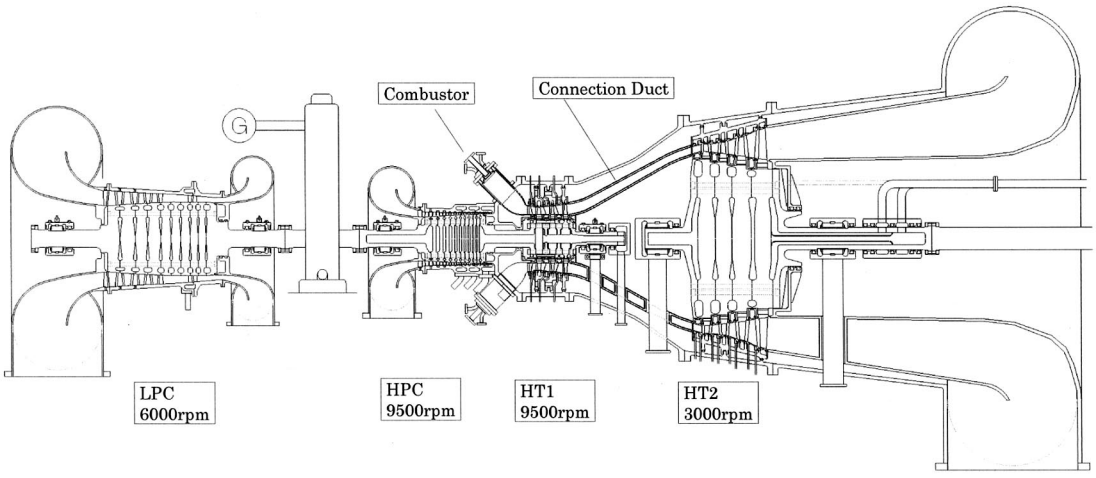


**Fig. 2 Structure of 1700°C class gas turbine**

turing becomes feasible. For the 1300°C-class HT2, 3000 rpm/4-stage turbine design was selected. Table 2 summarizes the specification of HT1 and HT2.

## High-Temperature Turbine Cooling System

Figure 5 indicates the schematic drawing of the HT1 cooling system. The turbine rotor consists of three turbine disks, two spacers, rear shaft and intermediate shaft (which connects with HPC), all of which are bolted together. The steam, individually supplied from the casing side, cools the nozzles. On the other hand, rotor cooling steam is supplied from the bore of the rear shaft. The rear shaft and one to two stage spacer disk have many radial channels to feed the coolant to the ring-shaped supply cavity just below the root of the blades. The steam, which cools the blades internally, is accumulated in the recovery cavity and then led to the combustor. This cooling steam flow also cools the rotor and spacer disks to sufficiently low temperature. Finally, a relatively small amount of steam is consumed as a hot gas seal at the disk to disk clearance.

In this type of internal cooling, the turbine hot parts such as the nozzle and blade act as a steam super-heater. And the thermal energy transmitted from the hot main flow gas to coolant is recovered in the combustor.

## Elemental Experiments

**Rotor Center Bore and Radial Channels Flow.** The steam flow in the rotor is complex, because of the rotational effects. And the pressure loss characteristics may be different from that of the stationary case. To design the inside-rotor coolant distribution, pressure loss characteristics need to be clarified. Therefore, the experimental measurements of the pressure loss of the rotor bore and radial distribution channel have been carried out.

Basically, the Coriolis and inertia force may dominate the flow in the rotating system under the gas turbine condition. So that in the model experiments, the ratio of Reynolds numbers $Re_r$ over $R_\omega$, namely $\Omega$, has been selected as the main experimental parameter and made nearly equal to the HT1 condition. $Re_r$, $R_\omega$, and $\Omega$ in the experimental and HT1 conditions are listed in Table 3.

$$R_\omega = \omega d^2/(2\nu) \tag{1}$$

$$Re_r = Vd/\nu \tag{2}$$

$$\Omega = R_\omega/Re_r \tag{3}$$

$$\zeta = \Delta P/(0.5\rho\ V^2) \tag{4}$$

Figure 6 shows the drawing of the test section. The axial inflow passage (center bore) is 80 mm in diameter. The radial distribution channels are 18.8 mm×18.8 mm square and the number was 12. A photograph of the apparatus is shown in Fig. 7. Experiments were carried out up to the rotational speed of 4000 rpm under the ambient air condition.

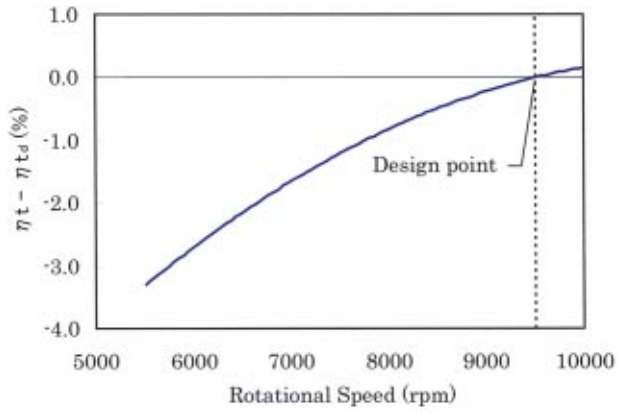


**Fig. 3 Variation of adiabatic efficiency with rotational speed (HT1)**

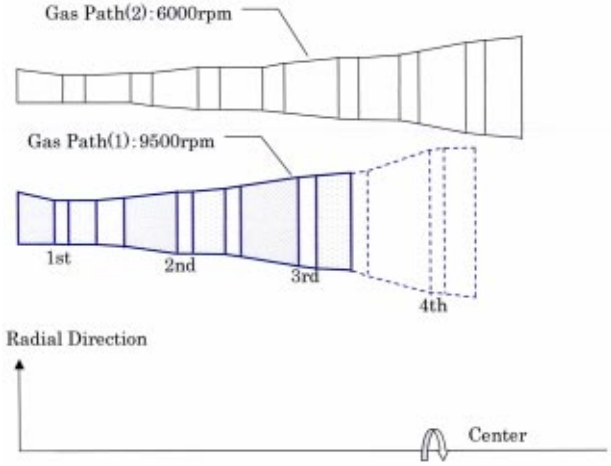


**Fig. 4 Gas path configuration (HT1)**

**Table 2 Specification of high-temperature turbine. Stage: N: Nozzle; B: Blade; Cooling Method: H: Hybrid cooling, C: Recovery cooling.**

| HT1 | | | | | | | | |
|---|---|---|---|---|---|---|---|---|
| Stage | 1N | 1B | 2N | 2B | 3N | 3B | | |
| Number of blades | 38 | 64 | 40 | 88 | 40 | 88 | | |
| Blade height mm | 101 | 101 | 119 | 119 | 142 | 142 | | |
| Blade mean diam mm | 824 | 824 | 843 | 843 | 866 | 866 | | |
| Blade chord (mean) mm | 93.6 | 57.6 | 107.3 | 43.1 | 109.7 | 45.7 | | |
| TBC | Y | Y | Y | Y | Y | Y | | |
| Cooling method | H | H | H | H | C | C | | |
| HT2 | | | | | | | | |
| Stage | 4N | 4B | 5N | 5B | 6N | 6B | 7N | 7B |
| Number of blades | 60 | 130 | 80 | 130 | 80 | 92 | 80 | 92 |
| Blade height mm | 100 | 112 | 149 | 171 | 243 | 289 | 400 | 464 |
| Blade mean diam. mm | 2674 | 2674 | 2674 | 2674 | 2702 | 2721 | 2763 | 2795 |
| Blade chord (mean) mm | 168.9 | 83 | 154.6 | 89.8 | 137.8 | 116.8 | 151.5 | 124.2 |
| TBC | Y | Y | Y | Y | Y | Y | Non | Y |
| Cooling method | C | C | C | C | C | C | Non | C |

Figure 8 shows the relationship between total pressure loss coefficient $\zeta$ and $\Omega$. In the figures, experimental and numerical results are plotted. It was found that the pressure loss coefficient $\zeta$ through the center bore was about 0.3–0.4; on the other hand, that of the radial channels (including the inlet/outlet effects) was 3.0–4.0. Furthermore, the pressure loss coefficients were nearly constant for $\Omega$ in the range of parameters studied herein. The CFD results obtained by using STAR-CD agree well with those obtained by the experiment. The resulting streamline visualization is shown in Fig. 9.

It is concluded that the radial distribution channel dominates the pressure loss of the turbine rotor coolant supply system. Moreover, it is clearly understood from the CFD results that the flow separation at the radial channel inlet and outlet generates large pressure loss. This flow separation was due to the strong flow direction change that occurred there. By using the pressure loss results, the HPT rotor system coolant distribution was rearranged.

**Blade Surface Heat Transfer.** The blade surface heat transfer distribution has been measured for the two-dimensional cascade with tip clearance in the low-speed wind tunnel. The blade profile used was that designed in the WE-NET project, since the purpose of the experimental study was to evaluate the ability of the numerical simulation procedure of the present design, the comparative evaluation is worthwhile. The numerical procedure will be used to estimate the 1700°C real gas turbine blades' thermal and hydraulic boundary conditions in the design.

Figure 10 shows the assembly of the two-dimensional model blade cascade. The main experimental parameters were the blade exit Reynolds number ($Re_m$) and the cascade inlet turbulent intensity (Tu). The maximum experimental $Re_m$ is $1.6\times10^6$ and is the same level as that under the HT1 condition. It is well known that the turbulent intensity has a strong impact on the heat transfer coefficient and distribution. However, Tu of a real machine is difficult to estimate. In the present experiments, large Tu was generated by positioning the turbulence grid upstream of the cascade and the effect was studied. The measured Tu at the blade inlet was 1.4% for the without-grid condition and 12.4% for the with-grid condition.

Using the unique thermochromic liquid crystal technique, which utilizes the color (RGB) information of a liquid crystal to estimate temperature [6–8], performed the measurement of the heat transfer coefficient. The blade surface heat transfer coefficient was calculated from heat flux and temperature. Heat flux of the blade surface was estimated from metal foil heater energy input, considering the inter-solid heat loss calculated by heat conduction analysis. Blade surface temperature has been converted from video recorded color of the liquid crystal.

Figures 11, 12, and 13 show the comparison between experi-

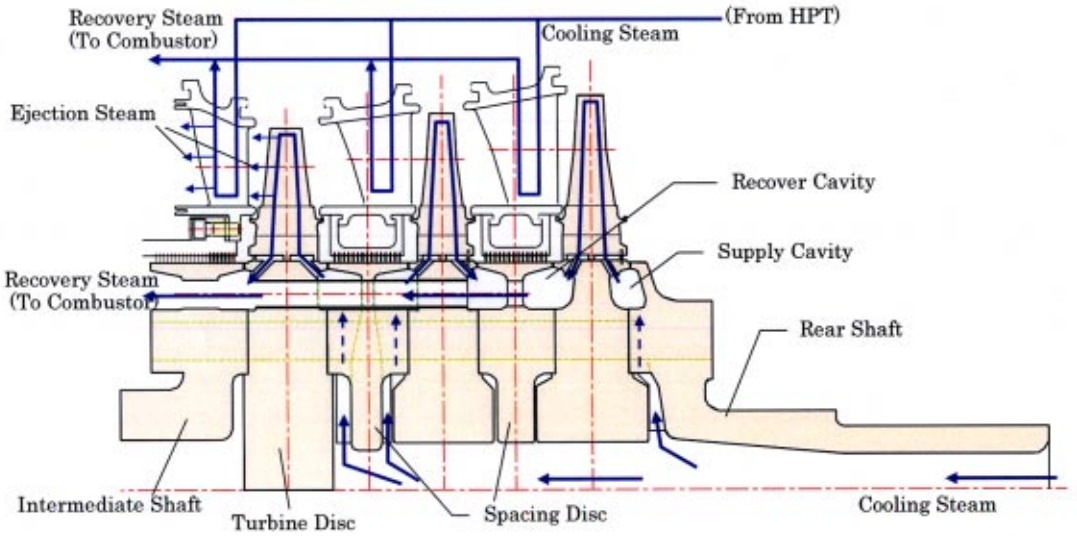


**Fig. 5 Schematic of turbine cooling system**

**Table 3 Range of parameter in experimental study**

| | | $R_\omega$ | $\mathrm{Re}_r$ | $\Omega$ |
|---|---|---|---|---|
| Center bore | Test range | $0-1.2\times10^5$ | $2-5\times10^5$ | 0–0.43 |
| | HT1 | $9.83\times10^6$ | $1.48\times10^7$ | 0.66 |
| Radial channel (inlet) | Test range | $0-6\times10^4$ | $0.4-1.1\times10^5$ | 0–1.3 |
| | HT1 | $2.31\times10^6$ | $2.08\times10^6$ | 1.11 |

mental results and numerical predictions for the first stage nozzle and blade at the mean height position. The nozzle surface heat transfer measurements have already been reported by Okamura et al. [4]. The two-dimensional simulation was performed by boundary layer code [9] and the three-dimensional prediction was executed by the multiblock Navier-Stokes code [10,11]. The turbulence model used in the three-dimensional CFD was a low Reynolds number version k-epsilon model of Launder and Sharma [12] with the Kato and Launder production model [13].

The measured, two-dimensional prediction and three-dimensional simulation show good agreement for the nozzle surface heat transfer distribution. And the suction side sudden heat transfer augmentation caused by the boundary layer transition is predicted well.

On the other hand, blade surface heat transfer characteristics show a big difference between measurement and prediction. The pressure side difference may be caused by the flow instability and separation that occurred under the strong adverse pressure gradient at the location, pressure side just downstream of the leading edge. On the suction side, the experiments indicate the increase of heat transfer with the increase of Tu, but the three-dimensional CFD could not predict such a big difference. The turbulence modeling and grid resolution may partly cause this inconsistency.

The blade profile has been redesigned for the present project to account for the changes in the main flow conditions and with consideration of an acceleration factor to suppress separation.

Figures 14 and 15 indicate the visualization of numerical heat transfer distributions and a near-endwall velocity vector direction. The color indicates the relative level of the Stanton number (St), red represents high St, and blue represents low St. The basic three-dimensional characteristics of the flow, the generation of the horseshoe vortex, passage vortex, and suction surface separation, may be simulated well by the present CFD procedure. Figure 16 shows the streamline visualization of two-dimensional blade cascade flow field observed from the downstream direction. The top half of the figure indicates the formation of the tip leak vortex and the bottom half of the figure indicates the secondary flow and generation of the separation region near the blade root.

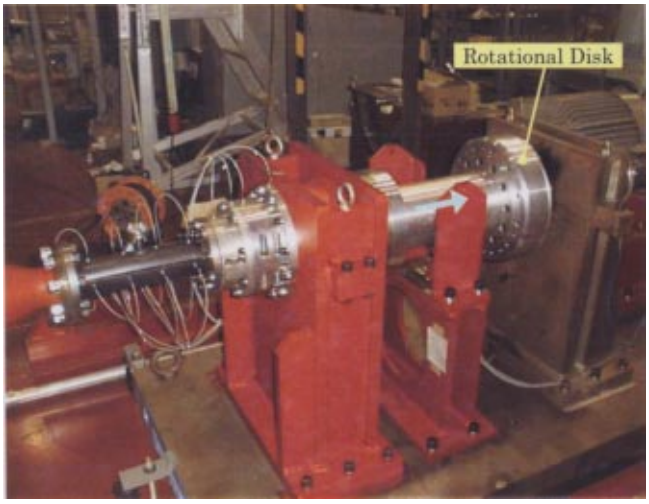


**Fig. 7 Photograph of rotor cooling flow test apparatus**

**Internal Cooling Channel Heat Transfer.** It is important to enhance the blade internal surface heat transfer by using turbulence promoters. In the present study, heat transfer of the skewed broken rib (4-rows) has been studied in comparison with the conventional 45 deg skewed continuous rib. The skewed broken rib was expected to increase the heat transfer coefficient by generating the three-dimensional vortex from the rib's leading edge and by thinning the thermal boundary layer thickness on the rib surface by discontinuity. Experimental measurements have been performed to focus on the heat transfer and pressure loss characteristics.

Figure 17 shows the photograph of the experimental apparatus. The test section was a 50 mm $\times$50 mm square channel and 1300 mm long, with a ribbed length of 540 mm in the middle, made of acrylic resin. Three test sections with a smooth wall, continuous ribbed wall, and broken ribbed wall, respectively, were prepared. To simulate the blade internal cooling channel, only two walls were equipped with ribs. The total heat transfer ability of the rib roughened surface is comprised of the wall surface and the rib surface. To measure the mean heat transfer coefficient on the rib surface, a copper rib test section has also been used.

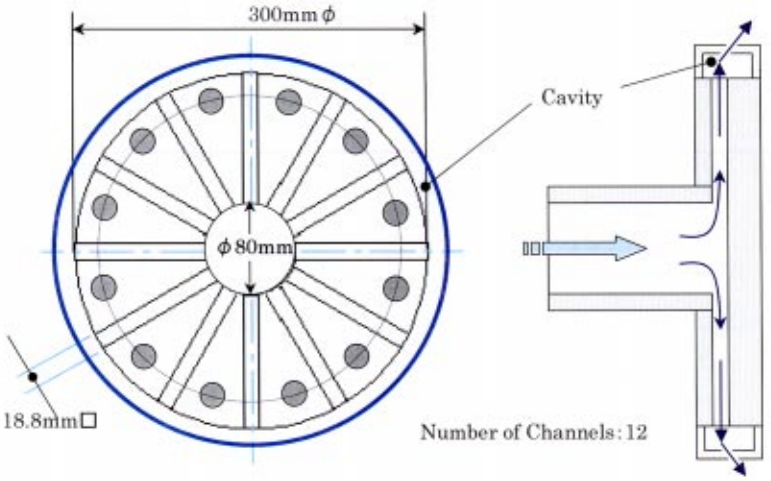


**Fig. 6 Rotor cooling flow test section**

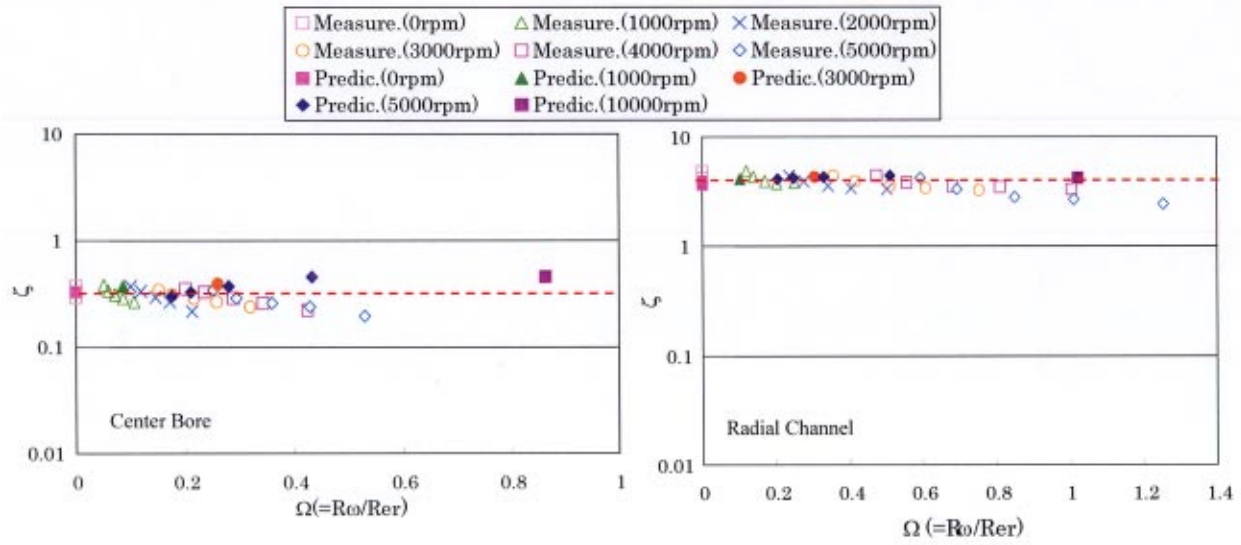


**Fig. 8 Pressure loss coefficient in rotor cooling passage**

For the wall surface, the thermochromic liquid crystals technique was used for the heat transfer measurement. The channel Reynolds number ($Re_c$) ranged from $10^4$ to $10^5$.

The measured heat transfer coefficient of the smooth wall channel agreed well with the turbulent channel correlation. And the rib effect was measured by the ratio of the Nusselt number (Nu) to that of the smooth wall condition ($Nu_0$). The value is called heat transfer enhancement in this paper.

Figure 18 shows the local heat transfer enhancement distribution for the broken ribbed wall at $Re_c = 8 \times 10^4$ as an example of liquid crystal measurements. It can be seen from the figure that the local heat transfer augmentation due to the vortex formation from the rib leading edge is not obvious. However, it was found that the rib surface heat transfer for the broken rib was about 2.0 to 2.3 times higher than that for the continuous rib. This leads to the conclusion that the broken rib heat transfer enhancement comes from the rib surface thermal boundary layer thinning effect.

Figure 19 indicates the Reynolds number dependency of mean heat transfer enhancement including both walls and rib surfaces. It was found that the present smooth side wall results agreed well

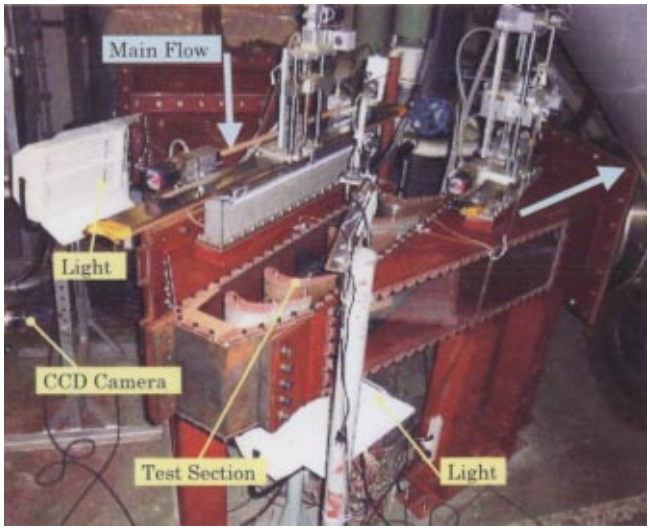


**Fig. 10 Photograph of heat transfer cascade test apparatus**

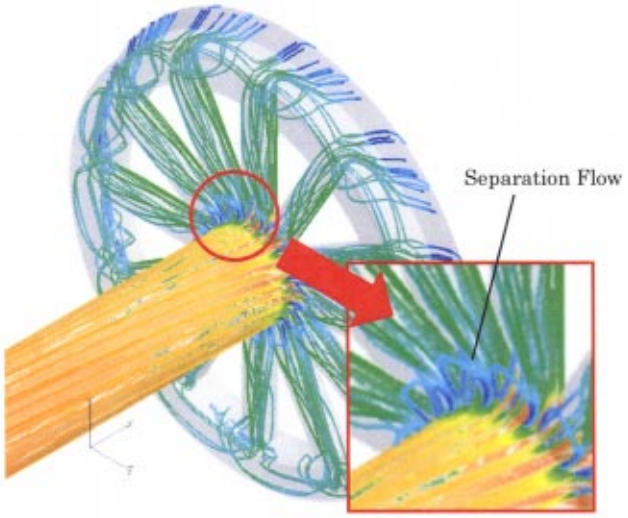


**Fig. 9 Streamlines on the rotor cooling passage**

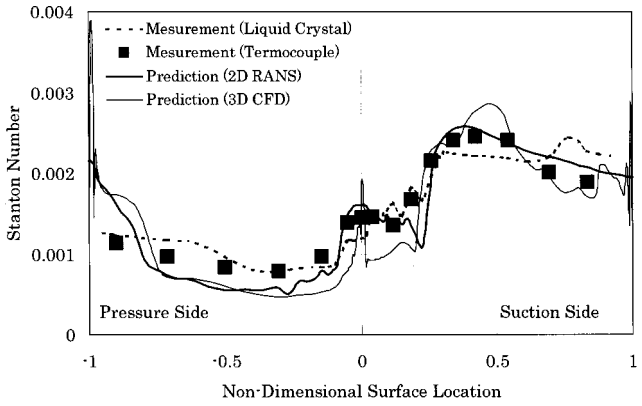


**Fig. 11 Distribution of Stanton number on nozzle surface (Re $=1.6\times10^6$, Tu=2.1%)**

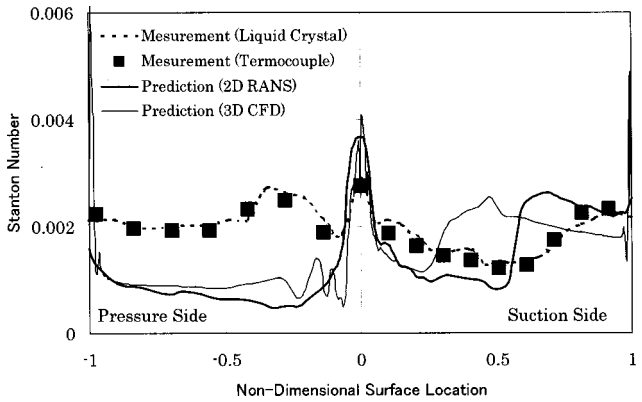


**Fig. 12 Distribution of Stanton number on blade surface (Re $=8.1\times10^5$, Tu=1.4%)**

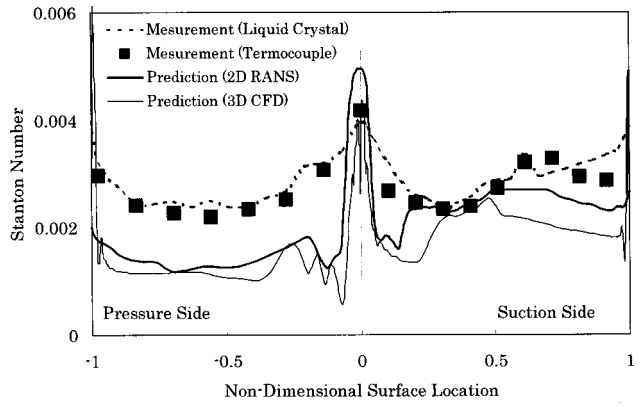


**Fig. 13 Distribution of Stanton number on blade surface (Re $=8.1\times10^5$, Tu=12.4%)**

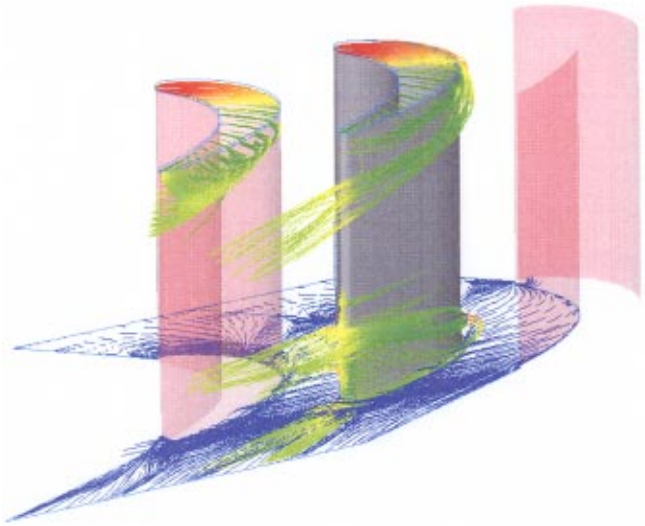

**Fig. 16 Numerical streamline visualization on two-dimensional bucket flow field with tip clearance**

with the results reported by Han et al. [14,15], and the broken rib has heat transfer ability 25% higher than that of the continuous rib. Figure 20 shows the measured mean friction factor ($C_f$) and compares it with that reported by Han et al. [15]. The friction factor was found to be at the same level for the broken rib and the continuous rib.

Following the results of the experimental study, the four-rows-type broken rib was adopted for the internal channel of the present high-temperature gas turbine blades.

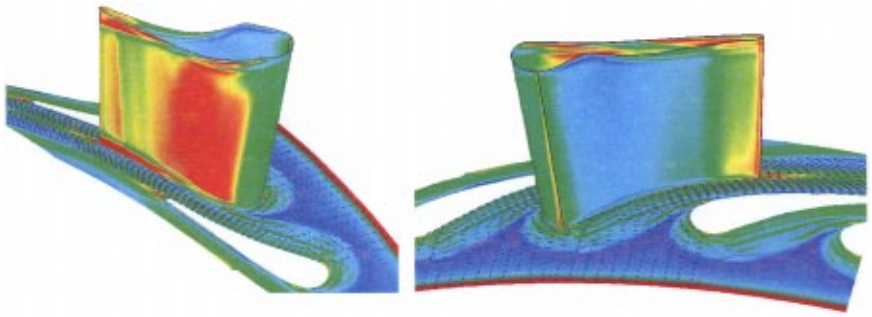

**Fig. 14 Computed Stanton number distribution on nozzle surface (Re=$1.6\times10^6$, Tu =2.1%)**

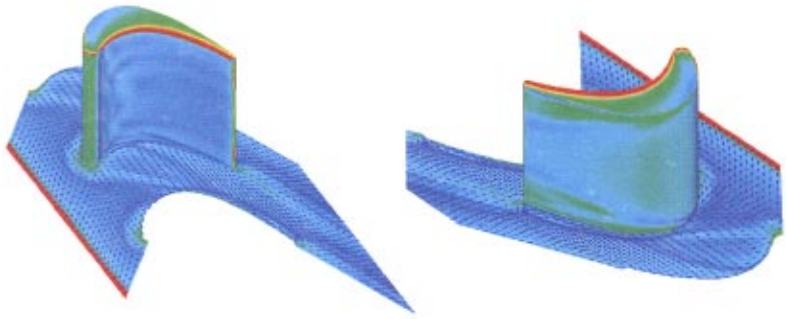

**Fig. 15 Computed Stanton number distribution on blade surface (Re=8.1 $\times10^5$, Tu=12.4%)**

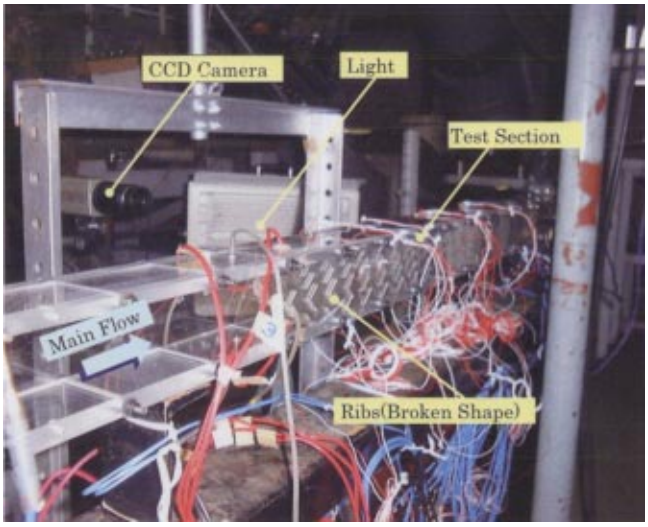


Fig. 17 Photograph of ribbed wall heat transfer test apparatus

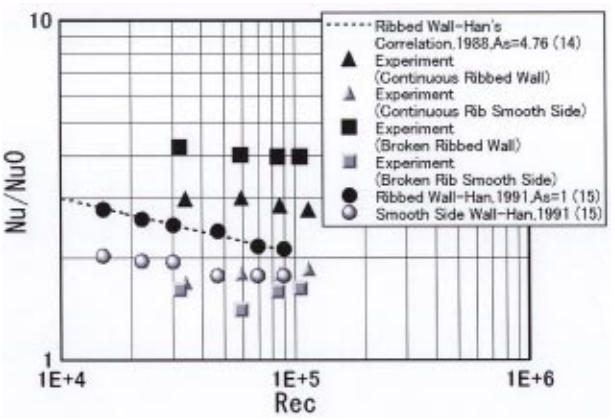


Fig. 19 Mean Nusselt number augmentation on the ribbed wall

## Design of HT1 First Stage Blades

**First Stage Nozzle and Blade Cooling Structure.** Table 4 lists the main flow gas and cooling steam specifications and cascade design parameters. The former WE-NET Project conditions are also indicated for reference. The allowable temperatures for TBC surface and base metal were assumed to be 1300°C (2370°F) and 950°C (1740°F), respectively.

Figure 21 indicates the designed cooling configuration of the first stage nozzle and blade. The leading edge part of the nozzle and blade suffer from the severe heat invasion from the hot gas, and are cooled by the shower-head-type film cooling. As can be seen from the figure, diffusion-shaped-type film cooling rows were added at the locations of the high heat load on the nozzle surface. The mid-chord internal cooling structure employed multipass serpentine passage with a broken-type rib.

These blades will be manufactured by precision casting. And inserts are installed in the nozzle channels to apply impingement cooling.

**Nozzle and Blade Cooling Effectiveness and Coolant Consumption.** The turbine nozzle and blade shown in Fig. 21 were redesigned utilizing the following advanced technologies. (1) Optimization of the cooling channel arrangement. (2) Adoption of the broken rib on the channel surface. (3) The utilization of newly developed TBC [16,17] and Ni-based high-temperature supperalloy [18].

Figure 22 shows the resulting blade surface temperature distributions at the mean height cross section. The blade surface heat transfer distributions were calculated by using the previously mentioned CFD codes. And the TBC and metal temperatures were calculated by coupling the heat and fluid analysis of internal channels with the heat conduction analysis of blade metal and TBC. Again, the allowable temperatures of TBC and metal surfaces were 1300°C and 950°C, respectively, in the present project. It can be seen from the figure that the maximum temperatures of TBC and metal were lower than these allowable limits.

Figure 23 shows the comparison of the coolant flow ratio for the first stage nozzle and blade. The coolant flow rate ($G_c$) over the main stream gas flow rate ($G_g$), namely, the coolant flow ratio ($G_c/G_g$) has been decreased by about 40% (from 6.3% to 4% for the nozzle, from 7% to 4.2% for the blade) in the first stage, compared with that of the WE-NET project. In particular, the ejection coolant flow rates have been decreased by 50% and 29% for the nozzle and blade, respectively.

Here, it must be noted that under the fixed turbine nozzle inlet temperature, the blade row inlet temperature changes and depends on the nozzle cooling scheme. Namely, the blade row inlet temperature decreases with the increase of the ejection cooling flow rate, because of hot main flow gas and cold coolant gas mixing. The internal cooling has less effect on the working gas temperature. This gas temperature decrease caused by cooling results in the decrease of plant efficiency.

And the above-mentioned coolant reduction contributes to the increase of blade row inlet temperature of about 30°C (54°F).

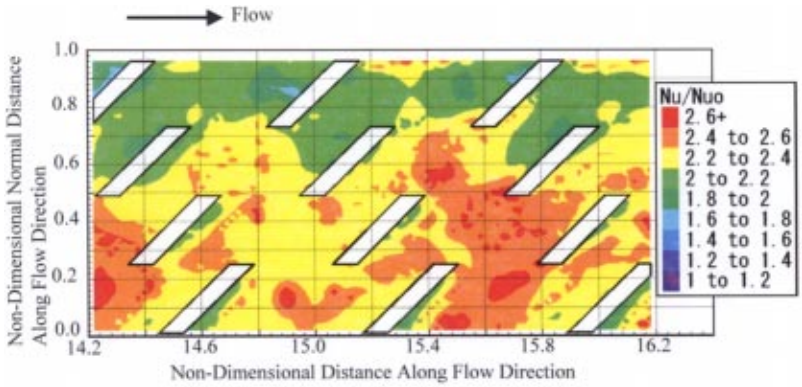


Fig. 18 Heat transfer distribution on the floor equipped with broken rib (Re $=8.4\times10^4$)

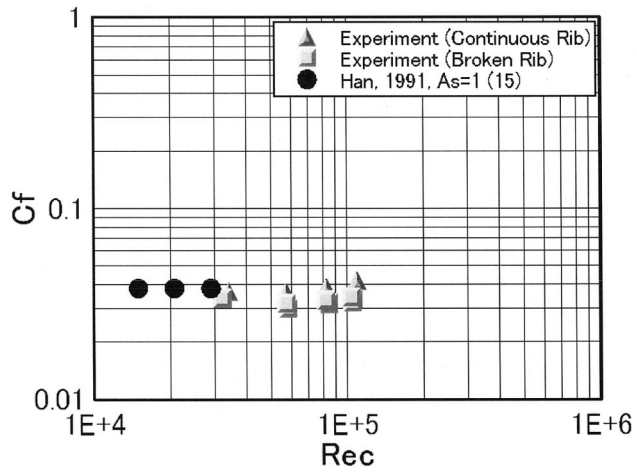


**Fig. 20 Friction factor of the ribbed wall**

**Table 4 Specification of the first stage turbine nozzle and blade**

| | ACRO-GT2000 | | WE-NET | |
|---|---|---|---|---|
| | Nozzle | Blade | Nozzle | Blade |
| Main flow | | | | |
| Inlet mean temp. (°C) | 1700 | 1600[a] | 1700 | 1570[a] |
| Inlet max. temp. (°C) | 1810 | 1670[a] | 1810 | 1640[a] |
| Inlet pressure (MPa) | 4.51 | 3.68[b] | 4.74 | 3.71[b] |
| Total flow (kg/s) | 278 | 286 | 222.4 | 231.6 |
| Cooling flow | | | | |
| Inlet temperature (°C) | 328 | 374 | 350 | 374 |
| Inlet pressure (MPa) | 5.3 | 6.03 | 5.4 | 5.69 |
| Ratio of main flow (%) | 3.94 | 4.20 | 6.40 | 6.90 |
| Allowable max. temp. | | | | |
| Base-metal (°C) | 950 | 950 | 930 | 930 |
| TBC (°C) | 1300 | 1300 | 1200 | 1200 |
| TBC thickness (mm) | 0.2 | 0.15 | 0.2 | 0.15 |

[a]Relative temperature
[b]Relative pressure

**Nozzle and Blade Structural Integrity.** Finally, nozzle and blade structural integrity has been evaluated by the three-dimensional FEM analysis using ABAQUS.

In the temperature analysis, external gas heat transfer distributions were considered as in the previous section. However, the mean gas temperature distribution in the blade height direction was treated by the simple pattern factor-based method. The pattern factor is a measure of the highest to mean temperature ratio. In the present study, 10% and 7% were assumed for nozzle and blade inlet, respectively. The resulting metal temperature distribution was used to analyze the thermal stress.

In the structural stress analysis, the external fluid pressure and rotational effect (for blade) were considered, since the bending stress generated by the gas pressure difference is important for the nozzle and the centrifugal stretch force is important for the blade. Furthermore, the anisotropy of single-crystal metal was taken into account in these stress analyses.

Figure 24 shows the results of the stress analysis. The overall stress levels of the nozzle and blade were found to be lower than 500 MPa (72.5 ksi) and 300 MPa (43.5 ksi), respectively, and the maximum local stress was found to be about 600 MPa (87.0 ksi) for the blade. Following the stress and temperature distributions of the blade in the height direction, the strength was evaluated. And it was found to be lower than 70% of the 0.2%-proof stress of the single-crystal metal. The strain of the blade was in the range of elastic deformation, and the possibility of crack generation may be small. The local stresses in the nozzle end-wall and the blade platform were also beyond the 0.2%-proof stress. However, the minor improvement of the cooling channel of the endwall and platform can reduce the stress to the range of elastic deformation.

## Conclusions

The conceptual design and the development of the blade for a 1700°C-class high-temperature gas turbine in a closed cycle power generation system has been carried out.

(1) The shaft arrangement and gas path design have been performed for the high-temperature turbine. The optimization has been performed, considering the aerodynamic efficiency and productivity results in the two-shaft design with the rotational speed and stage number of 9500/3 stages and 3000 rpm/4 stages for HT1 and HT2, respectively.

(2) The blade surface heat transfer has been experimentally measured by using the thermochromic liquid crystals technique in

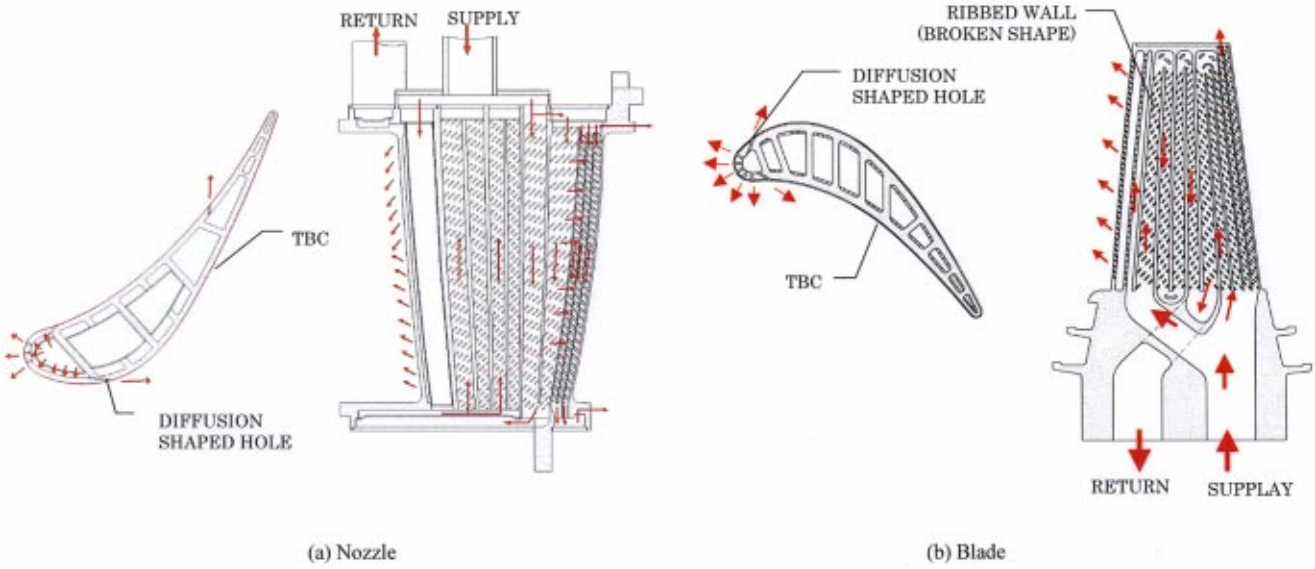


**Fig. 21 Cooling configurations of first stage nozzle and blade**

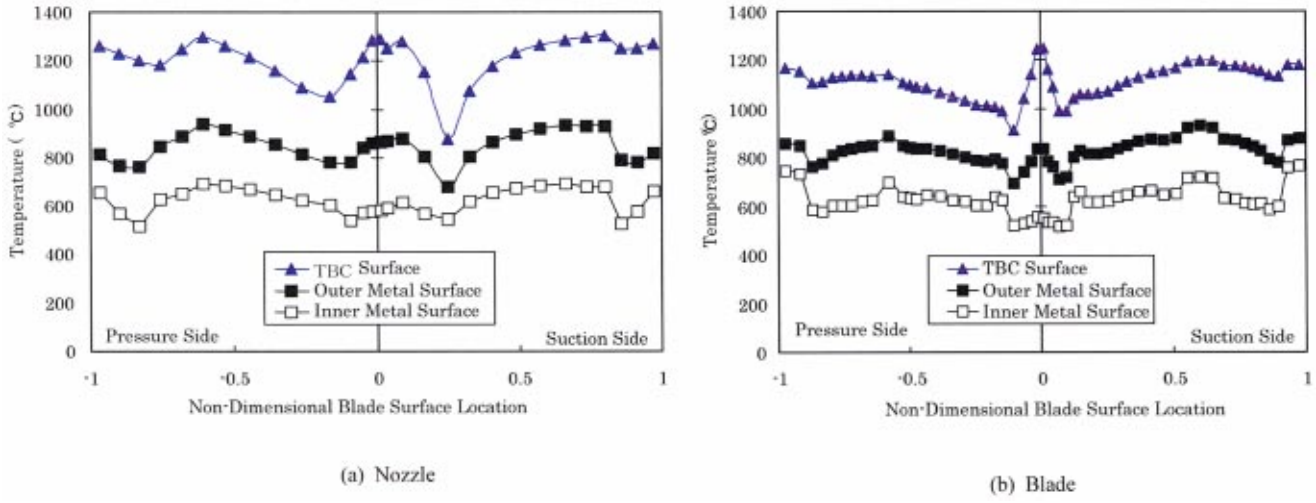


**Fig. 22 Blade mean height temperatures distributions**

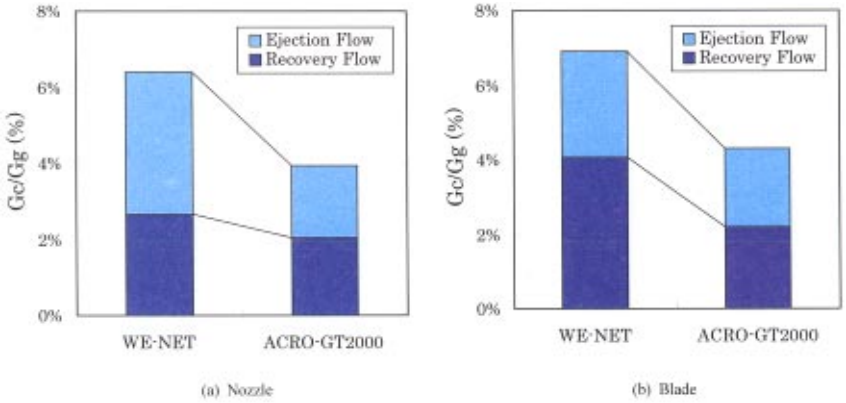


**Fig. 23 A comparison of the coolant flow rate for the first stage nozzle and blade**

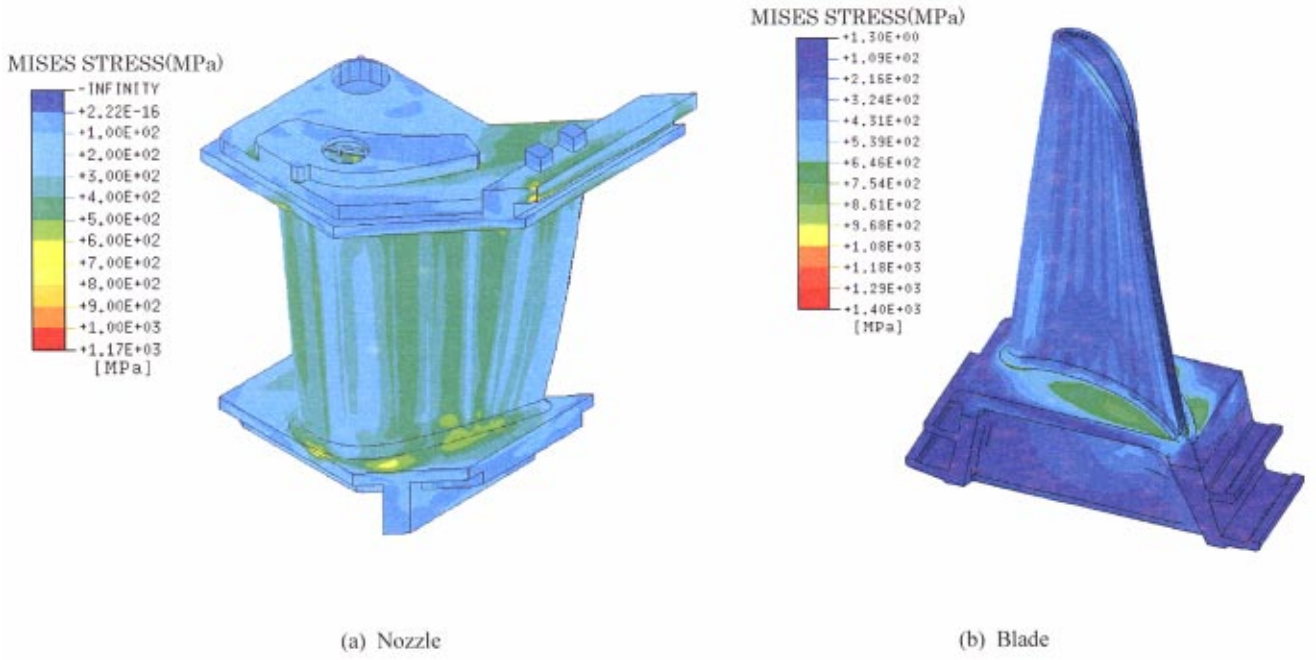


**Fig. 24 Nozzle and blade surface stress distributions**

the low-pressure wind tunnel and the design of the three-dimensional numerical simulation code has been evaluated. The results suggest that the numerical prediction is partly valid for the heat transfer analysis.

(3) The broken rib-type turbulence promoter heat transfer and pressure loss have been measured. It was found that the overall heat transfer ability including the wall surface and the rib was about 25% higher than in the case of a continuous rib. This increase in heat transfer is due to the heat transfer increase of about 2.0 to 2.3 times on the rib surface. So, the broken rib was adopted for the cooling design advancement.

(4) The pressure loss of the inter-rotor center bore and the distribution radial passage has been evaluated by a model experiment. Based on the experimental results, rotor system flow distribution and coolant supply pressure have been rearranged.

(5) The redesigned hybrid cooling first stage nozzle and blade realized a decrease of about 40% in coolant consumption compared with that of the WE-NET 1700°C stage. In particular, the 50% ejection coolant reduction at the first stage nozzle can increase the blade row inlet gas temperature by about 30°C. This contributes to the increase of plant thermal efficiency.

(6) The structural integrity of the first-stage nozzle and blade has been evaluated by FEM thermal and structural stress analysis. And it was confirmed that the effective stress was well below the 0.2% proof-stress of the base metal.

The conceptual design phase of the project has been finished. However, the confirmation and the operating experience accumulation for the complex closed-loop Brayton cycle/Rankin cycle system and the long-term durability tests for the newly introduced materials are necessary for the realization.

## Acknowledgments

This work was supported by the New Energy and Industrial Technology Development Organization (NEDO) as part of the ACRO-GT-2000 program, and was directly entrusted by the Central Research Institute of Electric Power Industry (CRIEPI). The authors would like to thank these organizations for their support.

## Nomenclature

As = channel aspect ratio
$C_f$ = friction factor
d = diameter (m)
$G_c$ = cooling mass flow rate (kg/s)
$G_g$ = main stream (hot) gas flow rate (kg/s)
Nu = Nusselt number
$Nu_0$ = Nusselt number for smooth wall
$Re_c$ = Reynolds number for channel
$Re_m$ = Reynolds number for blade
$Re_r$ = Reynolds number for rotor cooling passage
$R_\omega$ = rotational Reynolds number
St = Stanton number
Tu = inlet turbulence intensity
V = velocity (m/s)
$\Delta P$ = pressure drop (Pa)
$\rho$ = density ($kg/m^3$)
$\eta_t$ = turbine adiabatic efficiency
$\eta_{td}$ = turbine adiabatic efficiency at design point
$\zeta$ = total pressure loss coefficient
$\nu$ = kinetic viscosity ($m^2/s$)
$\omega$ = rotational speed (1/s)
$\Omega$ = rotational ratio ($=R_\omega/Re_r$)

## References

[1] Koda, E., Takahashi, T., Uematsu, K., and Yamashita, K., 2002, "Study on the Highly Efficient Closed-Cycle Gas Turbine System for $CO_2$ Collection," J. Gas Turbine Soc. Jpn., **30**, pp. 63–67 (in Japanese).
[2] Jackson, J. B. A., Neto, A. C., Whellens, M., and Audus, 2000, "Gas Turbine Performance Using Carbon Dioxide as Working Fluid in Closed Cycle Operation," ASME, 2000-GT-153.
[3] Jeriche, H., and Gottlich, E., 2002, "Conceptual Design for An Industrial Prototype Graz Cycle Power Plant," ASME, GT-2002-30118.
[4] Okamura, T., Koga, A., Ito, S., and Kawagishi, H., 2000, "Evaluation of 1700°C Class Turbine Blades in Hydrogen Fueled Combustion Turbine System," ASME, 2000-GT-0615.
[5] Ito, S., Koga, A., Kawagishi, H., Matsuda, H., Suga, T., and Okamura, T., 2000, "Hydrogen Combustion Wind Tunnel Test of 1700°C Class Turbine Cooling Blades," J. Gas Turbine Soc. Jpn., **28**, pp. 23–28 (in Japanese).
[6] Matsuda, H., Ikeda, K., Nakata, Y., Otomo, F., Suga, T., and Fukuyama, Y., 1999, "A New Thermochromic Liquid Crystal Temperature Identification Technique Using Color Space Interpolations and Its Application to Film Cooling Effectiveness Measurements," *Proceedings of PSFVIP-2*, PF053.
[7] Saeki, H., Ito, S., Matsuda, H., and Okamura, T., 1999, "Heat Transfer Measurements on Turbine Nozzle Using Liquid Crystals," *International Gas Turbine Congress '99 Kobe*, TS-47, pp. 607–613.
[8] Saeki, H., and Fukuyama, Y., 2002, "Heat Transfer Measurements on a Gas Turbine Blade for ACRO-GT-2000," ISROMAC-9, Paper HT-ABS-025.
[9] Biswas, D., and Fukuyama, Y., 1993, "Calculation of Transitional Boundary Layer With an Improved Low Reynolds Number Version of the k-$\varepsilon$ Turbulence Model," ASME, 93-GT-73.
[10] Fukuyama, Y., Otomo, F., Sato, M., Kobayashi, Y., and Matsuzaki, H., 1995, "Prediction of Vane Surface Film Cooling Effectiveness Using Compressible Navier–Stokes Procedure and k-Epsilon Turbulence Model With Wall Function," ASME, 95-GT-25.
[11] Kubo, R., Otomo, F., Fukuyama, Y., and Nakata, Y., 1998, "Aerodynamic Loss Increase Due to Individual Film Cooling Injections From Gas Turbine Nozzle Surface," ASME, 98-GT-497.
[12] Launder, B. E., and Sharma, B. I., 1979, "Application of the Energy-Dissipation Model of Turbulence to the Calculation of Flow Near a Spinning Disc," Lett. Heat Mass Transfer, **1**, pp. 131–138.
[13] Kato, M., and Launder, B. E., 1993, "The Modeling of Turbulent Flow Around Stationary and Vibrating Square Cylinders," 9th *Symposium on Turbulent Shear Flows*, Kyoto Japan, 10-4.
[14] Han, J. C., and Park, J. S., 1988, "Developing Heat Transfer in Rectangular Channels With Rib Turbulators," Int. J. Heat Mass Transfer, **31**, pp. 183–195.
[15] Han, J. C., Zhang, Y. M., and Lee, C. P., 1991, "Augmented Heat Transfer in Square Channels With Parallel, Crossed, and V-Shaped Angled Ribs," ASME J. Heat Transfer, **113**, pp. 590–596.
[16] Hisamatsu, T., 2002, "Development of Thermal Barrier Coating for $CO_2$-Recovering Closed Gas Turbine," J. Gas Turbine Soc. Jpn., **30**, pp. 519–525 (in Japanese).
[17] Hisamatsu, T., Nitta, A., Nakayama, M., Torigoe, T., Mori, K., Okada, I., Hino, T., Kameda, T., Ito, Y., Arikawa, H., Kojima, Y., and Nishi, K., 2002, "Development and Evaluation of Thermal Barrier Coating for 1700°C-Class Gas Turbine in the $CO_2$-Turbine Project," Report of the 123rd Committee on Heat-Resisting Materials and Alloys Japan Society for Promotion of Science, Vol. 43, No. 3, pp. 325–340 (in Japanese).
[18] Koizumi, Y., Kobayashi, T., Yokokawa, T., Kimura, T., Osawa, M., and Harada, H., 1998, "Third Generation Single Crystal Superalloys With Excellent Processability and Phase Stability," *Proceedings of Materials for Advanced Power Engineering 1998*, Part II, pp. 1089–1098.

# Application of "H Gas Turbine" Design Technology to Increase Thermal Efficiency and Output Capability of the Mitsubishi M701G2 Gas Turbine

**Y. Fukuizumi**
Mitsubishi Heavy Industries,
3-1, Minatomirai 3-chome, Nishi-ku,
Yokohama, Kanagawa 220-8401, Japan

**J. Masada**

**V. Kallianpur**

Mitsubishi Power Systems,
2287 Premier Row,
Orlando, FL 32809

**Y. Iwasaki**
Mitsubishi Heavy Industries,
2-1-1 Shinhama Arai-cho,
Takasago, Hyogo 676-8686, Japan

*Mitsubishi completed design development and verification load testing of a steam-cooled M501H gas turbine at a combined cycle power plant at Takasago, Japan in 2001. Several advanced technologies were specifically developed in addition to the steam-cooled components consisting of the combustor, turbine blades, vanes, and the rotor. Some of the other key technologies consisted of an advanced compressor with a pressure ratio of 25:1, active clearance control, and advanced seal technology. Prior to the M501H, Mitsubishi introduced cooling-steam in "G series" gas turbines in 1997 to cool combustor liners. Recently, some of the advanced design technologies from the M501H gas turbine were applied to the G series gas turbine resulting in significant improvement in output and thermal efficiency. A noteworthy aspect of the technology transfer is that the upgraded G series M701G2 gas turbine has an almost equivalent output and thermal efficiency as H class gas turbines while continuing to rely on conventional air cooling of turbine blades and vanes, and time-proven materials from industrial gas turbine experience. In this paper we describe the key design features of the M701G2 gas turbine that make this possible such as the advanced 21:1 compressor with 14 stages, an advanced premix DLN combustor, etc., as well as shop load test results that were completed in 2002 at Mitsubishi's in-house facility.* [DOI: 10.1115/1.1850490]

## 1 Introduction

The M701G2 gas turbine is built by enhancing the original M701G with some of the advanced technologies that were developed for Mitsubishi's steam-cooled M501H gas turbine [1]. The original M701G gas turbines went into commercial operation in 1999, and the lead unit has logged more than 25 000 operating hours at close to 100% reliability. The M701G2 is presently Mitsubishi's most advanced commercial offering for the 50 Hz power generation market. Table 1 compares the performance of the M701G and the M701G2 gas turbines. Note that the latter has a simple cycle efficiency and output of 39.5% and 334 MW, respectively. For a 1×1 combined cycle configuration those figures for the M701G2 are 58.7% and 489 MW, respectively. The primary design approach of the M701G2 gas turbine was to introduce key H technologies, without upsetting the proven reliability track record of the original M701G gas turbine. Greater output and performance were achieved by using an advanced compressor with 15% greater mass flow, and a pressure ratio of 21:1. The only steam-cooled hardware in the M701G2 consist of the combustor transitions, and the turbine blade rings, whereas in the original M701G gas turbine only the combustor transitions are steam cooled. On the other hand, the steam-cooled components in the M501H gas turbine consist of combustor transitions, blade rings, row 1 and row 2 turbine blades and vanes, and the rotor.

The full-scale load verification test of the steam-cooled M501H gas turbine in a combined cycle power plant was completed successfully in 2001. New technologies were applied in the development of the M501H for its 15 stage 25:1 pressure ratio compressor and steam cooled components. These include advanced 3D aero, mass transport and heat transfer analytical techniques and critical material compatiability evaluations for long-term reliability in a steam environment [2].

The selective advanced technologies from the M501H development were applied to increase the output and performance of the original M701G dramatically.

Table 2 compares the M701G2 with previous 50 Hz gas turbines from Mitsubishi. The development approach retained the same evolution path such as retaining design feature commonality and scaling practices across the 50 and 60 Hz models. A factory load test of the M701G2 was conducted to further confirm the reliability of the gas turbine.

## 2 Design Features

Figure 1 shows a picture of the M701G2 gas turbine rotor. The unit rotor is of bolted construction. There are 12 bolts in the compressor, and 12 in the turbine in conjunction with positive torque carrying features such as radial pins and curvic couplings, respectively. The rotor is supported by two 23-in. diameter two-element

**Table 1 Performance of M701G vs M701G2**

| Performance | M701G | M701G2 |
|---|---|---|
| G/T Power (MW) | 271 | 334 |
| G/T thermal efficiency (%—LHV) | 38.7 | 39.5 |
| Combined cycle (1 on 1) power (MW) | 405 | 489 |
| Combined cycle (1 on 1) efficiency (%—LHV) | 57.0 | 58.7 |

Contributed by the International Gas Turbine Institute (IGTI) of THE AMERICAN SOCIETY OF MECHANICAL ENGINEERS for publication in the ASME JOURNAL OF ENGINEERING FOR GAS TURBINES AND POWER. Paper presented at the International Gas Turbine and Aeroengine Congress and Exhibition, Atlanta, GA, June 16–19, 2003, Paper No. 2003-GT-38956. Manuscript received by IGTI, October 2002, final revision, March 2003. Associate Editor: H. R. Simmons.

**Table 2 M701 series evolution**

| Engine | M701D | M701F | M701G2 |
|---|---|---|---|
| Initial operation | 1981 | 1992 | 2002 |
| G/T power (MW) | 144.09 | 270.3 | 334 |
| G/T heat rate (Btu/kWh) | 9810 | 8930 | 8630 |
| Air flow (kg/s/Lb/s) | 441/972 | 651/1435 | 737/1625 |
| Exhaust temp. (Deg.C/Deg.F) | 542/1009 | 586/1087 | 587/1089 |
| Pressure ratio | 14 | 17 | 21 |
| No. of comp. stages | 19 | 17 | 14 |
| No. of turb. stages | 4 | 4 | 4 |
| Combined cycle (2 on 1) Power (MW) | 427 | 800 | 982 |
| Combined-cycle (2 on 1) Heat rate (Btu/kWh) | 6610 | 5956 | 5795 |

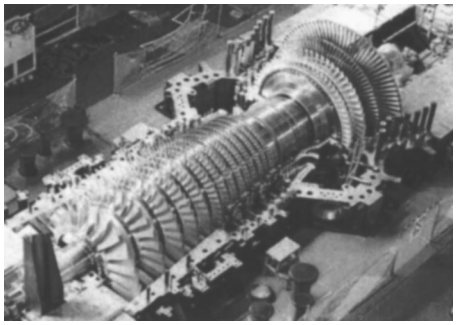

**Fig. 1 M701G2 gas turbine rotor**

tilting pad bearings, and an upper half fixed bearing. The thrust bearing is a double-acting bearing that uses the Leading Edge Groove lubrication system.

The air inlet system, which contains a silencer, delivers air to the compressor via a plenum bell mouth, and houses the inlet, main journal and thrust bearings.

The advanced axial flow compressor has 14 stages with a 21:1 pressure ratio.

There are four stages in the turbine so as to maintain moderate aerodynamic loadings even at the increased firing temperature and pressure ratio, as in the case of all Mitsubishi large frame industrial gas turbines. All engine casings are horizontally split so as to facilitate maintenance with the rotor in place, and use the same proven design construction and materials as before. The inlet casing is made of nodular cast iron, while cast steel is used for the casings in the compressor, combustor, turbine, and exhaust casings. The inlet bearing housing is supported on eight radial struts. The aft end bearing housing is supported with six tangential struts. Airfoil-shaped covers protect the tangential struts from the blade path gases, and support the inner and outer diffuser cones. Tangential struts respond slowly during transients and maintain the alignment of the bearing housing by rotating it as required to accommodate the thermal expansion. Individual inner casings (blade rings) are used for each turbine stationary stage. The blade rings can be readily removed and replaced or serviced with the rotor in place. Similar blade rings are used in the compressor latter stages (6–14). Another feature of these blade rings is that they have a high thermal response that is independent of the outer casing. The turbine rings function is to maintain concentric alignment of the rotor, prevent blade rubs, minimize clearance between blades and casing, which result in improving performance.

Cooling circuits for the M701G2 turbine section (see Fig. 2) are similar to those used on the M501F and M701F. They consist of a rotor cooling circuit and four stationary cooling circuits. Rotor cooling air is provided by compressor discharge air extracted from the combustor shell. This air is externally cooled and filtered before returning to the torque tube casing for seal air supply and for cooling the turbine disks as well as the first, second, and third stage turbine rotor blades. This cooled, filtered air provides a blanket of cooling air below the hot blade path gaseous layer.

Compressor discharge air is directly used to cool the row 1 vane, while the bleed air also cools the stage 2, 3, and 4 vane segments and rotor disks and inter-stage seal flow, and stage 2 and 3 ring segments. Closed-loop steam is used for cooling turbine blade rings, and for cooling the combustor transition piece. This steam is supplied from the Heat Recovery Steam Generator, and subsequently returned to it after cooling.

The stationary vanes and rotating blades of the first two turbine stages are coated with a thermal barrier coating. Compressor dia-

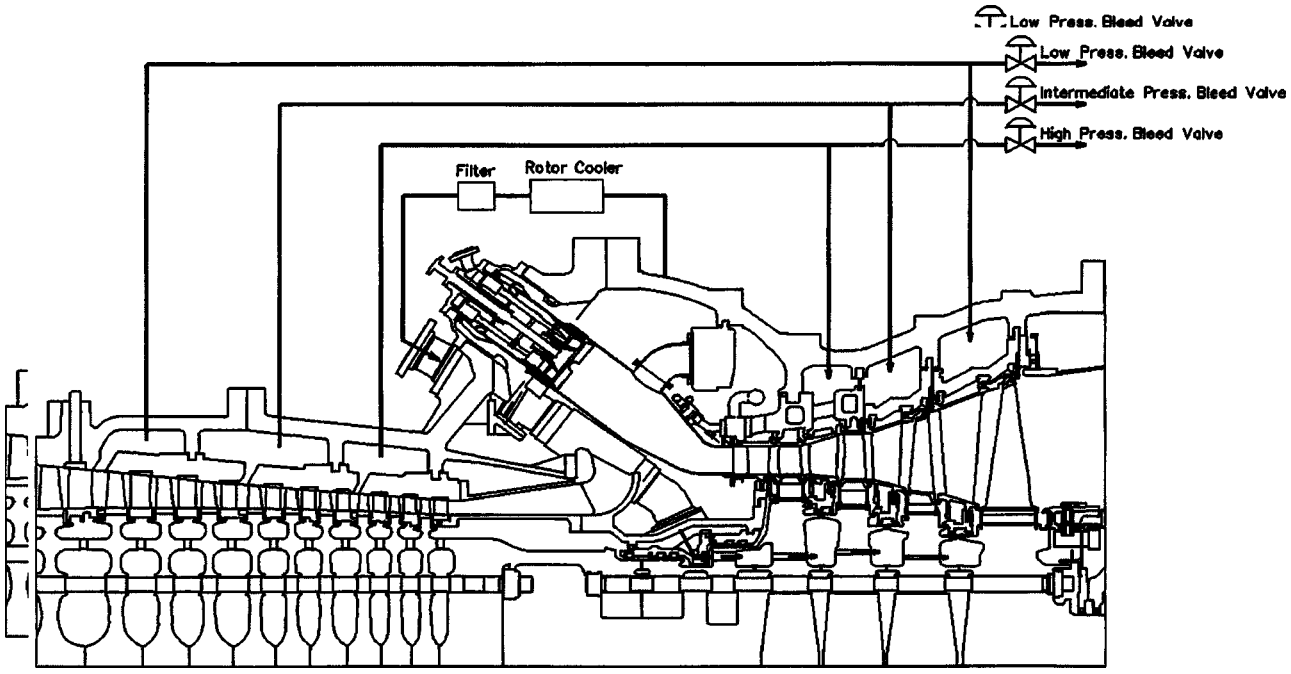


**Fig. 2 M701G2 gas turbine cooling circuit**

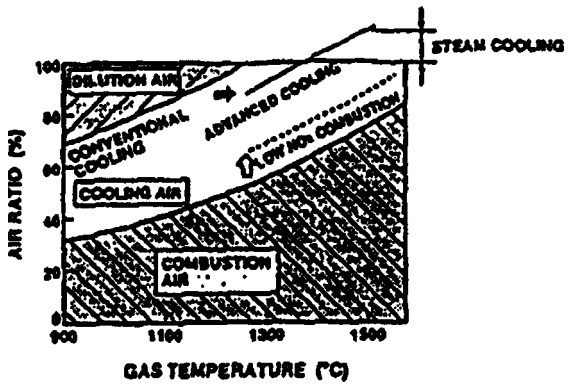


Fig. 3 Air distribution in a combustor

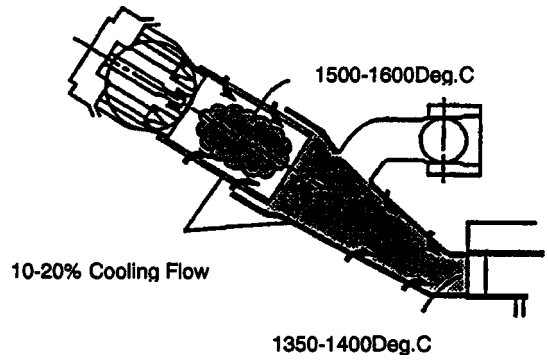


Fig. 5 M701F combustion system

phragms are also coated to improve aerodynamic performance and corrosion protection. For some environments, the compressor blades are coated for added corrosion protection.

## 3 Combustor Design

The combustor is based on the successful premix dry low $NO_x$ combustor developed for the M501F/M701F. This combustor operates at 25 ppm $NO_x$ level at 1400°C (2552°F) turbine inlet temperature. To achieve $NO_x$ levels of 25 ppm, the flame temperature has to be kept in the range of 1500°–1600°C, by supplying all air into the combustion zone, as shown in Fig. 3. Therefore, the M701G and M701G2 combustor use steam cooling for the transition piece to achieve the same $NO_x$ reduction at the higher firing temperature. Figure 4 shows the configuration of this new combustor. By eliminating the transition cooling air, virtually all the combustion air is introduced into the primary zone of the combustor, thus maintaining the similar flame temperature as the Mitsubishi F class gas turbines (i.e., M501F and M701F turbines). Therefore, $NO_x$ levels are also similar to the M501F/M701F level (see Fig. 5 and Fig. 6).

## 4 Turbine Design

Mitsubishi scaling philosophy uses the same turbine airfoils for rows 1 and 2 for 50 and 60 Hz applications (i.e., the same respective blade and vane geometries between the M501G and the M701G gas turbine). Improvements in aerodynamic airfoil shapes were achieved using fully three-dimensional viscous Euler analysis. This approach assures that the turbine has the highest practical aerodynamic efficiency, with the least cooling flow usage. There are 15% fewer airfoils compared to the M701F. The first two turbine blade rows are unshrouded. The third and fourth rows of blades are shrouded as on the M701F.

No changes were made in the turbine gas path materials. Table 3 shows that those materials are also used in the M701F gas turbines. The first turbine stationary row consists of 40 precision-cast, single-vane segments of MGA2400, a nickel base superalloy that was developed by Mitsubishi. As in previous designs, the row 1 vanes are removable, without any cover lift, through access manways. Inner shrouds are supported from the torque tube casing to limit flexural stresses and distortion, thus maintaining control of the critical row 1 vane angles. This method has been successfully used on M501F and M701F models as well. There are 22 precision-cast double vane segments of MGA2400 material in the second turbine stationary row. The third and fourth turbine stationary rows are precision-cast vane segments with 18 three-vane and 14 four-vane segments, respectively.

The rotating blades are precision cast of MGA1400 for all rows. Row 1 and row 2 blades are directionally solidified (i.e. DS). All rows utilize long blade root extensions or transitions in order to minimize the three-dimensional stress concentration factors that results when load is transferred between cross sections of different size and shape. The blade roots are the same geometric

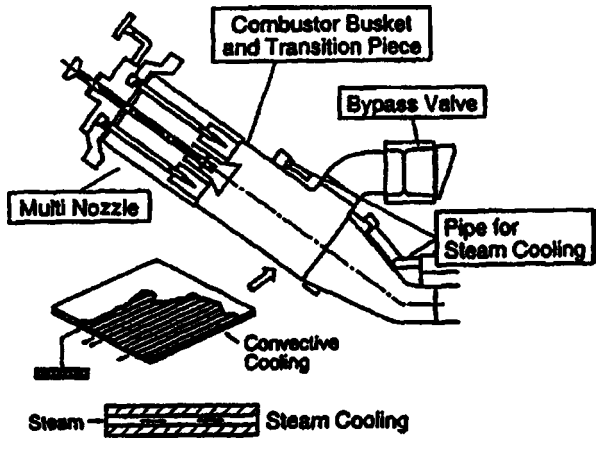


Fig. 4 Combustor configuration

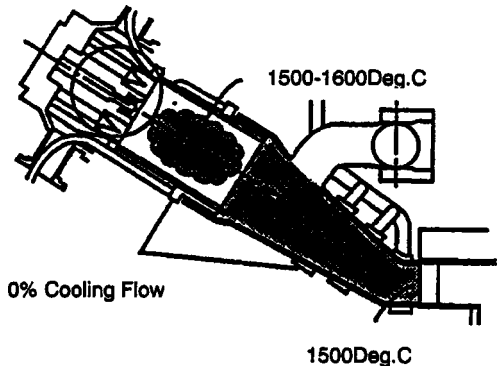


Fig. 6 M701G2 combustion system

Table 3 Material of turbine vanes and blades

| | | M701F | M701G2 |
|---|---|---|---|
| Vane | Row 1 | MGA2400CC | MGA2400CC |
| | Row 2 | MGA2400CC | MGA2400CC |
| | Row 3 | MGA2400CC | MGA2400CC |
| | Row 4 | X-45 | MGA2400CC |
| Blade | Row 1 | MGA1400DS | MGA1400DS |
| | Row 2 | MGA1400CC | MGA1400DS |
| | Row 3 | MGA1400CC | MGA1400CC |
| | Row 4 | MGA1400CC | MGA1400CC |

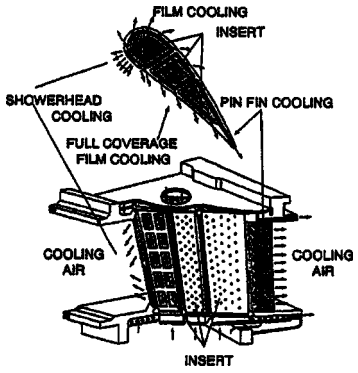


**Fig. 7 M701FG2 row 1 vane**

multiple serration type used on past designs with four serrations used on the first two rows and five serrations used on the last two stages.

Each row of vane segments is supported in a separate inner casing (blade ring) that is keyed and supported to permit radial and axial thermal response independent of possible external cylinder distortions. Blade ring distortion in the M701G (and M701G2) turbine is further minimized by the use of segmented isolation rings that support the vane segments and also ring segments over the rotor blades to form a thermal barrier between the flow path and the blade ring. As in all past designs, the interstage seal housings are uniquely supported from the inner shrouds of rows 2, 3, and 4 vane segments by radial keys that permit the thermal response of the seal housings to be independent of the more rapid thermal response of the vane segments.

The row 1 vane cooling is provided by impingement, convection and film cooling. The film cooling holes are fan shaped and both the airfoil and shrouds will be coated with a ceramic thermal barrier coating. The row 1 vane cooling design is shown in Fig. 7. This highly effective configuration utilizes state-of-the-art concepts with three impingement inserts in combination with an array of film cooling holes and a trailing edge pin fin system.

Film cooling is used at the leading edge as well as at selected pressure and suction side locations. This limits vane wall thermal gradients and external surface temperatures.

Particular attention is paid to the inner and outer shrouds because of the relatively flat temperature profile from the dry low $NO_x$ combustor. Cooling of shrouds is provided by impingement plates and film cooling as well as convection cooling via drilled holes.

The row 1 blade cooling consists of convectional serpentine cooling with angled turbulators. The film cooling utilizes fan shaped cooling holes for more effective cooling. The blade also

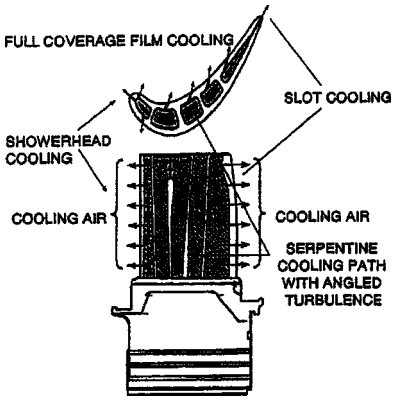


**Fig. 8 M701G2 row 1 blade**

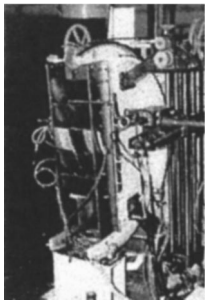

**Fig. 9 Measurement of film cooling effectiveness in a low speed cascade**

features extensive film cooling at the tip to reduce the metal temperature of squealer tip and platform cooling holes to positively cool the inner platforms. The airfoil is coated with a thermal barrier coating (Fig. 8).

Blade and vane cooling flows have been kept to a minimum while maintaining similar metal surface temperatures, as in the case of the M701F. These advanced turbine cooling schemes are developed through heat transfer model tests and cooled turbine

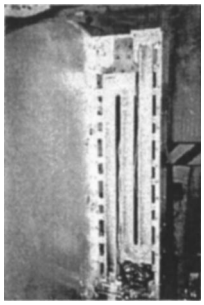

**Fig. 10 Serpentine cooling passage test under rotation**

**Fig. 11 Measurement of airfoil heat transfer coefficient using a liquid crystal**

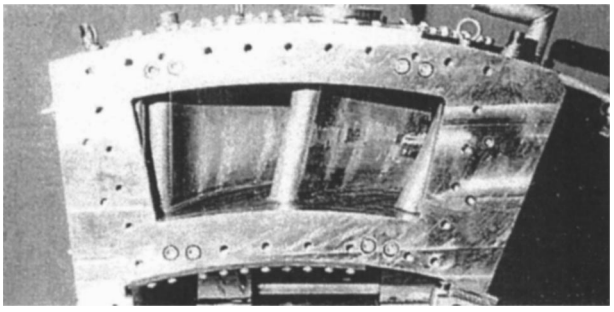

**Fig. 12 Hot cascade test**

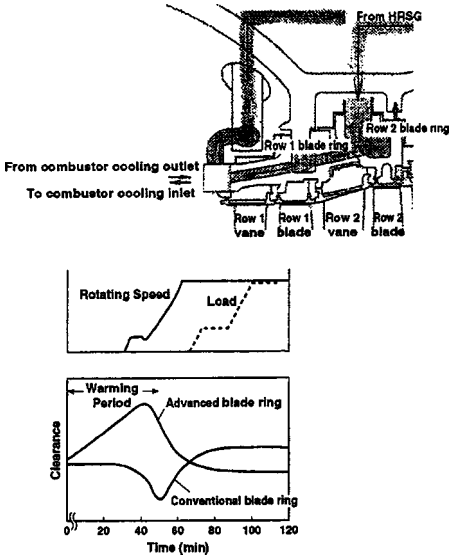


**Fig. 13 Startup hot gas type blade ring**

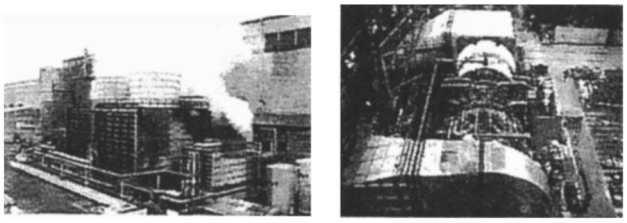

**Fig. 14 M701G2 factory load test condition**

(A) Performance

1 Air flow
2 Inlet temp. & Press
3 Exhaust temp. & Press
4 Fuel flow
5 Generator output
6 Compressor
(Surge margin, Efficiency)
(Stage temp. & press distribution)
7 Turbine
(Stage efficiency)
(Diffuser efficiency)

(B) METAL TEMP.

8 Combustor transition piece
9 #1, 2 Steam coooled blade ring
10 Turb. row 1, 2 vane
11 Bearing metal
12 Outer casing
13 Inner casing
14 Exhaust cylinder

(C) STRESS/VIBRATION

15 Compressor blade
16 Compressor vane
17 Combustor transition piece
18 Rotor. Vibration
19 Casing Vibration
20 Rotor torsional Vibration

(D) OTHERS

21 Cooling air network
• Flow
• Temperature
• Pressure
22 Thrust load
23 Exhaust emission
24 Rotor/casing Expansion
25 Noise
26 Lube oil temp.

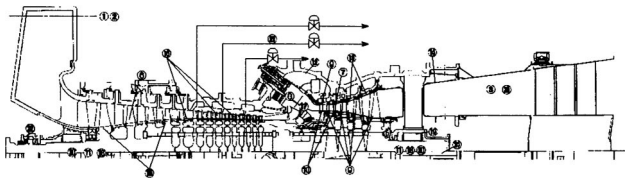

**Fig. 15 Itemized measurement on M701G2**

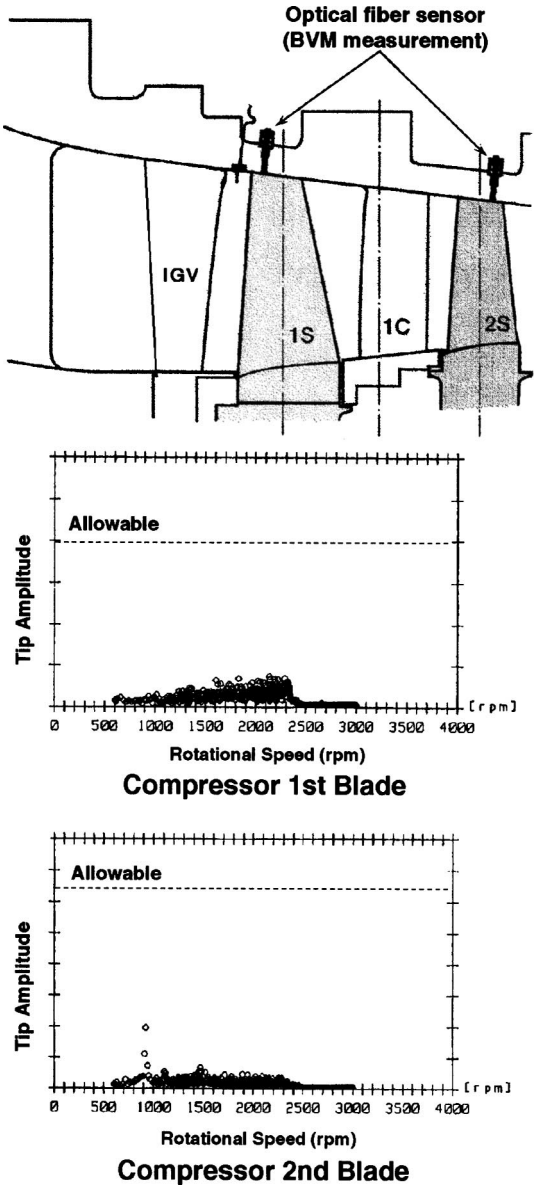


**Fig. 16 Working compressor, stationary vane vibration stress measurement result**

hot cascade tests. Those were also verified through a high-temperature demonstration unit by testing scaled-down turbine airfoils at the actual operating temperature. Figure 9 shows the film cooling test in a low-speed cascade to measure the film cooling effectiveness around the airfoil. Figure 10 shows the test of serpentine cooling passage with a turbulence promoter to measure the heat transfer characteristics under rotating conditions. Figure 11 shows the airfoil heat transfer measurements using a liquid crystal. Figure 12 shows the hot cascade test section. This cascade test allows a measurement of airfoil cooling performance under actual firing conditions.

The row 2 vane is cooled by a combination of impingement cooling via the inserts and film cooling using fan shaped cooling holes. With the row 1 vane, intensive cooling schemes were developed to the inner and outer shrouds using impingement and convection cooling.

The row 2 blade is cooled by convection with no film cooling. The airfoil is coated with a thermal barrier coating. The row 3 blade cooling is unique in that it positively cools the blade tip

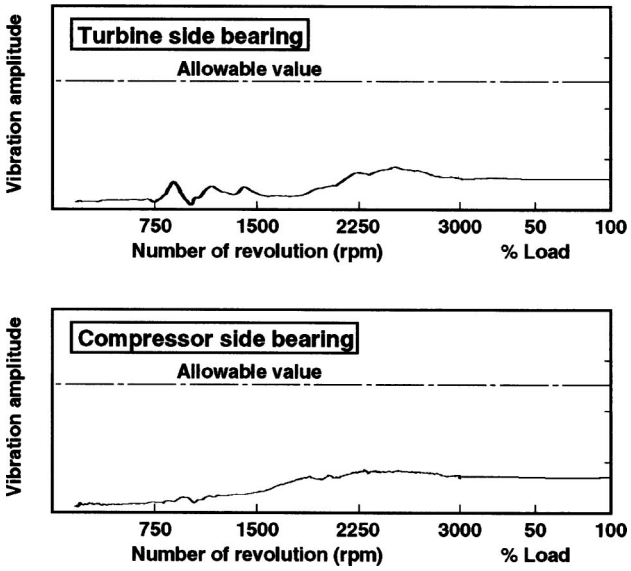


**Fig. 17 Rotor vibration measurement result**

shroud. Because of the flatter (or relatively flat) profile from the combustor, it was decided to allow for positive cooling of the tip shroud.

Compressor bleed air from the eighth stage is used to supply cooling air to the third-stage blade ring cavity. Cooling air is directed to the inlet cavity of a five-cavity multipass convective cooled vane airfoil. Leading edge cavity flow also supplies the interstage seal and cooling system while the fifth pass cavity exits through pressure side ''holes'' on the vane surface near the trailing edge. The fourth-stage vane is not cooled but does transport fifth-stage compressor bleed air for the fourth-row interstage seal and cooling system. The cooling system shown in Fig. 2 maintains the NiCrMoV turbine disk temperatures below 400°C (752 F), which ensures the safe operation of the disks below the creep range, thereby assuring long service life.

The structure and the characteristic of the advanced blade ring are shown in Fig. 13. By means of steam, heating, the blade ring is enlarged during start-up. During the rated load, the steam temperature is lower than the gas temperatures surrounding the blade ring. This cools the blade ring, causing a relative contraction and establishes the suitable clearance.

## 5 Factory Load Test of M701G2

In order to confirm the performance and the reliability of the M701G2, the factory load test was conducted in April and May 2002. This load test facility is located at Mitsubishi Heavy Industries Takasago Machinery Works. The factory load test facility is shown in Fig. 14. Over 1800 points were monitored with special sensors, as shown in Fig. 15.

The test results confirmed that the performance, reliability, and start-up characteristic of the compressor scaled accurately from the M501H gas turbine. In Fig. 16, the measured vibration stress of the compressor and the stationary vane are shown. The vibration stress of the blade was measured by using optical fiber sensor. It was confirmed that the measured vibration stress is lower than the allowable value ensuring reliability. As shown in Fig. 17, it was confirmed that gas turbine axial vibration was extremely low.

The tests confirmed the overall performance capability and reliability of the M701G2 gas turbine.

## 6 Conclusion

The M701G2 successfully incorporates M501H gas turbine technology without changing hot gas path materials or rotor materials and without shifting to steam cooling for the turbine blades and vanes. The output and heat rates are almost equivalent to that of H technology. The factory load tests of the M701G2 were conducted in April 2002 by monitoring over 1800 points with special sensors and confirmed that high mechanical reliability is achievable.

## References

[1] Aoki, S., ''Trend and Key Technologies for Gas Turbine Combined Cycle Power Generation in a Globally Competitive Market and Environmental Regulations,'' IJPGC2000-15084, 2000.

[2] Koeneke, C., Kallianpur, V., Arimura, H. et al., ''Maintaining Long Term Steam Cooling Reliability in Mitsubishi Advanced Industrial Gas Turbines: Approach, Technology & Field Experience,'' PowerGen 2002.

# Heat Transfer Measurements Using Liquid Crystals in a Preswirl Rotating-Disk System

**Gary D. Lock**
**Youyou Yan**[1]
**Paul J. Newton**
**Michael Wilson**
**J. Michael Owen**

Department of Mechanical Engineering,
University of Bath,
Bath BA2 7AY, UK

*Preswirl nozzles are often used in gas turbines to deliver the cooling air to the turbine blades through receiver holes in a rotating disk. The distribution of the local Nusselt number, Nu, on the rotating disk is governed by three nondimensional fluid-dynamic parameters: preswirl ratio, $\beta_p$, rotational Reynolds number, $Re_\phi$, and turbulent flow parameter, $\lambda_T$. A scaled model of a gas turbine rotor–stator cavity, based on the geometry of current engine designs, has been used to create appropriate flow conditions. This paper describes how a thermochromic liquid crystal, in conjunction with a stroboscopic light and digital camera, is used in a transient experiment to obtain contour maps of Nu on the rotating disk. The thermal boundary conditions for the transient technique are such that an exponential-series solution to Fourier's one-dimensional conduction equation is necessary. A method to assess the uncertainty in the measurements is discussed and these uncertainties are quantified. The experiments reveal that Nu on the rotating disk is axisymmetric except in the region of the receiver holes, where significant two-dimensional variations have been measured. At the higher coolant flow rates studied, there is a peak in heat transfer at the radius of the preswirl nozzles. The heat transfer is governed by two flow regimes: one dominated by inertial effects associated with the impinging jets from the preswirl nozzles, and another dominated by viscous effects at lower flow rates. The Nusselt number is observed to increase as either $Re_\phi$ or $\lambda_T$ increases.*
[DOI: 10.1115/1.1787509]

## 1 Introduction

Preswirl nozzles are often used in gas turbines to deliver the cooling air to the turbine blades, as illustrated in Fig. 1. The stationary nozzles swirl the cooling air in the direction of rotation of the turbine disk, thereby reducing the temperature of the air relative to the blades. The designer needs to know the effect of the preswirl ratio, $\beta_p$, the coolant flow rate, and the rotational speed, $\Omega$, on the pressure drop and temperature difference between the preswirl nozzles and the receiver holes in the disk. It is also important to know the effect of these parameters on the distribution of Nusselt number, Nu, over the surface of the rotating disk.

Owen and Rogers [1] described early studies of preswirl systems, and Owen and Wilson [2] gave a brief review of more recent heat transfer research. Metzger, Bunker, and Bosch [3] were the first to apply a thermochromic liquid crystal to the case of a rotating disk with jet impingement. Karabay, Wilson, and Owen [4] carried out a combined experimental and computational study of flow in a ''cover-plate'' (rotating cavity) preswirl system. A theoretical analysis was used to show that there was an optimal value of the preswirl ratio, for which the average Nusselt number for a heated rotating disk would be a minimum. Pilbrow et al. [5] presented experimental and computational results for heat transfer in the same cover-plate system, showing that the structure of these flows is governed principally by the values of $\beta_p$, and the turbulent-flow parameter, $\lambda_T$. For a detailed discussion of the significance of $\lambda_T$, the reader is referred to Ref. [1]. The heat transfer is governed by the above two parameters as well as by the rotational Reynolds number, $Re_\phi$, and by the temperature distribution on the rotating disk.

Designers can obtain some information using turbine-based rigs running close to engine-operating conditions. However, deeper insight can be gained from fundamental research that measures, computes, and explains the flow and heat transfer in generic, fully instrumented rigs operating under more benign conditions. Computational codes, validated on these detailed measurements, can then be used to conduct calculations extrapolated to engine conditions.

This paper describes a generic rig, which has been constructed to study the fluid dynamics and heat transfer in preswirl systems. The experimental facility is a simplified model of a gas turbine rotor–stator system designed to accommodate pressure and temperature instrumentation in the test section and to provide optical access to the wheel space. The fluid dynamics has been investigated both experimentally and computationally by Yan et al. [6]. The effects of rotational speed, flow rate, preswirl ratio, and the number of preswirl nozzles on the flow field and on the total pressure losses in the system have been reported. These measurements and computations showed that there was a significant loss of total pressure between the outlet from the preswirl nozzles and the rotating core of fluid in the wheel space. This loss increased as the preswirl flow rate and inlet swirl ratio increased, and as the number of nozzles decreased. The discharge coefficient of the receiver holes increased as the swirl ratio at the receiver-hole radius approached unity.

The complementary measurements of heat transfer using thermochromic liquid crystals (TLCs) are discussed here, featuring the novel technique of stroboscopic lighting and an exponential-series solution to Fourier's conduction equation. Contour maps of Nu on the rotating disk have been measured, including detailed two-dimensional patterns around the blade receiver holes. Al-

[1]Present address: City University, London, Northampton Square, London EC1V 0HB, U.K.

Contributed by the International Gas Turbine Institute (IGTI) of THE AMERICAN SOCIETY OF MECHANICAL ENGINEERS for publication in the ASME JOURNAL OF ENGINEERING FOR GAS TURBINES AND POWER. Paper presented at the International Gas Turbine and Aeroengine Congress and Exhibition, Atlanta, GA, June 16–19, 2003, Paper No. 2003-GT-38123. Manuscript received by IGTI, October 2002, final revision, March 2003. Associate Editor: H. R. Simmons.

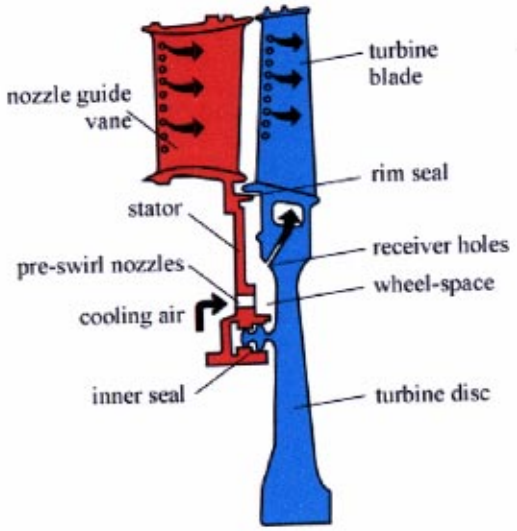


**Fig. 1 Simplified diagram of typical preswirl cooling-air system for a gas turbine**

though some authors have measured the radial distribution of Nu, there are no published records of contour maps over the disk surface.

## 2 Experimental Apparatus and Instrumentation

**2.1 Apparatus.** Experiments were conducted using a scaled model of a gas-turbine rotor–stator system. The geometry, which was based on information obtained for existing engine designs, is illustrated schematically in Fig. 2. The air entered the test section through the stator at low radius via preswirl nozzles and flowed radially outward between the rotating disk and the stator, exiting through receiver holes in the rotating disk representing the entrance to the blade-cooling passages in the engine.

The disk radius was $b=216$ mm, and the other principal dimensions are the inner-to-outer radius ratio $a/b=0.67$ and the gap ratio $s/b=0.051$. The stator was machined from aluminum, and contained 24 circular preswirl nozzles angled at 20 deg to the tangential direction. The rotating disk was machined from transparent polycarbonate, with sectors sprayed with TLC and black paint, and contained 60 axial receiver holes with a length-to-diameter ratio of 1.25. The nondimensional radius of the nozzles, $x_p=r_p/b=0.74$, was less than that of the receiver holes, $x_b=r_b/b=0.93$, and the area ratio of the receiver holes to that of the nozzles is 2.9.

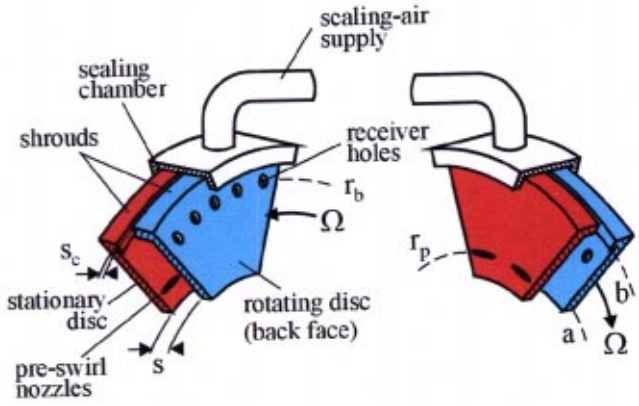


**Fig. 2 Schematic diagram of test-section geometry**

The outer shroud has two sections, one attached to the stator and the other the rotor, which were separated by an axial clearance, $s_c$. The inner seal, not shown in Fig. 2, was stationary. A stationary, annular ''sealing chamber'' was fitted around the periphery of the cavity, and the chamber was pressurised by a separate flow to form a labyrinth seal. Some of the preswirl air was allowed to leak past the labyrinth seal, and this leakage flow rate was controlled by the air supplied to the seal. It was therefore possible to control independently the mass flow rates of the preswirl, blade cooling, and sealing flows. These mass flow rates were chosen to simulate engine-representative values of $\beta_p$ and $\lambda_T$.

The disk could be rotated up to speeds of 5000 rpm, providing a maximum rotational Reynolds numbers, $\mathrm{Re}_\phi$ (based on disk radius) up to $1.2\times10^6$. This value is typically an order of magnitude less than those found in gas turbines. However, as discussed above, the flow structure within the rotating cavity depends principally on $\beta_p$ and $\lambda_T$ and only weakly on $\mathrm{Re}_\phi$. Hence the flow structure is considered to be representative of that found in cooling systems of engines. Nusselt numbers were measured for around 20 test conditions covering the following parametric range: $0.78\times10^6<\mathrm{Re}_\phi<1.2\times10^6$; $0.125<\lambda_T<0.36$; $0.5<\beta_p<1.5$.

**2.2 Instrumentation.** A total-temperature probe and pitot tube located in the outlet of the nozzles, together with a static-pressure tap between the nozzles, were used to measure the total and static temperature and the velocity of the inlet flow. Static pressure taps were located at nine radial stations in the stator, and nine pitot tubes were located at the same radii in the midaxial plane of the wheel space. This enabled the measurement of the radial distribution of static and total pressure, and of $V_\phi$, the tangential velocity of the air in the core outside the boundary layers. As the ''blade-cooling air'' discharged directly to atmosphere, it was also possible to measure the discharge coefficient of the receiver holes. Measurements of the fluid dynamics of the experimental facility are presented by Yan et al. [6].

Local heat transfer coefficients on the rotating disk were determined from surface-temperature measurements using TLCs. The experiments, which were transient and conducted under known thermal boundary conditions, relied on the accurate measurement of the time taken for the narrow-band TLCs on the rotor surface to reach a unique value of hue, which had been calibrated against temperature. The crystals were sprayed on the disk in sectors inside the wheel space, which could be viewed through the transparent polycarbonate by a digital video camera, running at 25 frames per second, under the illumination of a strobe light synchronized to the disk frequency. A thin layer of black paint was used to provide contrast to the color play of the TLC. The in situ calibration of the TLC is discussed in the next section, though it should be noted that the hue was measured as a function of temperature over a range of strobe frequencies corresponding to rotational disk speeds up to 5000 rpm. The strobe had a flash duration of less than 8 $\mu$s which, at 5000 rpm, corresponded to 0.24 deg angular rotation of the disk.

Figure 3 is a schematic diagram illustrating the arrangement of pipes providing the air flow to the test section, where all mass flow rates were measured using orifice plates designed to British Standards (BS1042). A mesh heater, designed using the method of Gillespie, Wang, and Ireland [7], was used to generate a sudden change in the air temperature and to create a well-controlled thermal boundary condition for the transient experiments. The mesh was made of 90-$\mu$m-diam stainless-steel wire with an open area of 38% and overall dimensions of $60\times120$ mm. The mesh was soldered to bus bars, and the additional support of three strengthening rods of 3 mm diameter was required due to the pressure drop across the mesh. A welding unit and control box provided a current of typically 150 A, which increased the air temperature across the mesh heater by 40°C (with a standard deviation of 0.2°C) for a mass flow rate of 0.1 kg/s. All pipework downstream of the

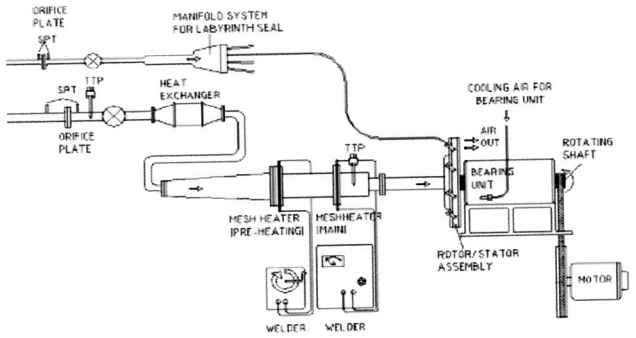


**Fig. 3 Schematic layout of experiment**

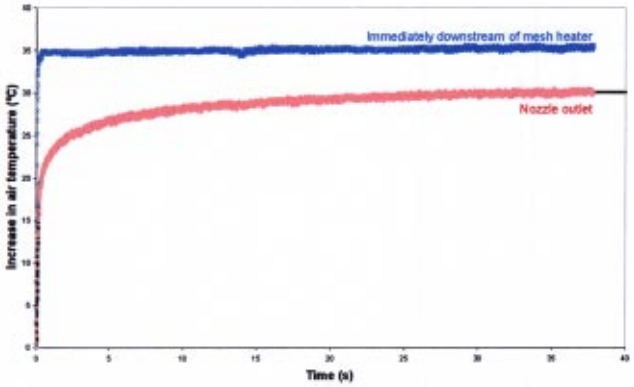


**Fig. 4 Increase in air temperature with time measured at two locations; a fitted curve is also shown for $m=3$**

mesh heater was thermally insulated using low-conductivity Rhoacell, a closed-pore structural foam with low thermal conductivity. This pipework had three main components: a 350-mm length of rectangular cross section, a 350-mm length of circular cross section, and a radial diffuser; there was also a short entry length into the preswirl nozzles. The temperature history of the air leaving the preswirl nozzles is described in Sec. 3.

Before the main mesh heater was switched on, the apparatus was left running, at the required speed and flow rate, to enable it to reach thermal equilibrium. When the air from the compressor was not equal to the ambient temperature in the laboratory, it was either cooled by a heat exchanger or heated by a second mesh heater upstream of the main heater. In practice, it was not possible to achieve perfect thermal equilibrium, and there was always a small temperature difference between the rotating disk and the air, as discussed in Sec. 4.

## 3 Temperature Measurement

**3.1 Total-Temperature Probes.** A conventional total-temperature probe usually contains a thermocouple, the bead of which is located inside a stainless-steel tube. Such probes have a large recovery factor ($\approx$0.95) but a poor time response. For the tests described here, a K-type bare-wire thermocouple, made from wires of 25 $\mu$m diameter, was constructed. The wires were contained inside a stainless steel tube with the bead outside; there was a distance of 3.5 mm (or 140 wire diameters) between the exposed bead and the tip of the tube. This construction method supported the thermocouple wires but reduced the thermal error resulting from transient conduction from the bead to the tube. The result was a robust probe with a time constant of less than 40 ms. A consistent probe recovery factor of 0.78 was measured over a range of air speeds up to 120 m/s.

Figure 4 shows a typical increase in air temperature with time measured by the probe immediately downstream of the mesh heater and at the outlet of the preswirl nozzles. Downstream of the heater there is a good approximation to a step change. Owing to the thermal inertia of the ducting between the heater and the test section, a step change is not produced at the nozzles; it can be seen that a good fit to the temperature is provided by an exponential series of $m=3$ terms (see Sec. 4.2). It seems likely that three terms are required in the exponential fit because there are three distinct geometric sections to the duct downstream of the heater mesh, as discussed above. Typically the TLC color-change times on the disk surface ranged between 1 and 20 s (depending on the local heat transfer coefficient), and these times are of similar magnitude to the time constants of the exponential rise in air temperature.

**3.2 Calibration of TLCs.** Microencapsulated TLCs were purchased commercially in the form of a water-based slurry. Three types of TLC were used: two narrow-band crystals optically active over a temperature range of around 1°C near 30°C (R30C1W) and 40°C (R40C1W), and one wide-band crystal (R18C20W) active from approximately 18°C over a 20°C range.

The crystals were calibrated against temperature by recording the red, green, and blue (RGB) signals of light reflected from the TLC, under known temperature and illumination, using a digital camera, an isothermal copper block, and an AGEMA 870C infrared-imager [8]. The RGB signals were converted into hues, which increase monotonically with temperature.

The TLC was applied to the rotor surface using an airbrush, and black paint was sprayed on top of the TLC to provide contrast to the color play from the crystals. The overall thickness (TLC and paint) was approximately 25 $\mu$m. During the experiments the TLC was viewed through the transparent polycarbonate disk using the stroboscopic light synchronized to the rotational speed of the disk. For the calibration, the stator was removed to gain direct optical access to the front surface of the disk, which was coated in TLC under black paint and heated quasiaxisymmetrically by a jet of hot air. The surface temperature of the front face was measured using an infrared imager. The back face of the disk was simultaneously illuminated by the stroboscopic light and the TLC was viewed by the digital camera, located behind the disk. The locations of the stroboscopic light and camera were the same as those used in the experiments, creating an in situ calibration.

It has been shown [8,9] that rotational speed has no significant effect on the calibration of TLCs, and so the calibrations were conducted with the disk stationary. To ensure that the strobe frequency had no effect, calibrations were carried out for frequencies corresponding to 3000, 4000, and 5000 rpm.

Figure 5 shows the calibrated variation of temperature with

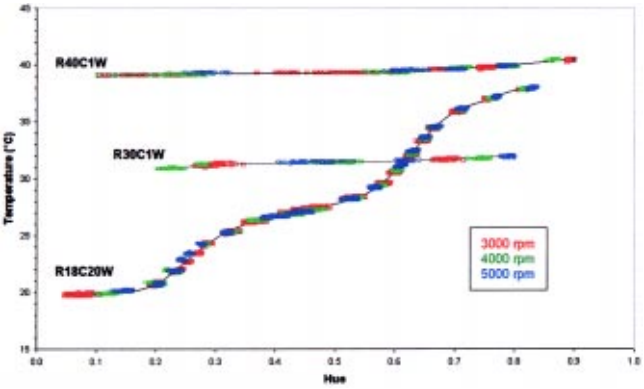


**Fig. 5 Calibrated temperature versus normalized hue for three crystals at three strobe frequencies**

normalized hues for all three crystals. The hue changed from 0 to 1 as the TLC changed color from red through green to blue as it was activated through its transition temperature. In all cases, the effect of the strobe frequency is insignificant. The estimated random uncertainties are ±1°C for the wide-band and ±0.1°C for the narrow-band crystals.

## 4 Analysis of Experimental Data

This section presents a technique for determining the convective heat transfer coefficient, $h$, for transient experiments where the air temperature, which is used as a boundary condition for Fourier's one-dimensional conduction equation, is represented by an exponential series.

**4.1 Definition of the Heat Transfer Coefficient.** Before proceeding, it is convenient to define $h$ as

$$q_w = h(T_{aw} - T_w), \tag{4.1}$$

where $q_w$ is the surface heat flux from the air to the wall, $T_w$ is the surface temperature of the wall, and $T_{aw}$ is the adiabatic-wall temperature. $T_{aw}$ depends on the total-temperature of the air, $T_a$, and on the fluid dynamics. For example, for boundary layer flow over a flat plate,

$$T_{aw} = T_a - (1-R)\frac{U^2}{2c_p}, \tag{4.2}$$

where $U$ is the free stream velocity and $R$ is the recovery factor. For the case where $U$ is invariant with time, Eq. (4.2) can be expressed as

$$T_{aw} = T_a + F, \tag{4.3}$$

where $F$ is a time-invariant term. In general, $F$ depends on the flow, but for the above case, $F=(R-1)U^2/2c_p$.

**4.2 Solution of Fourier's Equation.** In a typical transient test, a step change in air temperature is generated, and a narrow-band TLC is used to determine the surface temperature, $T_w$, of the test piece. Knowing the time, $t$, at which the surface reaches $T_w$, $h$ (assumed time-invariant) can be calculated from the solution of Fourier's one-dimensional conduction equation for the case of a semi-infinite plate subjected to a step change in air temperature.

In the tests described here, the mesh heater created an effective step change in the air temperature, but at the test section an exponential type of behavior (or so-called "slow transient") was produced, as shown in Fig. 4. The air temperature, $T_a$, could be fitted by an exponential series of m terms, such that

$$T_a(t) = T_{a,0} + \sum_{j=1}^{m} T_{a,j}(1 - e^{-t/\tau_j}), \tag{4.4}$$

where $T_{a,0}$ is the air temperature at $t=0$, and $T_{a,j}$ and $\tau_j$ are the constant amplitudes and time constants, respectively.

The adiabatic wall temperature can be written as

$$T_{aw}(t) = T_a(t) + F, \tag{4.5}$$

where $F$ is a time-invariant parameter that depends on the flow. As $t \to \infty$,

$$T_{aw,\infty} = T_0 + \sum_{j=1}^{m} T_{a,j} \tag{4.6}$$

where $T_0$ is the initial temperature of the wall, such that

$$T_0 = T_{a,0} + F. \tag{4.7}$$

Fourier's conduction equation for a semi-infinite slab has been solved by Gillespie, Wang, and Ireland [10] for the case where there is a simple exponential increase in the air temperature, corresponding to the case where $m=1$ in Eq. (4.4). The solution is

$$\Theta = \frac{T_w - T_0}{T_{aw,\infty} - T_0} = g(\beta, \beta_\tau), \tag{4.8}$$

where

$$g(\beta,\beta_\tau) = 1 - \frac{1}{1+\beta_\tau^2} e^{\beta^2}\,\mathrm{erfc}(\beta) - e^{-t/\tau}\frac{\beta_\tau^2}{1+\beta_\tau^2} \times \left\{ 1 + \frac{1}{\beta_\tau}\left[ \frac{1}{\pi}\sqrt{\frac{t}{\tau}} + \frac{2}{\pi}\sum_{n=1}^{\infty} \frac{1}{n} e^{-n^2/4} \sinh\left( n\sqrt{\frac{t}{\tau}} \right) \right] \right\}, \tag{4.9}$$

$$\beta = \frac{h\sqrt{t}}{\sqrt{\rho c k}}, \tag{4.10}$$

and

$$\beta_\tau = \frac{h\sqrt{\tau}}{\sqrt{\rho c k}}. \tag{4.11}$$

For the case where $\tau=0$, Eq. (4.8) simplifies to

$$\Theta = f(\beta), \tag{4.12}$$

where

$$f(\beta) = 1 - e^{\beta^2}\,\mathrm{erfc}(\beta), \tag{4.13}$$

which is the well-known solution of Fourier's equation for a step change in the air temperature.

The general solution for an exponential series, corresponding to Eq. (4.6), is given by Newton et al. [11] as

$$\Theta = \sum_{j=1}^{m} \frac{T_{a,j}}{T_{aw,\infty} - T_0} g(\beta, \beta_{\tau_j}). \tag{4.14}$$

For the special case where $m=1$, $T_{a,1} = T_{aw,\infty} - T_0$ and Eq. (4.14) reduces to Eq. (4.8).

**4.3 Data Analysis.** The experimental data were analyzed by making a least-squares fit of an exponential series (Eq. (4.4)) to the measured variation of air temperature with time. This enabled $T_{aw,\infty}$ and $T_{a,j}$ to be calculated for $j=1$ to $m$; a value of $m=3$ was found to give an acceptable fit in all cases tested.

The initial wall temperature, $T_0$, was determined using Eq. (4.7) with measured values of $T_{a,0}$ and a theoretical value of $F$. The value of $T_0$ found in this way was similar to, but considered to be more accurate than, the value obtained using wide-band TLCs (see Ref. [11]). The value of $T_w$ was determined from an appropriate narrow-band crystal. With knowledge of $T_w$, $T_0$, and $T_{aw,\infty}$, $\Theta$ was calculated, and $h$ was obtained from the numerical solution of Eq. (4.14).

An alternative procedure for experiments featuring a slow transient is to use a wide-band TLC (with a transition temperature range of, say, 20°C) to measure the complete variation of surface temperature with time. By use of Duhamel's method, Fourier's solution can be solved and $h$ determined. However, the uncertainty in measurement of surface temperature using wide-band TLCs is generally much greater than that using narrow-band TLCs, and this results in a large uncertainty in $h$ [12,13]. The advantage of the analysis presented here is that, just as for the step-change case, which is the limit of the exponential-series solution, it is not necessary to know the wall-temperature history: only a single narrow-band TLC is needed to determine $h$. This allows the accuracy of the simple step-change method to be brought to the more difficult case of the slow transient. A typical case is discussed below.

## 5 Typical Test Case

Figures 6(*a*) to 6(*d*) are raw color images selected from a time sequence obtained by the digital camera (operating at 25 frames

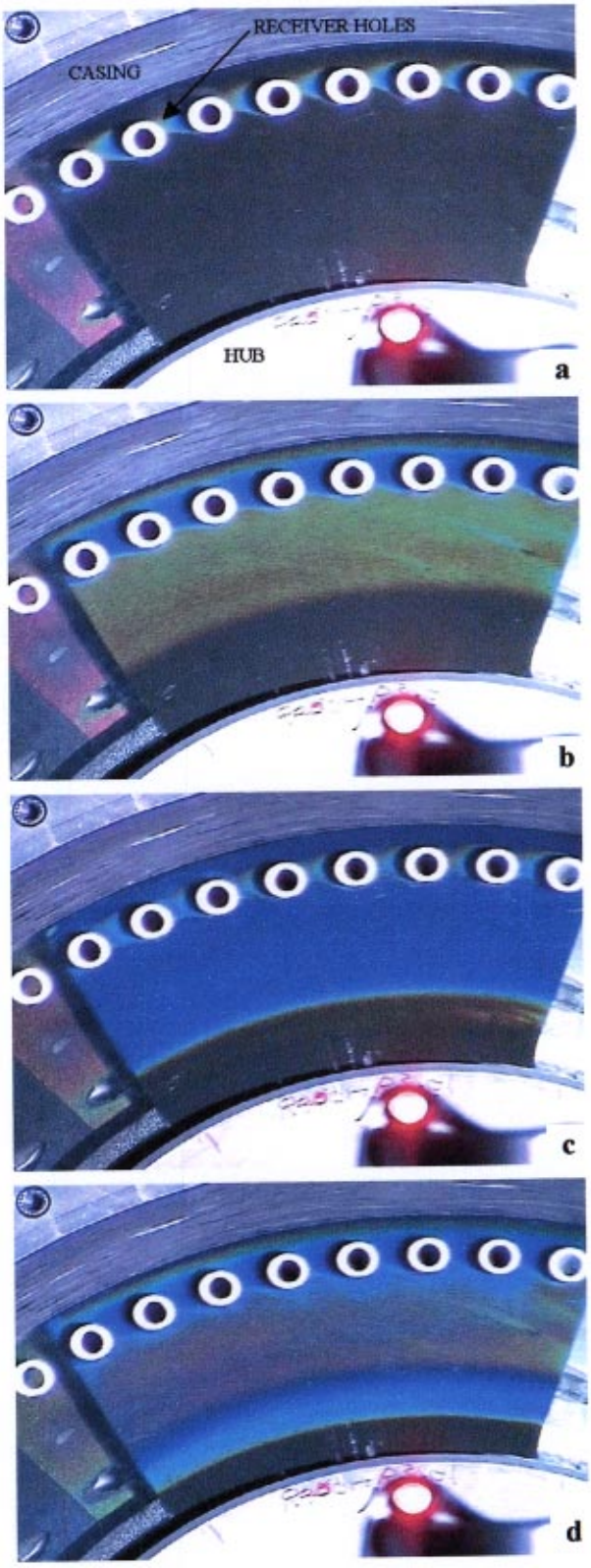


**Fig. 6** ***a–d*** **(top to bottom) Video recordings of disk surface showing change of color of TLC with time**

per second) during a typical experiment. These images show the color play of the TLC as viewed through the transparent polycarbonate disk. Initially clear when below its activation temperature, the TLC changed color from red to green to blue as the disk was

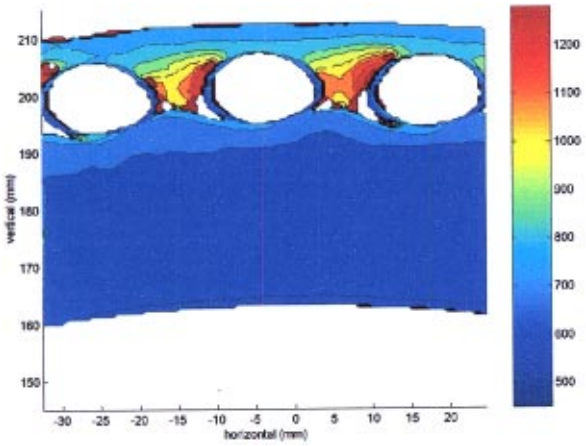


**Fig. 7 Contours of Nu: $Re_\phi \approx 0.8\times10^6$, $\lambda_T \approx 0.125$, $\beta_p \approx 0.5$; the disk is rotating clockwise**

heated by the hot gas entering through the preswirl nozzles. The images appear ''frozen'' because the rotor was illuminated by the stroboscopic light synchronized with the disk rotating at 5000 rpm.

A color version of Fig. 6 (and Figs. 7 and 8) appear in ASME paper GT-2003-38123. The hub and casing, at radii *a* and *b*, are marked in Fig. 6(*a*). The blade receiver holes, insulated using low-conductivity, white-colored Rhoacell foam, are also labeled. The narrow-band TLC and overcoat of black paint had been sprayed in a 48 deg sector on the disk covering 8 of the 60 receiver holes. To the left of this painted sector the stator, coated with a wide-band (initially red) TLC, and two of the 24 preswirl nozzles are visible through the transparent (unpainted) polycarbonate at low radius. Some shadows appear around the receiver holes due to constraints with the lighting and viewing angles.

In Fig. 6(*a*) the 30°C narrow-band TLC has been activated into its visible range (shown as blue) near the blade receiver holes. Elsewhere on the disk the TLC is still clear (showing black), indicating that there is a region of relatively high heat transfer around the holes. The virtually identical TLC patterns around each of the receiver holes clearly indicate the excellent periodicity of the flow structure. In Figs. 6(*b*) and 6(*c*), the 30°C crystal has been activated (green and blue, respectively) at radii between the preswirl nozzles and the receiver holes. In Fig. 6(*c*) the 40°C TLC has been activated by temperature (light blue) in the region around the receiver holes and has turned dark blue in Fig. 6(*d*). The 40°C TLC is activated at lower radii in Fig. 6(*d*) (red-green). Note that the stator, as indicated by the change in color of the wide-band TLC, has also been heated throughout this transient process.

These RGB images (of 800×600 pixels), recorded at 25 frames per second by the digital camera, were subsequently converted to hues on a PC. It was then possible to obtain the hue history of each pixel in the image and hence the time taken for the surface to reach a prescribed value of hue. Thus the time taken for the surface to reach the temperature of the calibrated narrow-band crystal, $T_w$, from an initial temperature, $T_0$, was measured at each pixel on the active surface of the disk in the field-of-view of the camera. A ''median filter,'' using the median of nine adjacent pixels, was used to reduce the uncertainty in the measured values of $T_w$.

## 6 Nusselt Number

Figure 7 shows contours of the measured Nusselt number on the rotating disk for $Re_\phi = 0.8\times10^6$, $\lambda_T \approx 0.125$, and $\beta_p \approx 0.5$; the direction of rotation of the disk is clockwise. The distribution of Nu is largely axisymmetric, except in the region around the re-

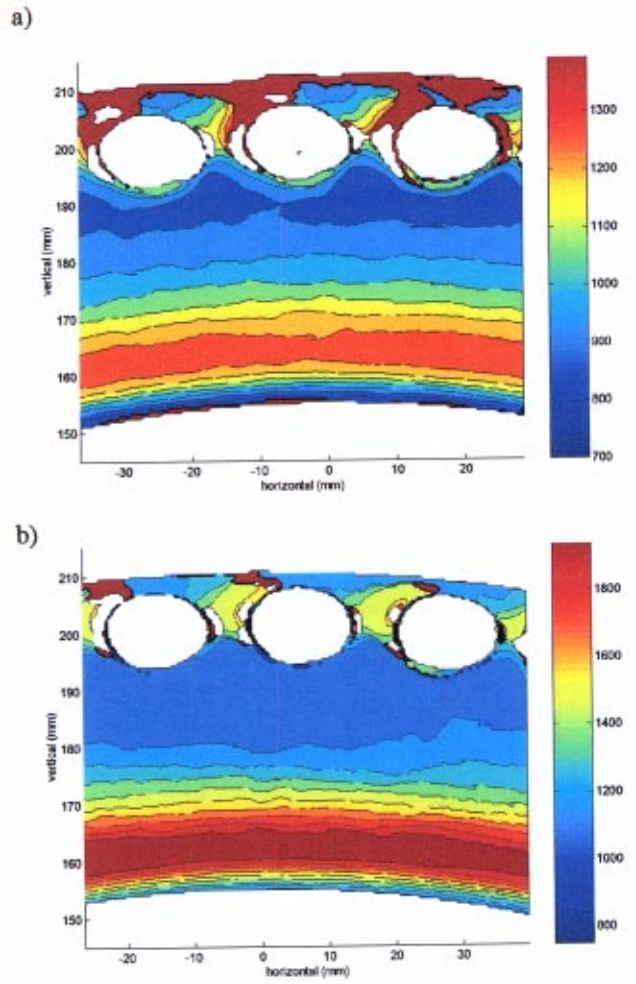


**Fig. 8 Effect of $Re_\phi$ on contours Nu for $\lambda_T \approx 0.36$ and $\beta_p \approx 1.4$: (*a*) $Re_\phi \approx 0.8\times10^6$, (*b*) $Re_\phi \approx 1.18\times10^6$; the disk is rotating clockwise**

ceiver holes. The highest heat transfer rates occur between the holes, and there is repeatability in both magnitudes and the variations of Nu between successive holes.

Figures 8(*a*) and 8(*b*) show contours of Nu for a higher flow rate, $\lambda_T \approx 0.36$, $\beta_p \approx 1.4$, for $Re_\phi = 0.8\times10^6$ and $Re_\phi = 1.18\times10^6$, respectively. The color scales have been chosen independently in order to show clearly the variations around the receiver holes. Comparing Fig. 4 and Fig. 5(*a*), for which $Re_\phi = 0.8\times10^6$ in both cases, there is higher heat transfer around the preswirl nozzle radius, $x_p = 0.74$, at the higher flow rate. There are similar variations (and similarly good repeatability of results) between the receiver holes on the disk; Nu is also higher in this region for the higher flow rate case. Figures 8(*a*) and 8(*b*) show that Nu increases generally with increasing $Re_\phi$.

**6.1 Effect of $Re_\phi$ on Radial Variation of Nu.** The variations of Nu with the parameters $\lambda_T$ and $\beta_p$, and with $Re_\phi$, are best observed by using results taken along a radial line midway between receiver holes. Figure 9 shows the effect of $Re_\phi$ on the measured radial variation of Nusselt number at two fixed values of $\lambda_T$ (0.125 and 0.36 approximately), for which $\beta_p \approx 0.5$ and 1.4, respectively. For each fixed value of $\lambda_T$ (and $\beta_p$), the magnitude of Nu increases with increasing $Re_\phi$, but there is little effect of $Re_\phi$ on the *shape* of the Nu distributions. For all cases, there is a peak in measured values of Nu in the region near the receiver holes on the disk. Figure 9(*a*) ($\lambda_T \approx 0.125$, $\beta_p \approx 0.5$) shows that Nu increases with radius between the preswirl nozzle radius, $x_p = 0.74$, and the receiver holes. This behavior is similar, qualitatively, to heat transfer in a simple rotor–stator system with a radial outflow [14], suggesting that heat transfer is controlled mainly by the boundary-layer flow on the rotating disk. For $x > 0.9$, there is a rapid rise in measured Nu. In this region, disk boundary layer fluid enters the receiver holes and there is strong flow axially toward the disk, causing an increase in heat transfer.

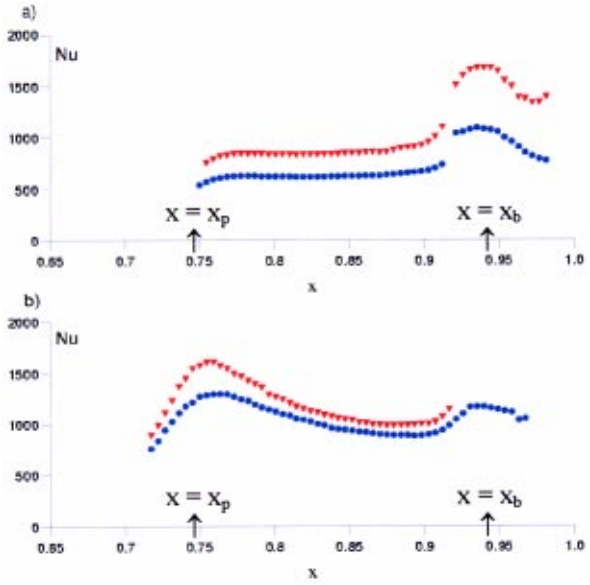


**Fig. 9 Effect of $Re_\phi$ on radial variation of Nu (*a*) $\lambda_T \approx 0.125$, $\beta_p \approx 0.52$; (*b*) $\lambda_T \approx 0.36$, $\beta_p \approx 1.4$ $Re_\phi \approx 0.8\times10^6$ ● $Re_\phi \approx 1.2\times10^6$ ▼**

Figure 9*b* shows that for $\lambda_T \approx 0.36$ ($\beta_p \approx 1.4$) a local peak in Nu occurs around the nozzle radius $x_p$, and Nu decreases for $x_p < x < x_b$. This suggests that inertial ''impingement'' effects have a more significant influence, due to the more powerful preswirl flow at this higher value of $\lambda_T$, than for the cases in Fig. 9(*a*).

**6.2 Effect of $\lambda_T$ and $\beta_p$ on the Radial Variation of Nu.** Figures 9(*a*) and 9(*b*) also show, respectively, the effect of varying $\lambda_T$ (and, as a consequence, varying $\beta_p$) on the measured radial variation of Nu for $Re_\phi \approx 0.8\times10^6$ (blue circles) and $1.2\times10^6$ (red triangles). At both values of $Re_\phi$, there is a similar transition in the variation of Nu with $x$, from the viscous behavior described above for $\lambda_T \approx 0.125$ ($\beta_p \approx 0.5$) to inertial behavior for $\lambda_T \approx 0.36$ ($\beta_p \approx 1.4$).

The combined effect of increasing $\lambda_T$ and $\beta_p$ at fixed $Re_\phi$ is greatest for $x < 0.9$, approximately. There is less sensitivity to $\lambda_T$ and $\beta_p$ for the region around and outward of the receiver holes, and this sensitivity also tends to decrease as $Re_\phi$ increases.

**6.3 Use of Two Crystals.** The method of analysis described in Sec. 4 only requires a measurement of a single narrow-band TLC. Two narrow-band TLCs were used to test the accuracy of the measurements. Figure 10 shows *h*, rather than Nu, again measured along a radius midway between two receiver holes for the viscous and inertial cases discussed above. Data from both the 30 and 40°C TLCs are shown.

There is good agreement between the data collected from the two TLCs for the viscous case. However, in the inertial case, *h* measured using the 40°C crystal is consistently higher than that obtained using the 30°C crystal. These cases are typical examples from a range of experimental data. Before discussing possible reasons for differences in the measurements of *h*, it is necessary to consider the uncertainties in these measurements.

The uncertainty analysis described by Owen, Newton, and Lock [13] was used to create the ''uncertainty bars'' shown in Fig. 10. Small, random uncertainties in the measured temperature can produce large uncertainties in the calculated values of *h*. If $P_{T_w}$, $P_{T_0}$,

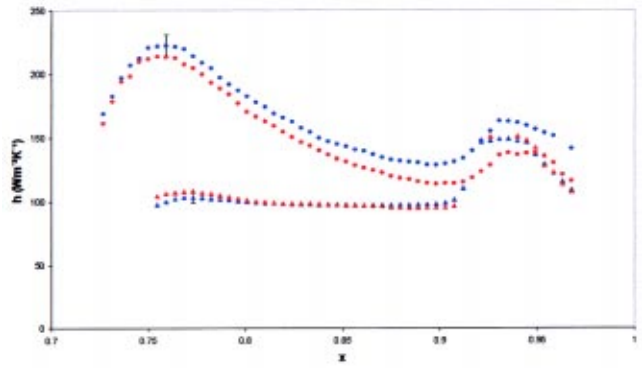

**Fig. 10 Heat transfer coefficient versus normalized radius for viscous and inertial flows. ▲ Viscous—H40; ● Inertial—H40; ▲ Viscous—H30; ● Inertial—H30. (*h* uncertainty for 0.2°C temperature uncertainty.)**

and $P_{T_{aw}}$ are the relative uncertainties (95% confidence estimates) in $T_w$, $T_0$ and $T_{aw}$, respectively, then $P_h$, the relative uncertainty in $h$, can be determined from

$$\frac{P_h}{h} = \Phi_h \frac{P_T}{T_{aw} - T_0}, \tag{6.1}$$

where $\Phi_h$ is the so-called *amplification parameter* and $P_T = \max(P_{T_w}, P_{T_0}, P_{T_{aw}})$.

The uncertainty bars in Fig. 10 are based on a 0.2°C temperature uncertainty. Despite the random uncertainties, there is no evidence of significant scatter in the results. The ''smoothness'' of the distribution of $h$ is attributed to the smoothing of the air temperature and to the median filtering used for the wall temperatures.

There are three suspected reasons for the differences in the measurements of $h$ from the two crystals: (i) incorrect values of $T_{aw}$; (ii) incorrect values of $T_0$; (iii) effect of radial distribution of $T_w$.

(i) $T_{aw}$, given by Eq. (4.5), depends on $T_a$, the local temperature in the fluid core. Unfortunately this temperature was not measured in the experiments but was assumed to be equal to the measured temperature at exit from the preswirl nozzles. It is speculated that, as heat flows from the air to the rotating disk, the temperature of the fluid in the core, and hence $T_{aw}$, will be less than $T_a$. Consequently the value of $T_{aw}$ given by Eq. (4.2) will overestimate the true value, which in turn would cause an underestimate in the true value of $h$. The values of $h$ calculated from the 40°C crystal should, by this argument, be closer to the true values than those from the 30°C crystal. This uncertainty in $T_a$ would have a more significant in the inertial regime than the viscous regime; in the former there is relatively high heat transfer and more mixing of air between the core and the region near the wall.

(ii) There is an uncertainty in the value of $T_0$ and this could bias the calculated values of $h$. A bias in $T_0$ would qualitatively affect both measurements of $h$ in the same way, though not in a quantitatively equal manner.

(iii) As discussed by Butler and Baughn [15], the distribution of $h$ is affected by the distribution of $T_w$. This effect is particularly significant in rotating-disk systems [1] where the radial distribution of $h$ depends strongly on the radial gradient of disk temperature. As the radial distributions of $T_w$ are, perforce, different for the two crystals, it is reasonable to speculate that the radial distribution of $h$ will be different. In addition, in regions of high local temperature gradients there is an effect of lateral conduction which can cause an overestimate in the value of $h$ from one-dimensional conduction analysis [16]. This error has not been quantified here.

The fact that differences in $h$, albeit within the limits of experimental uncertainty, could be measured is a tribute to the exponential-series technique and to the careful calibration of the TLCs. These measurements also reveal the benefits of using two crystals to evaluate $h$: one crystal would only provide the bliss of ignorance!

The measurements of $h$ obtained using the 40°C crystal are considered more accurate than those obtained using the 30°C crystal. All data in Figs. 7–9 are based on the 40°C crystal.

## 7 Conclusions

An experimental facility has been built to investigate the heat transfer and fluid dynamics of a rotor–stator system with preswirled air under engine-representative flow structure. The facility has been designed to accommodate pressure and temperature instrumentation in the test section and to provide optical access to the wheel space.

A thermochromic liquid crystal (TLC), in conjunction with a stroboscopic light and digital video camera, has been used to obtain contour maps of the Nusselt number, Nu, on the rotating disk. Both wide-band and narrow-band TLCs were used and carefully calibrated *in situ* using an infrared imager.

A mesh heater was used to generate an air temperature history in the test section, which was represented as an exponential series of three terms. An analysis has been developed to determine values of Nu by using this series as a boundary condition for Fourier's one-dimensional conduction equation. This technique has the advantage, in terms of accuracy and simplicity, that only a single narrow-band TLC is needed to determine $h$.

Two heat transfer regimes were observed experimentally: a viscous regime at relatively low values of $\lambda_T$, and an inertial regime at high values of $\lambda_T$. The viscous regime corresponds to axisymmetric boundary layer flow over most of the rotating disk: for $x < x_b$, Nu increases as $x$ increases. Three-dimensional flow near the receiver holes on the disk, at $x = x_b$, creates nonaxisymmetric flow in this region, with large values of Nu between and around the holes. The inertial regime corresponds to impingement on the rotating disk around the preswirl nozzle radius, $x = x_p$. There is a peak in Nu near $x = x_p$ and, for $x_p < x < x_b$, Nu decreases as $x$ increases; this behavior is also virtually axisymmetric. As for the viscous regime, there are large values and two-dimensional variations of Nu around the receiver holes. For both regimes, Nu increases as $\mathrm{Re}_\phi$, $\lambda_T$, and $\beta_p$ increase.


## Acknowledgment

This work was funded by Alstom Power, Ltd. and the U.K. EPSRC.


## Nomenclature

$a$ = inner radius of the disk
$b$ = outer radius of the disk
$c$ = specific heat of wall
$c_p$ = specific heat at constant pressure of air
$C_w$ = nondimensional mass flow rate ($= \dot{m}/\mu b$)
$f(\beta)$ = step-change solution of Fourier's equation
$F$ = time-invariant adiabatic-wall parameter ($= T_{aw} - T_a$)
$g(\beta, \beta_\tau)$ = exponential solution of Fourier's equation
$h$ = heat transfer coefficient [$= q_w/(T_{aw} - T_w)$]
$k$ = thermal conductivity of wall
$m$ = number of terms in exponential series
Nu = Nusselt number [$= q_w r/k(T_{aw} - T_w)$]
$P$ = uncertainty in measured value
$q_w$ = heat flux from air to wall
$r$ = radius from axis of rotation
$R$ = recovery factor
$\mathrm{Re}_\phi$ = rotational Reynolds number ($= \rho \Omega b^2/\mu$)
$s$ = gap width
$s_c$ = clearance spacing
$t$ = time
$T$ = temperature inside wall

$T_a$ = total temperature of air
$T_{aw}$ = adiabatic-wall temperature
$T_w$ = surface temperature of wall
$U$ = free-stream velocity
$V_\phi$ = tangential component of velocity
$x$ = nondimensional radius ($=r/b$)
$\alpha$ = thermal diffusivity of wall ($=k/\rho c$)
$\beta$ = parameter in step-change solution ($=h\sqrt{t/\rho ck}$)
$\beta_p$ = preswirl ratio ($=V_{\phi,p}/\Omega r_p$)
$\beta_\tau$ = parameter in exponential solution ($=h\sqrt{\tau/\rho ck}$)
$\lambda_T$ = turbulent flow parameter ($=C_{w,p}/\mathrm{Re}_\phi^{0.8}$)
$\rho$ = density
$\Theta$ = nondimensional temperature [$=(T_w-T_0)/(T_{aw,\infty}-T_0)$]
$\Phi$ = amplification parameter for uncertainties
$\mu$ = dynamic viscosity
$\Omega$ = angular speed of rotating disk
$\tau$ = time constant

### Subscripts

h = with reference to heat transfer coefficient
$j$ = $j$th term in series
$T$ = with reference to maximum value of $P_{T_w}$, $P_{T_0}$, and $P_{T_{aw}}$
$T_{aw}$ = with reference to adiabatic wall temperature
$T_0$ = with reference to initial temperature
$T_w$ = with reference to surface temperature
$p$ = preswirl nozzle
0 = value at $t=0$
$\infty$ = value as $t\to\infty$

## References


[1] Owen, J. M., and Rogers, R. H., 1989, *Flow and Heat Transfer in Rotating Disc Systems*: Vol. 1, *Rotor-Stator Systems*, Research Studies Press, Taunton, UK and Wiley, NY.

[2] Owen, J. M., and Wilson, M., 2000, "Some Current Research in Rotating-Disc Systems," in Turbine 2000 Int. Symp. on Heat Transfer in Gas Turbine Systems, Turkey, August 13–18, in Heat Transfer in Gas Turbine Systems, Annals of the New York Academy of Sciences, **934**, pp. 206–221.

[3] Metzger, D. E., Bunker, R. S., and Bosch, G., 1991, "Transient Liquid Crystal Measurement of Local Heat Transfer on a Rotating Disk With Jet Impingement," ASME J. Turbomach., **113**, pp. 52–59.

[4] Karabay, H., Wilson, M., and Owen, J. M., 2001, "Predictions of Effect of Swirl on Flow and Heat Transfer in a Rotating Cavity," Int. J. Heat Fluid Flow, **22**, pp. 143–155.

[5] Pilbrow, R., Karabay, H., Wilson, M., and Owen, J. M., 1999, "Heat Transfer in a 'Cover-Plate' Pre-Swirl Rotating-Disc System," ASME J. Turbomach., **121**, pp. 249–256.

[6] Yan, Y., Gord, M. F., Lock, G. D., Wilson, M., and Owen, J. M., 2002, Fluid dynamics of a pre-swirl rotating-disk system, ASME paper 2002-GT-30415 (to be published in the J Turbomachinery).

[7] Gillespie, D. R. H., Wang, Z., and Ireland, P. T., 2001, Heater element, European Patent No. 0847679.

[8] Syson, B. J., Pilbrow, R. G., and Owen, J. M., 1996, "Effect of Rotation on Temperature Response of Thermochromic Liquid Crystal," Int. J. Heat Fluid Flow, **17**, pp. 491–499.

[9] Camci, C., Glezer, B., Owen, J. M., Pilbrow, R. G., and Syson, B. J., 1996, "Application of Thermochromic Liquid Crystal to Rotating Surfaces," ASME J. Turbomach., **118**, pp. 408–413.

[10] Gillespie, D. R. H., Wang, Z., and Ireland, P. T., 1998, "Full Surface Local Heat Transfer Coefficient Measurements in a Model of an Integrally Cast Impingement Cooling Geometry," ASME J. Turbomach., **120**, pp. 92–99.

[11] Newton, P. J., Yan, Y., Stevens, N. E., Evatt, S. T., Lock, G. D., and Owen, J. M., 2003, "Transient Heat Transfer Measurements Using Thermochromic Liquid Crystal. Part 1: An Improved Technique," Int. J. Heat Fluid Flow, **24**, pp. 14–22.

[12] Yan, Y., and Owen, J. M., 2002, "Uncertainties in Transient Heat Transfer Measurements With Liquid Crystal," Int. J. Heat Fluid Flow, **23**, pp. 29–35.

[13] Owen, J. M., Newton, P. J., and Lock, G. D., 2003, "Transient Heat Transfer Measurements Using Thermochromic Liquid Crystal. Part 2: Experimental Uncertainties," Int. J. Heat Fluid Flow, **24**, pp. 23–28.

[14] Chen, J.-X., Gan, X., and Owen, J. M., 1996, "Heat Transfer in an Air-Cooled Rotor-Stator System," ASME J. Turbomach., **118**, pp. 444–451.

[15] Butler, R. J., and Baughn, J. W., 1996, "The Effect of the Thermal Boundary Condition on Transient Method Heat Transfer Measurements on a Flat Plate With a Laminar Boundary Layer," ASME J. Heat Transfer, **118**, pp. 831–837.

[16] Lin, M., and Wang, T., 2002, "A Transient Liquid Crystal Method Using a 3-D Inverse Transient Conduction Scheme," Int. J. Heat Mass Transfer, **45**, pp. 3491–3501.

# Direct-Transfer Preswirl System: A One-Dimensional Modular Characterization of the Flow

**M. Dittmann**
e-mail: Mario.dittmann@its.uni-karlsruhe.de

**K. Dullenkopf**

**S. Wittig**

Lehrstuhl und Institut für Thermische Strömungsmaschinen,
University of Karlsruhe,
76128 Karlsruhe, Germany

*In high-efficiency gas turbine engines, the cooling air for the high-pressure turbine stage is expanded through stationary preswirl nozzles, transferred through the preswirl chamber, and delivered to the blade feed holes of the rotor. By accelerating the cooling air in the direction of rotation, the total temperature relative to the rotor disk and the pressure losses occurring at the receiver hole inlet can be reduced. The discharge behavior of a direct-transfer preswirl system has been investigated experimentally for different number of receiver holes and different inlet geometries, varying axial gap widths between stator and rotor and for rotational Reynolds numbers up to* $Re_\phi = 2.3 \times 10^6$. *The discharge coefficients of the preswirl nozzles are given in the absolute frame of reference while the definition of the discharge coefficients of the receiver holes is applied to the rotating system in order to consider the work done by the rotor. A momentum balance is used to evaluate the deflection of the preswirled air entering the receiver holes. The flow in the preswirl chamber is characterized by introducing an effective velocity of the cooling air upstream of the rotor disk. The influences of geometrical parameters and operating points are reported and discussed in this paper.* [DOI: 10.1115/1.1787514]

## Introduction

In modern gas turbine engines two different preswirl systems are established in the internal air system of the high-pressure turbine [1]. In a ''cover-plate'' system, the preswirl nozzles are located at a small radius and the cooling air flows radially outward between the turbine disk and the cover plate to create a free vortex before entering the blade feed holes of the rotating turbine disk. In ''direct-transfer'' systems the stationary preswirl nozzles are located at a large pitch radius similar to the pitch radius of the blade feed holes in the rotor. The cooling air is accelerated in circumferential direction, passes the preswirl chamber, and is directly supplied to the receiver holes. Theoretically, lower cooling air temperatures can be achieved in direct-transfer systems. Furthermore, no cover plate is needed which is beneficial with respect to the engines weight.

Meierhofer and Franklin [2] were the first to measure the total temperature of the cooling air in the rotating blade feed holes of a direct-transfer system. A relatively good correlation was obtained in which the system effectiveness is given as a function of the velocity ratio of the circumferential velocity of the receiver holes to the effective velocity of the preswirled cooling air. The system's performance was found to be insensitive to several geometric and flow parameters. A combined experimental and numerical study was presented by El-Oun and Owen [3]. The effectiveness was calculated with a simple theoretical model, based on the Reynolds analogy. In their numerical study, Wilson et al. [4] used an axisymmetric elliptic solver to determine the flow structure and the heat transfer in a direct-transfer system. The discharge behavior of the preswirl nozzles and the receiver holes was characterized by Dittmann et al. [5]. As the determination of an effective time averaged velocity of the preswirled air at the inlet of the receiver hole is difficult, the flow inside the preswirl chamber was assumed to be isentropic. Thus the performance of the preswirl chamber could not be directly described.

Contributed by the International Gas Turbine Institute (IGTI) of THE AMERICAN SOCIETY OF MECHANICAL ENGINEERS for publication in the ASME JOURNAL OF ENGINEERING FOR GAS TURBINES AND POWER. Paper presented at the International Gas Turbine and Aeroengine Congress and Exhibition, Atlanta, GA, June 16–19, 2003, Paper No. 2003-GT-38312. Manuscript received by IGTI, Oct. 2002, final revision, Mar. 2003. Associate Editor: H. R. Simmons.

However, a characterization of all three components of the direct-transfer system, namely the preswirl nozzles, the preswirl chamber, and the receiver holes, is favorable. Based on the experimental data, in particular the measured torque of the driving shaft, the Euler equation for an axial compressor or turbine is used within this paper to calculate the specific work and to estimate the deflection of the preswirled air. Hence the occurring losses can be assigned to each single component of the preswirl system. The influence of geometric and flow parameters on the performance of the preswirl chamber will be discussed.

## Experimental Setup

A detailed description of the experimental setup, geometrical dimensions, and the instrumentation of the rig was given by Dittmann et al. [5]. Figure 1 shows a sectioned view of the direct-transfer preswirl system. Cooling air was discharged from a settling chamber through the flange of the rig to the preswirl plate. In total, four preswirl plates were available to vary the axial distance $s_1$ between stator and rotor and the number of preswirl nozzles $N_N$. All preswirl nozzles were 8 mm in diameter and inclined 20° to the stator surface in circumferential direction. The preswirled air entered an annulus of 46.8-mm radial height and left the test section to ambient conditions through receiver holes at a pitch radius of $r_m = 0.22$ m. The outer seal between rotor disk and casing could be fed with sealing air to reduce the leakage flow. In some test cases a radial outflow was superimposed to the swirled mainflow. Therefore air was discharged into the inner wheelspace close to the hub region of the rig. The superimposed cooling air passed the inner radial seal, was mixed with the mainflow inside the preswirl chamber, and left the test section radially through a lip seal arrangement in the casing.

The total area ratio of receiver holes to preswirl nozzles was kept constant while the number of receiver holes $N_R$ was varied. Therefore the diameter of the receiver holes had to be reduced with an increasing number of receiver holes. As the receiver holes were milled into the 40-mm thick titan-aluminum alloy rotor the $1/d$ ratio automatically changed with $N_R$. The rotor was connected to the driving shaft by two flexible clutches and a torque meter and could be accelerated up to 7000 rpm. This is equivalent

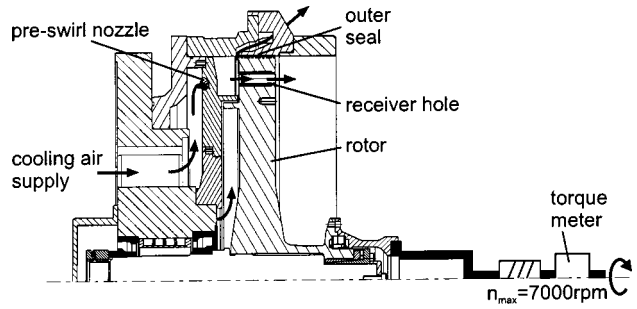


**Fig. 1 Setup of the preswirl rig**

to a circumferential velocity of the receiver holes of $u_R = 161$ m/s, or a rotational Reynolds number of $\mathrm{Re}_\phi = 2.3 \times 10^6$.

The mass flow rate discharged to the preswirl nozzles was measured by an orifice-metering system according to European standards with an uncertainty of 1 percent. The radially superimposed outflow was measured with hot-film sensors calibrated to an uncertainty of 1 percent. Pressure measurements were accomplished by means of a pressure transducer in combination with a Scanivalve system. The torque on the driving shaft could be determined with an uncertainty of 0.02 Nm. Based on the maximum measured torque, this corresponds to an accuracy of 0.25 percent. Using the method of Kline and McClintock [6] the uncertainty in the values of $c_D$ were found to be less than $\pm 2.5$ percent in most test cases, increasing to lower pressure ratios. The uncertainty of the effective velocity ratio was estimated to be lower than $\pm 3$ percent.

During the experiments the total pressure ratio $\pi$ was kept constant while the rotational speed of the rotor was varied. Different total pressure ratios across the preswirl rig were investigated. The radial mass flow rate was set to 30 or 50 percent of the preswirled mass flow rate.

## Definitions

The discharge coefficient is commonly used to characterize the occurring losses of the flow through restricting elements. For stationary setups, like the preswirl nozzles, a definition of the discharge coefficient in the absolute frame of reference is convenient. However, a transformation into the relative frame of reference is preferable for rotating configurations such as rotating holes or receiver holes within a preswirl system (Zimmermann et al. [7]). The work transferred to the fluid is considered and therefore discharge coefficients greater than unity do not occur, which is illogical under these circumstances.

A sketched view of the preswirl system is shown in Fig. 2. To clearly identify the properties of the fluid, the preswirl system is divided into five stages as indicated by the numbers 0–4. All representative temperatures and pressures are indicated in Fig. 2 and experimentally determined. In addition, the characteristic velocities of the preswirl system are sketched. The arrows indicate the positive direction of the velocities in the absolute and relative frame of reference. Two different velocity triangles are presented: one for the ideal flow without deceleration of the preswirled air inside the preswirl chamber; the other considering frictional effects and a widening of the air jets penetrating the preswirl chamber, as indicated by the dashed arrows. This results in a lower absolute approach velocity of the cooling air with respect to the receiver hole.

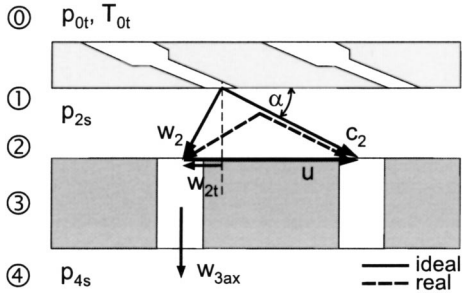


**Fig. 2 Velocities in the absolute and relative frame of reference**

The discharge coefficient is defined by the ratio of the discharged mass flow rate to the ideal mass flow rate, which can be determined by the total temperature and total pressure of the fluid upstream and the static pressure downstream of the restricting flow element. According to Popp et al. [8], the total properties upstream of the receiver holes have to be transformed into the relative frame of reference. As total temperature and total pressure change with relative motion, the circumferential velocity of the receiver holes and the tangential velocity of the preswirled cooling air have to be considered. The total properties in the relative system are determined by Eqs. (1) and (2). Finally, the discharge coefficients of the preswirl nozzles $c_{DN}$ and the receiver holes $c_{DR}$ can be calculated according to Eqs. (3) and (4),

$$\frac{T_{2\,\mathrm{tot,rel}}}{T_{2\,\mathrm{tot}}} = 1 + \frac{u^2 - 2uc_{2t}}{2c_p T_{2\,\mathrm{tot}}}, \tag{1}$$

$$\frac{p_{2\,\mathrm{tot,rel}}}{p_{2\,\mathrm{tot}}} = \left(1 + \frac{u^2 - 2uc_{2t}}{2c_p T_{2\,\mathrm{tot}}}\right)^{\kappa/(\kappa-1)}, \tag{2}$$

$$c_{DN} = \frac{\dot{m}}{\frac{A_N p_{0\,\mathrm{tot}}}{\sqrt{RT_{0\,\mathrm{tot}}}} \sqrt{\frac{2\kappa}{\kappa-1}\left[\left(\frac{p_{1s}}{p_{0\,\mathrm{tot}}}\right)^{2/\kappa} - \left(\frac{p_{1s}}{p_{0\,\mathrm{tot}}}\right)^{(\kappa+1)/\kappa}\right]}}, \tag{3}$$

$$c_{DR} = \frac{\dot{m}}{\frac{A_R p_{2\,\mathrm{tot,rel}}}{\sqrt{RT_{2\,\mathrm{tot,rel}}}} \sqrt{\frac{2\kappa}{\kappa-1}\left[\left(\frac{p_{4s}}{p_{2\,\mathrm{tot,rel}}}\right)^{2/\kappa} - \left(\frac{p_{4s}}{p_{2\,\mathrm{tot,rel}}}\right)^{(\kappa+1)/\kappa}\right]}}. \tag{4}$$

An accurate experimental determination of the tangential effective velocity of the cooling air upstream of the receiver hole is difficult or even impossible for small axial distances between stator and rotor. Geis et al. [9] presented a technique to measure the radial and tangential velocity distribution in the midplane between stator and rotor by means of particle image velocimetry (PIV). A remarkable deceleration of the cooling air jet was ascertained for the configuration investigated.

A further decrease of the jet velocity with larger distance from the nozzle exit seems to be obvious. To evaluate the performance of the preswirl chamber, a determination of the effective preswirl velocity at the exit is necessary. Thus the effectiveness of the preswirl chamber and the discharge behavior of the receiver holes can be characterized correctly. To separate the occurring losses, a momentum model, based on the Euler equation, is applied to the preswirl system.

## Momentum Model

The accurate determination of the approach velocity of the receiver holes is the major task necessary to characterize the preswirl system and its components. Depending on the pressure ratio in combination with the rotational speed of the rotor, the preswirled air is either accelerated or decelerated to the circumferential velocity of the receiver holes. Due to the relatively large $1/d$ ratios investigated in this study it can be assumed, that the cooling air leaves the receiver holes in the relative frame of reference axially. Thus the deflection of the cooling air entering the receiver holes and the velocity difference $\Delta c_t$ of the air, being transferred from the stationary to the rotating components, can be calculated by using the measured momentum on the driving shaft. For low rotational speed the preswirl system acts like a turbine and the

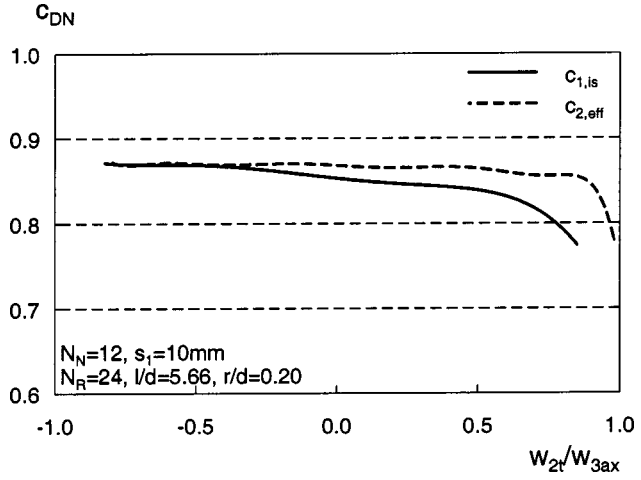


**Fig. 3 Discharge coefficients $c_{DN}$ for the preswirl nozzles**

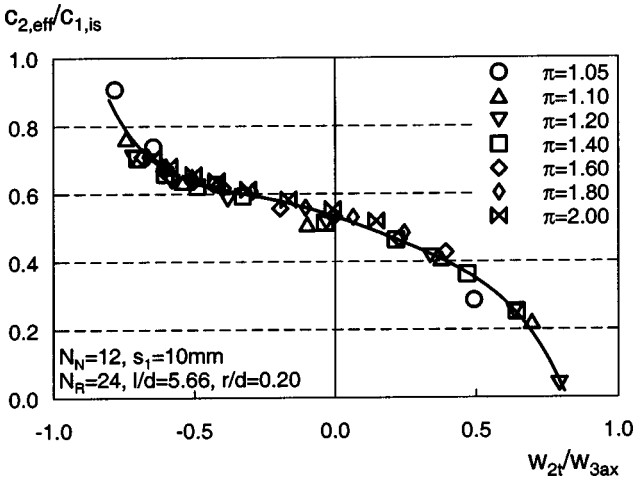


**Fig. 4 Effective velocity ratio of the preswirl system**

rotor has to be decelerated by the electric motor. Whereas a positive momentum is needed, if the fluid has to be brought up to rotor speed. These operating conditions can be compared to a compressor flow,

$$a_u = u_2 c_{2t} - u_3 c_{3t} = u \Delta c_t , \tag{5}$$

$$M = \dot{m} r_m \Delta c_t . \tag{6}$$

A characterization of the discharge behavior of the rotating receiver holes in the relative frame of reference is preferable as several theoretical constraints can be applied. According to Dittmann et al. [5], the discharge coefficients are plotted against the velocity ratio $w_{2t}/w_{3ax}$. As the rotational work is considered, the discharge coefficient of the receiver holes $c_{DR}$ cannot exceed unity. Furthermore, all operating points are limited to the velocity range of $|w_{2t}/w_{3ax}| \leqslant 1$.

Assuming that the time averaged flow direction of the cooling air jet is equal to the inclination angle of the preswirl nozzles, the effective approach velocity upstream of the receiver holes can be determined. The tangential fluid velocity $w_{2t}$ relative to the rotor disk is defined by Eq. (7). The ideal axial velocity of the receiver flow in the relative frame of reference for an isentropic expansion is determined by Eq. (8),

$$w_{2t} = u - c_{2t} , \tag{7}$$

$$w_{3ax} = \sqrt{\frac{2\kappa}{\kappa - 1} R T_{2\ \mathrm{tot,rel}} \left[ 1 - \left( \frac{p_{4s}}{p_{2\ \mathrm{tot,rel}}} \right)^{(\kappa-1)/\kappa} \right]} . \tag{8}$$

Prior to a discussion of the effect of geometric and flow parameters on the performance of the preswirl chamber all three components of the direct-transfer preswirl system should be characterized for one configuration. A setup with 12 preswirl nozzles, $s_1 = 10$-mm axial gap width and 24 receiver holes with radiused inlet was chosen.

Figure 3 shows the discharge coefficients of the preswirl nozzles $c_{DN}$. The discharge coefficients are plotted against the velocity ratio $w_{2t}/w_{3ax}$ as this parameter proves to characterize the operating conditions of the preswirl system quite well. Furthermore, the performance of the preswirl chamber as well as the discharge behavior of the receiver holes strongly depend on this velocity ratio. All data points were fitted by one curve to characterize the discharge behavior depending on the operating conditions. Two different methods to calculate the velocity ratio $w_{2t}/w_{3ax}$ were used. The solid line represents the discharge characteristic of the preswirl nozzles when the flow through the preswirl nozzles and the preswirl chamber is assumed to be isentropic. $c_{DN}$ first remains constant and then gradually decreases with increasing rotor disk speed. If the Euler equation is used to determine the reduced effective velocity of the preswirled air, the absolute values of $c_{DN}$ are not altered but displaced horizontally to higher velocity ratios, according to Eq. (7). The discharge coefficient is nearly constant for all investigated velocity ratios but sharply drops for values exceeding 0.85. For these data points the effective area ratio of preswirl nozzles and receiver holes is lower than unity. Thus the preswirl nozzles do not represent the smallest cross section of the preswirl system any more and an upstream influence of the receiver holes on the flow becomes noticeable.

The performance of the preswirl chamber can be characterized by the deceleration of the velocity of the preswirled air between preswirl nozzle exit and receiver hole inlet. To avoid an iterative procedure to calculate the polytropic exit velocity of the preswirl nozzle flow, the velocity ratio $c_{2,\mathrm{eff}}/c_{1,\mathrm{is}}$ is used to determine the effectiveness of the preswirl chamber. In Fig. 4 the effective velocity ratio is shown for different overall pressure ratios $\pi$ across the preswirl rig. As the circumferential velocity of the receiver holes was limited to $u_R = 161$ m/s, the maximum realized characteristic velocity ratio $w_{2t}/w_{3ax}$ was continuously reduced with increasing pressure ratio. Obviously, the pressure ratio does not influence the performance of the preswirl chamber. Hence a fitting curve can be used to characterize its effectiveness. In principal, an identical progression of the effectiveness was determined by Meierhofer and Franklin [2]. They found the system effectiveness to be a function of the rotor disk to the effective preswirl velocity ratio $u/c_{2,\mathrm{eff}}$. The effectiveness is continuously decreasing with increasing velocity ratio. In accordance to the results of Meierhofer and Franklin [2] the characteristic curve shows an inflection point at $w_{2t}/w_{3ax} \approx 0.0$. At these operating points straight inflow in the relative frame of reference occurs for the receiver holes. Generally, the maximum effectiveness of the system could be expected at this point. Considering the effects of geometry and flow parameters on the performance of the preswirl chamber, this special progression of the curve, which has been somewhat surprising to Meierhofer and Franklin [2], became clear.

Finally, the discharge coefficients of the receiver holes $c_{DR}$ are given in Fig. 5. The solid line represents the discharge behavior if the total properties of the fluid upstream of the receiver hole inlet were calculated without considering losses inside the preswirl nozzle and the preswirl chamber. Thus the approach velocity in the absolute frame of reference is overpredicted and perpendicular inflow into the receiver holes occurs at smaller velocity ratios $w_{2t}/w_{3ax}$ as already discussed by Dittmann et al. [5]. By using the Euler equation, the effective velocity of the preswirled air at the inlet of the receiver holes could be determined. Consequently, the corrected total properties of the fluid in the relative frame of reference differ as the transferred work is considered. The data points are shifted to higher velocity ratios and the absolute value of the

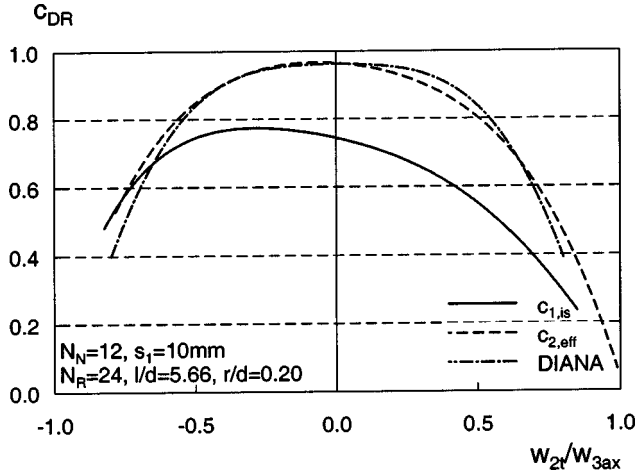


**Fig. 5 Discharge coefficients $c_{DR}$ for receiver hole and a rotating orifice**

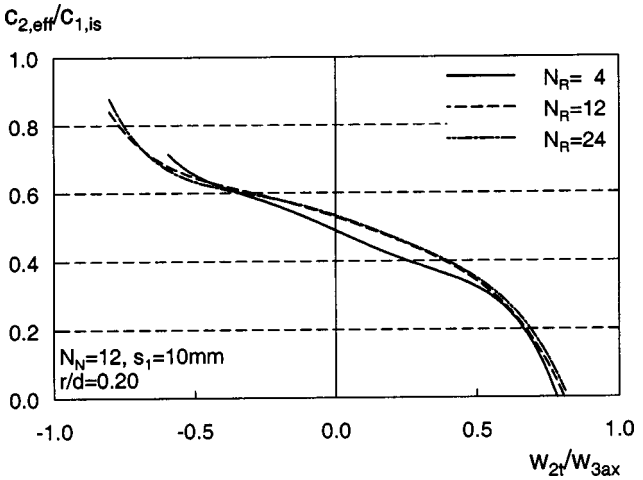


**Fig. 6 Effect of $N_R$, $1/d$ for $N_N=12$, $s_1=10$ mm, $r/d=0.2$**

discharge coefficient is altered. The discharge behavior of a rotating orifice without preswirl, predicted by the correlation DIANA, is given in Fig. 5, additionally. According to the correlation DIANA, which was presented by Wittig et al. [10] and is based on the correlation of McGreehan and Schotsch [11] for stationary orifices, the discharge coefficient of the receiver holes decreases continuously with increasing angle of the approaching flow. The maximum of the discharge coefficient of either the receiver hole with preswirl or the rotating orifice without preswirl is located at a velocity ratio of zero. At these operating conditions straight inflow occurs and the separation region at the inlet is minimized. In general, the discharge behavior of the receiver hole and the rotating orifice does agree very well, if the flow is analyzed in the relative frame of reference.

As the discharge behavior of the preswirl nozzles and the receiver holes is not significantly influenced by the investigated geometry and flow parameters, only the effect on the effective velocity ratio of the preswirl chamber will be discussed in the next section.

## Results

The preswirl system was investigated for several different configurations to determine the effect of each individual parameter. Therefore the number of receiver holes $N_R$, the inlet geometry of the receiver holes, the axial distance $s_1$ between stator and rotor and the flow distribution was varied. For all setups the overall pressure ratio was varied from 1.05 to 2.00 and the rotor disk speed was increased up to 7000 rpm. As the pressure ratio does not affect the effective velocity ratio of the preswirl chamber, a fitting curve can be used to characterize the system. The effect on the performance of the preswirl chamber due to the variation of each parameter is given in the following graphs.

In Fig. 6 the effective velocity ratio of the preswirl chamber is shown depending on the number of receiver holes. As the total cross sectional area of the receiver holes was kept constant, the $1/d$ ratio was changed, while the $r/d$ ratio was identical. The effectiveness of the preswirl chamber is improved slightly, if the number of receiver holes is increased from 4 to 12. A further increase of $N_R$ hardly influences the effectiveness of the system. Surprisingly, the effective velocity for operating conditions with $w_{2t}/w_{3ax}<-0.45$ is higher with the smallest number of receiver holes. This phenomenon can be explained by the definition of the effective velocity ratio as discussed later on.

The effect of the inlet geometry of the receiver holes is shown in Fig. 7. A setup with 11 preswirl nozzles and 4 receiver holes was investigated. Three different inlet geometries were tested. At $w_{2t}/w_{3ax}=0.0$ the $r/d$ ratio does not affect the effective velocity ratio. However, the slope of the characteristic curve is reduced with increasing inlet radius. For velocity ratios greater than zero the effectiveness of the preswirl chamber is higher with radiused receiver holes. This can be easily understood as the discharge characteristic of a rotating hole with radiused inlet is not as sensitive to the angle of the approaching flow as a sharp edged orifice. Thus the smaller separation region at the rounded inlet has a positive influence on the effective velocity ratio for $w_{2t}/w_{3ax}>0.0$. For negative velocity ratios, where the circumferential velocity of the preswirled air is greater than the circumferential velocity of the receiver holes, the tendency of the calculated effective velocity ratio is just inverted.

The effective velocity ratios of the preswirl chamber for different axial gap widths between stator and rotor are shown in Fig. 8. The axial distance $s_1$ was varied between 5 and 24 mm. The number of the preswirl nozzles and the receiver holes was kept constant. At least in the velocity range of $-0.6<w_{2t}/w_{3ax}<0.6$ all three characteristic curves representing the performance of the preswirl chamber are almost parallel. Thereby the effective velocity ratio is reduced with increasing axial distance. The jet of the preswirled cooling air widens and consequently decelerates continuously while penetrating the preswirl chamber. Thus the greatest length of the flow path between nozzle exit and receiver inlet for $s_1=24$ mm results in the lowest effective velocity ratio.

Finally, the influence of a superimposed radially outflow was investigated for two different mass flow ratios. Cooling air was

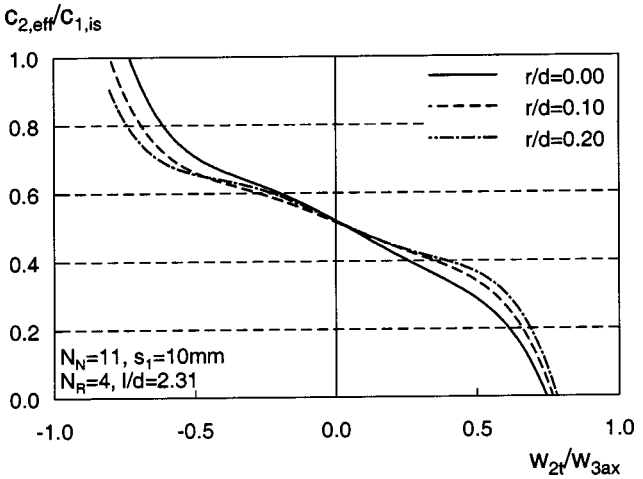


**Fig. 7 Effect of $r/d$ for $N_N=11$, $s_1=10$ mm, $N_R=4$**

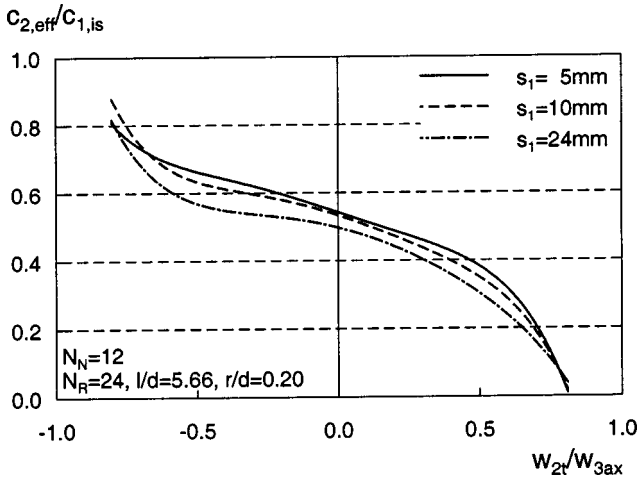


**Fig. 8 Effect of $s_1$ for $N_N=12$, $N_R=24$, $r/d=0.2$**

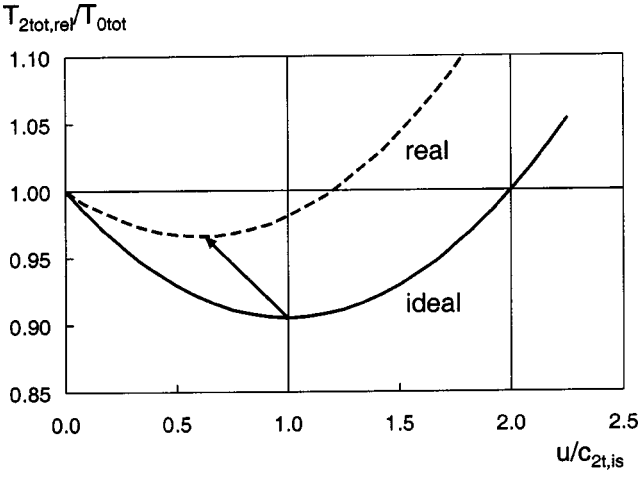


**Fig. 10 Cooling air total temperature in the relative frame of reference**

fed into the rotor-stator wheelspace near the hub region. The radial mass flow rate was set to 30 or 50 percent of the preswirled mainflow. The same percentage of the total mass flow rate left the preswirl chamber through a lip seal arrangement in radial direction, respectively. The effect of the superimposed radial flow on the effective velocity ratio is depicted in Fig. 9. As shown by Dittmann et al. [5] the radial outflow of coolant scarcely influences the discharge behavior of the receiver holes but obviously has a strong impact on the effective preswirl velocity. With increasing radial mass flow rate the effectiveness of the preswirled air is continuously diminished. The circumferential velocity of the fluid, which enters the preswirl chamber radially, can hardly be estimated. Both the rotational speed of the rotating lip of the inner seal and the axial through flow velocity do affect the swirl of the air exiting the inner seal. Nevertheless, the circumferential velocity of the secondary flow is definitely lower than the corresponding velocity component of the preswirled air. Consequently, the effective swirl of the mixed flow inside the preswirl chamber is reduced. The shift of the infection point of the characteristic curves to positive velocity ratios may result from the few data points available for this configuration.

As already mentioned, the progression of the effective velocity ratio was expected to be symmetric to the operation point where straight inflow of the receiver holes in the relative frame of reference occurs. In addition, the performance of the preswirl chamber should be best for these conditions. An explanation for the continuous decrease of the effective velocity ratio can be clarified by the total temperature ratios sketched in Fig. 10. The theoretical curve for an isentropic flow of the preswirl system is given by the solid line. According to Eq. (1), the total temperature of the cooling air in the relative frame of reference is equal to the total temperature in the absolute frame of reference for $u/c_{2t,is}=0.0$ and 2.0. For velocity ratios smaller than 2.0, the total enthalpy of the cooling air is reduced in the relative frame of reference. Due to the work done by the rotor, $T_{2\ tot,rel}$ exceeds $T_{2\ tot}$ for velocity ratios higher than 2.0. The maximum total temperature reduction of the cooling air in the relative system is achieved at $u/c_{2t,is}=1.0$. The dashed line represents the total temperature ratio of the preswirl system considering all occurring losses. The approach velocity of the receiver holes in the absolute frame of reference is lower, thus the maximum total temperature reduction in the relative system is reduced. Furthermore, straight inflow to the receiver holes in the relative frame of reference occurs at $u/c_{2t,is}<1.0$. The displacement of this special operating point regarding the ideal and the real case is indicated by the arrow. The discrepancy between two corresponding data points continuously increases with increasing velocity ratio. Thus a gradual decrease of the effective velocity ratio, characterizing the performance of the preswirl chamber, seems to be reasonable. The actual total temperature reduction depends on the pressure ratio across the preswirl nozzles and the velocity ratio.

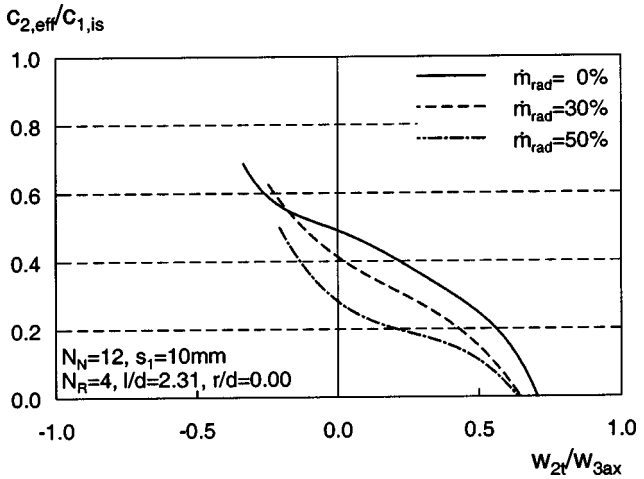


**Fig. 9 Effect of $\dot{m}_{rad}$ for $N_N=12$, $s_1=10$ mm, $N_R=4$, $r/d=0.0$**

Another possibility to characterize the performance of the preswirl chamber would be to determine the actual total temperature difference between absolute and relative system based on the maximum temperature reduction, which can be achieved for an isentropic flow. For positive velocity ratios $w_{2t}/w_{3ax}$ this newly gained characteristic line will correspond to the curves presented in Figs. 6–9. Congruence for negative velocity ratios will be achieved if the left part of the curve is mirrored across a horizontal line through the ordinate interception at $w_{2t}/w_{3ax}=0.0$. Therewith all investigated effects of geometric and flow parameters on the effective velocity ratio characterizing the preswirl chamber become comprehensible.

## Summary

A direct-transfer preswirl system was investigated experimentally. By separating the occurring losses of the flow, all three components, namely the preswirl nozzles, the preswirl chamber, and the receiver holes, could be characterized.

Discharge coefficients of the preswirl nozzles $c_{DN}$ were determined in the absolute frame of reference, whereas the discharge coefficients of the receiver holes $c_{DR}$ were defined in the relative frame of reference. Thus the work done by the rotor and the

change of the total enthalpy of the cooling air could be taken into account. The Euler equation was applied to the preswirl system to estimate the velocity of the preswirled cooling air at the inlet of the receiver holes. If the deceleration of the fluid is considered, the discharge behavior of the receiver holes can be compared to the discharge characteristic of rotating orifices with parallel approaching flow to the orifice axis. The discharge behavior of the receiver holes is strongly dependant on the velocity ratio $w_{2t}/w_{3ax}$, which indicates the flow angle relative to the receiver hole axis.

Finally, the performance of the preswirl chamber was characterized by the effective velocity ratio of the preswirled flow. Several geometric parameters of the preswirl system were varied to investigate the effect on the systems effectiveness. Additionally a radial outflow was superimposed to the preswirled mainflow. In general, the effective velocity ratio does not depend on the overall pressure ratio across the preswirl system but is strongly influenced by the operating point defined by the velocity ratio $w_{2t}/w_{3ax}$. Additionally, the performance of the preswirl system can be defined by the total temperature ratio $T_{2\,\mathrm{tot,rel}}/T_{0\,\mathrm{tot}}$. The highest performance is achieved at operating conditions where straight inflow of the receiver holes in the relative frame of reference occurs.

Based on the investigated parameters the following tendencies were obtained. The effect of the number of receiver holes seems to be secondary, as long as $N_R$ is equal or higher than the number of preswirl nozzles. In principal, the systems performance increases with increasing number of receiver holes. Radiusing the inlet of the rotating receiver holes minimizes the separation region of the flow at the inlet, especially for operating conditions where the approaching flow in the relative frame of reference is inclined to the orifice axis. Therefore the sensitivity of the preswirl chamber effectiveness regarding the velocity ratio $w_{2t}/w_{3ax}$ is reduced with increasing $r/d$. A reduction of the axial gap width between stator and rotor improves the systems efficiency. However, it should be mentioned that unstable flow phenomena were ascertained by Dittmann et al. [5], predominantly occurring for $s_1=5$ mm, which deteriorated the discharge behavior and the effectiveness of the preswirl system. The occurrence of this acoustic phenomenon is not understood yet. Superimposing a radial outflow significantly reduces the effective velocity of the preswirled air. As the circumferential velocity of the fluid exiting the inner seal is remarkably lower than that of the preswirled mainflow, the systems performance is diminished continuously with increasing radial mass flow rate.

## Acknowledgments

The authors wish to thank the ''Forschungsvereinigung Verbrennungskraftmaschinen e.V.'' for supporting the work described in this paper. The work was also partly funded by the EU.

## Nomenclature

$A$ = cross-sectional area $m^2$
$c$ = velocity in the absolute frame of reference m/s
$c_D$ = discharge coefficient
$c_p$ = specific heat J/(kg K)
$d$ = diameter of receiver holes m
$l$ = length of receiver holes m
$\dot{m}$ = mass flow rate kg/s
$M$ = momentum on the rotor Nm
$n$ = rotational speed 1/min
$N$ = number of holes
$p$ = pressure $N/m^2$
$r$ = radius m
$r_m$ = pitch radius of the receiver holes m
$R$ = specific gas constant J/(kg K)
$\mathrm{Re}_\phi$ = rotational Reynolds number, $\mathrm{Re}_\phi=\omega r_m^2/\nu$
$s_1$ = axial gap between stator and rotor m
$T$ = temperature K
$u$ = circumferential velocity m/s
$w$ = velocity in the relative frame of reference m/s
$\alpha$ = inclination of preswirl nozzles deg
$\kappa$ = isentropic exponent
$\nu$ = kinematic viscosity $m^2/s$
$\pi$ = total pressure ratio, $\pi=p_{0\,\mathrm{tot}}/p_{4s}$
$\omega$ = angular velocity of rotor 1/s

### Subscripts

ax = axial
eff = effective
is = isentropic
$N$ = preswirl nozzle
$R$ = receiver hole
rad = radial
rel = relative system
$s$ = static
$t$ = tangential
tot = total
0–4 = position 0–4

## References

[1] Scricca, J. A., and Moore, K. D., 1997, ''Effects of 'Cooled' Cooling Air on Pre-Swirl Nozzle Design,'' Tech. Rep. NASA/CP-98-208527, Pratt & Whitney.
[2] Meierhofer, B., and Franklin, C. J., 1981, ''An Investigation of a Preswirled Cooling Airflow to a Turbine Disc by Measuring the Air Temperature in the Rotating Channels,'' ASME Paper 81-GT-132.
[3] El-Oun, Z. B., and Owen, J. M., 1988, ''Pre-Swirl Blade-Cooling Effectiveness in an Adiabatic Rotor-Stator System,'' ASME J. Turbomach., **111**, pp. 522–529.
[4] Wilson, M., Pilbrow, R., and Owen, J. M., 1997, ''Flow and Heat Transfer in a Pre-Swirl Rotor-Stator System,'' ASME J. Turbomach., **119**, pp. 364–373.
[5] Dittmann, M., Geis, T., Schramm, V., Kim, S., and Wittig, S., 2002, ''Discharge Coefficients of a Preswirl System in Secondary Air Systems,'' ASME J. Turbomach., **124**, pp. 119–124.
[6] Kline, S., and McClintock, F. A., 1953, ''Describing Uncertainties in Single-Sample Experiments,'' Mech. Eng. (Am. Soc. Mech. Eng.), **75**, pp. 3–8.
[7] Zimmermann, H., Kutz, J., and Fischer, R., 1998, ''Air System Correlations Part 2: Rotating Holes and Two Phase Flow,'' ASME Paper 98-GT-207.
[8] Popp, O., Zimmermann, H., and Kutz, J., 1998, ''CFD-Analysis of Coverplate Receiver Flow,'' ASME J. Turbomach., **120**, pp. 43–49.
[9] Geis, T., Rottenkolber, G., Dittmann, M., Richter, B., Dullenkopf, K., and Wittig, S., 2002, ''Endoscopic PIV-Measurements in an Enclosed Rotor-Stator System With Pre-Swirled Cooling Air,'' *11th International Symposium on Applications of Laser Techniques to Fluid Mechanics*, Lisbon, Portugal.
[10] Wittig, S., Kim, S., Scherer, T., Jakoby, R., and Weißert, I., 1995, ''Durchfluß an rotierenden Wellen- und Scheibenbohrungen und Wärmeübergang an rotierenden Wellen,'' Forschungsvereinigung Verbrennungskraftmaschinen (FVV), Abschlußbericht, Vorhaben Nr. 465 und 536, Heft 574.
[11] McGreehan, W. F., and Schotsch, M. J., 1988, ''Flow Characteristics of Long Orifices With Rotation and Corner Radiusing,'' ASME J. Turbomach., **110**, pp. 213–217.

# Parametric Study on Economic Feasibility of Microturbine Cogeneration Systems by an Optimization Approach

**Satoshi Gamou**[1]
**Ryohei Yokoyama**
**Koichi Ito**

Department of Energy Systems Engineering,
Osaka Prefecture University,
1-1 Gakuen-cho,
Sakai, Osaka 599-8531, Japan

*Economic feasibility of microturbine cogeneration systems is investigated by analyzing relationships between the optimal number of microturbine units and the maximum energy demands under various conditions. For this purpose, a method to obtain the maximum energy demand at which the optimal number changes is proposed by combining a nonlinear equation problem and an optimal unit sizing problem hierarchically. Based on the proposed method, a map expressing the aforementioned relationships can be illustrated. Through numerical studies carried out on systems installed in hotels by changing the electrical generating efficiency and the capital unit cost of the microturbine cogeneration unit as parameters, the influence of the parameters on the economic feasibility of the microturbine cogeneration system is clarified.* [DOI: 10.1115/1.1806836]

## Introduction

Microturbine generator units with capacities under 100 kW have been recently paid attention to as distributed power sources [1]. The reason for this attention lies in the expectation that the microturbine generator units will have the advantages of low initial capital cost, high electrical generating efficiency for their small capacities, high reliability, low $NO_x$ emission, and so on. Moreover, microturbine generators can avoid operating at lower part load for a broad range of electricity demand by installing plural numbers of microturbine generators. Besides, they are expected as main equipment of cogeneration systems for commercial and public purposes [2]. Although their total energy efficiency becomes high, they have some disadvantages in this case. For example, their initial capital cost becomes expensive because of additional heat recovery devices, and utilization of exhaust heat from the microturbine generator unit with a recuperator is not efficient because of its lower temperature than large scale gas turbine generators. Therefore, it is important to investigate feasibility of microturbine cogeneration systems for commercial and public purposes from an economic viewpoint. Moreover, it is also important to investigate effects of installing plural numbers of microturbine cogeneration units on their economic feasibility.

The purpose of this paper is to evaluate the aforementioned economic feasibility rationally for various parameters, such as a capital unit cost and an electrical generating efficiency of the microturbine cogeneration unit. For this purpose, a method to obtain the maximum energy demand at which the optimal number changes is proposed by combining a nonlinear equation problem and an optimal unit sizing problem hierarchically. Based on this method, the aforementioned feasibility is evaluated by examining the relationships between the optimal number and the maximum energy demands. In the following, the configurations of microturbine cogeneration systems investigated here are first described. Second, the evaluation method is described. Finally, numerical parametric studies are carried out on systems installed in hotels.

[1]To whom correspondence should be addressed.

Contributed by the International Gas Turbine Institute (IGTI) of THE AMERICAN SOCIETY OF MECHANICAL ENGINEERS for publication in the ASME JOURNAL OF ENGINEERING FOR GAS TURBINES AND POWER. Paper presented at the International Gas Turbine and Aeroengine Congress and Exhibition, Atlanta, GA, June 16–19, 2003, Paper No. 2003-GT-38382. Manuscript received by IGTI, October 2002, final revision, March 2003. Associate Editor: H. R. Simmons.

## System Configurations

Figure 1 shows a schematic diagram of a microturbine cogeneration system. The system has the microturbine cogeneration unit (MTU), a single-stage absorption refrigerator (RW), a gas-fired absorption refrigerator (RG), a gas-fired boiler (BG), a radiator (RD), and a device for purchasing and reversing electricity (EP). In this figure, though only one unit is illustrated for each kind of equipment, there may be several units. Solid, dot-dash, dotted, and broken lines show flows of hot water, electricity, cold water, and natural gas, respectively.

In the system, electricity is supplied to users by purchasing electricity through the EP from an outside electric power company and by operating the MTU. Electricity is also used to drive cooling towers and other auxiliary machinery. Moreover, electricity can be reversed through the EP to the electric power company. Exhaust heat generated from the MTU is recovered in the form of hot water, and it is reused for space cooling through the RW, space heating, and other usage in a cascade way. Surplus exhaust heat is disposed of by the RD. Cold water for space cooling is supplied by the RW and the RG, and hot water for space heating and other usage is supplied by the recovered exhaust heat, the RG, and the BG.

## Evaluation Method

To evaluate the feasibility of the microturbine cogeneration systems from an economic viewpoint, we clarify the relationship between the number of the microturbine cogeneration units (MTUs) and the maximum energy demands. In order to achieve this purpose, we consider the problem of finding the maximum energy demand at which the optimal number changes its value. Its maximum energy demand is the one at which the minimum annual total cost, which is the sum of the annual capital cost and the annual operational cost, for the system with $n$ MTUs is equal to that for the system with $n+1$ MTUs. Figure 2 shows the concept for the problem of finding the aforementioned maximum energy demand when the kind of the number of energy demands is one. When the kind of the number of energy demands is two, the minimum annual total cost in Fig. 2 is not a curved line but a curved surface. Then, the maximum energy demand is found as a border curve at which two curved surfaces intersect. Similarly, when the kind of the number of energy demands is three or more, the maximum energy demand is found as a border surface or a border hypersurface. By finding the aforementioned maximum en-

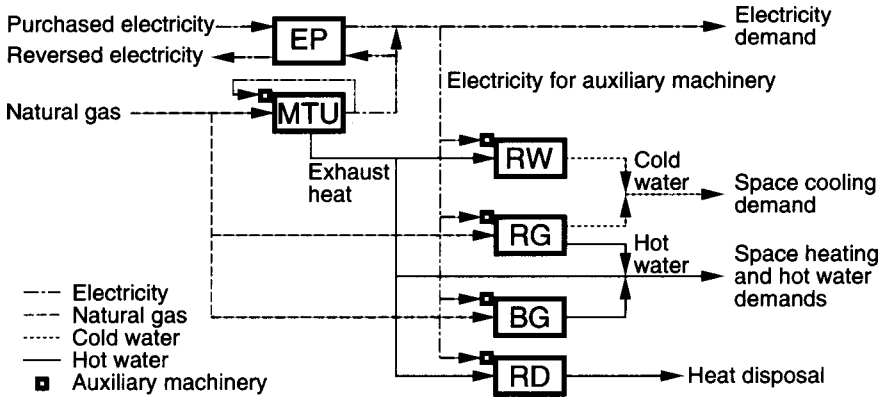


**Fig. 1 Schematic diagram of a microturbine cogeneration system**

ergy demand, we can obtain the map expressing the relationships between the optimal numbers and the maximum energy demands as an example shown in Fig. 3. In this paper, the feasibility of the MTU is evaluated using the map. A brief description on the aforementioned mathematical problem and procedure to obtain the map follows.

**Structure of Problem.** The aforementioned problem is resulted in the following nonlinear equation problem:

$$f_n(\boldsymbol{s}) - f_{n+1}(\boldsymbol{s}) = 0, \tag{1}$$

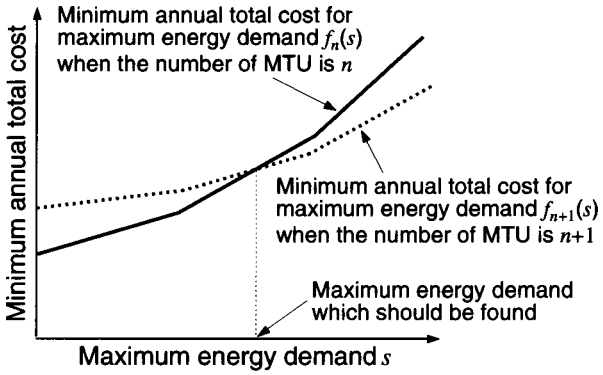


**Fig. 2 Concept for problem of finding maximum energy demand at which optimal number of MTU changes**

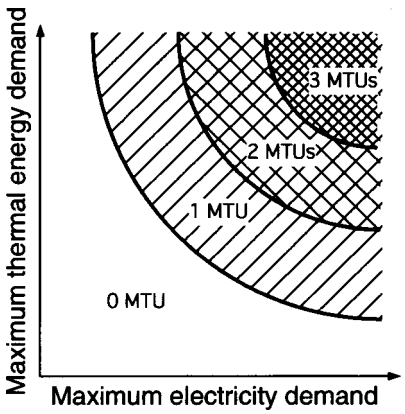


**Fig. 3 Example of map expressing the relationship between the optimal numbers and the maximum energy demands**

where $\boldsymbol{s}$ is a vector composed of the maximum energy demands, and $f_n$ is the minimum annual total cost when the number of the MTU is $n$, and is a function of the maximum energy demands $\boldsymbol{s}$. At this point, $f_n$ is obtained as the minimum value of the objective function for the following optimal unit sizing problem: equipment capacities and maximum contract demands of utilities are determined together with the systems' operational strategies so as to minimize the annual total cost subject to satisfaction of energy demand requirements for given maximum energy demands $\boldsymbol{s}$ and given number of the MTU $n$. In this optimal unit sizing problem, the capacity of the MTU is assumed to be given so as to make it easy to understand the maps expressing optimal numbers.

Therefore, the aforementioned problem becomes the nonlinear equation one which has the inner optimization problem. In the following, the outline of the optimization problem will be explained simply.

**Mathematical Formulation of Optimization Problem.** In formulating the optimization problem, it is defined that the annual operational hours in a year are discretized by employing several representative days and by dividing each day into several daily sampling times. For each sampling time, average energy demands are estimated. In addition, peak energy demands are estimated for winter and summer peak demand days.

In the following mathematical formulation of the problem, the subscript $t$ denotes the index for the sampling time, the symbol $T$ denotes the set of all the values of $t$ for a year, and the symbol $d_t$ denotes the annual operational hours for the sampling time $t$. Moreover, the subscripts $n$ and $\boldsymbol{s}$ denote the number of the MTU and the maximum energy demands, respectively.

*Decision Variables.* Decision variables are composed of design variables and operational variables. The design variables are equipment capacities except for the MTU and the utility maximum contract demands expressed by a vector $\boldsymbol{x}$. The vector $\boldsymbol{x}$ denotes continuous variables. On the other hand, the operational variables express the operational strategy at each sampling time $t$ expressed by vectors $\boldsymbol{y}_t$ and $\boldsymbol{z}_t$. The vector $\boldsymbol{y}_t$ denotes continuous variables which express energy flow rates, and the vector $\boldsymbol{z}_t$ denotes binary and integer variables which express the on/off status of operation of the equipment and the number of active MTUs for the discrete sampling time, respectively.

*Objective Function.* The annual total cost is adopted as the objective function to be minimized from the viewpoint of long-term economics. It is evaluated as the sum of the annual capital and operational costs based on the annualized costs method [3]. The annual capital costs of pieces of equipment are considered here as functions of their capacities. The annual operational costs of utilities are the sum of customer, demand, and energy charges. The customer and demand charges are considered as functions of

the maximum contract demands of utilities. The energy charge is calculated from the system's operational strategy. As a result, the objective function to be minimized $J_{n,s}$ i.e., the annual total cost, is defined by

$$J_{n,s}=F_{n,s}(\boldsymbol{x}_{n,s})+G_{n,s}(\boldsymbol{x}_{n,s})+\sum_{t\in T} V_{n,s,t}(\boldsymbol{x}_{n,s},\boldsymbol{y}_{n,s,t},\boldsymbol{z}_{n,s,t})d_t, \tag{2}$$

where $F$ is the annual capital cost, $G$ is the annual customer/demand charges, and they are functions of $\boldsymbol{x}$; and $V$ is the hourly energy charge, and it is a function of $\boldsymbol{x}$, $\boldsymbol{y}_t$ and $\boldsymbol{z}_t$. At this point, the value of $f_n(\boldsymbol{s})$ shown in Eq. (1) is the minimum value of $J_{n,s}$.

*Constraints.* As constraints of the optimization problem, it is necessary to consider performance characteristics of pieces of equipment together with hourly energy balance and supply-demand relationships of each energy flow.

The performance characteristics are formulated as relationships between input and output energy flow rates by adopting the piecewise linear approximation [4]. For example, a part of these relationships for the MTUs is expressed for each sampling time by the following equations:

$$\begin{gathered} v_{\mathrm{MTU}}=p_{\mathrm{MTU}}u_{\mathrm{MTU}}+q_{\mathrm{MTU}}\lambda, \\ \underline{u}_{\mathrm{MTU}}\lambda\leqslant u_{\mathrm{MTU}}\leqslant\overline{u}_{\mathrm{MTU}}\lambda, \\ \lambda\leqslant n, \end{gathered} \tag{3}$$

where $p$ and $q$ denote performance characteristic values, and $\underline{u}$ and $\overline{u}$ denote lower and upper limits of input energy flow rate for one unit, respectively; $\lambda$ denotes an integer variable expressing the number of the active MTUs in a single sampling time, which is an element of the vector $\boldsymbol{z}_t$, and $u$ and $v$ are input and output energy flow rates for several units, respectively, which are elements of the vector $\boldsymbol{y}_t$. The relationships between input and output energy flow rates for one unit of other pieces of equipment are, for example, expressed by the following equations:

$$\begin{gathered} v=p(x)u+q(x)\delta, \\ \underline{u}(x)\delta\leqslant u\leqslant\overline{u}(x)\delta, \\ \delta\in\{0,1\}, \end{gathered} \tag{4}$$

where $\delta$ denotes a binary variable expressing the on/off status of operation of equipment, which is an element of the vector $\boldsymbol{z}_t$. In Eq. (4), $p$, $q$, $\underline{u}$, and $\overline{u}$ are expressed as functions of equipment capacity $x$ which is an element of the design variables $\boldsymbol{x}$, because the performance characteristics of equipment depend on the equipment capacity. At this point, let us suppose that $\underline{p}(x)=p'$, $q(x)=q'x+q''$, $\underline{u}(x)=\underline{u}'x+\underline{u}''$, and $\overline{u}(x)=\overline{u}'x+\overline{u}''$. Then, $p(x)u=p'u$, and, consequently, $p(x)\underline{u}$ becomes a linear term. On the other hand, $q(x)\delta$, $\underline{u}(x)\delta$, and $\overline{u}(x)\delta$ include the nonlinear term, i.e., $x\delta$. Let $x\delta$ be replaced with $\xi$, and this nonlinear term can be linearized strictly by the following linear equations:

$$\begin{gathered} \underline{x}\delta\leqslant\xi\leqslant\overline{x}\delta, \\ x+\overline{x}(\delta-1)\leqslant\xi\leqslant x, \end{gathered} \tag{5}$$

where $\underline{x}$ and $\overline{x}$ denote lower and upper limits of $x$. In Eq. (5), when $\delta=0$, it is derived from the upper two inequalities that $\xi=0$, and $\xi$ becomes equal to $x\delta$. Then, the lower two inequalities of Eq. (5) are inactive constraints. On the other hand, when $\delta=1$, it is derived from the lower two inequalities that $\xi=x$, and $\xi$ becomes equal to $x\delta$ as well. Then, the upper two inequalities are inactive constraints. As a result, Eq. (4) is rewritten by

$$\begin{gathered} v=p'u+q'\xi+q''\delta, \\ \underline{u}'\xi+\underline{u}''\delta\leqslant u\leqslant\overline{u}'\xi+\overline{u}''\delta, \\ \underline{x}\delta\leqslant\xi\leqslant\overline{x}\delta, \\ x+\overline{x}(\delta-1)\leqslant\xi\leqslant x, \\ \delta\in\{0,1\}. \end{gathered} \tag{6}$$

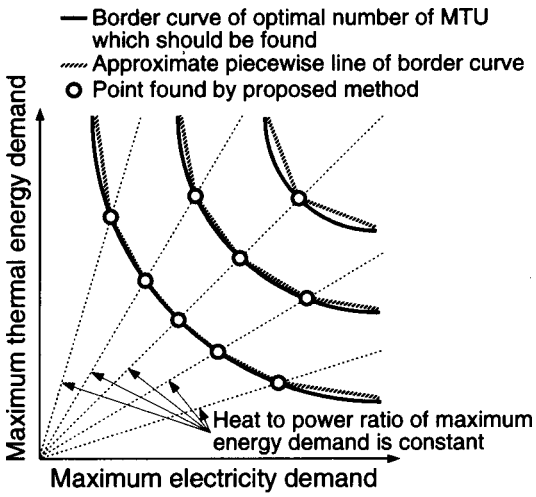


**Fig. 4 Concept for solution method**

On the other hand, energy balance and supply–demand relationships are formulated by linear equations with energy flow rates $\mathbf{y}_t$ at each junction for each energy flow illustrated in Fig. 1.

All these constraints are expressed simply for each sampling time $t$ by

$$\boldsymbol{C}_{n,s,t}(\boldsymbol{x}_{n,s},\boldsymbol{y}_{n,s,t},\boldsymbol{z}_{n,s,t})=\mathbf{0} \quad (t\in T), \tag{7}$$

where $\boldsymbol{C}$ is the vector composed of constraint functions.

**Solution Method.** The problem formulated and described in the previous section is complex and of nonlinear nature because it has the inner optimization problem. As mentioned previously, this problem is also one of finding the maximum energy demands as border curves, surfaces, or hypersurfaces for the several kinds of the number of energy demands. Since it is very difficult to directly find the border curves and so on numerically, in this paper we find the curves approximately by connecting points found as shown in Fig. 4. Though Fig. 4 is an example for two kinds of the number of energy demands, similarly we find border surfaces or hypersurfaces approximately by finding more points for several kinds of the number of energy demands.

The aforementioned points are found in the following way. When the kind of the number of energy demands is one and the number of the MTU $n$ is given, Eq. (1) is one of finding one maximum energy demand. Therefore, first heat-to-power ratio of the maximum energy demands is assumed to be constant, and under the assumption we find the points where the optimal number of the MTU changes as shown in Fig. 4. Next, we find more points by changing the ratio and the number, and finally we obtain the border curves, surfaces, or hypersurfaces by connecting the obtained points.

Equation (1) of finding one maximum energy demand is solved by Brent's algorithm [5], which is one combining a bisection method with a secant one using not differential values but only the value of the function $f$. The value of function $f$ is obtained by the optimization problem formulated in the previous section. The problem results in a mixed-integer linear programming one, and it is solved by the GAMS (General Algebraic Modeling System)/CPLEX solver [6], which is a commercial one combining the branch and bound method with the simplex method.

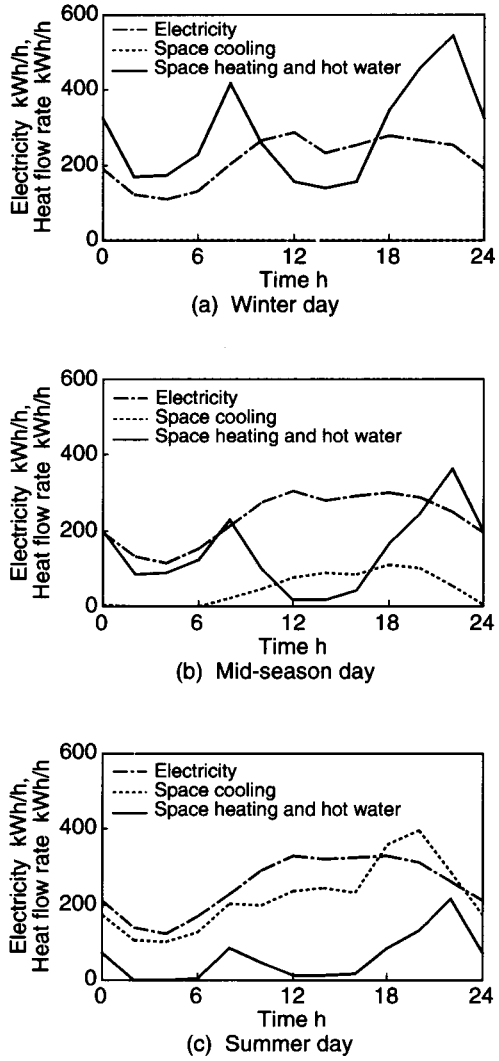


**Fig. 5 Hourly energy demands (hotel with maximum electricity demand of 400 kWh/h)**

## Numerical Study

**Input Data.** Cogeneration systems typically utilized in hotels are investigated in these numerical studies. Energy demands are estimated at each of 12 discrete daily sampling times on 5 representative days in a year, i.e., winter, mid-season, summer, winter peak demand, and summer peak demand days. As an example,

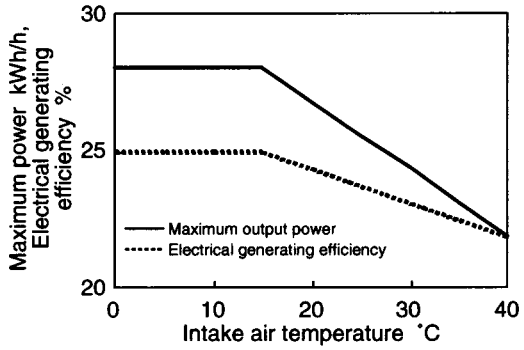


**Fig. 6 Relationship between intake air temperature and maximum output power or electrical generating efficiency at rated load**

Fig. 5 shows the hourly energy demands on winter, mid-season, and summer days in the hotel with the maximum electricity demand of 400 kWh/h. The ratio of maximum demands of electricity : space cooling : space heating and hot water is 1:1.2:1.6. In this numerical study, it is assumed that the ratio of the maximum space cooling demand to the maximum space heating and hot water ones is fixed, whereas the ratio of the maximum electricity demand to the maximum thermal energy one is changed. By this assumption, the independent kind of the number of energy demands becomes two, and consequently it is easy to understand results as two-dimensional illustrations as shown in Figs. 3 and 4. At this point, according to the change in the ratio of the maximum electricity demand to the maximum thermal energy one, the demand pattern shown in Fig. 5 changes linearly.

Representative values of performance characteristics and capital unit costs of equipment are summarized in Table 1. These data are based on practical systems currently used in Japan. In Table 1, the electrical generating efficiency, exhaust heat recovery efficiency, and capital unit cost of the microturbine cogeneration unit (MTU) are shown as parameters $\eta_e$, $\eta_h$, and $\alpha$, respectively. The MTU investigated here is based on a unit of Capstone and its capacity is 28 kW. The maximum output power and the electrical generating efficiency at the rated load of this unit are dependent greatly on intake air temperature. Figure 6 shows the relationships between the intake air temperature and the maximum output power or the electrical generating efficiency at the rated load of this unit when $\eta_e = 0.25$ at 15°C. These data are based on measurement data and catalogs of Capstone unit. An ambient air temperature is adopted as the intake air temperature in these studies, and the hourly ambient air temperature on each representative day is shown in Fig. 7. The rates for purchased/reversed electricity and

**Table 1 Performance characteristics values and capital unit costs of equipment**

| Equipment | Performance characteristic value (rated load) | | Capital unit cost |
|---|---|---|---|
| Micro gas turbine cogeneration unit 1 | Electrical generating efficiency<br>Exhaust heat recovery efficiency | 0.288*1,*2<br>0.351*1,*2 | $150.0\times10^3$ yen/kW |
| Micro gas turbine cogeneration unit 2 | Electrical generating efficiency<br>Exhaust heat recovery efficiency | 0.247*1,*2<br>0.498*1,*2 | $150.0\times10^3$ yen/kW |
| Electric compression refrigerator | Coefficient of performance | 4.2 | $32.7\times10^3$ yen/kW |
| Gas-fired absorption refrigerator | Coefficient of performance<br>Thermal efficiency | 1.12*1 (space cooling)<br>0.93*1 (space heating) | $38.7\times10^3$ yen/kW |
| Single-stage absorption refrigerator | Coefficient of performance | 0.69 | $43.7\times10^3$ yen/kW |
| Gas-fired boiler | Thermal efficiency | 0.91*1 | $12.9\times10^3$ yen/kW |
| Radiator | Electricity consumption rate | 0.0096 | $12.8\times10^3$ yen/kW |
| Receiving device for purchased electricity | – | | $56.0\times10^3$ yen/kW |

*1 The net thermal efficiency is calculated under the assumption that the lower heating value of natural gas is 11.55 kWh/m$^3$
*2 When intake air temperature is 15 ˚C

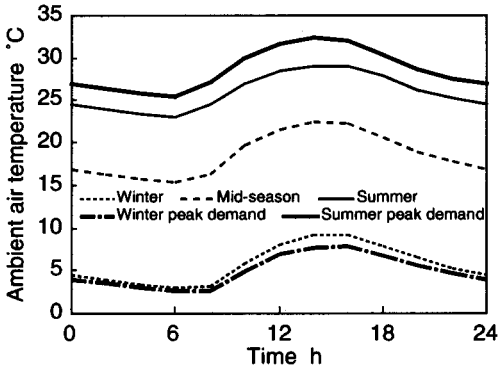


**Fig. 7 Ambient air temperature**

natural gas adopted in these studies are given in Table 2. These rates are used in order to calculate the hourly energy charge $V_t$ and the annual customer/demand charges $G$, including in Eq. (2). The rate for natural gas is a certain incentive one for the MTU in Japan.

In evaluating the annual capital cost, it is assumed that the interest rate, the ratio of salvage value, and the life of equipment are 0.03, 0.1, and 15 y, respectively. Moreover, the maintenance cost of the MTU is set to 2 yen/kWh.

**Studied Cases.** Concerning the parameters such as the electrical generating efficiency $\eta_e$, the exhaust heat recovery efficiency $\eta_h$, and the capital unit cost $\alpha$ of the microturbine cogeneration unit (MTU), the following four case studies are carried out to investigate the economic feasibility of the microturbine cogeneration systems.

Case 1: $\eta_e=0.25$, $\eta_h=0.50$, and $\alpha=250.0\times10^3$ yen/kW
Case 2: $\eta_e=0.35$, $\eta_h=0.40$, and $\alpha=250.0\times10^3$ yen/kW
Case 3: $\eta_e=0.25$, $\eta_h=0.50$, and $\alpha=150.0\times10^3$ yen/kW
Case 4: $\eta_e=0.35$, $\eta_h=0.40$, and $\alpha=150.0\times10^3$ yen/kW

The values of $\eta_e$, and $\eta_h$ in cases 2 and 4 are ones for the future improvement of the MTU's performance characteristics, and the values of $\alpha$ in cases 3 and 4 are ones for the future initial cost reduction of the MTU.

For all the above case studies, the relationship between the optimal number of the MTU and the maximum energy demands are surveyed using the method mentioned in the previous chapter.

**Results and Discussion.** First, Figs. 8–11 show maps expressing the relationship between the optimal numbers and the maximum energy demands for cases 1–4, respectively, which are obtained by calculating border curves for the optimal number of the microturbine cogeneration unit (MTU) using the proposed method. In these figures, the horizontal axis denotes the maximum electricity demand, and the vertical axis denotes the maximum thermal energy demands. Moreover, the range in which the optimal number of the MTU does not change is hatched, and the values in parentheses denote the total capacity of the MTU. According to Fig. 8, the border curves B to D on which the optimal numbers of the MTU change are drawn like the letter L. This

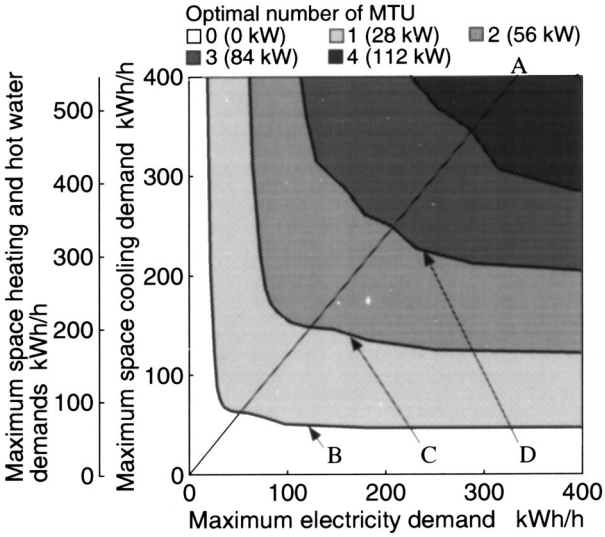


**Fig. 8 Map expressing relationship between optimal numbers and maximum energy demands (case 1)**

result shows that the optimal number of the MTU depends only the maximum electricity demand in the range where the maximum thermal energy demands are large, and that it does only the maximum thermal energy demands in the range where the maximum electricity demand are large. Moreover, the MTU is not installed unless the maximum electricity and thermal energy demands are larger than about 30 and 50 kWh/h, respectively. Besides, it is found from Fig. 8 that the maximum optimal number of the MTU is 4 (total capacity is 112 kW) in the range where both the maximum electricity and the maximum space cooling demands are less than 400 kWh/h. According to Fig. 9 for case 2 where the electrical generating efficiency of the MTU $\eta_e$ are higher than case 1, the border curves for the optimal number of the MTU are drawn like the letter L as well as Fig. 8. However, the maximum optimal number of the MTU is larger than that in Fig. 8, and it is 10 (total capacity is 280 kW) in Fig. 9. This result shows that the installation of the MTU is greatly promoted by the improvement of $\eta_e$. Besides, the MTU can be installed even if the maximum thermal energy demands are 0 kWh/h, when the maximum electricity demand is larger than about 100 kWh/h. It is also found from Fig. 10 that in case 3 where the capital unit cost of the MTU $\alpha$ is lower than case 1 the MTU can be installed even if the maximum thermal energy demands are 0 kWh/h. However, the number of the MTU for case 3 is fewer than that for case 2. This result shows that the effect of the improvement by 10% of $\eta_e$ on the promotion of the installation of the MTU is larger than that of the reduction by $100\times10^3$ yen/kW of $\alpha$. According to Fig. 11 for case 4 where $\eta_e$ is higher than case 1 and $\alpha$ is lower than case 1, the optimal number of the MTU depends almost only on the maximum electricity demand, and it is found that the installation feasibility of the MTU is very high.

**Table 2 Rates for purchase/reversed electricity and natural gas**

| Utility | Unit cost | | |
|---|---|---|---|
| | Customer charge | Demand charge | Energy charge |
| Purchased electricity | — | 1 620 yen/(kW·month) | 14.15(summer) yen/kWh<br>12.86(other seasons) yen/kWh |
| Reversed electricity | | | 8.30(10:00~17:00 in summer) yen/kWh<br>6.20(8:00~22:00 except above hours) yen/kWh<br>3.40(22:00~8:00) yen/kWh |
| Natural gas | 24 800 yen/month | 850 yen/(Nm$^3$/h·month) | 43.13 yen/Nm$^3$ |

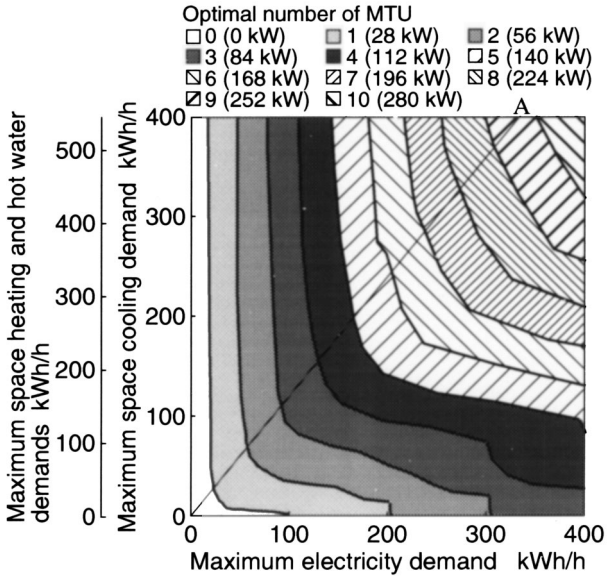


**Fig. 9 Map expressing relationship between optimal numbers and maximum energy demands (case 2)**

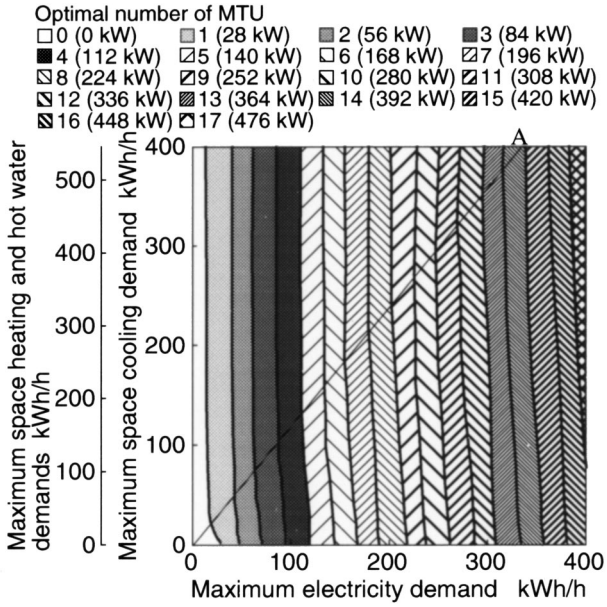


**Fig. 11 Map expressing relationship between optimal numbers and maximum energy demands (case 4)**

Next, the relationships between the annual total cost and the maximum electricity demand for various numbers of the MTU on the lines connecting the origin and point A shown in Figs. 8–11 are shown in Figs. 12–15 for cases 1–4, respectively. The line connecting the origin and point A corresponds the one on which the ratio of the maximum electricity demand to the maximum thermal energy one shown in Fig. 5 is constant. According to these figures, it is found that the annual total cost for the optimal number of the MTU increase in almost proportional to the maximum electricity demand. On the other hand, the annual total cost for the fixed number of the MTU increases greatly with the maximum electricity demand. Moreover, the difference between the annual total costs for the optimal number of the MTU and 0 MTU increases with the maximum electricity demand. Figure 16 shows the reduction rate of the annual total cost for the optimal number

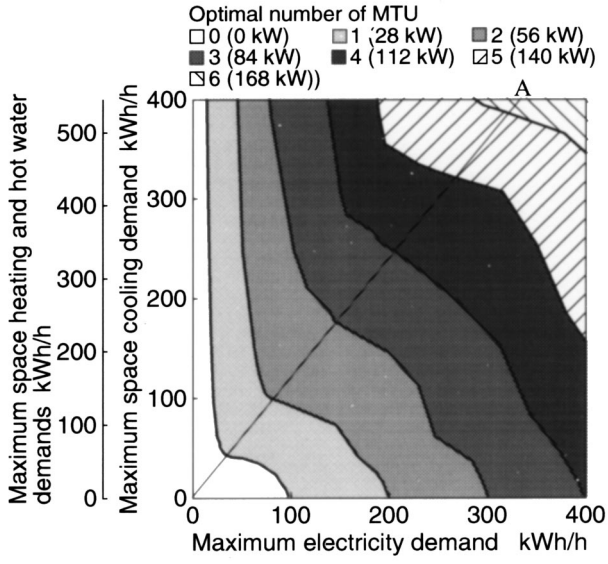


**Fig. 10 Map expressing relationship between optimal numbers and maximum energy demands (case 3)**

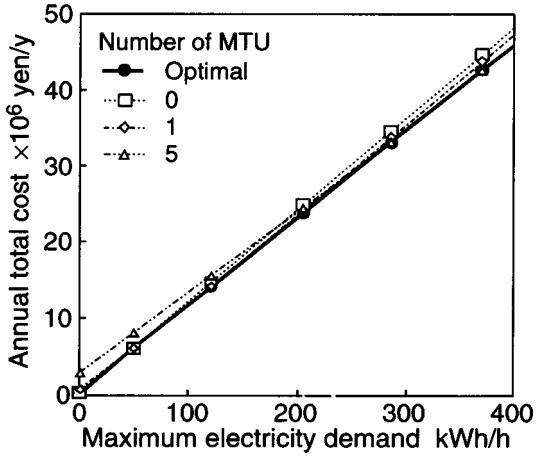


**Fig. 12 Annual total cost (case 1)**

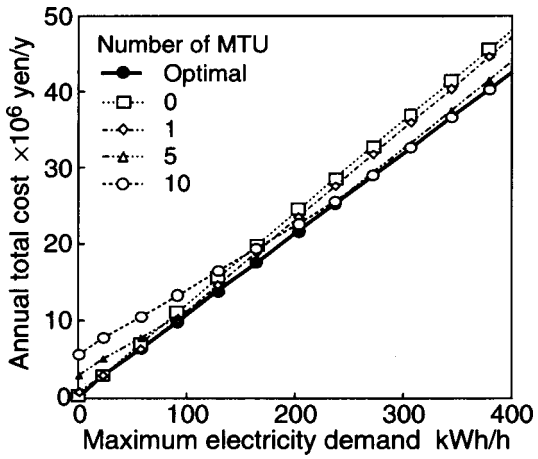


**Fig. 13 Annual total cost (case 2)**

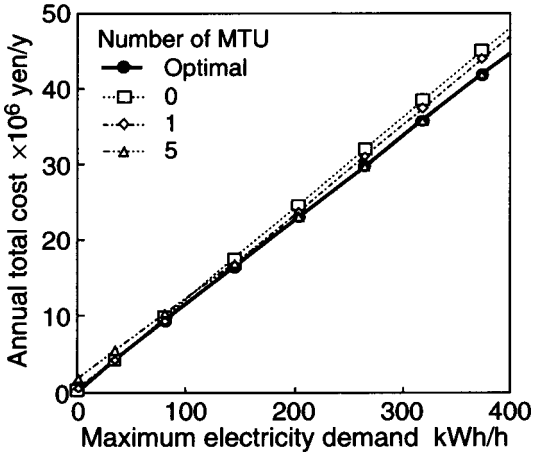


Fig. 14 Annual total cost (case 3)

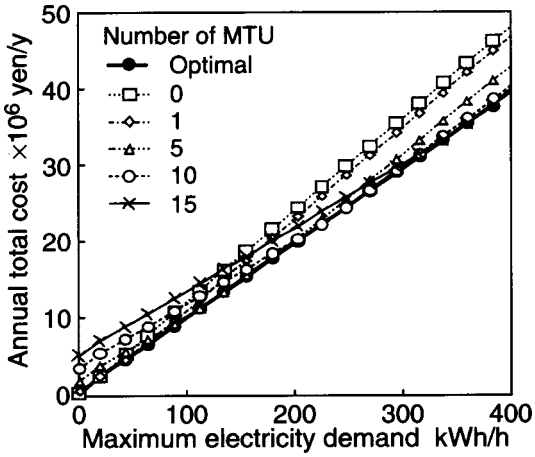


Fig. 15 Annual total cost (case 4)

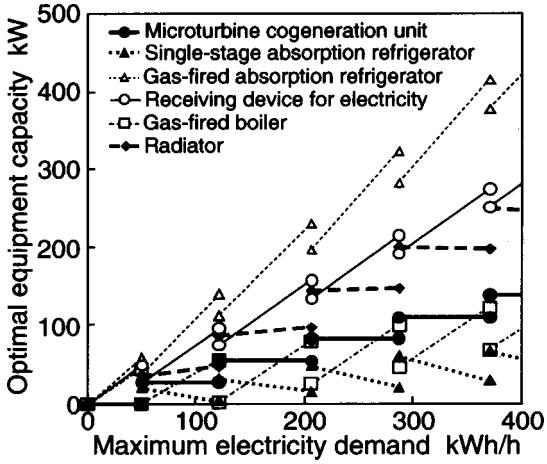


Fig. 17 Optimal equipment capacity (case 1)

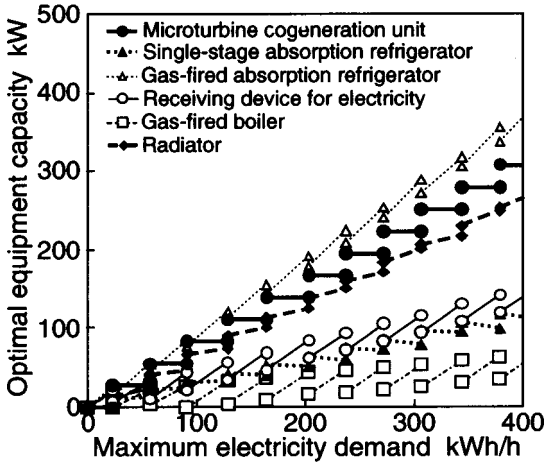


Fig. 18 Optimal equipment capacity (case 2)

of the MTU to that for 0 MTU, i.e., system without the MTU, for cases 1–4. In this figure, the numerals over the lines denote the optimal number of the MTU. According to this figure, it is found that the reduction rate of the annual total cost for each case becomes large by installing the plural numbers of the MTU. However, the reduction rate of the annual total cost changes its value hardly in the case where the optimal number is more than 4. Their reduction rates in cases 1–4 are respectively about 4%, 11%, 7%, and 18%, and it is found that the economic feasibility of the MTU becomes high by improving the electrical generating efficiency and reducing the capital unit cost.

Finally, Figs. 17–20 show the relationship between optimal equipment capacities and the maximum electricity demand for

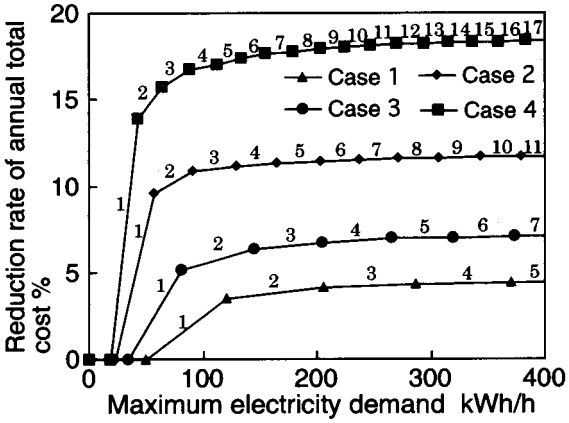


Fig. 16 Reduction rate of annual total cost

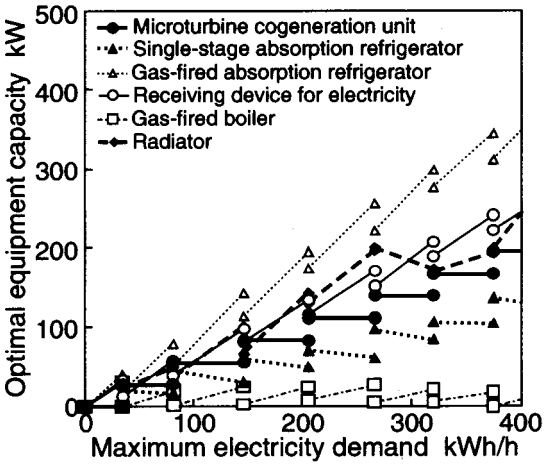


Fig. 19 Optimal equipment capacity (case 3)

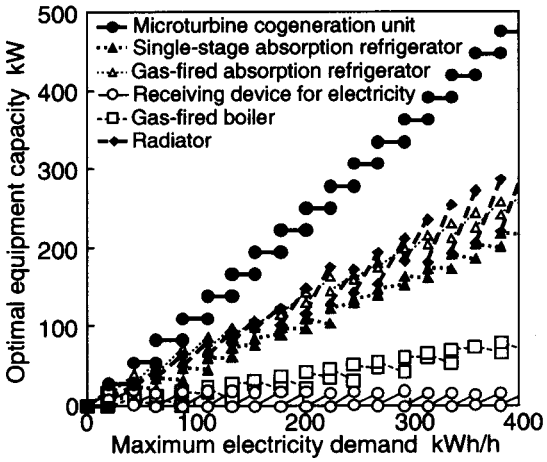


**Fig. 20 Optimal equipment capacity (case 4)**

cases 1–4, respectively. According to these figures, it is found that the optimal capacities of the gas-fired absorption refrigerator (RG), the receiving device for electricity (EP), and the gas-fired boiler (BG) decrease by increasing the optimal number of the MTU, whereas the optimal capacity of the single-stage absorption refrigerator (RW) increases. Moreover, when the optimal number of the MTU is fixed, the optimal capacities of the RG, the BG, and the EP increase with the maximum electricity demand, whereas the optimal capacity of the RW decreases.

## Conclusions

In this paper, the economic feasibility of the microturbine cogeneration systems has been evaluated by examining the relationships between the optimal number of the microturbine cogeneration units (MTUs) and the maximum energy demands under various conditions based on the proposed method which has been able to illustrate the relationships as a map. Through the numerical studies carried out on the systems installed in hotels, it has been found that the improvement of the electrical generating efficiency and the reduction of the capital unit cost of the MTU have greatly promoted the installation of the MTU, and that the reduction rate of the annual total cost by installing the plural numbers of the MTU has been about 4%–18%.

## Nomenclature

$\boldsymbol{C}$ = vector composed of constraint functions
$d$ = annual operational hours, h/y
$F$ = annual capital cost, yen/year[1]
$f$ = minimum annual total cost, yen/year[1]
$G$ = annual customer/demand charges, yen/year[1]
$J$ = annual total cost, yen/year[1]
$n$ = number of microturbine cogeneration unit
$p$, $q$, $p'$, $q'$, $\underline{q}''$, $\underline{u}'$, $\underline{u}''$, $\overline{u'}$, $\overline{u''}$ = performance characteristic values of a certain piece of equipment
$\boldsymbol{s}$ = vector composed of maximum energy demands, kWh/h
$s$ = maximum energy demand, kWh/h
$T$ = set of all the values of $t$ through a year
$t$ = index for a sampling time
$u$, $v$ = input and output energy flow rates of a certain piece of equipment, respectively, which are elements of vector $\boldsymbol{y}$, $Nm^3/h$, kWh/h
$V$ = hourly energy charge, yen/h[1]
$\boldsymbol{x}$ = vector composed of continuous variables for equipment capacities and utility maximum contract demands, kW, $Nm^3/h$
$x$ = capacity of a certain piece of equipment, which is an element of vector $\boldsymbol{x}$, kW
$\boldsymbol{y}$ = vector composed of continuous variables for energy flow rates, $Nm^3/h$, kWh/h
$\boldsymbol{z}$ = vector composed of binary and integer variables for on/off status of operation of equipment and the number of active microturbine cogeneration units, respectively
$\alpha$ = capital unit cost of microturbine cogeneration unit, yen/kW[1]
$\delta$ = binary variable expressing on/off status of operation of a certain piece of equipment, which is an element of vector $\boldsymbol{z}$
$\eta_e$ = electrical generating efficiency of microturbine cogeneration unit
$\eta_h$ = exhaust heat recovery efficiency of microturbine cogeneration unit
$\lambda$ = integer variable expressing number of active microturbine cogeneration units in a single sampling time, which is an element of vector $\boldsymbol{z}$
$\xi$ = discrete variable equal to product of $x$ and $\delta$
$\underline{(\ )}$, $\overline{(\ )}$ = lower and upper limits

### Equipment Symbols (Subscripts)

EP = device for purchasing and reversing electricity
MTU = microturbine cogeneration unit
RW = single-stage absorption refrigerator
RG = gas-fired absorption refrigerator
BG = gas-fired boiler
RD = radiator

### Subscripts

$n$ = number of microturbine cogeneration unit
$\boldsymbol{s}$ = vector composed of maximum energy demands
$t$ = index for sampling time

[1] 1 $≒120 yen.

## References


[1] Scott, W. G., 1998, "Micro-Turbine Generator for Distribution Systems," IEEE Ind. Applic. Mag., **4**(3), pp. 57–62.
[2] Carnö, J., Cavani, A., and Liinanki, L., 1998, "Microturbine for Combined Heat and Power in Distributed Generation," *Proceedings of the International Gas Turbine & Aeroengine Congress & Exhibition*, **98-GT-309**, pp. 1–6.
[3] Witte, L. C., Schmidt, P. S., and Brown, D. R., 1988, *Industrial Energy Management and Utilization*, Hemisphere, Washington, pp. 68–69.
[4] Ito, K., Yokoyama, R., Akagi, S., and Matsumoto, Y., 1990, "Influence of Fuel Cost on the Operation of a Gas Turbine-Waste Heat Boiler Cogeneration Plant," ASME J. Eng. Gas Turbines Power, **112**, pp. 122–128.
[5] Brent, R. P., 1973, *Algorithms for Minimization without Derivatives*, Prentice–Hall, Englewood Cliffs, NJ.
[6] Brooke, A., Kendrick, D., and Meeraus, A., 1996, *GAMS Release 2.25 a User's Guide*, GAMS Development Corp.

**Rattan Tawney**
**Zahid Khan**
**Justin Zachary**

Bechtel Power Corporation,
5275 Westview Drive,
Frederick, MD 21703

# Economic and Performance Evaluation of Heat Sink Options in Combined Cycle Applications

*This paper is a guideline to selecting the most appropriate technology for the power plant heat sink based on water availability, site location, and wastewater disposal requirements. The paper discusses wet as well as dry cooling systems and evaluates the impact of the heat sink technology on the performance and cost of combined cycle power plants. Cogeneration applications and cycling plant operations are also considered. For each proposed option, the performance, relative costs, and noise issues will be presented.*
[DOI: 10.1115/1.1839924]

## Heat Sink Technologies

In accordance with the laws of thermodynamics, a steam cycle rejects heat at a temperature that is much lower than the temperature at which heat is added. A power plant that dissipates heat at the lowest possible temperature will maximize cycle efficiency and minimize the amount of heat rejected. For combined cycles, the heat dissipation scheme to the environment consists of a steam surface condenser and/or a wet or dry cooling system. This package is referred to as the heat sink. Typical heat sink technologies in combined cycle applications include the following:

- Wet Cooling Technologies
  - Wet cooling tower
  - Once-through cooling system
- Dry Cooling Technologies
  - Direct dry cooling system (Air-Cooled Condenser)
  - Indirect dry cooling system (Heller system)
- Hybrid Cooling Technology
  - Wet-dry cooling system (Wet Surface Air Cooler)

**Wet Cooling Tower.** The heat of condensing steam is removed in a shell and tube heat exchanger by a continuous loop circulating water system. The hot water is then cooled by evaporation in contact with air in a tower, and the heat of evaporation is dissipated into the atmosphere. Figure 1 shows a typical flow diagram for a wet evaporative cooling tower. Theoretically, the lowest heat sink temperature achievable with a wet cooling tower is the ambient air wet bulb temperature. Because of inefficiencies in the cooling process, the cooling tower can only approach the wet bulb temperature. The closer the wet bulb is approached, the larger and more expensive the cooling tower becomes. Apart from the steam condensing heat load, other auxiliary cooling loads are also dissipated in the wet cooling tower.

Makeup water for this heat sink option is required to compensate for evaporation, blowdown, and drift losses from the cooling tower. Chemicals are added to the cooling tower forebay to control circulating water pH, scale/corrosion, and biological growth.

**Once-Through Cooling.** A once-through cooling system uses cold water from a nearby river, lake, or ocean and circulates it through the condenser to remove condensation heat and returns the hot water to the source. Because of the lower heat sink temperature relative to a wet cooling tower, once-through cooling is the most efficient cycle heat rejection system design. Figure 2 shows a typical flow diagram for a once-through cooling system. The heat sink condensation temperature depends on the temperature of the coldwater source. Specially designed intake and outfall structures are required to direct the cooling water from the source to the power plant and then back to the source again. The water is first channeled through an intake structure where screening equipment prevents trash and debris from reaching the main circulating water pumps. Flow straightening elements designed to provide streamlined flow to the pumps are also contained in the intake structure. The design of the intake structure must also account for changes in the water level due to seasonal or tidal variations. After flowing through the condenser, the hot water is returned to the environment through an outfall structure designed to discharge the water at an optimal velocity and within the thermal discharge limit.

**Direct Dry Cooling With an Air-Cooled Condenser.** Dry cooling systems transfer heat by convection and radiation instead of evaporation as in wet cooling. This typically results in higher heat sink temperatures and lower cycle efficiencies relative to wet towers. This is because the heat transfer process removes latent heat from the condensing steam to the sensible heat of the ambient air. The ambient dry bulb temperature controls the condensing temperature and pressure achievable with dry cooling. This is always higher than the wet bulb temperature, which is the controlling variable for the wet towers. In an air-cooled condenser (ACC), the condensing heat is dissipated directly into the atmosphere without using an intermediate medium such as cooling water. Figure 3 shows a typical flow diagram for an ACC. In this arrangement, the steam exhausting the turbine is piped to the condenser by a large diameter duct. The steam condenses in the air-cooled tube bundles. The fin tube bundles are mounted in an A-frame configuration and mounted on a steel structural support. The steam enters the tube bundles at the top of the A frame and condenses in the tube. The heat is removed by air blown over the exterior of the tube bundle surface by a forced draft fan. Noncondensibles are drawn off by air ejection equipment. The condensate drains into a collection tank and is then sent back to the heat recovery steam generator's (HRSG's) feedwater system.

**Indirect Dry Cooling System (Heller).** The indirect dry cooling system uses circulating water (steam condensed to water) to transfer the condensation heat to the air-cooled heat exchanger bundles. Cooled water from the dry cooling tower flows back to a jet condenser causing the turbine exhaust steam to condense. The direct contact between the circulating water and the condensing steam results in a small condenser volume. The ambient dry bulb controls the heat sink temperature in this arrangement. Because the indirect system requires the use of two heat transfer processes (steam condenser and air-cooled heat exchangers), the logarithmic

Contributed by the International Gas Turbine Institute (IGTI) of THE AMERICAN SOCIETY OF MECHANICAL ENGINEERS for publication in the ASME JOURNAL OF ENGINEERING FOR GAS TURBINES AND POWER. Paper presented at the International Gas Turbine and Aeroengine Congress and Exhibition, Atlanta, GA, June 16–19, 2003, Paper No. 2003-GT-38834. Manuscript received by IGTI, October 2002, final revision, March 2003. Associate Editor: H. R. Simmons.

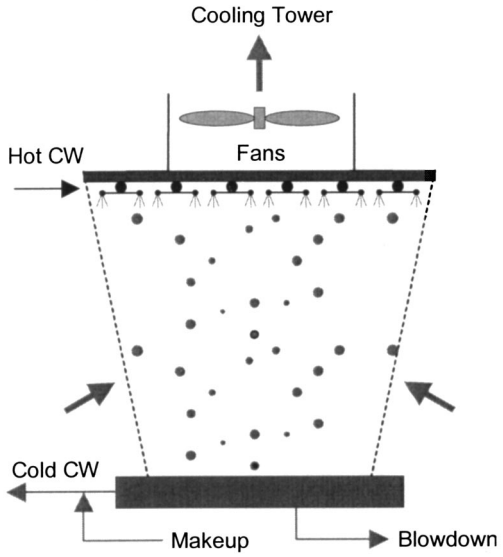


**Fig. 1 Typical flow diagram for a wet evaporative cooling tower**

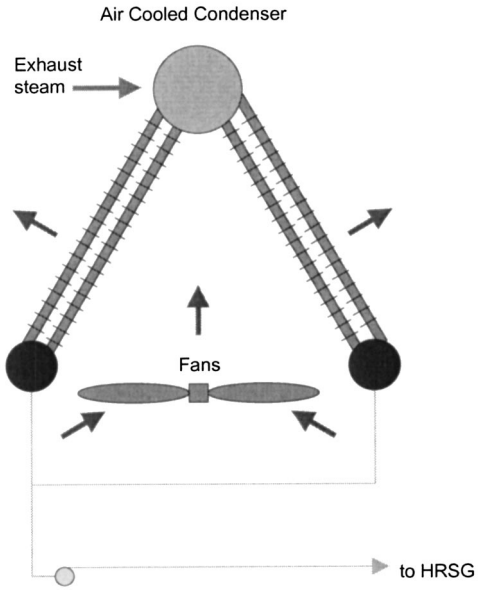


**Fig. 3 Typical ACC flow diagram**

mean temperature difference (LMTD) for the overall heat transfer process is lower than that for the direct dry cooling system. This can only be compensated for by using a larger cooling surface, increased cooling airflow, or both. Figure 4 shows a typical flow diagram for an indirect dry cooling system.

The circulating water is condensate quality and is circulated in a closed system. The circulating water pumps are equipped with hydraulic energy recovery turbines to recuperate the excess head in the return header from the dry cooling tower. The power recovered by the hydraulic turbines provides part of the pumping power for the circulating water pumps. The indirect dry cooling system incorporates large underground storage tanks to drain the system for maintenance purposes.

**Wet-Dry Cooling Tower (Wet Surface Air Cooler).** The wet surface air cooler (WSAC) condenses the steam inside tube bundles that are constantly oversprayed with water from the cooling tower basin. The process heat is released to the cascading water and is then transferred from the water to the air stream by vaporization. Motor-driven fans induce airflow over the sprayed tube bundles and discharge the humidified air vertically. Primary cooling is achieved by evaporating the spray water into the air stream. The ambient air wet and dry bulb temperatures control the heat sink temperature. Figure 5 shows a typical flow diagram for a WSAC.

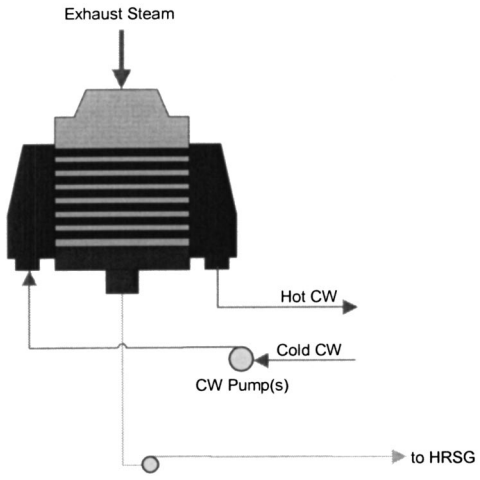


**Fig. 2 Typical flow diagram for a once-through cooling system**

## Selection of Heat Sink Technology

The selection of the heat sink technology should be initiated in the early stages of project development. The elements that significantly affect the selection of the heat sink and the overall power plant performance and cost include:

- Availability and quality of water
- Disposal of water
- Site configuration

Once the heat sink option has been selected, its performance can be optimized based on historical weather data for the wet bulb (relative humidity) and dry bulb temperatures at the site. Equipment design parameters such as temperature approaches are then determined in order to achieve maximum cycle efficiency at the lowest cost.

**Availability and Quality of Water.** A simplified overview of the heat sink technology selection process based on water availability is presented in Fig. 6.

If a source of water is identified and abundant cooling water is available, the preferred choice should be a once-through system or a wet cooling tower, depending on site configuration.

The quality of makeup water, used in cooling tower applications, is another parameter to be taken into consideration. The following makeup water quality and quantity issues need to be addressed during the design of the power plant:

- Characteristics of the makeup water—quantity and quality
- Variations in required flow due to different heat rejection loads
- Seasonal variations in water characteristics

The relative cost (capital and operating) of treating various sources of makeup water is shown in Fig. 7. The analysis uses low total dissolved solids (TDS) water (e.g., well water with less than a 1000 mg/l of total dissolved solids) as the basis of comparison for the relative cost of water treatment. The assessment indicates that use of either agricultural or industrial wastewater will cost

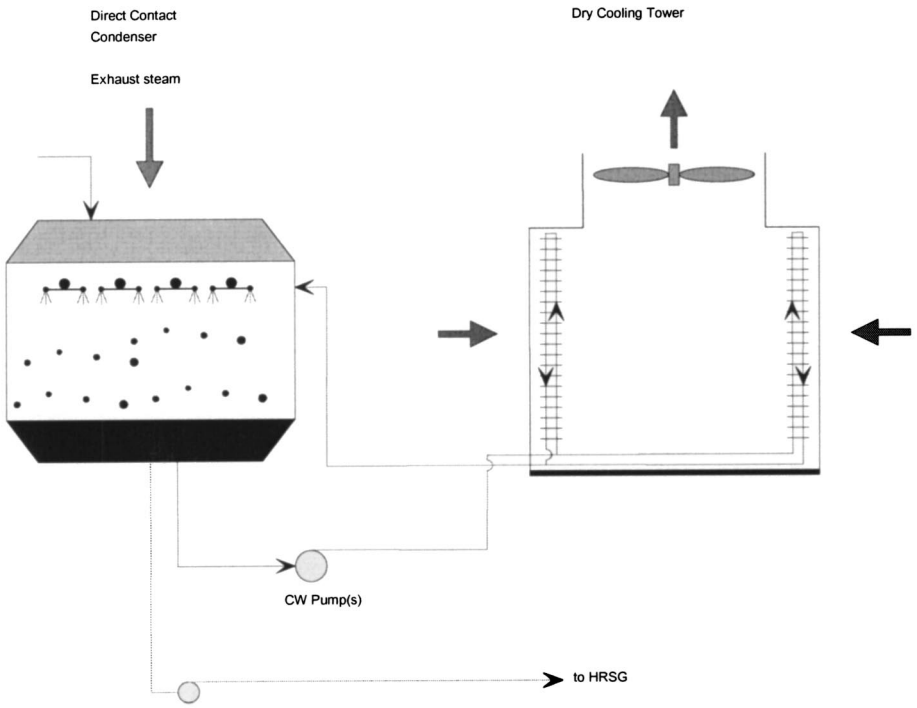


**Fig. 4 Typical flow diagram for a Heller system**

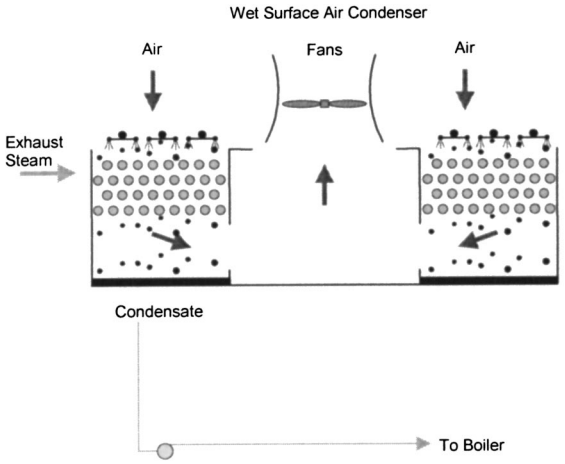


**Fig. 5 Typical WSAC flow diagram**

about 2–2.5 times more than low TDS water. Recovering cost of gray water or black water for heat sink use is up to twice the cost of low TDS water because of the complexity of the purification equipment required. Seawater used for once-through systems will also be approximately 25% more expensive than the base case due to the screening, filtration, and chlorination process.

**Disposal of Wastewater.** Another economic consideration is the relative cost of wastewater disposal (blowdown from cooling tower) after the wastewater has been concentrated in a wet cooling tower. The options for wastewater discharge depend on the plant location and the local regulations. Wastewater discharge options include stream discharge, creek discharge, sewer discharge, evaporation ponds, and zero discharge. For the once-through heat sink type, the returning sea or river hot water could be considered as wastewater. There are severe permitting limitations on its thermal discharge temperature and amount. The restrictions can be serious enough to require a reevaluation of the feasibility for this option.

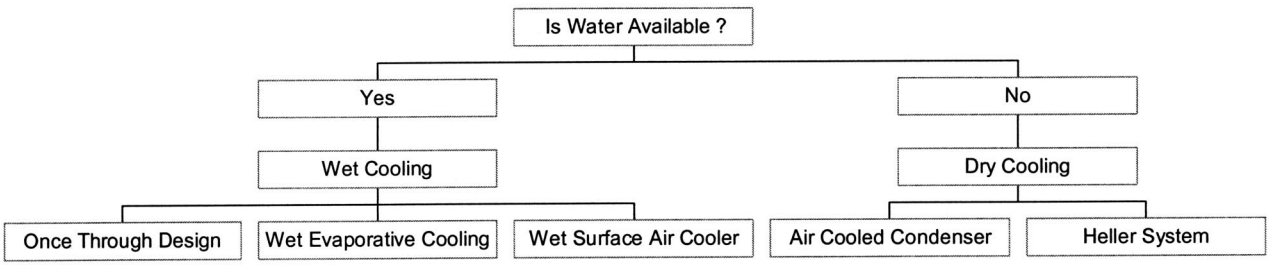


**Fig. 6 Heat sink selection process based on water availability**

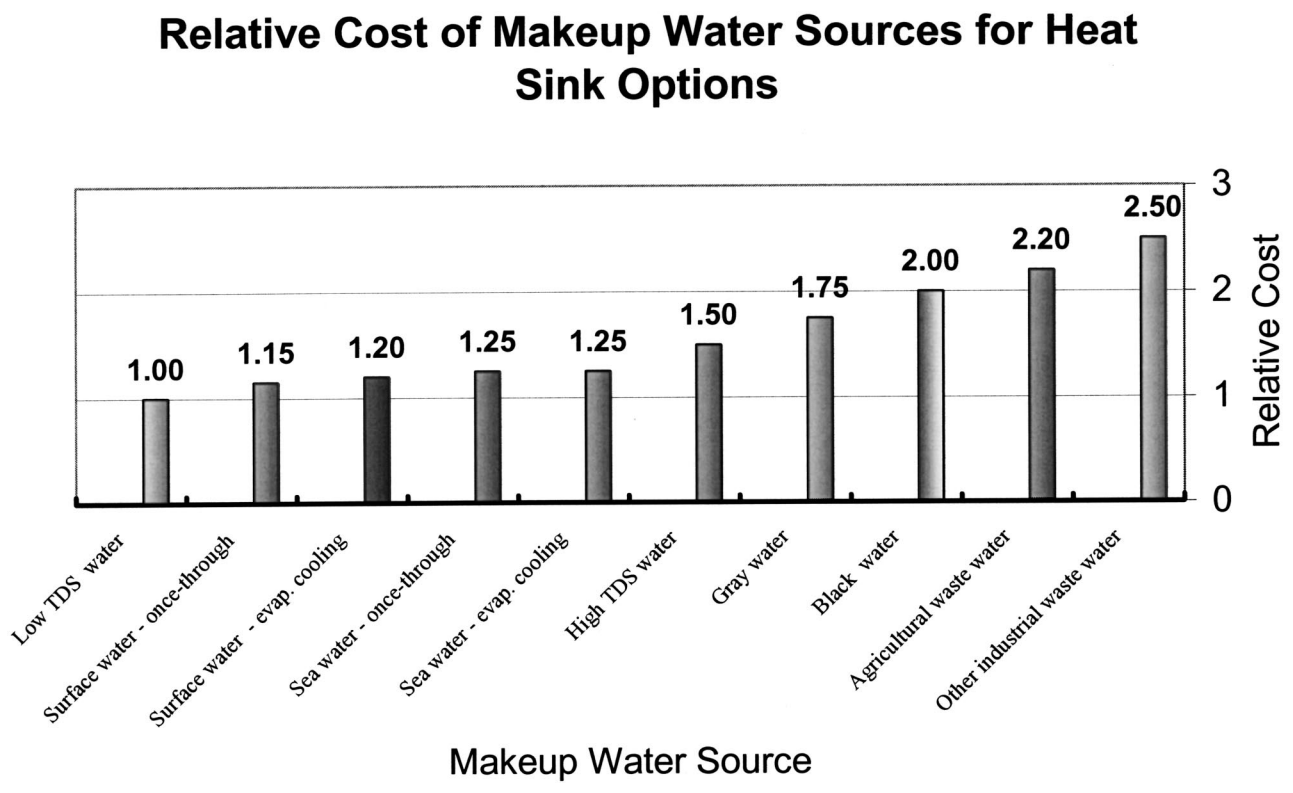


**Fig. 7 Cost of makeup water sources for heat sink options relative to low TDS water**

The results of a cost analysis conducted to assess the relative cost (capital and operating) of wastewater disposal are summarized in Fig. 8. The analysis uses the cooling pond as the basis of comparison for the relative cost of water treatment.

From the analysis, the ''zero discharge'' option is the most expensive and could cost as much as four times more than the cooling pond option. Therefore, the zero discharge option should be used only where stringent environmental laws require it. Success-

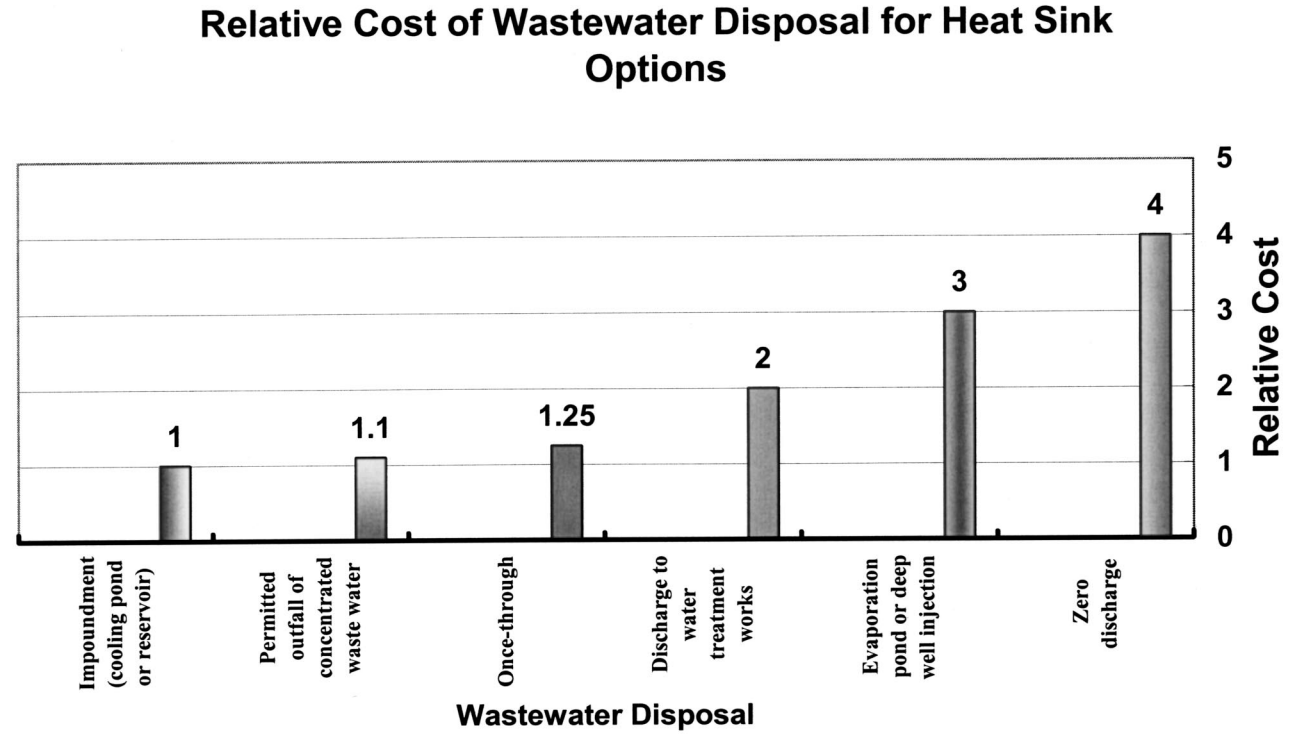


**Fig. 8 Cost of wastewater disposal for heat sink options relative to an impoundment system**

ful removal of contaminated water for zero discharge conditions involves very complex hardware and systems integration processes. Other disposal alternatives, such as discharge to water treatment plants, are at least twice the basic cost due to associated cost of the water treatment.

**Site Configuration.** Each heat sink option has specific layout requirements. For mechanical draft wet cooling towers, spacing and orientation affect thermal performance due to re-circulation and wind direction. Rectangular cooling towers are oriented parallel to the prevailing wind so that the exit air is blown away from the inlet.

Once-through cooling systems must be located near a large natural body of water. If the source for the body of water is not nearby, the necessary extended lengths of circulating water piping and larger pumps will increase the equipment cost as well as parasitic pumping power. Under such conditions, a detailed evaluation should be conducted to confirm the viability of this option.

Direct and indirect dry cooling systems require a large amount of space. Their location within the site perimeter should avoid restrictions to the inlet airflow.

Air-cooled condensers should be located close to the turbine building to minimize the pressure drop between the steam turbine and the condenser, reducing steam duct cost and improving cycle efficiency. In general, ACCs require a large, symmetrical plot space to accommodate their rectangular shape. Any irregular lot or unusual site requires creative and unconventional solutions.

## Cycling and Cogeneration Considerations

**Cycling Considerations.** The merchant plant concept implies that electric power must be supplied to the grid only when it is commercially justifiable. Such requirements must typically be met on very short notice. Therefore, these plants need to be started up quickly and should have flexible operating ranges. Merchant plants are normally in cycling service, which can be considered part-load operation or daily on/off operation. Heat sink considerations for a cycling plant require special features as described below:

- Use an auxiliary boiler to sparge the condenser hotwell to prevent the condensate from subcooling
- Maintain condenser vacuum during periods of shutdown
- Use a cooling tower bypass to shut-off cells for low load operation
- Use pre-coat condensate treatment (condensate polisher) with ACC, which may have large surface areas of carbon steel in contact with steam and condensate
- Include provisions to control all heat sink fans from the control room

**Cogeneration Applications.** Cogeneration is the simultaneous production of electrical and thermal energy. Cogeneration plants must also consider the quality and quantity of water returned to the power plant from the process. Depending on the quality of the returned water, further deaeration and chemical treatment may be necessary. If all the exported water is not returned, additional cycle makeup will be required. An external deaerator will be required if the total cycle makeup exceeds 3%–5%.

## Comparative Analysis

**Comparative Analysis of Heat Sink Technologies.** To assess the impact of different heat sink options, a combined cycle plant computer model was developed using a standard, commercially available simulation package (Thermoflow, Inc. software). The base case for this comparison of different heat sink technologies is the wet cooling tower. In our modeling, the plant configuration and ambient conditions were maintained identical for all cases. The only variations allowed were due to the changes in the heat sink design parameters. The selected configuration includes two gas turbines, two HRSGs, and one steam turbine (2×2×1). No steam extraction from the cycle was considered. No restrictions on either the water availability or the site configuration was considered in the model. In calculating net power output and heat rate, the specific auxiliary loads associated with each type of heat sink option were subtracted. Plant thermal performance was evaluated by the different condensing pressures resulting from each particular heat sink technology. A higher backpressure results in a lower power output and worse heat rate. The heat dissipation capability of each of the technologies is dependent on ambient conditions. The thermal performance is dependent on the wet bulb temperature for the wet cooling tower and is related to dry bulb temperature for the ACC and indirect dry cooling tower. For the once-through condenser using river or seawater, the heat sink temperature for the process is the river or seawater temperature. To produce meaningful results for the comparison, design parameters for condensing and/or heat dissipation equipment sizing, such as approach temperatures, rise, and other applicable criteria, are based on industry trends. The results of the analysis for the thermal performance and associated cost on a comparative basis are illustrated in the bar chart format.

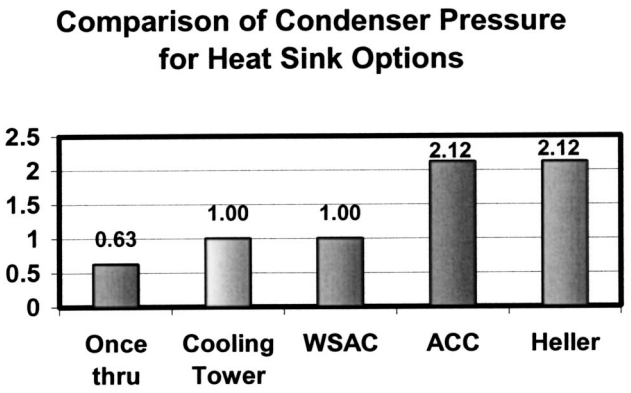


**Fig. 9 Condenser pressure comparison relative to a wet cooling tower**

**Condenser Pressure.** Figure 9 presents the expected backpressures for each heat sink option. The results are relative, based on the wet cooling tower backpressure equal to 1. A WSAC will have the same backpressure as the wet cooling tower at the same ambient wet bulb temperature. Under these conditions, a plant substituting an ACC or a indirect dry cooling tower for a wet tower will have a backpressure that is approximately 2.1 times higher, because the ACC and indirect dry cooling towers are governed by the dry bulb temperature. In contrast, a once-through condenser will have a backpressure that is about 40% lower than the base case.

**Electrical Power Output.** The electrical power output comparison in Fig. 10 shows that the net output is higher at lower heat sink temperatures with corresponding backpressures. The comparison indicates that ''dry options,'' such as ACC and indirect dry cooling systems, are about 4%–5% lower in power output compared with a wet cooling tower. Direct use of cooling water as shown in the once-through condenser could yield approximately 2% more power output.

**Heat Rate.** The impact on the net plant heat rate is shown in Fig. 11. A once-through condenser option will have about 2% better heat rate than the wet cooling tower. For this option it should be emphasized that, in addition to lower condensing pressure and temperature, the auxiliary loads are relatively smaller. The net plant heat rate of dry tower options such as ACC and indirect dry cooling systems can be about 5% worse than that of the wet cooling tower.

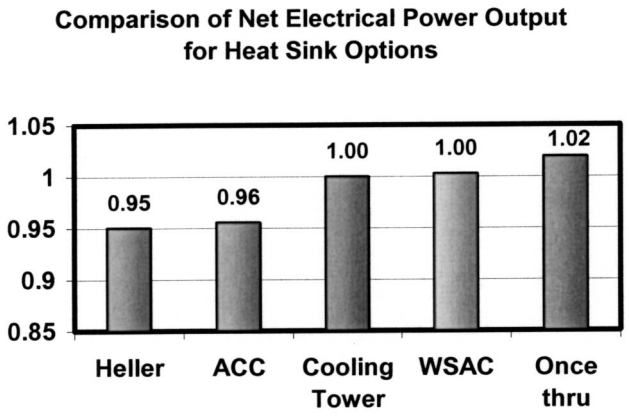


**Fig. 10 Net electrical power output comparison relative to a wet cooling tower**

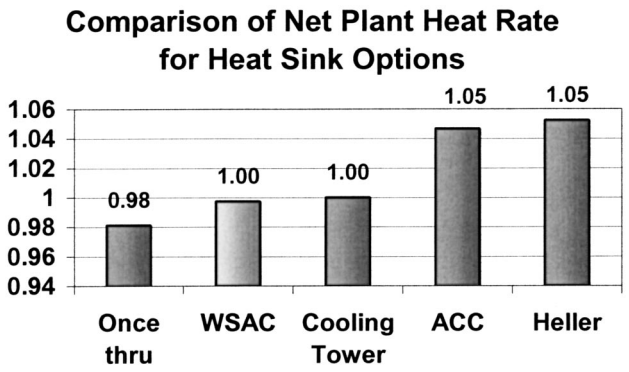


**Fig. 11 Net plant heat rate comparison relative to a wet cooling tower**

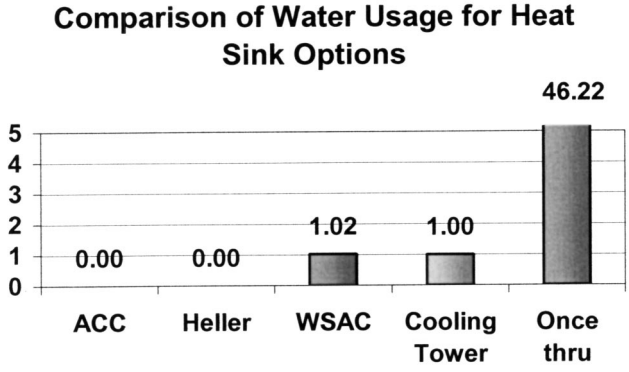


**Fig. 12 Makeup water usage comparison relative to a wet cooling tower**

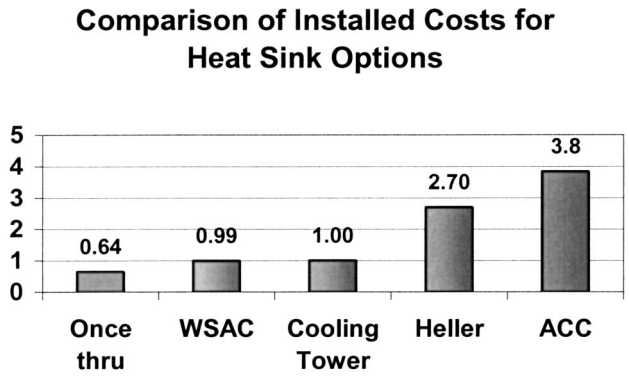


**Fig. 13 Total installed costs comparison relative to a wet cooling tower**

**Makeup Water.** An additional comparison of the use of makeup water is given in Fig. 12. The reference to makeup water in this paper is related only to the needs of the water as cooling media and not as the power plant cycle makeup. As expected, the indirect dry cooling system and ACC do not use any water. In a once-through condenser, the cooling water, in an open loop configuration, uses approximately 46 times more water than a wet cooling tower, where the water is cooled and recycled.

**Total Installed Cost.** The total installed cost for each of the options is given in Fig. 13. Installed costs for once-through designs may vary, depending on the distance to the water source from site location. The cost of the wet cooling tower includes a separate surface condenser.

Dry heat sinks are about three to four times more expensive than the conventional wet cooling tower/surface condenser combination. The differential between Heller and the ACC installed costs depends on the particular design being considered (e.g., natural draft or mechanical draft Heller versus ACC). The once-through option is about 40% less expensive than the wet cooling tower.

## Advantages and Challenges of Heat Sink Technologies

The advantages and challenges of each heat sink option compared with the wet cooling tower are summarized in Table 1.

**Once-Through System.** The advantages of this system are lower installed costs, lower operating costs, lower auxiliary loads, and a higher cycle efficiency compared with a wet cooling tower. The challenges of this design include higher makeup water requirements, complexity of intake and outfall structure design, and limitation on thermal discharge.

**Wet Cooling Tower.** The current trend in the fossil power industry is to use wet cooling towers if sufficient water is available year round at site. Because this design is often used in power plants, it is considered the base case for the purposes of discussion in this paper.

**Table 1 Advantages and challenges of heat sink options**

| Wet cooling tower | Once-thru | ACC | Heller | WSAC |
|---|---|---|---|---|
| ⇒ Base Installed cost | ⇒ Lower | ⇒ Higher | ⇒ Higher | ⇒ Almost same |
| ⇒ Base aux. loads | ⇒ Lower | ⇒ Higher | ⇒ Higher | ⇒ Lower |
| ⇒ Base cycle efficiency | ⇒ Higher | ⇒ Lower | ⇒ Lower | ⇒ Same |
| ⇒ Base noise | ⇒ Lower | ⇒ Higher | ⇒ Higher | ⇒ Lower |
| ⇒ Base land usage | ⇒ Lower | ⇒ Higher | ⇒ Higher | ⇒ Higher |
| ⇒ Base make-up water usage | ⇒ Higher | ⇒ Lower | ⇒ Lower | ⇒ Almost same |
| ⇒ Base wastewater disposal requirements | ⇒ Higher | ⇒ Lower | ⇒ Lower | ⇒ Lower |
| ⇒ Base chemical usage | ⇒ Lower | ⇒ Lower | ⇒ Lower | ⇒ Almost same |

The advantages of this system are moderate installed and operating costs, auxiliary loads with moderate makeup water requirements, and relatively good cycle efficiency. The challenges of this design include cooling tower blowdown disposal, plume formation at colder ambient temperatures, and disposal of any wastes (such as sludges) which may result from treatment of the makeup water.

For wet cooling towers, plume formation and blowdown disposal are major concerns. To solve the plume problem, the wet cooling tower manufacturers have developed systems to abate its formation. However, below certain ambient temperatures, the abatement process becomes ineffective and the plume reappears and gradually increases in size.

**Dry Cooling With Air-Cooled Condenser.** The advantages of this system are that water usage requirements are minimal and that no issues are associated with blowdown disposal and plume formation. The challenges of this design are higher installed costs, relatively higher noise emissions, larger footprint, and lower cycle efficiency than the base case (wet cooling tower).

**Indirect Dry Cooling System.** The advantages of this system are lower auxiliary loads and lower noise for natural draft-type Heller systems, minimal water usage requirements, and absence of issues associated with blowdown disposal and plume formation. The challenges of this design are higher installed costs, relatively larger footprint, and lower cycle efficiency. An increased quantity of oxygen scavenger is also required because the jet condenser achieves an oxygen level of only 15–20 ppb in the condensate, which is higher than the typical values seen in a deaerating condenser. The challenges of a mechanical draft-type Heller system includes higher auxiliary loads and higher noise.

**Wet Surface Air Cooler.** The advantages of this system are lower auxiliary loads, low noise, and slightly lower water usage requirements. The wet surface air cooler has a direct temperature approach to the wet bulb. This provides more efficient cooling than an ACC, which has an approach to the dry bulb temperature. At this time, this technology is not widely accepted in power plant applications.

## Conclusion

The heat sink option is often governed by factors such as site configuration, availability of water, and water disposal. The heat sink option selection process should be initiated in the early stages of project development to take these factors into account.

The plant performance in terms of power output and efficiency is best for the once-through option and worst for the indirect dry cooling system. The installed cost is highest for the ACC, closely followed by the indirect dry cooling system unit and lowest for the once-through system. The highest amount of make-up water will be consumed by the once-through option, while the indirect dry cooling system will consume the least. The probability of plume formation is greatest for the wet cooling tower option, whereas it is almost zero for the dry cooling systems such as ACC and Heller. The noise level is highest for the ACC, while it is almost zero for the once-through system. The wet cooling tower will generate the most wastewater for disposal, while dry systems such as ACC and indirect dry cooling will produce almost zero wastewater for disposal. The amount of real estate space needed is greatest for the indirect dry cooling option and least for the once-through system.

The relative cost of make-up water and the cost of wastewater disposal are also important considerations in the selection of heat sink options. The plants using black water or industrial wastewater have much higher costs. An expensive alternative for wastewater disposal will be zero discharge, with a disposal cost possibly four times that of a cooling pond.

The selection of a heat sink option is often site specific and is based on variables that include water availability, site configuration, water disposal, ambient conditions, level of target power output, anticipated hours of operation, Power Purchase Agreement structure, and Owner's economic evaluation factors for plant output, heat rate, and operations and maintenance costs.

While it is difficult to make any specific recommendations, the following conclusions would be valid for a majority of situations:

- For sites with scarce water resources, dry cooling systems such as the ACC and indirect dry cooling options will most likely be the preferred choice.
- For regions with adequate water availability and provisions for water disposal, wet cooling systems such wet cooling tower and WSAC will most likely be the preferred choice.
- For sites with a nearby river, ocean, lake, etc., once-through and/or wet cooling tower will be the option of choice.
- For regions near residential areas where noise is an issue, ACC may not be preferred.
- For peaking applications where electricity can be sold at a high price, once-through or wet cooling tower may offer a reasonable solution.
- For sites with limited water availability, parallel condensing systems consisting of an ACC and a wet cooling tower may be considered.

## Acknowledgments

Thanks to Sam Keith and Dave Ugolini, from Bechtel, for their valuable contributions and comments regarding this paper.

## Nomenclature

ACC = air cooled condenser
CW = circulating water
LMTD = logarithmic mean temperature difference
TDS = total dissolved solids
WSAC = wet surface air cooler
HRSG = heat recovery steam generator

# Cogeneration System Simulation and Control to Meet Simultaneous Power, Heating, and Cooling Demands

**Francisco Sancho-Bastos**

**Horacio Perez-Blanco**

Department of Mechanical and Nuclear Engineering,
The Pennsylvania State University,
137 Reber Building,
University Park, PA 16802-1412

*Gas turbines are projected to meet increasing power demand throughout the world. Cogeneration plants hold the promise of increased efficiency at acceptable cost. In a general case, a cogen plant could be able to meet power, heating and cooling demands. Yet those demands are normally uncoupled. Control and storage strategies need to be explored to ensure that each independent demand will be met continuously. A dynamic model of a mid-capacity system is developed, including gas and steam turbines, two heat recovery steam generators (HRSG) and an absorption-cooling machine. Controllers are designed using linear quadratic regulators (LQR) to control two turbines and a HRSG with some novelty. It is found that the power required could be generated exclusively with exhaust gases, without a duct burner in the high-pressure HRSG. The strategy calls for fuel and steam flow rate modulation for each turbine. The stability of the controlled system and its performance are studied and simulations for different demand cases are performed.*
[DOI: 10.1115/1.1789993]

## Introduction

In the present work we address how a cogeneration system can be controlled to satisfy transient power, heating and cooling demands, which are essentially independent of each other. The increasingly used [1] Brayton cycle discharges waste heat of considerable exergetic value. Hence, cogeneration schemes [2–7] have been studied, leading to the combination of Brayton and Rankine cycles [8], where the waste heat from the Brayton cycle drives the Rankine cycle. In some applications, some of the waste heat is used to cool the inlet air for the gas turbine, resulting in increased power output, but not in increased generating efficiency [6].

In cogen systems the products of combustion are used at high temperature by one component or cycle, and reject heat is used at progressively lower temperatures by other components. Each component in the energy cascading chain must be working at design. The transient nature of utility demand negates, in most cases, the possibility that all subsystems will work constantly at their design capacity. Clearly, the goal should be to fully use every unit of fuel to satisfy demand, but this may not always be possible, even if storage of some type of energy is adopted [4]. Some fuel use as backup may be called for. The issue of controlling thermal systems comprising multiple components has been addressed in the literature [2,3,7]. Generally, it was concluded that power-generating systems can respond to faults effectively, and that also they can follow loads within specified limits.

The system considered here provides power, heat, and cooling (Fig. 1) and it is somewhat more complex than previously studied power-generating facilities. A gas turbine supplies power to a user and the exhaust gas produces high-pressure steam to run a steam turbine. Low-pressure steam serves a thermal demand and, via an absorption machine, a cooling demand. As far as power generation goes, the system under consideration is not unlike a medium-capacity cogeneration system that could be installed in an industrial concern or small city. The low-pressure HRSG with two independent users is not commonly found, and to ascertain its feasibility and control is part of the thrust of this work.

In what follows, we describe the models and controls adopted for each component and how each element was integrated into a system. We also explain how we selected different loads, attempting to reflect demand profiles commonly found. We complete simulations at different ambient temperatures and with different parameters. The ability of each subsystem to respond to changes in loads or to store energy is studied.

## Plant Models

In the system schematic (Fig. 1), we describe each stream with a number. In the gas turbine, the power production rate (1) is determined by the mass flow rate of natural gas (2) and the position of the Inlet Guide Vanes (IGVs). Controlled variables are the rotational speed (3) and the exhaust gas temperature (5). The former two determine the amount and rate of potential heat recovery. The exhaust gas stream (5) flows to HRSG I, where the superheated steam stream (6) necessary to activate the steam turbine is produced. The steam turbine produces power (7), and the low-pressure exit steam (8) flows to the condenser. After condensation, the water is returned to HRSG I. The combined power production from both turbines meets the total electric power demand.

The exhaust gas from HRSG I (9), flows to the low-pressure HRSG II. A design capacity of 16 kg/s of steam was adopted for the former, whereas lower capacity of 4 kg/s was adopted for the latter. The capacities depend on the selected steam pressure levels and could change responding to design optimization, not attempted here. The steam generated by HRSG II is used to cover the steam requirements of the absorption-cooling machine and of a process heat consumer. The cooling machine provides air conditioning to a load with a time profile akin to those of office buildings, whereas the steam demand varies stepwise in time. Hence, various intermittent process heating operations, such as drying or water heating, are simulated.

A burner is added to the second HRSG for those instances when the exhaust gas mass flow rate is not large enough to meet the

Contributed by the International Gas Turbine Institute (IGTI) of THE AMERICAN SOCIETY OF MECHANICAL ENGINEERS for publication in the ASME JOURNAL OF ENGINEERING FOR GAS TURBINES AND POWER. Paper presented at the International Gas Turbine and Aeroengine Congress and Exhibition, Atlanta, GA, June 16–19, 2003, Paper No. 2003-GT-38840. Manuscript received by IGTI, Oct. 2002; final revision, Mar. 2003. Associate Editor: H. R. Simmons.

  

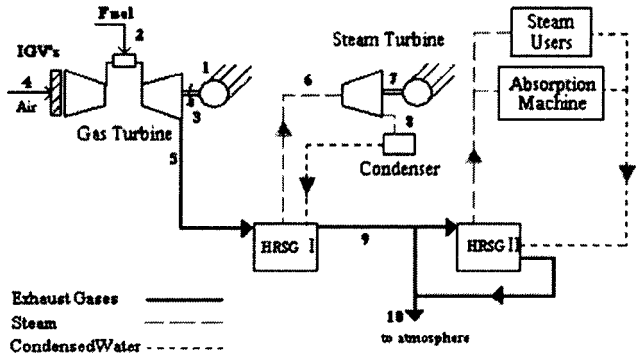


**Fig. 1 Cogeneration plant diagram**

requirements of the HRSG. Each component is modeled and controlled separately. The models are invalid for startup or shutdown transients.

**Gas Turbine.** The gas turbine model is based on the work of Camporeale [9,10]. In general, the ratio of the Laplace transform of the output to the Laplace transform of the input of a plant depends on the parameters of the plant and on the value of the transform variables. Since the gas turbine model has two inputs, namely, fuel mass flow rate and IGV position, and two outputs, namely, angular velocity and exhaust temperature, either input can influence either output. The two inputs and two outputs in the gas turbine model will have four transfer functions that are presented in a 2×2 transfer matrix (Eq. (1)) [11–13].

$$F(s)=\begin{pmatrix} \dfrac{\varpi_{GT}(s)}{\dot{m}_f(s)} & \dfrac{\varpi_{GT}(s)}{r_{IGV}(s)} \\ \dfrac{T_{GT}(s)}{\dot{m}_f(s)} & \dfrac{T_{GT}(s)}{r_{IGV}(s)} \end{pmatrix} \tag{1}$$

The transfer functions in the *s* plane readily yield insights into gas turbine stability and response to simple inputs. Yet, the model presents multiple outputs and multiple inputs, which are better handled for optimization purposes in the state-space representation. Hence, the model of Eq. (1) was translated into state space.

Minor changes were made to the original model proposed by Camporeale [14], allowing larger air and fuel mass flow rates, adjusted to meet the efficiency and rotational inertia of the selected turbine. An additional feature in the present model allows simulation of the effect of ambient temperature on power production.

**Steam Turbine.** The steam turbine model is a simplified version of the gas turbine one. In the steam turbine, the angular velocity is of importance, but the exhaust temperature is not. Then, the exhaust temperature state was eliminated from the turbine model, resulting in a SISO system [15], where the only input is the power generated, and the only output is the rotational speed. The mass of steam is considered a disturbance (in a control sense) introduced by the HRSG I in order to maintain its steam temperature and pressure at the set point as it will be explained later on. Model parameters were adjusted to obtain a realistic time response to a step input.

**HRSG I and II.** Detailed HRSG simulation is difficult, for the attending heat transfer equations are nonlinear. In addition, each pressure level within the HRSG requires an economizer tube bundle for preheating the condensate, an evaporator bundle, and a superheater bundle to ensure dry steam output. Each section of the HRSG is connected to the same drum, and there is a drum for each pressure level. The difficulty of modeling a HRSG lies on the counter flow nature of the arrangement, and the complexity ensuing from the arrangement required the simplifying assumptions below.

Applying the First Law of Thermodynamics and assuming overall constant vapor quality in the HRSG we get [14]

$$\dot{Q}=\mathrm{MHRSG}\frac{dT_H}{dt}+\dot{m}_{s,e}(h_e-u_{1,\mathrm{sat}})+\dot{m}_{s,i}(u_{1,\mathrm{sat}}-h_i) \tag{2}$$

The rate of heat transfer from the gas to the steam is a function of the heat transfer coefficients for each HRSG section, and of the temperature difference for each section. Modeling this complex situation has proven difficult in some studies, even at steady state [6,16], and consequently, a simplification was sought. It was reasoned that when steady-state conditions apply, the evaporator pinch (i.e., the temperature difference between the gas and the steam at the evaporator section gas exit) determines the amount of steam produced. If this pinch increases, heat transfer rates will increase for the three sections of the HRSG, and the converse will occur if it decreases. Hence, the HRSG capacity was simply made a function of the pinch, namely,

$$\dot{Q}=UA(T_{gp}-T_{\mathrm{evap}}) \tag{3}$$

where $T_{gp}$ is the vaporization temperature of the steam, which is the variable to be controlled in order to maintain the steady-state pressure. The gas temperature at the pinch is calculated by the following equation, which represents the HRSG energy balance:

$$T_{gp}=\frac{\dot{m}_{s,e}(h_e-h_{1,\mathrm{sat}})}{\dot{m}_g c_{pg}}+T_{gi} \tag{4}$$

In forced convection applications, the convective heat transfer coefficient is proportional to the 0.8 power of the flow rate, if the flow is turbulent. Assuming this to be the case, and factoring in the fact that the gas side tends to control the heat transfer rate, we obtain finally,

$$\dot{Q}=k\dot{m}_g^{0.8}\left(\frac{\dot{m}_{s,e}(h_e-h_{1,\mathrm{sat}})}{\dot{m}_g c_{pg}}+T_{gi}-T_{\mathrm{evap}}\right) \tag{5}$$

Rearranging terms we arrive at

$$\dot{Q}=\frac{k\dot{m}_g^{0.8}\dot{m}s,_e(h_e-h_{1,\mathrm{sat}})}{\dot{m}_g c_{pg}}+k\dot{m}_g^{0.8}T_{gi}+k\dot{m}_g^{0.8}T_{\mathrm{evap}} \tag{6}$$

Combining Eqs. (2), (5), and (6) yields,

$$\mathrm{MHRSG}\frac{dT_{\mathrm{evap}}}{dt}+\dot{m}_{s,e}(h_e-u_{1,s})+\dot{m}_{s,i}(u_{1,s}-h_i)$$
$$=\frac{k\dot{m}_g^{0.8}m_{s,e}(h_e-h_{1,\mathrm{sat}})}{\dot{m}_g c_{pg}}+k\cdot\dot{m}_g^{0.8}T_{gi}-\dot{k}\dot{m}_g^{0.8}T_{\mathrm{evap}} \tag{7}$$

The simplification embodied in Eq. (3) results in a SISO system where the only state is the steam evaporation temperature for each HRSG I and II. For HRSG I the only input is the mass of steam released to the steam turbine, and it presents two different disturbances that are the mass flow of gas from the gas turbine and its temperature. The rest of the coefficients were assumed to be constants, namely, their calculated values at design conditions were adopted. For HRSG II the input is the mass flow rate of exhaust gas, and the mass of steam delivered to users and chiller and the exhaust gas temperature are considered control disturbances.

In order to be able to apply linear control theory, it is necessary to linearize Eq. (7) about the design values for both HRSGs. The linearization yields two first-order differential equations for each HRSG of the form,

$$\mathrm{MHRSG}\cdot c_{\mathrm{HRSG}}\frac{dT_{\mathrm{evap}}}{dt}+K_1T_{\mathrm{evap}}=K_2\dot{m}_{s,e} \tag{8}$$

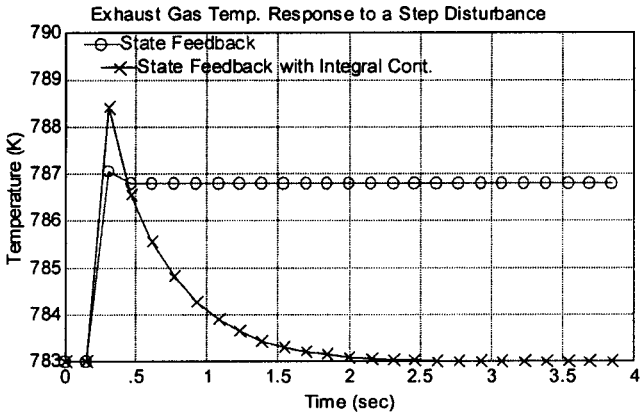


**Fig. 2 Exhaust gas temperature variation to a 20% decrease of the power demand**

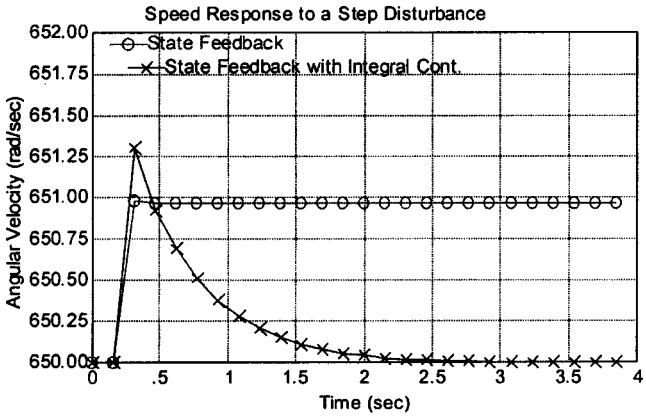


**Fig. 3 Rotational speed variation to a 20% decrease of the power demand**

**Absorption Cooling Machine and Condenser.** A first-order model is implemented for the capacity of the absorption machine, namely:

$$\frac{dq_{AM}}{dt} + k_1 q_{AM} = k_2 \dot{m}_s \tag{9}$$

Also, the condenser model responds to ambient temperature in a first-order fashion

$$\frac{dm_s \Delta h}{dt} + k_3 \ \dot{m}_s \ \Delta h = q_C(T_a) \tag{10}$$

As the ambient temperature rises, the condensed steam flow decreases, because the capacity $q_c$ decreases with increasing ambient temperature. Hence, the capacity of the steam turbine can be limited by that of the condenser in our model, and some steam can occasionally be derived to the absorption machine or to the steam user.

## Control Strategy

Controllers were designed for each component, and their stability was studied. The reader may recall that the zeros of the denominator of any transfer functions are called poles, and that the pole locations determine stability.

**Turbines.** The variables to be controlled in the gas turbine are the rotational speed and the exhaust gas temperature, and in the steam turbine the rotational speed. The rotational speed must be controlled closely. Similarly, the exhaust gas temperature must be controlled for acceptable HRSG performance. The gas turbine operational variables are affected by the change in the power load.

An LQR (linear quadratic regulator) [11,13] was designed and enhanced with an integral control [6]. The LQR is a control approach that minimizes an objective function, the latter being made up of states and of controlling forces. For instance, a state variable is the rotational speed of the turbine, and a controlling force is the fuel flow rate. The designer can specify the weight assigned to the states and to the forces, and the LQR algorithms will minimize the temporal integral of deviation from set points plus forces, each weighted as desired by the user. In our case, the rotational speed and fuel flow rate are given much more weight than the IGVs or exhaust temperatures.

The LQR then controls multiple process variables to minimize an objective function. In our case, the LQR varies the fuel mass flow rate and the position of the IGVs to keep controlled variables at their set points without steady state error, while minimizing the error and the total fuel mass into the unit. The response of the LQR controlled gas turbine to a step input is shown in Figs. 2 and 3. The response is calculated for simple state feedback and for state feedback with an integral controller that integrates the error over time and allows the LQR to correct for the integrated magnitude. Similar responses for the steam turbine are shown in Fig. 4.

**HRSG I and II.** The HRSG I receives the exhaust gases from the gas turbine with variable temperatures and mass flow rate. Since the mass flow rate and the temperature are subject to change, also the pressure and temperature of the steam will oscillate depending upon the power demand if all the other variables are kept constant. To keep the HRSG I and II pressures constant, a prescribed steam temperature is set for each.

In the present configuration, HRSG I accepts the total flow of exhaust gases. In contrast, the gas flow into HRSG II can vary. A proportional integral controller is designed for both HRSGs in order to control the steam temperature. In the case of the HRSG I, the controller varies the steam outflow to keep constant temperature. For HRSG II, the controller varies the input gas flow. The root-locus technique was used to determine the integral and proportional gains. Both proportional, and proportional-integral controls were studied. The response to a unit step input can be seen in Fig. 5 for HRSG I and in Fig. 6 for HRSG II.

**Absorption Cooling Machine.** Depending on the cooling demand, the capacity of the absorption-cooling machine will have to vary; therefore, a controller was designed to determine the mass flow rate of steam needed to cover the cooling demand.

First-order models call for a two-pole controller to meet ramp loads with zero steady-state error [14]. Hence an open-loop transfer function with two poles at zero in the *s* plane is adopted for the

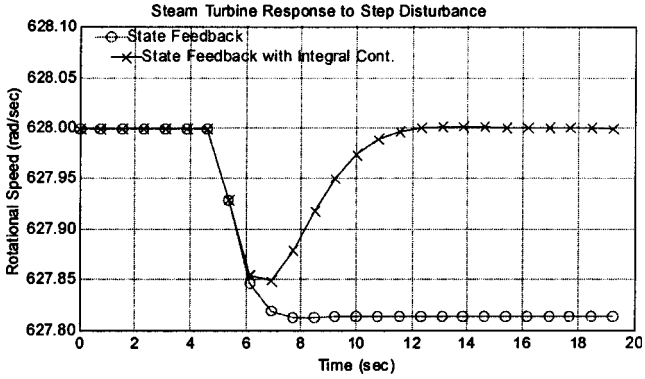


**Fig. 4 Steam turbine rotational-speed variation to a step decrease of the flow rate of steam**

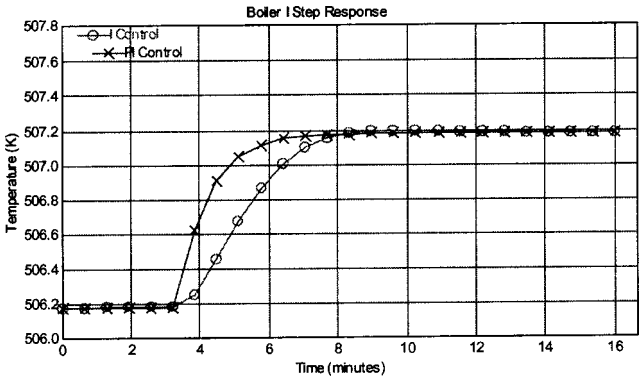


**Fig. 5 Response on the steam temperature in HRSG I for a step variation in the exit flow of steam**

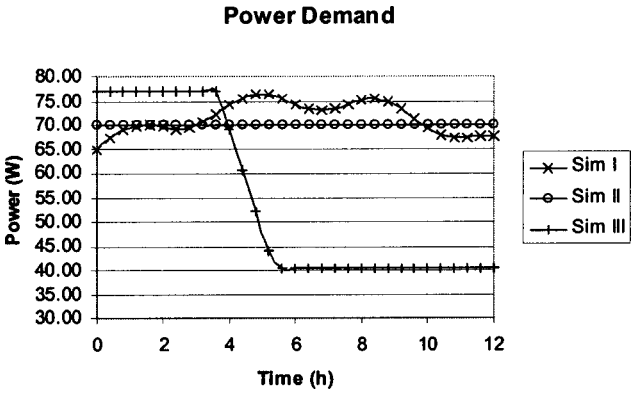


**Fig. 8 Power demand**

control algorithm. Figure 7 shows how the controller eliminates the steady state error of the response to a ramp input.

**Cogeneration Plant.** The overall system was projected to comply with the following guidelines.

1. The gas turbine generates part of the power demand and is controlled to keep constant speed and gas temperature.
2. The HRSG I produces steam that will have a mass flow rate determined by its controller in order to maintain constant pressure and temperature (assuming that the condenser can handle all the steam from HRSG I).
3. The output of the HRSG I is sent to the steam turbine. The steam turbine controller determines the power produced to maintain a constant speed.
4. The condenser capacity varies with the ambient temperature. If it cannot handle all the steam, then the extra amount is sent to the absorption machine and the steam users via a pressure-reducing valve to reduce the load of HRSG II.
5. The absorption machine and the steam users define the amount of steam that HRSG II must produce. To produce the required steam the HRSG II controller determines the exhaust gas mass flow rate needed. If the mass flow rate is equal to that from HRSG I, then a damper is fully open. If the required mass flow rate is smaller than the available, then some of the exhaust gas is sent to the ambient. Finally, if the mass flow rate is smaller than required, then the burner is activated, supplying the deficit of exhaust gas to HRSG II, to enable required steam production.

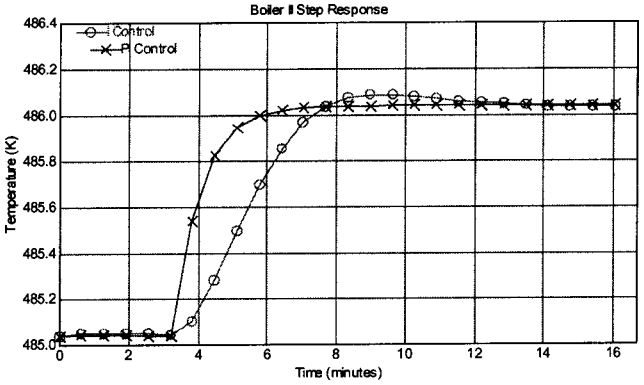


**Fig. 6 Response on the steam temperature in HRSG II for a step variation in the inlet flow of exhaust gas**

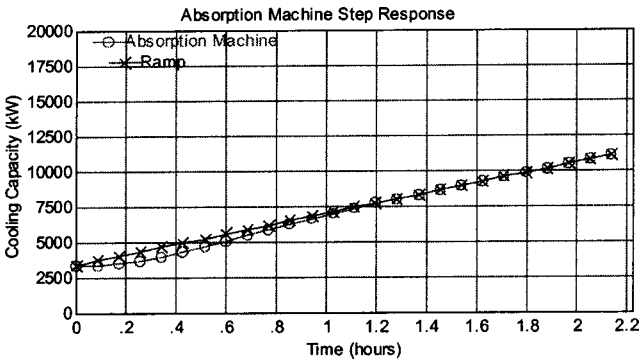


**Fig. 7 Capacity response of the controlled absorption-cooling machine to a ramp variation on the steam**

## Results

Three cases were simulated. In the first simulation (Sim I) typical power-, cooling-, and steam-demand curves for an average day in a facility [17,18] were adopted. A second and third simulation (Sim II and Sim III) were run, Sim II keeping the three different demands constant at a high value and Sim III keeping the cooling and steam demand constant while sharply reducing the electric load. For the simulations, the ambient temperature was assumed at 15°C. Figures 8–10 show the different demands for each of the three simulations.

Figure 11 displays the total power demand, the total power generated and the power generated by each of the turbines for Sim I. It can be seen that the power generated by both turbines met the total power demand. The system also met the power demand closely in Sim II and III [14]. Figure 12 plots the cooling demand

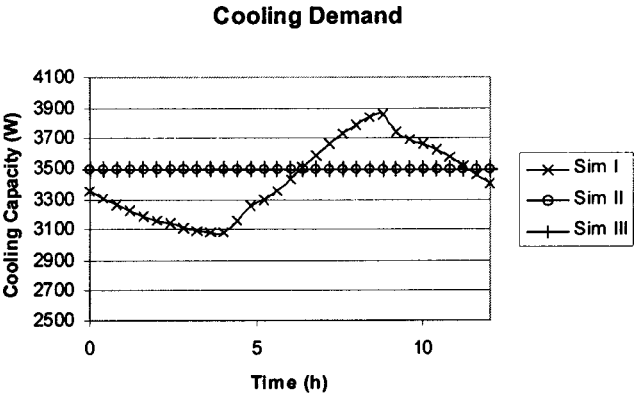


**Fig. 9 Cooling demand**

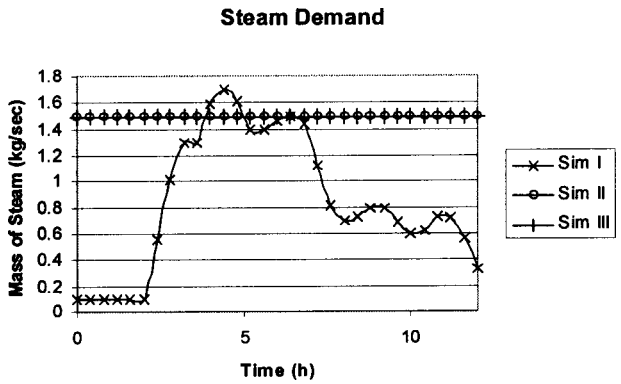


Fig. 10 Steam demand

and the cooling capacity with respect to time for Sim I. In Sim I, the steam demand was likewise followed closely. Similarly, all loads were met in Sim II and III.

The various efficiencies adopted for cogen merit evaluation are defined as follows:

$$\eta_{GT} = \frac{\int_0^{t_f} p_{GT} \cdot dt}{\int_0^{t_f} \dot{m}_f \cdot dt \cdot \Delta H} \tag{11}$$

$$\eta_p = \frac{\int_0^{t_f} (p_{GT} + p_{ST}) \cdot dt}{\int_0^{t_f} \dot{m}_f \cdot dt \cdot \Delta H} \tag{12}$$

$$\eta_{\text{total}} = \frac{\int_0^{t_f} (p_{GT} + p_{ST} + p_{H2}) \cdot dt}{\int_0^{t_f} \dot{m}_f \cdot dt \cdot \Delta H} \tag{13}$$

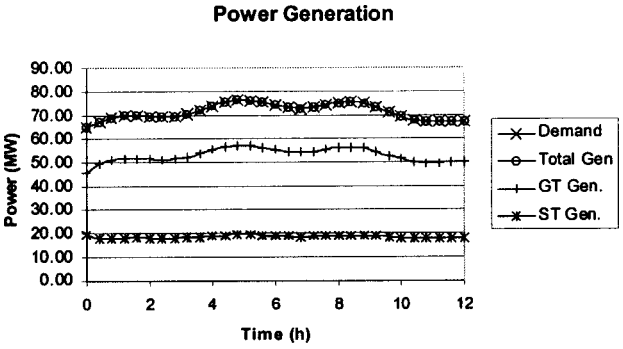


Fig. 11 Distribution of the power generation for Sim I

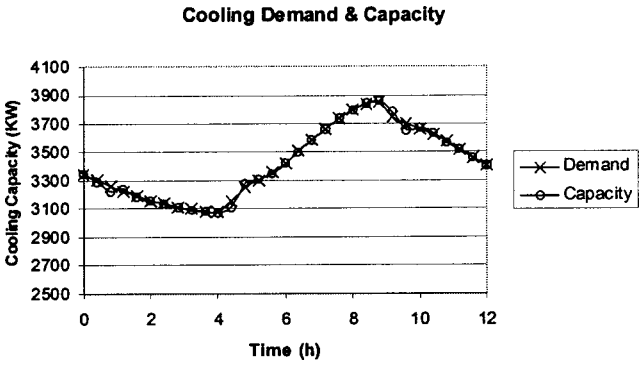


Fig. 12 Cooling demand and capacity for Sim I

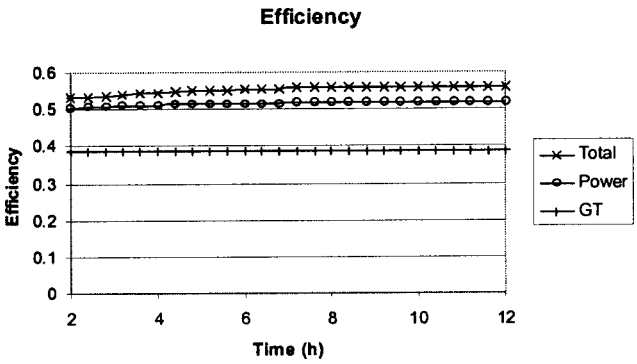


Fig. 13 Efficiencies for Sim I (typical demands)

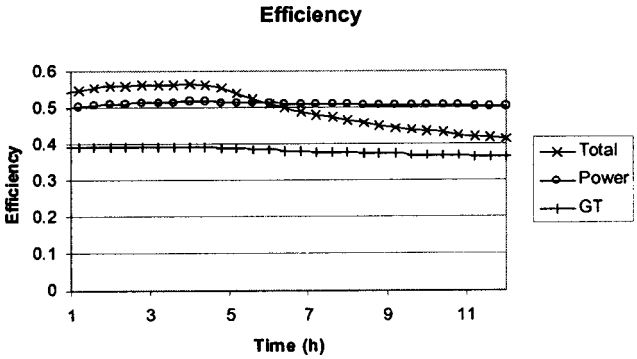


Fig. 14 Efficiency for Sim III

The efficiencies of the gas turbine, the power generation, and the total cogeneration plant (Eqs. 11–13) were calculated for the three simulations. Figure 13 displays the values for Sim I.

As expected, Fig. 14 shows how the total efficiency drops from approximately 56% to approximately 43% when the power demand falls. Since the exhaust gases from the power generation are not enough to meet the steam and cooling demand, the external burner has to start producing hot gases at a low efficiency, therefore, the efficiency decreases. The power and GT efficiencies tend to stay constant because the additional fuel consumed does not appear in their definition.

A fourth simulation was run were the power demand was kept constant at 70 MW and the ambient temperature varied from 40°C to −20°C. The controllers reacted in the following way: as the ambient temperature decreased, the steam turbine produced more power, and the gas turbine less power. This was done in order to decrease the consumption of fuel, while using the additional exhaust gas (due to increased air inlet density at low temperatures) to drive HRSGI to greater capacity.

## Conclusions

In the present work dynamic models are used to develop a control system for a cogeneration plant with the objective of meeting multiple transient demands, namely, power, heating, and cooling. The dynamic models vary in sophistication, but they retain one feature throughout: determining the constants that characterize the response of the equipment to step or ramp inputs would be a relatively straightforward experimental undertaking. The models apply to quasy steady-state operation.

Each subsystem has its own controls, and the fast response of the gas turbine, coupled with the thermal storage capabilities of the HRSGI, allowed implementation of a LQR that minimizes fuel input and departures of rotational speed from set point, while meeting the power demand. Hence, the power generated by the steam turbine is varied so that all the exhaust gases from the gas

turbine are used. Consequently, it is possible to eliminate the use of a duct or external burner before HRSG I most of the time.

Temporal simulations of the cogeneration system show that it is possible to meet all demands with conventional equipment and controls for the load profiles employed in this study. Future work should focus on more accurate modeling of the HRSG and on the possibilities afforded by setting controls off-site previous to equipment shipment and installation by means of simulations similar to that presented here.

## Acknowledgments

The authors gratefully acknowledge the support of the Penn State Mechanical Engineering Department and of Chevron Texaco in the form of teaching and research assistantships.

## Nomenclature

$a$ = ambient
$A$ = active heat transfer area, $m^2$
$c$ = fluid heat capacity, kJ/s-K, specific heat, kJ/kg-K
$\Delta h$ = enthalpy of vaporization, kJ/kg
$h$ = specific enthalpy, kJ/kg
HRSG = heat recovery steam generator
$K$, $k$, $k_1$, $k_2$, $k_3$ = constants
LQR = linear quadratic regulator
$m$ = mass, kg
$M$ = HRSG metal mass, kg
MHRSG = HRSG thermal mass, kg
$\dot{m}$ = mass flow rate, kg/s
$\dot{q}$ = capacity, kW
$\dot{Q}$ = heat transfer rate, kW
$r_{\mathrm{IGV}}$ = inlet guide vanes position.
SISO = single input single output
ST = steam turbine
$s$ = Laplace transform complex variable
$T$ = temperature, K
$T_{gp}$ = exhaust gas temperature at evaporator exit, K
$T_{\mathrm{evap}}$ = steam evaporation temperature, K
$\dot{U}$ = overall heat transfer coefficient
$u_e$ = specific internal energy, kJ/kg
$\eta$ = efficiency
$\varpi$ = angular velocity, rad/s

### Subscripts

$A$ = ambient
$AM$ = absorption cooling machine
$C$ = condenser
$f$ = fuel
$GT$ = gas turbine
$e$ = exit
$g$ = exhaust gas
$H$ = heat recovery steam generator, (HRSG)
$H_1$ = HRSG I
$H_2$ = HRSG II
$i$ = inlet
IGV = inlet guide vanes
$l$ = liquid
$M$ = HRSG metal mass
$p$ = exit of evaporator section of HRSG
$s$ = steam
Sat = saturated
$v$ = vapor

## References

[1] Langston, L., 2002, "Electrically Charged," Mech. Eng. (Am. Soc. Mech. Eng.), **124**, No. 6.
[2] Fairchild, P. D., Labinov, S. D., Zaltash, A., and Rizy, D. T., 2001, "Experimental and Theoretical Study of Microturbine-Based BCHP Sytem," ASME Winter Annual Meeting, Nov.
[3] Kim, B. H., Park, Y. M., Choi, M. S., and Lee, J. W., 1996, "LQG/LTR Robust Controller of Cogeneration Plant for Disturbance Rejection in Electric Frequency and Steam Pressure," Int. J. Elec. Power Energy Syst., **18**, No. 4, pp. 239–250.
[4] Perez-Blanco, H., and Albright, P., 2001, "Heat Recovery System Control Strategy to Meet Multiple Transient Demands," ASME Turbo Expo, Land Sea and Air 2001, June.
[5] Takahashi, K., Yasuda, T., Endoh, M., and Kurosaki, M., 2002, "Application of Dynamic Simulation to CAES G/T Control System Development," ASME TurboExpo 2002, pp. 153–161.
[6] Sigler, J., Erickson, D., and Perez-Blanco, H., 2001, "Gas Turbine Inlet Air Cooling Using Absorption Refrigeration: A Comparison Based on a Combined Cycle Process," ASME Turbo Expo, Land Sea and Air 2001, New Orleans, June.
[7] http://www.fwc.com/publications/heat/heat_pdf/9604-040.pdf
[8] Jeffs, E., 2002, "Siemens Offers Fast Track Maintenance to Their IPP Clients," Turbomachinery Int., **43**, No. 1, pp. 17–19.
[9] Camporeale, S. M., Fortunato, B., and Dumas, A., 1998, "Dyanamic Modeling and Control of Regenerative Gas Turbines," ASME Int. Gas Turbine and Aeroengine Congress and Exhibition, Sweden, June.
[10] Camporeale, S. M., Fortunato, B., and Mastrovito, M., 2002, "A High-Fidelity Real-Time Simulation Code of Gas Turbine Dynamics for Control Applications," ASME Turbo Expo 2002, The Netherlands, June.
[11] Franklin, G. F., Powell, J. D., and Workman, M., 1997, *Digital Control of Dynamic Systems*, 3rd ed., Addison Wesley.
[12] Marlin, T. E., 2000, *Design Process and Control Systems for Dynamic Performance*, 2nd ed., McGraw-Hill, New York.
[13] Ogata, K., 1997, *Modern Control Engineering*, 3rd ed., Prentice-Hall, Englewood Cliffs, NJ.
[14] Sancho-Bastos, F., 2002, "Simulation and Control Strategy of a High Efficiency Cogeneration System to Provide Power, Heating and Cooling," MS Thesis, The Pennsylvania State University.
[15] Bonert, R., and Hoops, G., 1990, "Stand Alone Induction Generator With Terminal Impedance Controller and no Turbine Controls," IEEE Trans. Energy Conv., **5**, No. 1, pp. 28–31.
[16] Perez-Blanco, H., and Hinojosa, L., 1999, "The Virtual Energy Laboratory (VEL), a Didactic Graphical Simulator for Thermal Design," ASME-IGTI Paper No. 99-GT-083, Turbomachinery Conference and Exposition, Indianapolis.
[17] Harrison, J. A., 1999, "Electric Power Systems," Prentice-Hall.
[18] McQuiston, F. C., Parker, J. D., and Spitler, J. D., 2000, *Heating, Ventilating, and Air Conditioning Analysis and Design*, 5th ed., Wiley, New York.

# Resistance Reduction in Pulsating Turbulent Pipe Flows

**Marcello Manna**[1]
Dipartiamento di Ingegneria Meccanica per l'Energetica,
Universitá degli Studi di Napoli "Federico II,"
Via Claudio 21,
80125 Naples, Italy
e-mail: manna@unina.it

**Andrea Vacca**
Dipartimento di Ingegneria Civile,
Seconda Universitá di Napoli,
Via Roma 29,
81031 Aversa, Italy
e-mail: vacca@unina.it

*The paper describes the effects of forced harmonic oscillations of fixed frequency and amplitudes in the range $\Lambda = U_m/U_b = 1-11$ on the characteristics of a turbulent pipe flow with a bulk Reynolds number of 5900. The resulting Stokes layer $\delta$ is a fraction of the pipe radius ($\chi = R/\delta = 53$) so that the vorticity associated to the oscillating motion is generated in a small near wall region. The analysis is carried out processing a set of statistically independent samples obtained from wall-resolved large eddy simulations (LES); time and space averaged global quantities, extracted for the sake of comparison with recent experimental data, confirm the presence of a non-negligible drag reduction phenomenon. Phase averaged profiles of the Reynolds stress tensor components provide valuable material for the comprehension of the effects of the time varying mean shear upon the near wall turbulent flow structures. The large scales of motion are directly computed through numerical integration of the space filtered three-dimensional Navier-Stokes equations with a spectrally accurate code; the subgrid scale terms are parametrized with a dynamic procedure.* [DOI: 10.1115/1.1789511]

## Introduction

Pulsating turbulent flows in pipes and conduits consist of a superimposition of an oscillatory component with a zero mean to a stationary flow, here and after referred to as the *current* component. They occur in many engineering applications such as high head hydraulic networks fed with reciprocating pumps and in the intake/exhaust manifolds of internal combustion engines, to name two relevant examples. A great deal of attention to this class of flow problems is also paid by the biomedical community for which pulsating turbulent pipe flow represents a valid test bench of blood and pulmonary flows.

Despite its great practical relevance little is known on the effects of unsteadiness upon the characteristics of even simple turbulent shear flows (like pipe or channels), so much that even the proper scaling variables are a matter of debate [1]. The time dependence imposed to the *current* flow increases significantly the complexity of the problem because of the necessity of the addition of a time and a length scale [2]. By doing so the relevant similarity parameters increase from 1 (in the case of steady flow) to 3 (if an oscillation is superimposed to the previous equilibrium flow).

There is a considerable literature available on pulsating flow in circular pipes and channels [1,3–9], which, however, do not cover the whole parameter space. More precisely, if the *current dominated* regime is almost exhaustively covered, the *wave dominated* one is not. While in the former case the time averaged wall shear stress is equal or larger, and in many instances significantly larger, than the equivalent value of the nonpulsating flow, in the latter it may attain values smaller than those pertaining to the steady case. The only investigations concerning these flow regimes that we are aware of are due to Refs. [6], [8]; they showed that for a given combination of the relevant nondimensional parameters the cycle-averaged wall shear stress is considerably reduced. In this work we investigate numerically a few flow conditions for which experiments indicate resistance reduction; calculated data confirm this phenomenon and provide some insight on the qualification of the near wall turbulent features.

This article is organized as follows: In the first two sections the problem formulation, the numerical method, and the flow conditions are detailed. The results section reports the computed data both in terms of global and local distributions; the analysis is conducted extracting steady and phase locked averaged data out of the simulation, as well as inspecting the response of the turbulent structures to the harmonic forcing. The quality of the computed data is assessed in the Appendix where a grid refinement study is carried out.

## Numerical Method

The model problem investigated herein is the fully developed flow through a circular pipe with diameter $D=2R$ subject to a harmonic forcing consisting of a time-dependent pressure gradient. The method of analysis is the numerical solution of the unsteady three-dimensional space filtered incompressible Navier-Stokes equations (large eddy simulation (LES)) in cylindrical coordinates. The operation of filtering the governing equations leads to large scale motion equations in terms of the resolved (denoted with a tilde) components $\tilde{\mathbf{u}}$ and $\tilde{p}$:

$$\frac{\partial \tilde{\mathbf{u}}}{\partial t} + \nabla \cdot \tilde{\mathbf{u}}\tilde{\mathbf{u}} = -\frac{1}{\rho}\nabla \tilde{p} + \frac{1}{\mathrm{Re}}\nabla \cdot \tilde{\mathbf{S}} - \frac{1}{\rho}\nabla \cdot \tau, \tag{1}$$

$$\nabla \cdot \tilde{\mathbf{u}} = 0, \tag{2}$$

in which $\tilde{\mathbf{S}}$ and $\tau = \rho(\widetilde{\mathbf{u}\mathbf{u}} - \tilde{\mathbf{u}}\tilde{\mathbf{u}})$ are the resolved rate of strain and subgrid-scale stress tensors. In the present paper we have added the isotropic part of $\tau$ to the pressure term and parametrized the anisotropic part of the subgrid-stress tensor by an eddy viscosity assumption,

$$\tau - \tfrac{1}{3}\mathrm{Tr}(\tau) = -2\mu_T \tilde{\mathbf{S}} = -2C(r,t)\rho\Delta|\tilde{\mathbf{S}}|\tilde{\mathbf{S}}, \tag{3}$$

with $|\tilde{\mathbf{S}}| = \sqrt{\mathrm{Tr}(2\tilde{\mathbf{S}}^2)}$, Tr the trace operator, and $\Delta$ the length associated with the grid scale filter. Following Lilly's modification [10] to the Germano model [11] and introducing a second coarser spatial (test) filter characterized by a width $\hat{\Delta}$, the scalar function $C(r,t)$ is given by

$$C(r,t) = -\frac{1}{2}\frac{\langle \mathrm{Tr}(\mathbf{LM})\rangle}{\langle \mathrm{Tr}(\mathbf{MM})\rangle}, \tag{4}$$

where $\langle\cdot\rangle$ denotes averaging in both azimuthal and axial directions and

$$\mathbf{L} = \widehat{\tilde{\mathbf{u}}\tilde{\mathbf{u}}} - \hat{\tilde{\mathbf{u}}}\hat{\tilde{\mathbf{u}}}, \quad \mathbf{M} = \hat{\Delta}^2|\hat{\tilde{\mathbf{S}}}|\hat{\tilde{\mathbf{S}}} - \Delta^2\widehat{|\tilde{\mathbf{S}}|\tilde{\mathbf{S}}}. \tag{5}$$

[1]To whom correspondence should be addressed.

Contributed by the International Gas Turbine Institute (IGTI) of THE AMERICAN SOCIETY OF MECHANICAL ENGINEERS for publication in the ASME JOURNAL OF ENGINEERING FOR GAS TURBINES AND POWER. Paper presented at the International Gas Turbine and Aeroengine Congress and Exhibition, Atlanta, GA, June 16–19, 2003, Paper No. 2003-GT-38630. Manuscript received by IGTI, Oct. 2002, final revision, Mar. 2003. Associate Editor: H. R. Simmons.

  

Sharp Fourier cutoff is used as both grid and test filter in streamwise and azimuthal directions, while no test filtering is performed in the radial direction. The test filter width is such that $\hat{\Delta}/\Delta = 2$. Details on the potential and limitations of the dynamic eddy viscosity procedure for both steady and unsteady channel flow problems are discussed in great depth in Refs. [9], [12], and will be omitted.

The governing equations (1) and (2) have been solved using the initial value solver developed and validated in Ref. [13]. The numerical method relies on a spectral Chebyshev multidomain algorithm for the inhomogeneous (radial) direction and Fourier decomposition for the homogeneous (streamwise and azimuthal) ones. Time integration is carried out with a Crank-Nicolson scheme for the viscous terms. The nonlinear convective terms, in skew-symmetric form, are treated explicitly with an Adams-Bashforth scheme. Periodic boundary conditions are applied in streamwise and azimuthal directions, and no-slip boundary conditions at the solid walls.

## Problem Formulation

In what follows, we shall denote with $u$, $v$, $w$ the streamwise ($z$), radial ($r$), and azimuthal ($\theta$) velocity components, respectively. As customary in equilibrium computations the flow is assumed periodic in the streamwise (and obviously azimuthal) direction, with a periodicity length $L_z$ equal to $4\pi R$. This value has been shown, in the steady case, to be sufficient for the streamwise two point correlations of the velocity components to drop to zero at the largest separation distance [14]. In the unsteady case, especially when a drag reduction phenomenon is expected, the $L_z$ value should be increased; we have thus computed the $\Lambda=1$ and $\Lambda=11$ cases with different lengths, viz. $L_z=4\pi R$ and $L_z=6\pi R$, respectively.

The flow is driven in the streamwise direction by a sinusoidal oscillatory in time external pressure gradient of appropriate mean value, amplitude, and pulsation $\Delta p/L_z[1+\alpha\cos(\omega t)]$. The constant part of the pressure gradient $\Delta p/L_z$, together with the amplitude $\alpha\Delta p/L_z$ and the pulsation $\omega$ of the oscillation, were selected in order to achieve flow conditions in full similarity with the experimental setup of Ref. [8]. As anticipated in the Introduction, pulsating flows are fully characterized by three nondimensional parameters, namely

$$\mathrm{Re}_b=\frac{U_b D}{\nu},\quad \mathrm{Re}_\delta=\frac{U_m\delta}{\nu},\quad \Lambda=\frac{U_m}{U_b},$$

where $\delta=2\nu/\omega$ is the Stokes layer thickness, $\nu$ the kinematic viscosity, $U_b$ the cross-sectional mean velocity, and $U_m$ the maximum value of the oscillatory flow at the center of the pipe. Other triplets are of course possible [1,8]. For the sake of simplicity, i.e., to closely follow the experimental setup of Ref. [8], we shall also refer to the following additional parameter $\chi=R/\delta$. Obviously $\chi=\mathrm{Re}_b\Lambda/(2\,\mathrm{Re}_\delta)$. For oscillating flow with a $\mathrm{Re}_\delta<200$ and $R/\delta>10$ the velocity field follows very closely the theoretical Stokes distribution [2]; this is usually referred to as the laminar regime. Increasing the Reynolds number up to the critical value of $\mathrm{Re}_\delta\sim550$, small perturbations appear superimposed to the Stokes flow (disturbed laminar regime) [15]. Experimental and numerical data indicate the occurrence of turbulent flow conditions in the decelerating phase of the cycle when $\mathrm{Re}_\delta>1000$ (intermittently turbulent regime); fully turbulent flows across the whole cycle occur instead for values of $\mathrm{Re}_\delta$ larger than 3500 [16]. According to Ref. [8] there are four main regimes that completely characterize this three-dimensional state space, namely

$$\text{current dominated},\ \Lambda\leqslant 1:\ \begin{cases}\text{high-frequency regimes } \mathrm{Re}_\delta<1000\\ \text{low-frequency regimes } \mathrm{Re}_\delta>1000\end{cases},$$

$$\text{wave dominated},\ \Lambda\geqslant 10:\ \begin{cases}\text{high-frequency regimes } \mathrm{Re}_\delta<1000\\ \text{low-frequency regimes } \mathrm{Re}_\delta>1000\end{cases}.$$

**Table 1 Flow regimes investigated**

| | $\mathrm{Re}_b$ | $\mathrm{Re}_\delta$ | $\Lambda$ |
|---|---|---|---|
| Steady flow | 5900 | 0 | 0 |
| Current dominated | 6100 | 56 | 1 |
| Wave dominated | 5546 | 572 | 11 |

Here and after we shall assume that the *current* flow is turbulent, that is, $\mathrm{Re}_b>2300$. Unlike the oscillating flow for which the stability region is defined by a single value of $\mathrm{Re}_\delta$ ($\mathrm{Re}_{\delta,cr}\sim550$ for $\chi>10$), in the case of pulsating pipe flows the transition conditions are defined by a combination of both $\mathrm{Re}_\delta$ and $\mathrm{Re}_b$ [8]. Experimental data [6,8] indicate that in the wave dominated regime and for $\mathrm{Re}_\delta<\mathrm{Re}_{\delta,cr}$ a drag reduction phenomenon occur. Thus we have focused our attention on three flow regimes detailed in Table 1. In the last case we expect drag reduction. Both unsteady conditions are characterized by $\chi=53$.

## Results

The calculations were performed over a total integration time of 330 nondimensional units $tU_b/D$. Data reduction was carried out processing 160 statistically independent samples separated in time by 0.4 nondimensional time units, both in the steady and unsteady cases. All quantities are space averaged in the homogeneous $z$ and $\theta$ directions; furthermore, time and/or phase averaging is applied to collect the statistics. In what follows, we shall indicate with an overline or capital letters the time and space averaged quantities, with $\langle\cdot\rangle$ the phase and space averaged quantities and with prime the perturbation from their time averages.

We begin this section presenting in Table 2 some global quantities, computed for the steady and oscillating flow conditions; all data are space and time averaged. As discussed in the previous section, the simulations are carried out with either a constant or time varying forcing term; thus the effective flow rates and bulk or centerline Reynolds numbers are a results of the calculations and as such cannot be round numbers. The differences between the computed values and the expected ones are of double nature, viz. numerical and physical. In the Appendix we provide exhaustive evidence that the former, i.e., the uncertainties associated with the modeled subgrid terms, are comfortably small, so that the drag reduction phenomena can be evaluated with good confidence.

Returning to the global values of Table 2, we first notice that the ratio $U_{cl}/U_b$ between the centerline and bulk velocities is in both cases very close to the steady pipe value. This indicates that, at least in an average sense, the velocity profiles are somewhat similar. As it will be shown later, the radial distributions of the mean velocity still retain a clearly turbulent shape, with a well defined logarithmic region. The displacement and momentum thicknesses defined as

$$\delta^*(D-\delta^*)=2\int_0^R\left(1-\frac{\overline{u}(r)}{U_c}\right)r\,dr,$$

**Table 2 Mean flow quantities**

| $\Lambda$ | $\mathrm{Re}_b$ | $U_{\mathrm{cl}}/U_b$ | $\delta^*/R$ | $\theta^*/R$ | $H$ |
|---|---|---|---|---|---|
| 0 | 5900 | 1.32 | 0.129 | 0.069 | 1.87 |
| 1 | 6100 | 1.32 | 0.129 | 0.069 | 1.88 |
| 11 | 5546 | 1.29 | 0.121 | 0.059 | 2.05 |
| $\Lambda$ | $\mathrm{Re}_b$ | $\mathrm{Re}_\tau$ | $\delta^+$ | $U_m/U_{\mathrm{cl}}$ | $C_f/C_f^B$ |
| 0 | 5900 | 192 | | | 1.06 |
| 1 | 6100 | 194 | 3.67 | 0.76 | 0.90 |
| 11 | 5546 | 160 | 3.01 | 8.50 | 0.73 |

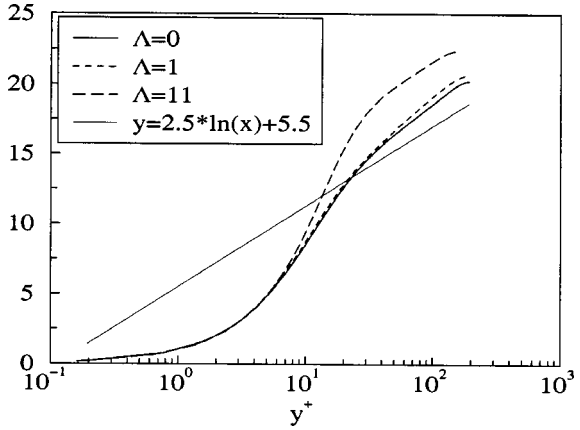


**Fig. 1 Mean velocity profiles**

$$\theta^*(D-\theta^*)=2\int_0^R\left(1-\frac{\overline{u}(r)}{U_c}\right)\frac{\overline{u}(r)}{U_c}rdr, \quad H=\frac{\delta^*}{\theta^*}$$

also show insignificant variations, while their ratio, i.e., the shape factor $H$ is seen to increase of about 9% in the case $\Lambda=11$, and to remain equal to the steady value in the case $\Lambda=1$. Recalling that the laminar value is 3.37 we may already foresee the occurrence of some resistance reduction; in fact, the skin friction coefficient $C_f=\tau_w/1/2\rho U_b^2$ is smaller than the corresponding Blasius value ($C_f^B=0.079\,\mathrm{Re}_b^{-1/4}$) for both unsteady cases (10% for $\Lambda=1$ and 27% for $\Lambda=11$). This is in accordance with the experimental data [8,6].

The radial distribution of the time averaged mean velocity is shown in inner coordinates in Fig. 1 for the three cases. In what follows we shall indicate with $y=(R-r)/R$ the distance from the solid wall. The wall values used for the normalization are space (in the homogeneous directions) and time averaged. The deviation from the logarithmic distribution $\overline{u}^+=1/\kappa\ln(y^+)+B$ (with $\kappa=0.41$ and $B=5.5$) is similar to the one observed in the experiments and calculations reported in Ref. [14].

In the current-dominated case the profile essentially collapses on the steady distribution. This is a nontrivial result, since for $\Lambda>1$ the amplitude of the velocity oscillation becomes greater than the local velocity close to the wall and thus flow reversal occurs. The somewhat surprising insensitivity of the mean flow profile to the imposed oscillations, in the case $\Lambda\sim1$, has not yet received, in the author's opinion, a convincing explanation. Tu et al. [3] have argued that whenever the oscillating frequency $f_o=D/(TU_b)$ is significantly below the bursting frequency $f_b$ there should be no effect of the pulsation on the mean velocity profile. In view of this argument, and since our data do not satisfy their criterion ($f_o\sim0.61>f_b\sim0.2$ [3]), we would expect to observe some modifications in the $\overline{u}$ radial distributions, which is apparently not the case. The absence of any significant departure from the steady condition, in the current dominated high-frequency regime, has also been observed in plane channel geometries both experimentally [1] and numerically [9] in similar flow conditions ($\mathrm{Re}_{cl}=8500$, $U_m/U_{cl}=0.64$, $\delta^+=8.1$ in Ref. [1] and $\mathrm{Re}_{cl}=7250$, $U_m/U_{cl}=0.75$, $\delta^+=4.4$ in Ref. [9]).

The oscillating case with $\Lambda=11$ still presents a logarithmic region with a slope $1/\kappa$ essentially equal to the corresponding steady slope but characterized by an upward shift. This shift and the consequent increase of the viscous sublayer thickness is typical of drag reducing flows.

Figure 2 shows, in inner coordinates, the radial distribution of the root-mean-square values of the fluctuating velocity components $\overline{u'u'}^+$, $\overline{v'v'}^+$, and $\overline{w'w'}^+$, for both oscillating cases. Also reported in the same figure are the steady distributions together with reference experimental and numerical data [1,9]. For the

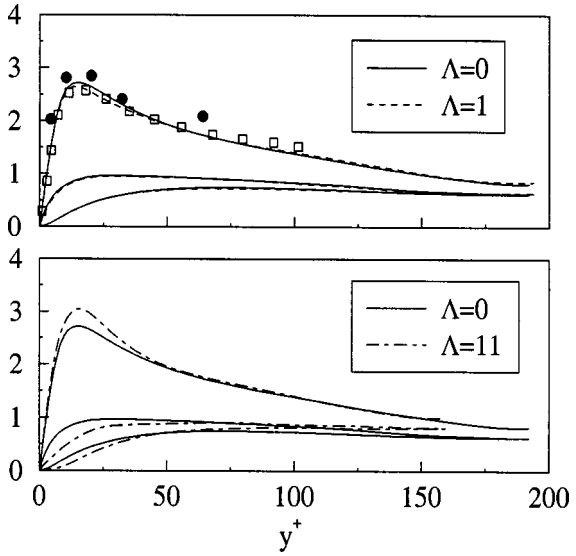


**Fig. 2 Mean turbulent intensities; ● experiments [1]; □ LES [9]**

lowest value of the amplitude $\Lambda=1$ all components show a good correspondence with the steady profiles, except for the maximum value of $\overline{u'u'}^+$. The largest difference is, however, small, i.e., $\sim3\%$. The above picture changes quite substantially in the $\Lambda=11$ case; on a general ground we note that the net effect of the large amplitude unsteady forcing on the normal stresses extends up to $y^+\sim50$, and basically consists of a reduction of all components. There are no experimental data available to corroborate these trends.

In Fig. 3 the space and time averaged data of the turbulent (resolved and subgrid-scale stress) and viscous stresses are reported for all simulations, in inner coordinates. The current dominated case does not show any significant departure from the steady flow distribution, either of the turbulent shear stress $\overline{u'v'}^+$ or of the viscous one $d\overline{u}^+/dy^+$. This is in accordance with the global data previously discussed. In the wave dominated regime, on the other hand, a remarkable reduction of $\overline{u'v'}^+$ across the whole pipe radius occurs. The inner coordinates representation highlights that the turbulent stress reduction is uniform, i.e., the whole wall layer is witnessing a weaker response of the turbulence to the unsteady forcing. However, $\overline{u'v'}^+$ is not at all negligible and thus the flow is definitely not in a reverse transition stage; note that neither is the extent of the overlap region substan-

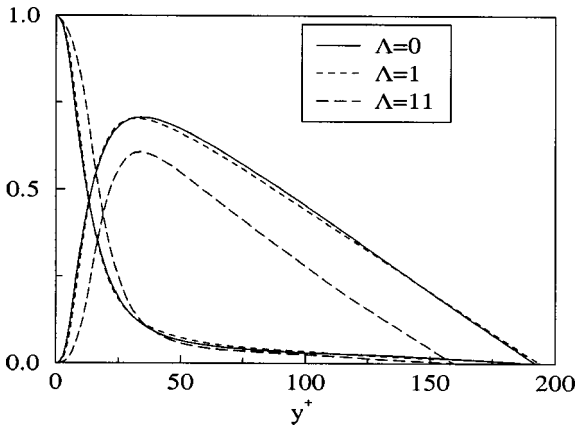


**Fig. 3 Turbulent and viscous shear stress**

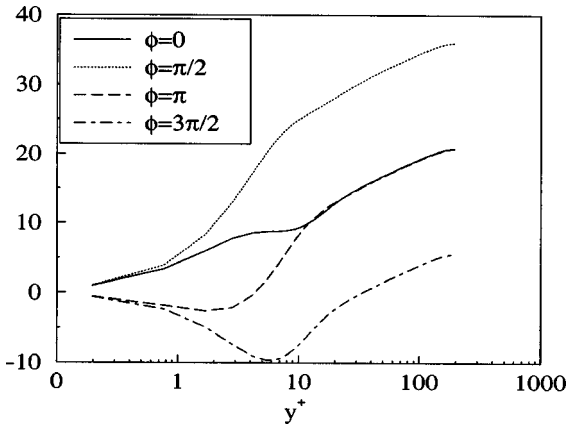


**Fig. 4 Phase averaged velocity profiles in inner coordinates ($\Lambda=1$)**

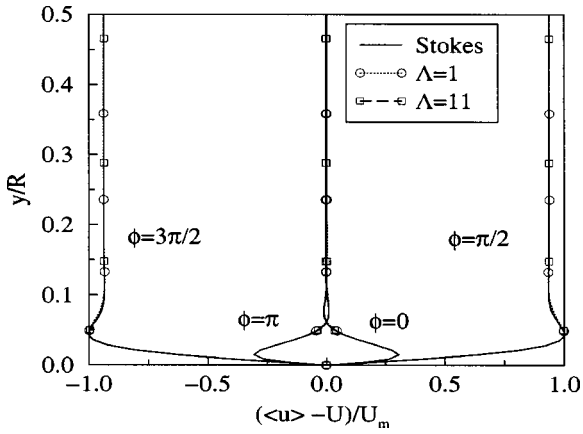


**Fig. 6 Phase averaged oscillating streamwise velocity profiles**

tially altered nor the location of the maximum Reynolds stress modified. Figures 4 and 5 show the phase averaged velocity profiles in inner coordinates for both cases $\Lambda=1$ and $\Lambda=11$; the phase angles $\phi(t/T)$ are defined as $\phi(t/T)=2\pi t/T$ with $t/T=0, \frac{1}{4}, \frac{1}{2}, \frac{3}{4}$. Given the high value of $\chi$, we may expect the logarithmic region not to be altered by the pulsating flow and its virtual origin to be displaced by a constant amount for each phase value. This conjecture is based on the unproven assumption that current and oscillating flows decouple for large enough values of $(R-r)/\delta$. The data seem to corroborate the above assumption outside the wall layer. The magnitude of the shift is obviously phase and $\Lambda$ dependent as clearly highlighted by the two graphs. Evident is the reverse flow region occurring at $\phi=\pi$ and $\phi=3/2\pi$ for both $\Lambda$ values. As concerns the wall layer we note that substantial differences take place; interesting are the local over- and undershoots at $y^+\sim 8$ which are addressed later on. We next further elaborate on the flow features decoupling. To this aim we present in Fig. 6 the phase averaged pure oscillating (i.e., obtained subtracting the mean value from the phase averaged ones) profiles of the streamwise velocity component as a function of the nondimensional coordinate $y$, for both cases. Reminding that for $\chi>10$, the critical value of $\mathrm{Re}_\delta$ defining the transitional value below which the oscillating flow is in laminar regimes is roughly 550, and because the present value of $\mathrm{Re}_\delta$ is much smaller ($\Lambda=1$) or comparable with ($\Lambda=11$) the critical value, it would be reasonable to assume the oscillating component of the flow to be in laminar regime. Therefore, the same figure reports, the Stokes solution computed with $\chi=53$, which is the only relevant nondimensional parameter in laminar flow conditions. In either cases both the amplitudes and the phase angles are very close to the Stokes values. Note that the maximum positive and negative velocity values occur at $y\sim 0.05$ corresponding to $y^+\sim 8$; thus the local peaks in the velocity representation of Figs. 4 and 5 are definitely connected with the underlying Stokes-like behavior. In the current dominated regime, the laminar behavior of the oscillating part of the flow has already been observed, in plane channel geometries, by Refs. [1] and [9]. According to Ref. [1] whenever the Stokes layer is sufficiently small, i.e., $\delta^+\leqslant 6$, there is no interaction of the unsteady vorticity (by diffusion) from the wall with the buffer layer; hence the only energy-transfer mechanism is of viscous diffusion nature. This result is consistent with the observed insensitivity of the time averaged turbulent quantities in the wall layer previously discussed. A Stokes-like behavior is also clear in the wave dominated regime. Therefore it appears that even though the oscillating component modifies substantially the time averaged quantities, the pulsating flow is not altered by the turbulent motion.

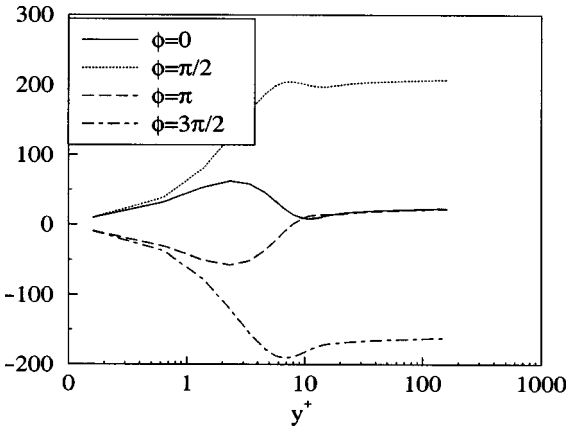


**Fig. 5 Phase averaged velocity profiles in inner coordinates ($\Lambda=11$)**

Figures 7 and 8 compare the phase averaged turbulence intensities distributions with the mean values. Apparently the radial component is the most affected by the oscillation cycle; in fact the perturbation from the mean at the position of the maximum value is non-negligible, as confirmed by Table 3. With reference to the streamwise normal stress, we further note that unlike the $\Lambda=1$ case, for which moderate changes within the phase interval occur, the $\Lambda=11$ data exhibit more pronounced variations. Not only are the amplitudes of those oscillations increased, but also the extent of the radial region affected by the these oscillations is enlarged. For $\Lambda=11$ the location of the peak moves away from the wall and its value decreases to disappear at $\phi=3/2\pi$; simultaneously the appearance of a secondary peak which will soon substitute the primary peak to close the cycle dynamic is remarked.

Figures 9 and 10 compare the phase averaged turbulent shear stress distributions with the mean values. The lines represent the sum of the supergrid and subgrid stress tensor components; incidentally we remark that the ratio of the subgrid to the total (resolved+SGS) stress is not exceeding 10% across the pipe radius. This is certainly due to the satisfactory grid resolution in both homogeneous directions. Similarly to the previously discussed Figs. 7 and 8 the phase variations of the turbulent stress in the $\Lambda=1$ case is significantly smaller than those pertaining to the $\Lambda=11$ case. Thus all time and phase averaged Reynolds stress components show a relative insensitivity to the harmonic oscillation of the driving force. In the case $\Lambda=11$ the changes during the oscillating period appear more pronounced. With reference to the beginning of the accelerating phase ($\phi=0$) negative values of the total shear stress are observed close to the wall, i.e., $y^+\sim 10$; at $\phi=\pi/2$ the above region is seen to increase in size. The negative

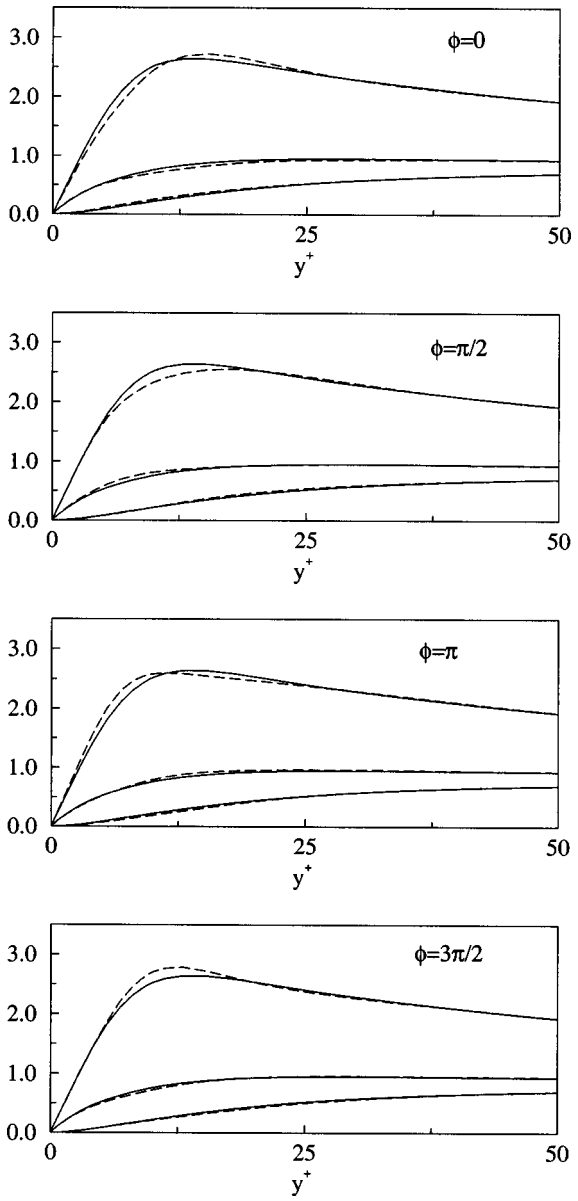


**Fig. 7 Phase averaged (– – –) and mean (——) turbulent intensities for $\Lambda=1$**

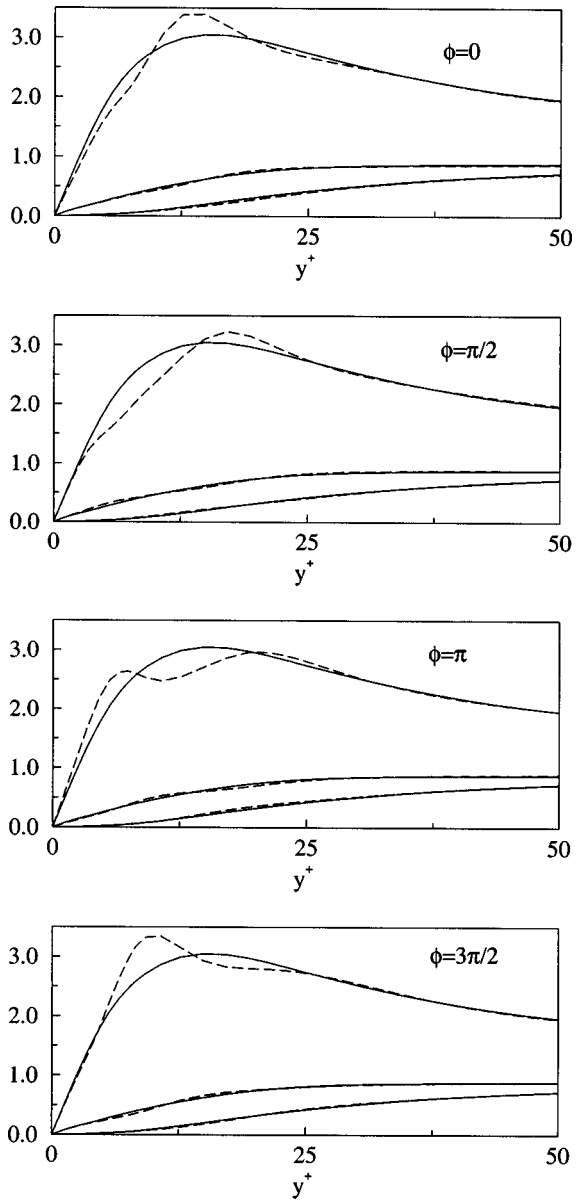


**Fig. 8 Phase averaged (– – –) and mean (——) turbulent intensities for $\Lambda=11$**

peak value position shifts towards the pipe core. The oscillations weaken considerably for $y^+>30$; this behavior is also shared by the $\Lambda=1$ case.

In Figs. 11 and 12 the temporal evolutions of both oscillating streamwise velocity and Reynolds stress tensor components at the position of maximum $\overline{u'u'}$ are shown; the data, normalized with the time mean values, are presented as a function of the phase angle $\phi$. As already evident from Fig. 6, the $u-\bar{u}$ fluctuation has an almost perfect harmonic shape, with a $\pi/2$ phase shift with respect to the driving forcing term. There is no appreciable effect of the $\Lambda$ parameter upon the shape of the profiles, except, of course, for the amplitudes which roughly differ by a factor 10. The scaling factor is not exactly 11 because the graphs pertain to the peak locations of $\overline{u'u'}$ which occur at slightly different radial positions (see caption of Fig. 11). Conversely, the Reynolds stress profiles show the appearance of temporal modes with higher (than 1) frequency contents and non-negligible amplitudes, which increase with $\Lambda$. Note the asymmetry of the positive and negative peaks. In addition there is considerable variation in the phase angles for the two $\Lambda$ cases. Thus the amplitude increase of the forcing induces a different response of the second-order moments despite the integral time scale of the mean flows is unchanged. We can therefore conclude that the response of the smaller turbulence scales to the external forcing is affected by the amplitude of the

**Table 3 Normal stress phase variation at $y^+=13$ ($\Lambda=1$) and $y^+=14.8$ ($\Lambda=11$)**

| $\Lambda=1$ | | | | |
|---|---|---|---|---|
| Phase angle | 0 | $\pi/2$ | $\pi$ | $3\pi/2$ |
| $\overline{u'u'}$ | 1.9% | −5.7% | −2.0% | 5.5% |
| $\overline{v'v'}$ | 10.6% | 4.7% | −11.0% | −6.4% |
| $\overline{w'w'}$ | −4.9% | 3.3% | 6.0% | −2.7% |
| $\Lambda=11$ | | | | |
| Phase angle | 0 | $\pi/2$ | $\pi$ | $3\pi/2$ |
| $\overline{u'u'}$ | 11.3% | 1.9% | −11.2% | −3.6% |
| $\overline{v'v'}$ | 13.0% | 7.2% | 13.5% | −11.8% |
| $\overline{w'w'}$ | 0% | −4.7% | −2.6% | 6.7% |

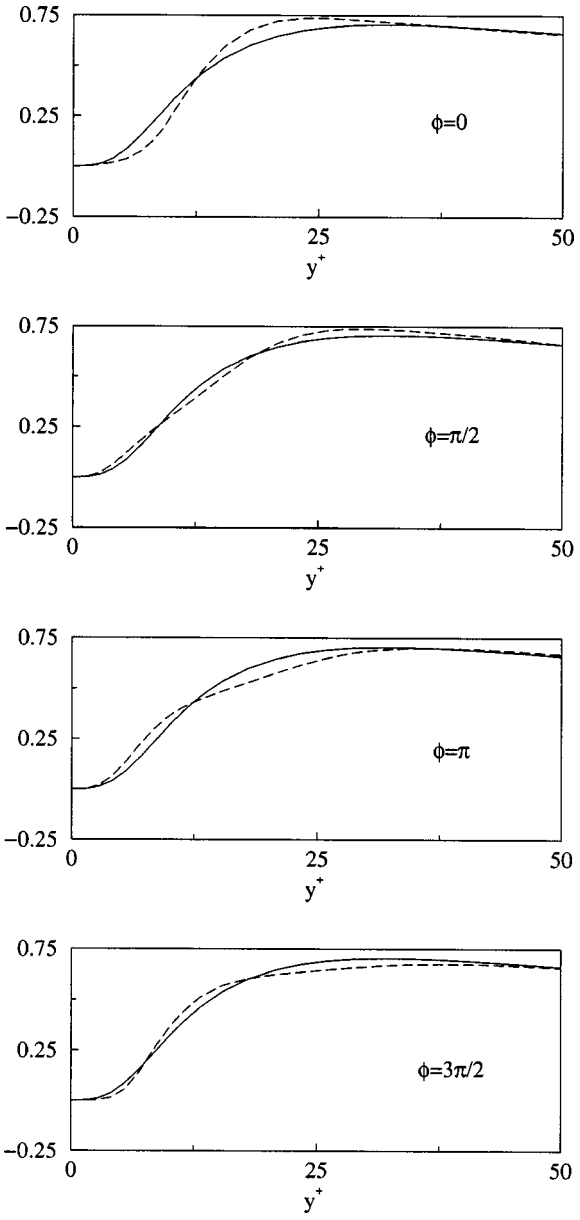


**Fig. 9 Phase averaged (– – –) and mean (——) turbulent shear stress (resolved+SGS) for $\Lambda=1$**

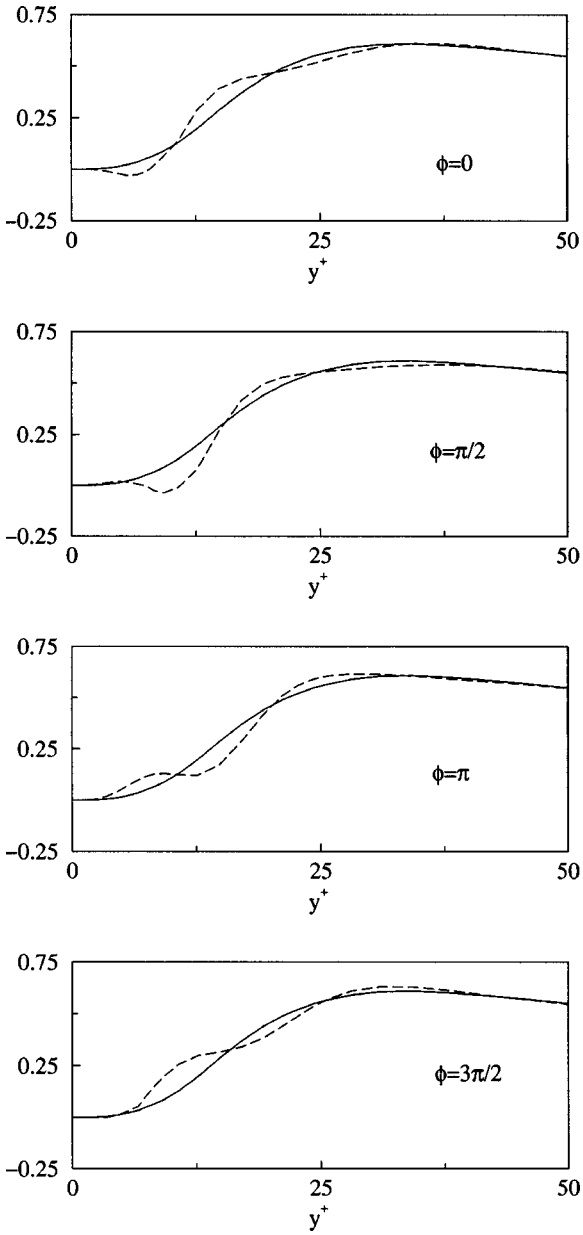


**Fig. 10 Phase averaged (– – –) and mean (——) turbulent shear stress (resolved+SGS) for $\Lambda=11$**

oscillating component, to which different integral time scales, viz. $\delta/U_m$, pertain. Additional data processing is required to establish this matter.

## Conclusions

Numerical data obtained from wall resolved large eddy simulations of pulsating turbulent pipe flows have been carried out in a range of amplitudes for a fixed frequency. The data indicate that, unlike the current dominated cases, in the wave dominated regimes the time and space averaged resistance may be substantially smaller than the corresponding nonpulsating case at the same bulk Reynolds number. This is in agreement with the experimental data of Refs. [8] and [6], who also observed drag reduction. The analysis of the radial distributions of the time and ensemble averaged quantities reveals that the resistance reduction is not due to a flow laminarization as suggested in Ref. [8]; turbulence remains sustained across the oscillation cycle although the harmonic forcing reduces the Reynolds stress tensor components to some nonnegligible extent. The oscillating flows obey the Stokes distribution even in the presence of resistance reduction. The phase locked analysis of the normal and shear stresses shows the appearance of temporal modes with frequencies higher than one of nonnegligible energy content which increases with $\Lambda$.

## Acknowledgments

The computing time on the SUN multiprocessor machine provided by the CDS (Centro servizi Didattico Scientifico) of the University of Naples *Federico II* and the technical support of Mr. Raffaele Ciotola are greatly acknowledged. Experimental data were kindly provided by the research group of the Department of Hydrodynamics and Water Resources, Technical University of Denmark ([8]).

## Appendix: Grid Refinement Study

In this appendix we check the quality of the computations performing a grid refinement study. The mesh used to build the sta-

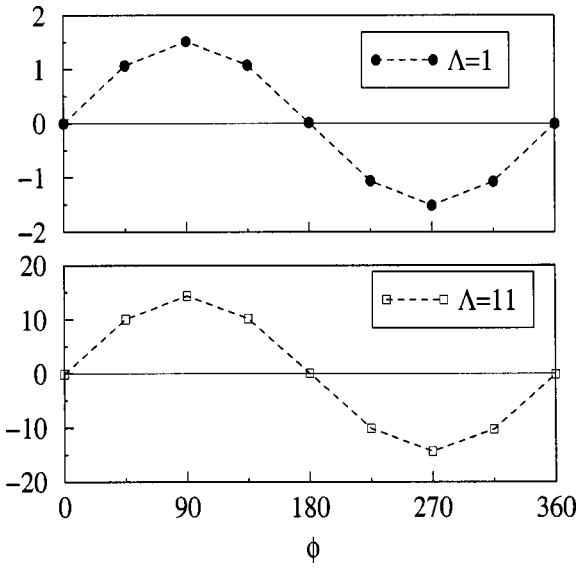


**Fig. 11 Temporal evolution of the phase averaged oscillating streamwise velocity component $(\langle u\rangle-\bar{u})/\bar{u}$; top $\Lambda=1$, $y^+=13$; bottom $\Lambda=11$, $y^+=14.8$**

tistics in both steady and current dominated regimes consists of six subdomains, each of which is characterized by 48 Fourier modes in the homogeneous (longitudinal and azimuthal) directions and 12 Chebyshev modes in the radial one. In the case of the wave dominated regime, we have kept the mesh spacing constant and therefore, since the pipe length was incremented, the number of nodes in the streamwise direction was increased by a factor 1.5. An analogous resolution has been used in the calculations of the pulsating turbulent channel flow of Ref. [9].

The accuracy of the data is tested performing the grid refinement study only in the steady case, and increasing the number of modes in the homogeneous $z$ and $\theta$ directions. In what follows we shall analyze the results computed with the grid systems described in Table 4. Statistics for all the grids were collected over identical averaging times, so that the sample size plays no role in the present discussion. The time steps of the simulation is $\Delta t^+ = \Delta t \overline{u}_\tau / D = 0.08\times 10^{-3}$. When the grid was refined in the azimuthal direction the time step was reduced to $\Delta t^+ = 0.03 \times 10^{-3}$.

**Table 4 Characteristics of the reference and refined grids**

| | Grid $(z,r,\theta)$ | $\Delta z^+$ | $\Delta r^+$ |
|---|---|---|---|
| LES1 | $6\times(48\times12\times48)$ | 49.7 | $0.19\leqslant\Delta r^+\leqslant7.8$ |
| LES2 | $6\times(48\times12\times96)$ | 49.7 | $0.19\leqslant\Delta r^+\leqslant7.8$ |
| LES3 | $6\times(96\times12\times48)$ | 24.9 | $0.19\leqslant\Delta r^+\leqslant7.8$ |
| | $(r\Delta\theta)^+_{\max}$ | | |
| LES1 | $(r\Delta\theta)^+_{\max}=26.0$ | | |
| LES2 | $(r\Delta\theta)^+_{\max}=13.0$ | | |
| LES3 | $(r\Delta\theta)^+_{\max}=26.0$ | | |

In Table 5 we analyzed the effect of the grid refinement, on some global parameters, and compare them with reference data ($u_\tau^B$ denotes the Blasius value of the friction velocity). The largest differences are of the order of a few percent.

In Fig. 13 we compare the mean velocity profiles and root-mean-square streamwise velocity distributions, in inner coordinates, with reference experimental and numerical data of Ref. [14]. Within plotting accuracy, there is essentially no difference

**Table 5 Mean flow quantities: steady flow conditions**

| | $\mathrm{Re}_b$ | $\mathrm{Re}_{\mathrm{cl}}$ | $\mathrm{Re}_\tau$ | $U_{\mathrm{cl}}/U_b$ |
|---|---|---|---|---|
| LES1 | 5900 | 7788 | 192 | 1.32 |
| LES2 | 5900 | 7664 | 191 | 1.30 |
| LES3 | 5900 | 7775 | 197 | 1.31 |
| DNS [14] | 5300 | 6950 | 180 | 1.31 |
| HWA [14] | 5600 | 7350 | 190 | 1.31 |
| | $u_\tau/u_\tau^B$ | $\delta^*/R$ | $\theta^*/R$ | $H$ |
| LES1 | 0.971 | 0.129 | 0.069 | 1.87 |
| LES2 | 0.962 | 0.122 | 0.066 | 1.85 |
| LES3 | 0.986 | 0.127 | 0.070 | 1.84 |
| DNS [14] | 0.998 | 0.127 | 0.068 | 1.82 |
| HWA [14] | 1.003 | 0.128 | 0.070 | 1.82 |

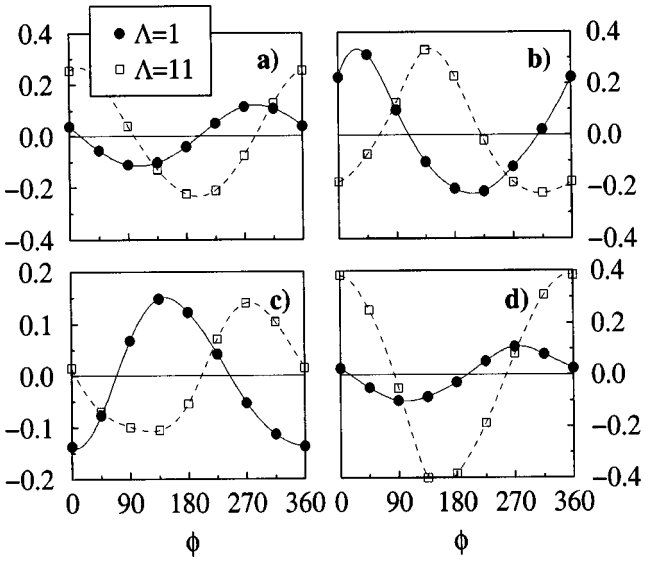


**Fig. 12 Temporal evolution of the phase averaged Reynolds stresses $(\langle u_i' u_j'\rangle-\overline{u_i'u_j'})/\overline{u_i'u_j'}$; $\Lambda=1$, $y^+=13$; $\Lambda=11$, $y^+=14.8$; (*a*) $i=j=1$; (*b*) $i=j=2$; (*c*) $i=j=3$; (*d*) $i=1$, $j=2$**

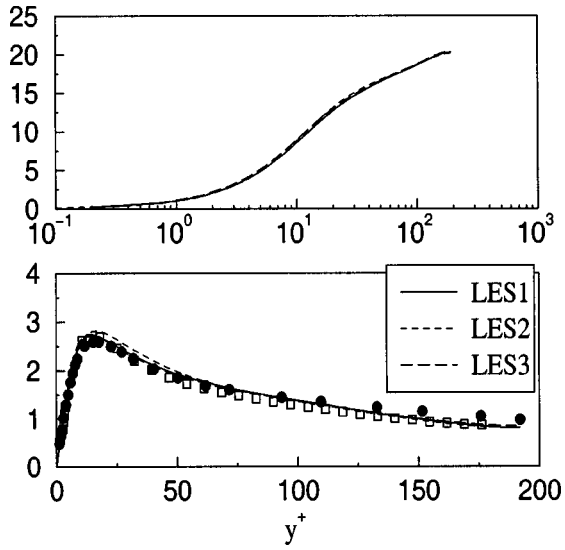


**Fig. 13 Streamwise velocity profiles (top); Reynolds stress trace (bottom). ● experiments [14]; □ DNS [14].**

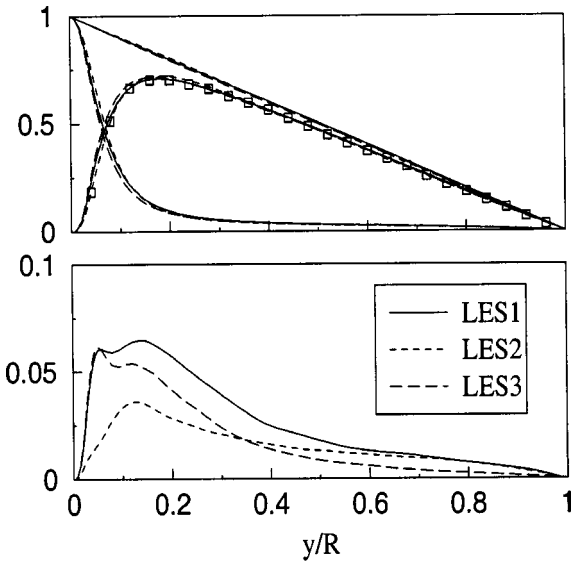


**Fig. 14 Turbulent and viscous stresses (top); SGS stresses (bottom); □ DNS [14]**

between LES1 and LES3, while LES2 differs from the other two in the wall layer by some small amount (the largest difference is 2.5% at $y^+ \sim 15$). We have therefore good confidence in the quality of the present results.

Figure 14 depicts, in inner coordinates, the viscous stress, the resolved+SGS turbulent stress along with the total ones (top half figure), together with the DNS data of Ref. [14]. Shown also are the subgrid stress distributions (bottom half); note the different scale on the $y$ axis. Interesting is the expected decrease of the SGS part in the outer layer when the streamwise resolution is increased (LES1 versus LES3) and the reverse phenomenon characterizing the azimuthally more resolved grid (LES2). This is an effect of the cylindrical coordinates which puts into evidence the role of the streamwise box size when $r \to 0$; conversely in the buffer layer there is clearly a demand for an enhanced resolution to properly describe the streaks dynamics.

From the foregoing we may argue that the multiple scale characteristics of this kind of wall bounded shear flows would be better accounted for, in a LES framework, with a nonconforming technology. Work is in progress in this direction.

## Nomenclature

### Dimensional Quantities

$\delta = \sqrt{2\nu/\omega}$ = Stokes layer thickness
$\delta^*$ = displacement thickness
$\Delta$ = filter size
$\kappa$ = von Kármán constant
$\mu_T$ = turbulent viscosity
$\nu$ = kinematic viscosity
$p$ = static pressure
$\theta$ = momentum thickness
$r$ = radial coordinate
$r\theta$ = azimuthal coordinate
$R, D$ = pipe radius, diameter
$\rho$ = fluid density
$\mathbf{S}$ = rate of strain tensor
$t$ = time coordinate
$T$ = oscillating period
$\tau$ = subgrid scale stress tensor
$u_z, u, u_1$ = axial velocity component
$u_r, v, u_2$ = radial velocity component
$u_\theta, w, u_3$ = azimuthal velocity component
$\mathbf{u}$ = velocity vector
$u_\tau$ = wall friction velocity
$y$ = distance from the wall
$z$ = axial coordinate
$\omega = 2\pi/T$ = oscillating frequency

### Nondimensional Quantities

$C_f$ = friction coefficient
$\phi = 2\pi t/T$ = phase angle
$H$ = shape factor
$\Lambda = U_m/U_b$ = amplitude oscillation parameter
$\mathrm{Re}_b = U_b D/\nu$ = bulk Reynolds number
$\mathrm{Re}_\tau = u_\tau R/\nu$ = Reynolds number
$\mathrm{Re}_\delta = U_m \delta/\nu$ = oscillating Reynolds number
$\chi = R/\delta$ = Stokes parameter

### Subscripts

$b$ = bulk, area averaged value
cl = centerline value
$m$ = maximum oscillatory value at $r = 0$
$w$ = wall value

### Superscripts

$+$ = wall coordinates
$'$ = fluctuating component
$B$ = Blasius value

### Averaging Operators

$\bar{\cdot}$ = time and space averaged
$\langle \cdot \rangle$ = phase and space averaged
$\tilde{\cdot}$ = resolved quantity

## References


[1] Tardu, S. F., Binder, G., and Blackwelder, R. F., 1994, "Turbulent Channel Flow With Large-Amplitude Velocity Oscillations," J. Fluid Mech., **267**, pp. 109–151.
[2] Akhavan, R., Kamm, R. D., and Shapiro, A. H., 1991, "An Investigation of Transition to Turbulence in Bounded Oscillatory Stokes Flows Part 1. Experiments," J. Fluid Mech., **225**, pp. 395–442.
[3] Tu, S. W., and Ramaprian, B. R., 1983, "Fully Developed Periodic Turbulent Pipe Flow. Part 1. Main Experimental Results and Comparison With Predictions," J. Fluid Mech., **137**, pp. 31–58.
[4] Tu, S. W., and Ramaprian, B. R., 1983, "Fully Developed Periodic Turbulent Pipe Flow. Part 2. The Detailed Structure of the Flow," J. Fluid Mech., **137**, pp. 59–81.
[5] Mao, Z. X., and Hanratty, T. J., 1986, "Studies of the Wall Shear Stress in a Turbulent Pulsating Pipe Flow," J. Fluid Mech., **170**, pp. 545–565.
[6] Mao, Z. X., and Hanratty, T. J., 1994, "Influence of Large-Amplitude Oscillations on Turbulent Drag," AIChE J., **40**(10), pp. 1601–1610.
[7] Tardu, S. F., and Binder, G., 1993, "Wall Shear Stress Modulation in Unsteady Turbulent Channel Flow With High Imposed Frequencies," Phys. Fluids, **5**, pp. 2028–2034.
[8] Lodahl, C. R., Sumer, B. M., and Fredosoe, J., 1998, "Turbulent Combined Oscillatory Flow and Current in a Pipe," J. Fluid Mech., **373**, pp. 313–348.
[9] Scotti, A., and Piomelli, U., 2001, "Numerical Simulation of Pulsating Turbulent Channel Flow," Phys. Fluids, **13**(5), pp. 1367–1384.
[10] Lilly, D. K., 1992, "A Proposed Modification of the Germano Subgrid-Scale Closure Method," Phys. Fluids, **4**(3), pp. 633–635.
[11] Germano, M., Piomelli, U., Moin, P., and Cabot, W. H., 1991, "A Dynamic Subgrid Scale Eddy Viscosity Model," Phys. Fluids, **3**, pp. 1760–1767.
[12] Piomelli, U., 1993, "High Reynolds Number Calculations Using the Dynamic Subgrid Scale Stress Model," Phys. Fluids, **5**(6), 1484–1490.
[13] Manna, M., and Vacca, A., 1999, "An Efficient Method for the Solution of the Incompressible Navier-Stokes Equations in Cylindrical Geometries," J. Comput. Phys., **151**, pp. 563–584.
[14] Eggels, J. G. M., Unger, F., Weiss, M. H., Westerweel, J., Adrian, R. J., Friedrich, R., and Nieuwstadt, F. T. M., 1994, "Fully Developed Turbulent Pipe Flow: A Comparison Between Direct Numerical Simulation and Experiments," J. Fluid Mech., **268**, pp. 175–209.
[15] Hino, M., Sawamoto, M., and Takasu, S., 1976, "Experiments on Transition to Turbulence in an Oscillatory Pipe Flow," J. Fluid Mech., **75**, pp. 193–207.
[16] Jensen, B., Sumer, B., and Fredosoe, J., 1989, "Turbulent Oscillatory Boundary Layers at High Reynolds Number," J. Fluid Mech., **206**, pp. 265–297.

# Feasibility Analysis for the Rotordynamic Performance of API617

**Hyeong-Joon Ahn**
e-mail: ahj@amed.snu.ac.kr

**Eric H. Maslen**
e-mail: ehm7s@virginia.edu

**Tetsuya Iwasaki**
e-mail: iwasaki@virginia.edu
Department of Mechanical and Aerospace Engineering,
University of Virginia,
122 Engineer's Way,
Charlottesville, VA 22904-4746

*The rotordynamic performance of API 617 standards provides two primary requirements. First, the standard stipulates system damping near the expected operating speed range. Second, the standard requires a specific bound of the worst case unbalance response. The problem this poses for machine designers is (1) feasibility: can bearings be designed for a given rotor to meet API 617 and (2) if so, how can these bearings be designed? Our primary effort in this research is to convert the API requirements to a control design objective for a bearing. This permits direct assessment of the feasible design problem as well as providing a means to synthesize optimal bearing dynamics. In addition to providing synthesis of magnetic bearings, the resulting bearing transfer functions give direct guidance to selection of more conventional fluid film or rolling element bearings.*
[DOI: 10.1115/1.1789492]

## Introduction

The rotordynamic performance of API 617 standards provides two primary requirements. First, the standard stipulates system damping near the expected operating speed range. This takes the form of a combination of damping requirements and separation margins, depending on where the system critical speeds lie relative to the operating range. Second, the standard requires a specific bound on the worst case unbalance response.

The problem this poses for machine designers is (1) feasibility: can bearings be designed for a given rotor to meet API 617 and (2) if so, how can these bearings be designed? This paper examines the feasibility problem. One possible approach to assessing feasibility would be to pick bearings, to model the final machine (including bearings), and to assess the resulting API 617 compliance. The problem with this approach is that the choice of bearing dictates the outcome and it may be difficult to select an optimal bearing for API 617. Consequently, failure of this test does not imply non-feasibility.

An alternative approach is to convert the API requirements to a control design problem. With this approach, it is not necessary to predesign or preselect the bearings: we can determine directly whether a bearing set exists that satisfies the control design problem. In this case, feasibility will not assure that a given type of bearing (fluid film, rolling element, . . . ) can meet the API standard, but it does imply that the requirement can be met through some mechanism (perhaps a magnetic bearing).

**Some Tools.** Constructing this control design problem requires three important mathematical tools: $H_\infty$ norms [1], $\mu$-analysis [2], and $\mu$ synthesis [3]. We present here a very brief synopsis: the full story can be found in Ref. [4].

The $H_\infty$ norm measures generalized peak of gain. Assume a dynamic system $y=G(s;N)f$. The response is a function of complex frequency, $s$, and may also depend on parameter(s) $N$ (which might be the rotor spin rate, for instance). At any given $s=j\omega$, the steady-state response $y$ to sinusoidal input $f$ is computed by evaluating the matrix function $G(j\omega)$. Because $G$ is a matrix, the gain from $f$ to $y$ depends on the direction of $f$. A bound on how large $y$ can be for a bounded $f$ is the maximum singular value $\bar{\sigma}(G(j\omega;N))$ [5]. The maximum singular value can be viewed as a composite summary of each of the individual transfer functions which constitute $G$.

The $H_\infty$ norm of $G(s;N)$ is the largest maximum singular value of $G(j\omega;N)$ when $\omega$ ranges from zero to infinity. If $G$ were a scalar function of $s$, then the $H_\infty$ norm of $G(s)$ would be the highest point on the Bode magnitude plot of $G(s)$.

$\mu$-analysis considers the stability problem where some stable system $G(s)$ is connected to some other uncertain (but stable) system $W(s)\Delta$, as shown in Fig. 1. Here, $W(s)$ describes the expected frequency response character of the uncertain system while $\Delta$ is a bound on its gain. For instance, if a rotor is connected to a seal with unknown damping: $-5\ \text{Nsec/m} < C_{\text{seal}} < 25\ \text{Nsec/m}$, then $G(s)$ would contain the nominal damping (10 Nsec/m), $W(s)$ might be the transfer function $15s$, and $\Delta$ would be $\pm 1$.

Now, ask: Is the closed loop system stable for all possible $\Delta$, where $\Delta$ is bounded (typically by $\pm 1$)? Using a very central result of control theory called the small gain theorem [6], $\mu$-analysis returns a figure of merit, $\mu$. If $\mu<1$, then the system is stable for all allowed values of $\Delta$ while if $\mu>1$, it may not be.

Finally, $\mu$-synthesis constructs a controller for an uncertain plant ($G(s)$ connected to $W(s)\Delta$) so that the resulting closed loop system will be stable for all possible $\Delta$. Therefore, the resulting closed-loop system is *robust* to uncertainties described by $\Delta$.

**The Feasibility Problem.** The unbalance response requirement is exactly a formal $H_\infty$ performance measure, but the separation margin requirement is not analytic so it is not simple to directly formulate this requirement as a linear system analysis problem. In this paper, the separation margin requirement is replaced by a pole placement problem: relatively large damping near the operating range. The pole placement problem can be approximated as a robust stability problem with frequency shaped uncertain modal damping. Since the unbalance response requirement can already be expressed as an $H_\infty$ problem, the two API 617 requirements can be cast as a single $\mu$-analysis problem. This permits direct assessment of the feasible design problem and also provides a means to synthesize optimal bearing dynamics. In addition to providing synthesis of magnetic bearings, the resulting bearing transfer functions may give direct guidance to selection of more conventional fluid film or rolling element bearings.

## The API 617 Standards [7]

Given a rotor-bearing system with a probe at a certain (important) location, one can experimentally find the vibration amplitude

Contributed by the International Gas Turbine Institute (IGTI) of THE AMERICAN SOCIETY OF MECHANICAL ENGINEERS for publication in the ASME JOURNAL OF ENGINEERING FOR GAS TURBINES AND POWER. Paper presented at the International Gas Turbine and Aeroengine Congress and Exhibition, Atlanta, GA, June 16–19, 2003, Paper No. 2003-GT-38596. Manuscript received by IGTI, October 2002, final revision, March 2003. Associate Editor: H. R. Simmons.

  

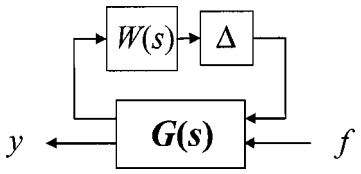


**Fig. 1 An example of an uncertain system**

$A$ [m] at the probe as a function of rotor speed $N$ [rpm]. If the $A(N)$ curve is plotted, it will typically have some peaks as illustrated by Fig. 2. The rotor speed at which a peak occurs is called a resonance speed (labeled by $N_R$ in Fig. 2). For each resonance speed, the amplification factor ($AF$) is defined by

$$AF \equiv \frac{N_R}{N_1 - N_2}, \quad A(N_1) = A(N_2) = \frac{A(N_R)}{\sqrt{2}}, \quad N_1 < N_2. \quad (1)$$

$AF$ is defined for each resonance speed $N_R$ so we may denote its dependence by $AF(N_R)$. If $AF$ is larger than 2.5 at some resonance speed $N_R$, then it is called a critical speed.

The procedure for checking satisfaction of the API 617 requirements is as follows.

1. Find resonance speeds by simply running the shaft or by analytical methods based on mathematical model of the system.
2. For each resonance speed, place unbalance weights at the locations that affect the resonance mode most adversely. The unbalance amount must be within the range specified below.
3. Run the shaft and measure the vibration amplitude at the probe at each rotor speed in the neighborhood of $N_R$.
4. Calculate $AF$ at $N_R$ and check if it is below the specified level, which is described below in detail.

**Unbalance Response Requirement.** The unbalance weight(s) must be chosen and placed so that the peak vibration amplitudes at the probes are not larger than

$$L_v := 25.4 \sqrt{\frac{12\,000}{N}}\, \mu\text{m}, \quad (2)$$

where $N$ [rpm] is the operating speed nearest to $N_R$. Given journal loadings $W$, the unbalance $mr$ at each plane has to be in the following interval:

$$2U_{\max} \leqslant mr \leqslant 8U_{\max}, \quad U_{\max} := 6350 \frac{W[\text{kg}]}{N_{\max}[\text{rpm}]} [\text{g}\cdot\text{mm}]. \quad (3)$$

When the probes are at the limit $L_v$, the rotor vibration cannot exceed 75% of the clearance at any location. Since the unbalance response requirement stipulates a specific bound on the worst case unbalance excitation, it is easily converted into a standard $H_\infty$ analysis problem: a norm bounded output for a worst case norm bounded input.

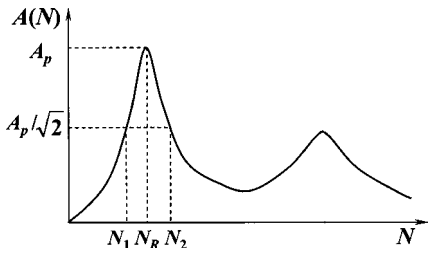


**Fig. 2 Relation between the rotor speed *N* and vibration *A***

**Separation Margin Requirement.** Let the operating speed range of the rotor-bearing system be given by $N_l \leqslant N \leqslant N_u$. The system passes the test at the resonance speed $N_R$ if one of the following conditions holds:

$$N_R \leqslant 0.83N_l, \quad N_R \geqslant 1.27N_u: \quad \text{no bound} \quad (4a)$$

$$0.83N_l \leqslant N_R \leqslant N_l: \frac{N_l - N_R}{N_l} \geqslant 0.17\left(\frac{AF - 2.5}{AF - 1.5}\right) \quad (4b)$$

$$N_l \leqslant N_R \leqslant 1.1N_u: AF \leqslant 2.5 \quad (4c)$$

$$1.1N_u \leqslant N_R \leqslant 1.27N_u: \frac{N_R - N_u}{0.1N_u} \geqslant 1 + 1.7\left(\frac{AF - 2.5}{AF - 1.5}\right) \quad (4d)$$

Clearly, the separation margin requirement is not analytic so it is difficult to formulate this as a linear system analysis problem.

## Interpreting the Separation Margin

Suppose that the rotor-bearing system at an operating speed in the neighborhood of a certain resonance speed $N_R$ can be adequately described by $y = G(s)f$ where $f \in \mathcal{R}^{nf}$ is the unbalance force vector and $y \in \mathcal{R}^{ny}$ is the displacement output at the probe. Assume that the transfer function $G(s)$ can be described by

$$M\ddot{q} + D\dot{q} + Kq = f, \quad y = Cq. \quad (5)$$

Let $\Phi$ be the unitary modal matrix that simultaneously diagonalizes $M$ and $K$:

$$\Phi^T M \Phi = I, \quad \Phi^T K \Phi = \Lambda, \quad \Phi^T D \Phi = Z, \quad (6)$$

where $\Lambda$ is a real diagonal matrix with non-negative entries. Assuming Rayleigh damping, the matrix $Z$ is also diagonal. In the modal coordinates $\xi := \Phi^T q$, the system can be described by

$$\ddot{\xi} + Z\dot{\xi} + \Lambda\xi = \Phi^T f, \quad y = C\Phi\xi \quad (7)$$

Suppose that the $i$th mode frequency corresponds to the resonance speed $N_R$. The unbalance force that would most excite the $i$th mode is given by

$$f(t) = mr\omega_e^2 \phi_i \sin \omega t, \quad (8)$$

where the excitation frequency $\omega_e$ is in the neighborhood of the resonance frequency and $\phi_i$ is the $i$th column of $\Phi$.

The steady state response $y$ to this excitation is

$$y(t) = |G(j\omega)\omega^2 \phi_i| mr \sin(\omega t + \varphi), \quad (9)$$

where $\varphi$ is an appropriate phase. Then the amplification factor at $N_R$ can be calculated using

$$M(s) := s^2 G(s) \phi_i = \frac{C\phi_i s^2}{s^2 + Z_i s + \Lambda_i}, \quad (10)$$

where $Z_i$ and $\Lambda_i$ are the $i$th diagonal entries of $Z$ and $\Lambda$.

Consider a second order system of (7) that has a resonance near the operating range,

$$M(s) := \frac{ks^2}{s^2 + 2\zeta\omega_n s + \omega_n^2}. \quad (11)$$

Assuming a small damping $\zeta$, we will calculate the $AF$ at the resonance frequency. Note that

$$|M(s)|^2 = \frac{k^2\omega^4}{(\omega_n^2 - \omega^2)^2 + 4\zeta^2\omega_n^2\omega^2}. \quad (12)$$

It is readily deduced that $|M(j\omega)|$ has the following peak:

$$\|M\|_\infty = \frac{k}{2\zeta\sqrt{1-\zeta^2}}, \quad N_R = \frac{\omega_n}{\sqrt{1-2\zeta^2}}. \quad (13)$$

The frequencies at half power are given by

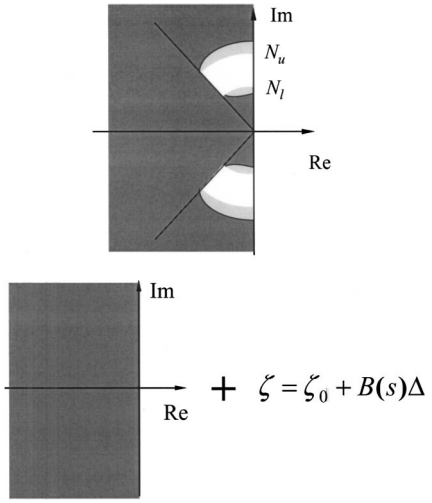


**Fig. 3 Interpretation of the separation margin (*a*) pole placement, (*b*) robust stability problem**

$$N_{1,2} := \frac{\omega_n}{\sqrt{1-2\zeta^2 \mp 2\zeta\sqrt{1-\zeta^2}}}. \tag{14}$$

Hence, the $AF$ may be approximated as

$$AF \doteq \frac{N_R}{N_2 - N_1} \approx \frac{\sqrt{1+\eta}-\sqrt{1-\eta}}{\sqrt{1-\eta^2}}, \quad \eta := \frac{2\zeta\sqrt{1-\zeta^2}}{1-2\zeta^2}. \tag{15}$$

When the damping is larger than 0.383, the resonance peak is not sharp enough to have a half-power frequency $N_{1,2}$ and hence the corresponding $AF$ may be considered as zero. In this manner, the separation margin requirement (4) can be converted exactly into a damping requirement.

**Pole Placement Problem.** The separation margin requirement can be described as the intersection of the following three conditions: system stability, required damping and operating range; that is, the system should be stable in the region of (4*a*) and should have the required damping near operating speed specified by (4*b*)–(4*d*). Therefore, the separation margin requires placement of the poles in the shaded region in Fig. 3.

**Robust Stability With Uncertain Modal Damping.** It is reasonable to ask, "Why is there a separation margin requirement in API 617: Is not the unbalance response requirement sufficient?" The separation margin requirement is derived from long experience with this class of machines. A likely linear systems interpretation of this requirement is that, if the amplification factor is high near operating speed, then small changes in system damping could abruptly lead to unsatisfactory unbalance response. Such a machine would be overly sensitive: it lacks robustness to uncertain modal damping.

This heuristic argument motivates the ensuing effort to substitute a robust stability analysis for the pole placement problem described above. The pole placement problem of Fig. 3 can be approximated as robust stability with frequency shaped uncertain modal damping, which is a stability problem of a system $\ddot{\xi} + 2\zeta\omega_n\dot{\xi} + \omega^2\xi = \phi f$ with uncertain modal damping $\zeta = \zeta_0 + B(s)$ as shown in Fig. 3. Here $B(s)$ captures the rather complicated speed dependency of (4): essentially a band pass filter encompassing the operating speed range (Fig. 6).

## Weighting Scheme for API 617 Requirements

The unbalance response requirement can be described by a transfer function $(SG)$ for the response from unbalance excitation $d$ to responses $e$ as shown in Fig. 4. In addition, a bearing specification in the form of a maximum force according to worst unbalance force $(T)$ is required. Therefore, a relatively simple weighting scheme for the API problem is

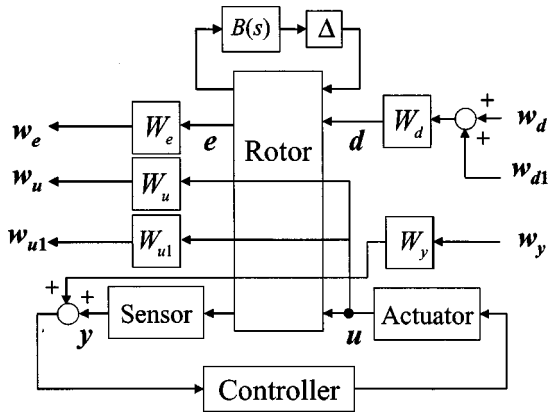


**Fig. 4 A weighting scheme for API 617 standard**

$$\begin{bmatrix} e(s) \\ u(s) \end{bmatrix} = \begin{bmatrix} SG(s) \\ T(s) \end{bmatrix} [d(s)]. \tag{16}$$

Input $w_w$ and output $w_{u1}$ are introduced to eliminate singularity in this simple formulation. In addition, another disturbance input is introduced to make the unbalance response requirement independent of the bearing specification. The inputs $w_d$, $w_{d1}$, and $w_y$ and output $w_e$, $w_u$, and $w_{u1}$ are chosen and augmented with the corresponding weighting functions. A frequency shaped modal uncertain damping $B(s)$ for the separation margin is introduced. The resulting augmented general plant is shown in Fig. 4.

Since the unbalance requirement and actuator specification are not related to the uncertain modal damping, the resulting $\mu$-synthesis for the API 617 standards can be expressed by

$$\min_k \text{ subject to} \|W_e S_0 G_0 W_d\|_\infty < \gamma, \quad \|W_u T_0 W_{d1}\|_\infty < \gamma, \quad \|W_{u1} C S_0 W_y\|_\infty < \gamma, \quad \text{and} \quad \mu_\Delta(H_{rs}) < 1. \tag{17}$$

The subscript 0 denotes the nominal transfer function ($\Delta = 0$) and $H_{rs}$ is defined as the transfer function seen by $\Delta$. This problem is not tractable but can be approximated by

$$\min_k \max_\Delta \mu(H), H(s) = \begin{bmatrix} W_e SGW_d & W_e SGW_{d1} & W_e TW_y \\ W_u TW_d & W_u TW_{d1} & W_u CSW_y \\ W_{u1} TW_d & W_{u1} TW_{d1} & W_{u1} CSW_y \end{bmatrix}, \tag{18}$$

where the underlying uncertainty structure for the $\mu(\cdot)$ operation is $\Delta_p := \text{diag}(\Delta_{p1}, \Delta_{p2}, \Delta_{p3})$, which is the performance block. This robust performance problem is further converted to a robust stability problem via the main loop theorem and then to the $D$-scaling $\mu$ upper bound problem for numerical tractability [4,8,9].

The weighting functions related to the unbalance requirement are $W_d$ and $W_e$: $W_d$ is for the worst case unbalance excitation and $W_e$ is for the allowed response. The unbalance excitation is proportional to the square of the rotor speed and is specified up to the maximum operating speed. This is well approximated by a 5th order Butterworth filter indicated in Fig. 5, which quickly attenuates the unbalance excitation above the maximum running speed. The allowed maximum response $W_e$ is given by

$$W_e^{-1} = \min(L_v, 0.75 C_{cl}). \tag{19}$$

If the bearing device is assumed to have a first order characteristic (constant capacity out to some typical cut-off frequency), the weighting $W_u$ for maximum bearing force can be approximated by

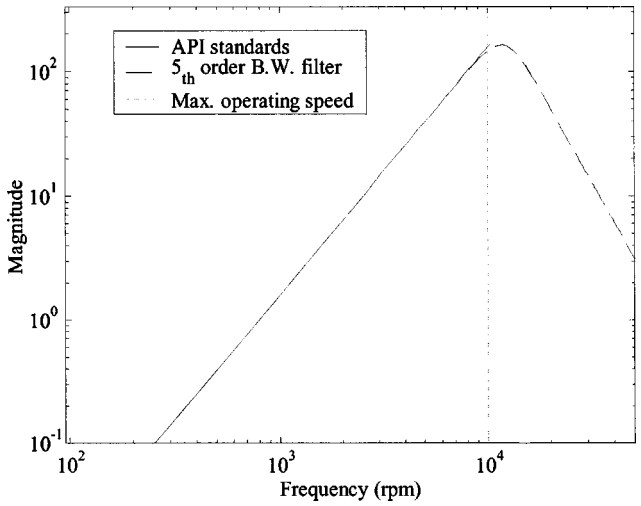


**Fig. 5 A weighting function for the worst case unbalance excitation**

$$W_u = \frac{(s+\omega_b)}{F_{\max}\omega_b(\varepsilon s+1)}, \tag{20}$$

where $\omega_b$ is the bandwidth of the bearing device. The factor $\varepsilon$ is simply chosen to be much smaller than $1/\omega_b$ and much smaller than $1/N_u$. For a fluid film bearing, $\omega_b$ may be taken as infinite so that $W_u$ becomes constant. $W_{u1}$ and $W_y$ are chosen as constants to have a small effect on the synthesis at first. However, these weighting functions will later play a significant role in reducing the conservativeness by weighting the control effort.

The frequency shaping implied by (4) for $B(s)$ can be approximated using a 7th order elliptic filter whose gain outside of the separation margin range is less than 0.001. The filter coefficients are determined through a least square algorithm [10]. The normalized separation margin requirement and an example elliptic filter are shown in Fig. 6.

## Example

The example system consists of a rotor, three sensors, and three AMBs as shown in Fig. 7. For simplicity, it is assumed that the three probe points and unbalance excitation locations for API standards are the same as the sensor and bearing locations.

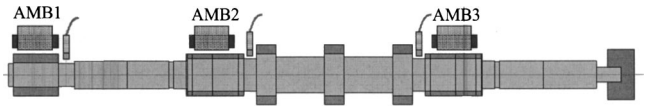


**Fig. 7 Example rotor model**

The rotor has three actuator sleeves, three midspan unbalance disks, and a coupling at the right end. The total mass is about 85 kg and total length is about 2.7 m. The first four natural frequencies in RPM are 8600, 19,268, 37,997, and 60,648.

The operating range is selected to be 8,000–10,000 rpm so that the first bending natural frequency is within the operating range. The calculated vibration limit at probes is 0.028 mm and the worst case unbalance is 14.4 g-mm from (2) and (3). The AMB capacities are assumed 6300 N up to the 265 Hz power signal bandwidth.

**Results.** To check if the API standards can be satisfied with these bearings, a synthesis is performed with small constant weightings for the control effort. If a rotor is assessed (by our method) to be infeasible for API standards, then we can be reasonably certain that there is no fluid film bearing which will meet API. On the other hand, if there is a controller, then there may be a bearing which also meets API, and it may be possible to approximate the computed controller as stiffness and damping of a bearing.

The peak $\mu$ value is 0.1574 and the API standard can be satisfied with the given actuator as shown in Fig. 8. The robust stability denotes the separation margin requirement, the nominal performance of the (1,1) diagonal block is for the unbalance response requirement and the nominal performance of the (2,2) diagonal block is for the actuator specification. The robust stability has most influence on the peak $\mu$ value near the operating range.

Figure 9 shows the pole/zero maps of the augmented open-loop plant and closed-loop system. The seven poles along the required damping line for the separation margin in Fig. 9(a) are related to the 7th order elliptic filter for the uncertain modal damping, while the three poles along the maximum operating range are related to the $5_{th}$ order Butterworth filter for the unbalance excitation. In addition, there is a lightly damped first bending mode (8600 rpm) near the imaginary axis, which is denoted by original pole. The pole of the lightly damped first bending mode moves farther be-

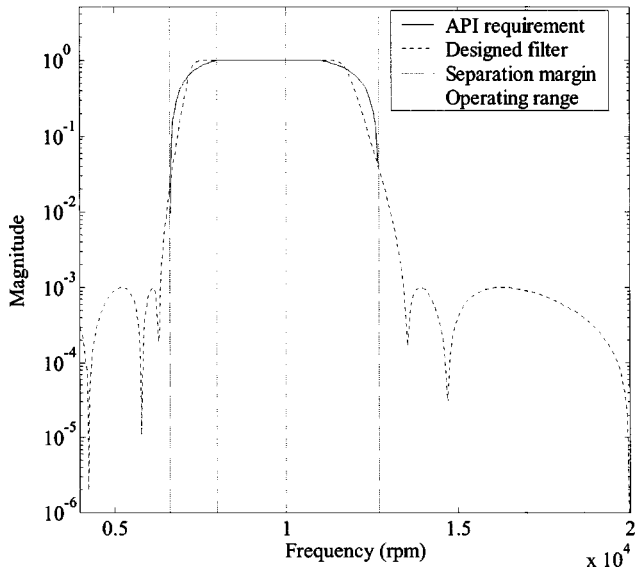


**Fig. 6 7th order elliptic filter for the uncertain modal damping**

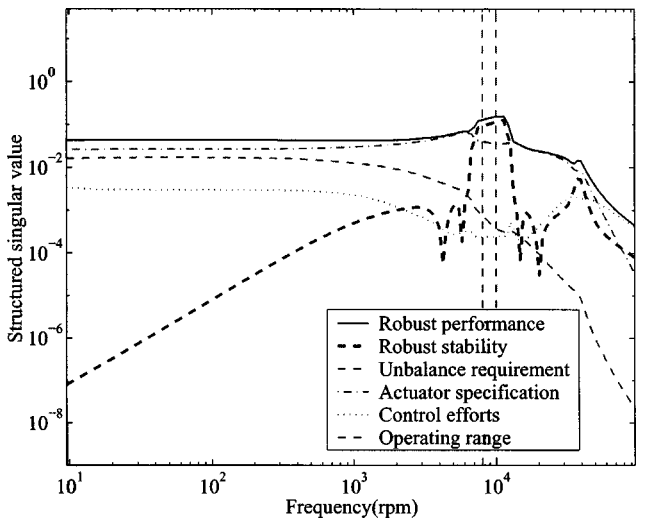


**Fig. 8 Results with the original actuator**

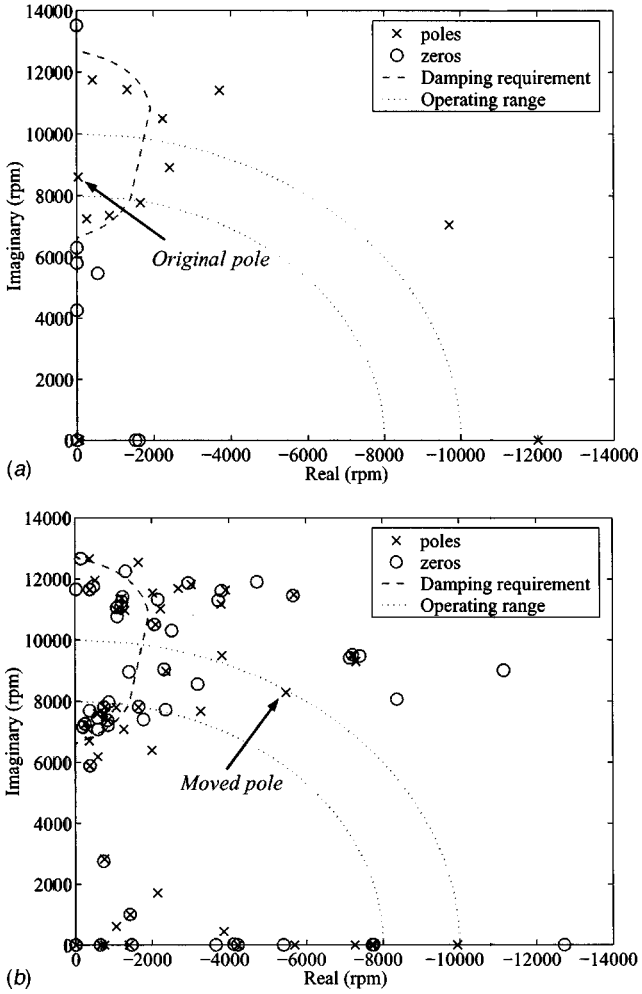


**Fig. 9 Pole/zero map: (*a*) augmented open-loop plant, (*b*) closed-loop system**

yond the required damping line than is required to meet the separation margin requirement, which is denoted by moved pole as shown in Fig. 9(b).

The maximum singular value of equivalent stiffness of the resulting control is shown in Fig. 10. The resulting controller does not exhibit the typical control shape of an AMB system, which is very similar to a PD control. In order to test how much control effort is required to meet the API standards, a simpler optimal design problem was solved. Here, the three bearings were assumed to be identical devices with fixed stiffness and damping. Thus, single values of stiffness and damping were found, which simultaneously satisfy $5.46 \cdot 10^5$ N/mm and $7.65 \cdot 10^3$ Nsec/mm, respectively. The equivalent stiffness at the bending natural frequency is $6.91 \cdot 10^6$ N/mm. The gain of the designed controller is much higher (the maximum value is $1.56 \cdot 10^8$ N/mm).

Although the API standards are satisfied, the designed controller is very conservative since all performance indices are much less than 1.0 (especially, the robust stability is 0.1283), which means that the control effort bound is unnecessarily high. In order to reduce the conservativeness of the synthesis and to find an economic controller meeting the API requirements with minimum control effort, the constant weighting for the control effort is changed. The synthesis procedure is as follows: all weightings are the same except for the control effort, whose initial values are the maximum force and vibration amplitude. Then, an optimal weighting constant is found to satisfy the API standard and the actuator specification through the bisection method. When the

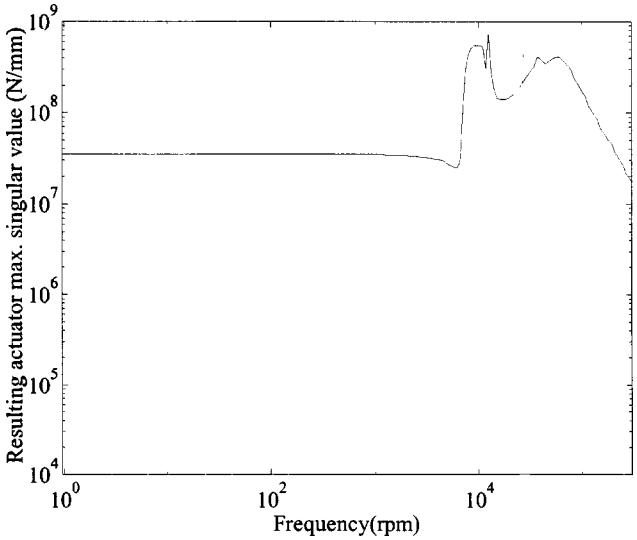


**Fig. 10 Stiffness of the designed controller**

maximum response is reduced by 11.4 times, the peak $\mu$ value is 1.8412 and robust stability is 0.9997. Both the API standards and the actuator specification are satisfied as shown in Fig. 11.

The pole/zero map of the closed-loop system is shown in Fig. 12. The moved pole is very close to the required damping line and the conservativeness is reduced significantly.

The maximum singular value of the equivalent stiffness of the second controller is shown in Fig. 13. The controller has the desired shape to stabilize an AMB rotor system similar to a PD control. The control effort is reduced significantly (particularly the gain at low frequencies) and the maximum equivalent stiffness is $1.53 \cdot 10^7$ N/mm, which is a little bit higher than expected; however, it is not unacceptably high considering non-collocation configuration and stabilization of an unstable AMB rotor system. That is, the $\mu$-analysis/synthesis is known to be conservative so it should not be expected to be exactly same as the API standards. However, it can be said is that if the proposed sythesis is successful, then there is definitely a bearing to meet the API standards.

## Conclusion

This paper discussed a possible control design problem for assessing the feasibility of meeting the API 617 requirements with a

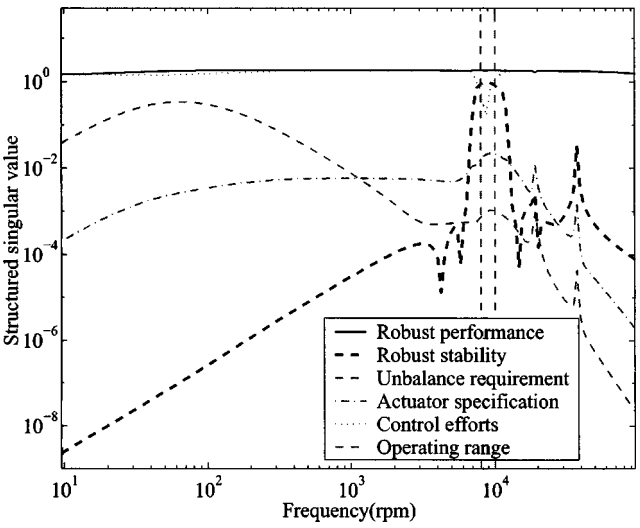


**Fig. 11 Results after reducing the conservativeness**

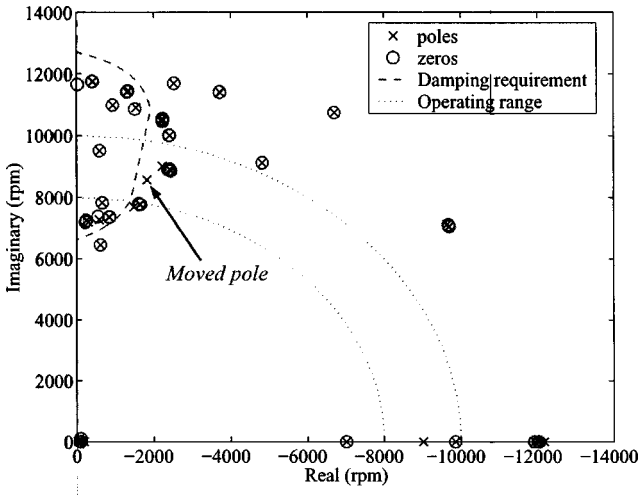


**Fig. 12 Pole/zero map of the closed-loop system after reducing the conservatism**

given rotor. The separation margin requirement is replaced by a pole placement problem: relatively large damping within the operating range. This pole placement problem can be approximated as a robust stability problem with a frequency-shaped uncertain modal damping. Since the unbalance response requirement can easily be expressed as an $H_\infty$ problem, the two API 617 requirements can be cast as a single $\mu$-analysis problem. Two simulations are performed with an example AMB rotor system: a feasibility test for API requirements with a given AMB actuator and a synthesis of economic controller meeting the API requirements with minimum control effort. The simulation shows that the proposed synthesis permits direct assessment of the feasible design problem as well as providing a means to synthesize optimal bearing dynamics.

The main point of the method, of course, is to be able to weed out (rotor/unbalance/clearance/bearing capacity) sets that simply cannot meet API standards. With the tool presented here, it is reasonably easy to play with clearances, unbalance specifications, and bearing capacities to determine what needs to be done to make the set feasible for API standards.

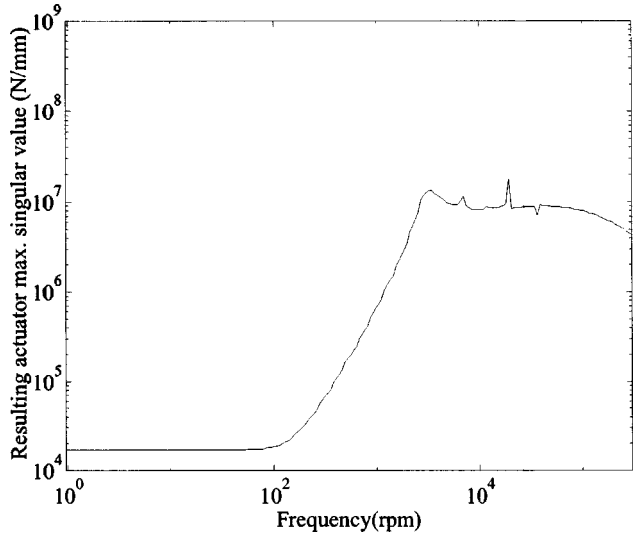


**Fig. 13 Stiffness of the controller after reducing the conservatism**


## Acknowledgment

The authors wish to acknowledge the support of Asea Brown Boveri, Ltd. in completing this research.


## Nomenclature

$A$, $A_p$ = vibration amplitude and peak vibration amplitude
$AF$ = amplification factor
$B(s)$ = bandpass filter for the separation margin
$C$ = output matrix
$C_{cl}$ = critical clearance
$C_{seal}$ = uncertain seal damping
$D$ = damping matrix
$d$ = plant input disturbance
$e$ = unbalance responses at probes
$f$ = force
$F_{\max}$ = maximum force of actuator
$G$ = plant (rotor) transfer matrix
$I$ = identity matrix
$K$ = stiffness matrix or controller
$k$ = residual
$L_v$ = vibration limit at probes
$M$ = mass matrix
$M(s)$ = unbalance response
$mr$ = unbalance
$N$ = rotor speed
$N_R$, $N_{1,2}$ = resonance and half power speeds
$N_l$, $N_u$ = lower and upper operating speeds
$nf$, $ny$ = numbers of unbalance force inputs and displacement outputs
$q$ = state vector
$R$ = real number
$S$ = sensitivity function
$s$ = frequency domain
$T$ = complementary sensitivity function
$u$ = controller input
$U$ = unbalance amount
$W(s)$ = example uncertainty
$W_e$ = allowed unbalance responses weighting function
$W_u$ = worst case bearing force weighting function
$W_d$ = worst case unbalance excitation weighting function
$W_y$ = allowed bearing input weighting function
$w$ = controller input disturbance
$y$ = response or output
$Z$ = modal damping matrix
$\Delta$ = uncertainty
$\varepsilon$ = factor for bearing force weighting
$\Phi$ = modal transformation matrix
$\phi$ = eigenvector
$\eta$ = constant for $AF$
$\varphi$ = phase angle
$\sigma$ = singular value
$\Lambda$ = diagonal eigenvalue square matrix
$\omega$ = frequency
$\omega_b$ = bandwidth of actuator
$\omega_e$, $\omega_n$, $\omega_r$ = excitation, natural, and resonance frequencies
$\xi$ = modal coordinate
$\zeta$, $\zeta_0$ = damping ratio and nominal damping ratio

## References


[1] Doyle, J. C., Glover, K., Khargonekar, P., and Francis, P., 1989, "State Space Solutions to Standard H-2 and H-infinity," IEEE Trans. Autom. Control, **AC-34**, pp. 831–847.

[2] Doyle, J. C., Packard, A., and Zhou, K., 1991, "Review of LFTs, LMIs, and $\mu$," *Proceedings of the 30th IEEE conference on Decision and Control*, **2**, pp. 1227–1232.

[3] Packard, A., and Doyle, J. C., 1993, "The Complex Structured Singular Value," Automatica, **29**, pp. 71–109.

[4] Zhou, K., Doyle, J. C., and Glover, K., 1996, *Robust and Optimal Control*, Prentice-Hall, Englewood Cliffs, NJ.
[5] Cloud, C. H., Foiles, W. C., Li, G., Maslen, E. H., and Barrett, L. E., 2002, ''Practical Applications of Singular Value Decomposition in Rotordynamics,'' in Proceedings of 6th International Conference on Rotor Dynamics.
[6] Zames, G., 1966, ''On the Input-Output Stability of Nonolinear Time-Varying Feedback Systems, Part I,'' IEEE Trans. Autom. Control, **11**, pp. 228–238.
[7] API 617, Axial and Centrifugal Compressors and Turboexpanders for Petroleum, Chemical and Gas Industry Services, American Petroleum Institute, Washinton D.C., 2002.
[8] Balas, G. J., Doyle, J. C., Glover, K., Packard, A. K., and Smith, R., 1995, *$\mu$ Analysis and Synthesis Toolbox User's Guide*, The MathWorks, Natick, MA.
[9] Skogestad, S., and Postlethwaite, I., 1996, *Multivariable Feedback Control: Analysis and Design*, Wiley, West Sussex, England.
[10] Branch, M. A., and Grace, A., 1996, *MATLAB Optimization Toolbox User's Guide*, The MathWorks, Natick, MA.

# Crack Detection in a Rotor Dynamic System by Vibration Monitoring—Part I: Analysis

**Itzhak Green**
Georgia Institute of Technology,
GWW School of Mechanical Engineering,
Atlanta, GA 30332
Fellow ASME

**Cody Casey**
Schlumberger,
14910 Airline Road,
Rosharon, TX 77583

*Many practical rotor dynamic systems contain shaft/rotor elements that are highly susceptible to transverse cross-sectional cracks due to fatigue. The early detection of mechanical malfunction that can be provided by an effective vibration monitoring system is essential. Two theoretical analyses, global and local asymmetry crack models, are utilized to identify characteristics of the system response that may be directly attributed to the presence of a transverse crack in a rotating shaft. A model consisting of an overhung whirling rotor is utilized to match an experimental test rig. A 2X harmonic component of the system response is shown to be the primary response characteristic resulting from the introduction of a crack. Once the unique characteristics of the system response are identified, they serve then as target observations for the monitoring system.*
[DOI: 10.1115/1.1789514]

## 1 Introduction

As rotating machinery is designed to operate at higher mechanical efficiency; operating speed, power, and load are increased as weight and dimensional tolerances are decreased. The result is a significantly increased level of operating stress in modern rotating machinery. As a consequence, many practical rotordynamic systems contain shaft/rotor elements that are highly susceptible to transverse cross-sectional cracks due to fatigue. To accurately predict the response of a system to the presence of a transverse crack, an appropriate crack model is essential. Once the crack is included in the system model, unique characteristics of the system response can be identified and attributed directly to the presence of the crack. These predicted indicators then serve as target observations for monitoring systems.

A significant amount of research involving the prediction of the response of shaft/rotor systems to the presence of a transverse crack, and the detection of transverse cracks in rotating shafts by vibration monitoring, has been completed in the last 30 to 40 years. This work is an extension of a body of research focused on a flexibly mounted rotor (FMR) mechanical face seal system [1]. The dynamics of the FMR mechanical face seal system have been extensively investigated [2–5]. In Ref. [2] the coupled dynamics of the seal and shaft is investigated including effects of shaft inertia and slenderness, fluid film, secondary seal, flexibly mounted rotating element, and an axial offset of the rotor center of mass. The steady-state response was investigated by implementing a complex extended transfer-matrix method. In Ref. [3] an experimental correlation is investigated between the presence of higher harmonic oscillations in the test rig system and seal face contact. The dynamics behavior of the FMR seal itself was investigated in Refs. [4] and [5]. Seal failure, diagnostics, control, and eventual performance restoration are extensively discussed in Refs. [6–10]. To achieve these goals it is imperative that failure characteristics of seal and shaft are well differentiated. The influence of a crack in a seal-driving shaft is the concern of this work.

An uncracked shaft has constant stiffness, and thus constant displacement under a fixed load, regardless of the angle of rotation. In a cracked shaft, the cracked portion of the cross section is not capable of supporting a tensile stress. Therefore the displacement, as a function of the stiffness, is minimum when the crack is closed and maximum when the crack is open. This opening and closing behavior, which is referred to as ''breathing,'' results in time-dependent stiffness coefficients in the equations of motion of the system, which is difficult to work with. Obtaining solutions usually requires making broad simplifying assumptions or some type of numerical approximation.

Systems in which static displacements and vibrational amplitudes remain very small result in a crack that remains essentially open regardless of the angle of rotation. This type of crack, which is essentially a local stiffness asymmetry, is referred to as a ''gaping'' crack. The analysis of systems containing a gaping crack is extremely useful since the response characteristics, or crack indicators, identified in the gaping crack analysis are also present in the analysis of systems containing a breathing crack. Furthermore, these indicators prove to be the most practical, in terms of implementation, in the detection of real cracks. Also, since the introduction of a crack into a rotating system, on the most basic level, results in a system with a stiffness asymmetry, the analysis of systems containing an asymmetry is fundamental to the study of the dynamics of cracked rotating systems.

The primary effect of the presence of a crack in a rotating shaft is clearly a local reduction in stiffness. This highly localized effect does not influence the stiffness of the regions of the rotor away from the cracked cross section. Regardless of the type of crack model used for analysis, the effective overall stiffness of the rotor is no longer symmetric. The analysis of the response of a rotor with designed-in asymmetry is therefore part of the fundamental basis for the analysis of the dynamics of shafts containing a transverse crack.

A free response of a two degree-of-freedom rotor with asymmetric moments of inertia [11] shows a range of shaft speeds in which the response is unstable. The appearance of a region of instability near the first natural frequency is confirmed in Ref. [12], as well as the $2X$ harmonic response in an analysis of a linearly asymmetric shaft. In Ref. [13] the $2X$ resonance is also predicted at approximately one-half of the first natural frequency. An intuitive explanation for the existence of a region of instability and a $2X$ harmonic response in shafts with dissimilar moments of inertia is given in Ref. [14]. It is important to note that for rotating systems, the terms ''natural frequency'' and ''whirl frequency'' are synonymous. Also, the term ''critical speed'' refers to a shaft speed for which one or more of the natural (whirl) frequencies of

Contributed by the International Gas Turbine Institute (IGTI) of THE AMERICAN SOCIETY OF MECHANICAL ENGINEERS for publication in the ASME JOURNAL OF ENGINEERING FOR GAS TURBINES AND POWER. Paper presented at the International Gas Turbine and Aeroengine Congress and Exhibition, Atlanta, GA, June 16–19, 2003, Paper No. 2003-GT-38659. Manuscript received by IGTI, October 2002, final revision, March 2003. Associate Editor: H. R. Simmons.

the system are equal to the shaft speed. Therefore the maximum $2X$ harmonic response occurs at shaft speeds that are approximately one-half of a critical speed, i.e., $\frac{1}{2}n_{cr}$.

In Ref. [15] a practical "hinge model" is developed that represents the crack as an additional flexibility in the direction perpendicular to the crack edge, for positive displacements in that direction. Similar displacement based breathing crack models have been utilized in Refs. [12,13,16–19]. In Ref. [20] the opening and closing of the crack is modeled as a step type function of the angle of rotation only. Other similar step and 1/rev continuous functions of the angle of rotation have been used to model the breathing behavior of the crack in Refs. [16–18,21–28].

The complicated system models resulting from the inclusion of a breathing crack model have been solved or approximated by a variety of methods. Analog computer simulations [12,15], Ritz basis functions based on the asymmetric solution [16], and numerical integration [13,17,18,20] have been used. Various transfer-matrix methods were employed as well [19,23,29]. Floquet theory stability analysis is performed in Refs. [21,27,30], and perturbation methods are utilized in Refs. [24,25].

The most significant result of the analysis of systems containing breathing crack models that is relevant to this work is the fact that the response characteristics due to a breathing crack model consist of the primary response characteristics of an asymmetric system plus some additional phenomena, in form of sub or higher harmonics [20,21,24,25,30–34]. The direction of the investigations into the response of rotating systems containing breathing crack models tends to focus on the $1X$ and $2X$ harmonic responses [17,23–25,33,34].

On the most basic level the introduction of a gaping crack results in a local system stiffness asymmetry that is time independent in a rotating coordinate frame. The additional flexibility introduced to the system by the presence of the crack is determined by methods such as finite element analysis or the Paris strain energy method [21,30]. The localization of the stiffness asymmetry is the key in this analysis.

In Refs. [21,30,33,34] the overall stiffness properties for their two and three degree-of-freedom systems is determined by conveniently placing the crack at the mid-span of the De-Laval rotor system. To arbitrarily place the crack at some location along the shaft in the system model, it is convenient to utilize a discrete representation of the system, such as a transfer-matrix method [29]. The presence of a gaping crack in the shaft of a rotating system tends to primarily affect the $1X$ synchronous response, and the $2X$ harmonics, which has a resonance at $\frac{1}{2}n_{cr}$.

In summary, the introduction of a gaping crack model into an existing system model has been shown to be a very effective method of obtaining reasonably accurate results from analysis, yet it avoids the inherent complexities of cracked shaft analysis due to breathing behavior. A discrete representation of the system allows the additional flexibility due to the crack to be placed arbitrarily along the axis of the shaft of the system. The $2X$ harmonic component of the system response is clearly the most practically implemented indicator for a monitoring and detection system. This work utilizes a global asymmetry crack model in a continuous representation of the system as well as a gaping crack model in a discrete representation of the system using a unique extended transfer-matrix formulation [2]. The theoretical analyses focus on the prediction of the behavior of the $2X$ component of the system response. For each crack model, free and forced response characteristics are investigated.

## 2 Global Asymmetry Crack Model

A shaft into which a transverse crack is introduced experiences a reduction in stiffness which, depending on the relative dimensions of the crack, can be quite small or quite large. As a first approximation we consider a shaft whose entire cross section is represented by the remaining uncracked cross section. Thus the resulting shaft is assumed to have an asymmetric cross section

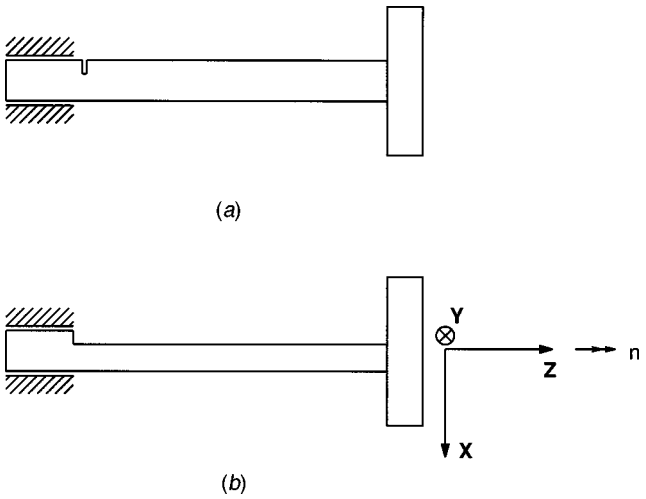


**Fig. 1 (*a*) Cracked system; (*b*) global asymmetry crack model**

over its entire length. This is referred to as a global asymmetry crack model, which is the worst case in terms of the amplitude of the resulting response characteristics. (Such an analysis is useful by itself since many rotor dynamic systems contain designed-in asymmetric components.)

In Fig. 1(*a*) the cross section of an overhung massless shaft with an attached rotor (which is a reasonable representation of the test rig system that is detailed in Ref. [35]) is shown to include a transverse crack. Figure 1(*b*) shows the same system including the global asymmetry crack model, which is essentially an asymmetric Euler-Bernoulli beam. Equations of motion for this system are derived in a rotating frame to avoid time-dependent stiffness coefficients. The $XYZ$ coordinate system rotates with the shaft, at shaft speed $n$, and is oriented such that the $X$ axis is perpendicular to the crack edge. The relationship between the rotating $XYZ$ coordinate system and the inertial $\xi\eta\zeta$ coordinate system is shown in Fig. 2. The equations of motion can be derived in the rotating $XYZ$ coordinate frame as detailed in Ref. [35], which is based upon the work in Ref. [36]. For the no damping case we have

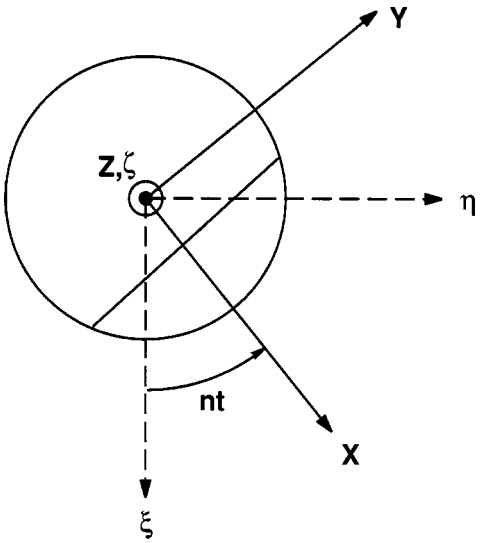


**Fig. 2 Coordinate systems**

$$\begin{bmatrix} m & 0 & 0 & 0 \\ 0 & m & 0 & 0 \\ 0 & 0 & I_t & 0 \\ 0 & 0 & 0 & I_t \end{bmatrix} \begin{Bmatrix} \ddot{X} \\ \ddot{Y} \\ \ddot{\gamma}_X \\ \ddot{\gamma}_Y \end{Bmatrix} + \begin{bmatrix} 0 & -2mn & 0 & 0 \\ 2mn & 0 & 0 & 0 \\ 0 & 0 & 0 & n(I_P-2I_t) \\ 0 & 0 & -n(I_P-2I_t) & 0 \end{bmatrix} \begin{Bmatrix} \dot{X} \\ \dot{Y} \\ \dot{\gamma}_X \\ \dot{\gamma}_Y \end{Bmatrix}$$
$$+ \begin{bmatrix} k_{11Y}-mn^2 & 0 & 0 & -k_{12Y} \\ 0 & k_{11X}-mn^2 & k_{12X} & 0 \\ 0 & k_{12X} & n^2(I_P-I_t)+k_{22X} & 0 \\ -k_{12Y} & 0 & 0 & n^2(I_P-I_t)+k_{22Y} \end{bmatrix} \begin{Bmatrix} X \\ Y \\ \gamma_X \\ \gamma_Y \end{Bmatrix} = \{F\}, \quad (1)$$

where $X$, $Y$, $\gamma_X$, and $\gamma_Y$ are displacements and tilts about the $X$ and $Y$ axes, respectively, $m$ is the mass or the rotor, $n$ is the shaft speed, $I_p$ and $I_t$ are the polar and transverse moments of inertia of the rotor, and $k_{ij}$ are stiffness elements, which are determined in the Appendix. Since in the tested system the mass of the shaft is significantly less than the mass of the rotor, it is neglected. The effects of internal energy dissipation in the free response analysis are negligible. Therefore internal damping will be incorporated into the equations of motion for the forthcoming forced response analysis. Equation (1) forms a system of coupled linear ordinary differential equations including gyroscopic effects, where $\{F\}$ is a vector of generalized applied forces.

**2.1 Undamped Free Response.** The goal of the free response analysis is to obtain the system eigenvalues, which are the natural, or whirl, frequencies. The homogeneous form of the matrix equation of motion given in Eq. (1) has the general form

$$[M]\{\ddot{S}\}+[C]\{\dot{S}\}+[K]\{S\}=\{0\}, \quad (2)$$

where $[M]$, $[C]$, and $[K]$ are inertia, "damping" (i.e., Coriolis and gyroscopic effects), and stiffness matrices, and $\{S\}$ is the generalized vector of displacements. The system is conveniently expressed in a state-variable form by defining the following $[A]$ and $[B]$ matrices:

$$[A]=\begin{bmatrix} -[K] & [0] \\ [0] & [M] \end{bmatrix}; \quad [B]=\begin{bmatrix} [0] & -[K] \\ -[K] & -[C] \end{bmatrix}. \quad (3)$$

The system expressed in state-variable form is then given by

$$\{\dot{\hat{S}}\}=[A]^{-1}[B]\{\hat{S}\}, \quad (4)$$

where $\{\hat{S}\}$ is the state vector of the displacements and tilts and their first derivatives, which is given by

$$\{\hat{S}\}=\{X \;\; Y \;\; \gamma_X \;\; \gamma_Y \;\; \dot{X} \;\; \dot{Y} \;\; \dot{\gamma}_X \;\; \dot{\gamma}_Y\}^T. \quad (5)$$

For this state vector form the state matrix is formed by $[A]^{-1}[B]$.

The eigenvalues and eigenvectors, or whirl frequencies and mode shapes, are then obtained, corresponding to the state vector expressed in the rotating $XYZ$ frame. For monitoring purposes the absolute whirl frequencies are of interest since the monitoring system is typically fixed in the inertial $\xi\eta\zeta$ coordinate frame. The absolute whirl frequencies, $\omega$, i.e., the eigenvalues expressed in the inertial $\xi\eta\zeta$ frame, can be obtained from

$$\omega=\omega_0+n, \quad (6)$$

where $\omega_0$ is the relative whirl frequency, and $n$ is the shaft speed. Since the state matrix, $[A]^{-1}[B]$, is $8\times8$, four conjugate pairs of eigenvalues are obtained. The eigenvalues are purely imaginary since damping or dissipation effects are neglected in this free response analysis.

In rotordynamics, the sign of the frequency is meaningful due to the fact that shaft whirl can occur with a negative sense, opposing the direction of shaft rotation, or a positive sense, in the direction of shaft rotation. The proper sign can be assigned to the magnitude of each eigenvalue pair which yields forward or backward whirl according to the analysis detailed in Ref. [35]. The relative whirl frequencies resulting from the analysis, $\omega_0$, are assigned the appropriate direction and the absolute whirl frequencies $\omega$ are obtained from Eq. (6). Figures 3 show the whirl frequencies as a function of shaft speed for simulated crack depths ranging from 0–40% of the shaft diameter. The "×" symbols along the horizontal axis of Fig. 3 indicate shaft speeds for which one or more of the eigenvalues has a positive real part, i.e., shaft speeds for which the response is unstable. This instability is solely due to an asymmetric cross section of a purely elastic shaft (recall that internal damping has been neglected in this section) (see also Refs. [11,12,14]). Two reference lines are also plotted in each of the figures. The intersection of the $\omega=n$ line with the locus of whirl frequencies indicates shaft speeds which are equivalent to a whirl frequency, i.e., primary $(1X)$ critical speeds. The intersection of the $\omega=2n$ line with the locus of whirl frequencies indicates shaft speeds which are one-half of a whirl frequency, i.e., secondary $(2X)$ critical speeds.

When operating at a secondary critical speed, the $2X$ component of the response of the system is occurring at a natural frequency of the system, and will therefore exhibit a resonance behavior. It is at these $2X$ critical speeds that the $2X$ response is expected to be maximum. Comparing the predicted shaft speeds at which the $2X$ resonance occurs for various crack depths clearly shows a decrease in the natural frequencies of the system due to the presence of the crack. This change in the system natural frequency is due to the reduction in system stiffness resulting from the crack. The predicted $2X$ resonance shaft speeds for the global asymmetry crack model are given in Table 1.

**2.2 Damped Forced Response.** The gravity forced response of the system model containing the global asymmetry crack model is fundamentally important when considering crack detection. The resulting $2X$ harmonic response is the most reliable and widely used indicator of crack existence.

Energy dissipation effects are included in this analysis in order to observe the influence of the introduction and propogation of the simulated crack on the magnitude of the system response at $2X$ resonance shaft speeds. The equivalent viscous damping coefficients are incorporated into the matrix equation of motion by defining a new damping matrix, $[\hat{C}]$, according to

$$[\hat{C}]=[C]+[D], \quad (7)$$

where $[C]$ is the matrix which contains the Coriolis and gyroscopic effects, and the $[D]$ matrix contains the equivalent viscous damping coefficients. The damping matrix $[D]$ is given by

$$[D]=\begin{bmatrix} d_{11_Y} & 0 & 0 & -d_{12_Y} \\ 0 & d_{11_X} & d_{12_X} & 0 \\ 0 & d_{12_X} & d_{22_X} & 0 \\ -d_{12_Y} & 0 & 0 & d_{22_Y} \end{bmatrix}, \quad (8)$$

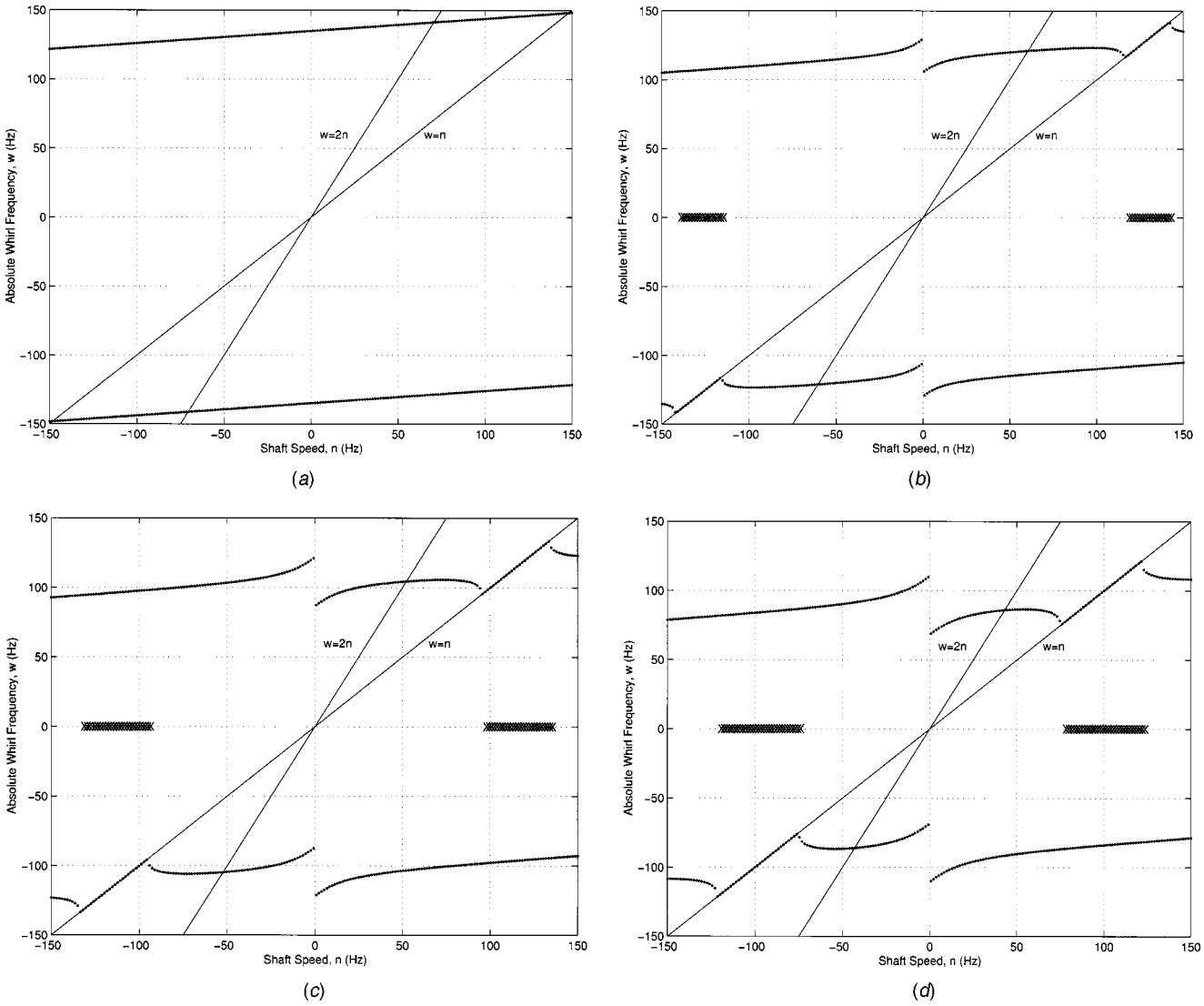


**Fig. 3 Global asymmetry model free response at various crack depth values: (*a*) uncracked; (*b*) 20%; (*c*) 30%; (*d*) 40%**

where $d_{ij_X}=d_{ij_Y}=c_{eq_{ij}}=\frac{1}{2}\overline{\beta}(k_{ij_X}+k_{ij_Y})/\omega$. Here average stiffness elements are used so that $d_{ij_X}$ and $d_{ij_Y}$ are equal. It is necessary to construct the complex equations of motion in the following analysis. The equation of motion, including internal damping, has the form

$$[M]\{\ddot{S}\}+[\hat{C}]\{\dot{S}\}+[K]\{S\}=\{F\}. \tag{9}$$

The equations of motion are derived in the shaft-fixed $XYZ$ coordinate frame. The direction along which gravity acts, which is a stationary vector along the $\xi$ axis of the inertial $\xi\eta\zeta$ coordinate frame, can be represented by a vector that is rotating with a negative sense in the $XYZ$ frame. Therefore the forcing function resulting from gravity has the form

$$F_g=mge^{-int}, \tag{10}$$

where $m$ is the mass of the rotor, $g$ is the gravitational acceleration and $n$ is the shaft speed. The vector of forces that is now included in the right-hand side of the equations of motion [Eq. (1)] is then given, in the rotating $XYZ$ coordinate frame, by

$$\{F\}=\begin{Bmatrix} mg\cos(nt) \\ -mg\sin(nt) \\ 0 \\ 0 \end{Bmatrix}. \tag{11}$$

The equations of motion are then combined by defining the following complex variables for the displacement $\rho$ and tilt $\phi$:

$$\rho=X+iY, \tag{12}$$

$$\phi=\gamma_X+i\gamma_Y. \tag{13}$$

The resulting complex equations of motion are

**Table 1 2*X* resonance shaft speeds—global asymmetry model free response**

| % cracked | Shaft speed (Hz) |
|---|---|
| 0 | 70.62 |
| 10 | 67.04 |
| 20 | 60.55 |
| 30 | 52.29 |
| 40 | 43.01 |

$$\ddot{\rho}+D_{11}\dot{\rho}+(\omega_\rho^2-n^2)\rho-\left(\frac{\Delta k_\rho}{k_\rho}\omega_\rho^2\right)\rho^*+(2n)i\dot{\rho}+D_{12_m}\dot{\phi}$$

$$+(\omega_{\rho\phi_m}^2)i\phi+\left(\frac{\Delta k_{\rho\phi}}{k_{\rho\phi}}\omega_{\rho\phi_m}^2\right)i\phi^*=ge^{-int}, \tag{14}$$

$$\ddot{\phi}+D_{22}\dot{\phi}+\left[n^2\left(\frac{I_p}{I_t}-1\right)+\omega_\phi^2\right]\phi+\left(\frac{\Delta k_\phi}{k_\phi}\omega_\phi^2\right)\phi^*-\left[n\left(\frac{I_p}{I_t}-2\right)\right]i\dot{\phi}$$

$$-D_{12_{I_t}}i\dot{\rho}-(\omega_{\rho\phi_{I_t}}^2)i\rho+\left(\frac{\Delta k_{\rho\phi}}{k_{\rho\phi}}\omega_{\rho\phi_{I_t}}^2\right)i\rho^*=0, \tag{15}$$

where the "*" denotes the complex conjugate of the variables in Eqs. (12) and (13), and

$$\omega_\rho=\frac{k_\rho}{m},\quad \omega_\phi=\frac{k_\phi}{I_t},\quad \omega_{\rho\phi_m}=\frac{k_{\rho\phi}}{m},\quad \omega_{\rho\phi_{I_t}}=\frac{k_{\rho\phi}}{I_t},$$

$$k_\rho=\tfrac{1}{2}(k_{11_X}+k_{11_Y}),$$

$$k_\phi=\tfrac{1}{2}(k_{22_X}+k_{22_Y}),\quad k_{\rho\phi}=\tfrac{1}{2}(k_{12_X}+k_{12_Y}),\quad \Delta k_\rho=k_\rho-k_{11_Y},$$

$$\Delta k_\phi=k_\phi-k_{22_Y},\quad \Delta k_{\rho\phi}=k_{\rho\phi}-k_{12_Y},\quad D_{11}=\frac{d_{11_X}}{m}=\frac{d_{11_Y}}{m},$$

$$D_{12_m}=\frac{d_{12_X}}{m}=\frac{d_{12_Y}}{m},\quad D_{12_{I_t}}=\frac{d_{12_X}}{I_t}=\frac{d_{12_Y}}{I_t},$$

$$D_{22}=\frac{d_{22_X}}{I_t}=\frac{d_{22_Y}}{I_t}.$$

To solve this system of equations, solutions of the following forms are chosen for the displacement $\rho$, and tilt $\phi$:

$$\rho=Ae^{int}+Be^{-int}, \tag{16}$$

$$\phi=Ce^{int}+De^{-int}, \tag{17}$$

where $A$, $B$, $C$, and $D$ are arbitrary complex numbers. These solutions are substituted into Eqs. (14) and (15) and the complex coefficients $A$, $B$, $C$, and $D$ are determined. Recalling that the displacement and tilt in the rotating $XYZ$ coordinate frame are given by Eqs. (16) and (17), the displacement $u$ and tilt $\gamma$ in the inertial coordinate frame are obtained according to

$$u=\rho e^{int}, \tag{18}$$

$$\gamma=\phi e^{int}. \tag{19}$$

The displacement and tilt expressed in the inertial coordinate frame are of interest since the experimental data provided by the monitoring system is also obtained in the inertial coordinate frame (according to Ref. [35]). From Eqs. (16)–(19) it is clear that the displacement and tilt in the inertial coordinate frame will have the form

$$u=Ae^{i2nt}+B, \tag{20}$$

$$\gamma=Ce^{i2nt}+D. \tag{21}$$

The presence of the $2X$ harmonic is evident in Eqs. (20) and (21). The magnitudes of coefficients $A$ and $C$ are the magnitudes of the $2X$ harmonic response, in the inertial frame, of the displacement and tilt, respectively. Equations (20) and (21) predict displacement and tilt responses which have circular shapes, having radii of $|A|$, and $|C|$, and are offset by $B$ and $D$. It is important to note that due to the form of the assumed solutions [Eqs. (16) and (17)], the resulting solutions [Eqs. (20) and (21)] are limited to predicting only circular orbit shapes of the $2X$ component.

Figures 4 show the predicted magnitude of the $2X$ tilt response, based on the global asymmetry crack model, as a function of shaft speed, for two speed ranges, and crack depths varying from 0 to 40% of the shaft diameter. The magnitudes plotted show the radii

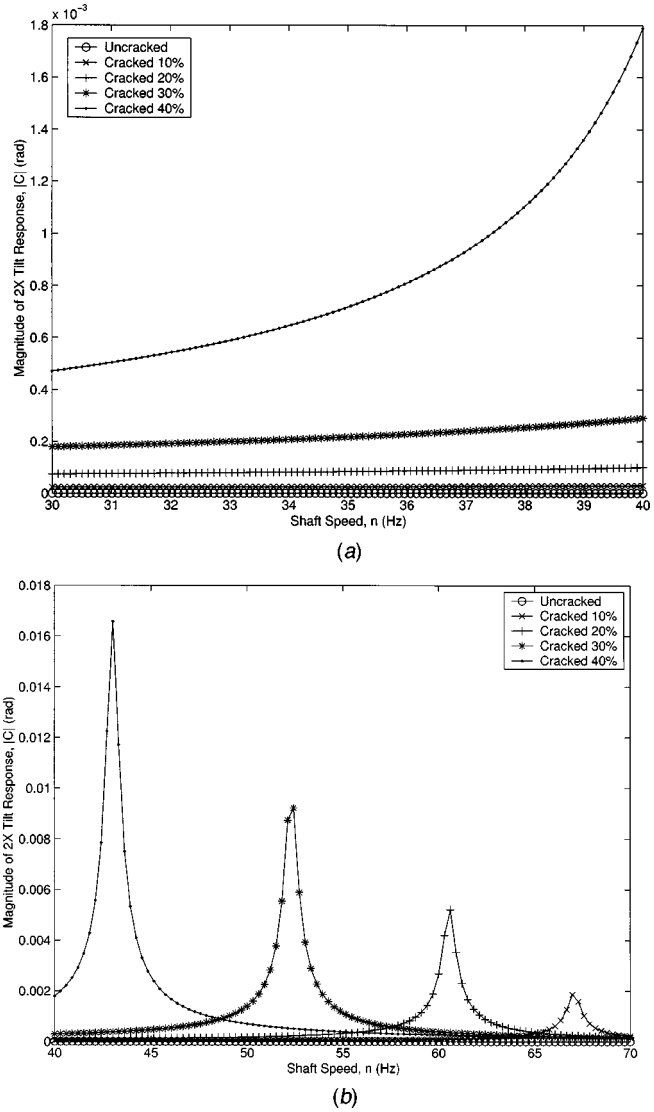


**Fig. 4 Global asymmetry model forced tilt $2X$ response: (*a*) Low-speed range; (*b*) high-speed range**

of the predicted circular $2X$ tilt responses. It is clear that for an arbitrary shaft speed, the amplitude of the $2X$ response is predicted to increase as the crack depth increases.

The magnitudes of the $2X$ component of the response plotted in Fig. 4(*a*) are significantly smaller than those plotted in Fig. 4(*b*). The range of shaft speeds shown in Fig. 4(*b*) contains $2X$ resonant speeds for each crack depth.

As predicted, the $2X$ resonant speeds decrease as the crack depth increases. The $2X$ resonance shaft speeds predicted based on this global asymmetry crack model forced response analysis are given in Table 2. These predicted $2X$ resonance shaft speeds agree with the $2X$ resonance shaft speeds predicted in the global asymmetry model free response analysis, which are given in Table 1. Since the 0% simulated crack depth results in a system with symmetric stiffness properties, no $2X$ resonance is predicted for the forced response analysis. Damping is light, thus numerically Tables 1 and 2 provide similar $2X$ results.

## 3 Local Asymmetry Crack Model

Perhaps the most important effect of the presence of a transverse crack in a rotating shaft is the highly localized flexibility

**Table 2 2X resonance shaft speeds—global asymmetry model forced response**

| % cracked | Shaft speed (Hz) |
|---|---|
| 0 | |
| 10 | 67.04 |
| 20 | 60.55 |
| 30 | 52.29 |
| 40 | 43.01 |

that is introduced. To locally represent the stiffness properties of a cracked cross section in an otherwise uncracked shaft, it is necessary to determine the additional flexibility due to the presence of the crack, and incorporate this flexibility into a discrete representation of the system. In this study a transfer-matrix method was employed to accomplish this desired localizing effect. Figure 5 shows the cracked system represented by three lumped stiffness elements; $[F_1]$, $[F_{\text{crack}}]$, and $[F_2]$, and one lumped inertia element $[P]$. Since the mass of the shaft is significantly less than the mass of the rotor, the mass of the shaft is neglected.

The purpose of this section is to present the analytical portion of the analysis of the cracked system including a local asymmetry crack model using the complex extended transfer-matrix method [2,37] for free and forced response analyses, along with relevant results. As previously, damping effects will be incorporated into the forced response analysis.

**3.1 Crack Flexibility.** The localized additional flexibility can be represented by a lumped parameter element. A section of a shaft containing a crack of depth $a$ is shown, under general loading, in Fig. 6($a$). Figure 6($b$) shows the cross section of the shaft section in Fig. 6($a$) at the location of the transverse crack. The generalized displacement $u_i$ in the $i$ direction is obtained by utilizing Castigliano's theorem [21,30]:

$$u_i = \frac{\partial}{\partial P_i} \int_0^{\alpha} J(Y)\, dY, \tag{22}$$

where $P_i$ is the generalized force associated with $u_i$, and $J(Y)$, according to Tada, Paris, and Irwin [37], is the strain energy density function given by

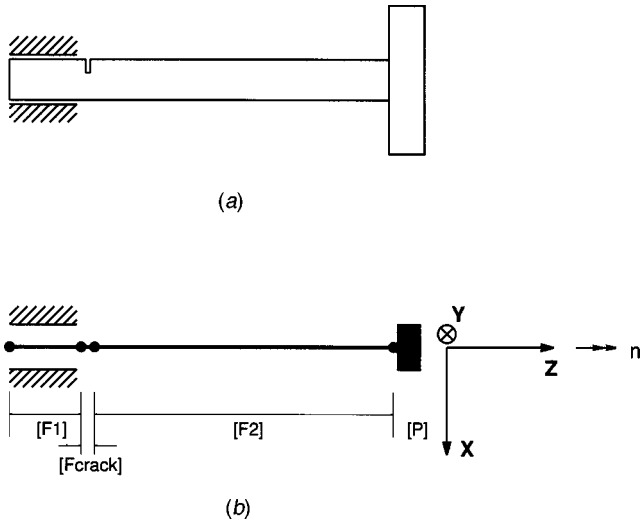


**Fig. 5 Local asymmetry crack model**

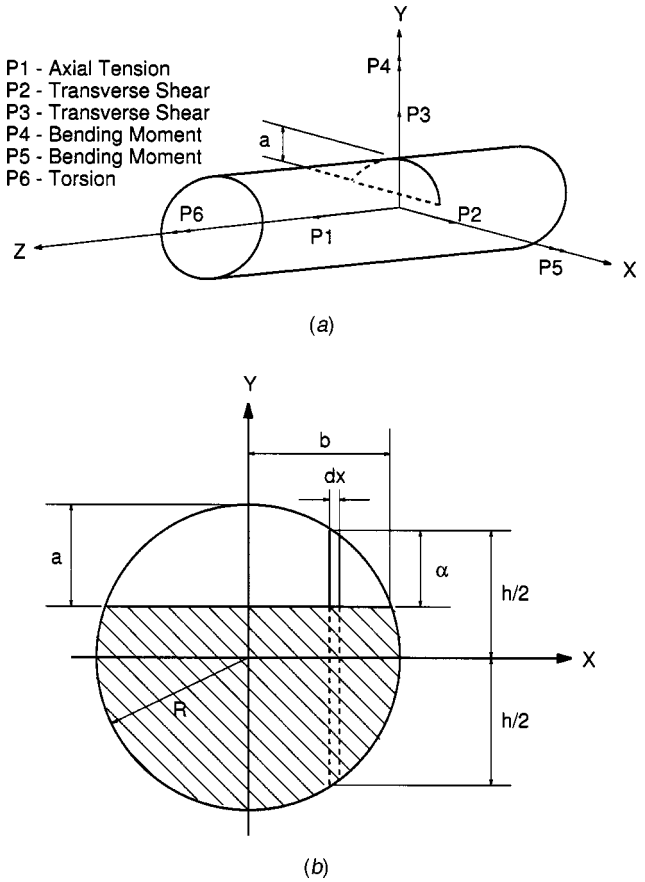


**Fig. 6 Local crack model: (*a*) shaft section containing a crack; (*b*) crack cross section**

$$J(\alpha) = \frac{1-\nu^2}{E}\left[\left(\sum_{i=1}^{6} K_{Ii}\right)^2 + \left(\sum_{i=1}^{6} K_{IIi}\right)^2 + (1+\nu)\left(\sum_{i=1}^{6} K_{IIIi}\right)^2\right], \tag{23}$$

where $\nu$ is Poisson's ratio, $E$ is Young's Modulus, and $K_{ni}$ is the crack stress intensity factor for mode $n$ due to $P_i$. The stress intensity factors for a unit width strip containing a crack of depth $\alpha$ are evaluated according to

$$K_{ni} = \sigma_i \sqrt{\pi \alpha} F_n\left(\frac{\alpha}{h}\right), \tag{24}$$

where $\sigma_i$ are the stresses due to the load $P_i$ at the crack, $F_n(\alpha/h)$ are appropriate intensity functions, and $h$ is the total strip length (see Fig. 6($b$)).

The additional flexibility due to the crack for a unit width strip can be written as

$$c_{ij} = \frac{\partial^2}{\partial P_i \partial P_j} \int_0^{\alpha} J(Y)\, dY \tag{25}$$

which, after integration along the crack edge, becomes

$$c_{ij} = \frac{\partial^2}{\partial P_i \partial P_j} \int_{-b}^{b} \int_0^{\alpha} J(Y)\, dY. \tag{26}$$

The current analysis is not concerned with torsion or axial displacement, hence only $c_{22}$, $c_{33}$, $c_{44}$, $c_{45}$, $c_{54}$, and $c_{55}$ are required. These elements are then given by

$$c_{22}=\frac{4(1-\nu^2)}{\pi E R}\int_0^{\bar{b}}\int_0^{\bar{a}}\bar{Y}F_{II}^2\left(\frac{\bar{Y}}{\bar{h}}\right)d\bar{Y}d\bar{X}, \tag{27}$$

$$c_{33}=\frac{4(1-\nu^2)}{\pi E R}\int_0^{\bar{b}}\int_0^{\bar{a}}\bar{Y}F_{II}^2\left(\frac{\bar{Y}}{\bar{h}}\right)d\bar{Y}d\bar{X}, \tag{28}$$

$$c_{44}=\frac{32(1-\nu^2)}{\pi E R^3}\int_0^{\bar{b}}\int_0^{\bar{a}}\bar{X}^2\bar{Y}F_{IY}^2\left(\frac{\bar{Y}}{\bar{h}}\right)d\bar{Y}d\bar{X}, \tag{29}$$

$$c_{45}=c_{55}=\frac{64(1-\nu^2)}{\pi E R^3}\int_0^{\bar{b}}\int_0^{\bar{a}}\bar{X}\bar{Y}\sqrt{1-\bar{X}^2}F_{IX}\left(\frac{\bar{Y}}{\bar{h}}\right)F_{IY}\left(\frac{\bar{Y}}{\bar{h}}\right)d\bar{Y}d\bar{X}, \tag{30}$$

$$c_{55}=\frac{64(1-\nu^2)}{\pi E R^3}\int_0^{\bar{b}}\int_0^{\bar{a}}(1-\bar{X}^2)\bar{Y}F_{IX}^2\left(\frac{\bar{Y}}{\bar{h}}\right)d\bar{Y}d\bar{X}, \tag{31}$$

where $\bar{b}=b/R$, $\bar{X}=X/R$, $\bar{Y}=Y/R$, $\bar{\alpha}=\alpha/R$, and $\bar{h}=h/R$. The corresponding intensity functions are given by

$$F_{IX}\left(\frac{\alpha}{h}\right)=\left[\frac{\tan(\beta_c)}{\beta_c}\right]^{1/2}[.932+.199(1-\sin(\beta_c))^4]/\cos(\beta_c), \tag{32}$$

$$F_{IY}\left(\frac{\alpha}{h}\right)=\left[\frac{\tan(\beta_c)}{\beta_c}\right]^{1/2}\left[.752+.202\left(\frac{\alpha}{h}\right)+.37(1-\sin(\beta_c))^3\right]\Big/\cos(\beta_c), \tag{33}$$

$$F_{II}\left(\frac{\alpha}{h}\right)=\left[1.122-.561\left(\frac{\alpha}{h}\right)+.085\left(\frac{\alpha}{h}\right)^2+.18\left(\frac{\alpha}{h}\right)^3\right]\Big/\left(1-\frac{\alpha}{h}\right)^{1/2}, \tag{34}$$

$$F_{III}\left(\frac{\alpha}{h}\right)=\left[\frac{\tan(\beta_c)}{\beta_c}\right]^{1/2}, \tag{35}$$

$$\beta_c=\left(\frac{\pi\alpha}{2h}\right). \tag{36}$$

The additional flexibilities due to the presence of the crack may therefore be obtained by numerically integrating Eqs. (27)–(31). Dimensionless flexibilities can be obtained according to

$$\bar{c}_{22}=c_{22}\frac{\pi E R}{(1-\nu^2)},\quad \bar{c}_{33}=c_{33}\frac{\pi E R}{(1-\nu^2)},$$
$$\bar{c}_{44}=c_{44}\frac{\pi E R^3}{(1-\nu^2)}\quad \bar{c}_{45}=c_{45}\frac{\pi E R^3}{(1-\nu^2)}, \tag{37}$$
$$\bar{c}_{55}=c_{55}\frac{\pi E R^3}{(1-\nu^2)},$$

where the overbar indicates the nondimensional value. These dimensionless flexibilities are plotted in Fig. 7, for crack depths up to 50% of the shaft diameter. These local flexibilities may now be introduced appropriately into the discrete representation of the system.

**3.2 Transfer Matrix.** The transfer-matrix method is a lumped parameter method in which inertial properties of the system are lumped into point matrices, and stiffness properties of the system are represented by lumped field matrices [2]; both relate state vectors at the two ends of a shaft element. The state vector at station *i*, expressed in the rotating *XYZ* coordinate frame, is defined as

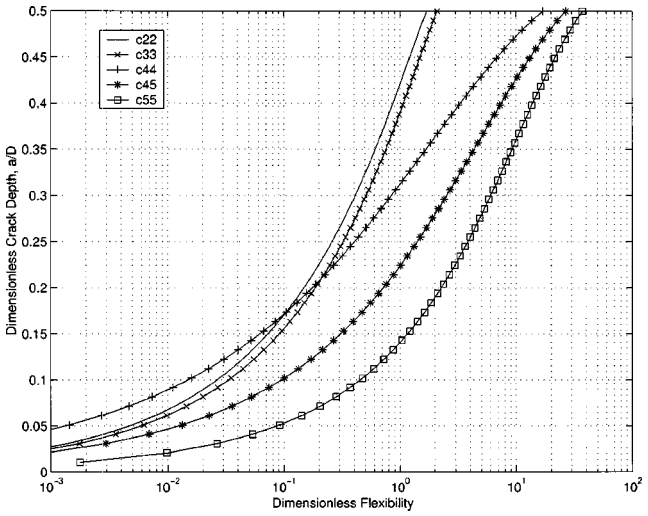


**Fig. 7 Dimensionless crack flexibilities**

$$\{Z\}_i=\{u_X\ \ \theta_Y\ \ M_Y\ \ -V_X\ \ -u_Y\ \ \theta_X\ \ M_X\ \ V_Y\}^T, \tag{38}$$

where $u$, $\theta$, $M$, and $V$ are the complex magnitudes of the displacement, tilt, moment, and shear force, respectively.

*The Field Matrix.* The state vector at the left of station *i*, $\{Z\}_i^L$, is related to the state vector at the right of station $i-1$, $\{Z\}_{i-1}^R$, by the field matrix $[F_i]$:

$$\{Z\}_i^L=[F_i]\{Z\}_{i-1}^R. \tag{39}$$

The field matrix $[F_i]$ has the form

$$[F_i]=\begin{bmatrix} 1 & l_i & \frac{l_i^2}{2EI} & \frac{l_i^3}{6EI} & 0 & 0 & 0 & 0 \\ 0 & 1 & \frac{l_i}{EI} & \frac{l_i^2}{2EI} & 0 & 0 & 0 & 0 \\ 0 & 0 & 1 & l_i & 0 & 0 & 0 & 0 \\ 0 & 0 & 0 & 1 & 0 & 0 & 0 & 0 \\ 0 & 0 & 0 & 0 & 1 & l_i & \frac{l_i^2}{2EI} & \frac{l_i^3}{6EI} \\ 0 & 0 & 0 & 0 & 0 & 1 & \frac{l_i}{EI} & \frac{l_i^2}{2EI} \\ 0 & 0 & 0 & 0 & 0 & 0 & 1 & l_i \\ 0 & 0 & 0 & 0 & 0 & 0 & 0 & 1 \end{bmatrix}, \tag{40}$$

where $l_i$ is the length of the field, $E$ is Young's modulus, and $I$ is the area moment of inertia of the field cross section.

*The Crack Matrix.* The crack is represented by a field matrix which contains the additional flexibilities introduced by the presence of the crack. The crack field matrix $[F_{\text{crack}}]$ has the form

$$[F_{crack}]=\begin{bmatrix} 1 & 0 & 0 & -c_{22} & 0 & 0 & 0 & 0 \\ 0 & 1 & c_{44} & 0 & 0 & 0 & c_{45} & 0 \\ 0 & 0 & 1 & 0 & 0 & 0 & 0 & 0 \\ 0 & 0 & 0 & 1 & 0 & 0 & 0 & 0 \\ 0 & 0 & 0 & 0 & 1 & 0 & 0 & -c_{33} \\ 0 & 0 & c_{54} & 0 & 0 & 1 & c_{55} & 0 \\ 0 & 0 & 0 & 0 & 0 & 0 & 1 & 0 \\ 0 & 0 & 0 & 0 & 0 & 0 & 0 & 1 \end{bmatrix}, \tag{41}$$

where the elements $c_{ij}$ are determined in Eqs. (27)–(36). Notably, in an uncracked shaft, $a=0$, $c_{ij}=0$, and $[F_{\text{crack}}]=[I]$.

*The Point Matrix.* The state vector at the right of the lumped mass at station $i$, $\{Z\}_i^R$, is related to the state vector at the left of the lumped mass at station $i$, $\{Z\}_i^L$, by the point matrix $[P_i]$:

$$\{Z\}_i^R=[P_i]\{Z\}_i^L. \tag{42}$$

The solution is sought in the rotating frame, $XYZ$, thus

$$[P_i]=\begin{bmatrix} 1 & 0 & 0 & 0 & 0 & 0 & 0 & 0 \\ 0 & 1 & 0 & 0 & 0 & 0 & 0 & 0 \\ 0 & n^2(I_p-I_t)-I_t\omega_0^2 & 1 & 0 & 0 & in\omega_0(2I_t-I_p) & 0 & 0 \\ m(\omega_0^2+n^2) & 0 & 0 & 1 & -2in\omega_0 m & 0 & 0 & 0 \\ 0 & 0 & 0 & 0 & 1 & 0 & 0 & 0 \\ 0 & 0 & 0 & 0 & 0 & 1 & 0 & 0 \\ 0 & in\omega_0(2I_t-I_p) & 0 & 0 & 0 & n^2(I_p-I_t)-I_t\omega_0^2 & 1 & 0 \\ 2in\omega_0 m & 0 & 0 & 0 & m(\omega_0^2+n^2) & 0 & 0 & 1 \end{bmatrix}, \tag{43}$$

where $m$ is the rotor mass, $I_t$ and $I_p$ are the transverse and polar mass moments of inertia, respectively, $n$ is the shaft speed, and $\omega_0$ is the relative whirl frequency (see Eqs. (1) and (6)).

*The Overall Transfer Matrix.* The overall transfer matrix for this system, $[U]$, is constructed according to

$$[U]=[P][F_2][F_{\text{crack}}][F_1]. \tag{44}$$

The state at the support, $\{Z\}_{\text{support}}$, is then related to the state at the right of the lumped mass $\{Z\}_1^R$ by the following:

$$\{Z\}_1^R=[U]\{Z\}_{\text{support}}. \tag{45}$$

*Undamped Free Response.* Applying the clamped-free boundary conditions, which are no displacement or tilt at the support boundary and no shear or moment at the end of the shaft, to the overall transfer matrix expression given in Eq. (45) leads to the following relations:

$$\begin{bmatrix} U_{33} & U_{34} & U_{37} & U_{38} \\ U_{43} & U_{44} & U_{47} & U_{48} \\ U_{73} & U_{74} & U_{77} & U_{78} \\ U_{83} & U_{84} & U_{87} & U_{88} \end{bmatrix} \begin{Bmatrix} M_Y \\ -V_X \\ M_X \\ V_Y \end{Bmatrix}_{\text{support}} \triangleq [\text{Freq}] \begin{Bmatrix} M_Y \\ -V_X \\ M_X \\ V_Y \end{Bmatrix}_{\text{support}} = \begin{Bmatrix} 0 \\ 0 \\ 0 \\ 0 \end{Bmatrix}_1^R, \tag{46}$$

$$\begin{bmatrix} U_{13} & U_{14} & U_{17} & U_{18} \\ U_{23} & U_{24} & U_{27} & U_{28} \\ U_{53} & U_{54} & U_{57} & U_{58} \\ U_{63} & U_{64} & U_{67} & U_{68} \end{bmatrix} \begin{Bmatrix} M_Y \\ -V_X \\ M_X \\ V_Y \end{Bmatrix}_{\text{support}} \triangleq [\text{Switch}] \begin{Bmatrix} M_Y \\ -V_X \\ M_X \\ V_Y \end{Bmatrix}_{\text{support}} = \begin{Bmatrix} u_X \\ \theta_Y \\ -u_Y \\ \theta_X \end{Bmatrix}_1^R, \tag{47}$$

where $U_{ij}$ are elements of the overall transfer matrix $[U]$.

By solving the standard eigenvalue problem for Eq. (46), four complex-conjugate pairs of eigenvalues result. The problem of assigning whirl directions to each of the four frequency magnitudes is identical to the previous discussion. To obtain the mode shape for a given eigenvalue, which is essentially the displacement and tilt portion of the state vector at the end of the shaft, it is convenient to label the $4\times4$ matrices in Eqs. (46) and (47) as [Freq] and [Switch], respectively. From Eq. (47), the shear and moment portion of the state vector at the support is given by

$$\begin{Bmatrix} M_Y \\ -V_X \\ M_X \\ V_Y \end{Bmatrix}_{\text{support}} = [\text{Switch}]^{-1} \begin{Bmatrix} u_X \\ \theta_Y \\ -u_Y \\ \theta_X \end{Bmatrix}_1^R. \tag{48}$$

Substituting this expression for $\{M_Y\ -V_X\ M_X\ V_Y\}_{\text{support}}^T$ into Eq. (46) results in

$$[\text{Freq}][\text{Switch}]^{-1} \begin{Bmatrix} u_X \\ \theta_Y \\ -u_Y \\ \theta_X \end{Bmatrix}_1^R = \begin{Bmatrix} 0 \\ 0 \\ 0 \\ 0 \end{Bmatrix}. \tag{49}$$

For each frequency magnitude, given by the four pairs of eigenvalues, Eq. (49) forms a linearly dependent system of equations. Solving this eigenvalue problem results in the corresponding mode shape, i.e., the vector $\{u_X\ \theta_Y\ u_Y\ \theta_X\}^T$. Once the eigenvalues and corresponding eigenvectors, or mode shapes, are determined, whirl directions are also assigned (see previous discussion) to each frequency, and the true natural frequencies are plotted versus shaft speed.

Figure 8 shows the whirl frequencies as a function of shaft speed for crack depths ranging from 0 to 40% of the shaft diameter. The "×" symbols along the horizontal axis indicate shaft speeds for which one or more of the eigenvalues has a positive real part, i.e., shaft speeds for which the response is unstable. As previously, two reference lines indicating critical speeds and "2$X$ resonance" shaft speeds are also included in each figure. From

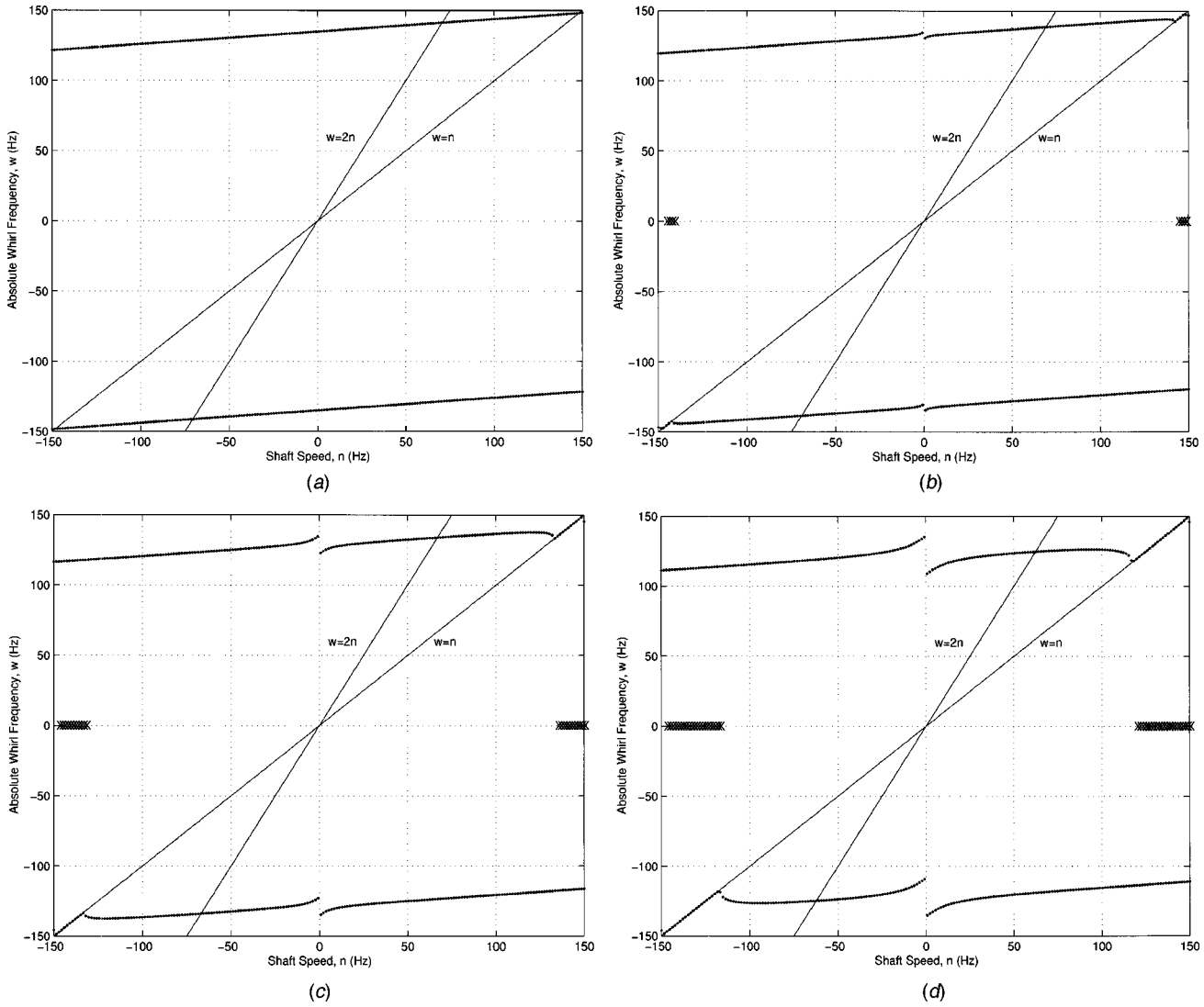


**Fig. 8 Local asymmetry model free response at various crack values: (*a*) uncracked; (*b*) 20%; (*c*) 30%; (*d*) 40%**

this analysis, shaft speeds at which the $2X$ response is maximum can be predicted for various crack depths. Table 3 gives the predicted $2X$ resonance shaft speeds based on the local asymmetry crack model. The decrease in the $2X$ resonance shaft speeds indicates the decrease in the natural frequencies of the system resulting from the increased flexibility introduced by the presence of the crack. This free response analysis of the system containing the local asymmetry crack model indicates that a decrease in natural frequencies, which may be observed as a decrease in primary and secondary critical speeds, is a characteristic of the system response that can be directly attributed to the presence of a transverse crack.

**Table 3 $2X$ resonance shaft speeds—local asymmetry model free response**

| % cracked | Shaft speed (Hz) |
|---|---|
| 0 | 70.62 |
| 10 | 70.34 |
| 20 | 69.24 |
| 30 | 66.97 |
| 40 | 62.44 |

*Damped Forced Response.* To account for a forcing function in the transfer-matrix method described above, the state vector and field and point matrices are extended to $9\times1$ and $9\times9$, respectively, similar to Ref. [2]. Likewise, the point matrix for this local asymmetry model forced response analysis will be modified to include damping effects.

The state vector for station $i$ now has the form

$$\{Z\}_i=\{u_X\ \ \theta_Y\ \ M_Y\ \ -V_X\ \ -u_Y\ \ \theta_X\ \ M_X\ \ V_Y\ \ 1\}^T. \quad (50)$$

The field matrices, including the crack matrix, are identical to those given in Eqs. (40) and (41) with an additional row and column of zeros, except for element (9,9), which is one unit. The damped forced response point matrix $[\hat{P}_i]$ contains damping effects, and is given by

$$[\hat{P}_i]=\begin{bmatrix}[P_i] & \{0\}\\ \{0\} & 1\end{bmatrix}+[\tilde{P}_i], \quad (51)$$

where $[P_i]$ is the $8\times8$ point matrix given in Eq. (43), and $[\tilde{P}_i]$ is the $9\times9$ matrix given by

$$[\tilde{P}_i]=\begin{bmatrix} 0 & 0 & 0 & 0 & 0 & 0 & 0 & 0 & 0 \\ 0 & 0 & 0 & 0 & 0 & 0 & 0 & 0 & 0 \\ i\omega d_{12_Y} & -i\omega d_{22_Y} & 0 & 0 & 0 & 0 & 0 & 0 & 0 \\ i\omega d_{11_Y} & -i\omega d_{12_Y} & 0 & 0 & 0 & 0 & 0 & 0 & mg \\ 0 & 0 & 0 & 0 & 0 & 0 & 0 & 0 & 0 \\ 0 & 0 & 0 & 0 & 0 & 0 & 0 & 0 & 0 \\ 0 & 0 & 0 & 0 & i\omega d_{12_X} & -i\omega d_{22_X} & 0 & 0 & 0 \\ 0 & 0 & 0 & 0 & i\omega d_{11_X} & -i\omega d_{12_X} & 0 & 0 & -img \\ 0 & 0 & 0 & 0 & 0 & 0 & 0 & 0 & 0 \end{bmatrix}, \tag{52}$$

where $d_{ij_q}=c_{eq_{ij_q}}=\overline{\beta}k_{ij_q}/\omega$, and $g$ is the acceleration due to gravity. This matrix contains the influence of internal damping and the forcing function. The overall transfer matrix is obtained by combining these $9\times9$ field and point matrices as in Eqs. (44) and (45). Applying the clamped-free boundary conditions, which are no displacement or tilt at the support boundary and no shear or moment at the end of the shaft, results in the following relations for the forced response:

$$\begin{bmatrix} U_{33} & U_{34} & U_{37} & U_{38} \\ U_{43} & U_{44} & U_{47} & U_{48} \\ U_{73} & U_{74} & U_{77} & U_{78} \\ U_{83} & U_{84} & U_{87} & U_{88} \end{bmatrix} \begin{Bmatrix} M_Y \\ -V_X \\ M_X \\ V_Y \end{Bmatrix}_{\text{support}} + \begin{Bmatrix} U_{39} \\ U_{49} \\ U_{79} \\ U_{89} \end{Bmatrix} = \begin{Bmatrix} 0 \\ 0 \\ 0 \\ 0 \end{Bmatrix}_1^R, \tag{53}$$

$$\begin{bmatrix} U_{13} & U_{14} & U_{17} & U_{18} \\ U_{23} & U_{24} & U_{27} & U_{28} \\ U_{53} & U_{54} & U_{57} & U_{58} \\ U_{63} & U_{64} & U_{67} & U_{68} \end{bmatrix} \begin{Bmatrix} M_Y \\ -V_X \\ M_X \\ V_Y \end{Bmatrix}_{\text{support}} = \begin{Bmatrix} u_X \\ \theta_Y \\ -u_Y \\ \theta_X \end{Bmatrix}_1^R. \tag{54}$$

The vector $\{M_Y\ -V_X\ M_X\ V_Y\}^T$ in Eq. (53) is obtained as the solution of a linearly independent system of equations. This solution is substituted into Eq. (54) and the forced response vector $\{u_X\ \theta_Y\ u_Y\ \theta_X\}^T$ is obtained. Each element of the state vector is a complex number. The displacement in the $X$ and $Y$ directions, for example, are of the form

$$u_X=u_{X_r}+iu_{X_i}, \tag{55}$$

$$u_Y=u_{Y_r}+iu_{Y_i}, \tag{56}$$

where the $r$ and $i$ subscripts denote real and imaginary components, respectively. The displacement in the $X$ and $Y$ directions, $X$ and $Y$, will be given by

$$X=\mathrm{Re}[u_Xe^{int}], \tag{57}$$

$$Y=\mathrm{Re}[u_Ye^{int}]. \tag{58}$$

So, taking the real part of each,

$$X=u_{X_r}\cos(nt)-u_{X_i}\sin(nt), \tag{59}$$

$$Y=u_{Y_r}\cos(nt)-u_{Y_i}\sin(nt). \tag{60}$$

Recalling that the point and field matrices were derived in the rotating coordinate frame $XYZ$,

$$\rho=X+iY=(u_{X_r}+iu_{Y_r})\cos(nt)-(u_{X_i}+iu_{Y_i})\sin(nt). \tag{61}$$

It is desired to observe the results in a stationary coordinate frame. The transformation from the rotating $XYZ$ coordinate frame to the inertial $\xi\eta\zeta$ coordinate frame is given by

$$u=\rho e^{int}, \tag{62}$$

so, the displacement of the rotor expressed in the stationary coordinate frame is

$$u=\tfrac{1}{2}[(u_{X_r}-iu_{x_i}+iu_{Y_r}+u_{Y_i})+(u_{X_r}+iu_{x_i}+iu_{Y_r}-u_{Y_i})e^{i2nt}]. \tag{63}$$

Similarly, the tilt of the rotor expressed in the stationary coordinate frame is

$$\gamma=\tfrac{1}{2}[(\theta_{X_r}-i\theta_{x_i}+i\theta_{Y_r}+\theta_{Y_i})+(\theta_{X_r}+i\theta_{x_i}+i\theta_{Y_r}-\theta_{Y_i})e^{i2nt}]. \tag{64}$$

It is clear from Eqs. (63) and (64) that the constant radial force of gravity acting on the cracked system results in a $2X$ harmonic response which is predicted by this analysis to have a circular shape. The predicted $2X$ circular tilt response has a radius of $\frac{1}{2}|(\theta_{X_r}-\theta_{Y_i})+i(\theta_{X_i}+\theta_{Y_r})|$ and is offset according to $\frac{1}{2}[(\theta_{X_r}+\theta_{Y_i})-i(\theta_{X_i}-\theta_{Y_r})]$. The magnitude of the $2X$ tilt response is plotted as a function of shaft speed in Fig. 9, shown separately for two low- and high-speed ranges, and for crack depths varying from 0 to 40% of the shaft diameter. It is clear that for an arbitrary shaft speed, the amplitude of the $2X$ response is predicted to increase as the crack depth increases. The range of shaft speeds shown contains $2X$ resonant speeds for each crack depth (Fig. 9(*b*)). As previously, the $2X$ resonant speeds decrease as the crack depth increases. The $2X$ resonance shaft speeds predicted based on this local asymmetry crack model forced response analysis are given in Table 4. Since the 0% crack depth results in a system with symmetric stiffness properties, no $2X$ resonance is predicted for the forced response analysis. Damping is light (typical damping ratios are less than 1%, as experimentally found [35]), thus numerically Tables 3 and 4 provide similar $2X$ results.

The amplitude of the $2X$ response at each $2X$ resonant speed is shown to increase in magnitude as the crack depth increases. The shaft speeds at which the $2X$ peaks occur decrease due to the reduced stiffness, which changes the system natural frequencies, resulting from the presence of the crack. The increased amplitude of the $2X$ component of the system response is due to the increased asymmetry as the crack depth increases. This forced response analysis of the system containing the local asymmetry crack model indicates that an increase in the amplitude of the $2X$ component of the system response, as well as a decrease in the shaft speed at which the $2X$ component of the response is maximum, are characteristics of the system response that may be directly attributed to the presence of a transverse shaft crack.

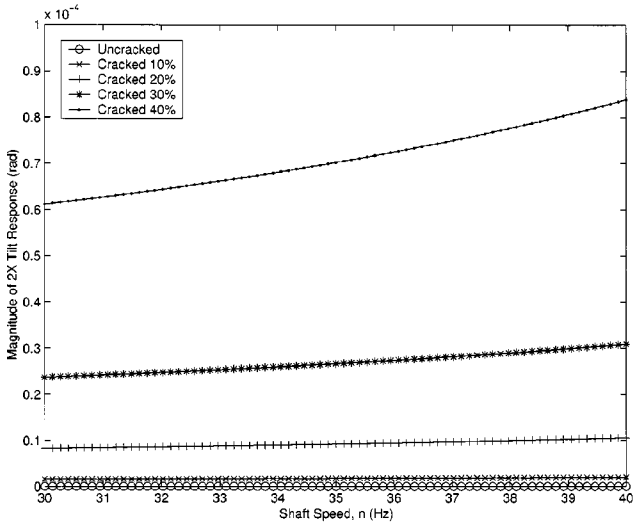


(*a*)

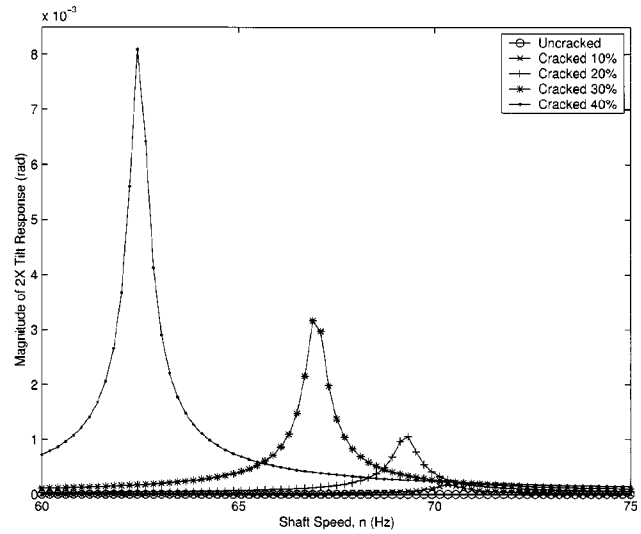


(*b*)

**Fig. 9 Local asymmetry model forced response: (*a*) low-speed range; (*b*) high-speed range**

## 4 Conclusions

Two theoretical analyses have been presented to identify characteristics of the system response that may be directly attributed to the presence of a transverse crack in the shaft of the test rig system. Both the global and local asymmetry crack model analyses qualitatively predict response characteristics which have been experimentally observed in the response of a system containing a gaping crack.

The behavior of the $2X$ harmonic component of the system response is an effective target observation for a monitoring system. The predicted behaviors of the $2X$ harmonic component of the system response include an increase in magnitude for increasing crack depth as well as a decrease in the shaft speed at which the $2X$ harmonic component of the system response is maximum. The presence of a transverse shaft crack has also been shown to induce an unstable response for some shaft speeds. The detection of changes in the magnitude of the $2X$ harmonic component of the system response becomes much more difficult for shaft speeds which are greater than $2X$ resonance speeds. Frequency-sweep tests, which pass through $2X$ resonance shaft speeds, would provide the most useful information; however, observation of the magnitude of the $2X$ component could also provide crack diagnostic information.

This research utilizes a method to account for a shaft crack in the transfer-matrix method. By employing these transfer matrices, coupled systems that include shafts, seals, bearings, etc., can be systematically analyzed in a modular fashion [2].

**Table 4 $2X$ resonance shaft speeds—local asymmetry model forced response**

| % cracked | Shaft speed (Hz) |
|---|---|
| 0 | |
| 10 | 70.34 |
| 20 | 69.24 |
| 30 | 66.97 |
| 40 | 62.44 |

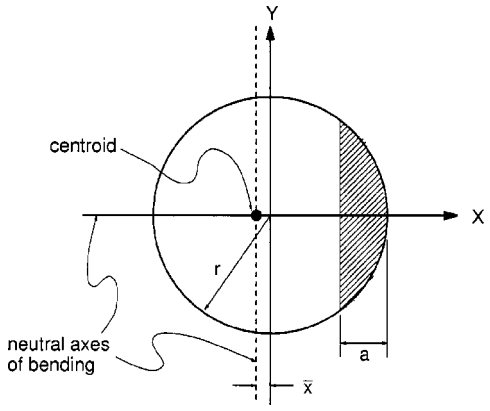


**Fig. 10 Asymmetric shaft cross section**


## Acknowledgments

This research was conducted under Grant No. N00014-95-1-0539 of the Office of Naval Research. Dr. Peter Schmidt was the Program Manger. This support is gratefully acknowledged.


## Appendix: Asymmetric Stiffness

The stiffness elements relate the displacement and tilt at the end of the shaft to the applied forces or moments in the $X$ and $Y$ directions. The stiffness relationships for a cantilever Euler-Bernoulli beam are obtained from general beam theory as

$$\begin{Bmatrix} F_X \\ M_Y \end{Bmatrix} = \begin{bmatrix} k_{11_Y} & -k_{12_Y} \\ -k_{21_Y} & k_{22_Y} \end{bmatrix} \begin{Bmatrix} X \\ \gamma_Y \end{Bmatrix} \tag{A1}$$

and

$$\begin{Bmatrix} F_Y \\ M_X \end{Bmatrix} = \begin{bmatrix} k_{11_X} & k_{12_X} \\ k_{21_X} & k_{22_X} \end{bmatrix} \begin{Bmatrix} Y \\ \gamma_X \end{Bmatrix}, \tag{A2}$$

where $k_{11_X}=12EI_X/l^3$, $k_{12_X}=k_{21_X}=6EI_X/l^2$, $k_{22_X}=4EI_X/l$, $k_{11_Y}=12EI_Y/l^3$, $k_{12_Y}=k_{21_Y}=6EI_Y/l^2$, and $k_{22_Y}=4EI_Y/l$.

The area moments of inertia, $I$, are calculated about the $X$ and $Y$ axes. For the uncracked case, the $X$ and $Y$ axes are also the neutral axes of bending.

The asymmetric stiffness relationships are obtained by calculating the appropriate asymmetric area moments of inertia and properly substituting them into the stiffness coefficients $k_{ij}$ above.

The cross section of the shaft at the location of the crack, which is shown in Fig. 10, has asymmetric area moments of inertia about the neutral axes of bending which are parallel to the $X$ and $Y$ axes. To find the area moments of inertia about the neutral axes of bending, the parallel axis theorem was utilized.

The area moments of inertia about the $X$ and $Y$ axes, $\hat{I}_X$ and $\hat{I}_Y$, are defined as

$$\hat{I}_X = \int_A Y^2 dA = \int_A Y^2 dX dY, \tag{A3}$$

$$\hat{I}_Y = \int_A X^2 dA = \int_A X^2 dX dY, \tag{A4}$$

where $A$ is the uncracked area of the cross section. The cross-coupled area moments of inertia, $I_{XY}$ and $I_{YX}$, are zero since the $X$ axis is an axis of symmetry. After integrating over the uncracked area, the following equations for $\hat{I}_X$ and $\hat{I}_Y$ result:

$$\hat{I}_X = \frac{\pi r^4}{8} + \frac{1}{4}\left[(r-a)(r^2-4ra+2a^2)\sqrt{2ra-a^2} + r^4 \sin^{-1}\left(\frac{r-a}{r}\right)\right], \tag{A5}$$

$$\hat{I}_Y = \frac{\pi r^4}{4} + \frac{(r-a)(2\Upsilon)^3}{12} - \frac{1}{4}\left[\Upsilon(2\Upsilon^2-r^2)\sqrt{r^2-\Upsilon^2} + r^4 \sin^{-1}\left(\frac{\Upsilon}{r}\right)\right], \tag{A6}$$

where $r$ is the shaft radius, $a$ is the crack depth, and $\Upsilon = \sqrt{a(2r-a)}$ for convenience.

The following expressions for the area of the cross section, $A$, and the distance from the $X$ axis to the centroid of the cross section, $\overline{X}$, can be obtained

$$A = (r-a)\sqrt{2ra-a^2} + r^2 \sin^{-1}\left(1-\frac{a}{r}\right) + \frac{\pi r^2}{2}, \tag{A7}$$

$$\overline{X} = \frac{2}{3A}(2ar-a^2)^{3/2}. \tag{A8}$$

The moments of inertia about the parallel centroidal axes, $I_X$ and $I_Y$, are then obtained according to the parallel axis theorem as

$$I_X = \hat{I}_X, \tag{A9}$$

$$I_Y = \hat{I}_Y - A\overline{X}^2. \tag{A10}$$

## References


[1] Zou, M., Dayan, J., and Green, I., 2000, "Dynamic Simulation and Monitoring of a Non-Contacting Flexibly Mounted Rotor Mechanical Face Seal," IMechE, Proc. Inst. Mech. Eng. **214**(C9), Part C, pp. 1195–1206.

[2] Lee, A. S., and Green, I., 1994, "Rotordynamics of a Mechanical Face Seal Riding on a Flexible Shaft," ASME J. Tribol., **116**(2), pp. 345–351.

[3] Lee, A. S., and Green, I., 1994, "Higher Harmonic Oscillations in a Noncontacting FMR Mechanical Face Seal Test Rig," ASME J. Vibr. Acoust., **116**(2), pp. 161–167.

[4] Lee, A. S., and Green, I., 1995, "An Experimental Investigation of the Steady-State Response of a Noncontacting Flexibly Mounted Rotor Mechanical Face Seal," ASME J. Tribol., **117**(1), pp. 153–159.

[5] Lee, A. S., and Green, I., 1995, "Physical Modeling and Data Analysis of the Dynamic Response of a Flexibly Mounted Rotor Mechanical Seal," ASME J. Tribol., **117**, pp. 130–135.

[6] Zou, M., and Green, I., 1999, "Clearance Control of a Mechanical Face Seal," STLE Tribol. Trans., **42**, pp. 535–540.

[7] Zou, M., Dayan, J., and Green, I., 1999, "Parametric Analysis of Contact Control of a Noncontacting Mechanical Face Seal," in *Proceedings of Vibration, Noise and Structural Dynamics*, pp. 493–499, April.

[8] Dayan, J., Zou, M., and Green, I., 2000, "Sensitivity Analysis for the Design and Operation of a Noncontacting Mechanical Face Seal," IMechE, Proc. Inst. Mech. Eng. **214**(C9), Part C, pp. 1207–1218.

[9] Zou, M., Dayan, J., and Green, I., 2000, "Feasibility of Contact Elimination of a Mechanical Face Seal Through Clearance Adjustment," ASME J. Eng. Gas Turbines Power, **122**, pp. 478–484.

[10] Dayan, J., Zou, M., and Green, I., 1999, "Contact Elimination in Mechanical Face Seals Using Active Control," in *Proceedings of the IEEE 7th Mediterranean Conference on Control and Automation (MED99)*, pp. 618–619, June.

[11] Tondl, A., 1965, *Some Problems in Rotor Dynamics*, Czechoslovakian Academy of Sciences, Chapman & Hall, London.

[12] Henry, T. A., and Okah-Avae, B. E., 1976, "Vibrations in Cracked Shafts," in *Conference on Vibrations in Rotating Machinery*, pp. 15–19.

[13] Murray, D. B., and McCraith, J. R., 1984, "Vibrational Method for the Detection of Cracks in Rotating Shafts," in *First Parsons International Turbine Conference*, pp. 229–236.

[14] Rao, J. S., 1991, *Rotor Dynamics*, 2nd edition, Wiley, New York.

[15] Gasch, R., 1976, "Dynamic Behavior of Simple Rotor With a Cross-Sectional Crack," in *Conference on Vibrations in Rotating Machinery*, p. 123.

[16] Mayes, I. W., and Davies, W. G. R., 1976, "The Vibrational Behavior of a Rotating Shaft System Containing a Transverse Crack," in *Conference on Vibrations in Rotating Machinery*, pp. 53–64.

[17] Imam, I., and Azzaro, S. H., 1989, "Development of an On-Line Rotor Crack Detection and Monitoring System," ASME J. Vib., Acoust., Stress, Reliab. Des., **111**(3), pp. 241–250.

[18] Huang, S. C., Huang, Y. M., and Shieh, S. M., 1993, "Vibration and Stability of a Rotating Shaft Containing a Transverse Crack," J. Sound Vib., **162**, pp. 387–401.

[19] Tsai, T., and Wang, W., 1998, "Vibration of a Rotor With a Transverse Open Crack," Proc. Natl. Sci. Counc., Repub. China, Part A: Phys. Sci. Eng., **22**, pp. 372–384.

[20] Grabowski, B., 1980, "The Vibrational Behavior of a Turbine Rotor Containing a Transverse Crack," ASME J. Mech. Des., **121**, pp. 140–146.

[21] Dimarogonas, A. D., and Paipetis, S. A., 1983, *Analytical Methods in Rotor Dynamics*, Applied Science.

[22] Herbert, R. G., 1987, "Turbine-Alternator Run-Down Vibration Analysis: Automated Crack Detection," in *11th Biennial Conference on Mechanical Vibration and Noise*, Vol. 2, pp. 631–636.

[23] Inagaki, T., Kanki, H., and Shiraki, K., 1982, "Transverse Vibrations of a General Cracked-Rotor Bearing System," ASME J. Mech. Des., **104**(2), pp. 345–355.

[24] Schmied, J., and Kraemer, E., 1984, "Vibrational Behavior of a Rotor With a Cross-Sectional Crack," in *Conference on Vibrations in Rotating Machinery*, pp. 183–192.

[25] Nelson, H. D., and Nataraj, C., 1986, "The Dynamics of a Rotor System With a Cracked Shaft," ASME J. Vib., Acoust., Stress, Reliab. Des., **108**, pp. 189–196.

[26] Sofker, D., Bajkowski, J., and Muller, P. C., 1993, "Crack Detection in Turbo Rotors, Vibrational Analysis and Fault Detection," in *Conference on Mechanical Vibration and Noise*, Vol. 60, pp. 277–287.

[27] Meng, G., and Hahn, E. J., 1994, "Dynamic Response of a Cracked Rotor With Some Comments on Crack Detection," in *Proceedings of the International Gas Turbine and Aeroengine Congress and Exposition*, June.

[28] Dirr, B. O., and Rothkegel, W., 1994, "Detection and Simulation of Small Transverse Cracks in Rotating Shafts," Arch. Appl. Mech., **64**(3), pp. 206–222.

[29] Inagaki, T., Kanki, H., and Shiraki, K., 1980, "Response Analysis of a General Asymmetric Rotor-Bearing," ASME J. Mech. Des., **102**(1), pp. 147–157.

[30] Dimarogonas, A. D., and Papadopoulos, C. A., 1983, "Vibration of Cracked Shafts in Bending," J. Sound Vib., **91**, pp. 583–593.

[31] Davies, W. G. R., and Mayes, I. W., 1984, "The Vibrational Behavior of a Multi-Shaft, Multi-Bearing System in the Presence of a Propogating Transverse Crack," ASME J. Vib., Acoust., Stress, Reliab. Des., **106**(1), pp. 146–153.

[32] Gasch, R., 1993, "A Survey of the Dynamic Behavior of a Simple Rotating Shaft With a Transverse Crack," J. Sound Vib., **160**, pp. 313–332.

[33] Papadopoulos, C. A., and Dimarogonas, A. D., 1987, "Stability of Cracked Rotors in the Coupled Vibration Mode," in *11th Biennial Conference on Mechanical Vibration and Noise*, Vol. 1, pp. 25–34.

[34] Papadopoulos, C. A., and Dimarogonas, A. D., 1987, "Coupled Longitudinal and Bending Vibrations of a Rotating Shaft With an Open Crack," J. Sound Vib., **117**, pp. 81–93.

[35] Casey, C., 2000, "Crack Detection in Rotor Dynamic System by Vibration Monitoring," M.S. thesis, Georgia Institute of Technology.

[36] Green, I., and Etsion, I., 1986, "A Kinematic Model for Mechanical Seals With Antirotation Locks or Positive Drive Devices," ASME J. Tribol., **108**(1), pp. 42–45.

[37] Tada, H., Paris, P. C., and Irwin, G. R., 1985, *The Stress Analysis of Cracks Handbook*, 2nd Ed., Paris Productions, St. Lous, MO.

**Andrew J. Provenza**
NASA Glenn Research Center,
Cleveland, OH 44135-3191
e-mail: andrew.j.provenza@nasa.gov

**Gerald T. Montague**
Army Research Lab,
NASA Glenn Research Center,
Cleveland, OH 44135
e-mail: gerald.t.montague@nasa.gov

**Mark J. Jansen**
University of Toledo,
Toledo, OH
e-mail: mark.j.jansen@nasa.gov

**Alan B. Palazzolo**
Department of Mechanical Engineering,
Texas A&M University,
College Station, TX
e-mail: a-palazzolo@tamu.edu

**Ralph H. Jansen**
University of Toledo,
Toledo, OH
e-mail: ralph.h.jansen@nasa.gov

# High Temperature Characterization of a Radial Magnetic Bearing for Turbomachinery

*Open loop, experimental force and power measurements of a radial, redundant-axis, magnetic bearing at temperatures to 1000°F (538°C) and rotor speeds to 15,000 rpm along with theoretical temperature and force models are presented in this paper. The experimentally measured force produced by a single C-core circuit using 22A was 600 lb (2.67 kN) at room temperature and 380 lb (1.69 kN) at 538°C. These values were compared with force predictions based on a one-dimensional magnetic circuit analysis and a thermal analysis of gap growth as a function of temperature. The analysis showed that the reduction of force at high temperature is mostly due to an increase in radial gap due to test conditions, rather than to reduced core permeability. Tests under rotating conditions showed that rotor speed has a negligible effect on the bearing's static force capacity. One C-core required approximately 340 W of power to generate 190 lb (845 N) of magnetic force at 538°C, however the magnetic air gap was much larger than at room temperature. The data presented are after bearing operation for eleven total hours at 538°C and six thermal cycles.* [DOI: 10.1115/1.1807413]

## Introduction

The gas turbine industry has a continued vested interest in improving engine performance and reducing net operating and maintenance costs. These goals are being realized because of advancements in materials, aeroelasticity & CFD analysis, and engine simulation. These advancements also aid in increasing engine thrust-to-weight ratios, pressure ratios, specific fuel consumption, and overall reliability through higher-efficiency engine operation at higher rotational speeds and temperatures.

Rolling element bearings and squeeze film dampers are currently used to support gas turbine engine rotors. These types of bearings are limited in temperature (<260°C) and speed (<2.5 million DN) and require both cooling air and a lubrication system. Rolling element bearings in gas turbines have been pushed to their limits and new bearing technologies must be developed to take full advantage of other aforementioned advancements.

Magnetic bearings are well suited to operate at elevated temperature, higher rotational speeds, and extreme altitudes (thin air atmosphere) and are a promising solution to current limitations.

Magnetic bearings in gas turbine engines would eliminate lubrication analysis, leaks, spills, contamination, and unnecessary maintenance due to faulty chip detection. The magnetic bearing could also provide health monitoring and adapt the rotor support to actively respond to transients such as hard aircraft landings and sudden imbalances. Magnetic bearings will enable engine designers to take full advantage of other technological advancements in turbine engine components by allowing rotor components to spin at higher speeds and at higher temperatures. As a result, turbine and compressor spools can be designed with higher operating temperatures and with significantly larger, faster, stiffer, highly damped rotors.

Contributed by the International Gas Turbine Institute (IGTI) of THE AMERICAN SOCIETY OF MECHANICAL ENGINEERS for publication in the ASME JOURNAL OF ENGINEERING FOR GAS TURBINES AND POWER. Paper presented at the International Gas Turbine and Aeroengine Congress and Exhibition, Atlanta, GA, June 16–19, 2003, Paper No. 2003-GT-38870. Manuscript received by IGTI, October 2002, final revision, March 2003. Associate Editor: H. R. Simmons.

## Literature Search

Magnetic bearing technology is being developed worldwide and is considered an enabling technology for new, hotter engine designs. There are several institutions which have been developing hardware for this high temperature application. Xu, Wang, and Schweitzer demonstrated 1 degree-of-freedom (DOF) levitation of a plate at 560°C and presented a design of a magnetic bearing system for 5 DOF in Ref. [1]. Vibration results for a blower used to recycle 700°C cathode gas, fully suspended by magnetic bearings operating at 400°C, was presented by Ohsawa et al. [2] Mekhiche et al. developed a high temperature magnetic bearing system that is described from design through room temperature testing in Refs. [3,4]. Field et al. described a complete, reliable magnetic bearing system targeted for high temperature application in Refs. [5,6]. Only in Ref. [2] can actual experimental data describing high temperature operation be found. But the data describe the vibration response of the suspended rotor at temperature. They do not present an assessment of the effects of temperature on magnetic bearing properties and system requirements.

High temperature magnetic properties of candidate magnetic materials were investigated in the 1960s by Kueser et al. [7], and recently by Kondoleon and Kelleher [8] and Fingers [9]. Hyperco 50 data in Ref. [7] does not indicate a significant decrease in permeability or saturation flux density at 538°C.

After reviewing the available literature, the authors believe that this paper provides the first baseline industry performance characteristics for actual magnetic bearing hardware during operation at temperatures up to 538°C.

The third generation high temperature, high load magnetic bearing, developed at the NASA Glenn Research Center, was first characterized at room temperature (RT) up to 20,000 rpm. It is capable of producing over 1000 lb (4.5 kN) of force per magnetic axis at RT and at speed. RT data for this bearing is presented in Ref. [10].

Data presented in this paper characterizes the third generation bearing at temperatures up to 538°C. Bearing force as a function of current, temperature, and speed to 15,000 rpm is shown. Bear-

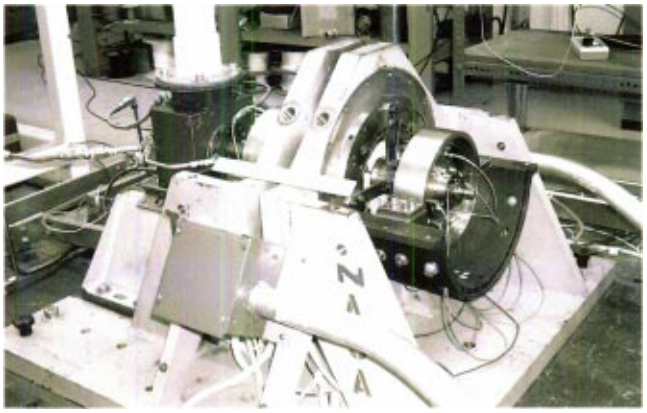

**Fig. 1 High-temperature magnetic bearing test facility at NASA Glenn Research Center**

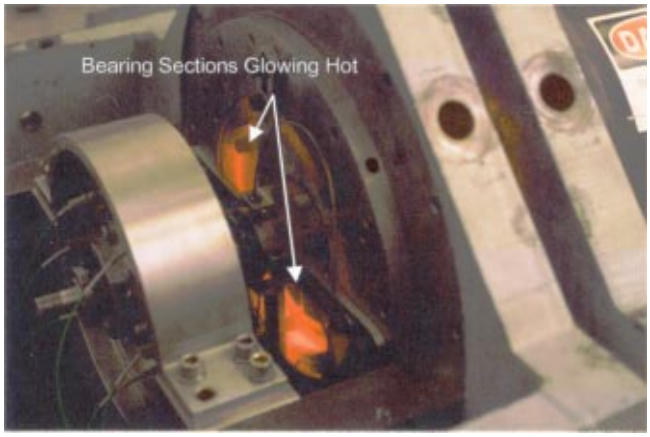


**Fig. 3 Magnetic bearing at 538°C (1000°F)**

ing power consumption measurements taken at several applied currents and temperatures are also presented. And finally, results of a simple analytical model are compared to the experimental force results.

## Test Facility

**Facility Description.** The high temperature magnetic bearing test facility is shown in Fig. 1. The structural support can accommodate thrust and radial bearings up to 22.8 cm diameter with a maximum axial loading of 22 kN and a maximum radial loading of 11.1 kN. The test facility has been configured a number of different ways [10,11].

The current configuration can be seen in Fig. 2. The magnetic bearing is located at the center of gravity of the 75-mm-diam rotor that weighs 8 kg. The 200-mm-diam stator weighs 23 kg. A 0.56 mm radial air gap exists between the stator poles and the rotor at RT. The rotor has interchangeable sleeves on each end that interface it with the support bearings, which, for these tests, are high-speed, grease packed, duplex ball bearings. For this configuration, the rotor was fitted with negative clearance sleeves so it was supported on pre-loaded ball bearings at both ends. This was done so that forces exerted by the magnetic bearing could be easily and directly measured outside the hot section at the support bearing locations. The outboard sleeve can be replaced with a positive clearance sleeve so that the magnetic bearing can support the rotor. An air turbine drives the rotor.

The magnetic bearing stator is an isolated C-core, 12-pole, heteropolar design, and is described in detail in Ref. [12]. The stator has an axial length of 76 mm. Each C-core is wrapped with two coils of 52 turns each of specially insulated and potted silver wire.

Power to the magnetic bearing is provided through tri-state, pulse width modulated (PWM) amplifiers. These components are passively filtered to remove high frequency amplifier noise that results from hard amplifier switching and for reducing EMI emissions from the bearing coils that are picked up by the eddy current position sensors.

Heat is supplied to the bearing through three, 3 kW band heaters wrapped around the stator (Fig. 2). Ground Fault Circuit Interrupts (GFCIs) have been incorporated into the heating system and the PWM amplifier circuits to protect the hardware and for safeguarding personnel. The facility is described in more detail in Ref. [12]. Figure 3 shows the facility at 538°C with the stator glowing ''orange'' hot.

**Sensors.** The facility is equipped with several different types of sensors that monitor load, temperature, rotor position, speed, and electric current.

High load, high bandwidth, piezoelectric load cells, with an accuracy of $\pm 1.5$ N, support the inboard and outboard rolling element bearings (Fig. 4). These load cells are capable of measuring loads up to 7.5 kN at 200 kHz and have a maximum operating temperature of 200°C. Two load cells are aligned along each of the three magnetic bearing axes on both support bearings for a total of 12 load cells. Each load cell was set with a preload of 1 kN. This preload value supplied symmetric structural rotor support, put the critical speed out of the operating range, and estab-

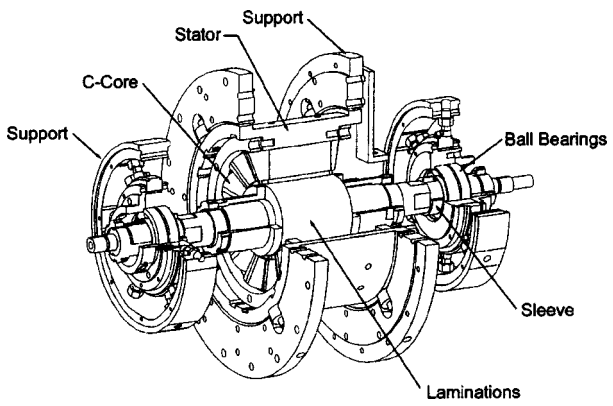


**Fig. 2 Third-generation high-temperature magnetic bearing test rig**

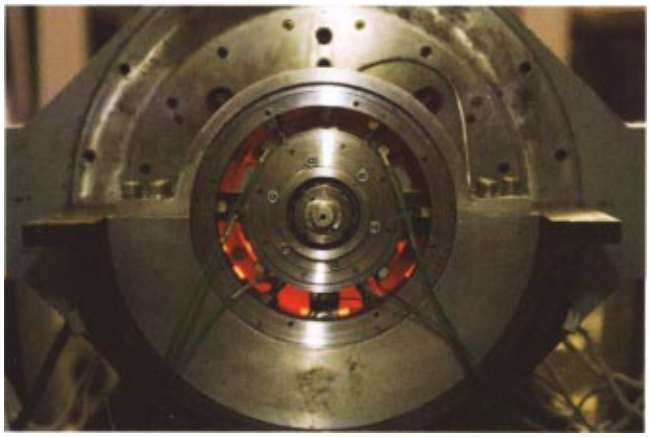

**Fig. 4 Six load cells supporting the outboard duplex ball bearing**

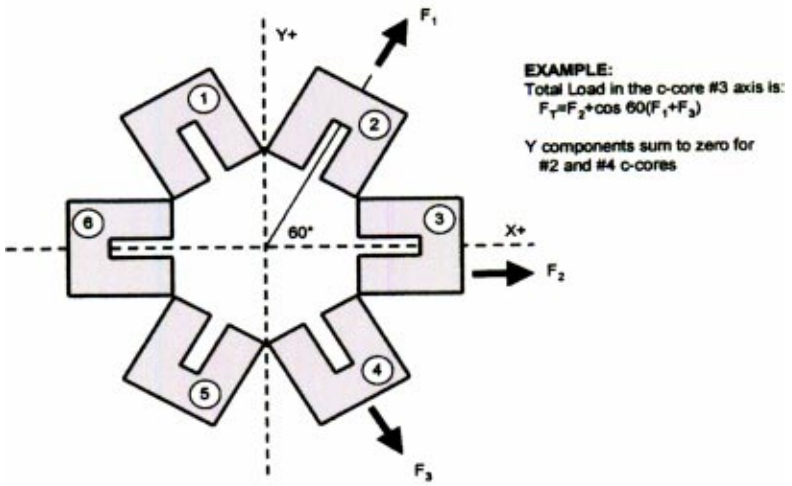


**Fig. 5 Maximum load on each magnetic axis is a vector sum of the forces from more than one C-core**

lished a large dynamic measurement range. This preload was electronically zeroed during testing and data acquisition.

Temperatures are recorded at several locations within the test rig. Both axial ends of the stator have three thermocouples mounted on them. Thermocouples are also mounted to each set of support bearings. A handheld infrared thermometer is also used periodically to gather additional thermal information about the shaft temperatures during rotation.

Commercially available, high-temperature eddy current displacement probes are used just outside the stator on both sides of the magnetic bearing to monitor rotor position. Each side has four probes $(X+, X-, Y+, Y-)$. The probes are capable of 0.0012 mm accuracy and are temperature compensated for a 538°C environment.

Other sensors include: an eddy current displacement probe used to measure rotor rpm and phase, magneto-resistive current sensors to measure C-core currents, and temperature and rpm sensors in the air turbine.

**Data Acquisition.** The facility data acquisition system is capable of capturing data at rates up to 15,000 samples per second per channel. Data are recorded for inboard and outboard bearing loads, support bearing and stator temperatures, $X$ and $Y$ axis displacements, rotor speed, and bearing C-core currents. Data are displayed in real time and can be saved directly into spreadsheet format.

## Experiment

For the tests reported in this paper, the shaft was mounted on zero clearance ball bearing supports so the load exerted by the magnetic bearing C-cores on the rotor could be measured outside of the hot section of the test facility.

The maximum load capacity for this bearing was determined by calculating the vector sum of the forces produced by any three C-cores along the middle core's centroidal axis. The primary force component is generated by the C-core inline with that axis. Each C-core adjacent to the primary C-core also contributed a component of force in the direction of the axis (Fig. 5). For example, the total load in the C-core #3 direction is the sum of the $F_2$ and the cosine of $F_1$ and $F_3$. The sine components of the $F_1$ and $F_3$ cancel each other out. This axis is referred to as the #2-3-4 magnetic axis.

**Maximum Force Produced by Single C-Core as a Function of Temperature.** Recorded data sets of load capacity versus temperature indicate the maximum load capacity of a single core and the current level where saturation begins. For these tests, C-core #1 was attached directly to a high power dc supply (100 V, 40 A) and load was measured while current was increased at five different temperatures.

Results are shown in Fig. 6. Force starts to become nonquadratic above about 12 A and saturation is almost complete at about 20 A if at lower temperatures. Saturation is less complete at higher temperatures. This suggests that forces attainable at RT can be achieved at elevated temperatures provided enough EMF can be generated to do so. Currents greater than 22 A were not applied due to concern over C-cores damage. The data also show that force production decreases by 37% at 22 A between RT and 538°C. In Ref. [11], Minihan et al. showed a similar force capacity degradation of 33% between RT and 538°C in saturation for the second generation high temperature magnetic bearing. The large decrease in load capacity for an applied current above room temperature is attributable to two causes: a minor decrease in permeability of the core material and a large increase in the radial air gap due to test conditions.

Figure 7 presents a subset of the C-core #1 data in log–log format. The top line indicates the quadratic form of the data since

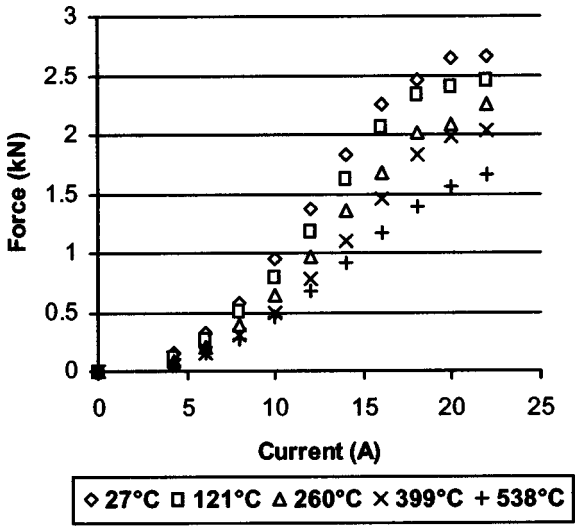


**Fig. 6 Force capacity for C-core #1 as a function of temperature**

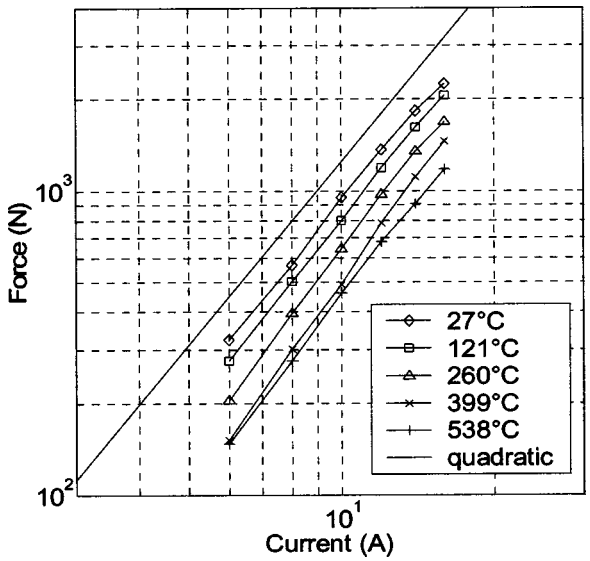


**Fig. 7 C-core #1 force data plotted on log–log plot**

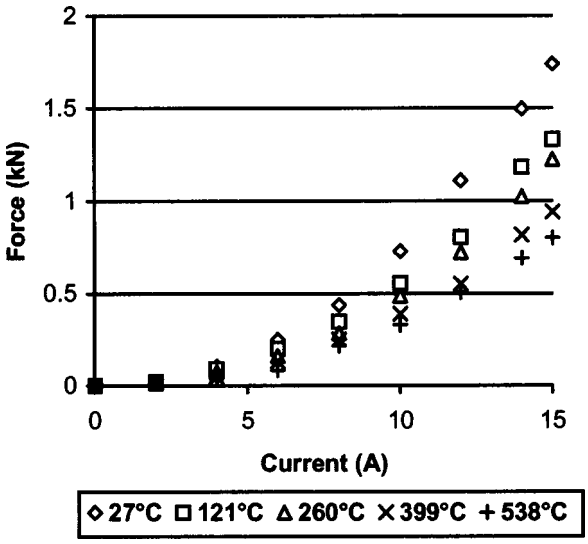


**Fig. 8 Force vs current for C-core #2 at 0 rpm**

each temperature data set is almost parallel to it. If the gap dimension was independent of temperature, then these curves would line up on top of each other. However, the actual gap dimension at each temperature can be backed out of this data using the assumption that the change in relative permeability of the core material is negligible and provided the initial gap at room temperature is known. Magnetization curves for 0.1 mm laminations of Hiperco 50 alloy in Ref. [7] do not appear to indicate an appreciable change with temperature (RT to 538°C) in relative permeability or induction for a fixed magnetizing force.

An inherent increase in gap length exists based solely upon the fact that the magnetic bearing lamination stacks are heating up. If the change in temperature of both the rotor and the stator is uniform, the gap grows by 0.5% at 538°C. One way to see this increase is to imagine replacing the air in the gap with lamination material. After applying heat, not only due the rotor and stator stacks expand, but so too does the gap material. Since this imaginary gap stack does not affect the growth of either the stator or the rotor stack, it can be concluded that the gap grows with temperature by a small amount as does the other metal components.

The coefficient of thermal expansion for Hyperco 50 is 5.28 $\times 10^{-6}$ in./(in. °F) and the gap is 0.022 in. An increase of 538°C thus results in a 0.5% increase in gap length, which results in a 1% loss in force capacity.

**Individual C-Core Force Capacity as a Function of Speed and Temperature.** Typical load capacity of a single C-core as a function of current, temperature, and speed is presented here. C-core #2 load capacity data at 0 and 15,000 rpm from 27 to 538°C is shown in Figs. 8 and 9.

The data show that speed does not have an appreciable effect on the force capacity of C-core #2 at any temperature or speed to 15,000 rpm. This same result was observed previously in Ref. [10].

Figure 10 shows just how close the data matches at 538°C. Slight variations are most likely associated with the timeliness of the measurements. Gap size affects these measurements and how long the stator took to get from RT to 538°C and how long it was there is critical. Possible nonuniform frictional forces generated within the rolling element bearings as the rotor gets hot, which are not accounted for, may also be a source of variation. Small net frictional forces in the direction of load could develop if the preloads are not perfectly balanced, or if the concentricity between the rotor and the outboard rolling element bearing changes. However, the ball bearings do provide a good load path from the rotating shaft and this effect seems minimal.

The option of measuring forces directly at the stator (Fig. 11) has been tried, with difficulty, prior to this publication. The main problem was that the load cells had to be in line with the stator mechanical support and an external actuator system was required. This support configuration permitted unwanted stator deflection and position slip during dynamic tests.

As the speed increases, rotor eddy current and hysteresis losses increase. However, these losses do not affect the static load production capability of this bearing at elevated temperatures to 15,000 rpm. These losses still have negative effects on actuator bandwidth.

For this particular C-core, a decrease in load capacity of 53% is evident at 15 A between RT and 538°C. This is considerably higher than previous results have shown. Since force is proportional to the inverse square of the total air gap, small changes in air gap can greatly affect bearing output for any current values. It would appear that Figs. 8 and 9 would have shown a more favorable result if data from C-core #1 was recorded. However, it is highly unlikely that the test rig reached an equilibrium temperature when Fig. 6 data were recorded.

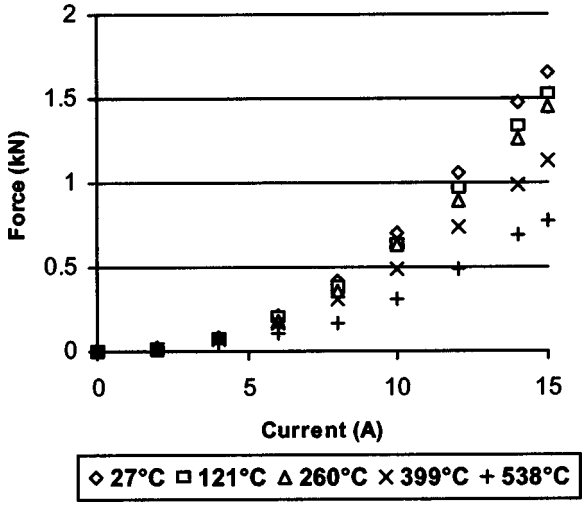


**Fig. 9 Force vs current for C-core #2 at 15,000 rpm**

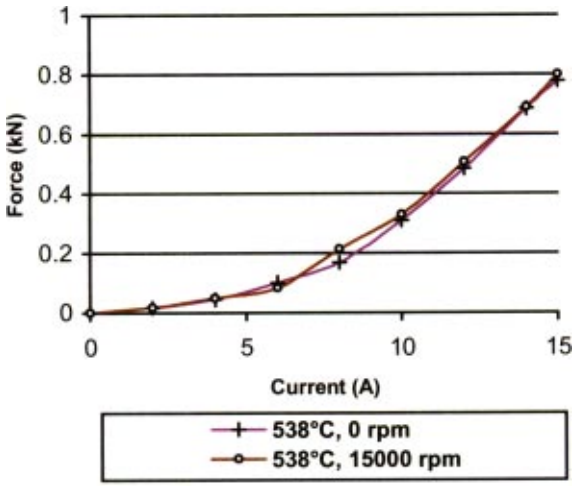


**Fig. 10 Force versus current and speed at 538°C**

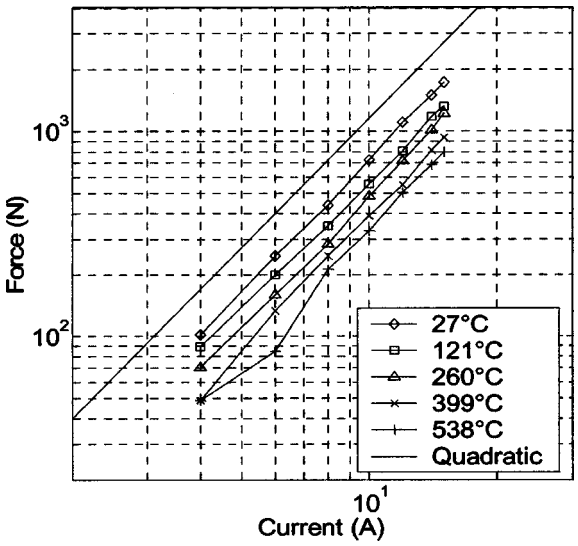


**Fig. 12 C-core #2 data at 0 rpm plotted on log–log plot**

C-core #2 tests were performed immediately when the stator had reached the desired temperature. Band heaters heat the back iron of the stator and the heat travels to all other components primarily through conduction and radiation. Consequently, the rotor takes longer to heat and therefore the air gap is larger than at room temperature. In fact, air gap size is a direct function of rotational speed, *and* the difference in temperature between the rotor and the stator.

Maintaining a constant uniform gap dimension for these tests is difficult. Concentricity within the rig has also been a challenge. The eight displacement sensors monitored *rotor* position during all the tests to ensure the rotor did not bow or change position relative to the support stand. However, the stator was not monitored, and its position may have changed slightly due to slipping, thus changing the air gap between the coils.

Figure 12 presents C-core #2 data in log–log format. The data are similar to that shown for core #1. Table 1 shows the % reduction in force and the % increase in gap for C-core #1 and #2 as a function of temperature. Force reductions were found by dividing each data set by the room temperature result. The increase in gap is directly proportional to the inverse square root of force.

**Force Capacity of an Axis as a Function of Speed and Temperature.** The previous tests were expanded upon to determine the load capacity for an axis under the condition where three adjacent C-cores all carry the same current and the opposing C-core coils carry none. The maximum load of an axis is a function of three adjacent C-cores. The two C-cores on either side of the main axis have a contribution to the total load in that axis (Fig. 5). Acting at an angle of 60 deg to the axis, these side C-cores contribute as much of the total force as the central C-core. The results of load versus current and temperature for 0 and 15,000 rpm using magnetic axis 2-3-4 are shown in Figs. 13 and 14.

Once again speed does not have an appreciable effect on the load capacity along an axis at any temperature—at least to 15,000 rpm.

To confirm that the applied magnetic force was in the same direction as the center C-core of that axis, the angle of the applied load was monitored. This was done by taking the load cell data in real-time and plotting the load vector direction versus true horizontal. The stator load angles matched the theoretical values (i.e., 0° for the #2-3-4 axis) to within a few degrees.

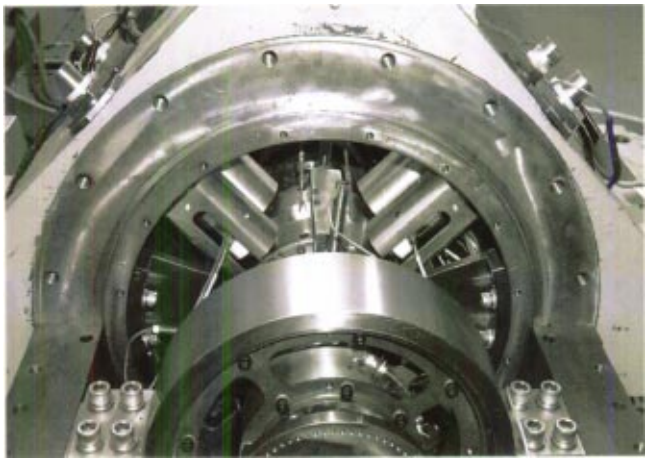

**Fig. 11 Load measurements at the stator using piezoelectric actuators**

## Power Characterization

**Power Consumption of Single Core.** The power required by the bearing C-cores as a function of magnetic force, current, temperature, and speed was also determined. At RT, the average resistance ($R$) for a C-core (2 coils) is 0.48 Ω and inductance ($L$) is 18 mH. The real power used by the C-core is a function of the output voltage of the pulse width modulation amplifier (22 kHz switching frequency) and the instantaneous current. Figure 15 shows the typical power system for one C-core.

The high switching frequency (22 kHz) of the PWM amplifier makes it difficult to measure the power required to produce bearing forces. Normal 60 Hz rms power measurement equipment cannot be used. An isolated, high impedance digital oscilloscope capable of acquiring data at one million samples per second was used to record the instantaneous voltage across the C-core coils as

**Table 1 Percent reduction in force and increase in gap as a function of temperature**

| | C-core #1 | | C-core #2 | |
|---|---|---|---|---|
| Temp (°C) | % force reduction | % gap increase | % force reduction | % gap increase |
| 121 | 13 | 7 | 21 | 13 |
| 260 | 30 | 20 | 33 | 22 |
| 399 | 44 | 34 | 47 | 37 |
| 538 | 51 | 43 | 55 | 49 |

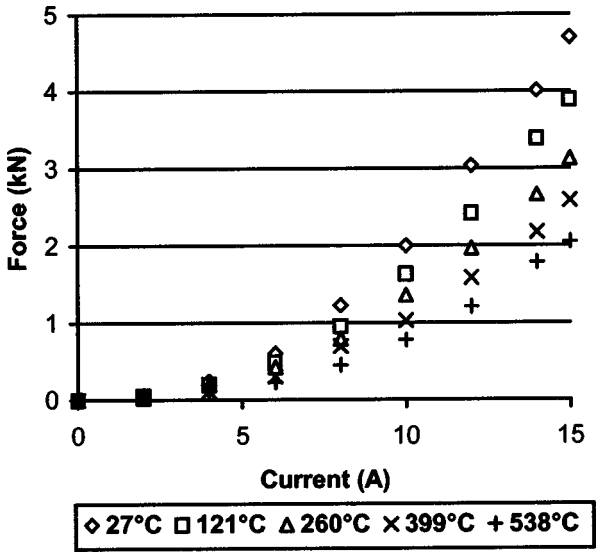


**Fig. 13 Force as a function of current and temperature for the #2-3-4 magnetic axes at 0 rpm**

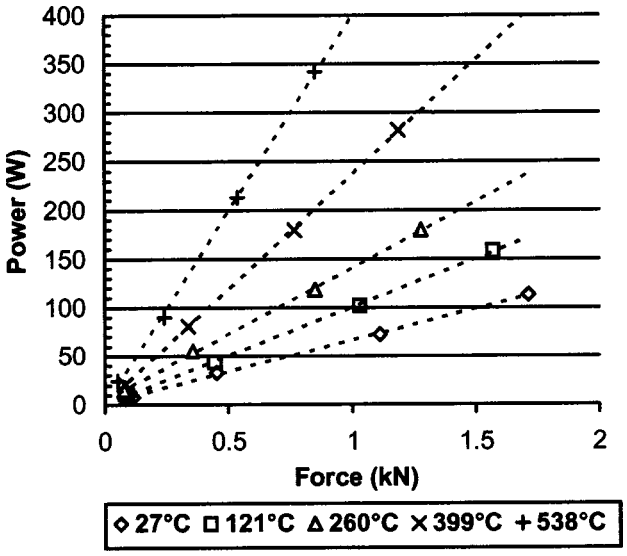


**Fig. 16 Power consumption of C-core #2 at 0 rpm**

well as the instantaneous current through the coils. Average power for each data point was calculated using a power factor equal to one.

**Full Axis Power Consumption.** Average power as a function of temperature was calculated for C-core #2 and the #2-3-4 magnetic axis at 0 rpm. The power for the magnetic axis is the sum of the power from the three C-cores in that axis. All the power calculations are shown in Figs. 16 and 17.

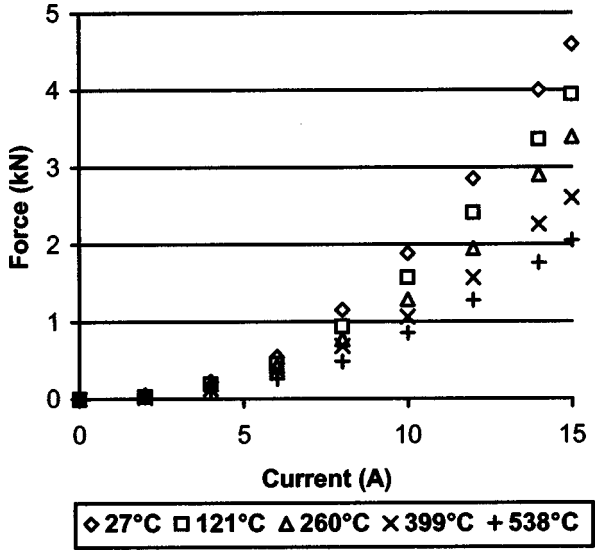


**Fig. 14 Force as a function of current and temperature for the #2-3-4 magnetic axes at 15,000 rpm**

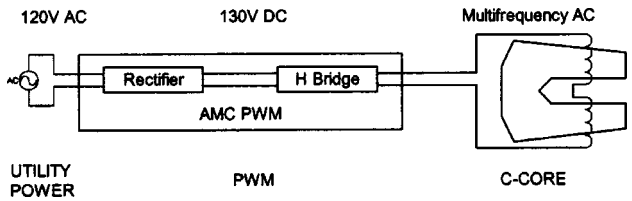


**Fig. 15 Power system for one C-core**

The largest power requirement was about 1 kW at 538°C to produce 2.3 kN on an axis. Power required to produce a specified load increases dramatically with temperature for several reasons. Resistive power loss increases since coil resistance increases. In fact, at 538°C, the resistance of the coils has increased by a factor of 3, thus required power will be at least three times as much based on this result alone. Slight degradation of the flux carrying capacity of the magnetic laminations also contributes to an increase. The other component here stems from an increase in gap dimension.

## Thermal Analysis

**Increase in Gap due to Thermal Expansion.** A major contributor to the decrease in load and the increase in power as temperature rises is the expanding gap between the rotor and the stator. Since the heaters are mounted directly on the outside of the stator, the stator heats up at a much higher rate then the rotor,

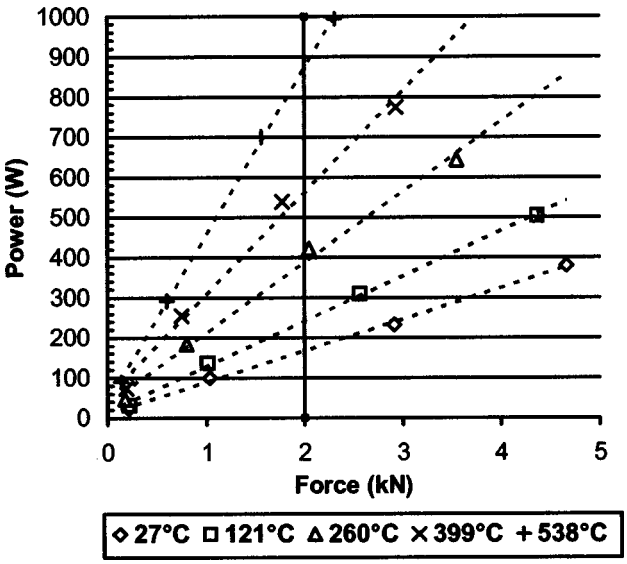


**Fig. 17 Power consumption of magnetic axis #2-3-4 at 0 rpm**

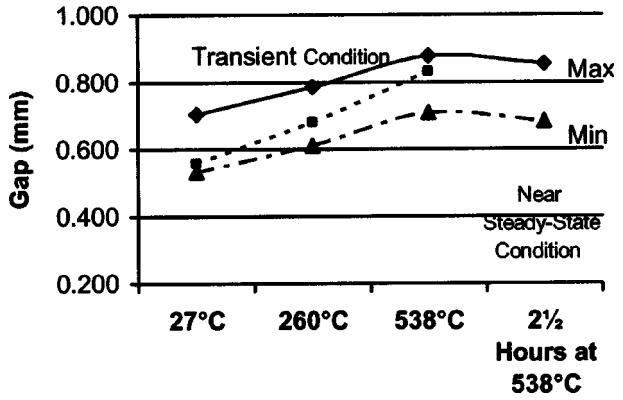


**Fig. 18 Theoretical gap between stator and rotor as a function of temperature using linear method**

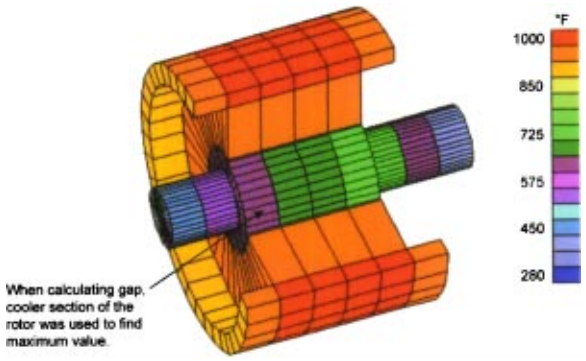


**Fig. 19 Thermal map (not FEA) of rotor and stator when rig first reaches 538°C**

which relies only on convection and radiation for heating. Thus, the rotor will not have expanded as much as the stator, and as a result, the gap will be larger than nominal.

In hindsight, it would seem advantageous to heat the rotor as well as the stator to alleviate thermal mismatch problems. With the current rig setup, however, this is not possible. Stresses generated from thermal expansion of the zero clearance bearing sleeves might cause the ball bearings to seize up. In addition, the grease used to lubricate these bearings is only rated to 135°C. In a future build, the ball bearings will be replaced with high temperature hydrostatic bearings to allow consideration of other heating methods. The hydrostatic bearings will also allow for continuous testing at higher speeds. Currently, the ball bearings heat up within minutes to their temperature limit in tests performed at high speed.

Constant gap dimension is important in the determination of force capacity and bearing power requirements, but the gap in a real engine application will not stay constant and could vary with time and external environmental conditions, such as inlet air temperature.

In order to better understand the growth of the gap, a linear thermal expansion analysis was conducted. The gap at any temperature has a minimum and maximum value just due to the tolerance stack up of the rotor and stator bearing components. The actual gap, which is somewhere between the max and min, will change with thermal mismatch. Thermal maps of the magnetic bearing section of the rotor were constructed using temperatures measured at several different points on the rig using a handheld infrared thermometer. Figure 18 shows that even after 2.5 h, the average gap dimension is greater than it is at room temperature. It is quite possible, that the rotor would never reach 538°C using the current heating method. The initial gap value for C-core #2 was determined using plastic shims to be approximately 0.56 mm. Using this reference and the values in Table 1, the actual gap can be determined. Values based on experiment and plotted in Fig. 18, fall between the max and min curves and thus provide confidence in the model.

The thermal map in Fig. 19 shows a temperature gradient on the rotor. This gradient was due to different heating rates of each of the three band heaters and also because the outer containment shell was removed for these tests allowing for convective cooling. The coolest rotor section is about 315°F. Figure 20 shows that the rotor did reach a uniform temperature of about 415°C after 2.5 h of steady heating after the stator poles reached 538°C.

In this model, the average radial gap at room temperature was 0.620 mm at 27°C. This gap increases to 0.792 mm at 538°C (Fig. 18). Since the magnetic force is a function of the inverse square of the gap distance (if core material is far from saturation), it is clear why the force at elevated temperature severely drops for a fixed supply current.

**Force Prediction.** A simple analytical prediction of force, made to verify the experimental results, is presented here. For a general magnetic actuator, the force produced by the magnetic flux in one air gap of area $A_g$ is

$$F = \frac{1}{2}\alpha\mu_0 A_g \left[\frac{NI}{2G + \frac{L_{\text{iron}}}{\mu_r}}\right]^2. \quad (1)$$

In this equation, $\mu_0$ is the magnetic permeability of free space and $NI$ is the ampere-turns of the coil(s) driving flux through the circuit. $2G$ represents the total effective magnetic air gap and $\alpha$ is a force de-rating factor, which accounts for leakage, fringing, and non-uniformity in flux density across the pole face [13]. $L_{\text{iron}}$ represents the average iron path component of the C-core circuit, and $u_r$ is the relative permeability of the iron laminations.

The actuator measurements in this paper are based on the performance of a complete C-core circuit. Each of the two C-core poles is 15° off-axis, therefore, the forced produced by a single C-core is 1.93 times that obtained using Eq. (1). Force predictions were made using the following parameters: $\alpha = 0.8$, $\mu_0 = 4\pi \times 10^{-7}$ N/A$^2$, N=52×2 turns, $A_g = 12.9$ cm$^2$, $G_0 = 0.559$ mm, $L_{\text{iron}} = 145$ mm, $\mu_r = 500$. A nominal $\mu_r$ was calculated from the local slope of the Hyperco 50 data in Ref. [7] at 12 Oe and RT. 12 Oe corresponds to about 10 A in these third generation radial bearing C-cores.

Figure 21 shows a comparison between the predicted force and the measured force for C-core #1. An initial gap, $G_0$, of 0.47 mm was used in the predictions since the force in C-core #1 was considerably higher than that in C-core #2. The trend for gap increase backed out of the measured data for C-core #1 shown in Table 1 was used to determine predicted gap values in C-core #1

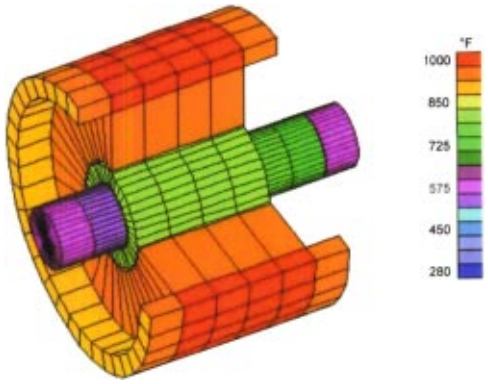


**Fig. 20 Thermal map (not FEA) of rotor and stator after rig at 538°C for 2.5 h**

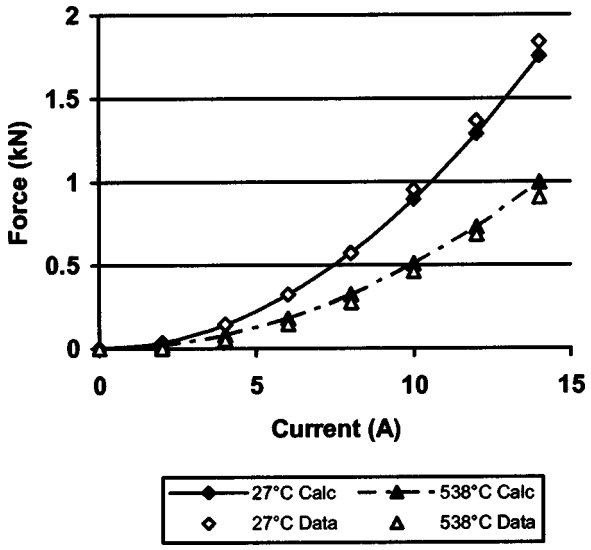


**Fig. 21 Theoretical force prediction versus actual measured values for C-core #1**

using $G_0$ as a reference. There is good agreement between the calculated load and the actual measurements when the variation in gap is considered.

It becomes quite clear that exact knowledge of the gap dimension is imperative to obtaining a detailed comparison between experimental results and analytical predictions. This measurement is not easy to obtain, however. The gap in this test rig is difficult to get at and high temperatures limit probe or shim materials.

## Concluding Remarks

Magnetic applied force and electric power for a high load, high speed, high temperature radial magnetic bearing for turbomachinery were measured. Even though the shaft is not doing any work and the rotor is not levitated, these tests provide baseline industry performance characteristics for actual hardware. Load capacity and power consumption of both a single C-core and a magnetic axis were measured from 27 to 538°C. Thermal analysis of the test rig to investigate gap growth due to non-uniform heating was performed. Theoretical force predictions were compared to actual results with good correlation. No appreciable decrease in static force production capability was observed due to rotation up to 15,000 rpm at any temperature. Future experimental work will include high temperature, high-speed levitation tests without the use of rolling element bearings and high temperature force measurements of a magnetic thrust bearing. Future analytical work will include the development of an advanced model that includes the effect of applied magnetizing force and temperature on the relative permeability of the core material as well as the effects of rotation and thermal mismatch on bearing air gap.

## Acknowledgments

This research was funded by NASA Glenn Research Center's Smart Efficient Components Program, which is managed by Robert D. Corrigan. The authors would like to thank Peter Kascak (University of Toledo) for his assistance in the power measurements, Julie Roden (Analex) for her thermal expansion analysis, John Poles (NASA Glenn) for his significant electrical contributions, and Tim Czaruk (QSS) for test support. The authors would also like to recognize Gerald Brown (NASA Glenn) and Albert Kascak (ARL at NASA Glenn) for their expert guidance and review. Final recognition is for Texas A&M students Randy Tucker, Jason Preuss, and Andrew Hunt who helped design and construct the high temperature coils used in this bearing.

## References

[1] Xu, L., Wang, L., and Schweitzer, G., 2000, "Development of Magnetic Bearings for High Temperature Suspension," *Proceedings of the 7th ISMB*.
[2] Ohsawa, M., Furuya, E., Marui, E. et al., 1998, "High Temperature Blower for a Molten Carbonate Fuel Cell Supported by Magnetic Bearings," *Proceedings of the 6th ISMB*, pp. 32–41.
[3] Mekhiche, M., Nichols, S., Oleksy, J., Young, J., Kiley, J., and Havenhill, D., 2000, "50K RPM, 1100°F Magnetic Bearings for Jet Turbine Engines," *Proceedings of the 7th ISMB*.
[4] Mekhiche, M., Nichols, S., Hevenhill, D. et al., 2000, "High-Speed, High-Temperature Magnetic Bearings for Jet Turbine Engine Application," *Proceedings of the International Conference on Electrical Machines* (ICEM).
[5] Field, R. J., and Iannello, V., 1998, "A Reliable Magnetic Bearing System for Turbomachinery," *Proceedings of the 6th ISMB*, pp. 42–51.
[6] Field, R. J., Sortore, C. K., and Iannello, V., 2000, "A Magnetic Bearing System for More-Electric Engines," Proceedings of ASME/IGTI Turbo Expo.
[7] Kueser, P. et al., 1967, "Properties of Magnetic Materials for Use in High-Temperature Space Power Systems," NASA SP-3043.
[8] Kondoleon, A., and Kelleher, W., 2000, "Soft Magnetic Alloys for High Temperature Radial Magnetic Bearings," *Proceedings of the 7th ISMB*.
[9] Fingers, R., 1999, "Creep Behavior of Thin Laminations of Iron-Cobalt Alloys for Use in Switched Reluctance Motors and Generators," AFRL-PR-WP-TR-1999-2053.
[10] Montague, G. T., Jansen, M. J., Provenza, A. P., Jansen, R. H., Ebihara, B., and Palazzolo, A., 2002, "Room Temperature Characterization of a Magnetic Bearing for Turbomachinery," NASA Tech. Memo-2002-211904.
[11] Minihan, T., Palazzolo, A., Provenza, A., Montague, G. T., and Kascak, A. F., 2002, "Fail Safe, High Temperature Magnetic Bearings," *Proceedings of the ASME/IGTI Turbo Expo*.
[12] Jansen, R. H., Ebihara, B. E., Montague, G. T., Provenza, A. J., Jansen, M. J., Palazzolo, A., Tucker, R., Preuss, J., and Hunt, A., 2003, "Design and Fabrication of a High Temperature, Radial Magnetic Bearing for Turbomachinery," NASA Tech. Memo, 2003-212300.
[13] Knospe, C. R., and Maslen, E. H., 1999, "Introduction to Active Magnetic Bearings," University of Virginia Short Course.

# Application of CFD Analysis for Rotating Machinery—Part I: Hydrodynamic, Hydrostatic Bearings and Squeeze Film Damper

**Zenglin Guo**
Post-Doctorate

**Toshio Hirano**
Visiting Research Engineer

**R. Gordon Kirk**
Professor

Rotor Dynamics Laboratory,
Mechanical Engineering Department,
Virginia Polytechnic Institute and State University,
Blacksburg, Virginia 24061

*The traditional method for bearing and damper analysis usually involves a development of rather complicated numerical calculation programs that may just focus on a simplified and specific physical model. The application of the general CFD codes may make this analysis available and effective where complex flow geometries are involved or when more detailed solutions are needed. In this study, CFX-TASCflow is employed to simulate various fixed geometry fluid-film bearing and damper designs. Some of the capabilities in CFX-TASCflow are applied to simulate the pressure field and calculate the static and dynamic characteristics of hydrodynamic, hydrostatic, and hybrid bearings as well as squeeze film dampers. The comparison between the CFD analysis and current computer programs used in industry has been made. The results show reasonable agreement in general. Some of the possible reasons for the differences are discussed. It leaves room for further investigation and improvement on the methods of computation.*
[DOI: 10.1115/1.1807415]

## Introduction

Various hydrodynamic, hydrostatic and hybrid bearings have been widely used in rotating machinery. The mechanism of hydrodynamic lubrication has been investigated and various bearings have been developed, which enable modern rotating machinery to operate with ever increasing speed, stability and efficiency. The majority of the analytical research work in hydrodynamic lubrication [1–6] has applied the classic Reynolds equation, which is a reduced form of the Navier–Stokes equations and the equation of continuity. Then the static performances, such as load capacity and flow rate, can be calculated by integrating the predicted pressure field. Furthermore, the dynamic stiffness and damping coefficients can also be obtained.

Because of the complexity of the structures and applied flow equations, most of the current standard bearing codes usually focus on a specific and simplified physical model. It has some limitations for application. These standard codes are usually adequate for common designs, but additional work may need to be done in order to meet the requirement when a new concept is desired or when a more accurate analysis is necessary. For example, in order to examine the effect of fluid inertia or complex flow geometries, researchers are required to build a new and more accurate physical model. This will require new equations developed from the general Navier–Stokes equations. Therefore, it would be very beneficial for the research work in the field of hydrodynamic lubrication if a general fluid flow commercial software could be applied for analysis of new bearing and damper designs.

Currently, initial CFD analysis has been conducted at the Virginia Tech Rotor Dynamics Laboratory, in which CFX-TASCflow is mainly employed to simulate fluid-film bearings, dampers and seals. In this paper, the application of CFX-TASCflow in the calculation of static and dynamic characteristics of hydrodynamic and hydrostatic bearings as well as a squeeze film damper is presented. In order to prove that the general CFD code can be applied for bearing and damper analysis with the appropriate accuracy, the results of the CFD analysis are compared to various standard lubrication theory numerical calculation programs [7–9]. The results show reasonable agreement, but leave room for future work to refine the methods of computation.

The simulation presented in this paper was conducted by using the CFX-TASCflow 2.11.1 [10]. For grid generation the CFX-Build 4.4 was employed. On the hardware side, one Intel 2×Pentium III 800 MHz CPU computer with 512 Mbytes RAM, and three Intel Pentium 4 1.7 GHz CPU computers with 2 Gbytes RAM, all operating on the Windows NT 4.0/2000 systems, were utilized, respectively. The typical simulation times ranged from a few minutes to several hours depending on the complexity of the models and the parameters used for the solver. More details of the required time of computation with the CFD analysis will be given in the following discussion of results.

## Hydrodynamic Bearing and Validation Study

Hydrodynamic journal bearings are very typical in various types of machinery requiring fluid-film lubrication. The convergent-wedge and squeeze film effect between the surface of the bearing and the journal create the dynamic pressure supporting the external load on the journal. In order to prove that the CFX-TASCflow program can be applied for fluid film bearing analysis, it must be shown that the results are appropriate and with the necessary accuracy. Hence, a validation study is conducted first on a conventional hydrodynamic bearing design that can be compared to the computer programs and results available for comparison. The standard lubrication numerical codes used for this comparison include: VT-FAST, DyRoBeS-BePerf, and VT-EXPRESS. VT-FAST is a rotordynamics software package developed by VT Rotor Lab that is currently used in both the classroom and industry [7]. DyRoBeS-BePerf is another software package for rotordynamics analysis developed by Chen [8]. VT-EXPRESS is a VT

Contributed by the International Gas Turbine Institute (IGTI) of THE AMERICAN SOCIETY OF MECHANICAL ENGINEERS for publication in the ASME JOURNAL OF ENGINEERING FOR GAS TURBINES AND POWER. Paper presented at the International Gas Turbine and Aeroengine Congress and Exhibition, Atlanta, GA, June 16–19; 2003, Paper No. 2003-GT-38931. Manuscript received by IGTI, October 2002, final revision, March 2003. Associate Editor: H. R. Simmons.

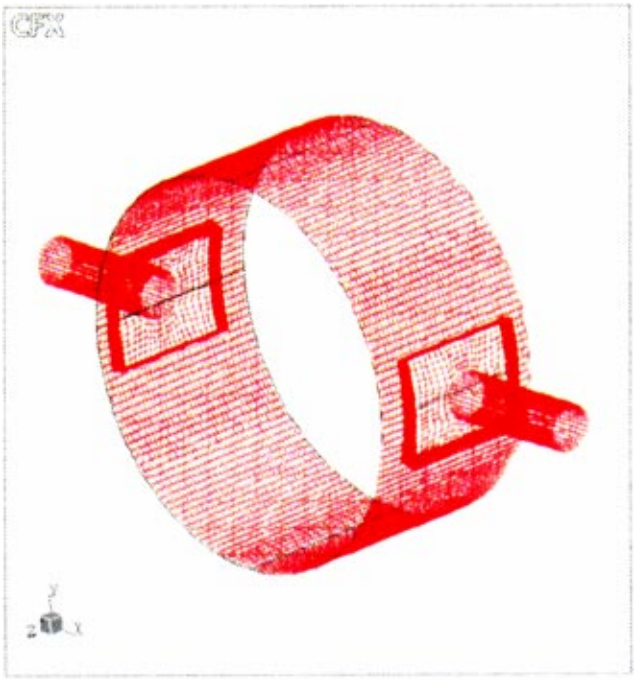

**Fig. 1 Hydrodynamic bearing model**

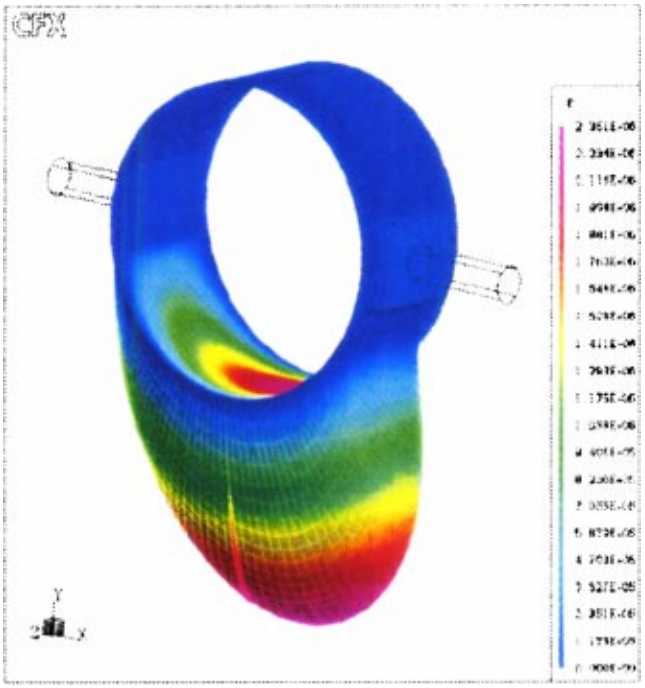

**Fig. 2 Pressure profile of hydrodynamic bearing**

Rotor Lab program mainly used for analysis of externally pressurized fluid-film journal bearings [9]. The solutions of these three standard codes are based on Reynolds equation, while CFX-TASCflow solves the general Navier–Stokes equations. In addition, these standard codes employ Reynolds condition to process the pressure boundary in the circumferential direction of the bearing while the Half- Sommerfeld condition is used in the following simulations by CFX-TASCflow. Both the standard codes and the CFD solutions utilized for the results presented in this paper are based on the assumption of incompressible fluid and laminar flow in the bearing.

*Example 1.* Consider a typical cylindrical journal bearing as shown in Fig. 1. Assume the diameter of the bearing $D=50$ mm (1.97 in.) with the width $B=25$ mm (0.984 in.) and radial clearance $h_0=0.05$ mm (1.97 mil). The included angle of inlet pocket is $\alpha=30°$ while its axial land width is $b=3.75$ mm (0.148 in.). The supply pressure of lubricating oil is $p_s=103\,000$ Pa (15 lbf/in.$^2$) and its dynamic viscosity is $\mu=1.25\times10^{-2}$ N s/m$^2$ ($1.81\times10^{-6}$ lbf s/in.$^2$). The spinning speed of journal is $\Omega=1000$ rad/s ($\approx$9550 rpm). The eccentricity ratio of journal is $\epsilon=0.5$.

Figure 1 is the geometry of the bearing model with 148 K mesh density. Figure 2 shows the pressure distribution obtained from the simulation by CFX-TASCflow on this hydrodynamic journal bearing with the same mesh density.

There are many factors that affect the correctness and accuracy of simulation by CFX-TASCflow. Two of these require special attention. The first is the mesh density of the geometry. Several mesh densities, including 52, 148, and 308 K, have been calculated and compared to the results by standard lubrication codes. The comparison of static calculation with different mesh density and the results by standard codes are shown in Table 1. It can be seen that the CFD simulation results are very close to that by the standard lubrication numerical solutions. The CPU time for each program is also given in Table 1, clearly illustrating the increased time required for the CFD analysis.

To balance the calculation accuracy and the requirements for proper use of machine's memory and simulation time, the 148 K mesh density is employed finally for this study. Table 2 gives the percent differences of the results utilizing 148 K mesh geometry relative to those of standard codes. It can be seen that the percent differences for the maximum pressure and load capacity are less than 1.2% while the difference for attitude angle is less than 3%. Because usually there is an allowable range of about half degree for the calculation of attitude angle in the traditional bearing calculations, these results show a very good agreement.

Most of the CPU times in Table 1 are based on the executions on the 1.7 GHz Pentium 4 machine. An exception is the CPU time of VT-EXPRESS, which runs on Pentium III machine with 800 MHz CPU. In addition, the CPU times for VT-FAST and DyRoBes-BePerf are the sum for both static and dynamic calculations. The other times in Table 1 are just for the static equilibrium calculation. It can be seen in Table 1 that the simulation by CFX-TASCflow requires a great deal of CPU time as compared to

**Table 1 Results of static calculations**

| | Maximum pressure ($10^6$ Pa) | Load capacity (N) | Attitude angle (deg) | CPU time (h:m:s) |
|---|---|---|---|---|
| VT-FAST | ··· | 1151 | 49.4 | 00:00:02 |
| DyRoBeS-BePerf | 2.328 | 1155 | 48.5 | 00:00:07 |
| VT-EXPRESS | 2.324 | 1143 | 49.3 | 00:00:05 |
| CFX-TASCflow (52 K mesh) | 2.336 | 1144 | 49.8 | 00:33:37 |
| CFX-TASCflow (148 K mesh) | 2.351 | 1156 | 49.8 | 02:05:28 |
| CFX-TASCflow (308 K mesh) | 2.352 | 1160 | 49.8 | 04:45:11 |

**Table 2 Percent differences for 148 K mesh geometry relative to comparison codes**

| Comparison code | Maximum pressure | Load capacity | Attitude angle |
|---|---|---|---|
| VT-FAST | ··· | 0.43% | 0.81% |
| DyRoBeS-BePerf | 0.99% | 0.09% | 2.68% |
| VT-EXPRESS | 1.16% | 1.14% | 1.01% |

**Table 3 Results of grid quality check**

| | Checked value | Required value |
|---|---|---|
| Skew angle (deg) | 19.22–168.85 | >10–20 |
| Aspect ratio | 1.01–4485.93 | <100–200 |

the standard lubrication codes. This proves the efficiency of the standard lubrication solutions. The ultimate purpose of applying this general CFD code for bearings and dampers is not to replace the current standard lubrication codes. Rather, it is necessary to understand how CFD analysis can be applied in those areas where a complicated structure is used or where a more detailed analysis is necessary.

The second factor affecting the simulation is the grid quality of geometry, which mainly includes the aspect ratio and skew angle of the grid. In CFX-TASCflow, the skew angle is required to be larger than 10 deg to 20 deg while the aspect ratio is recommended to be less than 100 or 200 for normal analysis. Due to the existence of the thin film in hydrodynamic bearings, the dominating feature for bearing CFD models is the large aspect ratio of the grid. To avoid the negative influence of this large aspect ratio, double precision calculations have been adopted per the suggestion of CFX-TASCflow documentation [10]. Table 3 gives the range of results for the grid quality check for the bearing model with 148 K mesh density. These results are for the entire range of eccentricity ratios from 0.1 to 0.9. For example, the model aspect ratio is 814.01 when the eccentricity ratio is equal to 0.5.

## Dynamic Calculation

**Calculation Method.** Consider the hydrodynamic bearing described in example 1. Using the small perturbation method, the increment of fluid-film force components can be described as follows:

$$\Delta F_x = k_{xx}x + k_{xy}y + c_{xx}\dot{x} + c_{xy}\dot{y},$$
$$\Delta F_y = k_{yx}x + k_{yy}y + c_{yx}\dot{x} + c_{yy}\dot{y}, \quad (1)$$

where $k_{ij}\,(i,j=x,y)$, $c_{ij}\,(i,j=x,y)$ represent the stiffness and damping coefficients of the bearing, and $x$, $y$, $\dot{x}$, $\dot{y}$ represent the perturbation of displacements and velocities in the $X$ direction and $Y$ direction, respectively. The coordinate system is the same as that shown in Fig. 1.

By giving small perturbations of displacement either in the $X$ direction or $Y$ direction, the stiffness coefficients can be obtained by differentiating the resultant fluid film force components on the displacements of perturbation. In standard lubrication programs, the dimensionless perturbation of displacements $x/h_0$, $y/h_0$ is usually between 0.01 and 0.005. For better comparison, in this study, three dimensionless perturbations are used: 0.01, 0.005, and 0.002 for selected CFD results.

In order to calculate the damping coefficients, a special capability in CFX-TASCflow, called ''Moving Grid,'' has been employed. The bearing surface and journal surface are specified as ''Frozen'' nodes and ''Moved'' nodes, respectively. Through the user's FORTRAN code, the ''Moved'' nodes can move in the fashion specified by the user. To match with the practice in standard codes, the dimensionless perturbations of velocity used in this study are $\dot{x}/\Omega h_0$, $\dot{y}/\Omega h_0 = 0.01$, 0.005, and 0.002.

**Table 4 Stiffness coefficients**

| | $K_{xx}$ ($10^6$ N/m) | $K_{xy}$ ($10^6$ N/m) | $K_{yx}$ ($10^6$ N/m) | $K_{yy}$ ($10^6$ N/m) |
|---|---|---|---|---|
| VT-FAST | 40.0 | −19.4 | 87.2 | 59.1 |
| DyRoBeS-BePerf | 38.0 | −15.2 | 84.8 | 65.2 |
| VT-EXPRESS | 33.9 | −13.1 | 85.3 | 65.0 |
| CFX-TASCflow ($x/h_0, y/h_0 = 0.01$) | 41.2 | −21.9 | 88.0 | 56.0 |
| CFX-TASCflow ($x/h_0, y/h_0 = 0.005$) | 41.1 | −22.1 | 88.0 | 56.0 |
| CFX-TASCflow ($x/h_0, y/h_0 = 0.002$) | 38.9 | −21.3 | 85.0 | 55.0 |

**Analysis of Results.** Table 4 shows the results of stiffness calculations by CFX-TASCflow and other standard lubrication codes for the bearing described in example 1. For better comparison, the CFD results with both $x/h_0$ *and* $y/h_0$ equal to 0.005 is selected for further comparison. The percent differences relative to the standard codes are shown in Table 5.

It can be seen from Table 4 that the stiffness coefficients by CFX-TASCflow are relatively closer to the results by VT-FAST than to the results by the other two standard codes. The percent differences for all of the four stiffness coefficients are less than 15%. It seems there is a big difference for the results of $K_{xy}$. Since this stiffness component usually has a very large slope, this difference may be better understood in future research investigation.

Table 6 shows the results of damping calculation. Table 7 is the percent differences for the CFD simulation with the 0.005 of dimensionless perturbation of velocity, relative to that of the standard codes. It can be seen that in general, the damping coefficients by CFX-TASCflow are larger than those by the standard codes. One of the possible reasons for this difference may be the influence of the fluid in inlet pockets. Generally speaking, this fluid body has more obvious effect on the damping of the bearing. In standard lubrication solutions, this effect was not considered. In

**Table 5 Stiffness coefficients percent difference for CFD simulation with $x/h_0$, $y/h_0 = 0.005$ relative to comparison codes**

| Comparison code | $K_{xx}$ | $K_{xy}$ | $K_{yx}$ | $K_{yy}$ |
|---|---|---|---|---|
| VT-FAST | 2.75% | 13.9% | 0.91% | −5.24% |
| DyRoBeS-BePerf | 8.16% | 45.4% | 3.77% | −14.1% |
| VT-EXPRESS | 21.2% | 68.7% | 3.16% | −13.8% |

**Table 6 Damping coefficients**

| | $C_{xx}$ ($10^4$ N s/m) | $C_{xy}$ ($10^4$ N s/m) | $C_{yx}$ ($10^4$ N s/m) | $C_{yy}$ ($10^4$ N s/m) |
|---|---|---|---|---|
| VT-FAST | 5.75 | 4.93 | 5.41 | 16.7 |
| DyRoBeS-BePerf | 4.86 | 4.29 | 4.29 | 16.1 |
| VT-EXPRESS | 4.38 | 3.87 | 4.50 | 15.9 |
| CFX-TASCflow ($\dot{x}/\Omega h_0, \dot{y}/\Omega h_0 = 0.01$) | 6.92 | 5.90 | 6.60 | 18.2 |
| CFX-TASCflow ($\dot{x}/\Omega h_0, \dot{y}/\Omega h_0 = 0.005$) | 7.16 | 5.92 | 6.40 | 18.4 |
| CFX-TASCflow ($\dot{x}/\Omega h_0, \dot{y}/\Omega h_0 = 0.002$) | 6.86 | 5.82 | 6.50 | 18.0 |

**Table 7 Damping coefficients percent difference for CFD simulation with $\dot{x}/\Omega h_0$, $\dot{y}/\Omega h_0 = 0.005$ relative to comparison codes**

| Comparison code | $C_{xx}$ | $C_{xy}$ | $C_{yx}$ | $C_{yy}$ |
|---|---|---|---|---|
| VT-FAST | 24.5% | 20.1% | 18.3% | 10.2% |
| DyRoBeS-BePerf | 47.3% | 38.0% | 49.2% | 14.3% |
| VT-EXPRESS | 63.4% | 52.9% | 42.2% | 15.7% |

**Table 8 Two cases for thermal solutions**

| | Feature | Property values |
|---|---|---|
| Case 1 | Constant properties | ISO VG32 at 50°C/122°F |
| Case 2 | Function properties | Functions for ISO VG32 |

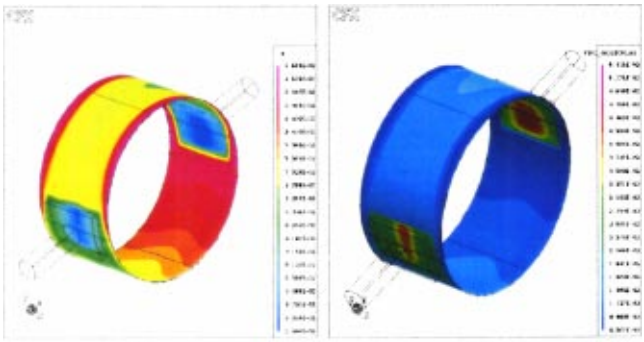


**Fig. 3 Temperature and viscosity distribution (case 2, 0.5 of eccentricity ratio, 9550 rpm of speed): (*a*) temperature, (*b*) dynamic viscosity**

addition, the differences in equation basis between two kinds of solutions may also be a cause. This will be a subject in future research work.

## Thermal Analysis

In the thermal analysis, another capability in CFX-TASCflow, ''Heat Transfer/Natural Convection,'' is activated. The fluid property functions are introduced by employing the user's FORTRAN code.

*Example 2*. Consider a cylindrical journal bearing as described in example 1 and Fig. 1. Here the lubricating oil is ISO VG32 (equivalent to DTE-LIGHT).

**Fluid Properties.** Two cases are calculated in this thermal analysis. The first case has an assumption of constant fluid properties, which is typical in normal lubrication analysis. The second case assumes the fluid properties are a function of temperature, which is a more realistic simulation. These two cases are described in Table 8.

**Simulation Results.** In Fig. 3, the profiles of temperature and viscosity for case 2 at 0.5 of eccentricity ratio and 9550 rpm of speed are displayed. The performances of the bearing both for case 1 and case 2 over the entire range of eccentricity ratios are shown in Fig. 4. For the purpose of comparison, the results by VT-EXPRESS are also displayed. Figure 5 is the maximum and average temperature curves of case 2.

**Availability for Extended Thermal Analysis.** The possibility to conduct further thermal solutions where the model to be analyzed includes both fluid film and solid elements, such as the bearing housing or journal, has been examined. This necessitates the ''Conjugate Heat Transfer'' capability in CFX-TASCflow. Figures 6 and 7 display the results of an initial simulation which has been conducted on a ''long bearing'' model. It can be seen that in

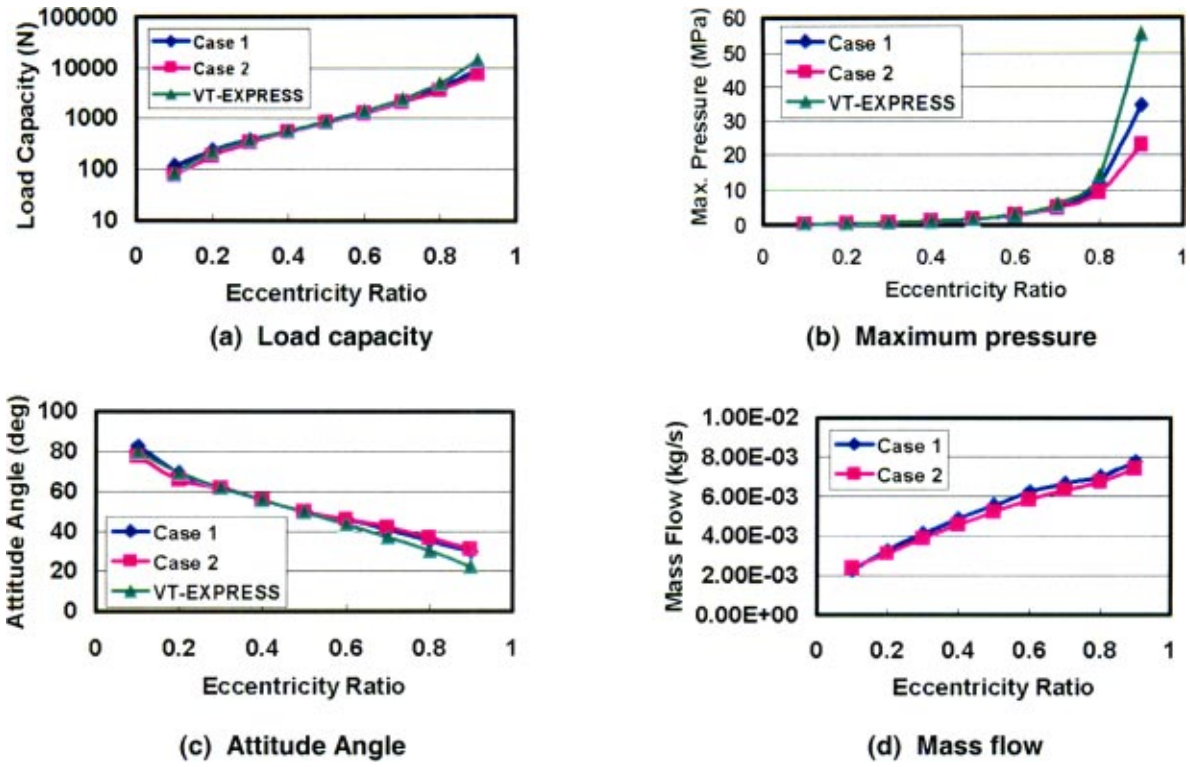


**Fig. 4 Bearing performances (5000 rpm of speed): (*a*) load capacity, (*b*) maximum pressure (*c*) attitude angle, (*d*) mass flow**

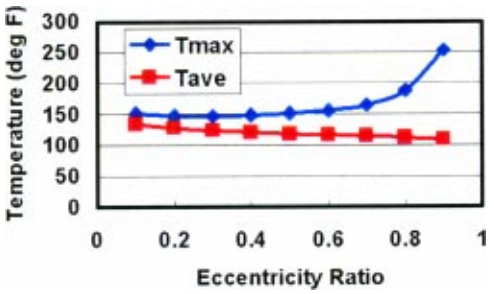


**Fig. 5 Average and maximum temperatures (case 2, 5000 rpm of speed)**

addition to the solutions of the fluid film, the temperature distribution within the bearing housing is also available for examination.

## Hydrostatic and Hybrid Bearings

The hydrostatic bearing is another type of widely used fluid-film lubrication bearing. This design employs an external high-pressure supply system to form the hydrostatic pressure in the bearing to supply the load capacity. In many circumstances, this kind of bearing is also called an externally pressurized bearing. Due to the rotation of the journal both hydrodynamic and hydrostatic lubrication effects can play essential roles in this kind of journal bearing. Hence, an externally pressurized journal bearing is a hybrid-operating bearing if the journal rotation speed is high.

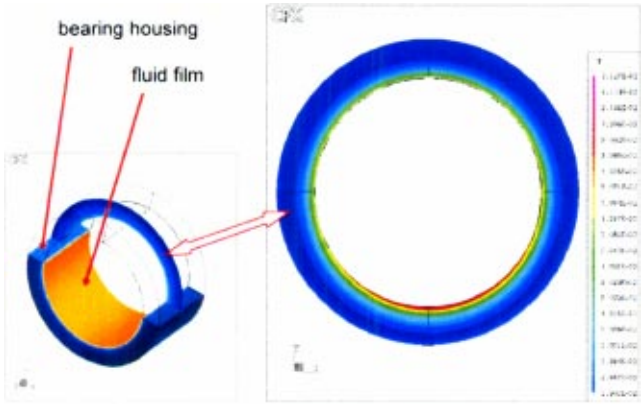


**Fig. 6 Temperature distribution on one cross section of bearing housing**

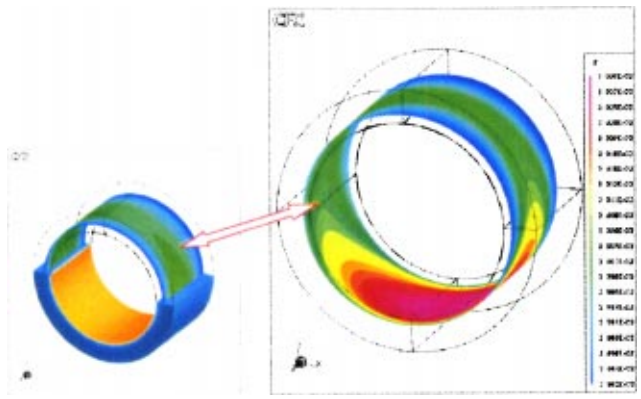

**Fig. 7 Temperature distribution on one circular layer of bearing housing**

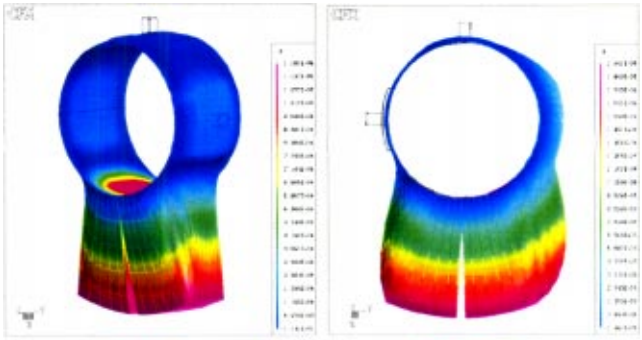


**Fig. 8 Pressure distribution of flow-constant hydrostatic bearing: (*a*) hydrostatic-operating, (*b*) hybrid-operating**

In addition, depending on the fluid supply system, there are two categories of hydrostatic bearing: flow-constant and pressure-constant.

**Flow-Constant Hydrostatic Bearing.** A set of pressure profiles for a flow-constant hydrostatic journal bearing with four pockets can be seen in Fig. 8. It can be seen that there is an obvious hydrodynamic effect in this hybrid-operating condition due to the rotation of the journal. In contrast, the pressure profile of a hydrostatic-operating bearing is symmetric relative to the eccentricity direction.

**Pressure-Constant Hydrostatic Bearing.** In pressure-constant hydrostatic bearings, a restrictor such as an orifice or a capillary, should be used to compensate the pocket pressures, to produce the load capacity of the bearing. The pressure-constant hydrostatic bearing is widely used in engineering applications.

Considering the difference between the sizes and grid numbers of the pocket and orifice, the grids could be built separately and attached together by using the GGI connection capability.

*Example 3.* Consider a typical four-pocket hydrostatic journal bearing with pressure-constant control system. Assume the diameter of bearing $D=30$ mm (1.18 in.) with the width $B=20$ mm (0.79 in.) and radial clearance $h_0=0.03$ mm (1.18 mil). The included angle of each pocket is $\beta=45°$ while its axial land width is $b=5$ mm (0.197 in.). The depth of pocket is $h_1=1$ mm (39.37 mil). The diameter of orifice is $d_0=0.6$ mm (23.6 mil). The supply pressure of lubricating oil is $p_s=5$ MPa (725 lbf/in.$^2$) at each orifice inlet and its dynamic viscosity is $\mu=9.93\times10^{-3}$ N s/m$^2$ ($1.47\times10^{-6}$ lbf s/in.$^2$). The eccentricity ratio of journal is $\epsilon=0.5$.

In this analysis, VT-EXPRESS is used as the comparison code. In addition to the difference of basic equations mentioned before, another difference between the two solutions is the process of pocket pressure distribution. In VT-EXPRESS, the pressure in the entire pocket area is assumed to be uniform, which is equal to the pocket inlet pressure (post-orifice). In the CFX-TASCflow simulation, the pocket area is solved at the same time as the other areas of the bearing.

The pressure distributions for both the hydrostatic-operating and hybrid-operating conditions are shown in Figs. 9 and 10, respectively. Figures 9(*a*) and 10(*a*) show the pressure changes pre- and post-orifices under two different operating conditions. From these two fringe plots, it can be seen clearly that the four pockets obtain a different pocket inlet pressure, due to the different clearance in each pocket region, while each pocket has the same supply pressure. Furthermore, due to the introduction of the hydrodynamic effect in the hybrid-operating bearing, the pocket inlet pressures for pockets 2 and 4 are different, as shown in Fig. 10.

Table 9 is the data results for two solution methods, CFX TASCflow and VT-EXPRESS. It can be seen that, essentially,

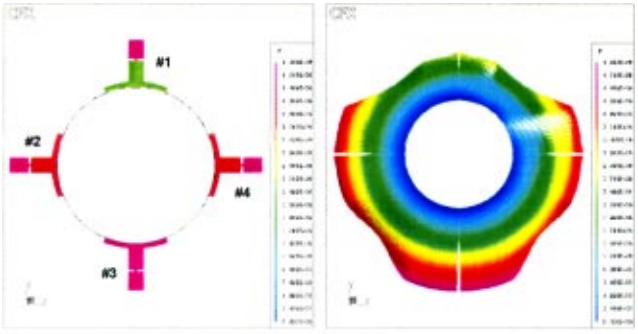


(*a*) (*b*)

**Fig. 9 Pressure distribution under hydrostatic-operating condition: (*a*) pre- and post-orifice, (*b*) bearing surface**

most of the results have a good agreement. The percent differences for all of pocket inlet pressures (the mean values at pocket inlets in CFD solutions) are less than 2%. But, it seems the load capacity is an exception. The load capacities by CFX-TASCflow under hydrostatic-operating and hybrid-operating conditions are higher by 13.2% and 8.3%, respectively, than that by VT-EXPRESS. Generally speaking, under the hydrostatic-operating condition, the load capacity of the bearing is proportional to the difference of pressures between the bottom and top pockets. By checking the pressure distribution in each pocket, it is found that in the top pocket area (pocket 1) there is an obvious decrease in the pressure field from the pocket inlet pressure (post-orifice pressure). Figure 11 shows this phenomenon in hydrostatic-operating condition. It can be seen that the pressure values on most areas in the top pocket are less than the pocket inlet pressure. This probably is because the clearance of the bearing in this area increases more than the other areas after applying the eccentricity. Although there is also a similar mechanism in the bottom pocket as well as the other two pockets, the simulation results show this influence is more evident right in the pocket opposite to the eccentricity direction. In the VT-EXPRESS solution, the pressure in each pocket was assumed to be the pocket inlet pressure. This phenomenon can also be found in the hybrid-operating conditions.

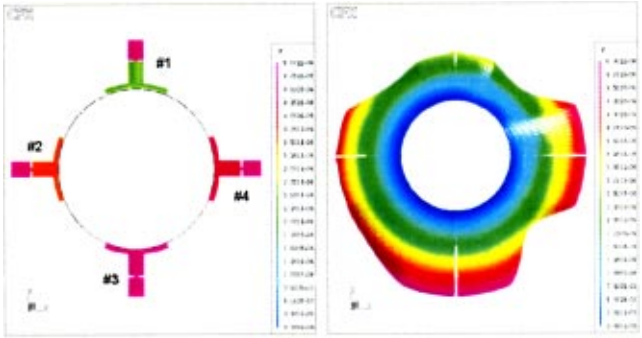


(*a*) (*b*)

**Fig. 10 Pressure distribution under hybrid-operating condition (9550 rpm of speed): (*a*) pre- and post-orifice, (*b*) bearing surface**

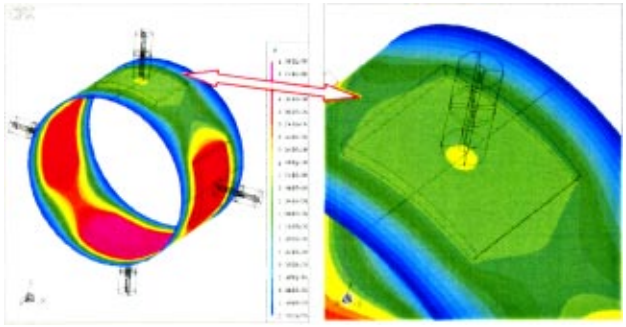

**Fig. 11 Pressure decrease within pocket area in hydrostatic-operating bearing**

## Squeeze Film Damper

A squeeze film damper (SFD) is a special kind of fluid-film bearing, which exclusively makes use of only the squeeze effect resulting from the whirl of the journal to influence the vibration of the supported rotor systems. Squeeze film dampers are utilized in

**Table 9 Comparison of results by two solutions**

| | Hydrostatic-operating | | | Hybrid-Operating | | |
|---|---|---|---|---|---|---|
| | CFX-TASCflow | VT-EXPRESS | % diff | CFX-TASCflow | VT-EXPRESS | % diff |
| #1 Pocket inlet pressure (MPa) | 2.657 | 2.650 | 0.3% | 2.671 | 2.724 | 1.9% |
| #2 Pocket inlet pressure (MPa) | 4.104 | 4.165 | 1.5% | 3.723 | 3.745 | 0.6% |
| #3 Pocket inlet pressure (MPa) | 4.959 | 4.975 | 0.3% | 4.980 | 4.987 | 0.1% |
| #4 Pocket inlet pressure (MPa) | 4.104 | 4.165 | 1.5% | 4.413 | 4.503 | 2.0% |
| Load capacity (N) | 722.7 | 638.1 | 13.2% | 727.0 | 670.9 | 8.3% |
| Attitude angle (deg) | 0 | 0 | 0% | 23.4 | 25.7 | 8.9% |
| Flow rate (kg/s) | 0.0324 | 0.0306 | 5.8% | 0.0318 | 0.0304 | 4.6% |

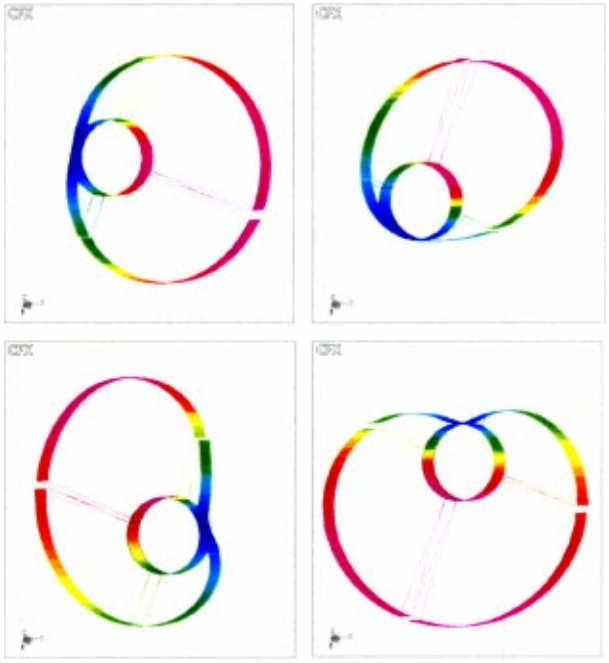

**Fig. 12 Whirling simulation of SFD**

jet aircraft engines to provide needed damping to control undesirable vibrations. They also are used in many land-based rotating machinery to enhance stability.

*Example 4*. Assume the diameter of a long damper $D=30$ mm (1.18 in.) with radial clearance $h_0=0.03$ mm (1.18 mil). The dynamic viscosity of lubricating oil is $\mu=9.93\times10^{-3}$ N s/m$^2$ ($1.47\times10^{-6}$ lbf s/in.$^2$). The radius of whirling orbit is $e=0.02$ mm (0.79 mil) and its circular frequency is $\omega=200$ rad/s ($\approx1910$ cpm).

By employing the ''Moving Grid'' capability and the user's FORTRAN code, the dynamic simulation of this SFD can be conducted. Some of the transient images of dynamic pressure at different instants are shown in Fig. 12.

## Conclusions

The application of the general CFD code, CFX-TASCflow, for analysis of hydrodynamic, hydrostatic, and hybrid bearings as well as a squeeze film damper, has been successfully conducted. The following conclusions can be stated:

1. The simulation results for static performances of hydrodynamic bearing have a good agreement with that of the standard lubrication solutions.
2. Considering the dynamic calculation of the hydrodynamic bearing, the stiffness coefficients by CFX-TASCflow are quite close to one of the standard codes. However, the damping coefficients by the CFD simulation are higher than that by the comparison codes, in general. One of the possible reasons is the inclusion, in the CFD simulation, of the influence of the fluid in the inlet pockets. The resolution of this discrepancy requires a new future investigation.
3. The CFD simulation of an externally pressurized bearing for both the hydrostatic and hybrid operating conditions shows that most of the static performance results have a reasonable agreement with that by a standard code. It also shows the load capacity in the hydrostatic-operating condition is higher than that by the standard code because of a further decrease of the pocket pressure values relative to its inlet pressure in the pocket opposite to the eccentricity direction. This may also affect the load capacity of the hybrid-operating bearing.
4. Certain capabilities in CFX-TASCflow can be used in the bearing and damper analysis. For example, ''Moving Grid'' is employed in the calculation of the bearing damping characteristics and the simulation of the squeeze film damper. The capability of ''Conjugate Heat Transfer'' makes the comprehensive simulation of both the fluid film and solid elements possible.
5. The simulation by CFX-TASCflow requires a great deal of CPU time if compared to the standard lubrication codes. However, it should be noted that the ultimate purpose of this research in applying this general CFD code for bearings and dampers is not to replace the current standard lubrication codes. CFD analysis will find its place in those areas where the complicated structure is used or when a more detailed system analysis is needed.

Although the current CFD results are encouraging, much work remains to be done in the future. Eventually CFD analysis will play an important role in the field of bearing and damper analysis.

## Acknowledgments

The authors express their gratitude to Virginia Tech Rotor Dynamics Lab Industry Affiliates Group and Toshiba Corporation for their support of this research work.

## References

[1] Pinkus, O., and Sternlicht, B., 1961, *Theory of Hydrodynamic Lubrication*, McGraw-Hill, New York.
[2] Lund, J. W., 1964, ''Spring and Damping Coefficients for the Tilting-Pad Journal Bearing,'' ASLE Trans., **7**(4), pp. 342–352.
[3] Nicholas, J. C., Gunter, E. J., and Allaire, P. E., 1979, ''Stiffness and Damping Coefficients for the Five Pad Tilting Pad Bearing,'' ASLE Trans., **22**(2), pp. 112–124.
[4] Nicholas, J. C., and Kirk, R. G., 1979, ''Selection and Design of Tilting Pad and Fixed Lobe Journal Bearings for Optimum Turbo-Rotor Dynamics,'' *Proceedings of the 8th Turbo-machinery Symposium*, Texas A&M University, College Station, Texas, pp. 43–58.
[5] Nicholas, J. C., and Kirk, R. G., 1981, ''Theory and Application of Multi-Pocket Bearings for Optimum Turbo Rotor Stability,'' ASLE Trans., **24**(2), pp. 269–275.
[6] San Andres, L., and Vance, J. M., 1986, ''Effects of Fluid Inertia and Turbulence on the Force Coefficients for Squeeze Film Dampers,'' ASME J. Eng. Gas Turbines Power, **108**(2), pp. 332–339.
[7] Kirk, R. G., Raju, K. V. S., and Ramesh, K., 1999, ''PC-Based Analysis of Turbomachinery Vibration,'' Shock Vib. Dig., **31**(6), pp. 449–454.
[8] Chen, W. J., ''DyRoBeS_BePerf Version 7.0,'' Eigen Technologies, © 1991–2002.
[9] Guo, Z., and Kirk, R. G., 2001, ''Analysis of Externally Pressurized Fluid-Film Bearings for High-Speed Rotating Machinery,'' *Proceedings ISCORMA'01*, South Lake Tahoe, California, August 20–24.
[10] AEA Technology, 2001, CFX-TASCflow 2.11.1 Documentation.